

nature

COMPACT SOURCE

Plasma-based acceleration
paves way to smaller
free-electron lasers



Firearm focus
Fresh funding
boosts US studies
on gun violence

Detecting emissions
How to verify
compliance with Paris
and Montreal treaties

Flow charts
How fluid dynamics
help a deep-sea sponge
feed and reproduce

Nature.2021.07.24

[Sat, 24 Jul 2021]

- [This Week](#)
- [News in Focus](#)
- [Opinion](#)
- [Work](#)
- [Research](#)
- [Amendments & Corrections](#)

| [Next section](#) | [Main menu](#) |

Donation

| [Next section](#) | [Main menu](#) |

This Week

- **[Responsible research assessment faces the acid test](#)** [21 July 2021]
Editorial • The University of Liverpool is planning to make lay-offs on the basis of controversial measures. How should the global movement for responsible research respond?
- **[Vulnerable nations lead by example on Sustainable Development Goals research](#)** [20 July 2021]
Editorial • A United Nations study of world science is a wake-up call that richer countries must also shift science towards the SDGs.
- **[While you sleep, a device harvests energy from your sweaty fingertips](#)** [15 July 2021]
Research Highlight • An energy collector in contact with the skin is efficient enough to power some electronic devices.
- **[Cruise ships could sail now-icy Arctic seas by century's end](#)** [09 July 2021]
Research Highlight • Without carbon cuts, many cargo ships could ply the Northwest Passage, between the Atlantic and Pacific oceans, in 2040.
- **[Tied in knots: Zika virus tangles are the most stable RNA known](#)** [16 July 2021]
Research Highlight • A dangerous virus uses a ring-shaped structure to make its RNA resistant to attack.
- **[Damage to a royal town on the Danube warns of seismic danger](#)** [14 July 2021]
Research Highlight • Documents and physical evidence hint that a major earthquake struck Visegrád in Hungary, once home to kings.
- **[Why a meat-free diet boosts health: protein levels might hit the spot](#)** [15 July 2021]
Research Highlight • An analysis shows that the amino-acid profiles of vegan, vegetarian and omnivorous diets are similar.
- **[Why breastfeeding is becoming less reliable for birth control](#)** [14 July 2021]

Research Highlight • As countries become more prosperous, people nursing their babies become fertile sooner after birth.

- **Destructive fires serve as pest control for lizards** [13 July 2021]

Research Highlight • Mediterranean lizards in burnt areas are less likely to be afflicted by mites than their neighbours in unburnt woodlands.

- EDITORIAL
- 21 July 2021

Responsible research assessment faces the acid test

The University of Liverpool is planning to make lay-offs on the basis of controversial measures. How should the global movement for responsible research respond?





•

[Download PDF](#)



The University of Liverpool is at odds with the responsible research movement. Credit: Education Images/Universal Images Group/Getty

A leading UK university has become mired in a public dispute over how it is assessing researchers' performance. The evolving situation at the University of Liverpool is being watched closely by concerned academics around the world — and is raising questions about whether more needs to be done to ensure that universities assess their researchers equitably. At the end of last month, the leaders of some of the world's foremost responsible-research initiatives — the Hong Kong Principles, the INORMS Research Evaluation Group, the Leiden Manifesto and the Metric Tide — wrote a strongly worded letter arguing that the University of Liverpool's proposals remain “squarely out of line with accepted practice”.

Liverpool wants to cut 32 posts from its Faculty of Health and Life Sciences. To keep their jobs, academics above the grade of lecturer need to demonstrate research income comparable with the average in their discipline for the 24-member Russell Group of research-intensive universities, to which Liverpool belongs. Candidates must also show a “substantial contribution” to two out of four additional categories — “world-leading”

publications, commercial or consulting income, teaching, and research impact.



[Row erupts over university's use of research metrics in job-cut decisions](#)

Many scientists are angry. Liverpool's criteria for assessing its academics do not represent the reality of how research is done. They do not include contributions to peer review, PhD supervision, mentoring or collaborations. Instead, the university is putting weight on criteria that mirror those used in rankings and measurements of research performance — notably the UK's Research Excellence Framework (REF).

When ranked according to the most recent REF results, from 2014, Liverpool's position in some categories — for example, the clinical sciences — is below that of a number of other research-intensive universities, including the 'Golden Triangle' universities in Cambridge, Oxford and London.

If Liverpool chooses to replace what it sees as underperforming academics with those who have more substantial research profiles, it is likely to attain a higher REF score. That would come with more government research funding — but it would also come at a cost to careers. Moreover, there are aspects of the process that are clearly unfair. The university has said that deans, heads of departments and researchers who sit on external committees — for

example, REF peer-review panels — will not be assessed for possible redundancy. In response to the threat of redundancies, researchers took industrial action during May, June and July.

One influential initiative is choosing to negotiate privately with the university. This is the organization behind the San Francisco Declaration on Research Assessment (DORA), an international voluntary agreement through which research organizations vow to conduct research assessment responsibly.



[Let's move beyond the rhetoric: it's time to change how we judge research](#)

DORA's signatories pledge not to use metrics such as the Journal Impact Factor to evaluate researchers, and to be transparent in the criteria used to make decisions on matters such as hiring and promotion. Liverpool is one of some 2,200 organizations that have signed the declaration. DORA is in talks with the university, but choosing not to reveal further details. A statement on DORA's website says that it expects signatories to abide by their pledges, while also reiterating that it is not a regulatory body.

DORA's approach — to resolve disputes constructively but without publicity — has had some effect. Liverpool initially included the field-weighted citation metric on its criteria for redundancies, but dropped that after consultation with DORA. However, there are conflicting views of whether

this puts Liverpool in the clear. The university told *Nature* its amended criteria are “in keeping with the principles of DORA”. In response, a DORA spokesperson said there are “ongoing concerns”. Such mixed messages show the limitations of quiet diplomacy. DORA and the university should at least agree on their public communications.

Evolving DORA

If a university insists on a system of assessing its academics that seems both unfair and unrepresentative of how research is done, it begs the question: does the research community need a body, or a mechanism, with the remit and resources to monitor the declaration and act more like a watchdog? Has the Liverpool episode tested the limits of the ‘critical friendship’ approach?

These are important questions because, if Liverpool does not further change its position as a result of the dialogue with DORA, others who have signed DORA might think that they can take similar action. DORA might be able to take the edge off unfair practices, but its leadership and management comprise a small team — just 1.2 full-time-equivalent staff and 29 volunteers. In its current form, it is no match for the resources that universities bring when challenged.



[University rankings need a rethink](#)

To monitor the more than 2,000 organizations signed up to DORA would require a very different institution, and that, in turn, would pose new challenges. The costs and logistics of setting up such a body could run into seven-figure sums. Such funds would require the involvement of governments or philanthropists, and would pose other risks — for example, to academic freedom.

A compliance-style organization isn't the only potential model, however. Another option is an approach that is used to recognize gender equality in universities. The Athena SWAN charter started in the United Kingdom and has since been adopted in several countries. Universities submit a self-assessment on their policies on inclusion and equality in hiring, promoting and retaining female staff. The assessments are judged independently, and institutions are awarded one of three grades: bronze, silver or (very rarely) gold. The initiative is funded by the institutions themselves, which pay into a common pool — as they would a membership fee. Each award lasts for a limited time, recently increased from four years to five, which ensures that institutions cannot rest on their laurels if they have achieved recognition once. Athena SWAN is not without its problems, but its underpinning principles could help universities to practise responsible research assessment.

DORA's team is working tirelessly to persuade more institutions to sign the declaration, as well as trying to resolve the University of Liverpool situation. But in the wake of this episode, a rethink might be needed. And it must not be for a small team to do alone. Everyone who values responsible research — including *Nature*'s publisher, Springer Nature, a signatory to DORA — has a stake in ensuring that its principles are implemented.

Nature **595**, 471-472 (2021)

doi: <https://doi.org/10.1038/d41586-021-01991-z>

Related Articles



- Row erupts over university's use of research metrics in job-cut decisions



- Let's move beyond the rhetoric: it's time to change how we judge research



- UK gender-equality scheme spreads across the world



- University rankings need a rethink



- Equality and diversity efforts do not 'burden' research



- Craft metrics to value co-production

Subjects

- Careers
- Research management
- Ethics

- [Institutions](#)

nature careers

[Jobs](#) >

- [Instrument scientist at the permanent end station REMI@FLASH](#)

German Electron Synchrotron (DESY)

Hamburg, Germany

- [AUSBILDUNG: 3 Auszubildende \(d/m/w\) zum/zur Elektroniker*in für Geräte und Systeme](#)

Helmholtz Centre for Heavy Ion Research GmbH (GSI)

Darmstadt, Germany

- [AUSBILDUNG: 3 Auszubildende \(d/m/w\) zum/zur Anlagenmechaniker*in \(d/m/w\) für Sanitär-, Heizungs- und Klimatechnik](#)

Helmholtz Centre for Heavy Ion Research GmbH (GSI)

Darmstadt, Germany

- [AUSBILDUNG: 3 Auszubildende \(d/m/w\) zum/zur Elektroniker*in \(d/m/w\) für Betriebstechnik](#)

Helmholtz Centre for Heavy Ion Research GmbH (GSI)

Darmstadt, Germany

[Download PDF](#)

Related Articles

-  [Row erupts over university's use of research metrics in job-cut decisions](#)
-  [Let's move beyond the rhetoric: it's time to change how we judge research](#)
-  [UK gender-equality scheme spreads across the world](#)
-  [University rankings need a rethink](#)
-  [Equality and diversity efforts do not 'burden' research](#)
-  [Craft metrics to value co-production](#)

Subjects

- [Careers](#)

- [Research management](#)
 - [Ethics](#)
 - [Institutions](#)
-

This article was downloaded by **calibre** from <https://www.nature.com/articles/d41586-021-01991-z>

| [Section menu](#) | [Main menu](#) |

- EDITORIAL
- 20 July 2021

Vulnerable nations lead by example on Sustainable Development Goals research

A United Nations study of world science is a wake-up call that richer countries must also shift science towards the SDGs.





•

[Download PDF](#)



Iraq's wetlands are threatened by climate change; the country is pivoting its research towards the SDGs. Credit: Murtadha Al-Sudani/Anadolu Agency/Getty

With the United Nations Sustainable Development Goals, world leaders pledged to end poverty and hunger, protect biodiversity and the climate, and get all children into schools by 2030. How have researchers and funders responded? Has there been a shift in research priorities?

The UN's Paris-based science and education agency has answers to these and other questions in the latest *UNESCO Science Report*, published last month (see go.nature.com/3zlojva). UNESCO says the 700-page report is a first attempt at understanding the impact of the Sustainable Development Goals (SDGs) on research priorities. The findings are a mixed picture.

Using the Scopus database, UNESCO mapped publications from almost 200 countries between 2011 and 2019 on 56 research topics relevant to the SDGs. For the most part, the high-income countries that account for 64% of the world's research spending — including Japan, South Korea, the United States and many European countries — showed relatively little change in the

number of publications produced concerning the SDGs, and a declining share of global research.



How science can put the Sustainable Development Goals back on track

But it's a different story for low- and middle-income countries, which have begun to shift their research priorities towards the goals.

For example, the share of publications on photovoltaics — which could address the SDG on boosting renewable energy — from low-income and lower-middle-income countries more than trebled, going from 6.2% to 22% of the world total in the study period. The share of papers on biofuels and biomass nearly trebled, from 8.5% to 23%.

Low-income countries more than doubled their share of research publications on crops that are more resilient to climate change, from 5% of the total to 11%. And researchers from sub-Saharan Africa contributed 361 out of 885 publications on smallholder farming in 2019 — more than the European Union's 294. Ecuador, Ethiopia, Indonesia, Iraq, Russia and Vietnam all increased their output on most topics, albeit from low starting points in some cases.

Much of the growth is powered by China. According to UNESCO, China's researchers now publish around half of the world's output on battery

efficiency, 43% on hydrogen energy and 41% on carbon pricing. Their research on carbon capture and storage increased from 1,300 publications between 2012 and 2015 to 2,049 in 2016–19. By contrast, high-income nations — including France, Germany and the United States — showed declining shares during the same period, and some showed declining numbers. One exception is research into floating marine plastics. The field, which barely existed a decade ago, recorded 853 publications in 2019, mostly from high-income nations. But, overall, wealthier nations reported falls in their share of publishing across 54 out of the 56 fields assessed.



Does the fight against hunger need its own IPCC?

It's disappointing to see so little progress from the richer countries. But it is something of a pattern. UNESCO's researchers calculated that, between 2000 and 2013, wealthy nations spent less than US\$25 billion on international development assistance in environmental areas such as climate change and biodiversity — about one-fifth of the \$130 billion given for assistance in industry and innovation.

At the same time, it's heartening to see scientific output being slowly revived in many low-income countries — some of which were engines of scholarship in times past. But UNESCO also finds that funding trends in these countries have become harder to track. Some 98 countries reported funding data in 2015, but this fell to 68 in 2018. Some 28% of high-income

and 78% of low- and middle-income countries are not reporting their science-funding data — and that is both problematic and troubling. The ability to correlate funding data with publishing information would provide a richer picture of the gains, and identify areas that would benefit from more resources. Countries need to comply with UNESCO's requests for information, partly because they are obliged to track these data for the SDGs.

Even before the pandemic, the [world was not on track to reach most of the Sustainable Development Goals](#). With less than a decade to go before the 2030 deadline to end poverty and protect the environment, the UNESCO report aptly says that the world is “running out of time”. The report needs to be read closely in every world capital. It’s still not too late for everyone to pivot science to sustainability.

Nature **595**, 472 (2021)

doi: <https://doi.org/10.1038/d41586-021-01992-y>

Related Articles

-  [Does the fight against hunger need its own IPCC?](#)
-  [How science can put the Sustainable Development Goals back on track](#)
-  [The UN Environment Programme needs new powers](#)



- [Reset Sustainable Development Goals for a pandemic world](#)

Subjects

- [Developing world](#)
- [Sustainability](#)
- [Biodiversity](#)
- [Government](#)
- [Climate change](#)

nature careers

[Jobs](#) >

- [Instrument scientist at the permanent end station REMI@FLASH](#)

German Electron Synchrotron (DESY)

Hamburg, Germany

- [AUSBILDUNG: 3 Auszubildende \(d/m/w\) zum/zur Elektroniker*in für Geräte und Systeme](#)

Helmholtz Centre for Heavy Ion Research GmbH (GSI)

Darmstadt, Germany

- [AUSBILDUNG: 3 Auszubildende \(d/m/w\) zum/zur Anlagenmechaniker*in \(d/m/w\) für Sanitär-, Heizungs- und Klimatechnik](#)

Helmholtz Centre for Heavy Ion Research GmbH (GSI)

Darmstadt, Germany

- [**AUSBILDUNG: 3 Auszubildende \(d/m/w\) zum/zur Elektroniker*in \(d/m/w\) für Betriebstechnik**](#)

Helmholtz Centre for Heavy Ion Research GmbH (GSI)

Darmstadt, Germany

[Download PDF](#)

Related Articles



- [**Does the fight against hunger need its own IPCC?**](#)



- [**How science can put the Sustainable Development Goals back on track**](#)



- [**The UN Environment Programme needs new powers**](#)



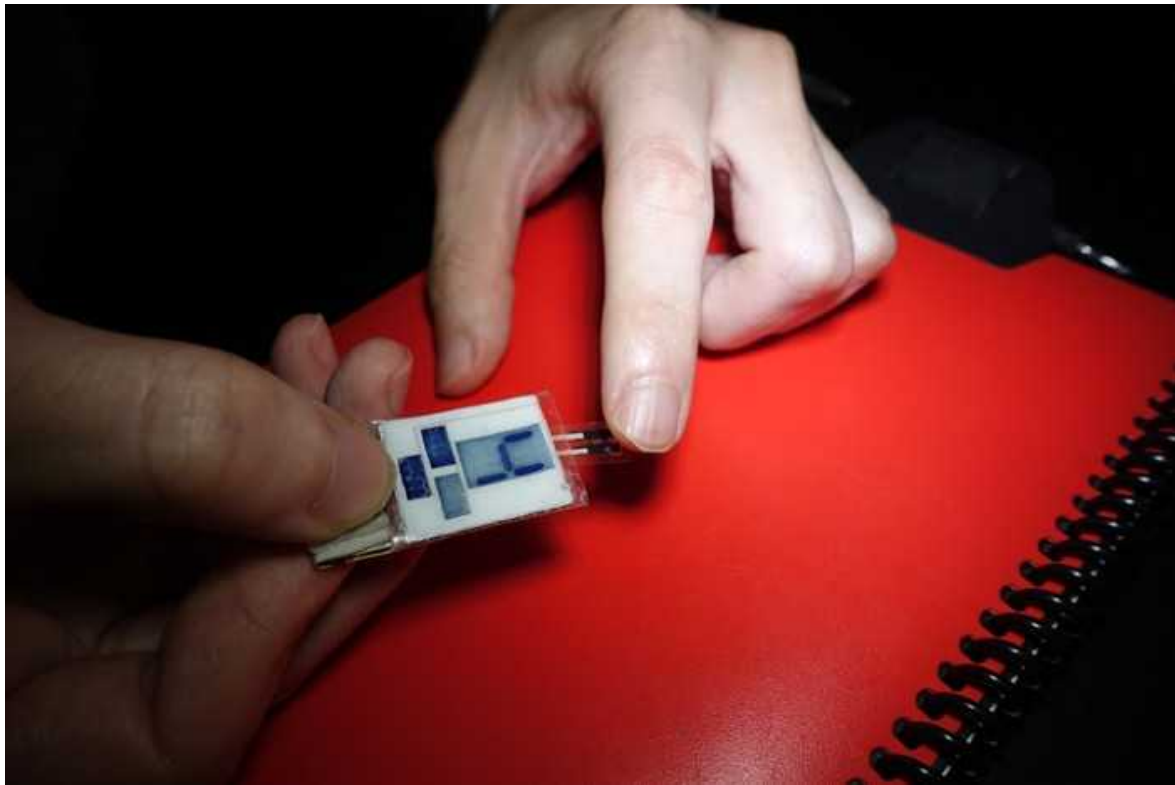
- [**Reset Sustainable Development Goals for a pandemic world**](#)

Subjects

- [Developing world](#)
 - [Sustainability](#)
 - [Biodiversity](#)
 - [Government](#)
 - [Climate change](#)
-

This article was downloaded by **calibre** from <https://www.nature.com/articles/d41586-021-01992-y>.

| [Section menu](#) | [Main menu](#) |



A flexible miniature fuel cell uses the sweat on a fingertip to make electricity, which powers a sensor (pictured) that measures vitamin C levels.
Credit: Lu Yin

Energy

15 July 2021

While you sleep, a device harvests energy from your sweaty fingertips

An energy collector in contact with the skin is efficient enough to power some electronic devices.





•

A thin, flexible device worn on a fingertip can harvest energy from a sleeping person's sweat to power small, wearable electronics.

From smart watches to health monitors, wearable technology is becoming an integral part of everyday life. But finding convenient power sources has been difficult.

To solve this problem, Joseph Wang and his colleagues at the University of California, San Diego, made a device that scavenges energy from chemicals in the perspiration on a fingertip. Unlike previous sweat-fuelled power sources, it does not require body movement. It is also the most efficient

device yet to collect energy from the body, harvesting hundreds of millijoules per square centimetre during a 10-hour sleep period.

The device collects enough energy while a person is sleeping to operate a sensor and display panel for environmental or health monitoring. It can also extract energy from light finger presses made, for example, when typing or texting.

The authors hope to improve the device's efficiency and durability and integrate it with other types of energy harvester.

Joule (2021)

- Energy

This article was downloaded by **calibre** from <https://www.nature.com/articles/d41586-021-01916-w>

| [Section menu](#) | [Main menu](#) |



An ice-breaker navigates Canada's Arctic waters, which could soon become accessible to ordinary vessels if global temperatures continue to climb.

Credit: Canadian Press/Shutterstock

Ocean sciences

09 July 2021

Cruise ships could sail now-icy Arctic seas by century's end

Without carbon cuts, many cargo ships could ply the Northwest Passage, between the Atlantic and Pacific oceans, in 2040.





•

The retreat and thinning of Arctic sea-ice projected by the end of the twenty-first century could allow ships of all kinds to safely sail Canada's northern seas and passages during much of the year.

Lawrence Mudryk at Environment and Climate Change Canada in Toronto and his colleagues used climate simulations to investigate how various levels of global warming expected by 2100 might affect the navigability of shipping routes along Canada's northern coast. This region has been unnavigable during cold months for all vessels but the strongest ice-breakers.

The models suggest that if global warming is above 2 °C, expected by around 2040 if carbon emissions remain high, the Beaufort Sea and parts of the Northwest Passage will become accessible for more than half the year to cargo and supply ships that can operate amid moderate amounts of thin sea-ice.

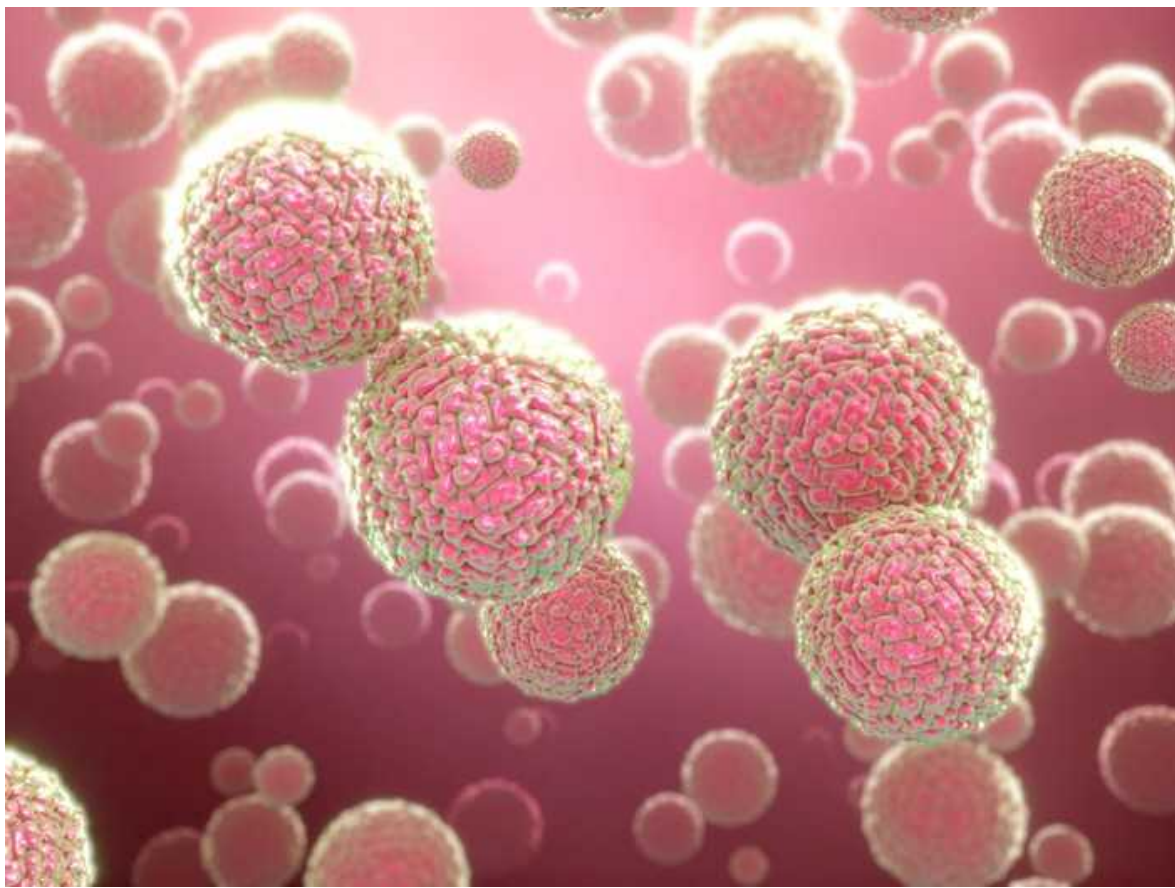
At 4 °C of warming, expected towards the end of the century, even light pleasure craft and cruise ships unequipped for sea-ice conditions should be able to safely navigate most of Canada's Arctic waters for as many as 200 days per year, the researchers say.

Nature Clim. Chan. (2021)

- [Ocean sciences](#)

This article was downloaded by **calibre** from <https://www.nature.com/articles/d41586-021-01889-w>

| [Section menu](#) | [Main menu](#) |



Zika virus (artist's impression), which can cause birth defects in the babies of women infected during pregnancy, ties its RNA in protective knots.
Credit: Maurizio De Angelis/Science Photo Library

Molecular biology

16 July 2021

Tied in knots: Zika virus tangles are the most stable RNA known

A dangerous virus uses a ring-shaped structure to make its RNA resistant to attack.





•

Some viruses tie their RNA into intricate knots to prevent hostile cells from digesting it. Experiments now show that the Zika virus's knotted RNA is the most stable RNA ever observed, paving the way to understanding how the virus eludes cellular defences.

To study the knot's mechanics, Meng Zhao and Michael Woodside at the University of Alberta in Canada used optical tweezers, which rely on a laser beam to hold and move microscopic objects. The authors applied force to both of the RNA strand's free ends, allowing them to repeatedly unfold and refold the knot and observe the steps involved in its formation. This revealed

that a ring-shaped structure blocks the cell's enzymes from digesting the RNA and generates the knot's unusual mechanical stability.

By working out the steps required to form the ring, the researchers offer potential targets for future therapeutics to prevent the RNA from knotting. Many members of the flavivirus family — which includes the Zika, West Nile, dengue and yellow fever viruses — contain RNA with knots, and the authors hope their findings will contribute to disarming these viruses.

Nature Chem. Biol. (2021)

- [Molecular biology](#)

This article was downloaded by **calibre** from <https://www.nature.com/articles/d41586-021-01911-1>

| [Section menu](#) | [Main menu](#) |



Now restored, Hungary's Salamon Tower was badly damaged by an earthquake in the sixteenth century, according to analysis of historical images. Credit: Shutterstock

Solid Earth sciences

14 July 2021

Damage to a royal town on the Danube warns of seismic danger

Documents and physical evidence hint that a major earthquake struck Visegrád in Hungary, once home to kings.





•

Scientific sleuthing has found evidence that a large earthquake in the sixteenth century severely damaged an ancient Hungarian town — one that is close to the site of a proposed modern dam.

In 1977, Czechoslovakia and Hungary agreed to build two large dams on the Danube River, one on each side of the international border. The project became mired in political and environmental disputes and was never completed.

Miklós Kázmer at Eötvös University in Budapest and his colleagues surveyed the medieval town of Visegrád, close to the proposed Hungarian dam site. Visegrád's Salomon Tower has been extensively reconstructed, but

the researchers found drawings and photographs from the nineteenth century that show a large vertical crack running through all six of the tower's floors. The crack resembles those produced by strong shaking of the ground during an earthquake.

Nearby, the authors mapped a giant depression in the floor of a fifteenth-century friary — evidence that the soil moved like liquid during an earthquake. A historical account suggests that there was a major earthquake in the region in August 1541.

Seismic risk near the proposed dam site is higher than previously suspected and higher than was accounted for in the dam's planning, the team concludes.

Seismol. Res. Lett. (2021)

- Solid Earth sciences

This article was downloaded by **calibre** from <https://www.nature.com/articles/d41586-021-01914-y>.

| [Section menu](#) | [Main menu](#) |



A vegan diet has an amino-acid composition similar to that of a diet that includes both plant and animal foods. Credit: Alexander Spatari/Getty

Metabolism

15 July 2021

Why a meat-free diet boosts health: protein levels might hit the spot

An analysis shows that the amino-acid profiles of vegan, vegetarian and omnivorous diets are similar.





•

Vegetarians, vegans and omnivores end up consuming similar ratios of amino acids, regardless of whether their menus lean more heavily on beef, beans or Greek yogurt — implying that protein type is not responsible for the health benefits of plant-based diets.

Plant-based diets have been linked to a reduced risk of cardiovascular disease and type 2 diabetes. Vegans and vegetarians tend to eat less protein than meat-eaters, but it's not clear which aspect of a meat-free diet confers benefits.

Michael MacArthur at the Swiss Federal Institute of Technology in Zurich and his colleagues found that the diets of people who are vegan, vegetarian

and omnivorous have similar amino-acid profiles — despite differences in the amino-acid composition of their food. This suggests that health might be influenced more by the total amount of protein a person consumes than the type.

The team fed mice diets that varied in amino-acid composition and quantity. Mice given the most protein had higher blood levels of sugar and fat than mice that consumed less protein, regardless of the protein source.

[Cell Metab. \(2021\)](#)

- [Metabolism](#)

This article was downloaded by **calibre** from <https://www.nature.com/articles/d41586-021-01934-8>

| [Section menu](#) | [Main menu](#) |



A woman in Taruma, Brazil, breastfeeds her son, a practice that in some countries is losing its effectiveness as a safeguard against pregnancy. Credit: Ricardo Oliveira/AFP/Getty

Public health

14 July 2021

Why breastfeeding is becoming less reliable for birth control

As countries become more prosperous, people nursing their babies become fertile sooner after birth.





•

Frequent and prolonged breastfeeding has been an excellent form of birth control that has helped to control population growth in many developing countries. But an analysis of data from more than 80 nations shows that breastfeeding's contraceptive effects have weakened, perhaps as a result of a rise in living standards.

After a person gives birth, hormonal changes that trigger production of breast milk also prevent the ovaries from releasing an egg. Without that step, pregnancy is impossible.

Nicolas Todd and Mathias Lerch at the Max Planck Institute for Demographic Research in Rostock, Germany, analysed 2.7 million births

between 1975 and 2019 in 84 low- and middle-income countries. They found that increases in a country's wealth, access to electricity and water and a mother's education level were associated with a reduced period of time without menstruation while breastfeeding.

In Asian countries, women that exclusively breastfed their children the first 6 months after birth spent on average 157 days without menstruation in the early 1990s, but only 129 days in the mid-2010s.

The authors call for more widespread contraception use as low- and middle-income economies grow.

[Proc. Natl Acad. Sci. USA \(2021\)](#)

- [Public health](#)

This article was downloaded by **calibre** from <https://www.nature.com/articles/d41586-021-01912-0>

| [Section menu](#) | [Main menu](#) |



A *Psammodromus algirus* lizard in Spain, where wildfires can confer long-lasting relief from parasites. Credit: Philippe Clement/Nature Picture Library

Ecology

13 July 2021

Destructive fires serve as pest control for lizards

Mediterranean lizards in burnt areas are less likely to be afflicted by mites than their neighbours in unburnt woodlands.





•

Occasional wildfires can help lizards to keep a clean house: the blazes cleanse natural areas of mites that can infest the reptiles' skin.

High-intensity fires in Mediterranean shrublands and woodlands renew vegetation, shoo away seed eaters and keep tree diseases in check. Lola Álvarez-Ruiz at the Desertification Research Centre in Valencia, Spain, and her colleagues were curious to know whether the flames could also be beneficial to animals.

Between 2016 and 2018, the researchers sampled *Psammodromus algirus*, a species of ground-dwelling lizard, in eight burnt and adjacent unburnt areas in Spain. They then counted either how many mites were attached to the

creatures' skin or how many raised scales the lizards had — an indication of previous infection with the parasite.

Lizards that lived in unburnt areas were four times more likely to carry mites than were those in recently scorched environments, and were also more likely to have raised scales. The results suggest that there was a lower incidence of parasitism even several years after a fire had occurred.

[Proc. R. Soc. B \(2021\)](#)

- [Ecology](#)

This article was downloaded by **calibre** from <https://www.nature.com/articles/d41586-021-01913-z>

| [Section menu](#) | [Main menu](#) |

News in Focus

- **[Inflammation clock, mini vaccine dose and genome editing](#)** [21 July 2021]
News Round-Up • The latest science news, in brief.
- **[Why England's COVID 'freedom day' alarms researchers](#)** [14 July 2021]
News • Easing restrictions amid rising infections raises the risk of new variants emerging and risks the health of those who are not vaccinated, say researchers around the world.
- **['Pregnant' male rat study kindles bioethical debate in China](#)** [09 July 2021]
News • Researchers question the value of the experiment — which involved sewing together male and female rats and led to the birth of live young.
- **[Long COVID and kids: scientists race to find answers](#)** [14 July 2021]
News • Children get long COVID too, but researchers are still working to determine how frequently and how severely.
- **[The rise of 'ARPA-everything' and what it means for science](#)** [08 July 2021]
News • Science agencies such as ARPA-Health hope to replicate the success of the US Defense Advanced Research Projects Agency, but researchers question whether they will thrive.
- **[COVID and the brain: researchers zero in on how damage occurs](#)** [07 July 2021]
News • Growing evidence suggests that the coronavirus causes 'brain fog' and other neurological symptoms through multiple mechanisms.
- **[Gun violence is surging — researchers finally have the money to ask why](#)** [21 July 2021]
News Feature • With historically high levels of new funding, US gun-violence research is starting to find its footing.

- NEWS ROUND-UP
- 21 July 2021

Inflammation clock, mini vaccine dose and genome editing

The latest science news, in brief.





•

[Download PDF](#)



Healthy people can have a biological age lower than their chronological one. Credit: Al Bello/Getty

‘Inflammation clock’ can reveal biological age

A new type of age ‘clock’ can assess chronic inflammation to predict whether someone is at risk of developing age-related disorders such as cardiovascular and neurodegenerative disease. The clock measures ‘biological age’, which takes health into consideration and can be higher or lower than a person’s chronological age.

The inflammatory ageing clock (iAge), reported on 12 July in *Nature Aging*, is one of the first tools of its kind to use inflammation to assess health ([N. Sayed et al. *Nature Aging* <https://doi.org/gnzm>; 2021](#)). It is based on the idea that as a person ages, their body experiences chronic, systemic inflammation because their cells become damaged and emit inflammation-causing

molecules. People who have a healthy immune system will be able to neutralize this inflammation to some extent, whereas others will age faster.

To develop iAge, a team including systems biologist David Furman and vascular specialist Nazish Sayed at Stanford University in California analysed blood samples from 1,001 people aged 8–96 who are part of the 1000 Immunomes Project, which aims to investigate how signatures of inflammation change as people age. The researchers used the participants' chronological ages and health information, combined with a machine-learning algorithm, to identify the protein markers in blood that most clearly signal systemic inflammation.

People aged 99 years and older who were tested with the tool had an iAge 40 years lower, on average, than their actual age.

The study “is a further reinforcement of the fact that the immune system is critical, not only for predicting unhealthy ageing, but also as a mechanism driving it”, says Vishwa Deep Dixit, an immunobiologist at Yale School of Medicine in New Haven, Connecticut.



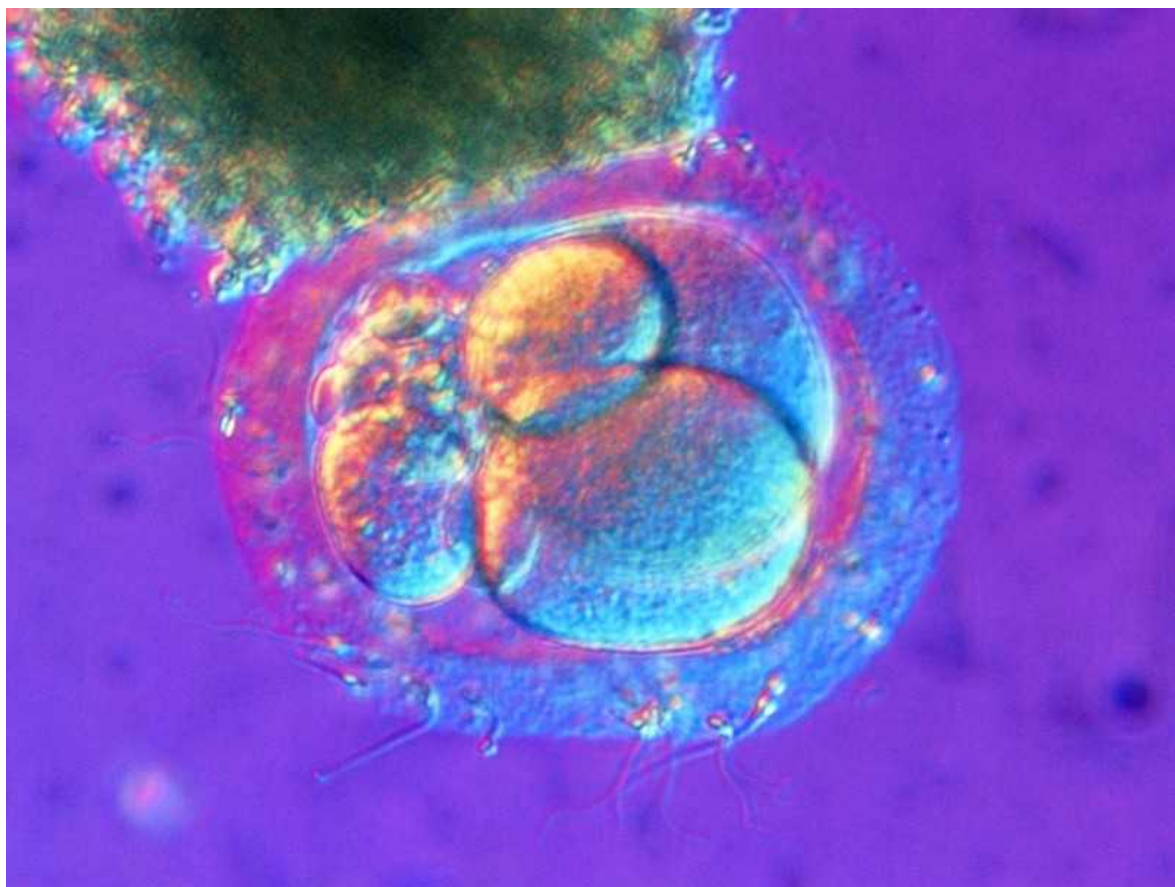
Workers prepare doses of Moderna's COVID-19 vaccine. Credit: Eugene Hoshiko/AP/Shutterstock

Quarter-dose of COVID vaccine rouses response

A preliminary study has hinted at the possibility of administering fractional doses of vaccines to stretch limited supplies and accelerate the global immunization effort. Tests found that two jabs that each contained only one-quarter of the standard dose of the Moderna COVID-19 vaccine gave rise to long-lasting antibodies.

In an early trial of the mRNA-based vaccine, study participants received one of three dose levels: 25, 100 or 250 micrograms. Initially, the 35 participants who had received the lowest dose seemed to have an insufficient immune response. But blood analyses 6 months after the second shot found that nearly all of the 35 participants had 'neutralizing' antibodies, which block the virus from infecting cells, the researchers reported in a preprint published on 5 July ([J. Mateus et al. Preprint at medRxiv](#) <https://doi.org/gn3t>; 2021). Levels of antibodies and T cells were comparable to those found in people who have recovered from COVID-19.

A half-dose now is more useful to an unvaccinated person than a full dose a year from now, says Alex Tabarrok, an economist at George Mason University in Fairfax, Virginia, which means that dose-stretching "is a way of promoting vaccine equity".



A human embryo shortly after fertilization, seen in a light micrograph. Credit: K. H. Kjeldsen/SPL

WHO advised to lead on genome-editing policies

A committee has advised the World Health Organization (WHO) to assume a leading, global role in efforts to regulate genome editing. The WHO should help national governments to coordinate their regulations, the advisers say, and genome editing should not yet be used to make modifications that can be passed on to later generations. The team also urged international collaboration in the governance of non-heritable gene editing, which has shown promise in treating disorders such as sickle-cell anaemia and transthyretin amyloidosis.

The group, which released its recommendations in two reports on 12 July, was formed after biophysicist He Jiankui, formerly at the Southern University of Science and Technology in Shenzhen, China, shocked the

world in 2018 by announcing that he had used the CRISPR genome-editing technique to alter embryos that led to the birth of two girls.

Another committee — convened by the US National Academy of Medicine, the US National Academy of Sciences and the UK Royal Society — concluded last September that the technology is not yet ready for use in human embryos (pictured) destined for implantation.

Nature **595**, 477 (2021)

doi: <https://doi.org/10.1038/d41586-021-01965-1>

Subjects

- [SARS-CoV-2](#)
- [Vaccines](#)
- [Genetics](#)

nature careers

[Jobs](#) >

- [**Instrument scientist at the permanent end station REMI@FLASH**](#)

German Electron Synchrotron (DESY)

Hamburg, Germany

- [**AUSBILDUNG: 3 Auszubildende \(d/m/w\) zum/zur Elektroniker*in für Geräte und Systeme**](#)

Helmholtz Centre for Heavy Ion Research GmbH (GSI)

Darmstadt, Germany

- [**AUSBILDUNG: 3 Auszubildende \(d/m/w\) zum/zur Anlagenmechaniker*in \(d/m/w\) für Sanitär-, Heizungs- und**](#)

Klimatechnik

Helmholtz Centre for Heavy Ion Research GmbH (GSI)
Darmstadt, Germany

- **AUSBILDUNG: 3 Auszubildende (d/m/w) zum/zur Elektroniker*in (d/m/w) für Betriebstechnik**

Helmholtz Centre for Heavy Ion Research GmbH (GSI)
Darmstadt, Germany

[Download PDF](#)

Subjects

- [SARS-CoV-2](#)
- [Vaccines](#)
- [Genetics](#)

This article was downloaded by **calibre** from <https://www.nature.com/articles/d41586-021-01965-1>

| [Section menu](#) | [Main menu](#) |

- NEWS
- 14 July 2021

Why England's COVID 'freedom day' alarms researchers

Easing restrictions amid rising infections raises the risk of new variants emerging and risks the health of those who are not vaccinated, say researchers around the world.

- [Philip Ball](#)

1. Philip Ball
[View author publications](#)

You can also search for this author in [PubMed](#) [Google Scholar](#)





•

[Download PDF](#)



A crowded train on the London Underground in June.Credit: Tolga Akmen/AFP/Getty

In less than a week, the UK government plans to drop nearly all measures for mitigating the spread of COVID-19 across England — despite steeply rising infections in the partially vaccinated population. The decision, widely hailed by its advocates as heralding a ‘freedom day’, has been sharply criticized by many scientific and public-health experts in the United Kingdom and beyond.

Some scientists call the relaxation an unprecedented public-health experiment that could result in large numbers of hospitalizations and deaths, and increase the chances of vaccine-resistant variants of SARS-CoV-2 emerging.

“There is absolutely no justification for relaxing restrictions now,” says Peter English, former chair of the British Medical Association’s Public

Health Medicine Committee. “If anything, they should be tightened, at least until the increase in case rates has reversed.”

Researchers worldwide are concerned in particular because of the potential for high infection rates in a partially vaccinated population to breed further concerning variants that could then be exported around the world. “The world has its eyes on the UK,” says Lauren Ancel Meyers, director of the University of Texas at Austin’s COVID-19 Modeling Consortium.

“The decision, and the way it has been presented, repeats a pattern of foolishly promising an outcome when dealing with a highly infectious agent,” says epidemiologist William Hanage, at the Harvard T. H. Chan School of Public Health in Boston, Massachusetts, alluding to the government’s earlier, premature assurances that the pandemic would soon be over.

From 19 July, all businesses in England will be allowed to open as normal, there will be no social-distancing requirements, and mask-wearing will no longer be legally mandated in public spaces. Yet infections in the United Kingdom are already at levels comparable to those in last winter’s devastating second wave of the pandemic and are still rising. The local governments of Scotland, Northern Ireland and Wales, which set public-health policy independently, do not plan to lift all restrictions yet.

A dangerous experiment

In late February, UK Prime Minister Boris Johnson announced a four-step road map that would take England from full lockdown to an ending of all restrictions on 21 June. That schedule was delayed for a month because of the spread of the more-infectious Delta variant of the virus.



Chris Whitty, chief medical adviser to the UK government, in a 12 July press conference with Prime Minister Boris Johnson (centre) and chief scientific adviser Patrick Vallance (right). Credit: Daniel Leal-Olivas/AFP/Getty

The government said that relaxation of restrictions would be guided by “data, not dates”, and that each stage of the opening up would happen only if certain criteria were satisfied. In particular, reopening would be postponed or reviewed if a rise in infection rates risked causing a surge in hospital admissions, or if new variants of the virus altered the picture. It is unclear whether those measures have been met for the reopening in July, say researchers. On 11 July, there were 31,000 recorded new cases of COVID-19 — total infections are now around 300 per 100,000 people. And [a new modelling study](#) shows an impending surge of hospitalizations, although the exact numbers are highly uncertain.

The government argues that, nonetheless, relaxation is justified — given the damage to the economy, livelihoods, education and mental health caused by

restrictions — because the country's good progress on vaccinations has weakened the link between infections and hospitalizations or deaths. As of early July, around 68% of the population had received at least one shot of a vaccine, and 52% had received two doses. Although current infections are comparable to the situation in February, hospitalizations and deaths are more than ten times lower.

The government has decided that this is an acceptable compromise, but many scientists and health professionals have grave doubts. "Even with lower hospitalization and fatality rates, current trends in the UK are likely to strain healthcare systems and lead to substantial public health consequences," says Meyers. On 7 July, *The Lancet* published a letter¹ with around 100 signatories from the United Kingdom and beyond, accusing the UK government of "embarking on a dangerous and unethical experiment".

Some are concerned that the government is willing to accept widespread infections among young people and children, who are not vaccinated and currently make up most of the known cases. Although this group is at far lower risk of serious illness and death than are older people, public-health specialists say that a policy that encourages the spread of infectious disease is unprecedented. Some think that the government is aiming to achieve 'herd immunity' in the population through a mix of natural infection and vaccination.

But Hanage sees no grounds for thinking that natural infection would be better than vaccination for generating population-level protection — not least because the vaccines are known to be safe, whereas COVID-19 is not.

Mike Ryan, executive director of the World Health Organization's Health Emergencies Program in Geneva, Switzerland, has said that a rush to re-open economies that accepted infections as inevitable and encouraged them to occur "sooner rather than later" amounted to "moral emptiness and epidemiological stupidity".

Grave risks

One particular concern with letting infections run high, even among groups, such as children, young people and vaccinated people, that are less likely to experience severe disease, is ‘long COVID’ — symptoms of COVID-19, such as exhaustion and difficulty concentrating, that persist for many months after infection. The UK Office for National Statistics currently says that close to a million people in the country have this condition. (Whether vaccines confer significant protection against long COVID is still unclear.) Chris Whitty, chief medical adviser to the UK government, has said that cases of long COVID seem sure to increase over the summer after opening up.

And, even among the vaccinated population, there will be more hospitalizations and deaths as infections rise. None of the vaccines used in the United Kingdom offers complete protection against hospitalization due to the Delta variant. For the widely used AstraZeneca vaccine, the protection has been found to be about 92%, so there will still be many casualties if infection rates are very high. People vulnerable to serious illness, for example those with compromised immune systems, will be put particularly at risk.

Many researchers acknowledge that compromises are needed: the economic and social costs of restrictions are too grave to impose indefinitely. “We should certainly be considering, in the light of all we’ve learned, which measures are most effective, and which we might be able to drop,” says English. But experts criticize the abandonment of measures that could reduce infection with minimal cost or inconvenience, particularly mandatory mask-wearing.

“Many of the relevant interventions are pretty mild”, says Hanage, “and getting people to accept small inconveniences for the greater good is what leadership is about.” He warns that forgoing minor interventions might end up necessitating a return to major disruptions and lockdowns later on.

English thinks that masks should remain compulsory in shops and on public transport, and that ventilation efficacy could be used to determine the rules in other spaces, as is currently done in Belgium. He also thinks that Germany’s practice of making restrictions and mitigations contingent on local rates of infection is a good model.

Johnson has insisted that the decision to open up reflects a judgement that the summer is the best time to do so. Spreading is reduced when people can be out in the open air, schools are on holiday, and hospitals are less pressured by seasonal ailments, such as flu, than they will be in the autumn and winter.

But English says relaxation when case numbers are high and rising does not make sense. Hanage says that a further delay of complete opening up could be used to vaccinate remaining age groups and thereby evade the worst consequences of a later relaxation.

Azra Ghani, an epidemic modeller at Imperial College London, agrees. “I think many of us in the scientific community would have preferred to see a more gradual relaxation,” waiting for all adults to have had the opportunity to get fully vaccinated, she says. “With a complete relaxation of interventions, we could see infection levels rise much higher than at any previous time during the pandemic.”

Once the change is implemented, “a very sharp spike in infections can be expected, maybe blunted a little by schools breaking up”, says Hanage. That was the experience in the Netherlands, where most restrictions were dropped on 26 June. Infections quickly began to soar, so the Dutch government was forced to reintroduce some safety measures from 10 July.

One of the gravest concerns is that if England’s number of infections grows as high as anticipated — some forecast up to 100,000 new infections per day over the summer — the chances of a variant emerging with even greater vaccine evasion are greatly increased. “All the experience we have with viruses”, says virologist Richard Tedder at Imperial College London, “is that if you let them replicate in a partially immune population, you will select inevitably for [vaccine] escape variants.”

So far, vaccines have mostly held up well against the concerning variants. But if more variants appear, this could cease to be true, at which point vaccines will need to be redesigned. “Why, at this point in time, with the virus on the rise again, are we prepared to rely on vaccines with the knowledge that if the vaccines fail then we’re going to have to rebuild them?” Tedder asks. More death and long COVID, although seriously

concerning, are minor problems compared to wiping out the efficacy of any vaccines, he says. "Once you've generated a lot of vaccine-resistant viruses, where do you go?"

Nature **595**, 479-480 (2021)

doi: <https://doi.org/10.1038/d41586-021-01938-4>

References

1. 1.

Gurdasani, D. *et al. Lancet* [https://doi.org/10.1016/S0140-6736\(21\)01589-0](https://doi.org/10.1016/S0140-6736(21)01589-0) (2021).

[Article](#) [Google Scholar](#)

[Download references](#)

Subjects

- [Epidemiology](#)
- [Virology](#)

nature careers

[Jobs](#) >

- [Instrument scientist at the permanent end station REMI@FLASH](#)

German Electron Synchrotron (DESY)

Hamburg, Germany

- [AUSBILDUNG: 3 Auszubildende \(d/m/w\) zum/zur Elektroniker*in für Geräte und Systeme](#)

Helmholtz Centre for Heavy Ion Research GmbH (GSI)

Darmstadt, Germany

- **AUSBILDUNG: 3 Auszubildende (d/m/w) zum/zur Anlagenmechaniker*in (d/m/w) für Sanitär-, Heizungs- und Klimatechnik**

Helmholtz Centre for Heavy Ion Research GmbH (GSI)

Darmstadt, Germany

- **AUSBILDUNG: 3 Auszubildende (d/m/w) zum/zur Elektroniker*in (d/m/w) für Betriebstechnik**

Helmholtz Centre for Heavy Ion Research GmbH (GSI)

Darmstadt, Germany

[Download PDF](#)

Subjects

- [Epidemiology](#)
- [Virology](#)

This article was downloaded by **calibre** from <https://www.nature.com/articles/d41586-021-01938-4>

- NEWS
- 09 July 2021

‘Pregnant’ male rat study kindles bioethical debate in China

Researchers question the value of the experiment — which involved sewing together male and female rats and led to the birth of live young.

- [Smriti Mallapaty](#)
 1. Smriti Mallapaty
[View author publications](#)

You can also search for this author in [PubMed](#) [Google Scholar](#)





•

[Download PDF](#)



It's not the first time research in China has led to controversy over ethics. Credit: APA Picturedesk GmbH/Shutterstock

An experiment to impregnate male rats stitched to female rats, by researchers at the Naval Medical University in Shanghai, has stirred debate in China and beyond about the ethics of the work.

Researchers say the experiment was highly contrived and unnecessarily distressing to the animals, and that it offers few insights into the possibility of pregnancy in people assigned male at birth — if anything, the poor success rate suggests that such a goal is a long way off.

But other scientists say the rat model could eventually be used to gradually tease apart what might be required to maintain pregnancy in people of any sex who wish to bear children. The study was detailed in a bioRxiv preprint posted online on 10 June¹.

“The experiment has no social value and just wasted the money taken from taxpayers,” says Qiu Renzong, a bioethicist at the Chinese Academy of Social Science in Beijing.

The paper has been particularly hotly debated among scholars and the public in China, where it was recently among the top-trending subjects on the Chinese social-media platform Weibo. Some researchers in China fear that [reckless biological experimentation](#) could blemish the country's reputation.

Issues with ethics in China

Chinese scientists are concerned that controversial research, such as this study, could reinforce an “already tainted image of Chinese science”, says Joy Zhang, a sociologist at the University of Kent in Canterbury, UK, who has conducted research in China over many years. The study is one of several in recent years that Chinese researchers feel have presented a “distorted image” of what they believe China’s research culture should be, she says.

In one high-profile case from 2018, a Chinese researcher announced the birth of the first genome-edited babies, which was [widely criticized](#) as highly unethical. The incident spurred efforts to [strengthen ethical governance](#) in China, including the formation of a [national committee](#) to advise the government on research ethics.



[Genome-edited baby claim provokes international outcry](#)

“There is also a deeper worry that the underlying trend of ‘science through PR’ — the mentality that experiments with outlandish objectives are a shortcut to public attention — would turn science into a form of entertainment business rather than a serious and responsible academic endeavour,” says Zhang.

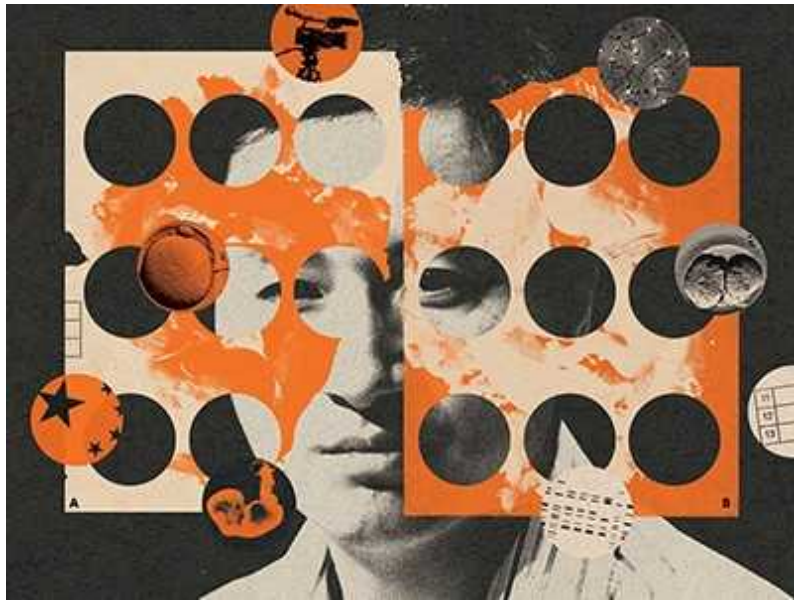
It is not clear whether the pregnancy experiment was approved by an independent ethics committee — a requirement for all publicly funded experiments involving laboratory animals — says Zhang Xinqing, a bioethicist at Peking Union Medical College in Beijing. Zhang adds that if it had been up to him, he would not have voted to approve this experiment.

The authors declined to comment on questions about the research from *Nature*. They stated in their manuscript that the work could have “a profound impact on reproductive biology”, but did not clarify why. In a public statement [on PubPeer](#), a website for post-publication peer review, one of the authors, Zhang Rongjia, said the work was performed “for our personal interests and curiosity”, and that they made efforts to reduce the number of animals used and to minimize their pain.

Birth of ten live pups

Pregnancy in males is extremely rare in nature, and is observed only in a group of fish that includes seahorses and pipefishes. To study the possibility of achieving it in mammals, the Chinese researchers sewed the elbows, knees and skins of pairs of rats together, each consisting of a castrated male and a female, to join their blood supply. This conjoined model, known as a parabiont, allows the animals to share blood.

Parabiosis is an established surgical technique for connecting animals to study the effects of infusing blood from one to the other — for example from an [elderly mouse](#) to a youthful one to study the process of ageing.



The CRISPR-baby scandal: what's next for human gene-editing

Six weeks after the castration and surgery, testosterone levels in the male rats had significantly declined — but their levels of oestrogen and progesterone mirrored those in the female rats.

Eight weeks after surgery, the researchers transplanted a uterus into each male rat, followed by embryos into both the male and female after another eight weeks. Three weeks into the embryos' development, and near the end of a normal rat pregnancy, the researchers delivered the pups by caesarean section.

Out of 842 embryos introduced into 46 conjoined pairs of rats, one-third of those in the female rats and one-tenth of those in the male rats developed into viable fetuses. Only 10 pups gestated in the male rats survived to adulthood — some 4% of the 280 embryos implanted in the male rats. The adult rats were subsequently separated, and all the males survived for another three months, until they were eventually euthanized.

The authors say the findings point to the importance of the pregnant female's blood supply, because the embryos did not mature in males that were attached to females without developing fetuses. The importance of the blood supply and the low rate of births suggest that "male pregnancy in humans is

not feasible at this stage”, Zhang wrote on PubPeer, adding: “If our result is correct, this is almost a death sentence for human male pregnancy.”

Limited scientific insights

But other researchers say the importance of a mother’s endocrine system is already common knowledge.

The study offers limited insights, says Chris O’Neill, a retired researcher formerly based at the University of Sydney in Australia, who has studied the biology of pregnancy. The model is effectively an *ex vivo* model of female pregnancy, he adds: a female uterus and blood supply within a castrated male. “It tells us that at least within the castrated male, there is no fundamental hostility of the male environment to carrying a fetus,” he says.

The intrusive surgical intervention also doesn’t lend itself to being applied to people, says Catherine Mills, a bioethicist at Monash University in Melbourne, Australia. “It is quite a long way from any real implication for human research,” she says. “In a sense, it is not an animal model; it is just an animal experiment.”

Study co-author Zhang declined to comment on the criticisms of the value of the work, stating in an e-mail to *Nature* that the authors “prefer to respond to external criticism by formally publishing academic papers”.



Reboot ethics governance in China

O'Neill says the study might provide a new experimental model for identifying nutrients or hormones in maternal blood that are crucial for a successful pregnancy.

There could be implications for other reproductive research in people as well. Some groups are already considering the possibility of uterine transplants in transgender women, says Mats Brännström, a reproductive-health researcher at Gothenburg University in Sweden, who led the first clinical trial of such a transplant in cisgender women without functioning uteri. Animal experiments such as the one by the Chinese researchers could be a first step in establishing the safety of such surgeries, says Brännström — and the findings offer a sense of the great challenge of such a task.

But others question whether there is any value to pregnancy in people assigned male at birth at all. “There may be some limited applications where trans women want to be able to gestate a child,” says Mills, but otherwise, “what is the therapeutic need?”

Nature **595**, 481 (2021)

doi: <https://doi.org/10.1038/d41586-021-01885-0>

References

1. 1.

Zhang, R. & Liu, Y. Preprint at bioRxiv
<https://doi.org/10.1101/2021.06.09.447686> (2021).

[Download references](#)

Related Articles



- [The CRISPR-baby scandal: what's next for human gene-editing](#)



- [Reboot ethics governance in China](#)



- [Genome-edited baby claim provokes international outcry](#)

Subjects

- [Ethics](#)
- [Physiology](#)
- [Developmental biology](#)

nature careers

[Jobs](#) >

- [**Instrument scientist at the permanent end station REMI@FLASH**](#)

German Electron Synchrotron (DESY)

Hamburg, Germany

- [**AUSBILDUNG: 3 Auszubildende \(d/m/w\) zum/zur Elektroniker*in für Geräte und Systeme**](#)

Helmholtz Centre for Heavy Ion Research GmbH (GSI)

Darmstadt, Germany

- [**AUSBILDUNG: 3 Auszubildende \(d/m/w\) zum/zur Anlagenmechaniker*in \(d/m/w\) für Sanitär-, Heizungs- und Klimatechnik**](#)

Helmholtz Centre for Heavy Ion Research GmbH (GSI)

Darmstadt, Germany

- [**AUSBILDUNG: 3 Auszubildende \(d/m/w\) zum/zur Elektroniker*in \(d/m/w\) für Betriebstechnik**](#)

Helmholtz Centre for Heavy Ion Research GmbH (GSI)

Darmstadt, Germany

[Download PDF](#)

Related Articles



- [**The CRISPR-baby scandal: what's next for human gene-editing**](#)



- [**Reboot ethics governance in China**](#)



- [**Genome-edited baby claim provokes international outcry**](#)

Subjects

- [Ethics](#)
- [Physiology](#)
- [Developmental biology](#)

This article was downloaded by **calibre** from <https://www.nature.com/articles/d41586-021-01885-0>

- NEWS
- 14 July 2021

Long COVID and kids: scientists race to find answers

Children get long COVID too, but researchers are still working to determine how frequently and how severely.

- [Dyani Lewis](#) ⁰
1. Dyani Lewis

1. Dyani Lewis is a freelance science journalist in Melbourne, Australia.

[View author publications](#)

You can also search for this author in [PubMed](#) [Google Scholar](#)





•

[Download PDF](#)



Children with COVID-19 are at risk of developing long-term symptoms.
Credit: Naveen Sharma/SOPA Images/LightRocket via Getty

As COVID-19 has ripped through communities, children have often been spared the worst of the disease's impacts. But the spectre of long COVID developing in children is forcing researchers to reconsider the cost of the pandemic for younger people.

The question is particularly relevant as the proportion of infections that are in [young people](#) rises in countries where many adults are now vaccinated — and as debates about the benefits of vaccinating children intensify.



Will COVID become a disease of the young?

Most people who survive COVID-19 recover completely. But for some, the poorly understood condition that's become known as long COVID can last for months — maybe even years. Nobody yet knows.

The condition was first described in adults. But several studies have now reported a similar phenomenon, including symptoms such as headache, fatigue and heart palpitations, in children, even though they rarely experience severe initial symptoms of COVID-19.

Estimates of how common long COVID is in children vary wildly. Researchers say that pinning this down is crucial, because decisions about school closures and vaccine roll-outs can hinge on the risk the virus poses to children. Getting solid numbers is “very, very important”, says Pia Hardelid, a child-health epidemiologist at University College London.

Alarm bells

Paediatrician Danilo Buonsenso, at the Gemelli University Hospital in Rome, led the first attempt to quantify long COVID in children. He and his colleagues interviewed 129 children aged 6–16 years, who had been diagnosed with COVID-19 between March and November 2020.

In January, they reported in a preprint that more than one-third had one or two lingering symptoms four months or more after infection, and a further one-quarter had three or more symptoms. Insomnia, fatigue, muscle pain and persistent cold-like complaints were common — a pattern similar to that seen in adults with long COVID. Even children who'd had mild initial symptoms, or were asymptomatic, were not spared these long-lasting effects, Buonsenso says.



[Long COVID: let patients help define long-lasting COVID symptoms](#)

The findings, published in a peer-reviewed journal in April¹, sparked a deluge of e-mails and calls from anxious parents. “It was like we opened the door, and everyone — mostly parents themselves — were starting to say, ‘Okay, so maybe this is something we should ask about,’” he says. The hospital now runs a weekly outpatient clinic to meet demand.

Data [released by the UK Office of National Statistics](#) (ONS) in February and updated in April also sparked concern. They showed that 9.8% of children aged 2–11 years and 13% aged 12–16 years reported at least one lingering symptom five weeks after a positive diagnosis. Another report released in April found that one-quarter of children who were surveyed after discharge from hospital in Russia post-COVID-19, had symptoms more than five months later².

The numbers reported aren't as high as they are for adults. The ONS data, for instance, show that about 25% of 35–69-year olds had symptoms at 5 weeks. But the numbers still set off alarm bells, because severe COVID-19 in children is much rarer than in adults, and most kids were therefore assumed to have been spared the impacts of long COVID, says Jakob Armann, a paediatrician at Dresden University of Technology in Germany.

If 10% or 15% of children, irrespective of the initial severity of the disease, do have long-term symptoms after all, "that's a true problem", he says, "so this needs to be studied".



A healthcare worker at a hospital in Havana, Cuba, administers a dose of vaccine to a 14-year-old boy.Credit: Alexandre Meneghini/Reuters

Not so high

But Armann suspects numbers might not be that high. Long-COVID symptoms include fatigue, headache, difficulty concentrating and insomnia. He says that other pandemic-related phenomena, such as school closures and

the trauma of seeing family members sick or dying from COVID-19 could result in those symptoms too, and artificially inflate long-COVID estimates. “You need a control group to tease out what is truly infection-related,” he says.

He and his colleagues have been taking blood samples from secondary-school children in Dresden since May 2020 to track rates of infection. In March and April this year, surveys were taken from more than 1,500 children — nearly 200 of whom had antibodies indicating previous SARS-CoV-2 infection — to see how many reported long COVID.

In May, Armann’s group reported in a preprint that it found no difference in rates of symptoms reported by the two groups³. “This was kind of striking,” says Armann, and suggests that long COVID in children is probably lower than some studies have indicated. That doesn’t mean that long COVID doesn’t exist in children, he says, but it does mean the number is probably below 10%, a level that would have been picked up in the study. The true figure is perhaps as low as 1%, he says.



Does vaccinating adults stop kids from spreading COVID too?

Hardelid tapped into data gathered by the Virus Watch study, which tracks infections and symptoms in more than 23,000 households across England and Wales. As they reported in a preprint in June, she and her colleagues found that 4.6% of children with evidence of SARS-CoV-2 infection had persistent symptoms lasting more than 4 weeks⁴.

Another UK study, posted as a preprint in May, found a similar rate. Of more than 1,700 schoolchildren who tested positive for SARS-CoV-2, 4.4% had symptoms, such as headache, fatigue and loss of smell, that persisted; 1.6% had symptoms that remained for at least 8 weeks⁵.

It will also be important to determine how long the condition lasts in children, says Armann. Headaches or trouble sleeping for just 6 months is a vastly different problem from having these symptoms all their life, even if it only happens for 1%, he says.

Defining the problem

Buonsenso says that one of the challenges in working out how many kids develop long COVID is that there are no set diagnostic criteria in adults, let alone in children. Surveys to detect symptoms usually cast a wide net, and are not yet specific enough to tease out long COVID from other conditions, he says. Nevertheless, he is convinced that some children — perhaps 5–10% of those with COVID-19 — do develop the condition.

If psychological distress were a big factor in the symptoms he's seeing, as Armann has suggested, Buonsenso argues there would have been more children with symptoms from the first wave of infections in 2020, when restrictions were harshest in Rome. Instead, the second wave resulted in more cases of children with symptoms of long COVID, he says.

A proper definition of long COVID is urgently needed, says Hardelid, so that studies can determine how much of a problem it presents in children, and which children are most at risk.

One suggestion, following a review of the literature in adults by the UK National Institute for Health Research, is that long COVID could be a collection of four different syndromes, including post-intensive care syndrome, post-viral fatigue syndrome and long-term COVID syndrome⁶. This could be the case in children, too, says Hardelid.

Buonsenso has also been looking at immunological changes that occur in people with long COVID, to see if there are biological markers that could

lead to treatments. In a small study posted as a preprint in May, he and his colleagues found that only the children with long COVID showed signs of chronic inflammation following infection⁷.

Such investigations into the biological basis of long COVID could have far-reaching effects. In general, we know very little about chronic post-viral conditions, says Buonsenso, because most clinical attention, and funding, has focused on the acute phase of infections.

Nature **595**, 482-483 (2021)

doi: <https://doi.org/10.1038/d41586-021-01935-7>

References

1. 1.

Buonsenso, D. *et al.* *Acta Paediatr.* <https://doi.org/10.1111/apa.15870> (2021).

[Article](#) [Google Scholar](#)

2. 2.

Osmanov, I. M. *et al.* Preprint at medRxiv
<https://doi.org/10.1101/2021.04.26.21256110> (2021).

3. 3.

Blankenburg, J. *et al.* Preprint at medRxiv
<https://doi.org/10.1101/2021.05.11.21257037> (2021).

4. 4.

Miller, F. *et al.* Preprint at medRxiv
<https://doi.org/10.1101/2021.05.28.21257602> (2021).

5. 5.

Molteni, E. *et al.* Preprint at medRxiv
<https://doi.org/10.1101/2021.05.05.21256649> (2021).

6. 6.

National Institute for Health Research. Living with Covid19
https://doi.org/10.3310/themedreview_41169 (NIHR, 2020).

7. 7.

Di Sante, G. *et al.* Preprint at medRxiv
<https://doi.org/10.1101/2021.05.07.21256539> (2021).

[Download references](#)

Related Articles

-  [Long COVID: let patients help define long-lasting COVID symptoms](#)
-  [Scientists set out to connect the dots on long COVID](#)
-  [Does vaccinating adults stop kids from spreading COVID too?](#)
-  [Will COVID become a disease of the young?](#)

Subjects

- [Infection](#)
- [SARS-CoV-2](#)
- [Epidemiology](#)

nature careers

[Jobs](#) >

- [Instrument scientist at the permanent end station REMI@FLASH](#)

German Electron Synchrotron (DESY)

Hamburg, Germany

- [AUSBILDUNG: 3 Auszubildende \(d/m/w\) zum/zur Elektroniker*in für Geräte und Systeme](#)

Helmholtz Centre for Heavy Ion Research GmbH (GSI)

Darmstadt, Germany

- [AUSBILDUNG: 3 Auszubildende \(d/m/w\) zum/zur Anlagenmechaniker*in \(d/m/w\) für Sanitär-, Heizungs- und Klimatechnik](#)

Helmholtz Centre for Heavy Ion Research GmbH (GSI)

Darmstadt, Germany

- [AUSBILDUNG: 3 Auszubildende \(d/m/w\) zum/zur Elektroniker*in \(d/m/w\) für Betriebstechnik](#)

Helmholtz Centre for Heavy Ion Research GmbH (GSI)

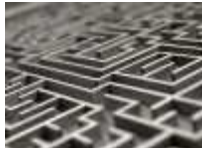
Darmstadt, Germany

[Download PDF](#)

Related Articles



- [Long COVID: let patients help define long-lasting COVID symptoms](#)



- [Scientists set out to connect the dots on long COVID](#)



- [Does vaccinating adults stop kids from spreading COVID too?](#)



- [Will COVID become a disease of the young?](#)

Subjects

- [Infection](#)
- [SARS-CoV-2](#)
- [Epidemiology](#)

This article was downloaded by **calibre** from <https://www.nature.com/articles/d41586-021-01935-7>

- NEWS
- 08 July 2021

The rise of ‘ARPA-everything’ and what it means for science

Science agencies such as ARPA-Health hope to replicate the success of the US Defense Advanced Research Projects Agency, but researchers question whether they will thrive.

- [Jeff Tollefson](#)
 1. Jeff Tollefson
[View author publications](#)

You can also search for this author in [PubMed](#) [Google Scholar](#)





•

[Download PDF](#)



Funding from ARPA-Energy has led to the creation of companies such as solar manufacturing firm 1366 Technologies (now CubicPV). Here, a technician shows off a solar cell at a demonstration plant in 2013. Credit: Pat Greenhouse/The Boston Globe/Getty

US President Joe Biden's administration wants to create a US\$6.5-billion agency to accelerate innovations in health and medicine — and revealed new details about the unit last month¹. Dubbed ARPA-Health (ARPA-H), it is the latest in a line of global science agencies now being modelled on the renowned US Defense Advanced Research Projects Agency (DARPA), whose work a generation ago laid the foundation for the modern Internet.

With more DARPA clones on the horizon, researchers warn that success in replicating DARPA's hands-on, high-risk, high-reward approach is by no means assured.

“The ARPA model has been successful, and we’ve learned a lot,” says Laura Diaz Anadon, who heads the Cambridge Centre for Environment, Energy and Natural Resource Governance at the University of Cambridge, UK. “But ARPA is not a magic bullet that will apply to everything.”



Plan to create UK version of DARPA lacks detail, say researchers

Enamoured with the innovation that DARPA fostered in the United States, governments around the world, including in Europe and Japan, have attempted to duplicate the agency within their own borders. Most recently, the United Kingdom [announced plans to create](#) its version, the Advanced Research and Invention Agency (ARIA), with an initial allocation of £800 million (US\$1.1 billion). And the Biden administration has proposed launching a second US agency, the \$500-million ARPA-Climate (ARPA-C), to spur technologies for fighting climate change.

Scientists who have studied the DARPA model say it works if applied properly, and to the right, ‘ARPA-able’ problems. But replicating DARPA’s recipe isn’t easy. It requires the managers who build and run an agency’s grant programmes to have the freedom to assemble research teams and pursue risky ideas in promising fields that have typically been neglected by conventional industrial research and development programmes. Critics aren’t yet sure how ARPA-H, ARPA-C and ARIA will fare.

Following the recipe

The US Department of Defense established DARPA in 1958, one year after the Soviet Union launched the world’s first satellite, Sputnik 1. The goal was to avoid falling behind the Soviets, and to ensure that the United States

remained a world leader in technology. DARPA was instrumental in early computing research, as well as in developing technologies such as GPS and unmanned aerial vehicles (See ‘Following in DARPA’s footsteps’).

DARPA functions differently from other major US science funding agencies, and has a leaner budget (\$3.5 billion). Its roughly 100 programme managers, borrowed for stints of 3–5 years from academia or industry, have broad latitude in what they fund, and actively engage with their teams, enforcing aggressive deadlines and monitoring progress along the way. By comparison, projects funded by agencies such as the US National Institutes of Health (NIH) typically see little engagement between programme managers and the researchers they fund, beyond annual progress reports. Projects funded by these agencies also tend towards being those that are likely to succeed — and thus typically represent more incremental advances, says William Bonvillian, a policy researcher at the Massachusetts Institute of Technology in Cambridge who has studied DARPA.

Following in DARPA’s footsteps

Beginning in the early 2000s, the United States and other nations began launching agencies that aimed to capture the magic of the US Defense Advanced Research Projects Agency (DARPA).

1958: The United States establishes what will eventually become DARPA, which initially focuses on space, missile defence and the detection of nuclear weapons.

1963: A DARPA project successfully launches the first of several Transit satellites, giving US Navy ships accurate location readings and laying the groundwork for the future GPS.

1966: DARPA initiates the ARPANET project in an effort to remotely and securely link computers. Years later, this effort gives rise to the Internet.

1988: A joint project between DARPA and the US Navy produces the first long-range, unmanned aerial vehicle, Amber, which flew non-stop for more than 38 hours.

2002: US Congress establishes the first DARPA clone, the Homeland Security ARPA.

2007: Former US president George W. Bush signs the America COMPETES Act, which authorizes the creation of ARPA-Energy (ARPA-E), with the aim of developing low-carbon technologies. Two years later, former president Barack Obama formally launches the agency.

2013: DARPA awards the first grants to firms such as Moderna in Cambridge, Massachusetts, and Pfizer in New York City to support [the development of messenger RNA vaccines](#), helping to lay the groundwork for the jabs deployed to fight the COVID-19 pandemic.

2018: Japan launches its largest DARPA-inspired programme, Moonshot, with an initial budget of ¥100 billion (US\$911 million) over five years.

2019: Germany launches the Federal Agency for Disruptive Innovation (SPRIN-D) with a budget of around €1 billion (US\$1.2 billion) over 10 years.

2020: The United Kingdom [announces plans to launch](#) the Advanced Research and Invention Agency (ARIA), which will receive £800 million (US\$1.1 billion) to cover its first few years.

2021: US President Joe Biden calls for the creation of ARPA-Health and ARPA-Climate in his first budget outline.

The DARPA model doesn't work if programme managers aren't given the space to fail, says Bonvillian. When the US government applied the model to developing national-defence technologies through the Homeland Security ARPA in 2002, he adds, this was the problem. The effort eventually collapsed. "If you don't get the culture right on day one, you have got a problem," says Bonvillian.

Researchers also point out that a successful ARPA needs a customer for the technologies it develops. In the case of DARPA, the US military was ready to purchase many promising inventions. ARPA-Energy (ARPA-E), which was launched in 2009 under former president Barack Obama to advance

low-carbon energy technologies, addressed this challenge by helping grant recipients to develop plans for commercialization from the outset — a model that Bonvillian says DARPA has also now imported.

ARPA-E had the independence it needed to function well, researchers say. Still running today, the agency, housed within the US Department of Energy (DoE), has invested \$2.8 billion in nearly 1,200 projects, which have attracted another \$5.4 billion in private-sector investments and led to the creation of 92 companies. Last month, one of those companies, 1366 Technologies in Bedford, Massachusetts, announced plans to build a \$300-million facility for manufacturing solar cells in India. The company, now known as CubicPV, received \$4 million from ARPA-E in 2009 to develop a cleaner, faster, cheaper way to manufacture the silicon semiconductors that go into solar panels.



Biden pursues giant boost for science spending

Because it can take decades for new technologies to have commercial and societal impact, whether ARPA-E will transform the energy industry remains to be seen. But scientists have documented preliminary signs of its success^{2,3}, as measured by patenting, publishing and, in some cases, attracting venture capital for technologies originally funded by the agency.

“The answer is yes, the [ARPA] model works, or at least it did in this case,” says Anna Goldstein, an energy researcher at the University of

Massachusetts Amherst who has analysed ARPA-E's worth. But that does not mean the model will solve all problems, she warns.

The new generation

Researchers have responded to Biden's latest ARPA proposals with trepidation. Some scientists have questioned the need to create ARPA-C, rather than expanding ARPA-E. They point out that the two have similar missions, even though DoE secretary Jennifer Granholm has said they will not overlap. As planned, ARPA-C would seek to foster "game-changing" energy and climate solutions, including technologies such as small, modular nuclear reactors and low-energy buildings — innovations that also fall under ARPA-E's purview.

Questions also abound about ARPA-H. The Biden administration proposed that it should be housed within the NIH, which critics worry could stifle innovation.

In a guest editorial published in *Science* last month¹, NIH director Francis Collins and other administration officials acknowledged that the NIH tends to fund incremental research rather than bold new technologies that could transform the marketplace, and agreed that ARPA-H's organization should be "flat, lean, and nimble", with a culture that values "bold goals with big potential impact". They cited potential breakthroughs in everything from vaccine development, to drug-delivery systems, to wearable medical devices.



DARPA investments have led to the creation of technologies such as unmanned aerial vehicles. Credit: US Air Force Photo/Alamy

The Biden administration is saying all the right things, says Bonvillian, although he still worries about whether ARPA-H will have the independence and the authority that it needs to operate within the biomedical-research behemoth. He also says the NIH will need to embrace the kind of interdisciplinary research that has been fundamental to technology development at agencies such as DARPA and ARPA-E. “If they set up an ARPA that is all biology all of the time, like NIH is, then they are going to radically limit its effectiveness,” he says.

Others worry that the scope of ARPA-H’s mission is too broad. Health care is a huge field. Given that there is already plenty of private investment in new drugs and medical therapies for prevalent diseases, Goldstein says, ARPA-H might be better placed to have an impact on neglected diseases that affect people living in impoverished and underprivileged communities. This area receives much less funding from other sources.

“The trick is setting the scope broad enough so that programme managers can wander intellectually and follow their noses, but not so broad that you try to boil the ocean,” says Eric Toone, a chemist who helped to set up ARPA-E and now works for Breakthrough Energy Ventures, a venture-capital firm based in Kirkland, Washington. This is also a potential concern with Britain’s ARIA, whose scope has yet to be defined, Toone adds.

Toone also recommends starting out small and letting new agencies grow over time. “The challenge you have with too much money is people’s expectations wind up in funny places.”

Nature **595**, 483–484 (2021)

doi: <https://doi.org/10.1038/d41586-021-01878-z>

References

1. 1.

Collins, F. S., Schwetz, T. A., Tabak, L. A. & Lander, E. S. *Science* <https://doi.org/10.1126/science.abj8547> (2021).

[Article](#) [Google Scholar](#)

2. 2.

Goldstein, A. P. & Narayananamurti, V. *Res. Policy* **47**, 1505–1512 (2018).

[Article](#) [Google Scholar](#)

3. 3.

Goldstein, A., Doblinger, C., Baker, E. & Díaz Anadón, L. *Nature Energy* **5**, 803–810 (2020).

[Article](#) [Google Scholar](#)

[Download references](#)

Related Articles



- [Plan to create UK version of DARPA lacks detail, say researchers](#)



- [Biden pursues giant boost for science spending](#)



- [How COVID unlocked the power of RNA vaccines](#)

Subjects

- [Technology](#)
- [Research management](#)
- [Policy](#)
- [Government](#)
- [Funding](#)

nature careers

[Jobs >](#)

- [Instrument scientist at the permanent end station REMI@FLASH](#)

German Electron Synchrotron (DESY)

Hamburg, Germany

- [AUSBILDUNG: 3 Auszubildende \(d/m/w\) zum/zur Elektroniker*in für Geräte und Systeme](#)

Helmholtz Centre for Heavy Ion Research GmbH (GSI)

Darmstadt, Germany

- [AUSBILDUNG: 3 Auszubildende \(d/m/w\) zum/zur Anlagenmechaniker*in \(d/m/w\) für Sanitär-, Heizungs- und Klimatechnik](#)

Helmholtz Centre for Heavy Ion Research GmbH (GSI)

Darmstadt, Germany

- [AUSBILDUNG: 3 Auszubildende \(d/m/w\) zum/zur Elektroniker*in \(d/m/w\) für Betriebstechnik](#)

Helmholtz Centre for Heavy Ion Research GmbH (GSI)

Darmstadt, Germany

[Download PDF](#)

Related Articles



- [Plan to create UK version of DARPA lacks detail, say researchers](#)



- [**Biden pursues giant boost for science spending**](#)



- [**How COVID unlocked the power of RNA vaccines**](#)

Subjects

- [Technology](#)
- [Research management](#)
- [Policy](#)
- [Government](#)
- [Funding](#)

This article was downloaded by **calibre** from <https://www.nature.com/articles/d41586-021-01878-z>

- NEWS
- 07 July 2021

COVID and the brain: researchers zero in on how damage occurs

Growing evidence suggests that the coronavirus causes ‘brain fog’ and other neurological symptoms through multiple mechanisms.

- [Michael Marshall](#)
 1. Michael Marshall
[View author publications](#)

You can also search for this author in [PubMed](#) [Google Scholar](#)





•

[Download PDF](#)



Since the beginning of the pandemic, researchers have been trying to understand how the coronavirus SARS-CoV-2 affects the brain. Credit: Stanislav Krasilnikov/TASS/Getty

How COVID-19 damages the brain is becoming clearer. New evidence suggests that the coronavirus's assault on the brain could be multipronged: it might attack certain brain cells directly, reduce blood flow to brain tissue or trigger production of immune molecules that can harm brain cells.

Infection with the coronavirus SARS-CoV-2 can cause memory loss, strokes and other effects on the brain. The question, says Serena Spudich, a neurologist at Yale University in New Haven, Connecticut, is: “Can we intervene early to address these abnormalities so that people don’t have long-term problems?”

With so many people affected — neurological symptoms appeared in 80% of the people hospitalized with COVID-19 who were surveyed in one study¹ — researchers hope that the growing evidence base will point the way to better treatments.

Breaking into the brain

SARS-CoV-2 can have severe effects: a preprint posted last month² compared images of people's brains from before and after they had COVID-19, and found loss of grey matter in several areas of the cerebral cortex. (Preprints are published without peer review.)

Early in the pandemic, [researchers speculated](#) that the virus might cause damage by somehow entering the brain and infecting neurons, the cells responsible for transmitting and processing information. But studies have since indicated³ that the virus has difficulty getting past the brain's defence system — the blood–brain barrier — and that it doesn't necessarily attack neurons in any significant way.



[COVID's toll on smell and taste: what scientists do and don't know](#)

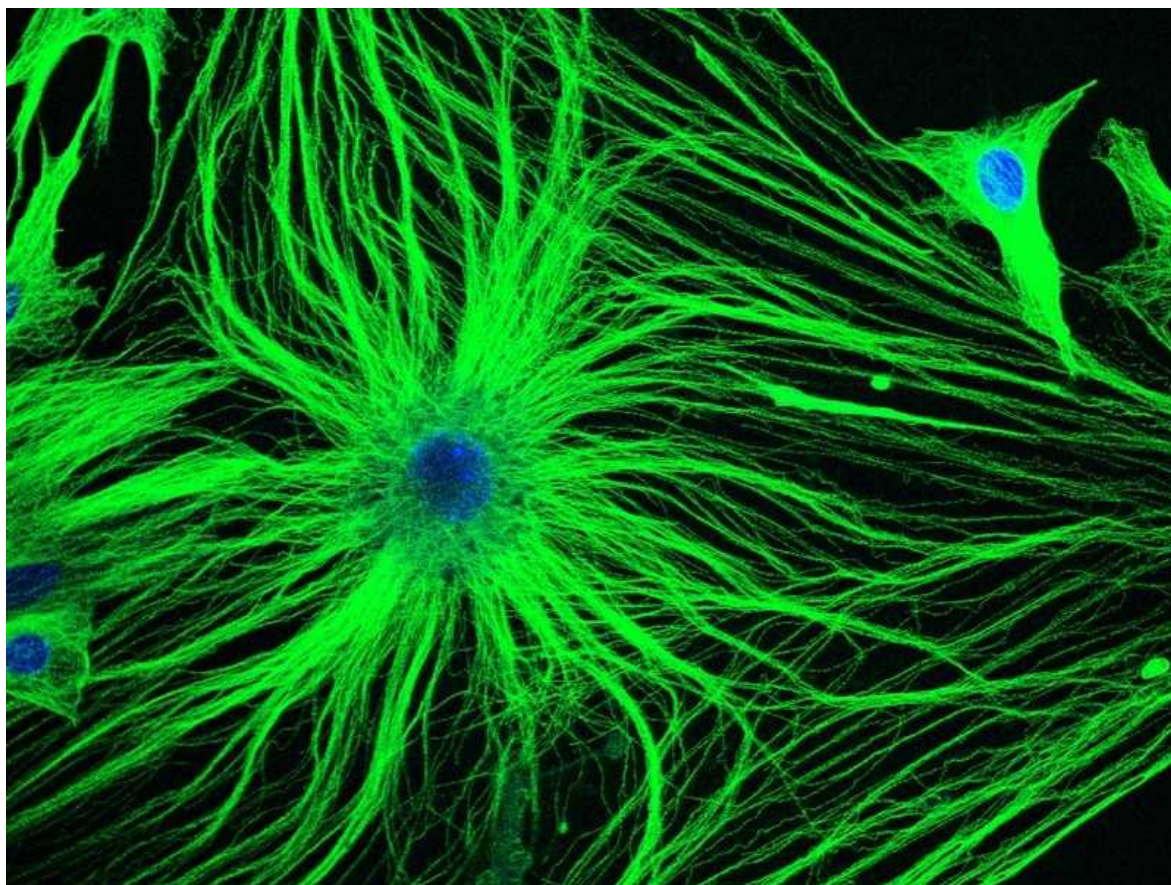
One way in which SARS-CoV-2 might be accessing the brain, experts say, is by passing through the olfactory mucosa, the lining of the nasal cavity, which borders the brain. The virus is often found in the nasal cavity — one reason that health-care workers test for COVID-19 by swabbing the nose.

Even so, "there's not a tonne of virus in the brain", says Spudich, who co-authored a review of autopsies and other evidence that was published online

in April⁴.

But that doesn't mean it is not infecting any brain cells at all.

Studies now suggest that SARS-CoV-2 can infect astrocytes, a type of cell that's abundant in the brain and has many functions. "Astrocytes do quite a lot that supports normal brain function," including providing nutrients to neurons to keep them working, says Arnold Kriegstein, a neurologist at the University of California, San Francisco.



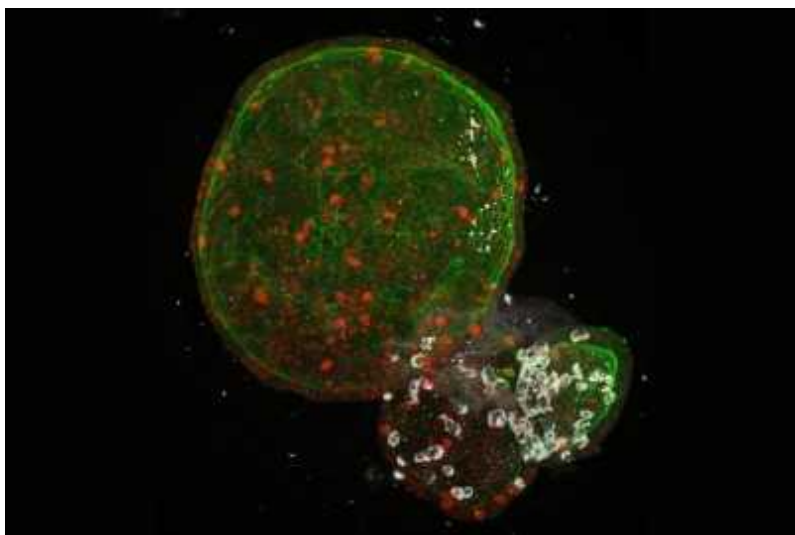
Astrocytes are star-shaped cells in the central nervous system that perform many functions, including providing nutrients to neurons. Credit: David Robertson, ICR/SPL

In a preprint posted in January, Kriegstein and his colleagues reported⁵ that SARS-CoV-2 preferentially infects astrocytes over other brain cells. The researchers exposed brain organoids — miniature brain-like structures

grown from stem cells in the lab — to the virus. SARS-CoV-2 almost exclusively infected astrocytes over all other cells present.

Bolstering these lab studies, a group including Daniel Martins-de-Souza, head of proteomics at the University of Campinas in Brazil, reported⁶ in a February preprint that it had analysed brain samples from 26 people who died with COVID-19. In the five whose brain cells showed evidence of SARS-CoV-2 infection, 66% of the affected cells were astrocytes.

Infected astrocytes could explain some of the neurological symptoms associated with COVID-19, especially fatigue, depression and ‘brain fog’, which includes confusion and forgetfulness, argues Kriegstein. “Those kinds of symptoms may not be reflective of neuronal damage, but could be reflective of dysfunctions of some sort. That could be consistent with astrocyte vulnerability.”



The mini lungs and other organoids helping to beat COVID

Astrocytes might be vulnerable even if they are not infected by the virus. A study published on 21 June⁷ compared the brains of 8 deceased people who had COVID-19 with the brains of 14 controls. The researchers found no trace of SARS-CoV-2 in the brains of the infected people, but they did find that gene expression had been affected in some astrocytes, which were not working properly.

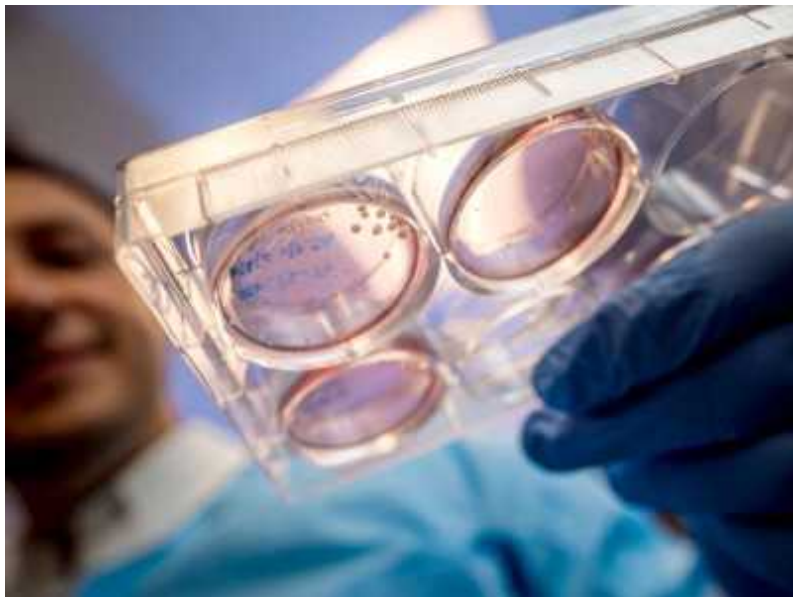
Given all these findings, researchers want to know how many brain cells need to be either infected or damaged to cause neurological symptoms, says Ricardo Costa, a physiologist at Louisiana State University Health in Shreveport whose team is studying SARS-CoV-2's effects on brain cells.

Unfortunately, there probably isn't a simple answer, says Kriegstein, pointing out that cells, including neurons, in some regions of the brain will cause more dysfunction than others, if damaged.

Blocking blood flow

Evidence has also accumulated that SARS-CoV-2 can affect the brain by reducing blood flow to it — impairing neurons' function and ultimately killing them.

Pericytes are cells found on small blood vessels called capillaries throughout the body — including in the brain. A February preprint reported that SARS-CoV-2 could infect pericyte-like cells in brain organoids⁸.



How COVID-19 can damage the brain

In April, David Attwell, a neuroscientist at University College London, and his colleagues published a preprint showing evidence that SARS-CoV-2 can

affect pericytes' behaviour⁹. The researchers observed that, in slices of hamster brain, SARS-CoV-2 blocks the functioning of receptors on pericytes, causing capillaries in the tissue to constrict. "It turns out this is a big effect," says Attwell.

It's a "really cool" study, says Spudich. "It could be something that is determining some of the permanent injury we see — some of these small-vessel strokes."

Attwell suggests that drugs used to treat high blood pressure, which involves blood-vessel restriction, might be useful in some cases of COVID-19. Two clinical trials are currently investigating the effect of the blood-pressure drug losartan to treat the disease.

Immune malfunction

There is also growing evidence that some neurological symptoms and damage are the result of the body's own immune system overreacting and even misfiring after encountering the coronavirus.

In the past 15 years, it has become clear that in response to infection, some people's immune systems inadvertently make 'autoantibodies' that attack their own tissue, says Harald Prüss, a neuroimmunologist at the German Center for Neurodegenerative Diseases in Berlin. This can cause long-term conditions such as neuromyelitis optica, in which people experience symptoms such as loss of vision, and weakness in their limbs. In a review published in May¹⁰, Prüss summarized evidence that these autoantibodies can pass through the blood–brain barrier, and contribute to neurological disorders ranging from memory impairment to psychosis.



Autopsy slowdown hinders quest to determine how coronavirus kills

This pathway might also operate in COVID-19. In a study published last year¹¹, Prüss and his colleagues isolated antibodies against SARS-CoV-2 from people, and found one that was able to protect hamsters from infection and lung damage. The aim was to create new treatments. But the researchers also found that some of the antibodies could bind to brain tissue, suggesting that they might damage it. “We’re currently trying to prove that clinically and experimentally,” says Prüss.

In a second paper, published online last December, a team including Prüss studied the blood and cerebrospinal fluid of 11 people critically ill with COVID-19, all of whom had neurological symptoms¹². All produced autoantibodies capable of binding neurons. And there is evidence that giving patients intravenous immunoglobulin, another type of antibody, to suppress the harmful autoantibodies’ action is “quite successful”, says Prüss.

These pathways — astrocytes, pericytes and autoantibodies — are not mutually exclusive, and are probably not the only ones: it is likely that people with COVID-19 experience neurological symptoms for a range of reasons. Prüss says a key question is what proportion of cases is caused by each of the pathways. “That will determine treatment,” he says.

Nature **595**, 484-485 (2021)

doi: <https://doi.org/10.1038/d41586-021-01693-6>

References

1. 1.

Chou, S. H.-Y. *et al.* *JAMA Netw. Open* **4**, e2112131 (2021).

[PubMed](#) [Article](#) [Google Scholar](#)

2. 2.

Douaud, G. *et al.* Preprint at medRxiv
<https://doi.org/10.1101/2021.06.11.21258690> (2021).

3. 3.

Serrano, G. E. *et al.* Preprint at medRxiv
<https://doi.org/10.1101/2021.02.15.21251511> (2021).

4. 4.

Farhadian S. F., Seilhean, D. & Spudich, S. *Curr. Opin. Neurol.* **34**, 417–422 (2021).

[PubMed](#) [Article](#) [Google Scholar](#)

5. 5.

Andrews, M. G. *et al.* Preprint at bioRxiv
<https://doi.org/10.1101/2021.01.17.427024> (2021).

6. 6.

Crunfli, F. *et al.* Preprint at medRxiv
<https://doi.org/10.1101/2020.10.09.20207464> (2021).

7. 7.

Yang, A. C. *et al.* *Nature* <https://doi.org/10.1038/s41586-021-03710-0> (2021).

[Article](#) [Google Scholar](#)

8. 8.

Wang, L. *et al.* Preprint at bioRxiv
<https://doi.org/10.1101/2021.02.09.430349> (2021).

9. 9.

Hirunpattarasilp, C. *et al.* Preprint at bioRxiv
<https://doi.org/10.1101/2021.04.01.438122> (2021).

10. 10.

Prüss, H. *Nature Rev. Immunol.* <https://doi.org/10.1038/s41577-021-00543-w> (2021).

[PubMed](#) [Article](#) [Google Scholar](#)

11. 11.

Kreye, J. *et al.* *Cell* **183**, 1058–1069.e19 (2020).

[PubMed](#) [Article](#) [Google Scholar](#)

12. 12.

Franke, C. *et al.* *Brain Behav. Immun.* **93**, 415–419 (2021).

[PubMed](#) [Article](#) [Google Scholar](#)

[Download references](#)

Related Articles

-  [How COVID-19 can damage the brain](#)



- [COVID's toll on smell and taste: what scientists do and don't know](#)



- [The mini lungs and other organoids helping to beat COVID](#)



- [Autopsy slowdown hinders quest to determine how coronavirus kills](#)

Subjects

- [Diseases](#)
- [SARS-CoV-2](#)
- [Neuroscience](#)

nature careers

Jobs >

- [Instrument scientist at the permanent end station REMI@FLASH](#)

German Electron Synchrotron (DESY)

Hamburg, Germany

- [AUSBILDUNG: 3 Auszubildende \(d/m/w\) zum/zur Elektroniker*in für Geräte und Systeme](#)

Helmholtz Centre for Heavy Ion Research GmbH (GSI)

Darmstadt, Germany

- [AUSBILDUNG: 3 Auszubildende \(d/m/w\) zum/zur Anlagenmechaniker*in \(d/m/w\) für Sanitär-, Heizungs- und Klimatechnik](#)

Helmholtz Centre for Heavy Ion Research GmbH (GSI)

Darmstadt, Germany

- [AUSBILDUNG: 3 Auszubildende \(d/m/w\) zum/zur Elektroniker*in \(d/m/w\) für Betriebstechnik](#)

Helmholtz Centre for Heavy Ion Research GmbH (GSI)

Darmstadt, Germany

[Download PDF](#)

Related Articles

-  [How COVID-19 can damage the brain](#)
-  [COVID's toll on smell and taste: what scientists do and don't know](#)
-  [The mini lungs and other organoids helping to beat COVID](#)



- [Autopsy slowdown hinders quest to determine how coronavirus kills](#)

Subjects

- [Diseases](#)
- [SARS-CoV-2](#)
- [Neuroscience](#)

This article was downloaded by **calibre** from <https://www.nature.com/articles/d41586-021-01693-6>

| [Section menu](#) | [Main menu](#) |

- NEWS FEATURE
- 21 July 2021

Gun violence is surging — researchers finally have the money to ask why

With historically high levels of new funding, US gun-violence research is starting to find its footing.

- [Nidhi Subbaraman](#)

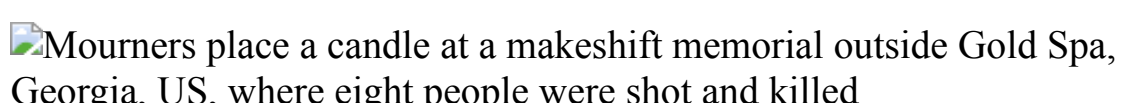
1. Nidhi Subbaraman
[View author publications](#)

You can also search for this author in [PubMed](#) [Google Scholar](#)





•



People light candles at a memorial to three women who were shot by a gunman at a spa in Atlanta, Georgia, in March. Credit: Chang W. Lee/NYT/Redux/eyevine

[Download PDF](#)

Maeve Wallace has studied maternal health in the United States for more than a decade, and a grim statistic haunts her. Five years ago, she published a study showing that being pregnant or recently having had a baby nearly

doubles a woman's risk of being killed¹. More than half of the homicides she tracked, using data from 37 states, were perpetrated with a gun.

In March 2020, she saw something she hadn't seen before: a funding opportunity from the US National Institutes of Health (NIH) to study deaths and injuries from gun violence. She had mentioned firearms in her studies before. But knowing that the topic is politically fraught, she often tucked related terms and findings deep within her papers and proposals. This time, she says, she felt emboldened to focus on guns specifically, and to ask whether policies that restrict firearms for people convicted of domestic violence would reduce the death rate for new and expecting mothers. Male partners are the killers in nearly half of homicides involving women in the United States. "This call for proposals really motivated me to ask the research questions that I may not have otherwise asked," says Wallace, an epidemiologist at Tulane University in New Orleans, Louisiana.

Wallace's group is one of several dozen funded by a new pool of federal money for gun-violence research in the United States, which has more firearm-related deaths than any other wealthy nation. Although other countries fund research on guns, it is often in the context of trafficking and armed conflict. US federal funding of gun-violence research has not reflected the death toll, researchers say.

The new money comes after more than two decades of what has essentially been a freeze on funding for the topic. And that's left a massive knowledge gap, says Asheley Van Ness, director of criminal justice at Arnold Ventures in New York City, a philanthropic organization that pledged US\$20 million to gun research in 2018, in part because of the paltry federal funding. "For decades we just have under-researched basic questions on gun violence," she says.



United States to fund gun-violence research after 20-year freeze

Spurred by advocacy that followed some high-profile school shootings, Congress has now authorized \$25 million for each of the past two years to go to the NIH and the US Centers for Disease Control and Prevention (CDC) for the study of gun violence as a public-health issue. In April, President Joe Biden suggested doubling that figure.

Although researchers were initially slow to answer the funding call, studies such as Wallace's are starting to look at how gun policies affect homicide rates. Others will investigate strategies to reduce suicides, which typically account for nearly two-thirds of gun deaths in the United States. And a handful of state health departments around the country are getting funding to collect better statistics on gun-related injuries.

The opening of the tap for federal dollars is considered an important advance, but those who have been watching the field for years say it will take more money and consistent investment to attract a committed cohort of researchers and fill in the data gaps. "That's like turning a ship," says David Studdert, who studies health law at Stanford Law School in California.

Meanwhile, gun violence in the United States shows no signs of slowing: [2020 emerged as the deadliest year in two decades](#), and the first few months of 2021 look even worse.



A young person holds a rifle at an annual meeting of the National Rifle Association in Dallas, Texas. Credit: Ashley Gilbertson/NYTRedux/eyevine

Control clause

Federal funds for firearms research have been heavily restricted ever since the 1996 Dickey Amendment, a clause added to that year's annual spending bill that barred the CDC from funding any effort that advocates or promotes gun control.

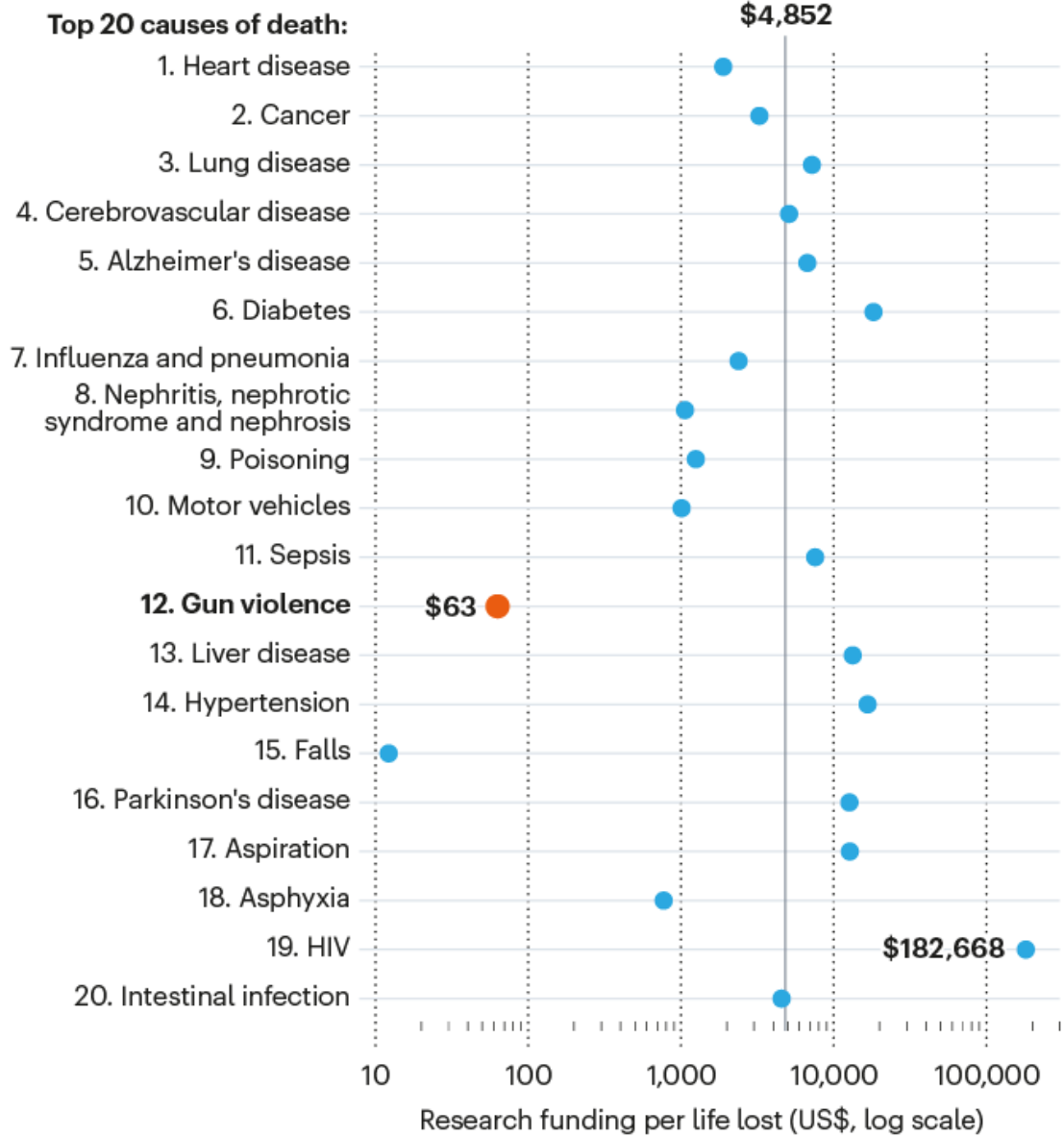
Although the amendment did not explicitly ban research on firearms, the CDC saw its budget cut by \$2.6 million in the year it passed — the same amount the agency was spending on the topic. CDC administrators saw the move as a message to steer clear, says Andrew Morral, a behavioural scientist at the Rand Corporation in Washington DC and director of the National Collaborative on Gun Violence Research, a consortium of foundations that fund firearms research.

The amendment remained in subsequent spending bills, and researchers who continued to work on gun violence say that their work received more scrutiny. “Any research we would put forward would create just a waterfall of backlash,” says Charles Branas, an epidemiologist at Columbia University’s Mailman School of Public Health in New York City. The gun lobby would argue that the work was biased, Branas says. Lawmakers would start asking questions. “That’s not something a cancer researcher has to contend with,” he says. “I think it scared off a lot of potential young scientists.”

The result has been an anaemic level of funding for research on one of the top 20 causes of mortality in the United States. One 2017 estimate² says that gun-violence research is funded at about \$63 per life lost, making it the second-most-neglected major cause of death, after falls (see ‘Dollars by death rate’). Private foundations have tried to fill the gap, but the levels are still low. The longest-running private funder, the Joyce Foundation in Chicago, Illinois, has invested \$32 million since 1993; its annual funding has surpassed \$2 million only once.

DOLLARS BY DEATH RATE

A 2017 estimate found that among the leading causes of death in the United States, gun violence was one of the least-funded areas of research.



©nature

Source: RAND/Ref. 2

Things began to change after 2012 when a gunman shot and killed 20 children and 6 staff, before killing himself, at Sandy Hook Elementary

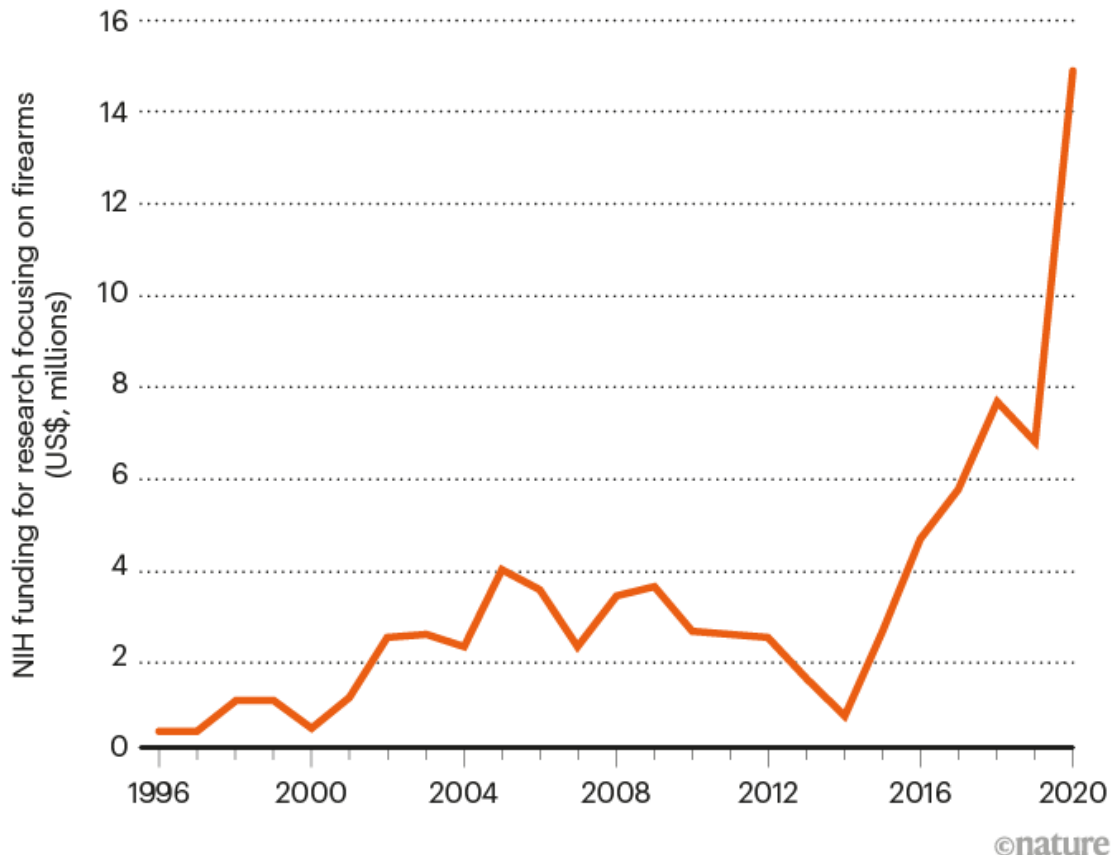
School in Newtown, Connecticut. Amid a raging political fight over gun control, then-president Barack Obama called on federal agencies to fund research on the topic, triggering a call for proposals at the NIH (but not at the CDC, where funding is more tightly controlled by congressional appropriations).

Sandy Hook set the stage for federal funding to open up, says Nina Vinik, a former programme director and now a consultant at the Joyce Foundation. Among the numerous efforts to push for gun policy, “advocates saw that the case for federal funding for research was just an easy one for people to understand and get behind”, she says.

Funding figures bear this out. According to data provided by the NIH, between 1996 and 2015 the agency spent just under \$2 million per year on average on research related to firearms. A new analysis by *Nature* estimates that the average more than tripled to just over \$6 million per year over the next four years (see ‘Gun-research funding in the United States’).

GUN-RESEARCH FUNDING IN THE UNITED STATES

Funding for gun-violence research from the US National Institutes of Health remained relatively meagre until a series of shootings a decade ago prompted calls for more resources. In 2020, Congress specifically allocated funds to study the topic.



Source: NIH Office of Extramural Research/*Nature* analysis using NIH RePORTER tool (go.nature.com/3WM3Q38)

Then, in February 2018, a shooter in Parkland, Florida, killed 17 people at the Marjory Stoneman Douglas High School, and injured 17 others before police arrested him. A national firestorm erupted over gun-control policies alongside renewed advocacy for research funding. The next month, lawmakers added language to the annual budget legislation that clarified the conundrum posed by the Dickey Amendment, stating that “the CDC has the authority to conduct research on the causes of gun violence”. Lawmakers

eventually authorized [dedicated funding in December 2019](#), giving \$12.5 million each to the CDC and the NIH specifically for gun-violence research. Congress approved a second round of funding for the 2021 fiscal year in December, and President Biden in his budget request for 2022 [asked for \\$50 million to go to the agencies](#).

Immediate impact

In March 2020, with the COVID-19 pandemic looming, the NIH put out a call for projects seeking to study public-health questions related to gun violence.

Wallace at Tulane was one of nine researchers funded through the mechanism. She says that her research on gun laws could have direct relevance to policy. Gathering evidence that rules in some states reduce deaths for pregnant people could persuade other states to enact similar measures. That would be huge, Wallace says, because it “identifies a policy that states can pass now and have an immediate impact”.

Lisa Wexler, a community-based participatory researcher at the University of Michigan in Ann Arbor, also answered the NIH’s funding call. She was looking for ways to involve families in her work to prevent suicides in rural Alaska. During the 1990s and 2000s, Wexler worked there as a mental-health counsellor and a community organizer, and saw the crisis faced by Alaska Native youth. Alaska’s Indigenous people are twice as likely to die by suicide as are non-native residents of the state, and it is the [leading cause of death for Alaska Native men under the age of 24](#).

She and her collaborators at the Maniilaq Association, an Alaska Native non-profit organization in Kotzebue that provides health services to Northwest Alaska residents, are laying the groundwork to test a new approach to gun safety. At health clinics, they will give people a brief talk about the need to safely store firearms at home, and offer them a lockable ammunition box or the option to have someone install a gun cabinet. “Making the environment safer is incredibly important, and it’s sort of an overlooked part of what we need to be doing for suicide prevention specifically in this country,” says Wexler. Past studies have shown that

limiting access to lethal means correlates with a decline in suicide rates^{3,4}. Wexler's programme, by involving all residents, acknowledges the Alaska Native values of community support and belonging — as well as the ubiquity and necessity of gun ownership in the region.



Los Angeles police ran a gun-buyback programme after an increase in shootings this year.Credit: Etienne Laurent/EPA-EFE/Shutterstock

“Hunting and fishing and gathering and living close to the land and animals and sea is still very deeply ingrained in the region here,” says Arlo Davis, Family Safety Net coordinator at the Maniilaq Association, who works with Wexler. “Our challenge is how do we do this research without shaming anybody — because most households have guns.”

Any shift in suicide trends will take some years to see, Wexler says, but she hopes such an approach will be one way to reduce the death toll.

Across the country in Philadelphia, implementation scientist Rinad Beidas at the University of Pennsylvania is testing whether routine paediatric visits can be an effective time to talk with new parents about gun safety. Like

Wexler, Beidas hopes to prevent suicides — the risk of death by suicide is higher when guns are easily accessible in a home. Her NIH-funded project will have paediatricians counselling parents about ways to limit gun access — for instance, by keeping firearms unloaded and locked away in their homes — alongside the conventional checklist of child-safety measures, including car seats and smoke alarms. Study volunteers will also receive locks for their guns from the programme. “Just like we made cars safer with seatbelts, we want to make homes safer around safe firearm storage,” she says.



[A murdered teen, two million tweets and an experiment to fight gun violence](#)

All told, the NIH disbursed about \$8.5 million to nine new proposals in 2020, short of the \$12.5 million authorized by Congress. The agency attributes the shortfall to the timing with the pandemic: “We did not receive as many applications to the [Funding Opportunity Announcement] as we would have liked,” a spokesperson for the NIH told *Nature* by e-mail. The agency applied the remaining money, plus another \$1.5 million, towards 12 other projects that included firearm research as an aspect of their proposal, for a total of about \$14 million.

Branas served on review committees evaluating research applications for both the NIH and the CDC, and says that, despite the low number of

applications specifically to the gun-research call, he was encouraged by the responses. “We felt like maybe there was some kind of pent-up interest in the topic, and people just didn’t have an outlet to apply.”

At the CDC, 18 research projects received just over \$8 million for multi-year studies. The CDC also spent \$2.2 million on an effort to gather data on emergency-room visits for non-fatal firearm injuries in ten states. The appropriation for this fiscal year will be used to fund the existing projects. “It was incredibly gratifying and important to receive this funding,” says James Mercy, director of the Division of Violence Prevention at the CDC’s Injury Center. “We’ve been operating for almost 25 years not being able to fully address the role of firearms in violence.”

Keeping momentum

It’s not yet clear whether the available funding levels will be sustained or expanded. One theme could be key to keeping bipartisan support for funding, says Mark Rosenberg, who led the CDC’s Injury Center at the time it was facing heat from Congress in 1996. In his view, more projects should be studying the impact that regulations have on those who own guns legally, because policy is often stymied by the perception that safety measures serve only to restrict rights. “I don’t know yet how to measure it effectively, but until you measure it, people will be free to say that any law impinges too much on the rights of law-abiding gun owners.”



The gun fighter

Some watchers are hopeful that the funding levels will increase, even if they don't hit Biden's target of \$50 million annually. "We've opened the door now and I don't see it closing," says Vinik. State governments seem to have momentum as well: lawmakers in California, New Jersey and Washington state, among others, have allocated funds for researching violence prevention and safety.

But what's still missing, researchers say, is federal support to tackle big, expensive, basic questions. For instance, nearly 40% of US households have a gun, and most people buying one say it's for protection. But the limited data that are available suggest that homes with guns are not safer, says Studdert. "That's a very fundamental disconnect between the admittedly somewhat modest science we have in this area, and the perspectives of most gun buyers in the United States."

Community organizations have for decades created and used violence-prevention techniques, but they have not been tested with field surveys. "Some of them probably work, some of them probably don't. But we need the research to identify the ones that work and the effective ingredients in those programmes," Morral says. "And that's expensive."

Morral and others think that more investment will be needed to fully address the public-health issue that guns present in the United States. An analysis commissioned by Arnold Ventures and the Joyce Foundation, published this month⁵, estimates that meeting public-health data collection and research needs on this topic will cost between \$587 million and \$639 million in federal funding over five years. That's a big gap. "Twenty-five million is a pittance," Branas says. "We need at least another zero at the end of that."

Nature **595**, 486–488 (2021)

doi: <https://doi.org/10.1038/d41586-021-01966-0>

References

1. 1.

Wallace, M. E., Hoyert, D., Williams, C. & Mendola, P. *Am. J. Obstet. Gynecol.* **215**, 364.e1–364.e10 (2016).

[Article](#) [Google Scholar](#)

2. 2.

Stark, D. E. & Shah, N. H. *JAMA* **317**, 84–85 (2017).

[PubMed](#) [Article](#) [Google Scholar](#)

3. 3.

Gunnell, D. *et al.* *Int. J. Epidemiol.* **36**, 1235–1242 (2007).

[PubMed](#) [Article](#) [Google Scholar](#)

4. 4.

Kreitman, N. *Br. J. Prev. Soc. Med.* **30**, 86–93 (1976).

[PubMed](#) [Google Scholar](#)

5. 5.

Health Management Associates. *Cost Estimate of Federal Funding for Gun Violence Research and Data Infrastructure* (HMA, 2021); available at <https://go.nature.com/3ztcjsf>

[Google Scholar](#)

[Download references](#)

Related Articles



- [United States to fund gun-violence research after 20-year freeze](#)



- [A murdered teen, two million tweets and an experiment to fight gun violence](#)



- [Fight the silencing of gun research](#)



- [The gun fighter](#)

Subjects

- [Public health](#)
- [Politics](#)

- [Human behaviour](#)

nature careers

[Jobs](#) >

- [Instrument scientist at the permanent end station REMI@FLASH](#)

German Electron Synchrotron (DESY)

Hamburg, Germany

- [AUSBILDUNG: 3 Auszubildende \(d/m/w\) zum/zur Elektroniker*in für Geräte und Systeme](#)

Helmholtz Centre for Heavy Ion Research GmbH (GSI)

Darmstadt, Germany

- [AUSBILDUNG: 3 Auszubildende \(d/m/w\) zum/zur Anlagenmechaniker*in \(d/m/w\) für Sanitär-, Heizungs- und Klimatechnik](#)

Helmholtz Centre for Heavy Ion Research GmbH (GSI)

Darmstadt, Germany

- [AUSBILDUNG: 3 Auszubildende \(d/m/w\) zum/zur Elektroniker*in \(d/m/w\) für Betriebstechnik](#)

Helmholtz Centre for Heavy Ion Research GmbH (GSI)

Darmstadt, Germany

[Download PDF](#)

Related Articles

-  [United States to fund gun-violence research after 20-year freeze](#)
-  [A murdered teen, two million tweets and an experiment to fight gun violence](#)
-  [Fight the silencing of gun research](#)
-  [The gun fighter](#)

Subjects

- [Public health](#)
- [Politics](#)
- [Human behaviour](#)

This article was downloaded by **calibre** from <https://www.nature.com/articles/d41586-021-01966-0>

Opinion

- **[Richard C. Lewontin \(1929–2021\)](#)** [13 July 2021]
Obituary • Pioneer of molecular evolution who campaigned against biological racism.
- **[Huge gaps in detection networks plague emissions monitoring](#)** [19 July 2021]
Comment • Plug gaps to measure ozone-destroying chemicals and greenhouse gases and verify compliance with Paris and Montreal treaties.
- **[ISSCR guidelines uphold human right to science for benefit of all](#)** [20 July 2021]
Correspondence •
- **[Six years as university rector changed how I do genetics](#)**
[20 July 2021]
Correspondence •
- **[Solar geoengineering research needs formal global debate](#)**
[20 July 2021]
Correspondence •
- **[Andes foothills protected by carbon-offset fund](#)** [20 July 2021]
Correspondence •

- OBITUARY
- 13 July 2021

Richard C. Lewontin (1929–2021)

Pioneer of molecular evolution who campaigned against biological racism.

- [Michael R. Dietrich](#) ⁰

1. [Michael R. Dietrich](#)

1. Michael R. Dietrich spent a sabbatical in Lewontin's laboratory in 1997. He has co-edited many books about iconoclastic biologists, and is a professor in the Department of History and Philosophy of Science at the University of Pittsburgh, Pennsylvania, USA.

[View author publications](#)

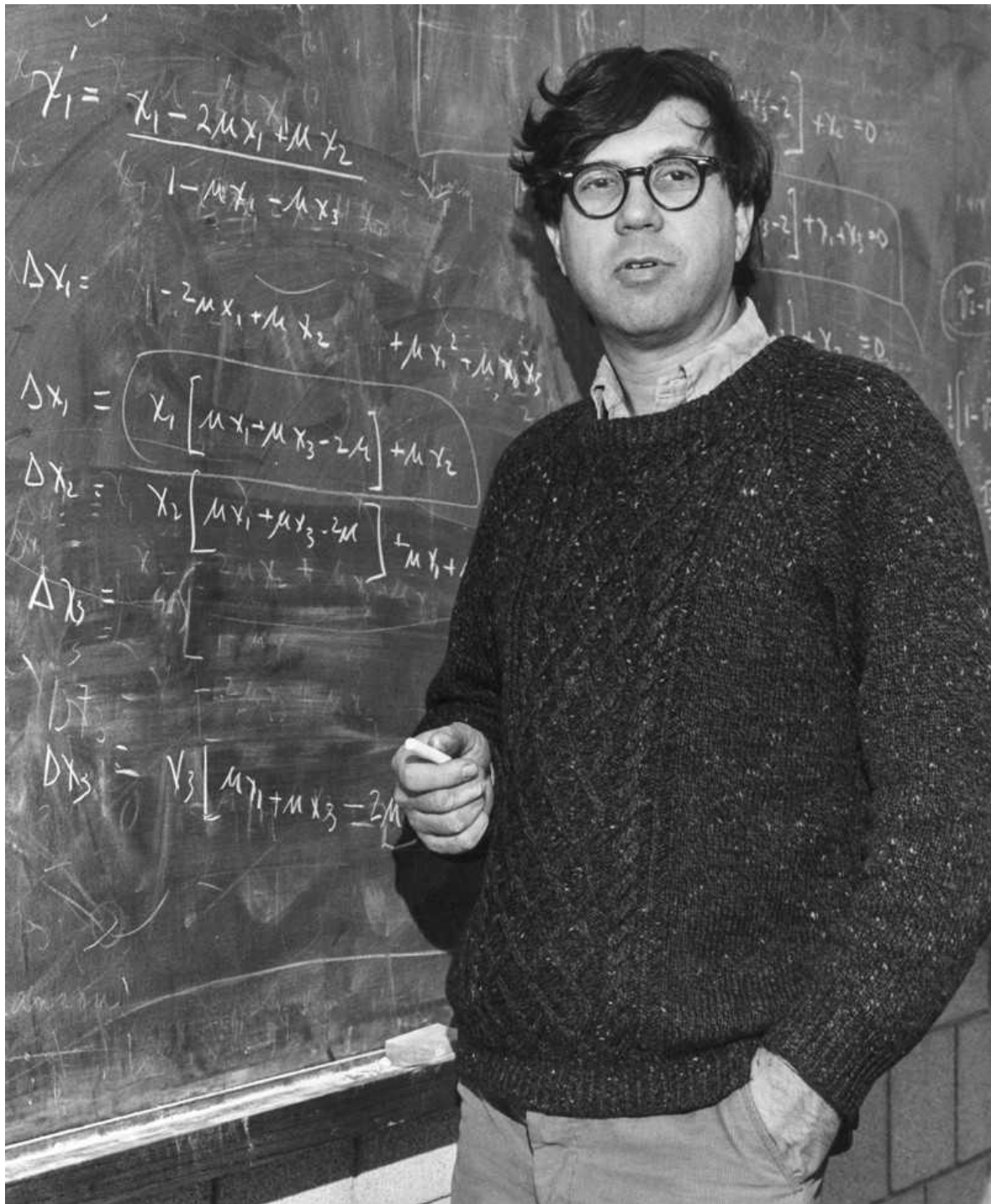
You can also search for this author in [PubMed](#) [Google Scholar](#)





•

[Download PDF](#)



Credit: Ernst Mayr Library and Archives of the Museum of Comparative Zoology, Harvard University

Richard Lewontin was a groundbreaking geneticist, best known for bringing molecular tools into evolutionary biology and for his advocacy against the

use of science to rationalize structural inequity. Lewontin and his collaborators revealed how natural selection acts to shape variation, exploring its effect on genes, groups and individuals. Moving between mathematical and statistical analysis, fieldwork and laboratory experiment, they set the course of molecular population genetics. Lewontin saw no place for his discipline in attempts to explain why “the children of oil magnates tend to become bankers, while the children of oil workers tend to be in debt to banks”.

Lewontin’s sometimes controversial critiques of science, often from a Marxist perspective, inspired new thinking on the relationship between science, politics and society. He was an [outspoken critic of sociobiology](#) and adaptationism (the idea that all traits evolved as adaptations of an organism to its environment). He despised the use of biology to justify racist ideology, especially with regard to IQ testing. His celebrated essay ‘The spandrels of San Marco and the Panglossian paradigm’, written with his colleague Stephen Jay Gould ([*Proc. R. Soc. Lond. B.* **205**, 581–598; 1979](#)) skewered, among other things, a “reliance upon plausibility alone as a criterion for accepting speculative tales”. Lewontin has died aged 92.

Richard Lewontin was born into an upper-middle-class Jewish family in New York City, and originally studied biology at Harvard University in Cambridge, Massachusetts, in the early 1950s. At the time, Harvard had no faculty member specializing in genetics, so Lewontin studied with a visitor, Leslie C. Dunn, from Columbia University in New York City. Dunn persuaded Lewontin to join the Columbia laboratory of Theodosius Dobzhansky, then the most influential evolutionary geneticist in the world. Lewontin adopted Dobzhansky’s investigation of the nature of selection and its impact on the variability of natural and laboratory populations. He completed his PhD in 1954.

That year, Lewontin joined the faculty at North Carolina State University in Raleigh. Here, he focused primarily on mathematical population genetics and worked with Ken-Ichi Kojima on genetic linkage, the tendency of neighbouring genetic sequences to be inherited together. After periods at the University of Rochester, New York, and the University of Chicago, Illinois, he spent the rest of his career at Harvard.

During his time at Rochester in the early 1960s, attempts to study genetic variation in natural populations were approaching an impasse. On a visit to the University of Chicago, Lewontin met Jack Hubby, who was adapting the biochemical technique of electrophoresis (which separates molecules by charge and size) to study the fruit fly *Drosophila*. They realized that detecting small differences between proteins could provide a new means of measuring genetic variability.

Lewontin moved to the University of Chicago and, with Hubby, published two landmark papers (*Genetics* 54, 577–594 and 595–609; 1966), which opened the way for the widespread application of electrophoresis and marked the beginning of molecular population genetics. These papers also revealed higher than expected amounts of genetic variability, addressing a long-standing dispute about whether natural selection maintains genetic variability in natural populations. In 1984, Martin Kreitman, working between Lewontin's and Walter Gilbert's laboratories at Harvard, brought DNA sequencing to bear on this question.

In Chicago in the 1960s, Lewontin became increasingly politically active, speaking out against racial discrimination, the Vietnam War and economic inequality. His fervent convictions led him to renounce his election to the US National Academy of Sciences, because of its support for secret war research. With ecologist Dick Levins and support from the Ford Foundation, he assembled a group to investigate the role of capital in agricultural research, such as the development of hybrid crop plants. Lewontin and Levins's collaboration also led to a series of essays on biology and society from a Marxist perspective, published later as *The Dialectical Biologist* (1985) and *Biology Under the Influence* (2007). Like his critiques of sociobiology, many of these essays treated science as politics, arguing against reductionism and determinism that favoured biological explanations of complex biosocial phenomena.

Lewontin also spoke up against biological racism. His landmark paper '[The Apportionment of Human Diversity](#)' (in *Evolutionary Biology* Vol. 6 (eds T. Dobzhansky *et al.*) Springer, 1972) found more variation within so-called 'racial groups' than between them, leading him to argue that such distinctions had no genetic basis. When biological arguments for race were again put forward in the context of mental testing in the 1980s, he opposed

them on scientific and social grounds, notably in *Not in Our Genes: Biology, Ideology, and Human Nature* (1984), co-authored with Steven Rose and Leon Kamin, and reissued in 2017 during the administration of US President Donald Trump. He continued to publish in this realm for decades.

Lewontin described himself as a pessimistic biologist. He was a profoundly critical thinker, willing to challenge the scientific and philosophical foundations of his discipline as well as their social, cultural and political consequences. His research and reflections set an agenda for generations of biologists, philosophers of biology and socially engaged scholars.

In keeping with his socialism, he disliked biography and its celebration of the individual. When, in 1997, I asked him how I should write about his life, he pulled out of his desk a list of every graduate student, postdoc and visitor at his laboratory — more than 100 people — and said I should write about all of them. They were his greatest source of pride as a scientist.

Nature **595**, 489 (2021)

doi: <https://doi.org/10.1038/d41586-021-01936-6>

Competing Interests

The author declares no competing interests.

Related Articles

-  [**Genetics: Under the skin**](#)

-  [**Racism in science: the taint that lingers**](#)



- [Genetic determinism rides again](#)



- [Nature still battles nurture in the haunting world of social genomics](#)



- [Manfred Eigen \(1927–2019\)](#)

Subjects

- [Genetics](#)
- [Evolution](#)
- [History](#)
- [Society](#)

nature careers

[Jobs](#) >

- [Instrument scientist at the permanent end station REMI@FLASH](#)

German Electron Synchrotron (DESY)

Hamburg, Germany

- [AUSBILDUNG: 3 Auszubildende \(d/m/w\) zum/zur Elektroniker*in für Geräte und Systeme](#)

Helmholtz Centre for Heavy Ion Research GmbH (GSI)

Darmstadt, Germany

- [AUSBILDUNG: 3 Auszubildende \(d/m/w\) zum/zur Anlagenmechaniker*in \(d/m/w\) für Sanitär-, Heizungs- und Klimatechnik](#)

Helmholtz Centre for Heavy Ion Research GmbH (GSI)

Darmstadt, Germany

- [AUSBILDUNG: 3 Auszubildende \(d/m/w\) zum/zur Elektroniker*in \(d/m/w\) für Betriebstechnik](#)

Helmholtz Centre for Heavy Ion Research GmbH (GSI)

Darmstadt, Germany

[Download PDF](#)

Related Articles



- [Genetics: Under the skin](#)



- [Racism in science: the taint that lingers](#)



- [Genetic determinism rides again](#)



- [Nature still battles nurture in the haunting world of social genomics](#)



- [Manfred Eigen \(1927–2019\)](#)

Subjects

- [Genetics](#)
- [Evolution](#)
- [History](#)
- [Society](#)

This article was downloaded by **calibre** from <https://www.nature.com/articles/d41586-021-01936-6>

| [Section menu](#) | [Main menu](#) |

- COMMENT
- 19 July 2021

Huge gaps in detection networks plague emissions monitoring

Plug gaps to measure ozone-destroying chemicals and greenhouse gases and verify compliance with Paris and Montreal treaties.

- [Ray F. Weiss](#) ⁰,
- [A. R. Ravishankara](#) ¹ &
- [Paul A. Newman](#) ²

1. [Ray F. Weiss](#)

1. Ray F. Weiss is an analytical atmospheric chemist and distinguished professor emeritus at the Scripps Institution of Oceanography, University of California, San Diego, USA.

[View author publications](#)

You can also search for this author in [PubMed](#) [Google Scholar](#)

2. [A. R. Ravishankara](#)

1. A. R. Ravishankara is an atmospheric chemist and university distinguished professor at Colorado State University in Fort Collins, USA.

[View author publications](#)

You can also search for this author in [PubMed](#) [Google Scholar](#)

3. [Paul A. Newman](#)

1. Paul A. Newman is the chief scientist for Earth sciences at the NASA Goddard Space Flight Center in Greenbelt, Maryland, USA.

[View author publications](#)

You can also search for this author in [PubMed](#) [Google Scholar](#)





•

[Download PDF](#)



Air conditioners (such as these units in New Delhi) proliferate as nations develop, releasing ozone-depleting and greenhouse gases. Credit: Biplov Bhuyan/*Hindustan Times* via Getty

In the decades after the 1987 Montreal Protocol, it seemed everything was on track to restore Earth's protective stratospheric ozone layer. Then, in 2018, came an alarming discovery: fresh emissions of the forbidden chlorofluorocarbon-11 (CFC-11), which destroys the ozone layer. Its production and use had been banned globally in 2010.

It was a wake-up call. But this surprise will not be the last unless something is done soon to improve the monitoring of other gases that destroy the ozone layer and cause climate change.

The Montreal Protocol has been hailed as a shining example of a successful treaty: it was universally ratified. Yet, as the CFC-11 incident showed, even the best treaties cannot be upheld, or the best regulations enforced, if compliance by individual parties cannot be assured. Many local and regional air-quality policies have failed to live up to their goals for this reason.

Corrective action requires knowing what is being emitted, how much and where.

The trick is to ‘trust but verify’, as is often said of nuclear disarmament. This tenet is the basis of the successful Comprehensive Nuclear-Test-Ban Treaty, which oversees the measurement and tracing of diagnostic radionuclides and isotopes in the atmosphere in key regions worldwide. Ensuring the health of our planet is as crucial as nuclear security.



[Chemists can help to solve the air-pollution health crisis](#)

Many of today’s environmental treaties rely on ‘bottom-up’ reporting. The Montreal Protocol depends on national accounting of production and consumption of chlorofluorocarbons and other halogenated gases. Of course, illegal or spurious production and emissions are not reported, as in the CFC-11 example. And what happens to the atmosphere, in the end, depends on actual emissions. Furthermore, products made in one place could eventually generate emissions elsewhere. So country-by-country reporting is an incomplete and potentially unreliable way to track emissions locally and regionally. Similarly, the Paris agreement relies on countries quantifying their own greenhouse-gas emissions.

Fortunately, emissions are also mapped and tallied ‘top-down’. Satellites and global monitoring stations give an overall picture of the abundances of gases

that persist in the atmosphere. Such global monitoring can quantify mismatches between the total reported and what is accumulating in the atmosphere. But specific sources are difficult to zero-in on from space.

To take action at national or regional levels, ground-based observations are needed. Networks of such stations exist, but there are huge holes in coverage, notably in low- and middle-income regions, where emissions are likely to rise as countries develop. These monitoring gaps must be filled urgently.

Detective work

Satellite and global monitoring measurements have confirmed that the Montreal Protocol has generally worked exceptionally well for decades. Atmospheric levels of chlorofluorocarbons (CFCs) have decreased since they peaked in 1993¹.

But in 2018, researchers reported that the fall in atmospheric concentrations of CFC-11 started to slow in 2012². At the same time, South Korean and Japanese air-monitoring stations in the East China Sea were detecting raised levels of the gas. Models of atmospheric transport then showed that most of the new emissions detected globally were coming from eastern China³.

An investigation by *The New York Times* determined a key source of these emissions. It was the production of polyurethane foam insulation in China, ironically driven, in part, by pressures to improve building insulation to reduce energy consumption for heating and cooling⁴⁻⁶. Ongoing atmospheric monitoring has shown that these emissions have now largely ceased, both globally⁷ and in eastern China⁸.

This was great detective work. But it relied on a lucky coincidence: that the emissions came from regions upwind of monitoring stations that collect data frequently.

It is unlikely that this will be the case next time.



The Mount Mugogo gas observing station in Rwanda is the only new station to be established in the past five years. Credit: Ministry of Education (MINEDUC) of Rwanda

Keeping watch

Several observational networks currently measure the distributions and trends of atmospheric gases that deplete the ozone layer and warm the planet. They include ground-based international collaborations such as the Network for the Detection of Atmospheric Composition Change (NDACC), which uses remote optical sensors to gather information on global changes in gas concentrations. There are also aircraft-based measurement programmes. Some use civil aviation and some are government-sponsored; these can identify local emissions but are sporadic.

Satellites can track the evolution of CFC-11 and other long-lived substances in the stratosphere. They can also help in identifying local emissions of abundant greenhouse gases, including carbon dioxide and methane. But they cannot measure with sufficient sensitivity many other harmful gases close to the surface. Also, satellites pass by only periodically, and cannot see through clouds.

At present, the most precise and accurate way to quantify regional emissions is from the ground.

The main networks for such high-frequency measurements are operated by the Advanced Global Atmospheric Gases Experiment (AGAGE) international consortium, and by the US National Oceanographic and Atmospheric Administration (NOAA). These were key to discovering and mapping the unexpected CFC-11 emissions.

Such networks can be highly informative. Stations that use automated mass-spectrometry and optical technologies can now measure precise concentrations of more than 50 gases (see ‘Gas watch’) hourly or even more frequently. Alternatively, air samples can be collected in flasks and sent to central laboratories for analysis.

Gas watch

Stations on the ground monitor more than 50 gases ranging in concentrations from parts per million to parts per trillion. These include:

Carbon dioxide (CO₂). The most abundant and long-lived greenhouse gas.

Methane (CH₄). A short-lived and potent greenhouse gas.

Nitrous oxide (N₂O). A long-lived ozone-depleting substance and greenhouse gas.

Chlorofluorocarbons (CFCs). Ozone-depleting industrial chemicals and greenhouse gases that have been phased out under the Montreal Protocol.

Hydrochlorofluorocarbons (HCFCs). Milder, ozone-depleting industrial chemicals that replaced CFCs; now also being phased out.

Hydrofluorocarbons (HFCs). Industrial chemicals that replaced CFCs and HCFCs. They do not deplete the ozone layer, but many are potent greenhouse gases.

Fully fluorinated carbon, sulfur and nitrogen gases. The most-potent and longest-lived greenhouse gases, they are emitted from high-tech industries.

Halons. Bromine-bearing industrial gases that are among the most potent ozone-depleting substances. They have largely been phased out under the Montreal Protocol.

Chlorocarbons and bromocarbons. A wide range of natural and anthropogenic ozone-depleting compounds containing chlorine or bromine.

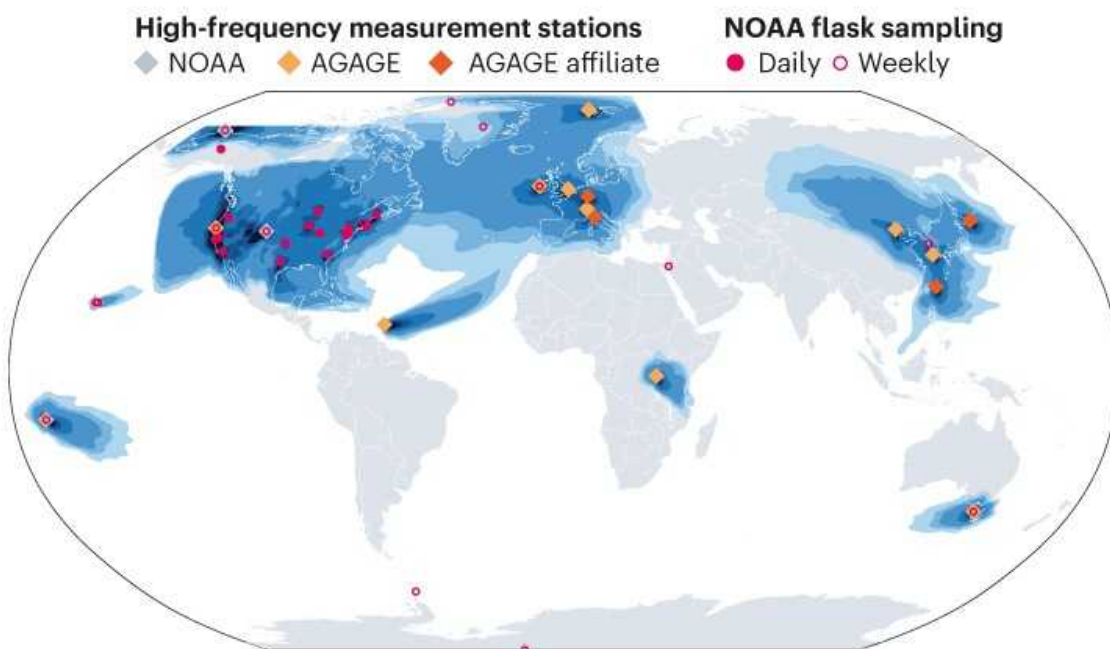
Observing stations are typically sensitive to emissions that occur within about 2,000 kilometres of them, as long as they are not overwhelmed by local pollution. Models that incorporate patterns of air movement, weather and variations in measured gas concentrations can then trace the emissions back to their source areas. By integrating these models over time, emissions

can be mapped and quantified across a ‘footprint’ area for each station. That is what happened in the case of the CFC-11 emissions from eastern China^{3,8}.

The problem is that there are vast blind spots. The AGAGE and NOAA stations (see ‘Gaps in emissions tracking’)⁹ cover large parts of the developed world. Potential emissions are relatively well sampled from areas such as eastern Asia, central North America and western Europe. Not covered are southern, western and central Asia, eastern Europe, all of South America, portions of North America, large parts of southeast Asia, Australia and New Zealand and most of Africa. It is in many of these regions that emissions are expected to increase with industrial and economic development.

GAPS IN EMISSIONS TRACKING

Networks of measurement stations and sampling sites can detect and quantify regional emissions of gases that deplete stratospheric ozone and warm the planet (darker blues show greater sensitivity). More sites are needed to cover most of Asia, Eastern Europe, South America, Australia and New Zealand, parts of North America and the majority of Africa.



Insufficient data are available to model air transport around the South Pole, central Alaska and parts of the Beaufort Sea.

Nature publications remain neutral with regard to contested jurisdictional claims in published maps.
AGAGE, Advanced Global Atmospheric Gases Experiment.
NOAA, National Oceanic and Atmospheric Administration.

©nature

Source: Ref. 9 and Courtesy of Luke Western, Univ. Bristol & Alistair Manning, UK Met Office

To date, expansions of AGAGE, NOAA and other ground-based observational networks have been largely ad hoc. They have been driven by a combination of individual investigators' scientific interests and needs, the funding interests and policy priorities of host and supporting entities and the availability of the necessary infrastructures and logistical support. Most stations are decades old. Just one new station has been established in the past five years, in Rwanda.

To meet the needs of the Montreal Protocol or the Paris agreement, the world needs a more systematic, coordinated international approach to building more stations. The United Nations Environment Programme, whose Ozone Secretariat is responsible for the Montreal Protocol, is a potential coordinator for such an effort for the substances that lie in its domain. The United Nations Framework Convention on Climate Change and the World Meteorological Organization could also have significant roles, particularly for emissions of potent synthetic greenhouse gases (such as fluorinated gases), which are covered by the Paris agreement.

New stations would ideally be sited downwind of emissions regions and away from polluted urban sites. To determine whether a proposed site is suitable, researchers can use Observing System Simulation Experiments. These model seasonal and annual variabilities in atmospheric transport patterns. Instruments capable of making high-frequency measurements are most useful when operated continuously in one place for a long time.



[Build a global Earth observatory](#)

Flask sampling can be used to augment coverage in areas of interest. Flask samples measured in central laboratories can also spot and correct systemic biases between different stations or programmes. Rigorous calibration, validation and standardized techniques are all needed to produce high-quality data for scientific analysis and policy. Most importantly, these data and their interpretive algorithms must be openly available for use by policymakers, regulators and the public, as is the case with the AGAGE and NOAA networks.

We estimate that adding approximately two dozen well-chosen stations to the existing networks would provide good regional coverage around the globe. The stations would monitor emissions inside their national borders, and those in neighbouring countries. This would build international confidence in the global network.

Money well spent

What would two dozen more stations cost? About US\$35 million to establish, plus \$4 million to \$5 million per year of operation. We estimate that it takes around \$1 million to establish a high-frequency measurement station, plus about \$400,000 for the instrumentation and ancillary

equipment. Annual operating costs are around \$200,000 per station, depending greatly on personnel costs. A philanthropic organization could, in theory, fund such a programme and thus also ensure its independence from national bias.

Compared with what is at stake, this price tag is minimal. Because many deployments would probably be in low- or middle-income countries, they would also build scientific capacity there. This could help to form a foundation to expand other observational and modelling capabilities in these regions, including those related to climate.

The 80 atmospheric observation stations of the Comprehensive Nuclear-Test-Ban Treaty have successfully monitored the world and warned of nuclear releases for decades. A similar network to measure and model regional emissions of a broad range of dangerous gases is crucial to responsible environmental policy and stewardship.

We cannot manage what we cannot measure. An investment in more ground-based, high-frequency monitoring stations will pay great dividends in the long run. It is a must for ensuring accountability under the Montreal and Paris treaties.

Nature **595**, 491-493 (2021)

doi: <https://doi.org/10.1038/d41586-021-01967-z>

References

1. 1.

World Meteorological Organization. *Scientific Assessment of Ozone Depletion: 2018, Global Ozone Research and Monitoring Project* (WMO, 2018).

[Google Scholar](#)

2. 2.

Montzka, S. A. *et al.* *Nature* **557**, 413–417 (2018).

[PubMed](#) [Article](#) [Google Scholar](#)

3. 3.

Rigby, M. *et al.* *Nature* **569**, 546–550 (2019).

[PubMed](#) [Article](#) [Google Scholar](#)

4. 4.

Buckley, C. & Fountain, H. ‘In a high-stakes environmental whodunit, many clues point to China’ *The New York Times* (24 June 2018).

5. 5.

Buckley, C. ‘More evidence points to China as source of ozone-depleting gas’ *The New York Times* (3 November 2018).

6. 6.

Cyranoski, D. *Nature* **571**, 309–310 (2019).

[PubMed](#) [Article](#) [Google Scholar](#)

7. 7.

Montzka, S. A. *et al.* *Nature* **590**, 428–432 (2021).

[PubMed](#) [Article](#) [Google Scholar](#)

8. 8.

Park, S. *et al.* *Nature* **590**, 433–437 (2021).

[PubMed](#) [Article](#) [Google Scholar](#)

9. 9.

United Nations Environment Programme. *Closing the Gaps in Top-down Regional Emissions Quantification: Needs and Action Plan* (UNEP, 2021).

[Google Scholar](#)

[Download references](#)

Competing Interests

R.F.W. is a participant in the AGAGE project.

Related Articles



- [**Build a global Earth observatory**](#)



- [**Chemists can help to solve the air-pollution health crisis**](#)



- [**Track urban emissions on a human scale**](#)



- [**Validate personal air-pollution sensors**](#)



- [Track climate pledges of cities and companies](#)



- [Paul J. Crutzen \(1933–2021\)](#)



- [Mario Molina \(1943–2020\)](#)

Subjects

- [Climate change](#)
- [Policy](#)
- [Environmental sciences](#)

nature careers

[Jobs](#) >

- [Instrument scientist at the permanent end station REMI@FLASH](#)

German Electron Synchrotron (DESY)

Hamburg, Germany

- [AUSBILDUNG: 3 Auszubildende \(d/m/w\) zum/zur Elektroniker*in für Geräte und Systeme](#)

Helmholtz Centre for Heavy Ion Research GmbH (GSI)

Darmstadt, Germany

- **AUSBILDUNG: 3 Auszubildende (d/m/w) zum/zur Anlagenmechaniker*in (d/m/w) für Sanitär-, Heizungs- und Klimatechnik**

Helmholtz Centre for Heavy Ion Research GmbH (GSI)

Darmstadt, Germany

- **AUSBILDUNG: 3 Auszubildende (d/m/w) zum/zur Elektroniker*in (d/m/w) für Betriebstechnik**

Helmholtz Centre for Heavy Ion Research GmbH (GSI)

Darmstadt, Germany

[Download PDF](#)

Related Articles



- [**Build a global Earth observatory**](#)



- [**Chemists can help to solve the air-pollution health crisis**](#)



- [**Track urban emissions on a human scale**](#)



- [**Validate personal air-pollution sensors**](#)



- [Track climate pledges of cities and companies](#)



- [Paul J. Crutzen \(1933–2021\)](#)



- [Mario Molina \(1943–2020\)](#)

Subjects

- [Climate change](#)
- [Policy](#)
- [Environmental sciences](#)

This article was downloaded by **calibre** from <https://www.nature.com/articles/d41586-021-01967-z>

- CORRESPONDENCE
- 20 July 2021

ISSCR guidelines uphold human right to science for benefit of all

- [Zubin Master](#)⁰,
- [Robin Lovell-Badge](#)¹ &
- [Bartha Knoppers](#)²

1. [Zubin Master](#)

1. Mayo Clinic, Minnesota, USA.

[View author publications](#)

You can also search for this author in [PubMed](#) [Google Scholar](#)

2. Robin Lovell-Badge

1. The Francis Crick Institute, London, UK.

[View author publications](#)

You can also search for this author in [PubMed](#) [Google Scholar](#)

3. Bartha Knoppers

1. McGill University, Quebec, Canada.

[View author publications](#)

You can also search for this author in [PubMed](#) [Google Scholar](#)





•

[Download PDF](#)

The International Society for Stem Cell Research (ISSCR) guidelines replace the 14-day limit on embryo research with case-by-case review (see go.nature.com/3gf1kw8). Some scientists, ethicists and lawyers advocate keeping the limit (or a substitute). They contend that it avoids ethical and political minefields, boosts public confidence and minimizes confusion (see [J. Johnston et al. *Nature* 594, 495 \(2021\)](https://www.nature.com/articles/nature594495); [R. M. Green et al. *Nature* 594, 333; 2021](https://www.nature.com/articles/nature594333)). In our view, the 14-day limit fails to uphold the human right to benefit from science.

This right was first recognized in the 1948 [Universal Declaration of Human Rights](#): “everyone has the right freely... to share in scientific advancement and its benefits”. According to the [International Covenant on Economic, Social and Cultural Rights](#), limitations must be “determined by law” and “solely for the purpose of promoting the general welfare in a democratic society”.

We maintain that the ISSCR guidelines respect this right: it is to everyone’s benefit to increase knowledge, identify the causes of miscarriage and congenital abnormalities and improve infertility treatments (see also [A. Boggio et al. CRISPR J. 2, 134–142; 2019](#)). Removal of a time limit ensures greater public debate on the governance of embryo research.

Nature **595**, 494 (2021)

doi: <https://doi.org/10.1038/d41586-021-01959-z>

Competing Interests

R.L-B. was Chair of ISSCR’s Task Force to Update the Guidelines. Z.M. and R.L-B serve on ISSCR’s Public Policy Committee and Z.M. is an ISSCR Goldstein Science Policy Fellow and Education Committee member.

Related Articles

- [See more letters to the editor](#)

Subjects

- [Stem cells](#)
- [Research management](#)
- [Society](#)

nature careers

[Jobs](#) >

- [**Instrument scientist at the permanent end station REMI@FLASH**](#)

German Electron Synchrotron (DESY)

Hamburg, Germany

- [**AUSBILDUNG: 3 Auszubildende \(d/m/w\) zum/zur Elektroniker*in für Geräte und Systeme**](#)

Helmholtz Centre for Heavy Ion Research GmbH (GSI)

Darmstadt, Germany

- [**AUSBILDUNG: 3 Auszubildende \(d/m/w\) zum/zur Anlagenmechaniker*in \(d/m/w\) für Sanitär-, Heizungs- und Klimatechnik**](#)

Helmholtz Centre for Heavy Ion Research GmbH (GSI)

Darmstadt, Germany

- [**AUSBILDUNG: 3 Auszubildende \(d/m/w\) zum/zur Elektroniker*in \(d/m/w\) für Betriebstechnik**](#)

Helmholtz Centre for Heavy Ion Research GmbH (GSI)

Darmstadt, Germany

[Download PDF](#)

Related Articles

- [**See more letters to the editor**](#)

Subjects

- [Stem cells](#)
 - [Research management](#)
 - [Society](#)
-

This article was downloaded by **calibre** from <https://www.nature.com/articles/d41586-021-01959-z>

| [Section menu](#) | [Main menu](#) |

- CORRESPONDENCE
- 20 July 2021

Six years as university rector changed how I do genetics

- [Giuseppe Novelli](#) ORCID: <http://orcid.org/0000-0002-7781-602X> 0
 1. [Giuseppe Novelli](#)
 1. University of Rome Tor Vergata, Italy.

[View author publications](#)

You can also search for this author in [PubMed](#) [Google Scholar](#)





•

[Download PDF](#)

There is a belief in academia that it is difficult, even impossible, to return to research after taking on administrative responsibility. That has not been my experience.

After six years as rector of the University of Rome Tor Vergata — intense years, filled with passion and sacrifice — I returned to my laboratory of medical genetics in late 2019. I went from coordinating an institution of 30,000 students and 2,400 faculty members and staff, with an annual budget of 300 million (US\$356 million), and signing contracts with institutions all

over the world, to designing experiments, writing grants and publishing numerous papers during the tough first year of the pandemic.

The relationships and alliances made during my years as rector opened my mind. Back at the bench, I found myself more efficient and motivated, more keen to collaborate with scientists from different disciplines and more deft in negotiation with funders. My lab joined the COVID Human Genetic Effort consortium (www.covidhge.com) to work on the bases of SARS-CoV-2 infection. Having overseen so many different research groups made it easier to integrate into a consortium of hundreds.

The administrative experience was a great help, not a hindrance. It taught me to look at the science more broadly. Complex challenges, such as those we face today, require lab heads and bureaucrats to work together to build a more sustainable future that leaves no one behind.

Nature **595**, 494 (2021)

doi: <https://doi.org/10.1038/d41586-021-01960-6>

Competing Interests

The author declares no competing interests.

Related Articles



- [**Research managers are essential to a healthy research culture**](#)
- [**See more letters to the editor**](#)

Subjects

- [**Research management**](#)

- [Careers](#)
- [Lab life](#)

nature careers

[Jobs](#) >

- [Instrument scientist at the permanent end station REMI@FLASH](#)

German Electron Synchrotron (DESY)

Hamburg, Germany

- [AUSBILDUNG: 3 Auszubildende \(d/m/w\) zum/zur Elektroniker*in für Geräte und Systeme](#)

Helmholtz Centre for Heavy Ion Research GmbH (GSI)

Darmstadt, Germany

- [AUSBILDUNG: 3 Auszubildende \(d/m/w\) zum/zur Anlagenmechaniker*in \(d/m/w\) für Sanitär-, Heizungs- und Klimatechnik](#)

Helmholtz Centre for Heavy Ion Research GmbH (GSI)

Darmstadt, Germany

- [AUSBILDUNG: 3 Auszubildende \(d/m/w\) zum/zur Elektroniker*in \(d/m/w\) für Betriebstechnik](#)

Helmholtz Centre for Heavy Ion Research GmbH (GSI)

Darmstadt, Germany

[Download PDF](#)

Related Articles



- [Research managers are essential to a healthy research culture](#)
- [See more letters to the editor](#)

Subjects

- [Research management](#)
- [Careers](#)
- [Lab life](#)

This article was downloaded by **calibre** from <https://www.nature.com/articles/d41586-021-01960-6>

| [Section menu](#) | [Main menu](#) |

- CORRESPONDENCE
- 20 July 2021

Solar geoengineering research needs formal global debate

- [Janos Pasztor](#) 0

1. [Janos Pasztor](#)

1. Carnegie Climate Governance Initiative, Geneva, Switzerland.

[View author publications](#)

You can also search for this author in [PubMed](#) [Google Scholar](#)





•

[Download PDF](#)

It is true that solar radiation modification (SRM) would require effective global governance that currently does not exist (see [F. Biermann *Nature* 595, 30; 2021](#)). It is for precisely this reason that meaningful conversations at the global level are needed on how, if at all, such frameworks could be put in place; if and how research might be governed; and whether or not SRM should be used. Silencing all formal debate piles risk upon risk, in my view.

SRM is not a substitute for mitigation. At best, it could supplement those efforts while temporarily cooling the planet — and possibly staving off potential planetary tipping points. The longer we take to radically slash emissions, the greater the possibility that the world might need to consider SRM. Of course, SRM would also generate new risks. There are no risk-free options. We need to weigh the risks of our present paths with those from the potential use of SRM.

The world needs a forum — such as the United Nations — where all voices and views can be expressed. There, the world should debate, and then it could decide on a moratorium on further research, or it could do the opposite. We need these conversations now.

The longer we delay, the greater the risk of hasty, ungoverned actions or decisions.

Nature **595**, 494 (2021)

doi: <https://doi.org/10.1038/d41586-021-01957-1>

Competing Interests

J.P. is executive director of the Carnegie Climate Governance Initiative, whose main mission is to address issues related to the governance of solar radiation modification. The content and eventual publication of this article, however, present no competing interests — neither financial nor any other.

Related Articles

- [See more letters to the editor](#)

Subjects

- [Climate change](#)
- [Society](#)
- [Policy](#)

Jobs >

- [**Instrument scientist at the permanent end station REMI@FLASH**](#)

German Electron Synchrotron (DESY)

Hamburg, Germany

- [**AUSBILDUNG: 3 Auszubildende \(d/m/w\) zum/zur Elektroniker*in für Geräte und Systeme**](#)

Helmholtz Centre for Heavy Ion Research GmbH (GSI)

Darmstadt, Germany

- [**AUSBILDUNG: 3 Auszubildende \(d/m/w\) zum/zur Anlagenmechaniker*in \(d/m/w\) für Sanitär-, Heizungs- und Klimatechnik**](#)

Helmholtz Centre for Heavy Ion Research GmbH (GSI)

Darmstadt, Germany

- [**AUSBILDUNG: 3 Auszubildende \(d/m/w\) zum/zur Elektroniker*in \(d/m/w\) für Betriebstechnik**](#)

Helmholtz Centre for Heavy Ion Research GmbH (GSI)

Darmstadt, Germany

[Download PDF](#)

Related Articles

- [See more letters to the editor](#)

Subjects

- [Climate change](#)
- [Society](#)
- [Policy](#)

This article was downloaded by **calibre** from <https://www.nature.com/articles/d41586-021-01957-1>

| [Section menu](#) | [Main menu](#) |

- CORRESPONDENCE
- 20 July 2021

Andes foothills protected by carbon-offset fund

- [Evert Thomas](#)⁰,
- [Marleni Ramirez](#)¹,
- [Lily Rodriguez](#)² &
- [Manuel Glave](#)³

1. [Evert Thomas](#)

1. CIMA Cordillera Azul, Lima, Peru

[View author publications](#)

You can also search for this author in [PubMed](#) [Google Scholar](#)

2. Marleni Ramirez

1. CIMA Cordillera Azul, Lima, Peru

[View author publications](#)

You can also search for this author in [PubMed](#) [Google Scholar](#)

3. Lily Rodriguez

1. CIMA Cordillera Azul, Lima, Peru

[View author publications](#)

You can also search for this author in [PubMed](#) [Google Scholar](#)

4. Manuel Glave

1. CIMA Cordillera Azul, Lima, Peru

[View author publications](#)

You can also search for this author in [PubMed](#) [Google Scholar](#)

•



•

[Download PDF](#)

At its creation in 2008, the United Nations REDD ('reducing emissions from degradation and deforestation') programme was hailed as a way to finance conservation with tools such as carbon offsets. Thirteen years on, little of that promise has been realized. A REDD transaction signed in March for the Cordillera Azul National Park, in the foothills of the Andes in Peru, offers hope.

The deal will support the conservation in perpetuity of the 13,500-square-kilometre park and its rich and pristine biodiversity. A trust fund to cover

all expenses is being set up by the non-governmental organization CIMA Cordillera Azul, which manages the park, and the Peruvian Service for Natural Protected Areas.

Investments in sustainable livelihoods will strengthen efforts to curb and reverse deforestation in the 23,000-km² buffer zone around the park — home to more than 300,000 people. Notably, they will boost development of sustainable products from forest restoration and agroforestry. For example, CIMA has built a cacao-processing plant to promote cacao agroforestry as an alternative to land use that relies on deforestation.

To our knowledge, this is the first REDD transaction to ensure that all conservation costs for a national park of this size are financed by private-sector carbon-credit sales, with minimal transaction costs. Similar deals around the globe could help to catalyse the carbon market.

Nature **595**, 494 (2021)

doi: <https://doi.org/10.1038/d41586-021-01958-0>

Competing Interests

The authors declare no competing interests.

Related Articles

- [See more letters to the editor](#)

Subjects

- [Conservation biology](#)
- [Climate change](#)
- [Environmental sciences](#)
- [Sustainability](#)

Jobs >

- [**Instrument scientist at the permanent end station REMI@FLASH**](#)

German Electron Synchrotron (DESY)

Hamburg, Germany

- [**AUSBILDUNG: 3 Auszubildende \(d/m/w\) zum/zur Elektroniker*in für Geräte und Systeme**](#)

Helmholtz Centre for Heavy Ion Research GmbH (GSI)

Darmstadt, Germany

- [**AUSBILDUNG: 3 Auszubildende \(d/m/w\) zum/zur Anlagenmechaniker*in \(d/m/w\) für Sanitär-, Heizungs- und Klimatechnik**](#)

Helmholtz Centre for Heavy Ion Research GmbH (GSI)

Darmstadt, Germany

- [**AUSBILDUNG: 3 Auszubildende \(d/m/w\) zum/zur Elektroniker*in \(d/m/w\) für Betriebstechnik**](#)

Helmholtz Centre for Heavy Ion Research GmbH (GSI)

Darmstadt, Germany

[Download PDF](#)

Related Articles

- [**See more letters to the editor**](#)

Subjects

- [Conservation biology](#)
 - [Climate change](#)
 - [Environmental sciences](#)
 - [Sustainability](#)
-

This article was downloaded by **calibre** from <https://www.nature.com/articles/d41586-021-01958-0>

| [Section menu](#) | [Main menu](#) |

Work

- **[The parenting penalties faced by scientist mothers](#)** [20 July 2021]
Career Feature • Starting a family at a key career stage comes at a cost to birthing parents — and many end up leaving the profession as a result.
- **[Single-cell analysis enters the multiomics age](#)** [19 July 2021]
Technology Feature • A rapidly growing collection of software tools is helping researchers to analyse multiple huge ‘-omics’ data sets.
- **[A monkey researcher fights to protect threatened and endangered primates](#)** [19 July 2021]
Where I Work • Andie Ang helps to build rope bridges in Singapore and is working to launch primate exchanges with other nations to keep imperilled species safe.

- CAREER FEATURE
- 20 July 2021

The parenting penalties faced by scientist mothers

Starting a family at a key career stage comes at a cost to birthing parents — and many end up leaving the profession as a result.

- [Kendall Powell](#) 0

1. Kendall Powell

1. Kendall Powell is a freelance writer in Boulder, Colorado.

[View author publications](#)

You can also search for this author in [PubMed](#) [Google Scholar](#)





•

[Find a new job](#)

[Download PDF](#)



Credit: Veronica Cerri

Yhasmin Moura's research was not the only thing on her mind in 2017 when she was considering postdoctoral positions in the United Kingdom and her home nation of Brazil. Moura was pregnant at the time, so parental-leave policies were a top concern.

Even though it meant moving far away from her extended family, Moura chose a placement at Lancaster University, UK, largely because it offered a full year of paid maternity leave. The Brazil placement would have given her only four months of unpaid maternity leave. "The pregnancy defined my position and determined a completely different future for me," says Moura, a geographer and remote-sensing researcher who is now a postdoc at the Karlsruhe Institute of Technology in Germany.

For many scientists, the transition from a PhD to a faculty position often happens when they are starting or building families, Moura says. It's no wonder, she adds, that many early-career researchers make crucial, life-

altering decisions based on institutions' policies and attitudes around parenthood.

Moura was among 176 attendees from 46 nations at a virtual conference organized in May by Mothers in Science (MiS), an international non-profit organization that aims to boost recruiting and retention of women in science careers. The conference highlighted the well-documented 'motherhood penalties' that mothers in science, technology, engineering and mathematics (STEM) face as they try to build their careers. Scientist-mothers face discrimination¹, drops in productivity² and inequities in wages and promotion^{3,4}, all of which contribute to them dropping out of the full-time STEM workforce⁵. The conference also pointed out that the COVID-19 pandemic revealed the stark pressures on mothers in STEM and highlighted the practices and policies that can help people to balance research and motherhood.

To better understand the penalties and barriers of motherhood, MiS conducted a survey in 2020 of nearly 9,000 people from 128 countries. The respondents came from all sectors of STEM careers and fields, and comprised 58% mothers, 22% women without children, 13% fathers and 7% men without children. Among the preliminary results presented at the conference, more than one-third (34%) of mothers in full-time careers in STEM globally had left those positions after their first child.



When Yhasmin Moura was choosing a postdoc while pregnant, she opted for a placement that offered a year of paid maternity leave. Credit: Yhasmin Mendes de Moura

A separate study⁵ by US-based researchers Erin Cech and Mary Blair-Loy found that, in the United States, where family-leave policies are often sparse or absent, the proportion of mothers in full-time STEM careers who leave after their first child is as high as 43%. As a result, scientist-mothers are under-represented at the topmost levels of academia in that nation and elsewhere. Women comprise less than one-quarter (24%) of the top earners at elite US universities, according to a 2021 study⁶ by the American Association of University Women.

Productivity penalty

At every career stage, the MiS survey found, scientist-mothers published fewer papers compared with scientist-fathers. This gap increases with time,

so that by nine years after their first child, mothers had on average published ten fewer papers than had fathers. These findings were consistent with another study² published this year and presented at the conference that found a significant productivity penalty for mothers.



Collection: Work-life balance

In the MiS survey, 38% of scientist-mothers worldwide said that they had received fewer offers for professional opportunities since becoming a parent, compared with just 13% of scientist-fathers. And nearly two-thirds (61%) of scientist-mothers, compared with 38% of scientist-fathers, said that parenthood had negatively affected their career.

Ryan Watkins, research manager for MiS and a planetary scientist for NASA who works from St Louis, Missouri, summarized the data for conference attendees: the barriers faced by scientist-mothers are systemic, structural and universal, she told the audience.

Keynote speaker Isabel Torres, co-founder and chief executive of MiS, noted the vicious cycle that scientist-mothers face. The barriers are largely invisible, so mothers — and their colleagues and supervisors — assume that they can persevere through hard work alone, she said in her talk. As a result, many scientist-mothers take on more teaching, service or outreach work to build up their CVs, even though they have fewer hours to spare. Then they

hit the wall. “Mothers can’t ‘do it all’ because they are already doing a lot more,” Torres said in her address. “Then, when a mom chooses to leave work or to work part-time, it looks like a personal decision.”

Scientist-fathers, she noted, rarely face this ‘choice’.



Isabel Torres co-founded Mothers in Science to boost the careers of researchers with children. Credit: Isabel Torres

Other researchers have corroborated both the ‘hidden’ nature of parenthood in academic research and the productivity penalty for academic scientist-mothers.

Aaron Clauset, a computer scientist at the University of Colorado Boulder, Allison Morgan, then a doctoral student, and their colleagues documented a publication deficit for scientist-mothers in a 2017–18 survey of more than 3,000 tenure-track faculty members from 450 departments at US and Canadian institutions. Respondents were in the fields of computer science,

business and history. The study's results, which Clauset presented at the conference, showed that mothers in the sample published 74–83% fewer papers than fathers during a 15-year span early in their careers².

Yet Clauset and Morgan's study found that, in the five years before a researcher's first child, future mothers' and fathers' productivity rates are nearly identical. With the arrival of the first child, the mothers' productivity drops immediately, by up to 48%. This drop in productivity is not seen for researcher-fathers, nor for non-parents who are the same age or at the same career stage. The analysis found that mothers in computer science produce, on average, nearly 18 fewer papers than do researcher-fathers over the 10 years after the birth of their first child — a gap that would take 5 extra years of work in a career to close.

Despite the barriers they face, mothers make up a significant slice of academia. Clauset and Morgan's study found that among faculty members over the age of 40, nearly three-quarters (71%) of women are mothers, and that 82% of men are fathers. “A large majority of faculty are parents, but we often hide our families from our jobs in academia,” says Clauset. “It gives the impression that we don't have a family, or that we don't care about our families. That is so wrong.”

Uneven parental leaves

More than one-third of institutions covered in the Clauset and Morgan study offered no paid parental leave. For those that did, the average length was 15 weeks for mothers and 12 weeks for fathers (for an interactive breakdown of these data, see go.nature.com/3aecocq).

All of this suggests to Clauset that parental-leave policies ignore opportunities to recruit and retain female faculty members. Universities should all be offering gender-neutral parental leave as a competitive advantage and making it easy to use, he says.



Science careers and mental health

Gender-neutral leave policies that give women and men equal time off are more helpful than policies that give women extra time, says Torres. Uneven policies “set families up for unequal childcare burdens later”, she says. “If only moms take leave, then they fall further behind in their careers.”

She points to a proposed law in Iceland as a model for equalizing parental leaves. The law would give both mothers and fathers six months of leave, with one month allowed to be transferred between the parents.

Biologist Fernanda Staniscuaski presented to conference attendees some ways that parent scientists have advocated for making maternity more visible in the Brazilian research ecosystem. She founded the group Parent in Science in 2016, which has promoted several solutions.

In 2018, the group petitioned Brazil’s National Council for Scientific and Technological Development (CNPq) — which runs a national database called [*Plataforma Lattes*](#) of nearly 7 million registered researchers and their CVs — to include a field on the CV to account for maternity leave. (In Brazil, mothers get 4–6 months of paid maternity leave, whereas fathers get 5–20 days.)

“It’s quite important, not just to show the reason for the drop in productivity, but also because it makes maternity visible,” says Staniscuaski, who is an associate professor at the Federal University of Rio Grande do Sul in Porto Alegre.



Fernanda Staniscuaski formed Parent in Science to advocate for scientists with children. Credit: Flávio Dutra

The Brazilian group also petitioned for a ‘maternity clause’ to be added to research grant or fellowship applications “to make the competition more fair for mothers”, Staniscuaski says. Since 2018, several Brazilian funding agencies have agreed to the clause, which uses either a longer span of years or a correction factor to equalize the assessment of mothers’ productivity with that of their non-parent peers.

In May, Staniscuaski’s university voted to implement the maternity clause during evaluations for newly recruited female staff who had taken maternity leave in the previous 6–7 years. “I thought it would be a harder fight than it

actually was,” she says. “But we have the productivity-drop data to back it up, and you cannot argue with the numbers.”

Buying time for new mothers

When Parent in Science surveyed Brazilian researchers during the pandemic⁷, just 10% of Black graduate-student mothers reported being able to continue their dissertation work. “We were afraid that this would drive them away from graduate school,” says Staniscuaski.



Shared parental leave: making it work for the whole family

So the group crowd-funded more than 100,000 Brazilian reais (US\$19,000) to support the cohort through the Tomorrow Program, which funds final-year doctoral-student mothers from minority ethnic groups. Each student receives 705 reais per month from April to December 2021 or until they graduate, whichever comes first. Recipients can use the funds for whatever will help them to finish their PhD programme. The need for the initiative was overwhelming, Staniscuaski says, with 750 applicants for 26 slots.

Similarly, the Christiane Nüsslein-Volhard Foundation in Germany, started by the eponymous Nobel-laureate developmental biologist in 2004, supports PhD-student and postdoc mothers. The programme supports 40–50 scientists

each year with €400 (US\$474) per month for up to 2 years. The mothers must either be getting or have earned a PhD in Germany, but use of the funds is unrestricted.

“It is buying them some freedom to cope with their duties” as both scientists and mothers, said Gerlind Wallon at the conference, who is deputy director of the European Molecular Biology Organization, based in Heidelberg, Germany, and a director of the foundation.

Getting leaders to take notice

In the wake of the conference, its organizers are wondering how to ensure that proven policies and solutions, such as fellowships for women returning to work (see ‘Support structure’) and Brazil’s maternity clause, become widespread globally.

Support structure

Birthing parents who take extended breaks from science, technology, engineering and mathematics (STEM) careers face an uphill climb to resume them. The UK Daphne Jackson Trust supports researchers returning to careers after a prolonged break of two years or more for family, caregiving or health reasons.

The charitable trust, based at the University of Surrey, arranges two- to three-year, part-time fellowships for researchers in the sciences, technology and other fields, matching them with a host institution and a funding sponsor. Typically, fellows are mothers returning from breaks of five to eight years spent caring for more than one child, but the fellowships are open to anyone.

Since 1986, the trust has awarded more than 400 fellowships and has an enviable track record — more than 90% of fellows remain long term in a STEM career, with 57% in research-based roles. Eight former fellows have become full professors⁸.

Chief executive Katie Perry says that success hinges not only on the funding for fellows, but also on the advocacy that the organization does. “We convince the host institutions, the research supervisors and the sponsors to work with us and facilitate the next step for the returners,” she says. Women who have taken childcare breaks often encounter a high level of discrimination in academia, says Perry. “That culture still persists. It’s bang out of order.”

Although no other organization is specifically devoted to giving returners hands-on help, some funding mechanisms support re-entry, including funding through the UK funder [Wellcome](#) and the [US National Institutes of Health](#) (NIH).

The NIH’s Research Supplements to Promote Re-Entry into Biomedical and Behavioral Research Careers (also called Re-Entry Supplements) can be applied for by any principal investigator holding a current NIH grant who wants to hire a postdoc or faculty member re-entering the research workforce after a one- to eight-year break caring for children or older people, or for personal health reasons. The supplements cover salary and benefits for up to three years, as well as US\$10,000 for supplies, travel or publication charges.

The US Society of Women Engineers also has a [STEM Re-entry Task Force](#) that works to connect returners with hirers.

Katie Perry, chief executive of the Daphne Jackson Trust, which supports UK scientists returning to research careers after family-care breaks, says that she pitches returners as those who have sharpened their multitasking, prioritizing and decision-making skills. But she thinks that real change will come when policies are hitched to funding, such as when the UK’s National Institute for Health Research required medical-school departments to [achieve a certain gender-equity ‘grade’ to receive funding](#). Decision-makers and other administrators took notice. “Gender equity suddenly went from a nicety to a necessity: we’ve got to do it or we will get left behind in the competition for funding,” she says.

Clauset agrees that funders have to get on board. “The federal grant-making process assumes families don’t exist,” says Clauset. And, he adds, funding

agencies need to make family-friendly policies more equitable among graduate students, postdocs and principal investigators.

Both Perry and Clauset promote another useful tactic: publicly identifying institutions that exacerbate and perpetuate bad practices. “I’d like to see slides at a scientific conference that have five examples of universities with excellent practices and five universities that should be doing better,” says Perry. “People do not want to be on the naughty list.”

Nature **595**, 611-613 (2021)

doi: <https://doi.org/10.1038/d41586-021-01993-x>

References

1. 1.

Correll, S. T., Benard, S. & Paik, I. *Am. J. Sociol.* **112**, 1297–1338 (2007).

[Article](#) [Google Scholar](#)

2. 2.

Morgan, A. C. *et al. Sci. Adv.* **7**, eabd1996 (2021).

[PubMed](#) [Article](#) [Google Scholar](#)

3. 3.

Chung, Y., Downs, B., Sandler, D. H. & Sienkiewicz, R. *The Parental Gender Earnings Gap in the United States* (US Census Bureau, 2017).

[Google Scholar](#)

4. 4.

Buffington, C., Harris, B. C., Jones, C. & Weinberg, B. A. *Am. Econ. Rev.* **106**, 333–338 (2016).

[PubMed](#) [Article](#) [Google Scholar](#)

5. 5.

Cech, E. A. & Blair-Loy, M. *Proc. Natl Acad. Sci. USA* **116**, 4182–4187 (2019).

[PubMed](#) [Article](#) [Google Scholar](#)

6. 6.

Silbert, A. & Dube, C. M. *The Power Gap Among Top Earners at America's Elite Universities* (Eos Foundation, 2021).

[Google Scholar](#)

7. 7.

Staniscuaski, F. *et al. Front. Psychol.* **12**, 1640 (2021).

[Article](#) [Google Scholar](#)

8. 8.

Daphne Jackson Trust. *Leading the Way for Returners: A Survey of Former Daphne Jackson Fellows, 2015* (Daphne Jackson Trust, 2015).

[Google Scholar](#)

[Download references](#)

Related Articles



- [Juggling research and family life: honest reflections from scientist dads](#)



- [Pandemic measures disproportionately harm women's careers](#)



- [Shared parental leave: making it work for the whole family](#)



- [Why scientist-mums in the United States need better parental-support policies](#)



- [Science careers and mental health](#)



- [Collection: Work-life balance](#)

Subjects

- [Careers](#)
- [Conferences and meetings](#)
- [Scientific community](#)

nature careers

Jobs >

- [Instrument scientist at the permanent end station REMI@FLASH](#)

German Electron Synchrotron (DESY)

Hamburg, Germany

- [**AUSBILDUNG: 3 Auszubildende \(d/m/w\) zum/zur Elektroniker*in für Geräte und Systeme**](#)

Helmholtz Centre for Heavy Ion Research GmbH (GSI)

Darmstadt, Germany

- [**AUSBILDUNG: 3 Auszubildende \(d/m/w\) zum/zur Anlagenmechaniker*in \(d/m/w\) für Sanitär-, Heizungs- und Klimatechnik**](#)

Helmholtz Centre for Heavy Ion Research GmbH (GSI)

Darmstadt, Germany

- [**AUSBILDUNG: 3 Auszubildende \(d/m/w\) zum/zur Elektroniker*in \(d/m/w\) für Betriebstechnik**](#)

Helmholtz Centre for Heavy Ion Research GmbH (GSI)

Darmstadt, Germany

[Download PDF](#)

Related Articles



- [**Juggling research and family life: honest reflections from scientist dads**](#)



- Pandemic measures disproportionately harm women's careers



- Shared parental leave: making it work for the whole family



- Why scientist-mums in the United States need better parental-support policies



- Science careers and mental health



- Collection: Work-life balance

Subjects

- Careers
- Conferences and meetings
- Scientific community

This article was downloaded by **calibre** from <https://www.nature.com/articles/d41586-021-01993-x>

- TECHNOLOGY FEATURE
- 19 July 2021
- Correction [21 July 2021](#)

Single-cell analysis enters the multiomics age

A rapidly growing collection of software tools is helping researchers to analyse multiple huge ‘-omics’ data sets.

- [Jeffrey M. Perkel](#)
 1. Jeffrey M. Perkel
[View author publications](#)

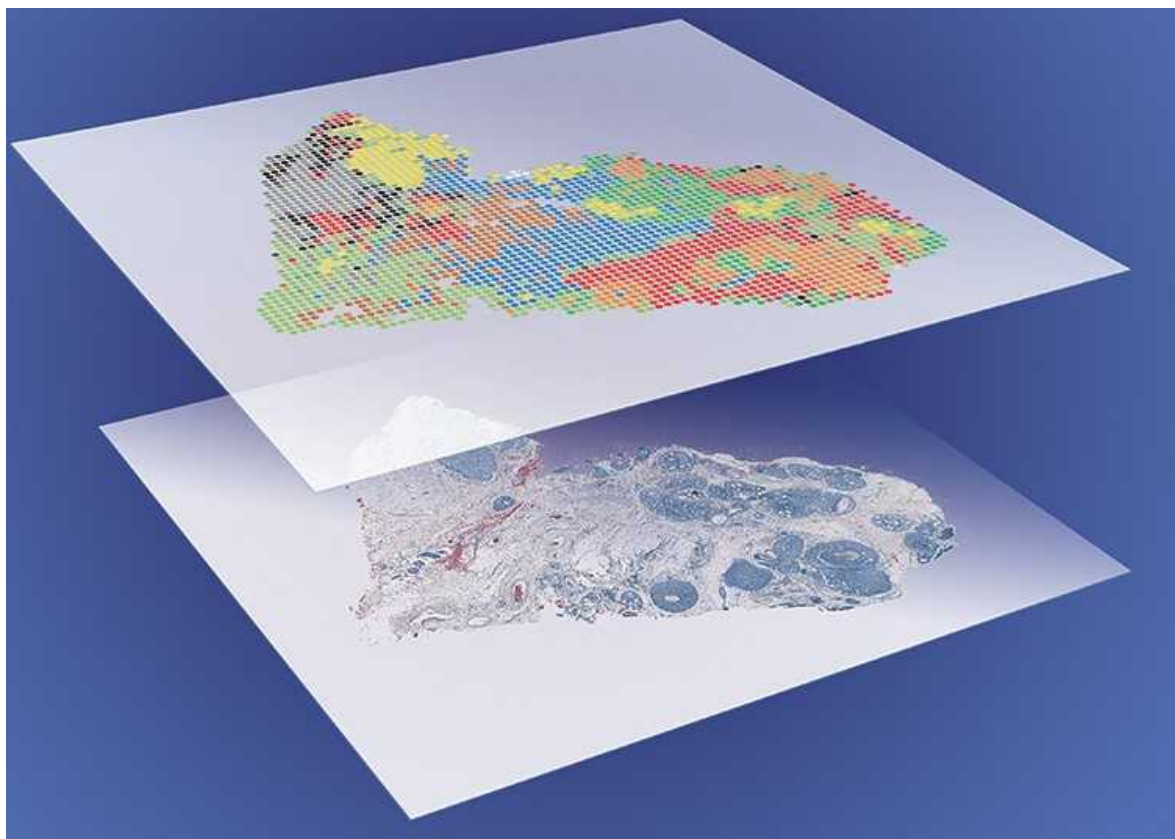
You can also search for this author in [PubMed](#) [Google Scholar](#)





•

[Download PDF](#)



Multiomics data are increasingly being combined with spatial information. Credit: 10x Genomics

It takes about 20 days for a mouse to grow from fertilized egg to newborn pup. Ricard Argelaguet and his colleagues were interested in what exactly happens inside the cells of a mouse embryo between days 4.5 and 7.5, when the stem cells shift into three layers: the ectoderm, which develops into the nervous system; the mesoderm, which develops into muscle and bone; and the endoderm, which develops into the gut and internal organs.

Researchers can easily distinguish between these three layers by looking at which genes are expressed in individual cells. But the team wanted a more nuanced picture. So, in 2019, the researchers combined the gene-expression data with two other sources of information¹. The first was methylation, a chemical modification that alters how genes are expressed. The second was chromatin accessibility: how modifications to chromatin, the knotty complex of proteins and DNA in eukaryotic nuclei, affect which parts of the DNA are

accessible for transcription into RNA. Both are factors in epigenetics, the non-genetic elements that influence how genes are expressed.

Combining the three data sources revealed something unexpected: in the absence of external stimuli, embryonic stem cells will become ectoderm. “This was the most essential contribution of the paper,” Argelaguet says. It showed “that there is kind of a hierarchy of cell fate specification at the epigenetic level”. Argelaguet, a computational biologist at the Babraham Institute in Cambridge, UK, was one of four first authors on the study, which was supervised by Babraham investigator Wolf Reik, as well as John Marioni at the EMBL-European Bioinformatics Institute in nearby Hinxton, and Oliver Stegle at the German Cancer Research Center in Heidelberg.

Their result explains the decades-old observation that embryonic stem cells in culture will preferentially differentiate into neurons. And it’s a finding, says Argelaguet, that would have been impossible to make using just a single type of data.

Genomics explosion

The past decade has witnessed an explosion in single-cell genomics. Single-cell RNA sequencing (RNA-seq), which profiles gene expression, is the most common technique. Other methods detail processes such as methylation, genetic variation, protein abundance and chromatin accessibility.

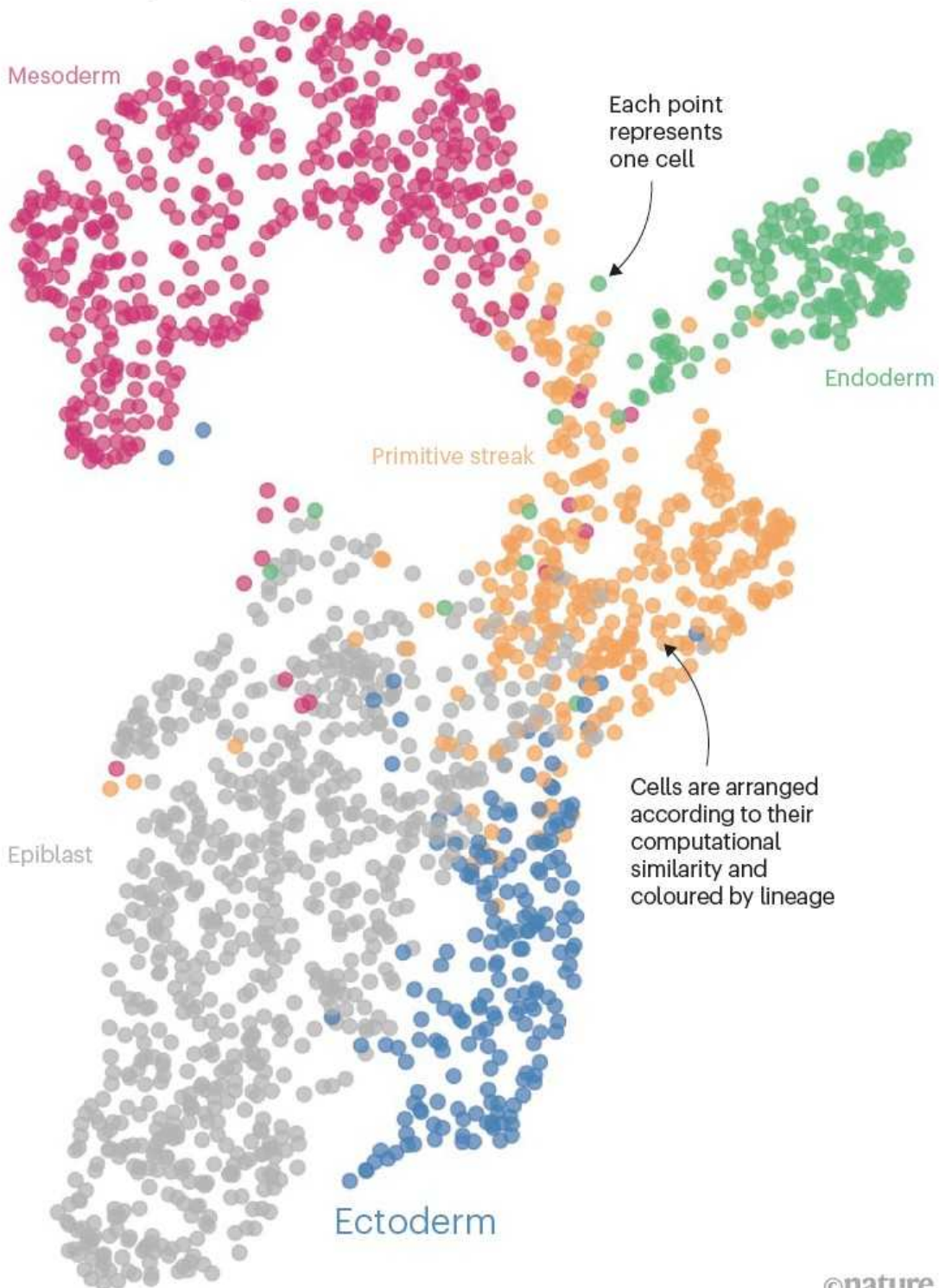
Now, researchers are increasingly combining these methods — and the resulting layers of data — in ‘multiomics’ experiments. Argelaguet, for instance, combined gene-expression profiling, methylation and chromatin accessibility in a technique called scNMT-seq. Another technique, CITE-seq, profiles both transcription and protein abundance. And G&T-seq captures both genomic DNA and RNA.

Whatever the acronym, all these techniques aim to glean complex biological insights that might be undetectable using any single method. But the task is computationally challenging, and making sense of the resulting data even more so. A fast-growing suite of software tools can help.

Almost all single-cell studies contain visualizations — sometimes called t-SNE or UMAP plots — which represent single cells as points on a 2D plane (see ‘UMAP-making’). Studying how those points aggregate, or cluster, can help researchers to discern biological structures. But the visualizations aren’t easy to create.

UMAP-MAKING

Dimensionality-reduction visualizations allow researchers to discern biological structures hidden in cell populations. This ‘uniform manifold approximation and projection’ (UMAP) plot represents 1,928 cells from a study on the early stages of mouse-embryo development.



For one thing, single-cell data sets have quickly become enormous. Back in 2019, Argelaguet captured individual cells in microtitre plates using a fluorescence-activated cell sorter, which limited him to analysing 200–300 cells per week¹. Now, he can process thousands of cells, thanks in part to a microfluidics platform developed by the biotechnology company 10x Genomics in Pleasanton, California. And a 2020 atlas of human fetal gene expression supervised by genome scientists Cole Trapnell and Jay Shendure at the University of Washington, Seattle, included four million cells². The result is basically a table with 80 billion entries — 4 million rows of cells by 20,000 genes.

And yet, “the overwhelming majority of the entries in that matrix are zero”, Trapnell says. This represents a key statistical and computational challenge, as scientists work to distinguish true zeroes — for instance, genes that are actually not expressed — from dropouts that result from sample handling or sensitivity issues. One option is to use imputation methods, which ‘borrow’ data from similar cells in the data set to fill in the gaps. As Stegle puts it: “Your neighbours tell you something about the unknown.”

Difficulty squared

Combining modalities only multiplies the difficulty, says Argelaguet. “All the weaknesses, all the noise, all the challenges from each technology, it just gets exacerbated by combining them into a multimodal assay.”

Argelaguet and his colleagues spent three months collecting their data set, and two years analysing it. Jason Buenrostro, an epigeneticist at Harvard University in Cambridge, Massachusetts, says that some of his team’s computations for a study describing a method called SHARE-seq took weeks to complete³.

The pay-off of the added detail, says Bernd Bodenmiller, who studies single-cell tumour biology at the University of Zurich, Switzerland, is that it helps researchers to “understand the biology”. And they can do so using existing data sets, such as the Human Cell Atlas and its 13.5 million cell profiles. In a preprint⁴ published in June, Chengxiang Qiu, a graduate student in Shendure’s lab, and his colleagues combined 1.4 million cells from 4

published atlases to tease apart how one cell type arises from another across 10 days of mouse development. The resulting “trajectories of mammalian embryogenesis” revealed more than 500 transcription factors that could have a role in cell-type specification.

Software tools

The information can be integrated in three main ways, depending on what features (or ‘anchors’) the data sets have in common, says Marioni, who has published a review⁵ on the topic. ‘Horizontal integration’ is used for data sets of the same type — two RNA-seq data sets, for instance. In that case, genes act as the anchors, “because you’re measuring the same set of genes in every population of cells”, Marioni says.

‘Vertical integration’ involves data sets collected from the same cells, such as for RNA-seq and chromatin accessibility. And ‘diagonal integration’ involves molecular measurements made across unrelated populations of cells. “The question is, what’s the common feature that you’re going to use?” Marioni says. One approach to vertical integration is to associate sites of chromatin accessibility with the genes they regulate, and then compute a probable gene-expression profile from the data.

“So, basically, you’re making it into a horizontal-integration problem, where genes become the anchors again,” Marioni says.



The secret life of cells

Integrating data sets, Trapnell says, is like aligning DNA sequences. “You’re assuming that a population of cells that you can see with one modality is visible with the other, and that for most cells or cell populations, there’s going to be a one-to-one mapping.” The trick, he says, is to align the sets so that you can be confident that any differences you see “are not due to your inability to find the similarities. And that’s the same spirit that motivates most sequence-alignment algorithms.”

Dozens of tools have been developed to achieve this, and many are indexed on the community-driven ‘[awesome-multi-omics](#)’ and ‘[awesome-single-cell](#)’ lists on GitHub.

[Seurat](#), for instance, developed by Rahul Satija’s team at the New York Genome Center, effectively aligns UMAP visualizations of two data sets to create a “shared, low-dimensional” space, says Tim Stuart, a computational biologist in Satija’s group. “That enables you to find neighbours of one data set in the other data set, and vice versa.” Other popular options include: Argelaguet’s MOFA, which he describes as a “kind of a multiomics generalization” of principal-component analysis; [Harmony](#), from Soumya Raychaudhuri’s team at Harvard Medical School in Boston, Massachusetts; and [LIGER](#), developed by Joshua Welch’s team at the University of Michigan in Ann Arbor. According to Welch, just as online retailers can

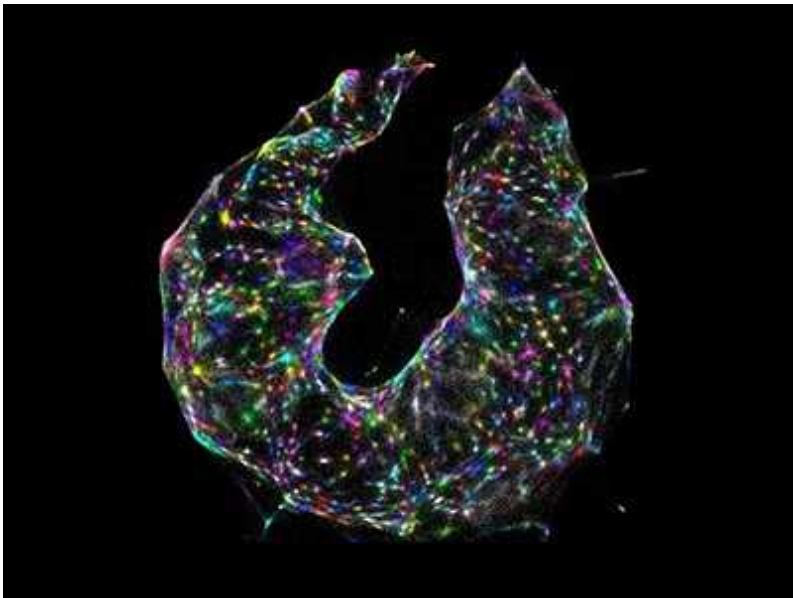
mine their customers' purchase histories to identify products that a user is likely to want, LIGER uses 'integrative non-negative matrix factorization' to identify related cells and cell clusters.

Spatial hackathon

With such a fast-growing tool set, researchers can struggle to know what they should use for which questions, and how to go about it. To help close those gaps, Elana Fertig at Johns Hopkins University in Baltimore, Maryland; Aedin Culhane at Harvard T. H. Chan School of Public Health in Boston; and Kim-Anh Lê Cao at the University of Melbourne, Australia, organized a virtual conference on single-cell omics data integration. As part of that event, held in June 2020, the organizers provided three curated data sets and challenged attendees to apply whichever algorithms and workflows they liked to integrate and interpret the data, in a series of 'hackathons'. Unlike in-person hackathons, in which researchers intensively collaborate on software projects in shorts bursts over a few hours or days, these were virtual events held over a month, with collaborators dispersed around the globe. One event focused on Argelaguet's mouse-embryo data set; the others concentrated on spatial-data-integration problems.

"We were interested to see what would be the challenges we should anticipate in multiomics," Lê Cao says. "We thought that it would be good to gather the different experts in the field and see how they would approach the analysis of multiomic studies in single cells."

Conventional single-cell experiments detail thousands of molecules at the expense of positional information. Spatial methods capture molecular identity without that dissociation step. By layering the two data types, researchers can compute the probable physical locations of dissociated cells, or flesh out spatial data sets with extra molecular detail.



Starfish enterprise: finding RNA patterns in single cells

“How a cell determines its fate, how it’s going to function, is a combination of many things,” says Marioni. “But something that’s very important is the physical location of the cell within the embryo: the mechanical pressures upon it, the local signalling environment, the shape of the embryo, how it’s changing through development. So, if we want to have a better understanding of cell-fate decisions, it’s really helpful to have these measurements in space.”

In one challenge, researchers were given both spatial and non-spatial RNA-expression data sets from a mouse visual cortex. They were then asked to use cell-type assignments computed in the non-spatial data to identify cell types in the spatial data, in which fewer genes are identified per cell. A second challenge asked whether it is possible to identify gene-expression signatures of cellular location in non-spatial transcriptional data. According to Fertig, the answer to that was mixed. “It depends on the data set and cell type,” she says.

Pratheepa Jeganathan, a statistician at McMaster University in Hamilton, Canada, tackled a third challenge, which involved protein-abundance data from different cohorts of people with breast cancer. Hackathon participants were tasked with integrating partially overlapping proteomics data sets; inferring the locations of cells for which no spatial data exist; and using non-

spatial data to predict the expression levels of proteins that were not measured in the spatial data.

Attendees approached these hackathons mostly by repurposing existing algorithms, says Lê Cao. Her students used a machine-learning approach called partial least squares, which they originally developed for bulk genomics data. “We are piling up our knowledge and methods and tweaking them, so we don’t reinvent the wheel,” she says.

Jeganathan used topic analysis, a natural-language processing technique that she adapted during her postdoc, to infer how microbial communities differ across environments. In the hackathon, she adapted the method again, to characterize the spatial distribution and composition of cells across data sets. According to Culhane, that kind of information can be clinically useful, because the distribution of immune cells around a tumour can influence how well a person responds to therapy. “The spatial orientation of the cells was actually informative for patient survival,” she says.

Gene regulatory networks

Two omics data types are particularly useful for determining the molecular mechanisms underlying cellular development.

Single-cell RNA-seq data identify which genes are expressed in a given cell, whereas chromatin accessibility assays highlight regulatory regions. By integrating those, researchers can identify the regulatory elements that act on a gene, the transcription factors that probably control those elements and when and where those factors are expressed. The result is a gene-regulatory network that researchers can probe to tease apart how cells’ fates are determined.

Buenrostro and his team applied this strategy to show how chromatin opens up, or becomes primed, in advance of cellular differentiation in mouse skin. They were then able to use the cell’s ‘chromatin potential’ to predict how individual cells were likely to differentiate. Chromatin, Buenrostro explains, “should always point in the direction of differentiation”. His team has released a software package called [FigR](#) to help define these networks.



NatureTech hub

[CellOracle](#), from Samantha Morris's team at Washington University in St. Louis, Missouri, allows researchers to simulate the effect of impeding or boosting impact of transcription factors on cell identity. Morris worked with researchers in Milan, Italy, to see how specific transcription factors affect the development of brain cells called medium spiny neurons in human embryos, which would be impossible to do using genetic manipulation⁶. Separately, her team has computationally modified some 200 transcription factors to identify those that are involved in formation of the axial mesoderm in embryonic zebrafish (*Danio rerio*). The axial mesoderm develops into the notochord, a skeletal rod that supports the embryo's body. The software predicted that the deletion of one of those transcription factors, *noto*, would not only prevent notochord development, which was already known, but also promote the growth of another developmental structure, which was not. When they knocked out *noto* in the lab, that is precisely what they saw. “We were able to predict a new phenotype in this knockout,” Morris says, “and then we validated that experimentally using single-cell RNA-seq.”

The kitchen sink

As the single-cell multiomics field accelerates, new tools are appearing at a dizzying pace. If cellular information can be captured by sequencing, single-

cell biologists are folding it into their experiments.

In June, researchers in the United States and Japan described a method⁷ of simultaneously capturing three pieces of information: chromatin accessibility, cell-surface protein abundance and cellular lineage, the last of which is measured using mitochondrial DNA.

The team initially called its method ASAP-seq. But during the revision of the paper, 10x Genomics released a new microfluidics kit to simplify the collection of gene-expression and chromatin-accessibility data from the same cells, and the researchers decided to blend that kit with ASAP-seq to fold in yet another layer of information: transcription.

The team dubbed its method DOGMA-seq — a nod to the ‘central dogma of molecular biology’, which states that DNA is transcribed into RNA, and RNA is translated into proteins. Among other things, the technique revealed lineage biases during bone-marrow differentiation⁷.

“The fact that a new assay was introduced as a revision experiment above all speaks to the breakneck speed at which the single-cell field is moving,” says Caleb Lareau, a computational biologist at Stanford University, California, and a member of the team.

Researchers can only try to keep up. Such is the pace of development that Buenrostro jokes that his students’ minds “implode” with each new publication as they scramble to work out how it affects their research.

And Lareau says that he and his colleagues have pre-emptively named their successor to DOGMA-seq. Their working title? ‘Kitchen-seq’, as in: “How can you sequence everything but the kitchen sink?”

Nature **595**, 614-616 (2021)

doi: <https://doi.org/10.1038/d41586-021-01994-w>

Updates & Corrections

- **Correction 21 July 2021:** An earlier version of the caption for the first image erroneously stated that the top section of the image represented single-cell data.

References

1. 1.

Argelaguet, R. *et al.* *Nature* **576**, 487–491 (2019).

[PubMed](#) [Article](#) [Google Scholar](#)

2. 2.

Cao, J. *et al.* *Science* **370**, eaba7721 (2020).

[PubMed](#) [Article](#) [Google Scholar](#)

3. 3.

Ma, S. *et al.* *Cell* **183**, 1103–1116 (2020).

[PubMed](#) [Article](#) [Google Scholar](#)

4. 4.

Qiu, C. *et al.* Preprint at bioRxiv
<https://doi.org/10.1101/2021.06.08.447626> (2021).

5. 5.

Argelaguet, R., Cuomo, A. S. E., Stegle, O. & Marioni, J. C. *Nature Biotechnol.* <https://doi.org/10.1038/s41587-021-00895-7> (2021).

[Article](#) [Google Scholar](#)

6. 6.

Bocchi, V. D. *et al.* *Science* **372**, eabf5759 (2021).

[PubMed](#) [Article](#) [Google Scholar](#)

7. 7.

Mimitou, E. P. *et al.* *Nature Biotechnol.* <https://doi.org/10.1038/s41587-021-00927-2> (2021).

[Article](#) [Google Scholar](#)

[Download references](#)

Related Articles

-  [Starfish enterprise: finding RNA patterns in single cells](#)
-  [The secret life of cells](#)
-  [Single-cell sequencing made simple](#)
-  [NatureTech hub](#)

Subjects

- [Computational biology and bioinformatics](#)
- [Transcriptomics](#)
- [Epigenetics](#)

Jobs >

- [Instrument scientist at the permanent end station REMI@FLASH](#)

German Electron Synchrotron (DESY)

Hamburg, Germany

- [AUSBILDUNG: 3 Auszubildende \(d/m/w\) zum/zur Elektroniker*in für Geräte und Systeme](#)

Helmholtz Centre for Heavy Ion Research GmbH (GSI)

Darmstadt, Germany

- [AUSBILDUNG: 3 Auszubildende \(d/m/w\) zum/zur Anlagenmechaniker*in \(d/m/w\) für Sanitär-, Heizungs- und Klimatechnik](#)

Helmholtz Centre for Heavy Ion Research GmbH (GSI)

Darmstadt, Germany

- [AUSBILDUNG: 3 Auszubildende \(d/m/w\) zum/zur Elektroniker*in \(d/m/w\) für Betriebstechnik](#)

Helmholtz Centre for Heavy Ion Research GmbH (GSI)

Darmstadt, Germany

[Download PDF](#)

Related Articles

-  [Starfish enterprise: finding RNA patterns in single cells](#)
-  [The secret life of cells](#)
-  [Single-cell sequencing made simple](#)
-  [NatureTech hub](#)

Subjects

- [Computational biology and bioinformatics](#)
- [Transcriptomics](#)
- [Epigenetics](#)

This article was downloaded by **calibre** from <https://www.nature.com/articles/d41586-021-01994-w>

- WHERE I WORK
- 19 July 2021

A monkey researcher fights to protect threatened and endangered primates

Andie Ang helps to build rope bridges in Singapore and is working to launch primate exchanges with other nations to keep imperilled species safe.

- [Virginia Gewin](#) ⁰

1. Virginia Gewin

1. Virginia Gewin is a freelance writer in Portland, Oregon.

[View author publications](#)

You can also search for this author in [PubMed](#) [Google Scholar](#)





•



Andie Ang is a primatologist at Mandai Nature, a research organization and funder in Singapore. Credit: James Chua

[Download PDF](#)

I was a ten-year-old in Singapore when I received a vervet monkey (*Chlorocebus pygerythrus*) as a pet. By the time I was 15, I knew that my family did not have the necessary international permit to own it legally. With help from local agencies, we sent the monkey to a rehabilitation sanctuary in Zambia, which ultimately released it into the wild. That

experience got me interested in learning more about wild monkeys and how to help them.

I research threatened and endangered leaf-eating primates known as Asian colobinae. They have specialized, multi-chambered stomachs, as do cows, and need a long rest after meals. They are shy and hard to find, so there has been less research on them than on orangutans or the great apes.

One species I study is the critically endangered Raffles' banded langur (*Presbytis femoralis*). Globally, there are just 320 individuals: 70 in Singapore and 250 in Malaysia. I work with national agencies, educational and non-governmental organizations and local communities to help protect these and other monkeys — especially those living between forest and urban areas. For example, in an area prone to roadkill, we installed a rope bridge to let langurs and other animals cross the road safely.

One of the biggest threats to these and other monkeys is inbreeding as their numbers shrink. We hope to exchange animals between Singapore and Malaysia to boost their population's genetic health.

In this picture from 2017, I was monitoring primate populations in a reserve in central Singapore when I saw these long-tailed macaques (*Macaca fascicularis*). Here, we are observing one another — and respecting each other's space.

I've started a website called Primate Watching to help observers learn about these primates and where to see them. People think monkeys are aggressive, but really they are just naturally curious. Still, the public should always keep a safe distance, not put a camera in their faces.

Nature **595**, 618 (2021)

doi: <https://doi.org/10.1038/d41586-021-01995-9>

Related Articles



- [Shell shock: A biologist's quest to save the endangered painted snail](#)



- [Mission marmoset](#)

Subjects

- [Careers](#)
- [Conservation biology](#)
- [Ecology](#)

nature careers

[Jobs](#) >

- [Instrument scientist at the permanent end station REMI@FLASH](#)

German Electron Synchrotron (DESY)

Hamburg, Germany

- [AUSBILDUNG: 3 Auszubildende \(d/m/w\) zum/zur Elektroniker*in für Geräte und Systeme](#)

Helmholtz Centre for Heavy Ion Research GmbH (GSI)

Darmstadt, Germany

- [AUSBILDUNG: 3 Auszubildende \(d/m/w\) zum/zur Anlagenmechaniker*in \(d/m/w\) für Sanitär-, Heizungs- und Klimatechnik](#)

Helmholtz Centre for Heavy Ion Research GmbH (GSI)

Darmstadt, Germany

- [AUSBILDUNG: 3 Auszubildende \(d/m/w\) zum/zur Elektroniker*in \(d/m/w\) für Betriebstechnik](#)

Helmholtz Centre for Heavy Ion Research GmbH (GSI)

Darmstadt, Germany

[Download PDF](#)

Related Articles



- [Shell shock: A biologist's quest to save the endangered painted snail](#)



- [Mission marmoset](#)

Subjects

- [Careers](#)
- [Conservation biology](#)
- [Ecology](#)

This article was downloaded by **calibre** from <https://www.nature.com/articles/d41586-021-01995-9>

Research

- [**Superconductivity in a graphene system survives a strong magnetic field**](#) [21 July 2021]

News & Views • A material system known as magic-angle twisted trilayer graphene exhibits superconductivity. The observation that this superconductivity persists under a strong magnetic field could lead to advances in quantum computation.

- [**A step closer to compact X-ray lasers**](#) [21 July 2021]

News & Views • Light sources known as free-electron lasers can produce intense X-ray radiation for a wide range of applications. The process usually needs huge particle accelerators, but an experiment shows how to overcome this limitation.

- [**Fluid flow through a deep-sea sponge could inspire engineering designs**](#) [21 July 2021]

News & Views • Sophisticated numerical simulations reveal that the beautiful structure of a sponge known as Venus's flower basket reduces hydrodynamic drag, and probably aids the capture of food particles, as well as sperm for sexual reproduction.

- [**Receptor–enzyme complex structures show how receptors start to switch off**](#) [14 July 2021]

News & Views • The structure of rhodopsin, an archetypal member of the G-protein-coupled family of receptors, in complex with its specific kinase enzyme, reveals the molecular mechanism of the first step of receptor inactivation.

- [**A multilayered immune system through the lens of unconventional T cells**](#) [21 July 2021]

Review Article • This Review provides an overview of our current understanding of the unconventional T cell compartment and discusses the development and function of unconventional T cells from an evolutionary perspective.

- [**The nightside cloud-top circulation of the atmosphere of Venus**](#) [21 July 2021]

Article • Cloud-top thermal images obtained by the Akatsuki orbiter show that Venus has almost null mean meridional circulation at the cloud top, because poleward circulation on the dayside is offset by equatorward circulation on the nightside.

- [**Free-electron lasing at 27 nanometres based on a laser wakefield accelerator**](#) [21 July 2021]

Article • Lasing in the extreme-ultraviolet range is demonstrated using a laser wakefield accelerator, as a step towards compact X-ray free-electron lasers.

- **Layer Hall effect in a 2D topological axion antiferromagnet**

[21 July 2021]

Article • A new type of Hall effect—the layer Hall effect—is produced in a 2D antiferromagnet that does not exhibit any net magnetization.

- **Pauli-limit violation and re-entrant superconductivity in moiré graphene**

[21 July 2021]

Article • A large violation of the Pauli limit and re-entrant superconductivity in a magnetic field is reported for magic-angle twisted trilayer graphene, suggesting that the spin configuration of the superconducting state of this material is unlikely to consist of spin singlets.

- **A natively flexible 32-bit Arm microprocessor**

[21 July 2021]

Article • Flexible electronic platforms would enable the integration of functional electronic circuitry with many everyday objects; here, a low-cost and fully flexible 32-bit microprocessor is produced.

- **Extreme flow simulations reveal skeletal adaptations of deep-sea sponges**

[21 July 2021]

Article • High-performance hydrodynamic simulations show that the skeletal structure of the deep-sea sponge Euplectella aspergillum reduces the hydrodynamic stresses on it, while possibly being beneficial for feeding and reproduction.

- **Orthogonal-array dynamic molecular sieving of propylene/propane mixtures**

[21 July 2021]

Article • A dynamic molecular sieve made from a metal–organic framework with orthogonally arrayed pockets is capable of separating propylene (C_3H_6) from a propylene (C_3H_6)/propane (C_3H_8) gas mixture.

- **Sexual arousal gates visual processing during Drosophila courtship**

[07 July 2021]

Article • Specific neurons in the fly brain that are activated when males are aroused modulate visual processing to underlie courtship.

- **Molecular logic of cellular diversification in the mouse cerebral cortex**

[23 June 2021]

Article • A single-cell atlas of the developing mouse cortex provides a temporal and spatial assessment of the molecular logic that drives the establishment and organization of cortical cell types.

- [Acetate differentially regulates IgA reactivity to commensal bacteria](#) [14 July 2021]
Article • Acetate—a major gut microbial metabolite—increases the production of IgA in the colon, alters the capacity of the IgA pool to bind to specific microorganisms and alters the localization of these bacteria within the colon.
- [Dysregulation of brain and choroid plexus cell types in severe COVID-19](#) [21 June 2021]
Article • Single-nucleus transcriptomes of frontal cortex and choroid plexus samples from patients with COVID-19 reveal pathological cell states that are similar to those associated with human neurodegenerative diseases and chronic brain disorders.
- [BNT162b2 vaccine induces neutralizing antibodies and poly-specific T cells in humans](#) [27 May 2021]
Article • In a phase-I/II trial in healthy adults, the BNT162b2 vaccine induces neutralizing antibodies and poly-specific T cells against SARS-CoV-2 epitopes that are conserved in a wide range of currently circulating variants.
- [Tissue-resident macrophages provide a pro-tumorigenic niche to early NSCLC cells](#) [16 June 2021]
Article • Single-cell RNA sequencing and imaging of macrophages in human non-small cell lung cancer and in a mouse model of lung adenocarcinoma show that tissue-resident macrophages have a key role in early tumour progression.
- [Clonal fitness inferred from time-series modelling of single-cell cancer genomes](#) [23 June 2021]
Article • Whole-genome sequencing of human cancer cells in patient-derived mouse xenograft models indicates a key role for TP53 in determining the fitness landscape of polyclonal cancer cell populations.
- [Phase separation drives aberrant chromatin looping and cancer development](#) [23 June 2021]
Article • The NUP98–HOXA9 oncogenic fusion protein found in leukaemia undergoes phase separation in the nucleus, which helps to promote activation of leukaemic genes and to establish aberrant chromatin looping.
- [A condensate-hardening drug blocks RSV replication in vivo](#) [07 July 2021]
Article • Cyclopamine and its chemical analogue A3E inhibit replication of human respiratory syncytial virus (RSV) by hardening the liquid–liquid phase-separated inclusion bodies, resulting in the inhibition of virus replication in the lungs of RSV-infected mice.
- [Structures of rhodopsin in complex with G-protein-coupled receptor kinase 1](#) [14 July 2021]

Article • Cryo-EM structures of complexes between GRK1 and rhodopsin shed light on how a small number of GRKs can selectively recognize and be activated by hundreds of different G-protein-coupled receptors.

- **cAMP binding to closed pacemaker ion channels is non-cooperative** [30 June 2021]

Article • Direct monitoring of individual cAMP molecules binding to HCN ion channels reveals the binding dynamics underlying the distinct physiological responses of ion channel isoforms.

- NEWS AND VIEWS
- 21 July 2021

Superconductivity in a graphene system survives a strong magnetic field

A material system known as magic-angle twisted trilayer graphene exhibits superconductivity. The observation that this superconductivity persists under a strong magnetic field could lead to advances in quantum computation.

- [Yi-Ting Hsu](#) 

1. [Yi-Ting Hsu](#)

1. Yi-Ting Hsu is in the Department of Physics, University of Notre Dame, Notre Dame, Indiana 46556, USA.

[View author publications](#)

You can also search for this author in [PubMed](#) [Google Scholar](#)



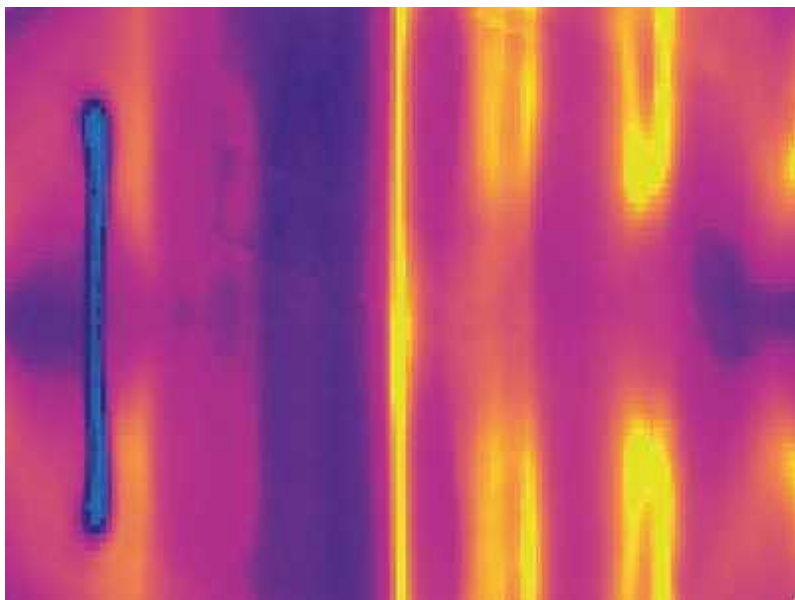


•

[Download PDF](#)

Quantum phases of matter known as superconductors transmit electrical current with zero resistance. Microscopically, this phenomenon arises from the fact that it is energetically favourable for electrons to bind into two-electron states, dubbed Cooper pairs, that move collectively and cooperatively without energy loss. A Cooper pair is said to be spin-singlet when its two electron spins (intrinsic angular momenta) point in opposite directions and the pair has a total spin of zero, whereas spin-triplet Cooper pairs have a total spin of 1, and the two electron spins can be aligned in the same direction. Most experimentally known superconductors have spin-

singlet Cooper pairs; these include metals (such as lead and niobium) that demonstrate conventional superconductivity, and cuprates (layered copper oxide compounds) that exhibit unconventional superconductivity. [Writing in Nature](#), Cao *et al.*¹ report evidence for unconventional superconductivity associated with spin-triplet Cooper pairs.

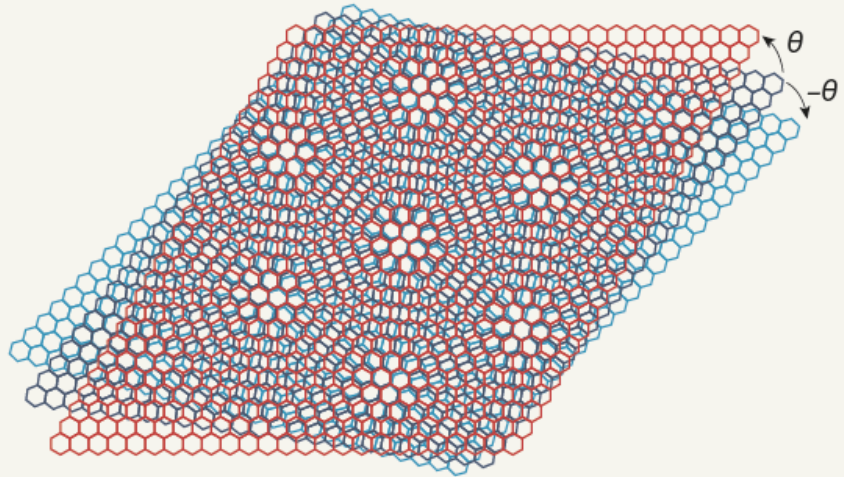


[Read the paper: Pauli-limit violation and re-entrant superconductivity in moiré graphene](#)

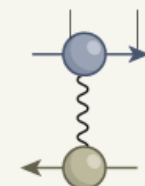
Two-dimensional spin-triplet superconductors have attracted widespread attention because many of them are predicted to host exotic zero-energy excitations called Majorana zero modes. A well-studied example of such a superconductor is a 2D chiral p -wave superconductor². This system breaks time-reversal symmetry (its physical properties would change if the direction of time were reversed), and Majorana zero modes are expected to exist in the cores of vortices (threads of magnetic flux) when a magnetic field is applied perpendicular to the system. Majorana zero modes are promising candidates for topological qubits — the building blocks of a type of ‘fault-tolerant’ quantum computation known as topological quantum computation^{3,4}. Therefore, given that most known spin-triplet superconductors are 3D, experimentally established 2D spin-triplet superconductors are much desired.

In the past four years, experimentalists have started to probe quasi-2D systems consisting of stacked but slightly misaligned layers of graphene — single sheets of hexagonally arranged carbon atoms (see refs 5 and 6, for example). Such systems have rapidly gained attention because they can be easily tuned experimentally and host a rich variety of correlated quantum phases. Earlier this year, superconductivity was reported in twisted trilayer graphene^{7,8}, which comprises three stacked graphene layers in which the top and bottom layers are rotated at angles of θ and $-\theta$, respectively, relative to the middle layer (Fig. 1). By tuning the value of θ , the physics in twisted trilayer graphene can be investigated in regimes ranging from one in which the electrons are essentially weakly coupled to each other to one in which they are strongly coupled.

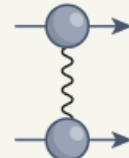
a Twisted trilayer graphene



b Electron Spin

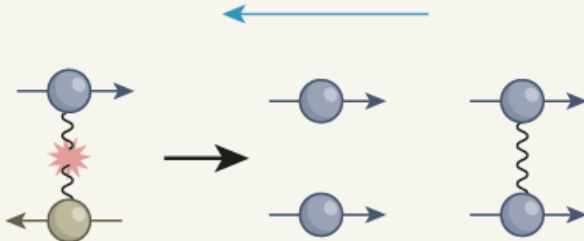


Spin-singlet
Cooper pair



Spin-triplet
Cooper pair

c Strong in-plane magnetic field



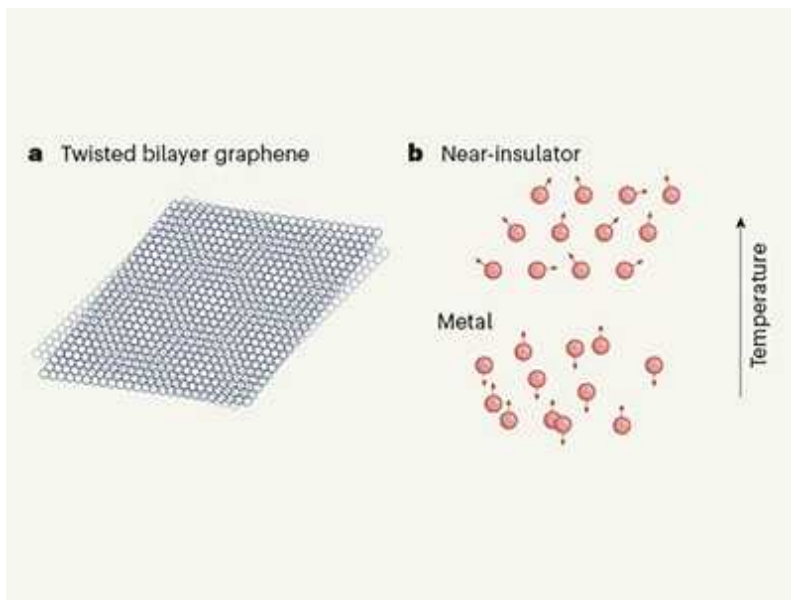
©nature

Figure 1 | Superconductivity in twisted trilayer graphene. a, Magic-angle twisted trilayer graphene (MATTG) is a system of three sheets of hexagonally arranged carbon atoms, stacked with a relative rotation angle θ of approximately 1.6° . **b,** Superconductivity results from electrons binding

into two-electron states called Cooper pairs. In a spin-singlet Cooper pair, the electron spins (intrinsic angular momenta) point in opposite directions; in a spin-triplet Cooper pair, they can be aligned in the same direction. c, In the presence of a strong magnetic field in the plane of the material, a spin-singlet Cooper pair breaks apart because a phenomenon known as the Zeeman effect causes the spins to align in the same direction. By contrast, a spin-triplet Cooper pair can survive such a field. Cao *et al.*¹ found that superconductivity in MATTG persists under a strong in-plane magnetic field, and suggest that this observation is evidence for spin-triplet Cooper pairs.

Cao *et al.* studied twisted trilayer graphene when θ is equal to the ‘magic’ angle of approximately 1.6° — the angle at which the system is expected to enter the strong-coupling regime. They observed superconductivity in such magic-angle twisted trilayer graphene (MATTG), and studied the spin properties of this superconductivity. Specifically, they measured the electrical resistance of MATTG at low temperatures (down to below 1 kelvin) and discovered a zero-resistance phase. They then applied a magnetic field to MATTG in the plane of the graphene layers and identified the critical field strength at which the observed superconductivity vanishes. They found that the superconductivity survives up to a surprisingly high critical field strength of nearly 10 tesla, which is not expected for spin-singlet superconductors.

Magnetic fields couple to the orbital angular momentum and spin of Cooper pairs in a superconductor. When a strong in-plane field is applied to a quasi-2D superconductor, the orbital effect is negligible. However, above a field strength called the Pauli limit, the spin effect tends to cause spin-singlet Cooper pairs, which have oppositely aligned electron spins, to break apart, because a phenomenon known as the Zeeman effect causes the spins to point in the same direction (Fig. 1). By contrast, spin-triplet Cooper pairs that have electron spins aligned in a single direction parallel to the field are compatible with such a spin effect and are not bound by the Pauli limit. The in-plane critical field strength measured by Cao *et al.* in MATTG is two to three times the Pauli limit and is therefore considered evidence of spin-triplet superconductivity.



Heating freezes electrons in twisted bilayer graphene

Cao and colleagues also detected a second superconducting phase that exists at even higher in-plane magnetic field strengths than does the first one, persisting above 10 tesla. On the basis of the resistance behaviour of MATTG when the field strength is increased compared with when it is decreased, the authors suggest that the two phases might be connected by a type of phase transition called a first-order phase transition. Such ‘re-entrant’ superconductivity is reminiscent of that observed in some 3D spin-triplet superconductors, such as uranium rhodium germanium⁹ and uranium telluride¹⁰, and in the spin-triplet superfluid (zero-viscosity liquid) helium-3¹¹. This similarity might provide hints about the nature of the two superconducting phases in MATTG.

The evidence reported by the authors for quasi-2D spin-triplet superconductivity in MATTG paves the way for unconventional superconductors that can be manipulated experimentally. High in-plane critical field strengths can typically develop in various ways other than in spin-triplet Cooper pairs. But these sources are unlikely to occur in MATTG owing to the negligible coupling between the spin and orbital angular momentum of electrons in graphene. Nevertheless, further measurements are needed to show whether the orbital structure of the Cooper pairs in MATTG is consistent with spin-triplet superconductivity.

Crucially, being spin-triplet does not imply that the observed superconductivity would be useful for topological quantum computation. Future work needs to study the topological properties of the superconductivity. For instance, researchers should determine whether it breaks time-reversal symmetry — an indication of possible chiral p -wave superconductivity. They should also look for direct evidence of zero-energy states in vortex cores, which would signal the presence of Majorana zero modes. The understanding gained from such studies could help physicists to develop promising platforms for topological quantum computation.

Nature **595**, 495-496 (2021)

doi: <https://doi.org/10.1038/d41586-021-01890-3>

References

1. 1.

Cao, Y., Park, J. M., Watanabe, K., Taniguchi, T. & Jarillo-Herrero, P. *Nature* **595**, 526–531 (2021).

[Article](#) [Google Scholar](#)

2. 2.

Read, N. & Green, D. *Phys. Rev. B* **61**, 10267 (2000).

[Article](#) [Google Scholar](#)

3. 3.

Kitaev, A. Y. *Ann. Phys.* **303**, 2–30 (2003).

[Article](#) [Google Scholar](#)

4. 4.

Nayak, C., Simon, S. H., Stern, A., Freedman, M. & Sarma, S. D. *Rev. Mod. Phys.* **80**, 1083–1159 (2008).

[Article](#) [Google Scholar](#)

5. 5.

Cao, Y. *et al.* *Nature* **556**, 43–50 (2018).

[PubMed](#) [Article](#) [Google Scholar](#)

6. 6.

Cao, Y. *et al.* *Nature* **556**, 80–84 (2018).

[PubMed](#) [Article](#) [Google Scholar](#)

7. 7.

Park, J. M., Cao, Y., Watanabe, K., Taniguchi, T. & Jarillo-Herrero, P. *Nature* **590**, 249–255 (2021).

[PubMed](#) [Article](#) [Google Scholar](#)

8. 8.

Hao, Z. *et al.* *Science* **371**, 1133–1138 (2021).

[PubMed](#) [Article](#) [Google Scholar](#)

9. 9.

Lévy, F., Sheikin, I., Grenier, B. & Huxley, A. D. *Science* **309**, 1343–1346 (2005).

[PubMed](#) [Article](#) [Google Scholar](#)

10. 10.

Ran, S. *et al.* *Nature Phys.* **15**, 1250–1254 (2019).

[Article](#) [Google Scholar](#)

11. 11.

Leggett, A. J. *Rev. Mod. Phys.* **47**, 331–414 (1975).

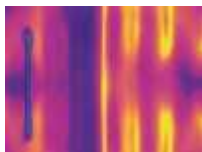
[Article](#) [Google Scholar](#)

[Download references](#)

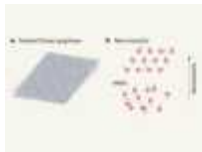
Competing Interests

The author declares no competing interests.

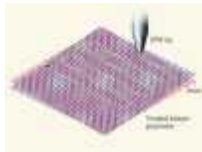
Related Articles



- [Read the paper: Pauli-limit violation and re-entrant superconductivity in moiré graphene](#)



- [Heating freezes electrons in twisted bilayer graphene](#)



- [Spectroscopy of graphene with a magic twist](#)
- [See all News & Views](#)

Subjects

- [Condensed-matter physics](#)

- [Materials science](#)

nature careers

[Jobs](#) >

- [Instrument scientist at the permanent end station REMI@FLASH](#)

German Electron Synchrotron (DESY)

Hamburg, Germany

- [AUSBILDUNG: 3 Auszubildende \(d/m/w\) zum/zur Elektroniker*in für Geräte und Systeme](#)

Helmholtz Centre for Heavy Ion Research GmbH (GSI)

Darmstadt, Germany

- [AUSBILDUNG: 3 Auszubildende \(d/m/w\) zum/zur Anlagenmechaniker*in \(d/m/w\) für Sanitär-, Heizungs- und Klimatechnik](#)

Helmholtz Centre for Heavy Ion Research GmbH (GSI)

Darmstadt, Germany

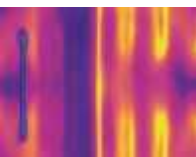
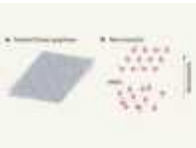
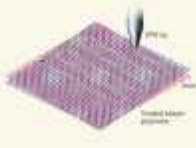
- [AUSBILDUNG: 3 Auszubildende \(d/m/w\) zum/zur Elektroniker*in \(d/m/w\) für Betriebstechnik](#)

Helmholtz Centre for Heavy Ion Research GmbH (GSI)

Darmstadt, Germany

[Download PDF](#)

Related Articles

-  [Read the paper: Pauli-limit violation and re-entrant superconductivity in moiré graphene](#)
-  [Heating freezes electrons in twisted bilayer graphene](#)
-  [Spectroscopy of graphene with a magic twist](#)
- [See all News & Views](#)

Subjects

- [Condensed-matter physics](#)
- [Materials science](#)

This article was downloaded by **calibre** from <https://www.nature.com/articles/d41586-021-01890-3>

- NEWS AND VIEWS
- 21 July 2021

A step closer to compact X-ray lasers

Light sources known as free-electron lasers can produce intense X-ray radiation for a wide range of applications. The process usually needs huge particle accelerators, but an experiment shows how to overcome this limitation.

- [Luca Giannessi](#) 0
1. [Luca Giannessi](#)
 1. Luca Giannessi is at the FERMI FEL facility, Elettra Synchrotron Trieste, 34149 Basovizza, Trieste, Italy, and at the National Institute for Nuclear Physics, National Laboratory of Frascati, Frascati, Italy.

[View author publications](#)

You can also search for this author in [PubMed](#) [Google Scholar](#)





•

[Download PDF](#)

The advent of new tools for investigating our world has always led to discoveries. Light sources called free-electron lasers (FELs) are examples of such tools. FELs can produce radiation in a broad array of wavelengths, including the extreme-ultraviolet¹ and X-ray² ranges, and can generate ultrashort pulses, at femtosecond³ (10^{-15} s) or even attosecond⁴ (10^{-18} s) timescales. At these spatial and temporal scales, there is little difference between biology, chemistry and physics, and FELs have revolutionized all three disciplines. FELs have enabled matter to be frozen in place and observed at the microscopic level, allowing scientists to resolve the motion

of atoms or electrons, control chemical reactions and follow the dynamics of chemical bonds or energy-transfer processes. In [a paper in *Nature*](#), Wang *et al.*⁵ report a milestone in the development of compact X-ray FELs.

FELs generate radiation from a high-energy electron beam traversing an undulator, a long array of magnets of alternating polarity (Fig. 1). The undulator causes the electrons to oscillate transversely, and the oscillating beam emits light at a wavelength proportional to the spatial period of the oscillation divided by the square of the beam energy. Therefore, the beam energy is one of the main parameters used to tune the output wavelength of the FEL light.

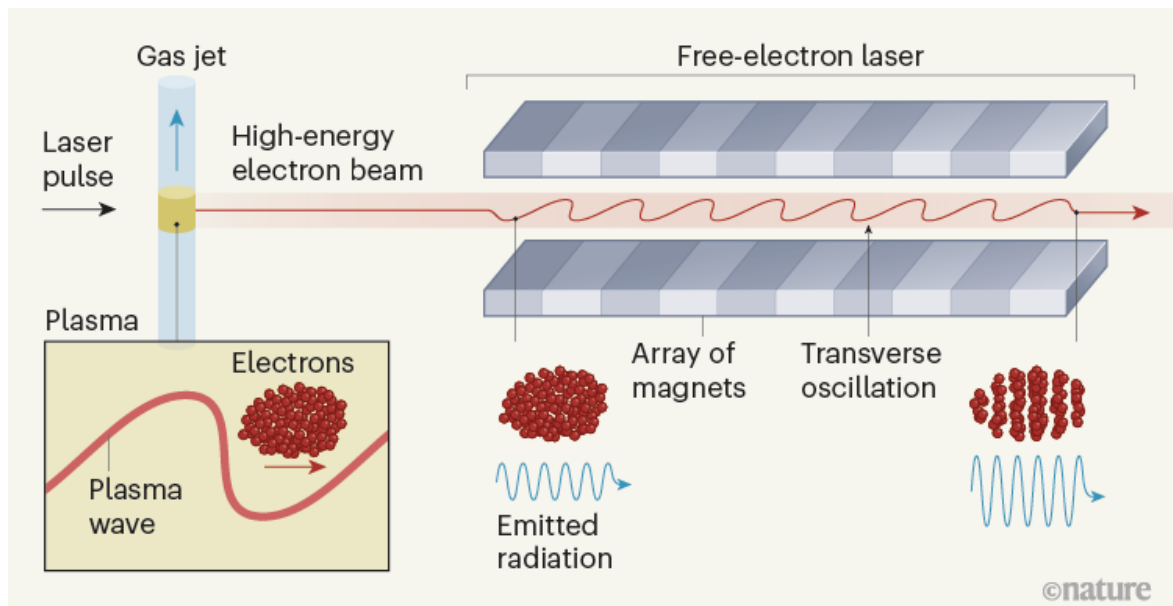
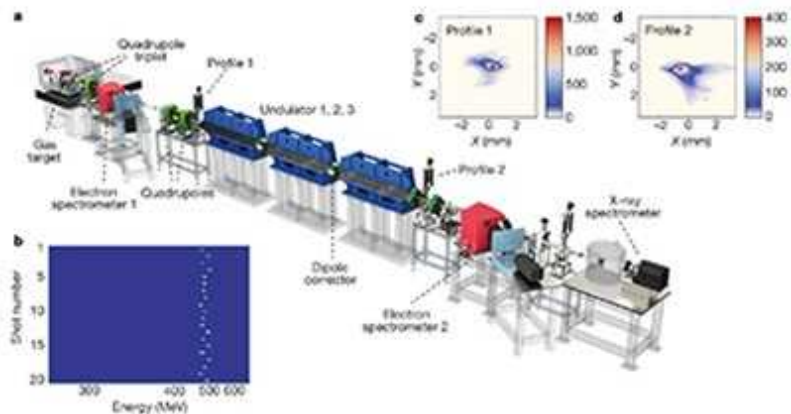


Figure 1 | A free-electron laser driven by electrons accelerated in a laser-excited plasma wave. Wang *et al.*⁵ fired a laser pulse at a gas jet to produce an ionized gas called a plasma. Electrons in the plasma were accelerated as they ‘surfed’ an electromagnetic wave known as a plasma wave. The authors directed the resulting high-energy electron beam into a light source called a free-electron laser, which comprises an array of magnets of alternating polarity (indicated by the two shades of grey). These magnets caused the beam to oscillate transversely and emit radiation. Initially, the electrons were randomly distributed and generated low-amplitude light. However, when leaving the magnets, the electrons were bunched into regions about the size of the radiation wavelength and emitted

high-amplitude light. This demonstration shows that high-energy electron beams for free-electron lasers can be produced in compact set-ups (Wang and colleagues' set-up was about 12 metres long), rather than requiring particle accelerators several hundred metres to a few kilometres in length.

Energy is efficiently transferred from the electron beam to the laser light if the beam has a high-enough current and is sufficiently monochromatic — that is, if the electrons have similar energies, follow similar trajectories and emit light with similar properties. When such a high-brightness beam interacts with the electromagnetic field of the light generated inside the undulator, the beam transfers part of its kinetic energy to the laser light. As a result, the light is amplified by several orders of magnitude while propagating through the undulator. FELs therefore require high-energy and high-brightness electron beams to generate intense laser light at short wavelengths, such as extreme-ultraviolet or X-ray wavelengths.



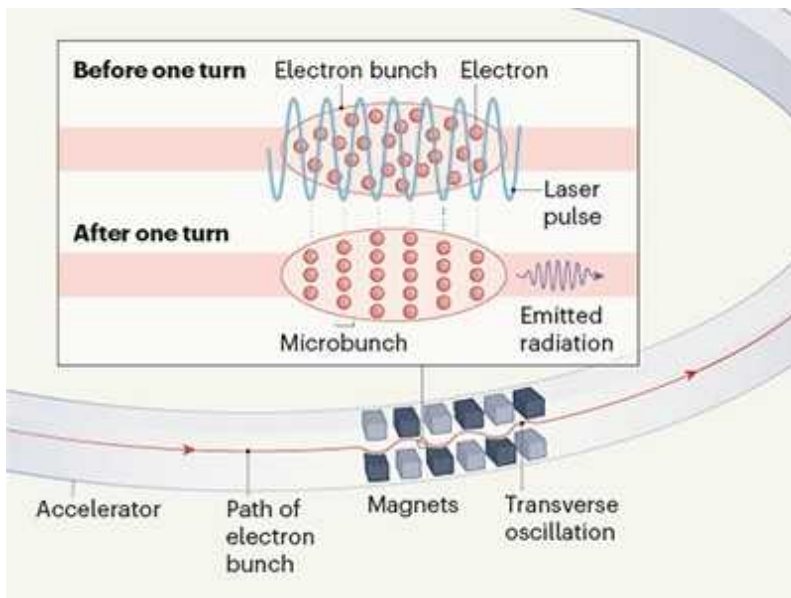
[Read the paper: Free-electron lasing at 27 nanometres based on a laser wakefield accelerator](#)

Electron beams are normally accelerated by injecting the electrons into a long sequence of hollow metal structures called resonant cavities, where the particles progressively gain energy by ‘surfing’ an electromagnetic wave. The final energy depends on the amplitude of the wave (that is, the strength of the accelerating field) and the length of the accelerator. Present

technology limits the field strength in accelerating cavities to a few tens of megavolts per metre. Therefore, an accelerator several hundred metres to a few kilometres in length is required to reach the beam energy of several gigaelectronvolts (GeV) needed by an X-ray FEL. High-energy electron beams therefore tend to be available only at large accelerator facilities, limiting the number of scientists who can access FELs or advanced investigation tools needing high-energy electrons.

This restriction is one of the motivations behind the search for alternative ways of producing strong accelerating fields to reduce the footprint and costs associated with accelerators. One promising idea involves exciting an electromagnetic wave in a plasma — an ionized gas — using the high power density of optical lasers⁶. Accelerating fields that are thousands of times stronger than those in conventional accelerating cavities can be generated in a plasma. With such fields, the electron-beam energy required by an X-ray FEL could be reached in a few tens of centimetres instead of a few kilometres.

A plasma wave can be excited by a laser pulse or the electron beam itself. Indeed, it is possible to shape the beam current in such a way that one part of the beam excites the wave, which then accelerates a second part of the same beam. Both approaches were explored previously, and enormous field strengths, similar to those predicted⁶, were demonstrated^{7,8}. But one of the missing ingredients to drive FELs successfully using these beams concerned the beam quality. Specifically, the energy difference between the electrons was too large, and the emitted radiation behaved as though generated by randomly distributed electrons, rather than by electrons bunched into regions about the size of the radiation wavelength, for which the light amplification is several orders of magnitude larger.



Accelerator-based light sources get a boost

Various teams are concentrating on finding the conditions for stable and reliable acceleration of an electron beam that is sufficiently monochromatic for FEL amplification⁹. Wang *et al.* have demonstrated, for the first time, that this amplification can be achieved using electrons accelerated in a laser-excited plasma wave (Fig. 1). The authors produced the plasma wave by firing a laser pulse at a gas jet that had a diameter of only 6 mm. By manipulating the density of the gas, they shaped the plasma density along the acceleration direction and loaded electrons from the plasma into the accelerating phase of the plasma wave. This technique ensured that the generated beam, with an energy of about 0.5 GeV, was of sufficient quality to amplify radiation in an extreme-ultraviolet FEL at an output wavelength of 27 nm.

The performance of Wang and colleagues' FEL cannot yet match that available in existing FEL facilities that produce radiation at similar wavelengths^{1,10}. However, this laser represents a technological breakthrough, and its stability, reproducibility and efficiency in transferring energy from the electron beam to the radiation will probably be improved in the future. The authors' experiment paves the way for FELs driven by extremely compact accelerators¹¹, which could be managed in university-scale facilities. One of the requirements for a new tool that will favour

discoveries is its availability, and this work promises to increase the availability of FEL light in the world.

Nature **595**, 496–497 (2021)

doi: <https://doi.org/10.1038/d41586-021-01892-1>

References

1. 1.

Feldhaus, J. *J. Phys. B* **43**, 194002 (2010).

[Article](#) [Google Scholar](#)

2. 2.

Emma, P. *et al.* *Nature Photon.* **4**, 641–647 (2010).

[Article](#) [Google Scholar](#)

3. 3.

Mirian, N. S. *et al.* *Nature Photon.* **15**, 523–529 (2021).

[Article](#) [Google Scholar](#)

4. 4.

Huang, S. *et al.* *Phys. Rev. Lett.* **119**, 154801 (2017).

[PubMed](#) [Article](#) [Google Scholar](#)

5. 5.

Wang, W. *et al.* *Nature* **595**, 516–520 (2021).

[Article](#) [Google Scholar](#)

6. 6.

Tajima, T. & Dawson, J. M. *Phys. Rev. Lett.* **43**, 267–270 (1979).

[Article](#) [Google Scholar](#)

7. 7.

Leemans, W. P. *et al.* *Phys. Rev. Lett.* **113**, 245002 (2014).

[PubMed](#) [Article](#) [Google Scholar](#)

8. 8.

Blumenfeld, I. *et al.* *Nature* **445**, 741–744 (2007).

[PubMed](#) [Article](#) [Google Scholar](#)

9. 9.

Pompili, R. *et al.* *Nature Phys.* **17**, 499–503 (2021).

[Article](#) [Google Scholar](#)

10. 10.

Allaria, E. *et al.* *Nature Photon.* **6**, 699–704 (2012).

[Article](#) [Google Scholar](#)

11. 11.

Assmann, R. W. *et al.* *Eur. Phys. J. Spec. Top.* **229**, 3675–4284 (2020).

[Article](#) [Google Scholar](#)

[Download references](#)

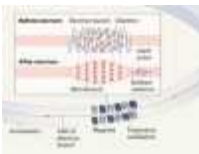
Competing Interests

The author declares no competing interests.

Related Articles



- [**Read the paper: Free-electron lasing at 27 nanometres based on a laser wakefield accelerator**](#)



- [**Accelerator-based light sources get a boost**](#)
-  A diagram illustrating the interaction between short proton bunches and energetic electrons, showing how the protons transfer energy to the electrons.
- [**Short proton bunches rapidly accelerate energetic electrons**](#)
- [**See all News & Views**](#)

Subjects

- [Optics and photonics](#)
- [Applied physics](#)
- [Physics](#)

nature careers

Jobs >

- [**Instrument scientist at the permanent end station REMI@FLASH**](#)

German Electron Synchrotron (DESY)

Hamburg, Germany

- **AUSBILDUNG: 3 Auszubildende (d/m/w) zum/zur Elektroniker*in für Geräte und Systeme**

Helmholtz Centre for Heavy Ion Research GmbH (GSI)

Darmstadt, Germany

- **AUSBILDUNG: 3 Auszubildende (d/m/w) zum/zur Anlagenmechaniker*in (d/m/w) für Sanitär-, Heizungs- und Klimatechnik**

Helmholtz Centre for Heavy Ion Research GmbH (GSI)

Darmstadt, Germany

- **AUSBILDUNG: 3 Auszubildende (d/m/w) zum/zur Elektroniker*in (d/m/w) für Betriebstechnik**

Helmholtz Centre for Heavy Ion Research GmbH (GSI)

Darmstadt, Germany

[Download PDF](#)

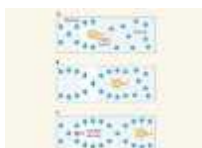
Related Articles



- **Read the paper: Free-electron lasing at 27 nanometres based on a laser wakefield accelerator**



-  **Accelerator-based light sources get a boost**
 - 
Short proton bunches rapidly accelerate energetic electrons
 - See all News & Views



Subjects

- Optics and photonics
 - Applied physics
 - Physics

This article was downloaded by **calibre** from <https://www.nature.com/articles/d41586-021-01892-1>

- NEWS AND VIEWS
- 21 July 2021

Fluid flow through a deep-sea sponge could inspire engineering designs

Sophisticated numerical simulations reveal that the beautiful structure of a sponge known as Venus's flower basket reduces hydrodynamic drag, and probably aids the capture of food particles, as well as sperm for sexual reproduction.

- [Laura A. Miller](#) ✉
 1. [Laura A. Miller](#)

1. Laura A. Miller is in the Departments of Mathematics and Biomedical Engineering, University of Arizona, Tucson, Arizona 85721, USA.

[View author publications](#)

You can also search for this author in [PubMed](#) [Google Scholar](#)





•

[Download PDF](#)

The deep-sea sponge *Euplectella aspergillum*, also known as Venus's flower basket, is celebrated for its intricate glass skeleton. This structure provides remarkable mechanical support and has inspired a generation of strong, lightweight bridges and skyscrapers¹. Water is continuously drawn into and out of the sponge's central body cavity through pores, to filter food particles and exchange gases. Although the mechanical properties of the sponge's skeleton are well documented, little is known about the detailed fluid flows around and through the organism. In [a paper in *Nature*](#), Falcucci *et al.*² use state-of-the-art fluid-dynamics simulations to resolve these flows. Their

results show that the sponge's structural elements reduce the impact of hydrodynamic forces on the organism and generate internal circulation patterns that might be used for feeding and sexual reproduction.

The skeleton of *E. aspergillum* consists of a regular square lattice that is diagonally reinforced and forms scaffolding for the sponge's hollow cylindrical body³ (Fig. 1). In addition, external ridges spiral around the main body and are superimposed on the lattice. To deconstruct the effect of each skeletal component on the fluid flows, Falcucci and colleagues generated several idealized models of the sponge for comparison. These models included a plain solid cylinder, a solid cylinder with helical ridges, a hollow cylindrical lattice and a hollow cylindrical lattice with helical ridges.

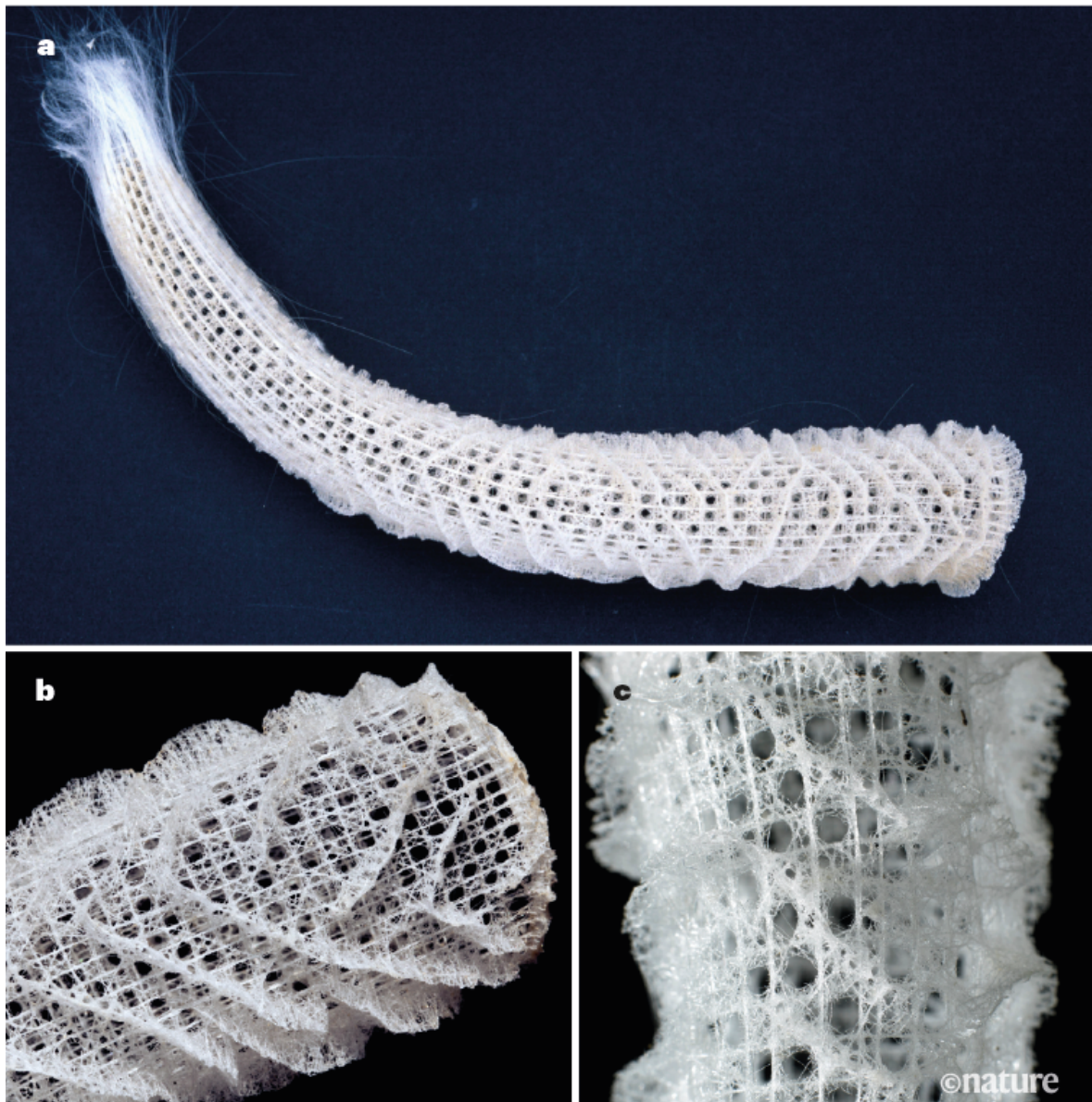
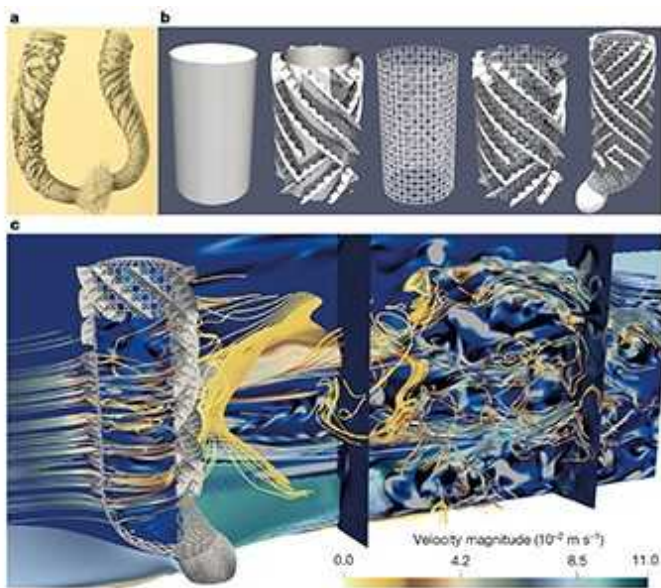


Figure 1 | Venus's flower basket. **a**, Falcucci *et al.*² used sophisticated fluid-dynamics simulations to study fluid flows through and around the intricate skeleton of a deep-sea sponge known as Venus's flower basket. The tubular skeleton can be up to 250 millimetres long. **b**, External ridges spiral around the main body of the sponge. The authors found that these ridges generate low-speed flow structures in the body cavity that probably enhance the capture of food particles. **c**, The ridges are superimposed on a regular square lattice that is diagonally reinforced. Falcucci and colleagues discovered that this porous skeleton reduces hydrodynamic drag, boosting the organism's robustness to strong ocean flows.

Determining the fluid flows for these different models required extremely accurate fluid-dynamics simulations. These can simultaneously resolve a level of detail from the microscopic flows around the skeleton all the way up to the bulk flows around the entire organism. To make these *in silico* experiments feasible, Falcucci *et al.* numerically solved the equations that govern such flows using a method that lends itself particularly well to parallel computing on electronic circuits called graphics processing units⁴. Moreover, the authors ran the simulations on Marconi100, one of the most powerful supercomputers in the world (see go.nature.com/3hzrzjp).

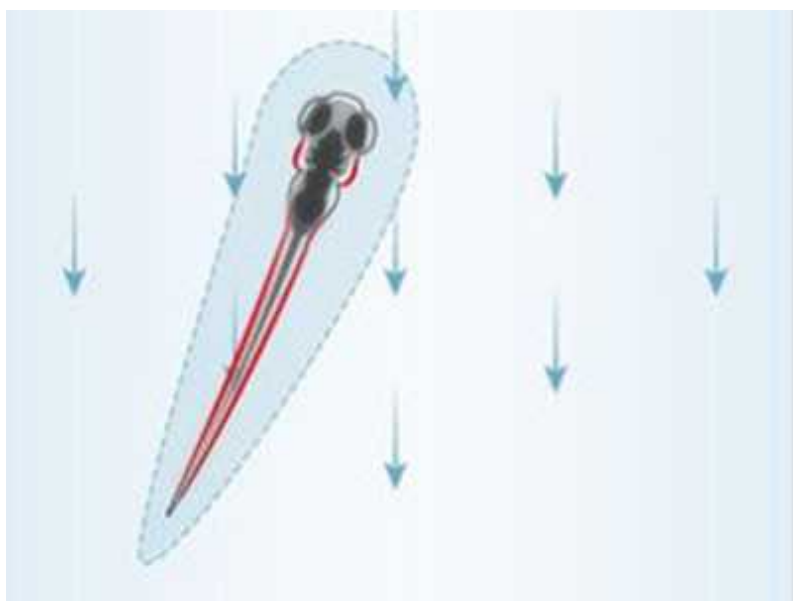


[Read the paper: Extreme flow simulations reveal skeletal adaptations of deep-sea sponges](#)

It is well documented that, in water flows of 1–10 centimetres per second or more, solid cylinders roughly the size of *E. aspergillum* undergo vortex shedding⁵ — a process in which repeating patterns of swirling vortices form on the downstream side of an object. This phenomenon results in large velocity fluctuations in the wake of the cylinder, as well as varying and increased hydrodynamic drag. Falcucci and colleagues' *in silico* experiments showed that a hollow cylindrical lattice acts as a porous object that suppresses such velocity fluctuations and decreases drag. Given that hydrodynamic forces can be powerful enough to dislodge a sea sponge, reduced drag improves the organism's robustness in the presence of strong flows.

The authors also found that the inclusion of helical ridges generates low-speed vortical structures in the cylinder's central cavity. For *E. aspergillum*, such flow structures probably improve the capture of food particles by increasing the rate of encounters between plankton and the sponge's body cavity. Similarly, these structures could increase the contact between free-swimming sperm and retained eggs, thereby boosting reproductive efficiency.

Although these *in silico* experiments have greatly advanced what is known about fluid flow through *E. aspergillum*, there is still much that is not understood. For instance, Falcucci *et al.* were able to show that the sponge's external helical ridges increase the residence time of particles in the central cavity. However, the extent to which this aids food uptake and gas exchange has not been quantified. Future work should consider how the low-speed vortical structures in the cavity might selectively filter particles of specific shapes and sizes.



How fish feel the flow

Furthermore, it is not yet understood how cells that actively drive fluid flow through the sponge by beating their hair-like extensions (flagella) interact with the environmentally driven flows. The *in silico* experiments also assumed that the oncoming flow is steady and that the sponge is rigid. Deformations of the sponge in unsteady currents probably produce

hydrodynamic forces that are different from the simplified case considered by the authors.

This work provides a striking example of how state-of-the-art numerical simulations can be used to explore problems in areas such as biomechanics, fundamental fluid dynamics and bioinspired design. Falcucci and colleagues' results suggest that many of the complex structures seen in marine invertebrates and other organisms have non-intuitive consequences for fluid dynamics. The authors' approach could be applied to a vast array of puzzles in nature related not only to food filtering, gas exchange and drag reduction, but also to pollen capture and heat loss. For example, such multiscale flow simulations could be used to understand the hydrodynamics of gas exchange through coral reefs⁶, or the aerodynamics of pollen capture⁷.

Moreover, this study of Venus's flower basket reveals how complex geometries can manipulate fluid flow for multiple functions, including drag reduction, mechanical support and particle filtering. The lessons learnt from this organism could inspire improved multifunctional engineering structures, such as sampling and filtering devices.

Nature **595**, 497–498 (2021)

doi: <https://doi.org/10.1038/d41586-021-01891-2>

References

1. 1.

Fernandes, M. C., Aizenberg, J., Weaver, J. C. & Bertoldi, K. *Nature Mater.* **20**, 237–241 (2021).

[PubMed](#) [Article](#) [Google Scholar](#)

2. 2.

Falcucci, G. *et al.* *Nature* **595**, 537–541 (2021).

[Article](#) [Google Scholar](#)

3. 3.

Weaver, J. C. *et al.* *J. Struct. Biol.* **158**, 93–106 (2007).

[PubMed](#) [Article](#) [Google Scholar](#)

4. 4.

Succi, S. *The Lattice Boltzmann Equation: For Complex States of Flowing Matter* (Oxford Univ. Press, 2018).

[Google Scholar](#)

5. 5.

Tritton, D. J. *J. Fluid Mech.* **6**, 547–567 (1959).

[Article](#) [Google Scholar](#)

6. 6.

Monismith, S. G. *Annu. Rev. Fluid Mech.* **39**, 37–55 (2007).

[Article](#) [Google Scholar](#)

7. 7.

Niklas, K. J. *Bot. Rev.* **51**, 328 (1985).

[Article](#) [Google Scholar](#)

[Download references](#)

Competing Interests

The author declares no competing interests.

Related Articles

-  [Read the paper: Extreme flow simulations reveal skeletal adaptations of deep-sea sponges](#)
-  [How fish feel the flow](#)
-  [The aerodynamics buzz from mosquitoes](#)
- [See all News & Views](#)

Subjects

- [Biomechanics](#)
- [Fluid dynamics](#)
- [Computational biology and bioinformatics](#)

nature careers

[Jobs](#) >

- [Instrument scientist at the permanent end station REMI@FLASH](#)

German Electron Synchrotron (DESY)

Hamburg, Germany

- **AUSBILDUNG: 3 Auszubildende (d/m/w) zum/zur Elektroniker*in für Geräte und Systeme**

Helmholtz Centre for Heavy Ion Research GmbH (GSI)

Darmstadt, Germany

- **AUSBILDUNG: 3 Auszubildende (d/m/w) zum/zur Anlagenmechaniker*in (d/m/w) für Sanitär-, Heizungs- und Klimatechnik**

Helmholtz Centre for Heavy Ion Research GmbH (GSI)

Darmstadt, Germany

- **AUSBILDUNG: 3 Auszubildende (d/m/w) zum/zur Elektroniker*in (d/m/w) für Betriebstechnik**

Helmholtz Centre for Heavy Ion Research GmbH (GSI)

Darmstadt, Germany

[Download PDF](#)

Related Articles

-  [Read the paper: Extreme flow simulations reveal skeletal adaptations of deep-sea sponges](#)

-  [How fish feel the flow](#)



- [**The aerodynamics buzz from mosquitoes**](#)
- [**See all News & Views**](#)

Subjects

- [Biomechanics](#)
- [Fluid dynamics](#)
- [Computational biology and bioinformatics](#)

This article was downloaded by **calibre** from <https://www.nature.com/articles/d41586-021-01891-2>

| [Section menu](#) | [Main menu](#) |

- NEWS AND VIEWS
- 14 July 2021

Receptor–enzyme complex structures show how receptors start to switch off

The structure of rhodopsin, an archetypal member of the G-protein-coupled family of receptors, in complex with its specific kinase enzyme, reveals the molecular mechanism of the first step of receptor inactivation.

- [Vsevolod V. Gurevich](#) ⁰ &
 - [Eugenia V. Gurevich](#)¹
1. [Vsevolod V. Gurevich](#)

1. Vsevolod V. Gurevich is in the Department of Pharmacology,
Vanderbilt University, Nashville, Tennessee 37232, USA.

[View author publications](#)

You can also search for this author in [PubMed](#) [Google Scholar](#)

2. Eugenia V. Gurevich

1. Eugenia V. Gurevich is in the Department of Pharmacology,
Vanderbilt University, Nashville, Tennessee 37232, USA.

[View author publications](#)

You can also search for this author in [PubMed](#) [Google Scholar](#)



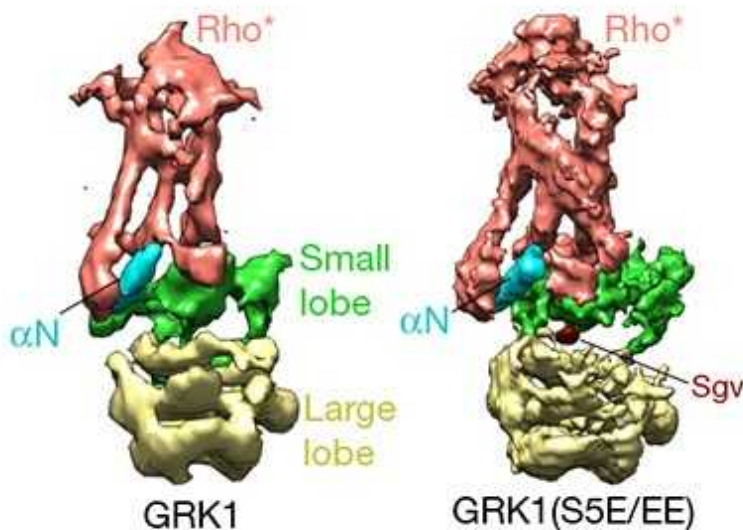


•

[Download PDF](#)

Cell behaviour is regulated by myriad external stimuli that act through specialized receptor proteins at the cell surface. G-protein-coupled receptors (GPCRs) are the largest family of receptors and mediate cellular responses to hormones, neurotransmitter molecules, light and other stimuli by activating G proteins inside cells. This signalling is terminated by a two-step mechanism: G-protein-coupled receptor kinase (GRK) enzymes add phosphate chemical groups to an active receptor, and the active phosphorylated receptor is then bound by arrestin proteins, precluding its further coupling to G proteins. [Writing in Nature](#), Chen *et al.*¹ report the first

structure of a GPCR–GRK complex: the light-responsive receptor rhodopsin bound to its specific kinase, GRK1 (also known as rhodopsin kinase).



[Read the paper: Structures of rhodopsin in complex with G-protein-coupled receptor kinase 1](#)

Phosphorylation of GPCRs by GRKs is the crucial, rate-limiting step in switching off receptors, a process called desensitization. The receptor–GRK interaction determines the dynamics of G-protein-mediated signalling because it affects the subsequent recruitment of arrestins, which bind to most GPCRs with high affinity only after the receptor is phosphorylated. Receptor-bound arrestins shut down G-protein-dependent signalling and initiate signalling through other pathways, which are determined by the pattern of phosphate groups attached to a receptor by a GRK (ref. 2)². The determination of the rhodopsin–GRK1 structure is an important step forward in understanding GPCR–GRK interactions that might transform our models of the regulation of GPCR signalling.

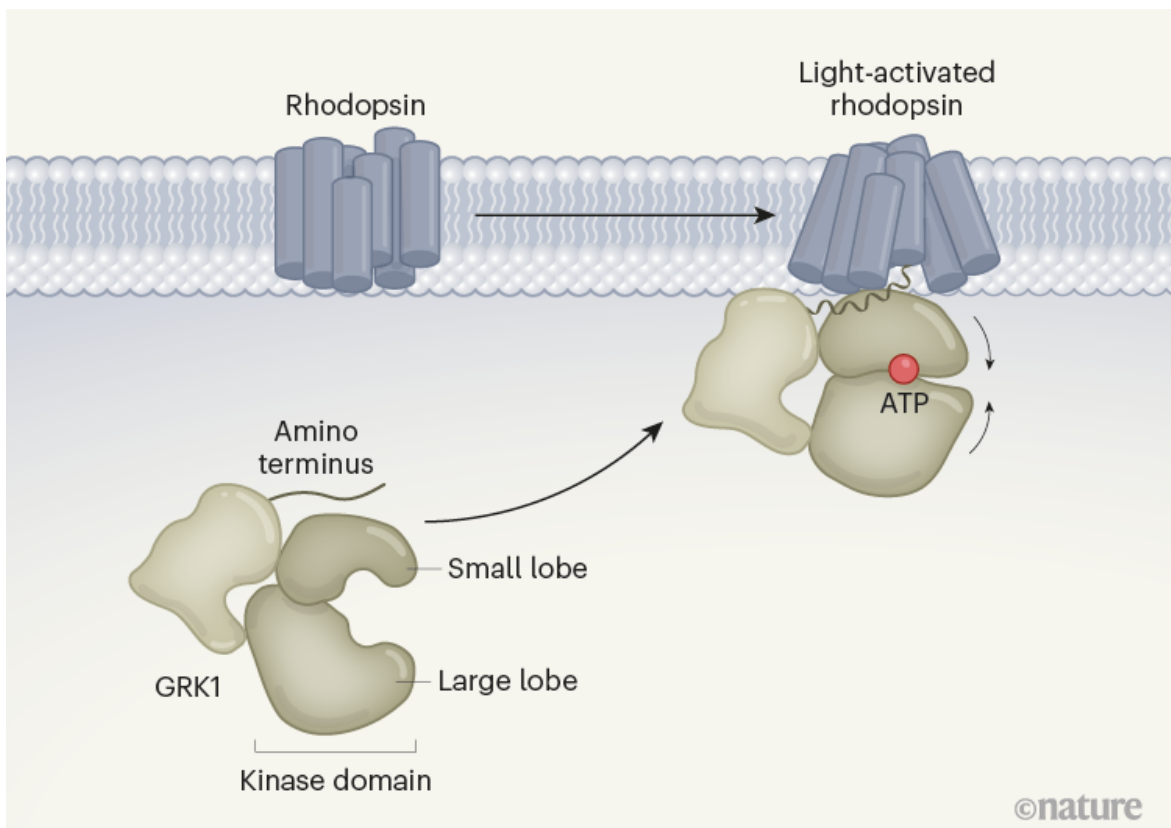
The structure presented by Chen and colleagues is a tour de force owing to its 4-ångström resolution and the biological insights it yields. GRKs bind to GPCRs only transiently, such that capturing a GPCR–GRK complex to determine its structure poses a considerable challenge. Two previous attempts at elucidating the structure of GPCR–GRK complexes^{3,4} involved various biochemical and biophysical methods, combined with negative-stain

electron microscopy and modelling. Because the proposed structures were deduced rather than determined, they were, naturally, unable to explain certain established biochemical findings.

In this context, the work by Chen *et al.*¹ presents the first real structure of a GPCR–GRK complex. To achieve this feat, the authors crosslinked the two proteins and used two different antibodies to make the complex stable for long enough to be characterized using cryo-electron microscopy. The resulting insights were certainly worth the effort.

Most GRKs, including GRK1, show a clear preference for activated GPCRs. Thus, conformational changes in receptors resulting from their activation must be recognized by GRKs to facilitate binding. The key question in GPCR biology is: what common features do active, as opposed to inactive, GPCRs have that ‘attract’ GRKs?

In the structure obtained by Chen *et al.*, the amino terminus of the GRK (which is specific to and shared by members of the GRK family) was found to insert into the cavity that opens up between the membrane-spanning helices of the receptor on GPCR activation⁵. This cavity is also engaged by other binding partners, such as transducin (the G protein activated by rhodopsin⁶) and visual arrestin-1 (ref. 7)⁷, that prefer active GPCRs over inactive ones. The N terminus of GRK1 forms an α -helix on binding to rhodopsin, as do the parts of transducin and arrestin-1 that engage the same receptor cavity (Fig. 1).



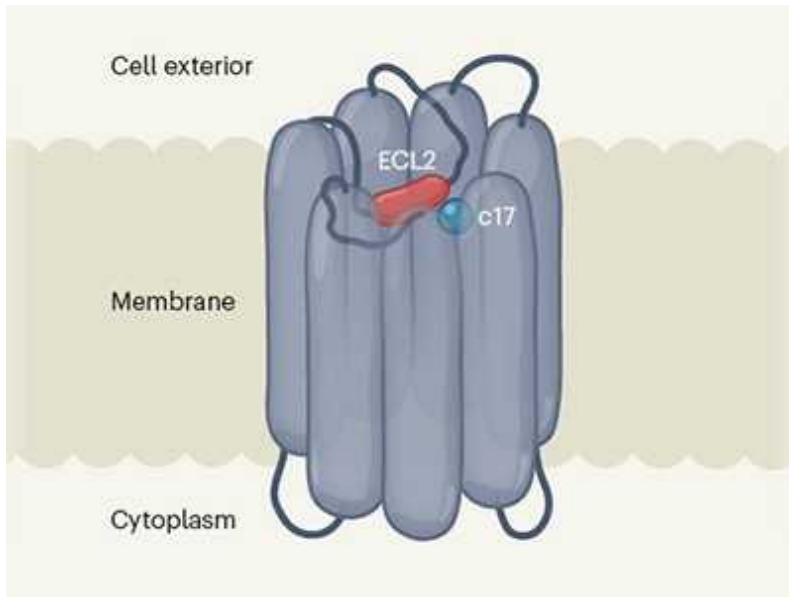
©nature

Figure 1 | A first step to switching off G-protein-coupled receptors. The switch-off (desensitization) of an active G-protein-coupled receptor protein (GPCR) is initiated when it binds to an enzyme called a G-protein-coupled receptor kinase (GRK). Chen *et al.*¹ used cryo-electron microscopy to determine the structure of the GPCR rhodopsin in complex with its GRK, GRK1. The inactive receptor does not attract GRK1 and, under baseline conditions, the small and large lobes of the kinase domain of GRK1 are misaligned, making it inactive. However, when rhodopsin is activated by a photon of light, the GRK amino terminus preferentially binds to active (rather than inactive) GPCRs by forming an α -helix and engaging the cavity that opens up between the membrane-spanning helices of the receptor. The receptor also binds to the kinase domain, ‘pushing’ its two lobes into alignment to create an active catalytic site that can bind to ATP molecules, which is necessary for transferring phosphates from them to the receptor.

It was previously known that the basal phosphorylating activity of GRKs is low, but increases dramatically when GRK binds to a receptor. As such, the receptor itself activates the kinase, serving as both a substrate and an

allosteric activator (that is, it activates the catalytic site of the kinase by binding to the enzyme at another site). The part of a GRK that is responsible for its phosphorylating activity — the kinase domain — consists of a small lobe and a large lobe. In the non-active GRK, the two lobes are misaligned, characteristic of inactive kinases generally⁸. For the receptor to activate GRKs⁹, it must force the alignment of the two GRK lobes to create an active catalytic site. In the structure resolved by Chen *et al.*, the receptor interacts with the kinase domain, suggesting that the binding of the receptor to this domain pushes the lobes into alignment¹, thereby promoting the kinase activity (Fig. 1).

Naturally, many questions remain. First, rhodopsin is a specialized receptor that responds to light and is expressed almost exclusively in rod photoreceptor cells in the retina, enabling vision. Similarly, GRK1 is a specialized kinase with a high preference for rhodopsin over non-visual GPCRs. By contrast, five of the seven mammalian GRK subtypes show widespread expression in various cell types, and each interacts with diverse GPCRs. Thus, the structures of GRKs bound to different GPCRs are needed to identify common mechanisms of GPCR regulation.



A self-activating orphan receptor

Second, the structure of the GPCR–GRK complex described here represents the final stage of the interaction between these proteins, and the process of

binding requires further study. In most cases, GRKs need to attach more than one phosphate group to a receptor to enable tight arrestin binding. Therefore, a GRK probably has to bind to an active GPCR more than once to phosphorylate several amino-acid residues in the GPCR.

The dynamics of GRK binding to a GPCR, as well as those of GRK activation, remain to be determined, for example using biophysical methods. Characterizing the steps that the two proteins go through to achieve the complex revealed by this structure is crucial for the development of molecular tools to modify or control this process, which in turn could be used to channel GPCR signalling towards a desired direction.

Nature **595**, 499–500 (2021)

doi: <https://doi.org/10.1038/d41586-021-01873-4>

References

1. 1.

Chen, Q. *et al.* *Nature* **595**, 600–605 (2021).

[Article](#) [Google Scholar](#)

2. 2.

Nobles, K. N. *et al.* *Sci. Signal.* **4**, ra51 (2011).

[PubMed](#) [Article](#) [Google Scholar](#)

3. 3.

He, Y. *et al.* *Cell Res.* **27**, 728–747 (2017).

[PubMed](#) [Article](#) [Google Scholar](#)

4. 4.

Komolov, K. E. *et al.* *Cell* **169**, 407–421 (2017).

[PubMed](#) [Article](#) [Google Scholar](#)

5. 5.

Weis, W. I. & Kobilka, B. K. *Annu. Rev. Biochem.* **87**, 897–919 (2018).

[PubMed](#) [Article](#) [Google Scholar](#)

6. 6.

Gao, Y. *et al.* *Mol. Cell* **75**, 781–790 (2019).

[PubMed](#) [Article](#) [Google Scholar](#)

7. 7.

Kang, Y. *et al.* *Nature* **523**, 561–567 (2015).

[PubMed](#) [Article](#) [Google Scholar](#)

8. 8.

Cato, M. C. *et al.* *Biomolecules* **11**, 447 (2021).

[PubMed](#) [Article](#) [Google Scholar](#)

9. 9.

Palczewski, K., Buczylko, J., Kaplan, M. W., Polans, A. S. & Crabb, J. W. *J. Biol. Chem.* **266**, 12949–12955 (1991).

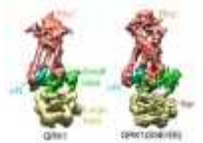
[PubMed](#) [Article](#) [Google Scholar](#)

[Download references](#)

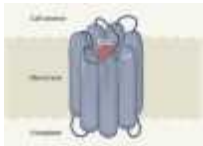
Competing Interests

The authors declare no competing interests.

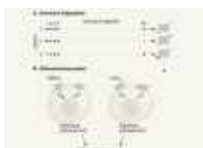
Related Articles



- [Read the paper: Structures of rhodopsin in complex with G-protein-coupled receptor kinase 1](#)



- [A self-activating orphan receptor](#)



- [Isoforms of GPCR proteins combine for diverse signalling](#)
- [See all News & Views](#)

Subjects

- [Structural biology](#)
- [Molecular biology](#)

nature careers

[Jobs](#) >

- [Instrument scientist at the permanent end station REMI@FLASH](#)

German Electron Synchrotron (DESY)

Hamburg, Germany

- [AUSBILDUNG: 3 Auszubildende \(d/m/w\) zum/zur Elektroniker*in für Geräte und Systeme](#)

Helmholtz Centre for Heavy Ion Research GmbH (GSI)

Darmstadt, Germany

- [AUSBILDUNG: 3 Auszubildende \(d/m/w\) zum/zur Anlagenmechaniker*in \(d/m/w\) für Sanitär-, Heizungs- und Klimatechnik](#)

Helmholtz Centre for Heavy Ion Research GmbH (GSI)

Darmstadt, Germany

- [AUSBILDUNG: 3 Auszubildende \(d/m/w\) zum/zur Elektroniker*in \(d/m/w\) für Betriebstechnik](#)

Helmholtz Centre for Heavy Ion Research GmbH (GSI)

Darmstadt, Germany

[Download PDF](#)

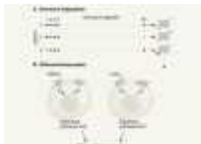
Related Articles



- [Read the paper: Structures of rhodopsin in complex with G-protein-coupled receptor kinase 1](#)



- [A self-activating orphan receptor](#)



- Isoforms of GPCR proteins combine for diverse signalling
- See all News & Views

Subjects

- Structural biology
- Molecular biology

This article was downloaded by **calibre** from <https://www.nature.com/articles/d41586-021-01873-4>

| [Section menu](#) | [Main menu](#) |

- Review Article
- [Published: 21 July 2021](#)

A multilayered immune system through the lens of unconventional T cells

- [Toufic Mayassi^{1,2},](#)
- [Luis B. Barreiro^{2,3,4},](#)
- [Jamie Rossjohn ORCID: orcid.org/0000-0002-2020-7522^{5,6,7}](#) &
- [Bana Jabri ORCID: orcid.org/0000-0001-7427-4424^{2,8,9,10}](#)

Nature volume **595**, pages 501–510 (2021) [Cite this article](#)

- 2239 Accesses
- 37 Altmetric
- [Metrics details](#)

Subjects

- [Mucosal immunology](#)
- [T cells](#)

Abstract

The unconventional T cell compartment encompasses a variety of cell subsets that straddle the line between innate and adaptive immunity, often reside at mucosal surfaces and can recognize a wide range of non-polymorphic ligands. Recent advances have highlighted the role of

unconventional T cells in tissue homeostasis and disease. In this Review, we recast unconventional T cell subsets according to the class of ligand that they recognize; their expression of semi-invariant or diverse T cell receptors; the structural features that underlie ligand recognition; their acquisition of effector functions in the thymus or periphery; and their distinct functional properties. Unconventional T cells follow specific selection rules and are poised to recognize self or evolutionarily conserved microbial antigens. We discuss these features from an evolutionary perspective to provide insights into the development and function of unconventional T cells. Finally, we elaborate on the functional redundancy of unconventional T cells and their relationship to subsets of innate and adaptive lymphoid cells, and propose that the unconventional T cell compartment has a critical role in our survival by expanding and complementing the role of the conventional T cell compartment in protective immunity, tissue healing and barrier function.

Access options

Subscribe to Journal

Get full journal access for 1 year

\$199.00

only \$3.90 per issue

[Subscribe](#)

All prices are NET prices.

VAT will be added later in the checkout.

Tax calculation will be finalised during checkout.

Rent or Buy article

Get time limited or full article access on ReadCube.

from \$8.99

Rent or Buy

All prices are NET prices.

Additional access options:

- [Log in](#)
- [Access through your institution](#)
- [Learn about institutional subscriptions](#)

Fig. 1: Comparison of TCR docking modes.

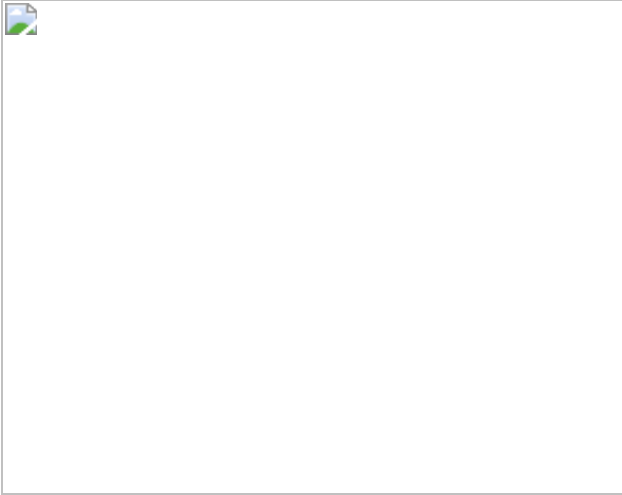


Fig. 2: Classification of non-classical T cells on the basis of central or peripheral development.



Fig. 3: Functional niche of unconventional T cells.

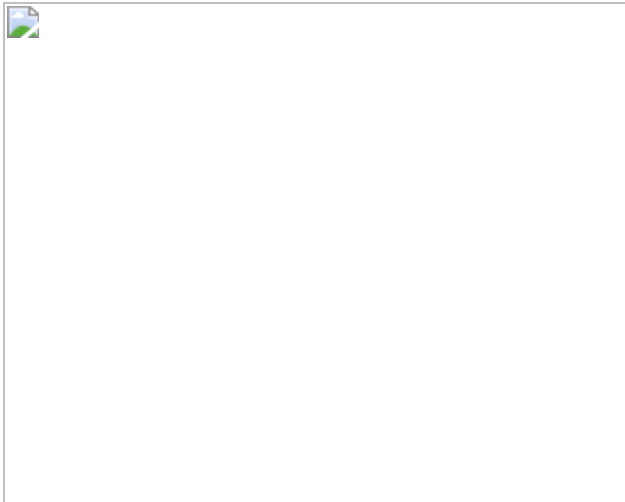
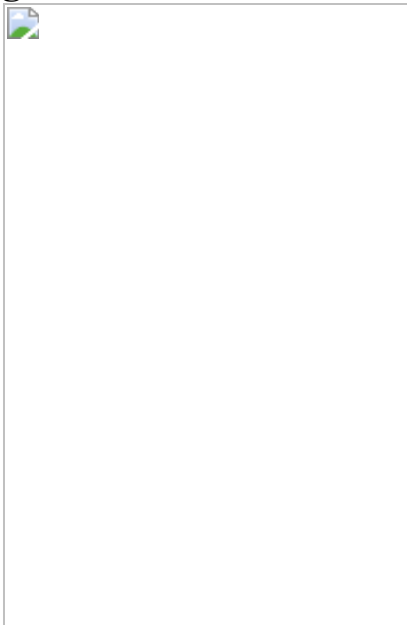


Fig. 4: Conservation and redundancy within the T cell compartment.



References

1. 1.

Godfrey, D. I., MacDonald, H. R., Kronenberg, M., Smyth, M. J. & Van Kaer, L. NKT cells: what's in a name? *Nat. Rev. Immunol.* **4**, 231–237 (2004).

[CAS](#) [PubMed](#) [Article](#) [Google Scholar](#)

2. 2.

Lu, L., Werneck, M. B. F. & Cantor, H. The immunoregulatory effects of Qa-1. *Immunol. Rev.* **212**, 51–59 (2006).

[CAS](#) [PubMed](#) [Article](#) [Google Scholar](#)

3. 3.

Colmone, A. & Wang, C.-R. H2-M3-restricted T cell response to infection. *Microbes Infect.* **8**, 2277–2283 (2006).

[CAS](#) [PubMed](#) [Article](#) [Google Scholar](#)

4. 4.

Bendelac, A., Savage, P. B. & Teyton, L. The biology of NKT cells. *Annu. Rev. Immunol.* **25**, 297–336 (2007).

[CAS](#) [PubMed](#) [Article](#) [Google Scholar](#)

5. 5.

Cohen, N. R., Garg, S. & Brenner, M. B. Antigen presentation by CD1 lipids, T cells, and NKT cells in microbial immunity. *Adv. Immunol.* **102**, 1–94 (2009).

[CAS](#) [PubMed](#) [Article](#) [Google Scholar](#)

6. 6.

Cheroutre, H., Lambolez, F. & Mucida, D. The light and dark sides of intestinal intraepithelial lymphocytes. *Nat. Rev. Immunol.* **11**, 445–456 (2011).

[CAS](#) [PubMed](#) [PubMed Central](#) [Article](#) [Google Scholar](#)

7. 7.

Kim, H.-J. & Cantor, H. Regulation of self-tolerance by Qa-1-restricted CD8⁺ regulatory T cells. *Semin. Immunol.* **23**, 446–452 (2011).

[CAS](#) [PubMed](#) [PubMed Central](#) [Article](#) [Google Scholar](#)

8. 8.

Godfrey, D. I., Uldrich, A. P., McCluskey, J., Rossjohn, J. & Moody, D. B. The burgeoning family of unconventional T cells. *Nat. Immunol.* **16**, 1114–1123 (2015).

[CAS](#) [PubMed](#) [Article](#) [Google Scholar](#)

9. 9.

Mayassi, T. & Jabri, B. Human intraepithelial lymphocytes. *Mucosal Immunol.* **11**, 1281–1289 (2018).

[CAS](#) [PubMed](#) [PubMed Central](#) [Article](#) [Google Scholar](#)

10. 10.

Ogg, G., Cerundolo, V. & McMichael, A. J. Capturing the antigen landscape: HLA-E, CD1 and MR1. *Curr. Opin. Immunol.* **59**, 121–129 (2019).

[CAS](#) [PubMed](#) [Article](#) [PubMed Central](#) [Google Scholar](#)

11. 11.

Legoux, F., Salou, M. & Lantz, O. MAIT cell development and functions: the microbial connection. *Immunity* **53**, 710–723 (2020).

[CAS](#) [PubMed](#) [Article](#) [PubMed Central](#) [Google Scholar](#)

12. 12.

Vantourout, P. & Hayday, A. Six-of-the-best: unique contributions of $\gamma\delta$ T cells to immunology. *Nat. Rev. Immunol.* **13**, 88–100 (2013).

[CAS](#) [PubMed](#) [PubMed Central](#) [Article](#) [Google Scholar](#)

13. 13.

Nielsen, M. M., Witherden, D. A. & Havran, W. L. $\gamma\delta$ T cells in homeostasis and host defence of epithelial barrier tissues. *Nat. Rev. Immunol.* **17**, 733–745 (2017).

[CAS](#) [PubMed](#) [PubMed Central](#) [Article](#) [Google Scholar](#)

14. 14.

Jouand, N. et al. HCMV triggers frequent and persistent UL40-specific unconventional HLA-E-restricted CD8 T-cell responses with potential autologous and allogeneic peptide recognition. *PLoS Pathog.* **14**, e1007041 (2018).

[PubMed](#) [PubMed Central](#) [Article](#) [CAS](#) [Google Scholar](#)

15. 15.

Bian, Y. et al. MHC Ib molecule Qa-1 presents *Mycobacterium tuberculosis* peptide antigens to CD8 $^{+}$ T cells and contributes to protection against infection. *PLoS Pathog.* **13**, e1006384 (2017).

[PubMed](#) [PubMed Central](#) [Article](#) [CAS](#) [Google Scholar](#)

16. 16.

Bendelac, A. et al. CD1 recognition by mouse NK1⁺ T lymphocytes. *Science* **268**, 863–865 (1995). **This paper demonstrates that NKT cells recognize CD1d.**

[ADS](#) [CAS](#) [PubMed](#) [Article](#) [Google Scholar](#)

17. 17.

Mattner, J. et al. Exogenous and endogenous glycolipid antigens activate NKT cells during microbial infections. *Nature* **434**, 525–529 (2005). **This paper and the following reference show that NKT cells promote defence against bacterial infections by recognizing either self or microbial glycolipids.**

[ADS](#) [CAS](#) [PubMed](#) [Article](#) [Google Scholar](#)

18. 18.

Kinjo, Y. et al. Recognition of bacterial glycosphingolipids by natural killer T cells. *Nature* **434**, 520–525 (2005).

[ADS](#) [CAS](#) [PubMed](#) [Article](#) [Google Scholar](#)

19. 19.

Kjer-Nielsen, L. et al. MR1 presents microbial vitamin B metabolites to MAIT cells. *Nature* **491**, 717–723 (2012). **This paper demonstrates that MR1 presents vitamin B metabolites to MAIT cells.**

[ADS](#) [CAS](#) [PubMed](#) [Article](#) [Google Scholar](#)

20. 20.

Corbett, A. J. et al. T-cell activation by transitory neo-antigens derived from distinct microbial pathways. *Nature* **509**, 361–365 (2014).

[ADS](#) [CAS](#) [PubMed](#) [Article](#) [PubMed Central](#) [Google Scholar](#)

21. 21.

Shawar, S. M., Rodgers, J. R., Cook, R. G. & Rich, R. R. Specialized function of the nonclassical MHC class I molecule Hmt: a specific receptor for N-formylated peptides. *Immunol. Res.* **10**, 365–375 (1991).

[CAS](#) [PubMed](#) [Article](#) [PubMed Central](#) [Google Scholar](#)

22. 22.

Lenz, L. L., Dere, B. & Bevan, M. J. Identification of an *H2-M3*-restricted *Listeria* epitope: implications for antigen presentation by M3. *Immunity* **5**, 63–72 (1996). **This paper shows that the non-classical MHC molecule H2-M3 presents bacterial formylated peptides.**

[CAS](#) [PubMed](#) [PubMed Central](#) [Article](#) [Google Scholar](#)

23. 23.

Tanaka, Y. et al. Natural and synthetic non-peptide antigens recognized by human gamma delta T cells. *Nature* **375**, 155–158 (1995).

[ADS](#) [CAS](#) [PubMed](#) [Article](#) [PubMed Central](#) [Google Scholar](#)

24. 24.

de Jong, A. et al. CD1a-autoreactive T cells recognize natural skin oils that function as headless antigens. *Nat. Immunol.* **15**, 177–185 (2014).

[PubMed](#) [Article](#) [CAS](#) [PubMed Central](#) [Google Scholar](#)

25. 25.

Birkinshaw, R. W. et al. $\alpha\beta$ T cell antigen receptor recognition of CD1a presenting self lipid ligands. *Nat. Immunol.* **16**, 258–266 (2015). **The crystal structures in this paper show the breaking of the co-recognition paradigm as defined by the requirement for a TCR to simultaneously recognize an antigen and the antigen-presenting molecule.**

[CAS](#) [PubMed](#) [PubMed Central](#) [Article](#) [Google Scholar](#)

26. 26.

Dimova, T. et al. Effector V γ 9V δ 2 T cells dominate the human fetal $\gamma\delta$ T-cell repertoire. *Proc. Natl Acad. Sci. USA* **112**, E556–E565 (2015).

[CAS](#) [PubMed](#) [PubMed Central](#) [Article](#) [Google Scholar](#)

27. 27.

Tomasec, P. et al. Surface expression of HLA-E, an inhibitor of natural killer cells, enhanced by human cytomegalovirus gpUL40. *Science* **287**, 1031 (2000).

[ADS](#) [CAS](#) [PubMed](#) [Article](#) [PubMed Central](#) [Google Scholar](#)

28. 28.

Braud, V., Jones, E. Y. & McMichael, A. The human major histocompatibility complex class Ib molecule HLA-E binds signal sequence-derived peptides with primary anchor residues at positions 2 and 9. *Eur. J. Immunol.* **27**, 1164–1169 (1997).

[CAS](#) [PubMed](#) [Article](#) [PubMed Central](#) [Google Scholar](#)

29. 29.

Jabri, B. et al. TCR specificity dictates CD94/NKG2A expression by human CTL. *Immunity* **17**, 487–499 (2002).

[CAS](#) [PubMed](#) [Article](#) [PubMed Central](#) [Google Scholar](#)

30. 30.

Braud, V. M. et al. HLA-E binds to natural killer cell receptors CD94/NKG2A, B and C. *Nature* **391**, 795–799 (1998).

[ADS](#) [CAS](#) [PubMed](#) [Article](#) [PubMed Central](#) [Google Scholar](#)

31. 31.

Oliveira, C. C. et al. The nonpolymorphic MHC Qa-1b mediates CD8⁺ T cell surveillance of antigen-processing defects. *J. Exp. Med.* **207**, 207–221 (2010).

[CAS](#) [PubMed](#) [PubMed Central](#) [Article](#) [Google Scholar](#)

32. 32.

Sakaguchi, S., Yamaguchi, T., Nomura, T. & Ono, M. Regulatory T cells and immune tolerance. *Cell* **133**, 775–787 (2008).

[CAS](#) [PubMed](#) [Article](#) [PubMed Central](#) [Google Scholar](#)

33. 33.

Barbee, S. D. et al. Skint-1 is a highly specific, unique selecting component for epidermal T cells. *Proc. Natl Acad. Sci. USA* **108**, 3330–3335 (2011). **This paper identifies SKINT-1 as the selecting ligand for DETCs.**

[ADS](#) [CAS](#) [PubMed](#) [PubMed Central](#) [Article](#) [Google Scholar](#)

34. 34.

Di Marco Barros, R. et al. Epithelia use butyrophilin-like molecules to shape organ-specific $\gamma\delta$ t cell compartments. *Cell* **167**, 203–218 (2016). **This paper identifies BTNL molecules as the selecting ligands for gut-specific $\gamma\delta$ T cells.**

[PubMed](#) [PubMed Central](#) [Article](#) [CAS](#) [Google Scholar](#)

35. 35.

Mayassi, T. et al. Chronic inflammation permanently reshapes tissue-resident immunity in celiac disease. *Cell* **176**, 967–981 (2019). **This paper characterizes the functional and transcriptional program of the gut innate-like human BTNL-specific $\gamma\delta$ T cells and shows how chronic inflammation permanently reshapes these niches.**

[CAS](#) [PubMed](#) [PubMed Central](#) [Article](#) [Google Scholar](#)

36. 36.

Groh, V., Steinle, A., Bauer, S. & Spies, T. Recognition of stress-induced MHC molecules by intestinal epithelial $\gamma\delta$ T cells. *Science* **279**, 1737–1740 (1998).

[ADS](#) [CAS](#) [PubMed](#) [Article](#) [PubMed Central](#) [Google Scholar](#)

37. 37.

Kong, Y. et al. The NKG2D ligand ULBP4 binds to TCR $\gamma\delta$ 2 and induces cytotoxicity to tumor cells through both TCR $\gamma\delta$ and NKG2D. *Blood* **114**, 310–317 (2009).

[CAS](#) [PubMed](#) [Article](#) [PubMed Central](#) [Google Scholar](#)

38. 38.

Crowley, M. P., Reich, Z., Mavaddat, N., Altman, J. D. & Chien, Y. The recognition of the nonclassical major histocompatibility complex (MHC) class I molecule, T10, by the $\gamma\delta$ T cell, G8. *J. Exp. Med.* **185**, 1223–1230 (1997).

[CAS](#) [PubMed](#) [PubMed Central](#) [Article](#) [Google Scholar](#)

39. 39.

Shin, S. et al. Antigen recognition determinants of $\gamma\delta$ T cell receptors. *Science* **308**, 252–255 (2005).

[ADS](#) [CAS](#) [PubMed](#) [Article](#) [PubMed Central](#) [Google Scholar](#)

40. 40.

Lantz, O. & Bendelac, A. An invariant T cell receptor α chain is used by a unique subset of major histocompatibility complex class I-specific CD4 $^{+}$ and CD4 $^{-}$ 8 $^{-}$ T cells in mice and humans. *J. Exp. Med.* **180**, 1097–1106 (1994).

[CAS](#) [PubMed](#) [Article](#) [PubMed Central](#) [Google Scholar](#)

41. 41.

Kawano, T. et al. CD1d-restricted and TCR-mediated activation of v α 14 NKT cells by glycosylceramides. *Science* **278**, 1626–1629 (1997).

[ADS](#) [CAS](#) [PubMed](#) [Article](#) [PubMed Central](#) [Google Scholar](#)

42. 42.

Tilloy, F. et al. An invariant T cell receptor α chain defines a novel TAP-independent major histocompatibility complex class Ib-restricted α/β T cell subpopulation in mammals. *J. Exp. Med.* **189**, 1907–1921 (1999).

[CAS](#) [PubMed](#) [PubMed Central](#) [Article](#) [Google Scholar](#)

43. 43.

Porcelli, S., Yockey, C. E., Brenner, M. B. & Balk, S. P. Analysis of T cell antigen receptor (TCR) expression by human peripheral blood CD4 $^{-}$ 8 $^{-}$ α/β T cells demonstrates preferential use of several V β genes and an invariant TCR α chain. *J. Exp. Med.* **178**, 1–16 (1993).

[CAS](#) [PubMed](#) [Article](#) [PubMed Central](#) [Google Scholar](#)

44. 44.

Treiner, E. et al. Selection of evolutionarily conserved mucosal-associated invariant T cells by MR1. *Nature* **422**, 164–169 (2003).

[ADS](#) [CAS](#) [PubMed](#) [Article](#) [PubMed Central](#) [Google Scholar](#)

45. 45.

Van Rhijn, I. et al. A conserved human T cell population targets mycobacterial antigens presented by CD1b. *Nat. Immunol.* **14**, 706–713 (2013).

[PubMed](#) [PubMed Central](#) [Article](#) [CAS](#) [Google Scholar](#)

46. 46.

Gras, S. et al. T cell receptor recognition of CD1b presenting a mycobacterial glycolipid. *Nat. Commun.* **7**, 13257 (2016).

[ADS](#) [PubMed](#) [PubMed Central](#) [Article](#) [Google Scholar](#)

47. 47.

Melandri, D. et al. The $\gamma\delta$ TCR combines innate immunity with adaptive immunity by utilizing spatially distinct regions for agonist selection and antigen responsiveness. *Nat. Immunol.* **19**, 1352–1365 (2018).

[CAS](#) [PubMed](#) [PubMed Central](#) [Article](#) [Google Scholar](#)

48. 48.

Castro, C. D., Luoma, A. M. & Adams, E. J. Coevolution of T-cell receptors with MHC and non-MHC ligands. *Immunol. Rev.* **267**, 30–55 (2015).

[CAS](#) [PubMed](#) [PubMed Central](#) [Article](#) [Google Scholar](#)

49. 49.

Linehan, J. L. et al. Non-classical immunity controls microbiota impact on skin immunity and tissue repair. *Cell* **172**, 784–796 (2018).
This paper demonstrates the role of H2-M3-restricted T cell responses in regulating the microbiota and wound healing in the skin.

[CAS](#) [PubMed](#) [PubMed Central](#) [Article](#) [Google Scholar](#)

50. 50.

Grant, E. J. et al. The unconventional role of HLA-E: the road less traveled. *Mol. Immunol.* **120**, 101–112 (2020).

[CAS](#) [PubMed](#) [Article](#) [PubMed Central](#) [Google Scholar](#)

51. 51.

McDonald, B. D., Bunker, J. J., Ishizuka, I. E., Jabri, B. & Bendelac, A. Elevated T cell receptor signaling identifies a thymic precursor to the TCR $\alpha\beta^+$ CD4 $^-$ CD8 β^- intraepithelial lymphocyte lineage. *Immunity* **41**, 219–229 (2014).

[CAS](#) [PubMed](#) [PubMed Central](#) [Article](#) [Google Scholar](#)

52. 52.

Mayans, S. et al. $\alpha\beta$ T cell receptors expressed by CD4 $^-$ CD8 $\alpha\beta^-$ intraepithelial T cells drive their fate into a unique lineage with unusual MHC reactivities. *Immunity* **41**, 207–218 (2014).

[CAS](#) [PubMed](#) [PubMed Central](#) [Article](#) [Google Scholar](#)

53. 53.

Park, S. H. et al. Selection and expansion of CD8 α/α^1 T cell receptor α/β^1 intestinal intraepithelial lymphocytes in the absence of both classical major histocompatibility complex class I and nonclassical CD1 molecules. *J. Exp. Med.* **190**, 885–890 (1999).

[CAS](#) [PubMed](#) [PubMed Central](#) [Article](#) [Google Scholar](#)

54. 54.

Gherardin, N. A., McCluskey, J., Rossjohn, J. & Godfrey, D. I. The diverse family of MR1-restricted T cells. *J. Immunol.* **201**, 2862–2871 (2018).

[CAS](#) [PubMed](#) [Article](#) [PubMed Central](#) [Google Scholar](#)

55. 55.

Uldrich, A. P. et al. CD1d-lipid antigen recognition by the $\gamma\delta$ TCR. *Nat. Immunol.* **14**, 1137–1145 (2013).

[CAS](#) [PubMed](#) [Article](#) [PubMed Central](#) [Google Scholar](#)

56. 56.

Luoma, A. M. et al. Crystal structure of V δ 1 T cell receptor in complex with CD1d-sulfatide shows MHC-like recognition of a self-lipid by human $\gamma\delta$ T cells. *Immunity* **39**, 1032–1042 (2013).

[CAS](#) [PubMed](#) [Article](#) [PubMed Central](#) [Google Scholar](#)

57. 57.

Le Nours, J. et al. A class of $\gamma\delta$ T cell receptors recognize the underside of the antigen-presenting molecule MR1. *Science* **366**, 1522–1527 (2019).

[ADS](#) [PubMed](#) [Article](#) [CAS](#) [PubMed Central](#) [Google Scholar](#)

58. 58.

Garcia, K. C. et al. An $\alpha\beta$ T cell receptor structure at 2.5 Å and its orientation in the TCR–MHC complex. *Science* **274**, 209–219 (1996).

[ADS](#) [CAS](#) [PubMed](#) [Article](#) [PubMed Central](#) [Google Scholar](#)

59. 59.

Garboczi, D. N. et al. Structure of the complex between human T-cell receptor, viral peptide and HLA-A2. *Nature* **384**, 134–141 (1996).

[ADS](#) [CAS](#) [PubMed](#) [Article](#) [PubMed Central](#) [Google Scholar](#)

60. 60.

Rossjohn, J. et al. T cell antigen receptor recognition of antigen-presenting molecules. *Annu. Rev. Immunol.* **33**, 169–200 (2015).

[CAS](#) [PubMed](#) [Article](#) [PubMed Central](#) [Google Scholar](#)

61. 61.

Beringer, D. X. et al. T cell receptor reversed polarity recognition of a self-antigen major histocompatibility complex. *Nat. Immunol.* **16**, 1153–1161 (2015).

[CAS](#) [PubMed](#) [Article](#) [PubMed Central](#) [Google Scholar](#)

62. 62.

Gras, S. et al. Reversed T cell receptor docking on a major histocompatibility class I complex limits involvement in the immune response. *Immunity* **45**, 749–760 (2016).

[CAS](#) [PubMed](#) [Article](#) [PubMed Central](#) [Google Scholar](#)

63. 63.

La Gruta, N. L., Gras, S., Daley, S. R., Thomas, P. G. & Rossjohn, J. Understanding the drivers of MHC restriction of T cell receptors. *Nat. Rev. Immunol.* **18**, 467–478 (2018).

[PubMed](#) [Article](#) [CAS](#) [PubMed Central](#) [Google Scholar](#)

64. 64.

Adams, E. J. & Luoma, A. M. The adaptable major histocompatibility complex (MHC) fold: structure and function of nonclassical and MHC class I-like molecules. *Annu. Rev. Immunol.* **31**, 529–561 (2013).

[CAS](#) [PubMed](#) [Article](#) [PubMed Central](#) [Google Scholar](#)

65. 65.

Van Rhijn, I., Godfrey, D. I., Rossjohn, J. & Moody, D. B. Lipid and small-molecule display by CD1 and MR1. *Nat. Rev. Immunol.* **15**, 643–654 (2015).

[PubMed](#) [PubMed Central](#) [Article](#) [CAS](#) [Google Scholar](#)

66. 66.

Saunders, P. M. et al. A bird's eye view of NK cell receptor interactions with their MHC class I ligands. *Immunol. Rev.* **267**, 148–166 (2015).

[CAS](#) [PubMed](#) [Article](#) [PubMed Central](#) [Google Scholar](#)

67. 67.

Hoare, H. L. et al. Structural basis for a major histocompatibility complex class Ib-restricted T cell response. *Nat. Immunol.* **7**, 256–264 (2006).

[CAS](#) [PubMed](#) [Article](#) [PubMed Central](#) [Google Scholar](#)

68. 68.

Borg, N. A. et al. CD1d-lipid-antigen recognition by the semi-invariant NKT T-cell receptor. *Nature* **448**, 44–49 (2007). **This paper provides the first insights into how unconventional TCR recognition differs from that of conventional TCRs in the form of type I NKT TCR–CD1d–lipid complex.**

[ADS](#) [CAS](#) [PubMed](#) [Article](#) [PubMed Central](#) [Google Scholar](#)

69. 69.

Rossjohn, J., Pellicci, D. G., Patel, O., Gapin, L. & Godfrey, D. I. Recognition of CD1d-restricted antigens by natural killer T cells. *Nat. Rev. Immunol.* **12**, 845–857 (2012).

[CAS](#) [PubMed](#) [PubMed Central](#) [Article](#) [Google Scholar](#)

70. 70.

Patel, O. et al. Recognition of vitamin B metabolites by mucosal-associated invariant T cells. *Nat. Commun.* **4**, 2142 (2013).

1. [ADS](#) [PubMed](#) [Article](#) [CAS](#) [PubMed Central](#) [Google Scholar](#)
2. 71.

Eckle, S. B. G. et al. A molecular basis underpinning the T cell receptor heterogeneity of mucosal-associated invariant T cells. *J. Exp. Med.* **211**, 1585–1600 (2014).

[ADS](#) [CAS](#) [PubMed](#) [PubMed Central](#) [Article](#) [Google Scholar](#)
3. 72.

Patel, O. et al. Recognition of CD1d-sulfatide mediated by a type II natural killer T cell antigen receptor. *Nat. Immunol.* **13**, 857–863 (2012).

[CAS](#) [PubMed](#) [Article](#) [PubMed Central](#) [Google Scholar](#)
4. 73.

Girardi, E. et al. Type II natural killer T cells use features of both innate-like and conventional T cells to recognize sulfatide self antigens. *Nat. Immunol.* **13**, 851–856 (2012).

[CAS](#) [PubMed](#) [PubMed Central](#) [Article](#) [Google Scholar](#)
5. 74.

Gherardin, N. A. et al. Diversity of T cells restricted by the MHC class I-related molecule MR1 facilitates differential antigen recognition. *Immunity* **44**, 32–45 (2016).

[CAS](#) [PubMed](#) [Article](#) [PubMed Central](#) [Google Scholar](#)
6. 75.

Wun, K. S. et al. T cell autoreactivity directed toward CD1c itself rather than toward carried self lipids. *Nat. Immunol.* **19**, 397–406

(2018).

[CAS](#) [PubMed](#) [PubMed Central](#) [Article](#) [Google Scholar](#)

7. 76.

Bendelac, A. Positive selection of mouse NK1⁺ T cells by CD1-expressing cortical thymocytes. *J. Exp. Med.* **182**, 2091–2096 (1995).

[CAS](#) [PubMed](#) [Article](#) [PubMed Central](#) [Google Scholar](#)

8. 77.

Seach, N. et al. Double-positive thymocytes select mucosal-associated invariant T cells. *J. Immunol.* **191**, 6002–6009 (2013).

[CAS](#) [PubMed](#) [Article](#) [PubMed Central](#) [Google Scholar](#)

9. 78.

Savage, A. K. et al. The transcription factor PLZF directs the effector program of the NKT cell lineage. *Immunity* **29**, 391–403 (2008). **This paper demonstrates the critical role of PLZF in the effector programming of unconventional T cells such as NKT cells and MAIT cells.**

[CAS](#) [PubMed](#) [PubMed Central](#) [Article](#) [Google Scholar](#)

10. 79.

Koay, H.-F. et al. A divergent transcriptional landscape underpins the development and functional branching of MAIT cells. *Sci. Immunol.* **4**, eaay6039 (2019).

[CAS](#) [PubMed](#) [Article](#) [PubMed Central](#) [Google Scholar](#)

11. 80.

Griewank, K. et al. Homotypic interactions mediated by Slamf1 and Slamf6 receptors control NKT cell lineage development. *Immunity* **27**, 751–762 (2007).

[CAS](#) [PubMed](#) [PubMed Central](#) [Article](#) [Google Scholar](#)

12. 81.

Urdahl, K. B., Sun, J. C. & Bevan, M. J. Positive selection of MHC class Ib-restricted CD8⁺ T cells on hematopoietic cells. *Nat. Immunol.* **3**, 772–779 (2002).

[CAS](#) [PubMed](#) [PubMed Central](#) [Article](#) [Google Scholar](#)

13. 82.

Bediako, Y. et al. SAP is required for the development of innate phenotype in H2-M3-restricted CD8⁺ T cells. *J. Immunol.* **189**, 4787–4796 (2012).

[CAS](#) [PubMed](#) [Article](#) [PubMed Central](#) [Google Scholar](#)

14. 83.

McDonald, B. D., Jabri, B. & Bendelac, A. Diverse developmental pathways of intestinal intraepithelial lymphocytes. *Nat. Rev. Immunol.* **18**, 514–525 (2018).

[CAS](#) [PubMed](#) [PubMed Central](#) [Article](#) [Google Scholar](#)

15. 84.

Wei, D. G. et al. Expansion and long-range differentiation of the NKT cell lineage in mice expressing CD1d exclusively on cortical thymocytes. *J. Exp. Med.* **202**, 239–248 (2005).

[CAS](#) [PubMed](#) [PubMed Central](#) [Article](#) [Google Scholar](#)

16. 85.

Guy-Grand, D. et al. Origin, trafficking, and intraepithelial fate of gut-tropic T cells. *J. Exp. Med.* **210**, 1839–1854 (2013).

[CAS](#) [PubMed](#) [PubMed Central](#) [Article](#) [Google Scholar](#)

17. 86.

Constantinides, M. G. et al. MAIT cells are imprinted by the microbiota in early life and promote tissue repair. *Science* **366**, eaax6624 (2019). **This paper demonstrates that there is a window in early life for the colonization of tissues by MAIT cells and stresses the role of MAIT cells in wound repair.**

[CAS](#) [PubMed](#) [PubMed Central](#) [Article](#) [Google Scholar](#)

18. 87.

Mazzarino, P. et al. Identification of effector-memory CMV-specific T lymphocytes that kill CMV-infected target cells in an HLA-E-restricted fashion. *Eur. J. Immunol.* **35**, 3240–3247 (2005).

[CAS](#) [PubMed](#) [Article](#) [PubMed Central](#) [Google Scholar](#)

19. 88.

Doorduijn, E. M. et al. T cells engaging the conserved MHC class Ib molecule Qa-1^b with TAP-independent peptides are semi-invariant lymphocytes. *Front. Immunol.* **9**, 60 (2018).

[PubMed](#) [PubMed Central](#) [Article](#) [CAS](#) [Google Scholar](#)

20. 89.

Havran, W. L. & Allison, J. P. Origin of Thy-1⁺ dendritic epidermal cells of adult mice from fetal thymic precursors. *Nature* **344**, 68–70 (1990).

[ADS](#) [CAS](#) [PubMed](#) [Article](#) [PubMed Central](#) [Google Scholar](#)

21. 90.

Benlagha, K., Weiss, A., Beavis, A., Teyton, L. & Bendelac, A. In vivo identification of glycolipid antigen-specific T cells using fluorescent CD1d tetramers. *J. Exp. Med.* **191**, 1895–1904 (2000).

[CAS](#) [PubMed](#) [PubMed Central](#) [Article](#) [Google Scholar](#)

22. 91.

Dusseaux, M. et al. Human MAIT cells are xenobiotic-resistant, tissue-targeted, CD161^{hi} IL-17-secreting T cells. *Blood* **117**, 1250–1259 (2011).

[CAS](#) [PubMed](#) [Article](#) [PubMed Central](#) [Google Scholar](#)

23. 92.

Mueller, S. N. & Mackay, L. K. Tissue-resident memory T cells: local specialists in immune defence. *Nat. Rev. Immunol.* **16**, 79–89 (2016).

[CAS](#) [PubMed](#) [Article](#) [PubMed Central](#) [Google Scholar](#)

24. 93.

Masopust, D. & Soerens, A. G. Tissue-resident T cells and other resident leukocytes. *Annu. Rev. Immunol.* **37**, 521–546 (2019).

[CAS](#) [PubMed](#) [PubMed Central](#) [Article](#) [Google Scholar](#)

25. 94.

Olszak, T. et al. Microbial exposure during early life has persistent effects on natural killer T cell function. *Science* **336**, 489–493 (2012).

[ADS](#) [CAS](#) [PubMed](#) [PubMed Central](#) [Article](#) [Google Scholar](#)

26. 95.

Chan, A. C. et al. Ex-vivo analysis of human natural killer T cells demonstrates heterogeneity between tissues and within established CD4⁺ and CD4⁻ subsets. *Clin. Exp. Immunol.* **172**, 129–137 (2013).

[CAS](#) [PubMed](#) [PubMed Central](#) [Article](#) [Google Scholar](#)

27. 96.

Loh, L. et al. Human mucosal-associated invariant T cells in older individuals display expanded TCRαβ clonotypes with potent antimicrobial responses. *J. Immunol.* **1950**, 1119–1133 (2020).

[Article](#) [CAS](#) [Google Scholar](#)

28. 97.

Zaid, A. et al. Persistence of skin-resident memory T cells within an epidermal niche. *Proc. Natl Acad. Sci. USA* **111**, 5307–5312 (2014).

[ADS](#) [CAS](#) [PubMed](#) [PubMed Central](#) [Article](#) [Google Scholar](#)

29. 98.

Hayday, A., Theodoridis, E., Ramsburg, E. & Shires, J. Intraepithelial lymphocytes: exploring the Third Way in immunology. *Nat. Immunol.* **2**, 997–1003 (2001).

[CAS](#) [PubMed](#) [Article](#) [PubMed Central](#) [Google Scholar](#)

30. 99.

Hinks, T. S. C. et al. Activation and in vivo evolution of the MAIT cell transcriptome in mice and humans reveals tissue repair functionality. *Cell Rep.* **28**, 3249–3262.e5 (2019).

[CAS](#) [PubMed](#) [PubMed Central](#) [Article](#) [Google Scholar](#)

31. 100.

Legoux, F., Salou, M. & Lantz, O. Unconventional or preset $\alpha\beta$ T cells: evolutionarily conserved tissue-resident T cells recognizing nonpeptidic ligands. *Annu. Rev. Cell Dev. Biol.* **33**, 511–535 (2017).

[CAS](#) [PubMed](#) [Article](#) [PubMed Central](#) [Google Scholar](#)

32. 101.

Guy-Grand, D., Cuénod-Jabri, B., Malassis-Seris, M., Selz, F. & Vassalli, P. Complexity of the mouse gut T cell immune system: identification of two distinct natural killer T cell intraepithelial lineages. *Eur. J. Immunol.* **26**, 2248–2256 (1996). **This paper provides the first evidence that intestinal tissue-resident unconventional intraepithelial T lymphocytes express NK receptors and mediate NK-cell-like killing.**

[CAS](#) [PubMed](#) [Article](#) [PubMed Central](#) [Google Scholar](#)

33. 102.

Toulon, A. et al. A role for human skin-resident T cells in wound healing. *J. Exp. Med.* **206**, 743–750 (2009).

[CAS](#) [PubMed](#) [PubMed Central](#) [Article](#) [Google Scholar](#)

34. 103.

Groh, V. et al. Broad tumor-associated expression and recognition by tumor-derived $\gamma\delta$ T cells of MICA and MICB. *Proc. Natl Acad. Sci. USA* **96**, 6879–6884 (1999).

[ADS](#) [CAS](#) [PubMed](#) [PubMed Central](#) [Article](#) [Google Scholar](#)

35. 104.

Pamer, E. G., Bevan, M. J. & Lindahl, K. F. Do nonclassical, class Ib MHC molecules present bacterial antigens to T cells? *Trends Microbiol.* **1**, 35–38 (1993).

[CAS](#) [PubMed](#) [Article](#) [PubMed Central](#) [Google Scholar](#)

36. 105.

Le Bourhis, L. et al. Antimicrobial activity of mucosal-associated invariant T cells. *Nat. Immunol.* **11**, 701–708 (2010).

[PubMed](#) [Article](#) [CAS](#) [PubMed Central](#) [Google Scholar](#)

37. 106.

Gaya, M. et al. Initiation of antiviral B cell immunity relies on innate signals from spatially positioned NKT cells. *Cell* **172**, 517–533 (2018).

[CAS](#) [PubMed](#) [PubMed Central](#) [Article](#) [Google Scholar](#)

38. 107.

Boismenu, R. & Havran, W. L. Modulation of epithelial cell growth by intraepithelial $\gamma\delta$ T cells. *Science* **266**, 1253–1255 (1994). **This paper was the first study to propose that TCR $\gamma\delta$ T cells have a role in wound healing.**

[ADS](#) [CAS](#) [PubMed](#) [Article](#) [PubMed Central](#) [Google Scholar](#)

39. 108.

Jabri, B. & Abadie, V. IL-15 functions as a danger signal to regulate tissue-resident T cells and tissue destruction. *Nat. Rev. Immunol.* **15**, 771–783 (2015).

[CAS](#) [PubMed](#) [PubMed Central](#) [Article](#) [Google Scholar](#)

40. 109.

Tortorella, D., Gewurz, B. E., Furman, M. H., Schust, D. J. & Ploegh, H. L. Viral subversion of the immune system. *Annu. Rev. Immunol.* **18**, 861–926 (2000).

[CAS](#) [PubMed](#) [Article](#) [PubMed Central](#) [Google Scholar](#)

41. 110.

Turtle, C. J. et al. Innate signals overcome acquired TCR signaling pathway regulation and govern the fate of human CD161^{hi} CD8α⁺ semi-invariant T cells. *Blood* **118**, 2752–2762 (2011).

[CAS](#) [PubMed](#) [PubMed Central](#) [Article](#) [Google Scholar](#)

42. 111.

Slichter, C. K. et al. Distinct activation thresholds of human conventional and innate-like memory T cells. *JCI Insight* **1**, e86292 (2016).

[PubMed](#) [PubMed Central](#) [Article](#) [Google Scholar](#)

43. 112.

Wesley, J. D., Tessmer, M. S., Chaukos, D. & Brossay, L. NK cell-like behavior of Vα14i NK T cells during MCMV infection. *PLoS Pathog.* **4**, e1000106 (2008).

[PubMed](#) [PubMed Central](#) [Article](#) [CAS](#) [Google Scholar](#)

44. 113.

Tyznik, A. J. et al. Cutting edge: the mechanism of invariant NKT cell responses to viral danger signals. *J. Immunol.* **181**, 4452–4456 (2008).

[CAS](#) [PubMed](#) [Article](#) [PubMed Central](#) [Google Scholar](#)

45. 114.

Strid, J. et al. Acute upregulation of an NKG2D ligand promotes rapid reorganization of a local immune compartment with pleiotropic effects on carcinogenesis. *Nat. Immunol.* **9**, 146–154 (2008).

[CAS](#) [PubMed](#) [Article](#) [PubMed Central](#) [Google Scholar](#)

46. 115.

Strid, J., Sobolev, O., Zafirova, B., Polic, B. & Hayday, A. The intraepithelial T cell response to NKG2D-ligands links lymphoid stress surveillance to atopy. *Science* **334**, 1293–1297 (2011).

[ADS](#) [CAS](#) [PubMed](#) [Article](#) [PubMed Central](#) [Google Scholar](#)

47. 116.

Wu, Y. et al. An innate-like V δ 1 $^+$ γ δ T cell compartment in the human breast is associated with remission in triple-negative breast cancer. *Sci. Transl. Med.* **11**, eaax9364 (2019).

[CAS](#) [PubMed](#) [PubMed Central](#) [Article](#) [Google Scholar](#)

48. 117.

Carnaud, C. et al. Cutting edge: cross-talk between cells of the innate immune system: NKT cells rapidly activate NK cells. *J. Immunol.* **163**, 4647–4650 (1999).

[CAS](#) [PubMed](#) [Google Scholar](#)

49. 118.

Godfrey, D. I., Le Nours, J., Andrews, D. M., Uldrich, A. P. & Rossjohn, J. Unconventional T cell targets for cancer immunotherapy. *Immunity* **48**, 453–473 (2018).

[CAS](#) [PubMed](#) [Article](#) [Google Scholar](#)

50. 119.

Crowther, M. D. et al. Genome-wide CRISPR–Cas9 screening reveals ubiquitous T cell cancer targeting via the monomorphic MHC class I-related protein MR1. *Nat. Immunol.* **21**, 178–185 (2020).

[CAS](#) [PubMed](#) [PubMed Central](#) [Article](#) [Google Scholar](#)

51. 120.

Edholm, E.-S., Banach, M. & Robert, J. Evolution of innate-like T cells and their selection by MHC class I-like molecules. *Immunogenetics* **68**, 525–536 (2016).

[CAS](#) [PubMed](#) [PubMed Central](#) [Article](#) [Google Scholar](#)

52. 121.

Mondot, S., Boudinot, P. & Lantz, O. MAIT, MR1, microbes and riboflavin: a paradigm for the co-evolution of invariant TCRs and restricting MHCI-like molecules? *Immunogenetics* **68**, 537–548 (2016).

[CAS](#) [PubMed](#) [Article](#) [Google Scholar](#)

53. 122.

Boudinot, P. et al. Restricting nonclassical MHC genes coevolve with TRAV genes used by innate-like T cells in mammals. *Proc. Natl Acad. Sci. USA* **113**, E2983–E2992 (2016).

[CAS](#) [PubMed](#) [PubMed Central](#) [Article](#) [Google Scholar](#)

54. 123.

Flajnik, M. F. & Kasahara, M. Origin and evolution of the adaptive immune system: genetic events and selective pressures. *Nat. Rev. Genet.* **11**, 47–59 (2010).

[CAS](#) [PubMed](#) [Article](#) [PubMed Central](#) [Google Scholar](#)

55. 124.

Rodgers, J. R. & Cook, R. G. MHC class Ib molecules bridge innate and acquired immunity. *Nat. Rev. Immunol.* **5**, 459–471 (2005).

[CAS](#) [PubMed](#) [Article](#) [PubMed Central](#) [Google Scholar](#)

56. 125.

Van Rhijn, I., Ly, D. & Moody, D. B. CD1a, CD1b, and CD1c in immunity against mycobacteria. *Adv. Exp. Med. Biol.* **783**, 181–197 (2013).

[PubMed](#) [Article](#) [CAS](#) [PubMed Central](#) [Google Scholar](#)

57. 126.

van Wilgenburg, B. et al. MAIT cells contribute to protection against lethal influenza infection in vivo. *Nat. Commun.* **9**, 4706 (2018).

[ADS](#) [PubMed](#) [PubMed Central](#) [Article](#) [CAS](#) [Google Scholar](#)

58. 127.

Legoux, F. et al. Microbial metabolites control the thymic development of mucosal-associated invariant T cells. *Science* **366**, 494–499 (2019).

[ADS](#) [CAS](#) [PubMed](#) [Article](#) [PubMed Central](#) [Google Scholar](#)

59. 128.

Fischer, A. Severe combined immunodeficiencies. *Immunodefic. Rev.* **3**, 83–100 (1992).

[CAS](#) [PubMed](#) [Google Scholar](#)

60. 129.

Barreiro, L. B. et al. Evolutionary dynamics of human Toll-like receptors and their different contributions to host defense. *PLoS Genet.* **5**, e1000562 (2009).

[PubMed](#) [PubMed Central](#) [Article](#) [CAS](#) [Google Scholar](#)

61. 130.

Barreiro, L. B. & Quintana-Murci, L. From evolutionary genetics to human immunology: how selection shapes host defence genes. *Nat. Rev. Genet.* **11**, 17–30 (2010).

[CAS](#) [PubMed](#) [Article](#) [Google Scholar](#)

62. 131.

Howson, L. J. et al. Absence of mucosal-associated invariant T cells in a person with a homozygous point mutation in *MRI*. *Sci. Immunol.* **5**, eabc9492 (2020).

[CAS](#) [PubMed](#) [Article](#) [PubMed Central](#) [Google Scholar](#)

63. 132.

Harsha Krovi, S. et al. Thymic iNKT single cell analyses unmask the common developmental program of mouse innate T cells. *Nat. Commun.* **11**, 6238 (2020).

[ADS](#) [CAS](#) [PubMed](#) [PubMed Central](#) [Article](#) [Google Scholar](#)

64. 133.

Constantinides, M. G., McDonald, B. D., Verhoef, P. A. & Bendelac, A. A committed precursor to innate lymphoid cells. *Nature* **508**, 397–401 (2014).

[ADS](#) [CAS](#) [PubMed](#) [PubMed Central](#) [Article](#) [Google Scholar](#)

65. 134.

Heinzel, A. S. et al. HLA-E-dependent presentation of Mtb-derived antigen to human CD8⁺ T cells. *J. Exp. Med.* **196**, 1473–1481 (2002).

[CAS](#) [PubMed](#) [PubMed Central](#) [Article](#) [Google Scholar](#)

66. 135.

Kabelitz, D. et al. The primary response of human γ/δ^+ T cells to *Mycobacterium tuberculosis* is restricted to V γ 9-bearing cells. *J. Exp. Med.* **173**, 1331–1338 (1991).

[CAS](#) [PubMed](#) [Article](#) [PubMed Central](#) [Google Scholar](#)

67. 136.

Gold, M. C. et al. Human mucosal associated invariant T cells detect bacterially infected cells. *PLoS Biol.* **8**, e1000407 (2010).

[PubMed](#) [PubMed Central](#) [Article](#) [CAS](#) [Google Scholar](#)

68. 137.

Nish, S. & Medzhitov, R. Host defense pathways: role of redundancy and compensation in infectious disease phenotypes. *Immunity* **34**, 629–636 (2011).

[CAS](#) [PubMed](#) [PubMed Central](#) [Article](#) [Google Scholar](#)

69. 138.

Borbulevych, O. Y., Santhanagopalan, S. M., Hossain, M. & Baker, B. M. TCRs used in cancer gene therapy cross-react with MART-1/Melan-A tumor antigens via distinct mechanisms. *J. Immunol.* **187**, 2453–2463 (2011).

[CAS](#) [PubMed](#) [Article](#) [PubMed Central](#) [Google Scholar](#)

70. 139.

Wun, K. S. et al. Human and mouse type I natural killer T cell antigen receptors exhibit different fine specificities for CD1d-antigen complex. *J. Biol. Chem.* **287**, 39139–39148 (2012).

[CAS](#) [PubMed](#) [PubMed Central](#) [Article](#) [Google Scholar](#)

[Download references](#)

Acknowledgements

We thank D. Littler for generating Fig. 1; A. Bendelac for sharing his insights on innate-like lymphocytes; D. Guy-Grand for sharing her insights on intraepithelial lymphocytes over many years; and M. Kronenberg and K. Sangani for discussions. This Review was supported by grants to B.J. from the National Institutes of Health (NIH: R01 DK67180 and R01 DK098435) and the Digestive Diseases Research Core Center at the University of Chicago (P30 DK42086); to J.R. from the Australian ARC Laureate Fellowship; and to L.B.B. from NIH: R01 GM134376.

Author information

Affiliations

1. Broad Institute of MIT and Harvard, Cambridge, MA, USA

Toufic Mayassi

2. Committee on Immunology, University of Chicago, Chicago, IL, USA

Toufic Mayassi, Luis B. Barreiro & Bana Jabri

3. Committee on Genetics, Genomics, and Systems Biology, University of Chicago, Chicago, IL, USA

Luis B. Barreiro

4. Section of Genetic Medicine, Department of Medicine, University of Chicago, Chicago, IL, USA

Luis B. Barreiro

5. Infection and Immunity Program, Biomedicine Discovery Institute, Monash University, Clayton, Victoria, Australia

Jamie Rossjohn

6. Department of Biochemistry and Molecular Biology, Biomedicine Discovery Institute, Monash University, Clayton, Victoria, Australia

Jamie Rossjohn

7. Institute of Infection and Immunity, Cardiff University, School of Medicine, Heath Park, Cardiff, UK

Jamie Rossjohn

8. Department of Medicine, University of Chicago, Chicago, IL, USA

Bana Jabri

9. Department of Pathology, University of Chicago, Chicago, IL, USA

Bana Jabri

10. Department of Pediatrics, University of Chicago, Chicago, IL, USA

Bana Jabri

Authors

1. Toufic Mayassi

[View author publications](#)

You can also search for this author in [PubMed](#) [Google Scholar](#)

2. Luis B. Barreiro

[View author publications](#)

You can also search for this author in [PubMed](#) [Google Scholar](#)

3. Jamie Rossjohn

[View author publications](#)

You can also search for this author in [PubMed](#) [Google Scholar](#)

4. Bana Jabri

[View author publications](#)

You can also search for this author in [PubMed](#) [Google Scholar](#)

Contributions

B.J. conceived the writing of the article. T.M. and B.J. conceptualized the framework and wrote the article, with input from J.R. on the ‘Modes of ligand recognition’ section and input from L.B.B. on the ‘Evolution and redundancy’ section. All authors reviewed and edited the manuscript before submission.

Corresponding author

Correspondence to [Bana Jabri](#).

Ethics declarations

Competing interests

The authors declare no competing interests.

Additional information

Peer review information *Nature* thanks Laurent Gapin, Paul Kleenerman and Laura Mackay for their contribution to the peer review of this work.

Publisher’s note Springer Nature remains neutral with regard to jurisdictional claims in published maps and institutional affiliations.

Rights and permissions

[Reprints and Permissions](#)

About this article



Check for
updates

Cite this article

Mayassi, T., Barreiro, L.B., Rossjohn, J. *et al.* A multilayered immune system through the lens of unconventional T cells. *Nature* **595**, 501–510 (2021). <https://doi.org/10.1038/s41586-021-03578-0>

[Download citation](#)

- Received: 15 December 2020
- Accepted: 23 April 2021
- Published: 21 July 2021
- Issue Date: 22 July 2021
- DOI: <https://doi.org/10.1038/s41586-021-03578-0>

Comments

By submitting a comment you agree to abide by our [Terms](#) and [Community Guidelines](#). If you find something abusive or that does not comply with our terms or guidelines please flag it as inappropriate.

[Access through your institution](#)

[Change institution](#)

[Buy or subscribe](#)

Advertisement

| [Section menu](#) | [Main menu](#) |

- Article
- [Published: 21 July 2021](#)

The nightside cloud-top circulation of the atmosphere of Venus

- [Kiichi Fukuya](#) ORCID: [orcid.org/0000-0001-8296-3940¹](#),
- [Takeshi Imamura](#) ORCID: [orcid.org/0000-0002-9470-4492²](#),
- [Makoto Taguchi](#) ORCID: [orcid.org/0000-0002-2907-2265³](#),
- [Tetsuya Fukuhara](#) ORCID: [orcid.org/0000-0001-7974-232X³](#),
- [Toru Kouyama](#) ORCID: [orcid.org/0000-0002-1060-3986⁴](#),
- [Takeshi Horinouchi](#) ORCID: [orcid.org/0000-0002-2296-1975⁵](#),
- [Javier Peralta](#) ORCID: [orcid.org/0000-0002-6823-1695^{6,7}](#),
- [Masahiko Futaguchi](#) ORCID: [orcid.org/0000-0001-5703-9561⁸](#),
- [Takeru Yamada](#) ORCID: [orcid.org/0000-0003-3103-7300³](#),
- [Takao M. Sato](#) ORCID: [orcid.org/0000-0002-7090-2689⁹](#),
- [Atsushi Yamazaki](#) ORCID: [orcid.org/0000-0001-6468-6812¹⁰](#),
- [Shin-ya Murakami](#) ORCID: [orcid.org/0000-0002-7137-4849¹⁰](#),
- [Takehiko Satoh](#) ORCID: [orcid.org/0000-0001-9071-5808¹⁰](#),
- [Masahiro Takagi](#) ORCID: [orcid.org/0000-0002-4629-6279¹¹](#) &
- [Masato Nakamura¹⁰](#)

[Nature](#) volume 595, pages 511–515 (2021) [Cite this article](#)

- 493 Accesses
- 178 Altmetric
- [Metrics details](#)

Subjects

- [Atmospheric dynamics](#)
- [Inner planets](#)

Abstract

Although Venus is a terrestrial planet similar to Earth, its atmospheric circulation is much different and poorly characterized¹. Winds at the cloud top have been measured predominantly on the dayside. Prominent poleward drifts have been observed with dayside cloud tracking and interpreted to be caused by thermal tides and a Hadley circulation^{2,3,4}; however, the lack of nightside measurements over broad latitudes has prevented the unambiguous characterization of these components. Here we obtain cloud-tracked winds at all local times using thermal infrared images taken by the Venus orbiter Akatsuki, which is sensitive to an altitude of about 65 kilometres⁵. Prominent equatorward flows are found on the nightside, resulting in null meridional velocities when these are zonally averaged. The velocity structure of the thermal tides was determined without the influence of the Hadley circulation. The semidiurnal tide was found to have an amplitude large enough to contribute to the maintenance of the atmospheric superrotation. The weakness of the mean meridional flow at the cloud top implies that the poleward branch of the Hadley circulation exists above the cloud top and that the equatorward branch exists in the clouds. Our results should shed light on atmospheric superrotation in other celestial bodies.

Access options

Subscribe to Journal

Get full journal access for 1 year

\$199.00

only \$3.90 per issue

[Subscribe](#)

All prices are NET prices.
VAT will be added later in the checkout.
Tax calculation will be finalised during checkout.

Rent or Buy article

Get time limited or full article access on ReadCube.

from \$8.99

[Rent or Buy](#)

All prices are NET prices.

Additional access options:

- [Log in](#)
- [Access through your institution](#)
- [Learn about institutional subscriptions](#)

Fig. 1: Processing of thermal images of Venus.

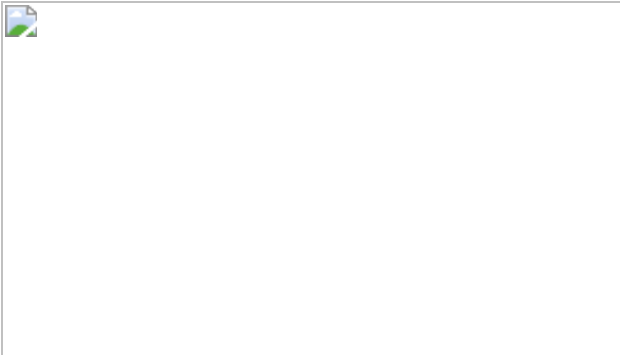


Fig. 2: Latitude–local time distributions of derived velocities.

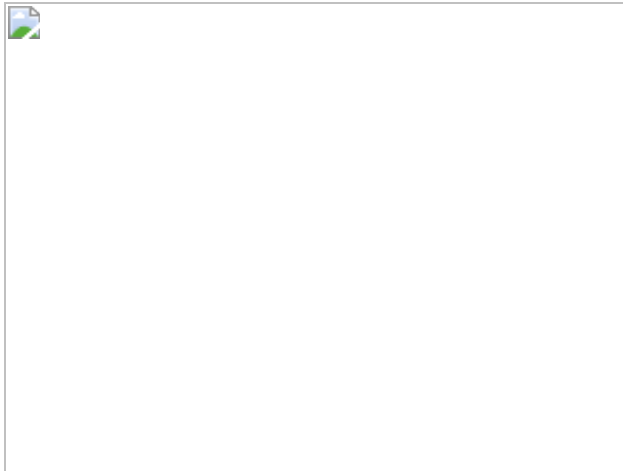


Fig. 3: Diurnal and semidiurnal components of derived velocities.

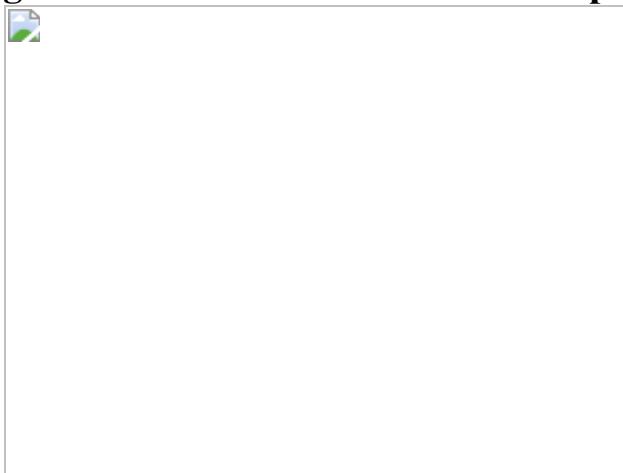


Fig. 4: Latitudinal variations of zonal-mean circulation.

Data availability

The Akatsuki LIR Level 3c data that support the findings of this study are available in Data Archives and Transmission System (DARTS) of JAXA⁵⁶ at <https://doi.org/10.17597/ISAS.DARTS/VCO-00019>. An internal version of the data (v20190401) was used, but it is essentially the same as the publicly available version. [Source data](#) are provided with this paper.

Code availability

Cloud tracking was conducted using the Python codes developed by K.F., which are available at <https://doi.org/10.5281/zenodo.4726329> and https://github.com/kiichi-f/Cloud_Tracking_using_Multiple_Images.

References

1. 1.
Sánchez-Lavega, A., Lebonnois, S., Imamura, T., Read, P. & Luz, D. The atmospheric dynamics of Venus. *Space Sci. Rev.* **212**, 1541–1616 (2017).
[ADS](#) [Article](#) [Google Scholar](#)
2. 2.
Schubert, G. et al. Structure and circulation of the Venus atmosphere. *J. Geophys. Res.* **85**, 8007–8025 (1980).
[ADS](#) [Article](#) [Google Scholar](#)
3. 3.
Newman, M. & Leovy, C. Maintenance of strong rotational winds in Venus' middle atmosphere by thermal tides. *Science* **257**, 647–650 (1992).
[ADS](#) [CAS](#) [PubMed](#) [Article](#) [Google Scholar](#)

4. 4.

Horinouchi, T. et al. How waves and turbulence maintain the super-rotation of Venus' atmosphere. *Science* **368**, 405–409 (2020).

[ADS](#) [MathSciNet](#) [CAS](#) [PubMed](#) [Article](#) [Google Scholar](#)

5. 5.

Taguchi, M. et al. Longwave Infrared Camera onboard the Venus Climate Orbiter. *Adv. Space Res.* **40**, 861–868 (2007).

[ADS](#) [Article](#) [Google Scholar](#)

6. 6.

Bird, M. K. et al. The vertical profile of winds on Titan. *Nature* **438**, 800–802 (2005).

[ADS](#) [CAS](#) [PubMed](#) [Article](#) [Google Scholar](#)

7. 7.

Read, P. L. & Lebonnois, S. Superrotation on Venus, on Titan, and elsewhere. *Annu. Rev. Earth Planet. Sci.* **46**, 175–202 (2018).

[ADS](#) [CAS](#) [Article](#) [Google Scholar](#)

8. 8.

Imamura, T. et al. Superrotation in planetary atmospheres. *Space Sci. Rev.* **216**, 87 (2020).

[ADS](#) [Article](#) [Google Scholar](#)

9. 9.

Showman, A., Tan, X. & Parmentier, V. Atmospheric dynamics of hot giant planets and brown dwarfs. *Space Sci. Rev.* **216**, 139 (2020).

[ADS](#) [Article](#) [Google Scholar](#)

10. 10.

Tomasko, M. G., Doose, L. R., Smith, P. H. & Odell, A. P. Measurements of the flux of sunlight in the atmosphere of Venus. *J. Geophys. Res.* **85**, 8167–8186 (1980).

[ADS](#) [Article](#) [Google Scholar](#)

11. 11.

Fels, S. B. & Lindzen, R. S. The interaction of thermally excited gravity waves with mean flows. *Geophys. Fluid Dyn.* **6**, 149–191 (1974).

[ADS](#) [Article](#) [Google Scholar](#)

12. 12.

Burt Pechmann, J. & Ingersoll, A. P. Thermal tides in the atmosphere of Venus: comparison of model results with observations. *J. Atmos. Sci.* **41**, 3290–3313 (1984).

[ADS](#) [Article](#) [Google Scholar](#)

13. 13.

Baker, N. L. & Leovy, C. B. Zonal winds near Venus' cloud top level: a model study of the interaction between the zonal mean circulation and the semidiurnal tide. *Icarus* **69**, 202–220 (1987).

[ADS](#) [Article](#) [Google Scholar](#)

14. 14.

Takagi, M. & Matsuda, Y. Effects of thermal tides on the Venus atmospheric superrotation. *J. Geophys. Res.* **112**, D09112 (2007).

[ADS](#) [Google Scholar](#)

15. 15.

Ingersoll, A. P. & Orton, G. S. Lateral inhomogeneities in the Venus atmosphere: analysis of thermal infrared maps. *Icarus* **21**, 121–128 (1974).

[ADS](#) [Article](#) [Google Scholar](#)

16. 16.

Schofield, J. T. & Taylor, F. W. Measurements of the mean, solar-fixed temperature and cloud structure of the middle atmosphere of Venus. *Q. J. R. Meteorol. Soc.* **109**, 57–80 (1983).

[ADS](#) [Article](#) [Google Scholar](#)

17. 17.

Zasova, L. V., Ignatiev, N., Khatuntsev, I. & Linkin, V. Structure of the Venus atmosphere. *Planet. Space Sci.* **55**, 1712–1728 (2007).

[ADS](#) [CAS](#) [Article](#) [Google Scholar](#)

18. 18.

Kouyama, T. et al. Global structure of thermal tides in the upper cloud layer of Venus revealed by LIR onboard Akatsuki. *Geophys. Res. Lett.* **46**, 9457–9465 (2019).

[ADS](#) [Article](#) [Google Scholar](#)

19. 19.

Ando, H. et al. Local time dependence of the thermal structure in the Venusian equatorial upper atmosphere: comparison of Akatsuki radio occultation measurements and GCM results. *J. Geophys. Res.* **123**, 2270–2280 (2018).

[Article](#) [Google Scholar](#)

20. 20.

Peralta, J. et al. Solar migrating atmospheric tides in the winds of the polar region of Venus. *Icarus* **220**, 958–970 (2012).

[ADS](#) [Article](#) [Google Scholar](#)

21. 21.

Lebonnois, S. et al. Superrotation of Venus' atmosphere analyzed with a full general circulation model. *J. Geophys. Res.* **115**, E06006 (2010).

[ADS](#) [Article](#) [Google Scholar](#)

22. 22.

Crisp, D. Radiative forcing of the Venus mesosphere, II: thermal fluxes, cooling rates, and radiative equilibrium temperatures. *Icarus* **77**, 391–413 (1989).

[ADS](#) [Article](#) [Google Scholar](#)

23. 23.

Gierasch, P. J. Meridional circulation and the maintenance of the Venus atmospheric rotation. *J. Atmos. Sci.* **32**, 1038–1044 (1975).

[ADS](#) [Article](#) [Google Scholar](#)

24. 24.

Yamamoto, M., Ikeda, K., Takahashi, M. & Horinouchi, T. Solar-locked and geographical atmospheric structures inferred from a Venus general circulation model with radiative transfer. *Icarus* **321**, 232–250 (2019).

[ADS](#) [CAS](#) [Article](#) [Google Scholar](#)

25. 25.

Imamura, T. & Hashimoto, G. L. Venus cloud formation in the meridional circulation. *J. Geophys. Res. Planets* **103**, 31349–31366 (1998).

[ADS](#) [CAS](#) [Article](#) [Google Scholar](#)

26. 26.

Imamura, T. & Hashimoto, G. L. Microphysics of Venusian clouds in rising tropical air. *J. Atmos. Sci.* **58**, 3597–3612 (2001).

[ADS](#) [Article](#) [Google Scholar](#)

27. 27.

Yamamoto, M. & Takahashi, M. An aerosol transport model based on a two-moment microphysical parameterization in the Venus middle atmosphere: model description and preliminary experiments. *J. Geophys. Res.* **111**, E08002 (2006).

[ADS](#) [Google Scholar](#)

28. 28.

Ando, H., Takagi, M., Sugimoto, N., Sagawa, H., Matsuda, Y. Venusian cloud distribution simulated by a general circulation model. *J. Geophys. Res.* **125**, e2019JE006208 (2020).

[ADS](#) [Article](#) [Google Scholar](#)

29. 29.

Limaye, S. S. Venus: cloud level circulation during 1982 as determined from Pioneer cloud photopolarimeter images: II. Solar longitude dependent circulation. *Icarus* **73**, 212–226 (1988).

[ADS](#) [Article](#) [Google Scholar](#)

30. 30.

Rossow, W. B., Del Genio, A. D. & Eichler, T. Cloud-tracked winds from Pioneer Venus OCPP images. *J. Atmos. Sci.* **47**, 2053–2084 (1990).

[ADS](#) [Article](#) [Google Scholar](#)

31. 31.

Hueso, R., Peralta, J., Garate-Lopez, I., Bandos, T. V. & Sánchez-Lavega, A. Six years of Venus winds at the upper cloud level from UV, visible and near infrared observations from VIRTIS on Venus Express. *Planet. Space Sci.* **113–114**, 78–99 (2015).

[ADS](#) [Article](#) [Google Scholar](#)

32. 32.

Horinouchi, T. et al. Mean winds at the cloud top of Venus obtained from two-wavelength UV imaging by Akatsuki. *Earth Planet Space* **70**, 10 (2018).

[ADS](#) [Article](#) [Google Scholar](#)

33. 33.

Takagi, M., Sugimoto, N., Ando, H. & Matsuda, Y. Three-dimensional structures of thermal tides simulated by a Venus GCM. *J. Geophys. Res.* **123**, 335–352 (2018).

[Article](#) [Google Scholar](#)

34. 34.

Imamura, T. Momentum balance of the Venusian midlatitude mesosphere. *J. Geophys. Res.* **102**, 6615–6620 (1997).

[ADS](#) [Article](#) [Google Scholar](#)

35. 35.

Lee, Y. J. et al. The radiative forcing variability caused by the changes of the upper cloud vertical structure in the Venus mesosphere. *Planet. Space Sci.* **113–114**, 298–308 (2015).

[ADS](#) [Article](#) [Google Scholar](#)

36. 36.

Fukuhara, T. et al. Absolute calibration of brightness temperature of the Venus disk observed by the Longwave Infrared Camera onboard Akatsuki. *Earth Planets Space* **69**, 141 (2017).

[ADS](#) [Article](#) [Google Scholar](#)

37. 37.

Fukuhara, T. et al. Large stationary gravity wave in the atmosphere of Venus. *Nat. Geosci.* **10**, 85–88 (2017).

[ADS](#) [CAS](#) [Article](#) [Google Scholar](#)

38. 38.

Kouyama, T., Imamura, T., Nakamura, M., Satoh, T. & Futaana, Y. Horizontal structure of planetary-scale waves at the cloud top of Venus deduced from Galileo SSI images with an improved cloud-tracking technique. *Planet. Space Sci.* **60**, 207–216 (2012).

[ADS](#) [Article](#) [Google Scholar](#)

39. 39.

Khatuntsev, I. V. et al. Cloud level winds from the Venus Express Monitoring Camera imaging. *Icarus* **226**, 140–158 (2013).

[ADS](#) [Article](#) [Google Scholar](#)

40. 40.

Limaye, S. S. Venus atmospheric circulation: known and unknown. *J. Geophys. Res.* **112**, E04S09 (2007).

[ADS](#) [Google Scholar](#)

41. 41.

Ignatiev, N. I. et al. Altimetry of the Venus cloud tops from the Venus Express observations. *J. Geophys. Res.* **114**, E00B43 (2009).

[Google Scholar](#)

42. 42.

Takagi, M. & Matsuda, Y. Sensitivity of thermal tides in the Venus atmosphere to basic zonal flow and Newtonian cooling. *Geophys. Res. Lett.* **32**, L02203 (2005).

[ADS](#) [Google Scholar](#)

43. 43.

Takagi, M. & Matsuda, Y. Dynamical effect of thermal tides in the lower Venus atmosphere. *Geophys. Res. Lett.* **33**, L13102 (2006).

[ADS](#) [Article](#) [Google Scholar](#)

44. 44.

Crisp, D. & Titov, D. V. in *Venus II* (eds Bouger, S. W. et al.) 353–384 (Univ. Arizona Press, 1997).

45. 45.

Smith, M. D. & Gierasch, P. J. Global-scale winds at the Venus cloud top inferred from cloud streak orientations. *Icarus* **123**, 313–323 (1996).

[ADS](#) [Article](#) [Google Scholar](#)

46. 46.

Walterscheid, R. L. et al. Zonal winds and the angular momentum balance of Venus' atmosphere within and above the clouds. *J. Atmos. Sci.* **42**, 1982–1990 (1985).

[ADS](#) [Article](#) [Google Scholar](#)

47. 47.

Sugimoto, N., Takagi, M. & Matsuda, Y. Waves in a Venus general circulation model. *Geophys. Res. Lett.* **41**, 7461–7467 (2014).

[ADS](#) [Article](#) [Google Scholar](#)

48. 48.

Peralta, J. et al. Morphology and dynamics of Venus's middle clouds with Akatsuki/IR1. *Geophys. Res. Lett.* **46**, (2019).

49. 49.

Sánchez-Lavega, A. et al. Variable winds on Venus mapped in three dimensions. *Geophys. Res. Lett.* **35**, L13204 (2008).

[ADS](#) [Article](#) [CAS](#) [Google Scholar](#)

50. 50.

Knutson, H. A. et al. A map of the day–night contrast of the extrasolar planet HD 189733b. *Nature* **447**, 183–186 (2007).

[ADS](#) [CAS](#) [Article](#) [Google Scholar](#)

51. 51.

Nakamura, M. et al. Akatsuki returns to Venus. *Earth Planets Space* **68**, 75 (2016).

[ADS](#) [Article](#) [Google Scholar](#)

52. 52.

Sato, T. M. et al. Dayside cloud top structure of Venus retrieved from Akatsuki IR2 observations. *Icarus* **345**, 113682 (2020).

[CAS](#) [Article](#) [Google Scholar](#)

53. 53.

Limaye, S. S. et al. Venus looks different from day to night across wavelengths: morphology from Akatsuki multispectral images. *Earth Planets Space* **70**, 24 (2018).

[PubMed](#) [PubMed Central](#) [Article](#) [Google Scholar](#)

54. 54.

Machado, P. et al. Venus cloud-tracked and Doppler velocimetry winds from CFHT/ESPaDOnS and Venus Express/VIRTIS in April 2014. *Icarus* **285**, 8–26 (2017).

[ADS](#) [Article](#) [Google Scholar](#)

55. 55.

Gonçalves, R. et al. Venus' cloud top wind study: coordinated Akatsuki/UVI with cloud tracking and TNG/HARPS-N with Doppler velocimetry observations. *Icarus* **335**, 113418 (2020).

[Article](#) [Google Scholar](#)

56. 56.

Murakami, S. et al. *Venus Climate Orbiter Akatsuki LIR Longitude-Latitude Map Data v1.0* (JAXA Data Archives and Transmission System, 2018).

57. 57.

Kouyama, T. et al. Topographical and local time dependence of large stationary gravity waves observed at the cloud top of Venus. *Geophys. Res. Lett.* **44**, 12,098–12,105 (2017).

[Article](#) [Google Scholar](#)

58. 58.

Ikegawa, S. & Horinouchi, T. Improved automatic estimation of winds at the cloud top of Venus using superposition of cross-correlation surfaces. *Icarus* **271**, 98–119 (2016).

[ADS](#) [Article](#) [Google Scholar](#)

59. 59.

Seiff, A., Schofield, J. T., Kliore, A. J., Taylor, F. W. & Limaye, S. S. Models of the structure of the atmosphere of Venus from the surface to 100 kilometers altitude. *Adv. Space Res.* **5**, 3–58 (1985).

[ADS](#) [Article](#) [Google Scholar](#)

60. 60.

Imamura, T. et al. Initial performance of the radio occultation experiment in the Venus orbiter mission Akatsuki. *Earth Planets Space* **69**, 137 (2017).

[ADS](#) [Article](#) [Google Scholar](#)

[Download references](#)

Acknowledgements

The data used in this study were provided by the Akatsuki project of JAXA. We thank the science members of the project for comments. This work was supported by JSPS KAKENHI grant numbers 20H01958 and 19H05605.

Author information

Affiliations

1. Department of Earth and Planetary Science, The University of Tokyo, Tokyo, Japan

Kiichi Fukuya

2. Graduate School of Frontier Sciences, The University of Tokyo, Kashiwa, Japan

Takeshi Imamura

3. College of Science, Rikkyo University, Tokyo, Japan

Makoto Taguchi, Tetsuya Fukuhara & Takeru Yamada

4. Digital Architecture Research Center, National Institute of Advanced Industrial Science and Technology, Tokyo, Japan

Toru Kouyama

5. Faculty of Environmental Earth Science, Hokkaido University, Sapporo, Japan

Takeshi Horinouchi

6. Instituto de Astrofísica e Ciências do Espaço, Lisbon, Portugal

Javier Peralta

7. Colegio Huerta de la Cruz, Algeciras, Spain

Javier Peralta

8. Omori Medical Center, Toho University, Tokyo, Japan

Masahiko Futaguchi

9. Space Information Center, Hokkaido Information University, Ebetsu, Japan

Takao M. Sato

10. Institute of Space and Astronautical Science, Japan Aerospace Exploration Agency, Sagamihara, Japan

Atsushi Yamazaki, Shin-ya Murakami, Takehiko Satoh & Masato Nakamura

11. Faculty of Science, Kyoto Sangyo University, Kyoto, Japan

Masahiro Takagi

Authors

1. Kiichi Fukuya

[View author publications](#)

You can also search for this author in [PubMed](#) [Google Scholar](#)

2. Takeshi Imamura

[View author publications](#)

You can also search for this author in [PubMed](#) [Google Scholar](#)

3. Makoto Taguchi

[View author publications](#)

You can also search for this author in [PubMed](#) [Google Scholar](#)

4. Tetsuya Fukuhara

[View author publications](#)

You can also search for this author in [PubMed](#) [Google Scholar](#)

5. Toru Kouyama

[View author publications](#)

You can also search for this author in [PubMed](#) [Google Scholar](#)

6. Takeshi Horinouchi

[View author publications](#)

You can also search for this author in [PubMed](#) [Google Scholar](#)

7. Javier Peralta

[View author publications](#)

You can also search for this author in [PubMed](#) [Google Scholar](#)

8. Masahiko Futaguchi

[View author publications](#)

You can also search for this author in [PubMed](#) [Google Scholar](#)

9. Takeru Yamada

[View author publications](#)

You can also search for this author in [PubMed](#) [Google Scholar](#)

10. Takao M. Sato

[View author publications](#)

You can also search for this author in [PubMed](#) [Google Scholar](#)

11. Atsushi Yamazaki

[View author publications](#)

You can also search for this author in [PubMed](#) [Google Scholar](#)

12. Shin-ya Murakami

[View author publications](#)

You can also search for this author in [PubMed](#) [Google Scholar](#)

13. Takehiko Satoh

[View author publications](#)

You can also search for this author in [PubMed](#) [Google Scholar](#)

14. Masahiro Takagi

[View author publications](#)

You can also search for this author in [PubMed](#) [Google Scholar](#)

15. Masato Nakamura

[View author publications](#)

You can also search for this author in [PubMed](#) [Google Scholar](#)

Contributions

K.F. developed the code and led the analysis and manuscript writing. T.I. designed the study and contributed to the analysis and manuscript writing. M. Taguchi is the principal investigator of LIR. T.F. mainly developed the instrument. M.F. also developed the instrument and supported calibration. T.K. developed the data processing tool and contributed to calibration. T.Y. contributed to data processing. S.-y.M. led the development of data processing pipeline. T.M.S. contributed to observation planning and A.Y. prepared commands for observations. T.S. led the coordination of the instrument suite including LIR as the project scientist. M.N. led the whole of Akatsuki's observation as the project manager. T.H. provided expertise on atmospheric dynamics and contributed to manuscript writing. J.P. contributed to the interpretation of the results and also helped with manuscript writing. M. Takagi contributed to the interpretation of the tidal structure.

Corresponding author

Correspondence to [Takeshi Imamura](#).

Ethics declarations

Competing interests

The authors declare no competing interests.

Additional information

Peer review information *Nature* thanks Nikolay Ignatiev, Arianna Piccialli and the other, anonymous, reviewer(s) for their contribution to the peer review of this work. Peer reviewer reports are available.

Publisher's note Springer Nature remains neutral with regard to jurisdictional claims in published maps and institutional affiliations.

Extended data figures and tables

[Extended Data Fig. 1 Zonal velocities obtained in first estimation.](#)

a–c, Results for template sizes of $30^\circ \times 30^\circ$ (**a**), $20^\circ \times 20^\circ$ (**b**) and $10^\circ \times 10^\circ$ (**c**). Cloud-tracked vectors that satisfy the criteria described in Methods are plotted as dots. The limit of the major axis length in criterion (3) is 60 m s^{-1} for **a**, 50 m s^{-1} for **b** and 45 m s^{-1} for **c**. The blue dotted line shows the moving average with a sliding window of 20° in latitude and the red solid line shows the rigid body rotation with an equatorial velocity of -95 m s^{-1} , which was adopted as the background zonal velocity in the second estimation

[Source data.](#)

[Extended Data Fig. 2 Examples of cross-correlation coefficient map in second estimation.](#)

The vertical axis represents the northward velocity and the horizontal axis represents the deviation of the eastward velocity from the assumed background velocity. The eastward velocities were divided by the cosine of the latitude. The crosses indicate the maxima, and the blue, green and black lines indicate the contours of the top 1%, 5% and 10% values, respectively. **a, b**, Two examples of accepted cases. **c**, Case rejected because of multiple local maxima. **d**, Case rejected because the major axis of the region of the top 5% is longer than 60 m s^{-1} .

Extended Data Fig. 3 Examples of cloud tracking.

a, Local time–latitude distribution of the accepted velocity vectors on the dayside obtained from a series of images spanning from 02:00 to 23:08 on 16 November 2018. **b**, A pair of images in the image series showing temporal development. **c**, Correlation maps showing the peaks that correspond to the tracking boxes shown by squares in **b**. **d–f**, Same as **a–c**, respectively, but for the dusk–nightside obtained from a series of images spanning from 23:08 on 17 December to 11:08 on 18 December. In **a, d**, arrows are scaled such that the distance occupied by 15° in latitude or 1 h in local time represents a speed of 50 m s^{-1} , and red (blue) colour represents northward (southward) movement. The vertical and horizontal axes of the correlation surfaces are the northward velocity and the deviation of the eastward velocity from the assumed background velocity, respectively. The crosses indicate the maxima, and the blue, green and black lines indicate the contours of the top 1%, 5% and 10% values, respectively.

Extended Data Fig. 4 Latitude–local time distribution of measurement dispersion.

a, b, Standard deviation (**a**) and standard error (**b**) of the cloud-tracked velocity in each grid.

Extended Data Fig. 5 Changes in latitude–local time distribution of velocity associated with change in background velocity adopted in second estimation.

a–c, The background velocity is the sum of a rigid body rotation with an equatorial velocity of -95 m s^{-1} and a constant offset of -15 m s^{-1} (**a**), 0 m s^{-1} (**b**) and 15 m s^{-1} (**c**). Velocity vectors (top) and the meridional velocity (bottom) are shown. Each velocity vector is defined by the deviation of the zonal velocity from the local-time average and the total meridional velocity. Arrows are scaled such that the distance occupied by 10° in latitude represents a meridional speed of 5 m s^{-1} and that occupied by 1 h in local time represents a zonal speed of 5 m s^{-1} .

[Extended Data Fig. 6 Sensitivity to template size.](#)

a–f, Latitude–local time distributions of the derived velocities for template sizes of $20^\circ \times 20^\circ$ (**a–c**) and $40^\circ \times 40^\circ$ (**d–f**). Zonal velocity (**a, d**), meridional velocity (**b, e**) and velocity vectors (**c, f**) are shown. Each velocity vector is defined by the deviation of the zonal velocity from the local-time average and the total meridional velocity. Arrows are scaled such that the distance occupied by 10° in latitude represents a meridional speed of 5 m s^{-1} and that occupied by 1 h in local time represents a zonal speed of 5 m s^{-1} .

[Extended Data Fig. 7 Stability of velocity field.](#)

a–f, Latitude–local time distributions of the velocities obtained from the first half (from 23 December 2016 to 13 February 2018; **a–c**) and the second half (from 25 February 2018 to 20 January 2019; **d–f**) of the dataset. Zonal velocity (**a, d**), meridional velocity (**b, e**) and velocity vectors (**c, f**) are shown. Each velocity vector is defined by the deviation of the zonal velocity from the local-time average and the total meridional velocity. Arrows are scaled such that the distance occupied by 10° in latitude represents a meridional speed of 5 m s^{-1} and that occupied by 1 h in local time represents a zonal speed of 5 m s^{-1} .

Supplementary information

[Peer Review File](#)

Video 1 Example of convergent flow on the nightside

Data taken from 18:01, 18 August 2018 to 19:08, 19 August 2018.

Animation of highpass-filtered images in a superrotating coordinate system with a duration of ~10 h, with noises being suppressed by applying a moving average in the time domain with a window length of ~10 h that corresponds to ~10 images. The red dashed line indicates noon, the black dashed line indicates midnight, and the blue solid lines indicate the terminator.

Video 2 Example of convergent flow on the nightside

Data taken from 06:01, 17 December 2018 to 11:08, 18 December 2018.

Animation of highpass-filtered images in a superrotating coordinate system with a duration of ~10 h, with noises being suppressed by applying a moving average in the time domain with a window length of ~10 h that corresponds to ~10 images. The red dashed line indicates noon, the black dashed line indicates midnight, and the blue solid lines indicate the terminator.

Video 3 Example of divergent flow on the dayside

Data taken from 09:01, 23 February 2018 to 06:08, 24 February 2018.

Animation of highpass-filtered images in a superrotating coordinate system with a duration of ~10 h, with noises being suppressed by applying a moving average in the time domain with a window length of ~10 h that corresponds to ~10 images. The red dashed line indicates noon, the black dashed line indicates midnight, and the blue solid lines indicate the terminator.

Video 4 Example of divergent flow on the dayside

Data taken from 02:00, 16 November 2018 to 07:08, 17 November 2018.

Animation of highpass-filtered images in a superrotating coordinate system with a duration of ~10 h, with noises being suppressed by applying a moving average in the time domain with a window length of ~10 h that corresponds to ~10 images. The red dashed line indicates noon, the black

dashed line indicates midnight, and the blue solid lines indicate the terminator.

Video 5 Example of the movements of tracking boxes on the dayside

Data taken from 07:00 to 20:01, 16 November 2018. Animation showing examples of the movements of tracking boxes corresponding to accepted velocity vectors. A moving average in the time domain with a window length of ~4 h was applied to be consistent with the cloud tracking procedure.

Video 6 Example of the movements of tracking boxes on the dusk-night side.

Data taken from 17:08, 17 December 2018 to 07:08, 18 December 2018. Animation showing examples of the movements of tracking boxes corresponding to accepted velocity vectors. A moving average in the time domain with a window length of ~4 h was applied to be consistent with the cloud tracking procedure.

Source data

[**Source Data Fig. 2**](#)

[**Source Data Fig. 3**](#)

[**Source Data Fig. 4**](#)

[**Source Data Extended Data Fig. 1**](#)

Rights and permissions

[**Reprints and Permissions**](#)

About this article



Cite this article

Fukuya, K., Imamura, T., Taguchi, M. *et al.* The nightside cloud-top circulation of the atmosphere of Venus. *Nature* **595**, 511–515 (2021). <https://doi.org/10.1038/s41586-021-03636-7>

[Download citation](#)

- Received: 20 November 2020
- Accepted: 12 May 2021
- Published: 21 July 2021
- Issue Date: 22 July 2021
- DOI: <https://doi.org/10.1038/s41586-021-03636-7>

Comments

By submitting a comment you agree to abide by our [Terms](#) and [Community Guidelines](#). If you find something abusive or that does not comply with our terms or guidelines please flag it as inappropriate.

[Access through your institution](#)

[Change institution](#)

[Buy or subscribe](#)

Advertisement

This article was downloaded by **calibre** from <https://www.nature.com/articles/s41586-021-03636-7>

| [Section menu](#) | [Main menu](#) |

- Article
- [Published: 21 July 2021](#)

Free-electron lasing at 27 nanometres based on a laser wakefield accelerator

- [Wentao Wang](#)¹^{na1},
- [Ke Feng](#) ORCID: orcid.org/0000-0003-0157-1297¹^{na1},
- [Lintong Ke](#)^{1,2},
- [Changhai Yu](#)¹,
- [Yi Xu](#)¹,
- [Rong Qi](#)¹,
- [Yu Chen](#)¹,
- [Zhiyong Qin](#)¹,
- [Zhijun Zhang](#)¹,
- [Ming Fang](#)¹,
- [Jiaqi Liu](#)¹,
- [Kangnan Jiang](#)^{1,3},
- [Hao Wang](#)¹,
- [Cheng Wang](#)¹,
- [Xiaojun Yang](#)¹,
- [Fenxiang Wu](#)¹,
- [Yuxin Leng](#)¹,
- [Jiansheng Liu](#) ORCID: orcid.org/0000-0002-5984-7965¹,
- [Ruxin Li](#) ORCID: orcid.org/0000-0002-2603-9814^{1,3} &
- [Zhizhan Xu](#)¹

- 3294 Accesses
- 30 Altmetric
- [Metrics details](#)

Subjects

- [Free-electron lasers](#)
- [Plasma-based accelerators](#)

Abstract

X-ray free-electron lasers can generate intense and coherent radiation at wavelengths down to the sub-ångström region^{1,2,3,4,5}, and have become indispensable tools for applications in structural biology and chemistry, among other disciplines⁶. Several X-ray free-electron laser facilities are in operation^{2,3,4,5}; however, their requirement for large, high-cost, state-of-the-art radio-frequency accelerators has led to great interest in the development of compact and economical accelerators. Laser wakefield accelerators can sustain accelerating gradients more than three orders of magnitude higher than those of radio-frequency accelerators^{7,8,9,10}, and are regarded as an attractive option for driving compact X-ray free-electron lasers¹¹. However, the realization of such devices remains a challenge owing to the relatively poor quality of electron beams that are based on a laser wakefield accelerator. Here we present an experimental demonstration of undulator radiation amplification in the exponential-gain regime by using electron beams based on a laser wakefield accelerator. The amplified undulator radiation, which is typically centred at 27 nanometres and has a maximum photon number of around 10^{10} per shot, yields a maximum radiation energy of about 150 nanojoules. In the third of three undulators in the device, the maximum gain of the radiation power is approximately 100-fold, confirming a successful operation in the exponential-gain regime. Our results constitute a proof-of-principle demonstration of free-electron lasing using a laser wakefield accelerator, and pave the way towards the

development of compact X-ray free-electron lasers based on this technology with broad applications.

Access options

Subscribe to Journal

Get full journal access for 1 year

\$199.00

only \$3.90 per issue

[Subscribe](#)

All prices are NET prices.

VAT will be added later in the checkout.

Tax calculation will be finalised during checkout.

Rent or Buy article

Get time limited or full article access on ReadCube.

from \$8.99

[Rent or Buy](#)

All prices are NET prices.

Additional access options:

- [Log in](#)
- [Access through your institution](#)
- [Learn about institutional subscriptions](#)

Fig. 1: Schematic layout of LWFA-based free electron laser experiment.

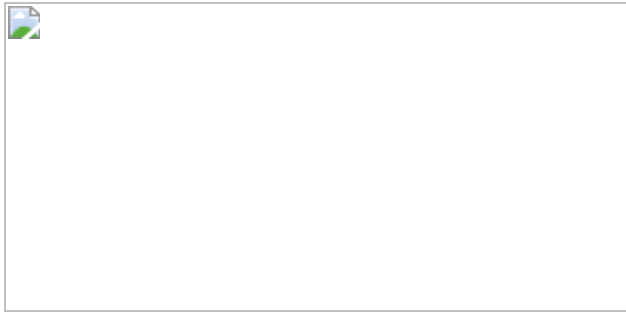


Fig. 2: Measurement of undulator radiation.

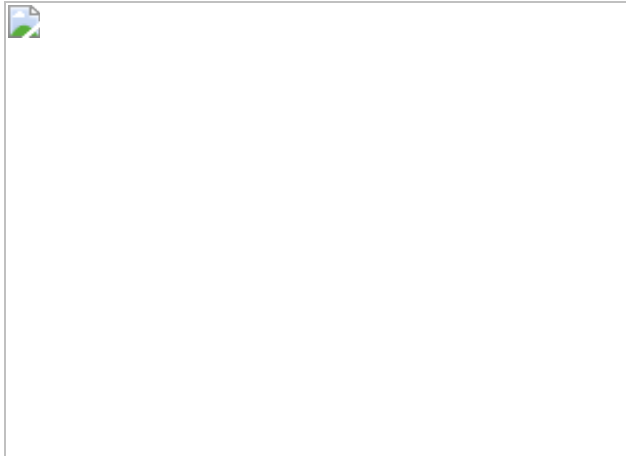
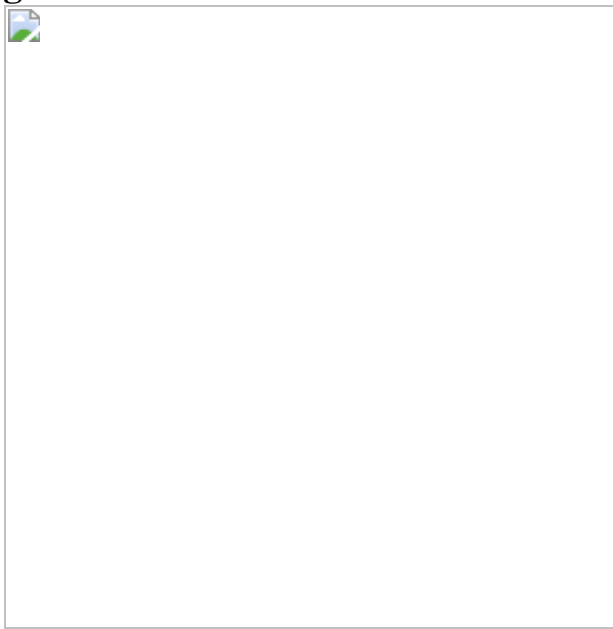


Fig. 3: Undulator radiation measurement at 27 nm.



Data availability

All data are available upon reasonable request from the corresponding authors. [Source data](#) are provided with this paper.

Code availability

All codes written for use in this study are available upon reasonable request from the corresponding authors.

References

1. 1.

Madey, J. M. J. Stimulated emission of bremsstrahlung in a periodic magnetic field. *J. Appl. Phys.* **42**, 1906–1913 (1971).

[ADS](#) [CAS](#) [Google Scholar](#)

2. 2.

Ackermann, W. et al. Operation of a free-electron laser from the extreme ultraviolet to the water window. *Nat. Photon.* **1**, 336–342 (2007).

[ADS](#) [Google Scholar](#)

3. 3.

Emma, P. et al. First lasing and operation of an angstrom-wavelength free-electron laser. *Nat. Photon.* **4**, 641–647 (2010).

[ADS](#) [CAS](#) [Google Scholar](#)

4. 4.

Ishikawa, T. et al. A compact X-ray free-electron laser emitting in the sub-angstrom region. *Nat. Photon.* **6**, 540–544 (2012).

[ADS](#) [CAS](#) [Google Scholar](#)

5. 5.

Allaria, E. et al. Highly coherent and stable pulses from the FERMI seeded free-electron laser in the extreme ultraviolet. *Nat. Photon.* **6**, 699–704 (2012).

[ADS](#) [CAS](#) [Google Scholar](#)

6. 6.

Bostedt, C. et al. Linac Coherent Light Source: the first five years. *Rev. Mod. Phys.* **88**, 015007 (2016).

[ADS](#) [Google Scholar](#)

7. 7.

Tajima, T. & Dawson, J. M. Laser electron accelerator. *Phys. Rev. Lett.* **43**, 267–270 (1979).

[ADS](#) [CAS](#) [Google Scholar](#)

8. 8.

Mangles, S. P. et al. Monoenergetic beams of relativistic electrons from intense laser-plasma interactions. *Nature* **431**, 535–538 (2004).

[ADS](#) [CAS](#) [Google Scholar](#)

9. 9.

Geddes, C. G. R. et al. High-quality electron beams from a laser wakefield accelerator using plasma-channel guiding. *Nature* **431**, 538–541 (2004).

[ADS](#) [CAS](#) [Google Scholar](#)

10. 10.

Faure, J. et al. A laser-plasma accelerator producing monoenergetic electron beams. *Nature* **431**, 541–544 (2004).

[ADS](#) [CAS](#) [Google Scholar](#)

11. 11.

Nakajima, K. Towards a table-top free-electron laser. *Nat. Phys.* **4**, 92–93 (2008).

[CAS](#) [Google Scholar](#)

12. 12.

Faure, J. et al. Controlled injection and acceleration of electrons in plasma wakefields by colliding laser pulses. *Nature* **444**, 737–739 (2006).

[ADS](#) [CAS](#) [Google Scholar](#)

13. 13.

Corde, S. et al. Observation of longitudinal and transverse self-injections in laser-plasma accelerators. *Nat. Commun.* **4**, 1501 (2013).

[ADS](#) [CAS](#) [Google Scholar](#)

14. 14.

Gonsalves, A. J. et al. Tunable laser plasma accelerator based on longitudinal density tailoring. *Nat. Phys.* **7**, 862–866 (2011).

[CAS](#) [Google Scholar](#)

15. 15.

Buck, A. et al. Shock-front injector for high-quality laser-plasma acceleration. *Phys. Rev. Lett.* **110**, 185006 (2013).

[ADS](#) [CAS](#) [Google Scholar](#)

16. 16.

Liu, J. S. et al. All-optical cascaded laser wakefield accelerator using ionization-induced injection. *Phys. Rev. Lett.* **107**, 035001 (2011).

[ADS](#) [CAS](#) [Google Scholar](#)

17. 17.

Wang, W. T. et al. High-brightness high-energy electron beams from a laser wakefield accelerator via energy chirp control. *Phys. Rev. Lett.* **117**, 124801 (2016).

[ADS](#) [CAS](#) [Google Scholar](#)

18. 18.

Steinke, S. et al. Multistage coupling of independent laser-plasma accelerators. *Nature* **530**, 190–193 (2016).

[ADS](#) [CAS](#) [Google Scholar](#)

19. 19.

Gonsalves, A. J. et al. Petawatt laser guiding and electron beam acceleration to 8 GeV in a laser-heated capillary discharge waveguide. *Phys. Rev. Lett.* **122**, 084801 (2019).

[ADS](#) [CAS](#) [Google Scholar](#)

20. 20.

Ta Phuoc, K. et al. All-optical Compton gamma-ray source. *Nat. Photon.* **6**, 308–311 (2012).

[ADS](#) [Google Scholar](#)

21. 21.

Sarri, G. et al. Ultrahigh brilliance multi-MeV γ -ray beams from nonlinear relativistic Thomson scattering. *Phys. Rev. Lett.* **113**, 224801 (2014).

[ADS](#) [CAS](#) [Google Scholar](#)

22. 22.

Yu, C. et al. Ultrahigh brilliance quasi-monochromatic MeV γ -rays based on self-synchronized all-optical Compton scattering. *Sci. Rep.* **6**, 29518 (2016).

[ADS](#) [CAS](#) [PubMed](#) [PubMed Central](#) [Google Scholar](#)

23. 23.

Schroeder, C. B., Esarey, E., Geddes, C. G. R., Benedetti, C. & Leemans, W. P. Physics considerations for laser-plasma linear colliders. *Phys. Rev. Spec. Top. Accel. Beams* **13**, 101301 (2010).

[ADS](#) [Google Scholar](#)

24. 24.

Pellegrini, C., Marinelli, A. & Reiche, S. The physics of X-ray free-electron lasers. *Rev. Mod. Phys.* **88**, 015006 (2016).

[ADS](#) [Google Scholar](#)

25. 25.

Huang, Z. & Kim, K.-J. Review of X-ray free-electron laser theory. *Phys. Rev. Spec. Top. Accel. Beams* **10**, 034801 (2007).

[ADS](#) [Google Scholar](#)

26. 26.

Anania, M. P. et al. An ultrashort pulse ultra-violet radiation undulator source driven by a laser plasma wakefield accelerator. *Appl. Phys. Lett.* **104**, 264102 (2014).

[ADS](#) [Google Scholar](#)

27. 27.

Fang, M. et al. Long-distance characterization of high-quality laser-wakefield-accelerated electron beams. *Chin. Opt. Lett.* **16**, 040201 (2018).

[Google Scholar](#)

28. 28.

van Tilborg, J. et al. Active plasma lensing for relativistic laser-plasma-accelerated electron beams. *Phys. Rev. Lett.* **115**, 184802 (2015).

[ADS](#) [Google Scholar](#)

29. 29.

Maier, A. R. et al. Demonstration scheme for a laser-plasma-driven free-electron laser. *Phys. Rev. X* **2**, 031019 (2012).

[Google Scholar](#)

30. 30.

Huang, Z., Ding, Y. & Schroeder, C. B. Compact X-ray free-electron laser from a laser-plasma accelerator using a transverse-gradient undulator. *Phys. Rev. Lett.* **109**, 204801 (2012).

[ADS](#) [Google Scholar](#)

31. 31.

Loulergue, A. et al. Beam manipulation for compact laser wakefield accelerator based free-electron lasers. *New J. Phys.* **17**, 023028 (2015).

[ADS](#) [Google Scholar](#)

32. 32.

Khojoyan, M. et al. Transport studies of LPA electron beam towards the FEL amplification at COXINEL. *Nucl. Instrum. Methods Phys. Res. A* **829**, 260–264 (2016).

[ADS](#) [CAS](#) [Google Scholar](#)

33. 33.

Seggebrock, T., Maier, A. R., Dornmair, I. & Grüner, F. Bunch decompression for laser-plasma driven free-electron laser demonstration schemes. *Phys. Rev. Spec. Top. Accel. Beams* **16**, 070703 (2013).

[ADS](#) [Google Scholar](#)

34. 34.

Schlenvoigt, H. P. et al. A compact synchrotron radiation source driven by a laser-plasma wakefield accelerator. *Nat. Phys.* **4**, 130–133 (2008).

[CAS](#) [Google Scholar](#)

35. 35.

Fuchs, M. et al. Laser-driven soft-X-ray undulator source. *Nat. Phys.* **5**, 826–829 (2009).

[CAS](#) [Google Scholar](#)

36. 36.

André, T. et al. Control of laser plasma accelerated electrons for light sources. *Nat. Commun.* **9**, 1334 (2018).

[ADS](#) [PubMed](#) [PubMed Central](#) [Google Scholar](#)

37. 37.

Ratner, D. et al. FEL gain length and taper measurements at LCLS. In *Proc. 2009 Free-Electron Laser Conference* 221–224 (JACoW, 2009).

38. 38.

Wu, F. X. et al. Performance improvement of a 200TW/1Hz Ti:sapphire laser for laser wakefield electron accelerator. *Opt. Laser Technol.* **131**, 106453 (2020).

[CAS](#) [Google Scholar](#)

39. 39.

Reiche, S. GENESIS 1.3: a fully 3D time-dependent FEL simulation code, *Nucl. Instrum. Methods Phys. Res. Nucl. Instrum. Methods Phys. Res.* **429**, 243–248 (1999).

[ADS](#) [CAS](#) [Google Scholar](#)

40. 40.

Hogan, M. et al. Measurements of high gain and intensity fluctuations in a self-amplified, spontaneous-emission free-electron laser. *Phys. Rev. Lett.* **80**, 289–292 (1998).

[ADS](#) [CAS](#) [Google Scholar](#)

41. 41.

Rosbach, J. et al. 10 years of pioneering X-ray science at the free-electron laser FLASH at DESY. *Phys. Rep.* **808**, 1–74 (2019).

[ADS](#) [CAS](#) [Google Scholar](#)

42. 42.

Maier, R. et al. Decoding sources of energy variability in a laser-plasma accelerator. *Phys. Rev. X* **10**, 031039 (2020).

[CAS](#) [Google Scholar](#)

43. 43.

Lehe, R. et al. A spectral, quasi-cylindrical and dispersion-free Particle-In-Cell algorithm. *Comput. Phys. Commun.* **203**, 66 (2016).

[ADS](#) [MathSciNet](#) [CAS](#) [MATH](#) [Google Scholar](#)

44. 44.

Jalas, S. et al. Accurate modeling of plasma acceleration with arbitrary order pseudo-spectral particle-in-cell methods. *Phys. Plasmas* **24**, 033115 (2017).

[ADS](#) [Google Scholar](#)

45. 45.

Borland, M. *ELEGANT: A flexible SDDS-compliant code for accelerator simulation*. Technical Report No. LS-287 (Argonne National Laboratory, 2000).

46. 46.

Flöttmann, K. ASTRA. A space charge tracking algorithm.
<https://www.desy.de/~mpyflo/> (DESY, 2007).

47. 47.

Xie, M. Exact and variational solutions of 3D eigenmodes in high gain FELs. *Nucl. Instrum. Methods Phys. Res. Sect. A* **445**, 59–66 (2000).

[ADS](#) [CAS](#) [Google Scholar](#)

[Download references](#)

Acknowledgements

We thank D. Wang and B. Liu for discussions and assistance. This work was supported by the Strategic Priority Research Program (B) (grant no. XDB16) and Center for Excellence in Ultra-intense Laser Science of Chinese Academy of Sciences (CAS), the National Natural Science Foundation of China (grant nos. 11127901, 11875065 and 11991072), the Natural Science Foundation of Shanghai (nos 18JC1414800 and 18ZR1444500) and the State Key Laboratory Program of the Chinese Ministry of Science and Technology and CAS Youth Innovation Promotion Association (Y201952).

Author information

Author notes

1. These authors contributed equally: Wentao Wang, Ke Feng

Affiliations

1. State Key Laboratory of High Field Laser Physics and CAS Center for Excellence in Ultra-intense Laser Science, Shanghai Institute of Optics and Fine Mechanics (SIOM), Chinese Academy of Sciences (CAS), Shanghai, People's Republic of China

Wentao Wang, Ke Feng, Lintong Ke, Changhai Yu, Yi Xu, Rong Qi, Yu Chen, Zhiyong Qin, Zhijun Zhang, Ming Fang, Jiaqi Liu, Kangnan Jiang, Hao Wang, Cheng Wang, Xiaojun Yang, Fenxiang Wu, Yuxin Leng, Jiansheng Liu, Ruxin Li & Zhizhan Xu

2. Center of Materials Science and Optoelectronics Engineering, University of Chinese Academy of Sciences, Beijing, People's

Republic of China

Lintong Ke

3. School of Physical Science and Technology, ShanghaiTech University, Shanghai, People's Republic of China

Kangnan Jiang & Ruxin Li

Authors

1. Wentao Wang

[View author publications](#)

You can also search for this author in [PubMed](#) [Google Scholar](#)

2. Ke Feng

[View author publications](#)

You can also search for this author in [PubMed](#) [Google Scholar](#)

3. Lintong Ke

[View author publications](#)

You can also search for this author in [PubMed](#) [Google Scholar](#)

4. Changhai Yu

[View author publications](#)

You can also search for this author in [PubMed](#) [Google Scholar](#)

5. Yi Xu

[View author publications](#)

You can also search for this author in [PubMed](#) [Google Scholar](#)

6. Rong Qi

[View author publications](#)

You can also search for this author in [PubMed](#) [Google Scholar](#)

7. Yu Chen

[View author publications](#)

You can also search for this author in [PubMed](#) [Google Scholar](#)

8. Zhiyong Qin

[View author publications](#)

You can also search for this author in [PubMed](#) [Google Scholar](#)

9. Zhijun Zhang

[View author publications](#)

You can also search for this author in [PubMed](#) [Google Scholar](#)

10. Ming Fang

[View author publications](#)

You can also search for this author in [PubMed](#) [Google Scholar](#)

11. Jiaqi Liu

[View author publications](#)

You can also search for this author in [PubMed](#) [Google Scholar](#)

12. Kangnan Jiang

[View author publications](#)

You can also search for this author in [PubMed](#) [Google Scholar](#)

13. Hao Wang

[View author publications](#)

You can also search for this author in [PubMed](#) [Google Scholar](#)

14. Cheng Wang

[View author publications](#)

You can also search for this author in [PubMed](#) [Google Scholar](#)

15. Xiaojun Yang

[View author publications](#)

You can also search for this author in [PubMed](#) [Google Scholar](#)

16. Fenxiang Wu

[View author publications](#)

You can also search for this author in [PubMed](#) [Google Scholar](#)

17. Yuxin Leng

[View author publications](#)

You can also search for this author in [PubMed](#) [Google Scholar](#)

18. Jiansheng Liu

[View author publications](#)

You can also search for this author in [PubMed](#) [Google Scholar](#)

19. Ruxin Li

[View author publications](#)

You can also search for this author in [PubMed](#) [Google Scholar](#)

20. Zhizhan Xu

[View author publications](#)

You can also search for this author in [PubMed](#) [Google Scholar](#)

Contributions

R.L., Jiansheng Liu and Z.X. conceived the project. R.L., W.W. and K.F. designed the experiments. W.W., K.F., L.K., C.Y., R.Q., Y.C., Z.Q., Z.Z., M.F., Jiaqi Liu, K.J., H.W., C.W. and Jiansheng Liu performed the experiments and collected the data. Y.L., Y.X., F.W. and X.Y. constructed and ran the Ti:sapphire laser system. K.F. conducted the simulations. K.F.

and L.K. analysed the experimental data. K.F., W.W. and R.L. co-wrote the paper. All authors contributed to the experiments and discussions.

Corresponding authors

Correspondence to [Wentao Wang](#) or [Jiansheng Liu](#) or [Ruxin Li](#).

Ethics declarations

Competing interests

The authors declare no competing interests.

Additional information

Peer review information *Nature* thanks Luca Giannessi, James Rosenzweig and the other, anonymous, reviewer(s) for their contribution to the peer review of this work. Peer reviewer reports are available.

Publisher's note Springer Nature remains neutral with regard to jurisdictional claims in published maps and institutional affiliations.

Extended data figures and tables

[Extended Data Fig. 1 Electron-beam spectra from LWFA.](#)

Energy spectra of the accelerated electron beams for 50 shots measured in spectrometer 1 located 2.3-m downstream of the gas target. Electron beams with an average peak energy of about 490 MeV, r.m.s. energy spread of 0.2–1.2%, r.m.s. divergence of 0.1–0.4 mrad and charges of 10–50 pC were experimentally obtained. The associated fluctuations of the electron beam peak energy were estimated to be less than 3%.

[Source data](#)

Extended Data Fig. 2 Particle-in-cell simulation results for single-stage LWFA.

a, b, Measured fringe pattern for plasma density diagnosis and the corresponding density profile along the optical axis. **c–e**, Longitudinal phase space of the trapped electrons and the corresponding accelerating electric field at different positions. **f**, Longitudinal phase space of the accelerated electrons at the exit of the plasma and the corresponding energy spectrum shown in red. s is the longitudinal position of the electron in an electron beam in the co-moving coordinate. The simulated electron beam had a peak energy of 495 MeV, charge of 25.4 pC, global energy spread of 0.67% in r.m.s. (93% of the total electrons), and normalized projected emittance of 0.23 mm mrad and 0.73 mm mrad in the horizontal and vertical directions, respectively.

[Source data](#)

Extended Data Fig. 3 Properties of simulated electron beam at the exit of the plasma.

a, Coordinate space distribution of accelerated electrons, with various colours representing the various energies. **b**, Beam current (blue) and slice energy spread (red) within the beam. RES, relative energy spread. **c**, Normalized slice emittance of the beam in the horizontal (enx , red) and vertical (eny , blue) directions. Each slice has a length of 31.25 nm, which was set as the grid size in the particle-in-cell simulation.

[Source data](#)

Extended Data Fig. 4 Electron-beam properties in the beamline.

a, b, Start-to-end simulation for horizontal and vertical envelopes of the electron beam along the beamline with a beam energy of 475 MeV (blue), 490 MeV (red) and 505 MeV (black). **c–e**, Measured transverse profiles of the electron beam at the entrance of the undulator located 4-m downstream

from the gas target without (**c**) and with (**d**) focusing and at the exit of the undulator located 9.5-m downstream from the gas target (**e**). With the quadrupoles installed, the measured r.m.s. size of the electron beam was reduced from approximately 0.8 mm to a minimum value of less than 0.1 mm in the horizontal and vertical directions. **f–h**, Shot-to-shot pointing distribution over 50 shots (**f**), and beam size statistics in the horizontal (**g**) and vertical (**h**) directions. The relative positions of the quadrupoles (green) and undulators (cyan) are shown in **a** and **b**.

[Source data](#)

Extended Data Fig. 5 Properties of an electron beam with a reference energy of 490 MeV along the beamline.

a–c, Simulated beam envelopes (**a**), normalized projected emittance (**b**) and Twiss parameters β (**c**) of the electron beam in the horizontal (red) and vertical (blue) directions. The beam used for tracking was directly derived from the FBPIC code.

[Source data](#)

Extended Data Fig. 6 Properties of the electron beam at the entrance of the undulator.

a, Beam current (blue) and slice energy spread (red) within the beam. **b**, Normalized slice emittance of the beam in the horizontal (red) and the vertical (blue) directions. Despite the slice emittance in the bunch tail increasing substantially (**b**) and causing an increase in projected emittance (Extended Data Fig. 5b), most of the electrons in the beam still showed a small slice emittance.

[Source data](#)

Extended Data Fig. 7 Electron-beam spectra detected at the exit of the undulators.

Energy spectra of electron beams for 200 consecutive shots detected with spectrometer 2. The average energy of the electron beam was estimated to be 485 MeV with energy fluctuations of 3.3% and a reproducibility of approximately 100%.

[Source data](#)

Extended Data Fig. 8 Measured spectra of undulator radiation.

a, b, Spectra of the undulator radiation with a groove density of the grating of 3,000 lines per mm (**a**) and 500 lines per mm (**b**). The radiation wavelength was typically centred at 27 nm with a corresponding electron beam energy of 492 MeV, which is reasonably consistent with the measured values shown in Extended Data Fig. 7. The minimum bandwidth was measured to be 2%, which indicated a reasonable agreement with the simulated values in the exponential-gain regime. The measured spectra of broadband spontaneous emission are also depicted with a bandwidth of approximately 7%.

[Source data](#)

Extended Data Fig. 9 Measured radiation energy at the exit of the undulator for various electron beam charges and relative energy spreads.

The black diamonds represent cases with energy spreads larger than 2% (exponential gain is typically not available under such conditions), and the corresponding linear fitting curve (black dashed line) indicates the spontaneous emission. The radiation emitted by a low-energy-spread electron beam (<1%) typically has energy one to two orders higher than that in spontaneous cases, thus indicating the operation in the exponential-gain regime in the present scheme. The exponential gain of the radiation is illustrated with the orbit kick method in the main text.

[Source data](#)

Supplementary information

Supplementary Video 1

The e beams continuously measured in the energy spectrometer I.

Supplementary Video 2

The e beams continuously measured in the energy spectrometer II.

Supplementary Video 3

Video recording for the generation of a continuous high-quality e beams.

Peer Review File

Source data

Source Data Fig. 1

Source Data Fig. 2

Source Data Fig. 3

Source Data Extended Data Fig. 1

Source Data Extended Data Fig. 2

Source Data Extended Data Fig. 3

Source Data Extended Data Fig. 4

Source Data Extended Data Fig. 5

[Source Data Extended Data Fig. 6](#)

[Source Data Extended Data Fig. 7](#)

[Source Data Extended Data Fig. 8](#)

[Source Data Extended Data Fig. 9](#)

Rights and permissions

[Reprints and Permissions](#)

About this article



Check for
updates

Cite this article

Wang, W., Feng, K., Ke, L. *et al.* Free-electron lasing at 27 nanometres based on a laser wakefield accelerator. *Nature* **595**, 516–520 (2021).
<https://doi.org/10.1038/s41586-021-03678-x>

[Download citation](#)

- Received: 05 August 2020
- Accepted: 28 May 2021
- Published: 21 July 2021
- Issue Date: 22 July 2021
- DOI: <https://doi.org/10.1038/s41586-021-03678-x>

Comments

By submitting a comment you agree to abide by our [Terms](#) and [Community Guidelines](#). If you find something abusive or that does not comply with our terms or guidelines please flag it as inappropriate.

[Access through your institution](#)

[Change institution](#)

[Buy or subscribe](#)

Associated Content

[**A step closer to compact X-ray lasers**](#)

- Luca Giannessi

Advertisement

This article was downloaded by **calibre** from <https://www.nature.com/articles/s41586-021-03678-x>

| [Section menu](#) | [Main menu](#) |

- Article
- [Published: 21 July 2021](#)

Layer Hall effect in a 2D topological axion antiferromagnet

- [Anyuan Gao](#) ORCID: [orcid.org/0000-0001-7151-500X¹](https://orcid.org/0000-0001-7151-500X),
- [Yu-Fei Liu¹](#),
- [Chaowei Hu²](#),
- [Jian-Xiang Qiu](#) ORCID: [orcid.org/0000-0002-3855-9374¹](https://orcid.org/0000-0002-3855-9374),
- [Christian Tzschaschel¹](#),
- [Barun Ghosh^{3,4}](#),
- [Sheng-Chin Ho¹](#),
- [Damien Bérubé¹](#),
- [Rui Chen⁵](#),
- [Haipeng Sun](#) ORCID: [orcid.org/0000-0002-5845-9688⁵](https://orcid.org/0000-0002-5845-9688),
- [Zhaowei Zhang](#) ORCID: [orcid.org/0000-0002-0603-6763⁶](https://orcid.org/0000-0002-0603-6763),
- [Xin-Yue Zhang](#) ORCID: [orcid.org/0000-0001-9726-4835⁷](https://orcid.org/0000-0001-9726-4835),
- [Yu-Xuan Wang⁷](#),
- [Naizhou Wang⁶](#),
- [Zumeng Huang⁶](#),
- [Claudia Felser](#) ORCID: [orcid.org/0000-0002-8200-2063⁸](https://orcid.org/0000-0002-8200-2063),
- [Amit Agarwal³](#),
- [Thomas Ding](#) ORCID: [orcid.org/0000-0001-6813-7271⁷](https://orcid.org/0000-0001-6813-7271),
- [Hung-Ju Tien⁹](#),
- [Austin Akey¹⁰](#),
- [Jules Gardener¹⁰](#),
- [Bahadur Singh](#) ORCID: [orcid.org/0000-0002-2013-1126¹¹](https://orcid.org/0000-0002-2013-1126),
- [Kenji Watanabe](#) ORCID: [orcid.org/0000-0003-3701-8119¹²](https://orcid.org/0000-0003-3701-8119),
- [Takashi Taniguchi](#) ORCID: [orcid.org/0000-0002-1467-3105¹³](https://orcid.org/0000-0002-1467-3105),

- [Kenneth S. Burch](#) ORCID: [orcid.org/0000-0002-7541-0245⁷](https://orcid.org/0000-0002-7541-0245),
- [David C. Bell](#) ORCID: [orcid.org/0000-0002-8215-127X^{10,14}](https://orcid.org/0000-0002-8215-127X),
- [Brian B. Zhou](#)⁷,
- [Weibo Gao](#) ORCID: [orcid.org/0000-0003-3971-621X⁶](https://orcid.org/0000-0003-3971-621X),
- [Hai-Zhou Lu](#)⁵,
- [Arun Bansil](#)⁴,
- [Hsin Lin](#) ORCID: [orcid.org/0000-0002-4688-2315¹⁵](https://orcid.org/0000-0002-4688-2315),
- [Tay-Rong Chang](#) ORCID: [orcid.org/0000-0003-1222-2527^{9,16,17}](https://orcid.org/0000-0003-1222-2527),
- [Liang Fu](#)¹⁸,
- [Qiong Ma](#)⁷,
- [Ni Ni](#) ORCID: [orcid.org/0000-0003-4602-3999²](https://orcid.org/0000-0003-4602-3999) &
- [Su-Yang Xu](#) ORCID: [orcid.org/0000-0002-9808-6572¹](https://orcid.org/0000-0002-9808-6572)

Nature volume **595**, pages 521–525 (2021) [Cite this article](#)

- 3260 Accesses
- 40 Altmetric
- [Metrics details](#)

Subjects

- [Topological matter](#)
- [Two-dimensional materials](#)

Abstract

Whereas ferromagnets have been known and used for millennia, antiferromagnets were only discovered in the 1930s¹. At large scale, because of the absence of global magnetization, antiferromagnets may seem to behave like any non-magnetic material. At the microscopic level, however, the opposite alignment of spins forms a rich internal structure. In topological antiferromagnets, this internal structure leads to the possibility that the property known as the Berry phase can acquire distinct spatial textures^{2,3}. Here we study this possibility in an antiferromagnetic axion

insulator—even-layered, two-dimensional MnBi₂Te₄—in which spatial degrees of freedom correspond to different layers. We observe a type of Hall effect—the layer Hall effect—in which electrons from the top and bottom layers spontaneously deflect in opposite directions. Specifically, under zero electric field, even-layered MnBi₂Te₄ shows no anomalous Hall effect. However, applying an electric field leads to the emergence of a large, layer-polarized anomalous Hall effect of about $0.5e^2/h$ (where e is the electron charge and h is Planck's constant). This layer Hall effect uncovers an unusual layer-locked Berry curvature, which serves to characterize the axion insulator state. Moreover, we find that the layer-locked Berry curvature can be manipulated by the axion field formed from the dot product of the electric and magnetic field vectors. Our results offer new pathways to detect and manipulate the internal spatial structure of fully compensated topological antiferromagnets^{4,5,6,7,8,9}. The layer-locked Berry curvature represents a first step towards spatial engineering of the Berry phase through effects such as layer-specific moiré potential.

Access options

Subscribe to Journal

Get full journal access for 1 year

\$199.00

only \$3.90 per issue

[Subscribe](#)

All prices are NET prices.

VAT will be added later in the checkout.

Tax calculation will be finalised during checkout.

Rent or Buy article

Get time limited or full article access on ReadCube.

from \$8.99

[Rent or Buy](#)

All prices are NET prices.

Additional access options:

- [Log in](#)
- [Access through your institution](#)
- [Learn about institutional subscriptions](#)

Fig. 1: Basic characterizations of the antiferromagnetic six-SL MnBi_2Te_4 .

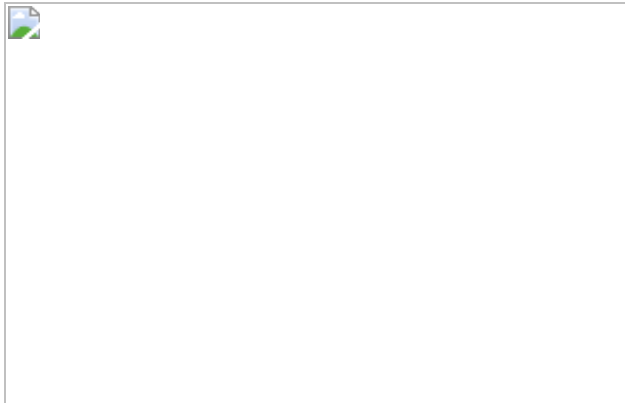


Fig. 2: Observation of the layer Hall effect.

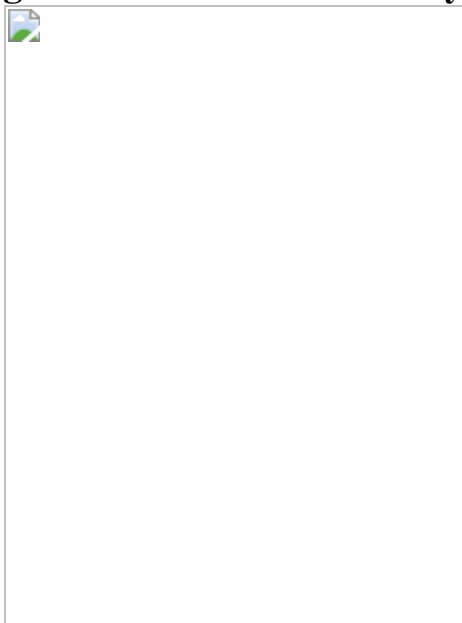
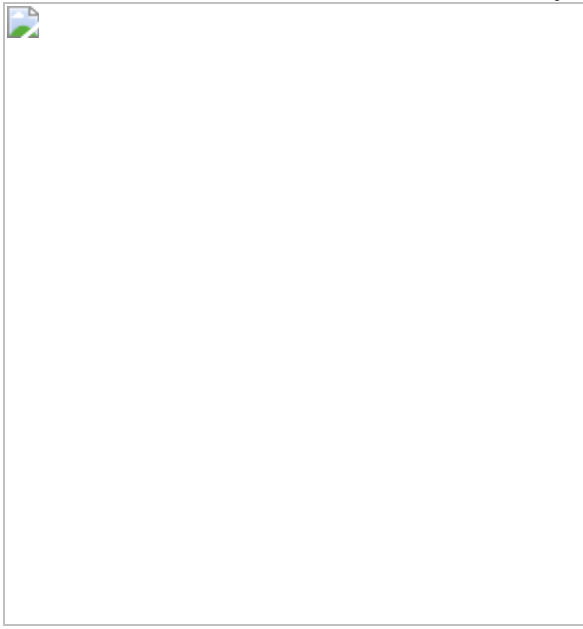


Fig. 3: Charge-density dependence of the layer Hall effect and the layer-locked Berry curvature.



Fig. 4: Manipulation of the layer-locked Berry curvature by the axion field $E \cdot B$ and electrical readout by the layer Hall effect.



Data availability

The data that support the plots within this paper and other findings of this study are available from the corresponding authors upon reasonable request. [Source data](#) are provided with this paper.

References

1. 1.

Néel, L. Nobel Lecture: Magnetism and the local molecular field. *Nobel Lectures, Physics 1963–1970* (Elsevier, 1970).

2. 2.

Li, X., Cao, T., Niu, Q., Shi, J. & Feng, J. Coupling the valley degree of freedom to antiferromagnetic order. *Proc. Natl Acad. Sci. USA* **110**, 3738–3742 (2013).

[ADS](#) [CAS](#) [PubMed](#) [PubMed Central](#) [Article](#) [Google Scholar](#)

3. 3.

Gao, Y., Yang, S. A. & Niu, Q. Field induced positional shift of Bloch electrons and its dynamical implications. *Phys. Rev. Lett.* **112**, 166601 (2014).

[ADS](#) [PubMed](#) [Article](#) [CAS](#) [Google Scholar](#)

4. 4.

Chen, H., Niu, Q. & MacDonald, A. Anomalous Hall effect arising from noncollinear antiferromagnetism. *Phys. Rev. Lett.* **112**, 017205 (2014).

[ADS](#) [PubMed](#) [Article](#) [CAS](#) [Google Scholar](#)

5. 5.

Nakatsuji, S., Kiyohara, N. & Higo, T. Large anomalous Hall effect in a non-collinear antiferromagnet at room temperature. *Nature* **527**, 212–215 (2015).

[ADS](#) [CAS](#) [PubMed](#) [Article](#) [Google Scholar](#)

6. 6.

Nayak, A. K. et al. Large anomalous Hall effect driven by a nonvanishing Berry curvature in the noncolinear antiferromagnet Mn₃Ge. *Sci. Adv.* **2**, e1501870 (2016).

[ADS](#) [PubMed](#) [PubMed Central](#) [Article](#) [CAS](#) [Google Scholar](#)

7. 7.

Šmejkal, L., Mokrousov, Y., Yan, B. & MacDonald, A. H. Topological antiferromagnetic spintronics. *Nat. Phys.* **14**, 242–251 (2018).

[Article](#) [CAS](#) [Google Scholar](#)

8. 8.

Tokura, Y., Yasuda, K. & Tsukazaki, A. Magnetic topological insulators. *Nat. Rev. Phys.* **1**, 126–143 (2019).

[Article](#) [Google Scholar](#)

9. 9.

Xu, Y. et al. High-throughput calculations of magnetic topological materials. *Nature* **586**, 702–707 (2020).

[ADS](#) [CAS](#) [PubMed](#) [Article](#) [Google Scholar](#)

10. 10.

Fiebig, M. Revival of the magnetoelectric effect. *J. Phys. D* **38**, R123–R152 (2005).

[ADS](#) [CAS](#) [Article](#) [Google Scholar](#)

11. 11.

Jungwirth, T., Marti, X., Wadley, P. & Wunderlich, J.
Antiferromagnetic spintronics. *Nat. Nanotechnol.* **11**, 231–241 (2016).

[ADS](#) [CAS](#) [PubMed](#) [Article](#) [Google Scholar](#)

12. 12.

Essin, A. M., Moore, J. E. & Vanderbilt, D. Magnetoelectric polarizability and axion electrodynamics in crystalline insulators. *Phys. Rev. Lett.* **102**, 146805 (2009).

[ADS](#) [PubMed](#) [Article](#) [CAS](#) [Google Scholar](#)

13. 13.

Sivadas, N., Okamoto, S. & Xiao, D. Gate-controllable magneto-optic Kerr effect in layered collinear antiferromagnets. *Phys. Rev. Lett.* **117**, 267203 (2016).

[ADS](#) [PubMed](#) [Article](#) [Google Scholar](#)

14. 14.

Wang, J., Lian, B. & Zhang, S.-C. Generation of spin currents by magnetic field in $\{\mathcal{T}\}$ -and $\{\mathcal{P}\}$ -broken materials. *Spin* **9**, 1940013 (2019).

[ADS](#) [CAS](#) [Article](#) [Google Scholar](#)

15. 15.

Zhang, D. et al. Topological axion states in the magnetic insulator MnBi_2Te_4 with the quantized magnetoelectric effect. *Phys. Rev. Lett.* **122**, 206401 (2019).

[ADS](#) [CAS](#) [PubMed](#) [Article](#) [Google Scholar](#)

16. 16.

Armitage, N. P. & Wu, L. On the matter of topological insulators as magnetoelectrics. *SciPost Phys.* **6**, 046 (2019).

[ADS](#) [MathSciNet](#) [CAS](#) [Article](#) [Google Scholar](#)

17. 17.

Šmejkal, L., González-Hernández, R., Jungwirth, T. & Sinova, J. Crystal time-reversal symmetry breaking and spontaneous Hall effect in collinear antiferromagnets. *Sci. Adv.* **6**, eaaz8809 (2020).

[ADS](#) [PubMed](#) [PubMed Central](#) [Article](#) [CAS](#) [Google Scholar](#)

18. 18.

Du, S. et al. Berry curvature engineering by gating two-dimensional antiferromagnets. *Phys. Rev. Res.* **2**, 022025 (2020).

[CAS](#) [Article](#) [Google Scholar](#)

19. 19.

Wang, H. & Qian, X. Electrically and magnetically switchable nonlinear photocurrent in $\{\mathcal{P}\}\{\mathcal{T}\}$ -symmetric magnetic topological quantum materials. *npj Comput. Mater.* **6**, 199 (2020).

[ADS](#) [CAS](#) [Article](#) [Google Scholar](#)

20. 20.

Fei, R., Song, W. & Yang, L. Giant linearly-polarized photogalvanic effect and second harmonic generation in two-dimensional axion insulators. *Phys. Rev. B* **102**, 035440 (2020).

[ADS](#) [CAS](#) [Article](#) [Google Scholar](#)

21. 21.

Li, R., Wang, J., Qi, X.-L. & Zhang, S.-C. Dynamical axion field in topological magnetic insulators. *Nat. Phys.* **6**, 284–288 (2010).

[CAS](#) [Article](#) [Google Scholar](#)

22. 22.

Nagaosa, N., Sinova, J., Onoda, S., MacDonald, A. & Ong, N. P. Anomalous Hall effect. *Rev. Mod. Phys.* **82**, 1539–1592 (2010).

[ADS](#) [Article](#) [Google Scholar](#)

23. 23.

Mak, K. F., McGill, K. L., Park, J. & McEuen, P. L. The valley Hall effect in MoS₂ transistors. *Science* **344**, 1489–1492 (2014).

[ADS](#) [CAS](#) [PubMed](#) [Article](#) [Google Scholar](#)

24. 24.

Otrokov, M. M. et al. Prediction and observation of an antiferromagnetic topological insulator. *Nature* **576**, 416–422 (2019).

[ADS](#) [CAS](#) [PubMed](#) [Article](#) [Google Scholar](#)

25. 25.

Rienks, E. D. L. et al. Large magnetic gap at the Dirac point in Bi₂Te₃/MnBi₂Te₄ heterostructures. *Nature* **576**, 423–428 (2019).

[ADS](#) [CAS](#) [PubMed](#) [Article](#) [Google Scholar](#)

26. 26.

Lee, S. H. et al. Spin scattering and noncollinear spin structure-induced intrinsic anomalous Hall effect in antiferromagnetic topological insulator MnBi₂Te₄. *Phys. Rev. Res.* **1**, 012011 (2019).

[CAS](#) [Article](#) [Google Scholar](#)

27. 27.

Yan, J.-Q. et al. Crystal growth and magnetic structure of MnBi₂Te₄. *Phys. Rev. Mater.* **3**, 064202 (2019).

[CAS](#) [Article](#) [Google Scholar](#)

28. 28.

Deng, Y. et al. Quantum anomalous Hall effect in intrinsic magnetic topological insulator MnBi₂Te₄. *Science* **367**, 895–900 (2020).

[ADS](#) [CAS](#) [PubMed](#) [Article](#) [Google Scholar](#)

29. 29.

Liu, C. et al. Robust axion insulator and Chern insulator phases in a two-dimensional antiferromagnetic topological insulator. *Nat. Mater.* **19**, 522–527 (2020).

[ADS](#) [CAS](#) [PubMed](#) [Article](#) [Google Scholar](#)

30. 30.

Ge, J. et al. High-Chern-number and high-temperature quantum Hall effect without Landau levels. *Natl Sci. Rev.* **7**, 1280–1287 (2020).

[CAS](#) [Article](#) [Google Scholar](#)

31. 31.

Liu, C. et al. Helical Chern insulator phase with broken time-reversal symmetry in MnBi₂Te₄. Preprint at <https://arxiv.org/abs/1910.13943> (2020).

32. 32.

Deng, H. et al. High-temperature quantum anomalous Hall regime in a MnBi₂Te₄/Bi₂Te₃ superlattice. *Nat. Phys.* **17**, 36–42 (2021).

[CAS](#) [Article](#) [Google Scholar](#)

33. 33.

Ovchinnikov, D. et al. Intertwined topological and magnetic orders in atomically thin Chern insulator MnBi₂Te₄. *Nano Lett.* **21**, 2544–2550 (2021).

[ADS](#) [CAS](#) [PubMed](#) [Article](#) [Google Scholar](#)

34. 34.

Mogi, M. et al. Tailoring tricolor structure of magnetic topological insulator for robust axion insulator. *Sci. Adv.* **3**, eaao1669 (2017).

[PubMed](#) [PubMed Central](#) [Article](#) [CAS](#) [Google Scholar](#)

35. 35.

Xiao, D. et al. Realization of the axion insulator state in quantum anomalous Hall sandwich heterostructures. *Phys. Rev. Lett.* **120**, 056801 (2018).

[ADS](#) [CAS](#) [PubMed](#) [Article](#) [Google Scholar](#)

36. 36.

Chang, C.-Z. et al. Experimental observation of the quantum anomalous Hall effect in a magnetic topological insulator. *Science* **340**, 167–170 (2013).

[ADS](#) [CAS](#) [PubMed](#) [Article](#) [Google Scholar](#)

37. 37.

Iyama, A. & Kimura, T. Magnetoelectric hysteresis loops in Cr₂O₃ at room temperature. *Phys. Rev. B* **87**, 180408(R) (2013).

[ADS](#) [Article](#) [CAS](#) [PubMed](#) [Article](#) [Google Scholar](#)

38. 38.

Jiang, S., Shan, J. & Mak, K. F. Electric-field switching of two-dimensional van der Waals magnets. *Nat. Mater.* **17**, 406–410 (2018).

[ADS](#) [CAS](#) [PubMed](#) [Article](#) [Google Scholar](#)

39. 39.

Matsukura, F., Tokura, Y. & Ohno, H. Control of magnetism by electric fields. *Nat. Nanotechnol.* **10**, 209–220 (2015).

[ADS](#) [CAS](#) [PubMed](#) [Article](#) [Google Scholar](#)

40. 40.

Tsai, H. et al. Electrical manipulation of a topological antiferromagnetic state. *Nature* **580**, 608–613 (2020).

[ADS](#) [CAS](#) [PubMed](#) [Article](#) [Google Scholar](#)

41. 41.

Zhang, S. et al. Experimental observation of the gate-controlled reversal of the anomalous Hall effect in the intrinsic magnetic topological insulator MnBi₂Te₄ device. *Nano Lett.* **20**, 709–714 (2020).

[ADS](#) [PubMed](#) [Article](#) [CAS](#) [Google Scholar](#)

42. 42.

Gordon, K. N. et al. Strongly gapped topological surface states on protected surfaces of antiferromagnetic MnBi₄Te₇ and MnBi₆Te₁₀.

Preprint at <https://arxiv.org/abs/1910.13943> (2019).

43. 43.

Chen, Y. J. et al. Topological electronic structure and its temperature evolution in antiferromagnetic topological insulator MnBi_2Te_4 . *Phys. Rev. X* **9**, 041040 (2019).

[CAS](#) [Google Scholar](#)

44. 44.

Hao, Y.-J. et al. Gapless surface Dirac cone in antiferromagnetic topological insulator MnBi_2Te_4 . *Phys. Rev. X* **9**, 041038 (2019).

[CAS](#) [Google Scholar](#)

45. 45.

Swatek, P. et al. Gapless Dirac surface states in the antiferromagnetic topological insulator MnBi_2Te_4 . *Phys. Rev. B* **101**, 161109 (2020).

[ADS](#) [CAS](#) [Article](#) [Google Scholar](#)

46. 46.

Huang, B. et al. Layer-dependent ferromagnetism in a van der Waals crystal down to the monolayer limit. *Nature* **546**, 270–273 (2017).

[ADS](#) [CAS](#) [PubMed](#) [Article](#) [Google Scholar](#)

47. 47.

Zhao, S. Y. F. et al. Sign reversing Hall effect in atomically thin high temperature superconductors. *Phys. Rev. Lett.* **122**, 247001 (2019).

[ADS](#) [CAS](#) [PubMed](#) [Article](#) [Google Scholar](#)

48. 48.

Deng, Y. et al. Gate-tunable room-temperature ferromagnetism in two-dimensional Fe₃GeTe₂. *Nature* **563**, 94–99 (2018).

[ADS](#) [CAS](#) [PubMed](#) [Article](#) [Google Scholar](#)

49. 49.

Zhang, Y. et al. Direct observation of a widely tunable bandgap in bilayer graphene. *Nature* **459**, 820–823 (2009).

[ADS](#) [CAS](#) [PubMed](#) [Article](#) [Google Scholar](#)

50. 50.

Taychatanapat, T. & Jarillo-Herrero, P. Electronic transport in dual-gated bilayer graphene at large displacement fields. *Phys. Rev. Lett.* **105**, 166601 (2010).

[ADS](#) [PubMed](#) [Article](#) [CAS](#) [Google Scholar](#)

51. 51.

Kresse, G. & Furthmüller, J. Efficient iterative schemes for *ab initio* total-energy calculations using a plane-wave basis set. *Phys. Rev. B* **54**, 11169–11186 (1996).

[ADS](#) [CAS](#) [Article](#) [Google Scholar](#)

52. 52.

Otrokov, M. M. et al. Unique thickness-dependent properties of the van der Waals interlayer antiferromagnet MnBi₂Te₄ films. *Phys. Rev. Lett.* **122**, 107202 (2019).

[ADS](#) [CAS](#) [PubMed](#) [Article](#) [Google Scholar](#)

53. 53.

Souza, I., Marzari, N. & Vanderbilt, D. Maximally localized Wannier functions for entangled energy bands. *Phys. Rev. B* **65**, 035109 (2001).

[ADS](#) [Article](#) [CAS](#) [Google Scholar](#)

54. 54.

Newhouse-Illige, T. et al. Voltage-controlled interlayer coupling in perpendicularly magnetized magnetic tunnel junctions. *Nat. Commun.* **8**, 15232 (2017).

[ADS](#) [CAS](#) [PubMed](#) [PubMed Central](#) [Article](#) [Google Scholar](#)

55. 55.

Kanai, S. et al. Electric field-induced magnetization reversal in a perpendicular-anisotropy CoFeB–MgO magnetic tunnel junction. *Appl. Phys. Lett.* **101**, 122403 (2012).

[ADS](#) [Article](#) [CAS](#) [Google Scholar](#)

56. 56.

Hirsch, S. Spin Hall effect. *Phys. Rev. Lett.* **83**, 1834–1837 (1999).

[ADS](#) [CAS](#) [Article](#) [Google Scholar](#)

57. 57.

Sodemann, I. & Fu, L. Quantum nonlinear Hall effect induced by Berry curvature dipole in time-reversal invariant materials. *Phys. Rev. Lett.* **115**, 216806 (2015).

[ADS](#) [PubMed](#) [Article](#) [CAS](#) [Google Scholar](#)

58. 58.

Manna, K. et al. From colossal to zero: controlling the anomalous Hall effect in magnetic Heusler compounds via Berry curvature design.

Phys. Rev. X **8**, 041045 (2018).

[CAS](#) [Google Scholar](#)

59. 59.

Yasuda, K. et al. Stacking-engineered ferroelectricity in bilayer boron nitride. *Science* **27**, eabd3230 (2021).

[Google Scholar](#)

[Download references](#)

Acknowledgements

We thank F. Zhao and P. Kim for allowing us to use their glovebox and sample preparation facilities. We thank T. I. Andersen, G. Scuri, H. Park and M. D. Lukin for their help with magnetic measurements. We also thank F. Zhao, P. Kim, Y. Gao and C. Liu for discussions. Work in the Xu group was supported partly by the Center for the Advancement of Topological Semimetals (CATS), an Energy Frontier Research Center (EFRC) funded by the US Department of Energy (DOE) Office of Science, through the Ames Laboratory under contract DE-AC0207CH11358 (fabrication and measurements) and partly through the STC Center for Integrated Quantum Materials (CIQM), National Science Foundation (NSF) award no. ECCS-2025158 (data analysis). S.-Y.X. acknowledges the Corning Fund for Faculty Development. Q.M. acknowledges support from the CATS, an EFRC funded by the US DOE Office of Science, through the Ames Laboratory under contract DE-AC0207CH11358. C.T. acknowledges support from the Swiss National Science Foundation under project P2EZP2_191801. Y.-F.L., A. Akey, J.G., D.C.B. and L.F. were supported by the CIQM, NSF award no. ECCS-2025158. This work was performed in part at the Center for Nanoscale Systems at Harvard University, a member of the National Nanotechnology Coordinated Infrastructure Network, which is supported by the NSF under NSF award no.1541959. Work at UCLA was supported by the US DOE, Office of Science, Office of Basic Energy Sciences (BES) under award no. DE-SC0021117 for bulk sample growth,

transport and magnetic property measurements. The work at Northeastern University was supported by the Air Force Office of Scientific Research under award number FA955-20-1-0322, and it benefited from the computational resources of Northeastern University's Advanced Scientific Computation Center (ASCC) and the Discovery Cluster. B.G. and A. Agarwal thank the Science Education and Research Board and the Department of Science and Technology of the government of India for financial support, and the computer centre IIT Kanpur for providing the High Performance Computing facility. T.-R.C. was supported by the Young Scholar Fellowship Program from the Ministry of Science and Technology (MOST) in Taiwan, under a MOST grant for the Columbus Program MOST110-2636-M-006-016, the National Cheng Kung University, Taiwan, and National Center for Theoretical Sciences, Taiwan. Work at NCKU was supported by MOST, Taiwan, under grant MOST107-2627-E-006-001 and Higher Education Sprout Project, Ministry of Education to the Headquarters of University Advancement at NCKU. H.L. acknowledges support by MOST in Taiwan under grant number MOST 109-2112-M-001-014-MY3. H.-Z.L. was supported by the National Natural Science Foundation of China (11925402), Guangdong province (2016ZT06D348, 2020KCXTD001), the National Key R&D Program (2016YFA0301700), Shenzhen High-level Special Fund (G02206304, G02206404), and the Science, Technology and Innovation Commission of Shenzhen Municipality (ZDSYS20170303165926217, JCYJ20170412152620376, KYTDPT20181011104202253), and Center for Computational Science and Engineering of SUSTech. R.C. was supported by the China Postdoctoral Science Foundation (grant no. 2019M661678) and the SUSTech Presidential Postdoctoral Fellowship. C.F. was supported by the ERC Advanced Grant no. 742068 'TOPMAT' and by the Deutsche Forschungsgemeinschaft (German Research Foundation) under Germany's Excellence Strategy through Würzburg-Dresden Cluster of Excellence on Complexity and Topology in Quantum Matter—ct.qmat (EXC 2147, project-id 390858490). K.S.B. is grateful for the support of the Office of Naval Research under award no. N00014-20-1-2308. K.W. and T.T. acknowledge support from the Elemental Strategy Initiative conducted by MEXT, Japan, grant no. JPMXP0112101001 and JSPS KAKENHI grant no. JP20H00354. Z.Z., N.W., Z.H. and W.G. thank the Singapore National Research Foundation through its Competitive Research Program (CRP

award no. NRF-CRP21-2018-0007, NRF-CRP22-2019-0004). X.-Y.Z., Y.-X.W. and B.B.Z. acknowledge support from NSF award no. ECCS-2041779.

Author information

Affiliations

1. Department of Chemistry and Chemical Biology, Harvard University, Cambridge, MA, USA

Anyuan Gao, Yu-Fei Liu, Jian-Xiang Qiu, Christian Tzschaschel, Sheng-Chin Ho, Damien Bérubé & Su-Yang Xu

2. Department of Physics and Astronomy and California NanoSystems Institute, University of California, Los Angeles, Los Angeles, CA, USA

Chaowei Hu & Ni Ni

3. Department of Physics, Indian Institute of Technology, Kanpur, India

Barun Ghosh & Amit Agarwal

4. Department of Physics, Northeastern University, Boston, MA, USA

Barun Ghosh & Arun Bansil

5. Shenzhen Institute for Quantum Science and Engineering and Department of Physics, Southern University of Science and Technology (SUSTech), Shenzhen, China

Rui Chen, Haipeng Sun & Hai-Zhou Lu

6. Division of Physics and Applied Physics, School of Physical and Mathematical Sciences, Nanyang Technological University, Singapore, Singapore

Zhaowei Zhang, Naizhou Wang, Zumeng Huang & Weibo Gao

7. Department of Physics, Boston College, Chestnut Hill, MA, USA

Xin-Yue Zhang, Yu-Xuan Wang, Thomas Ding, Kenneth S. Burch, Brian B. Zhou & Qiong Ma

8. Max Planck Institute for Chemical Physics of Solids, Dresden, Germany

Claudia Felser

9. Department of Physics, National Cheng Kung University, Tainan, Taiwan

Hung-Ju Tien & Tay-Rong Chang

10. Center for Nanoscale Systems, Harvard University, Cambridge, MA, USA

Austin Akey, Jules Gardener & David C. Bell

11. Department of Condensed Matter Physics and Materials Science, Tata Institute of Fundamental Research, Mumbai, India

Bahadur Singh

12. Research Center for Functional Materials, National Institute for Materials Science, Tsukuba, Japan

Kenji Watanabe

13. International Center for Materials Nanoarchitectonics, National Institute for Materials Science, Tsukuba, Japan

Takashi Taniguchi

14. Harvard John A. Paulson School of Engineering and Applied Sciences, Harvard University, Cambridge, MA, USA

David C. Bell

15. Institute of Physics, Academia Sinica, Taipei, Taiwan

Hsin Lin

16. Center for Quantum Frontiers of Research and Technology (QFort),
Tainan, Taiwan

Tay-Rong Chang

17. Physics Division, National Center for Theoretical Sciences, National
Taiwan University, Taipei, Taiwan

Tay-Rong Chang

18. Department of Physics, Massachusetts Institute of Technology,
Cambridge, MA, USA

Liang Fu

Authors

1. Anyuan Gao

[View author publications](#)

You can also search for this author in [PubMed](#) [Google Scholar](#)

2. Yu-Fei Liu

[View author publications](#)

You can also search for this author in [PubMed](#) [Google Scholar](#)

3. Chaowei Hu

[View author publications](#)

You can also search for this author in [PubMed](#) [Google Scholar](#)

4. Jian-Xiang Qiu

[View author publications](#)

You can also search for this author in [PubMed](#) [Google Scholar](#)

5. Christian Tzschaschel

[View author publications](#)

You can also search for this author in [PubMed](#) [Google Scholar](#)

6. Barun Ghosh

[View author publications](#)

You can also search for this author in [PubMed](#) [Google Scholar](#)

7. Sheng-Chin Ho

[View author publications](#)

You can also search for this author in [PubMed](#) [Google Scholar](#)

8. Damien Bérubé

[View author publications](#)

You can also search for this author in [PubMed](#) [Google Scholar](#)

9. Rui Chen

[View author publications](#)

You can also search for this author in [PubMed](#) [Google Scholar](#)

10. Haipeng Sun

[View author publications](#)

You can also search for this author in [PubMed](#) [Google Scholar](#)

11. Zhaowei Zhang

[View author publications](#)

You can also search for this author in [PubMed](#) [Google Scholar](#)

12. Xin-Yue Zhang

[View author publications](#)

You can also search for this author in [PubMed](#) [Google Scholar](#)

13. Yu-Xuan Wang

[View author publications](#)

You can also search for this author in [PubMed](#) [Google Scholar](#)

14. Naizhou Wang

[View author publications](#)

You can also search for this author in [PubMed](#) [Google Scholar](#)

15. Zumeng Huang

[View author publications](#)

You can also search for this author in [PubMed](#) [Google Scholar](#)

16. Claudia Felser

[View author publications](#)

You can also search for this author in [PubMed](#) [Google Scholar](#)

17. Amit Agarwal

[View author publications](#)

You can also search for this author in [PubMed](#) [Google Scholar](#)

18. Thomas Ding

[View author publications](#)

You can also search for this author in [PubMed](#) [Google Scholar](#)

19. Hung-Ju Tien

[View author publications](#)

You can also search for this author in [PubMed](#) [Google Scholar](#)

20. Austin Akey

[View author publications](#)

You can also search for this author in [PubMed](#) [Google Scholar](#)

21. Jules Gardener

[View author publications](#)

You can also search for this author in [PubMed](#) [Google Scholar](#)

22. Bahadur Singh

[View author publications](#)

You can also search for this author in [PubMed](#) [Google Scholar](#)

23. Kenji Watanabe

[View author publications](#)

You can also search for this author in [PubMed](#) [Google Scholar](#)

24. Takashi Taniguchi

[View author publications](#)

You can also search for this author in [PubMed](#) [Google Scholar](#)

25. Kenneth S. Burch

[View author publications](#)

You can also search for this author in [PubMed](#) [Google Scholar](#)

26. David C. Bell

[View author publications](#)

You can also search for this author in [PubMed](#) [Google Scholar](#)

27. Brian B. Zhou

[View author publications](#)

You can also search for this author in [PubMed](#) [Google Scholar](#)

28. Weibo Gao

[View author publications](#)

You can also search for this author in [PubMed](#) [Google Scholar](#)

29. Hai-Zhou Lu

[View author publications](#)

You can also search for this author in [PubMed](#) [Google Scholar](#)

30. Arun Bansil

[View author publications](#)

You can also search for this author in [PubMed](#) [Google Scholar](#)

31. Hsin Lin

[View author publications](#)

You can also search for this author in [PubMed](#) [Google Scholar](#)

32. Tay-Rong Chang

[View author publications](#)

You can also search for this author in [PubMed](#) [Google Scholar](#)

33. Liang Fu

[View author publications](#)

You can also search for this author in [PubMed](#) [Google Scholar](#)

34. Qiong Ma

[View author publications](#)

You can also search for this author in [PubMed](#) [Google Scholar](#)

35. Ni Ni

[View author publications](#)

You can also search for this author in [PubMed](#) [Google Scholar](#)

36. Su-Yang Xu

[View author publications](#)

You can also search for this author in [PubMed](#) [Google Scholar](#)

Contributions

S.-Y.X. conceived the experiment and supervised the project. A.G. fabricated the devices with help from Y.-F.L., J.-X.Q., D.B., C.F., K.S.B. and Q.M. A.G. performed the transport measurements and analysed data with help from Y.-F.L., C.T., J.-X.Q., S.-C.H., D.B., T.D. and Q.M. C.H. and N.N. grew the bulk MnBi₂Te₄ single crystals. Z.Z., N.W., Z.H., W.G., J.-X.Q., C.T. and A.G. performed optical magnetic circular dichroism measurements. X.-Y.Z., Y.-X.W. and B.B.Z. performed nitrogen-vacancy centre magnetometry experiments. B.G., R.C., H.S., A. Agarwal, C.T., S.-Y.X., H.-Z.L, H.-J.T., B.S., A.B., H.L., L.F. and T.-R.C. made theoretical studies including first-principles calculations and tight-binding modelling. A. Akey, J.G. and D.C.B. performed transmission electron microscopy measurements. J.-X.Q. performed atomic force microscopy measurements. K.W. and T.T. grew the bulk hBN single crystals. S.-Y.X., A.G. and Q.M. wrote the manuscript with input from all authors. S.-Y.X. was responsible for the overall direction, planning and integration among different research units.

Corresponding authors

Correspondence to [Ni Ni](#) or [Su-Yang Xu](#).

Ethics declarations

Competing interests

The authors declare no competing interests.

Additional information

Peer review information *Nature* thanks the anonymous reviewers for their contribution to the peer review of this work.

Publisher's note Springer Nature remains neutral with regard to jurisdictional claims in published maps and institutional affiliations.

Extended data figures and tables

Extended Data Fig. 1 Spatial engineering of Berry curvature.

a, Topological axion domain wall constructed by the axion field $\mathbf{E} \cdot \mathbf{B}$. **b**, Spatially modulated Berry curvature moiré superlattice enabled by a MnBi₂Te₄-twisted hBN heterostructure⁵⁹.

Extended Data Fig. 2 Topological Chern insulator state in MnBi₂Te₄.

a, Microscope image of the 6SL MnBi₂Te₄ device presented in the main text. The circuit for our transport measurements is noted. **b**, **c**, Longitudinal R_{xx} (**c**) and transverse (Hall) resistance R_{yx} (**b**) as a function of V_{BG} and B . **d**, R_{xx} and R_{yx} versus V_{BG} at -9 T.

Extended Data Fig. 3 Electric field dependence of the layer Hall effect in 6SL MnBi₂Te₄.

a, The AHE conductivity $(\{\sigma\}_{xy})^{\rm AHE}$ as a function of electric field. The charge density n is set in the hole-doped regime ($n = -1.4 \times 10^{12} \text{ cm}^{-2}$). **b**, Same as **a** but n is set in the electron-doped regime ($n = +1.5 \times 10^{12} \text{ cm}^{-2}$). **c**, **d**, First-principles calculated AHE conductivity $(\{\sigma\}_{xy})^{\rm AHE}$ as a function of electric field. **c**, Fermi level is set in the valence band (-10 meV). **d**, Fermi level is set in the conduction band (+30 meV).

Extended Data Fig. 4 Temperature-dependent measurements of 6SL MnBi₂Te₄.

a, Temperature-dependent R_{xx} data showing the Néel temperature T_N . **b**, R_{yx} versus B measurements at different temperatures. Data at different temperatures are offset by 4 kΩ for visibility at electric field 0.6 V nm⁻¹. **c**, AHE resistance as a function of temperature.

Extended Data Fig. 5 Schematic electronic structure and Berry curvature of even-layered MnBi₂Te₄.

a, b, Same antiferromagnetic state under opposite electric fields. **c, d**, Opposite antiferromagnetic states under the same electric field.

Extended Data Fig. 6 First-principles calculated band structures.

a–e, Calculated band structures of 6SL antiferromagnetic MnBi₂Te₄ for different theoretical electric fields E^{THY} .

Extended Data Fig. 7 Optical contrast of the MnBi₂Te₄ flakes.

a, Lower panel, optical image of few-layer flakes of MnBi₂Te₄ exfoliated on SiO₂ substrate. Upper panel, lattice of one SL MnBi₂Te₄. **b**, Optical contrast $C = (I_{\text{flake}} - I_{\text{substrate}})/(I_{\text{flake}} + I_{\text{substrate}})$ as a function of number of layers, which was independently determined by atomic force microscope. This process was repeated on many samples (each symbol in the figure represents an independent sample) to ensure a reproducible and reliable correspondence between C and layer number (see [Methods](#) and Supplementary Information section [V.1](#) for details).

Extended Data Fig. 8 Experimental data and microscopic picture for odd-layered MnBi₂Te₄.

a, b, The AHE for 5SL MnBi₂Te₄. In contrast to 6SL, the AHE in 5SL does not change sign as one tunes the charge density from the hole-doped regime to the electron-doped regime. Data at different n are offset by 200 μ S for visibility. **c–f**, In an odd-layered antiferromagnetic system, the top and bottom Dirac fermions experience the same magnetizations and hence open up gaps in the same fashion. As such, conduction and valence bands have the opposite Berry curvature. Therefore, the AHE remains the same sign in the hole-doped and electron-doped regimes. This conclusion is independent of E .

[Extended Data Fig. 9 Unconventional Hall effects in a wide range of quantum materials.](#)

a, The AHE in ferromagnets induced by the total Berry curvature. **b**, The valley Hall effect in gapped graphene and transition metal dichalcogenides induced by the valley-locked Berry curvature. **c**, The spin Hall effect in heavy metals induced by spin-locked Berry curvature. **d**, The layer Hall effect in the AFM axion state in even-layered MnBi₂Te₄ induced by layer-locked Berry curvature.

Supplementary information

[Supplementary Information](#)

This file contains Supplementary Information, including Supplementary Figures 1-29, Supplementary Tables 1-2, and Supplementary References.

Source data

[Source Data Fig. 1](#)

[Source Data Fig. 2](#)

[Source Data Fig. 3](#)

Source Data Fig. 4

Rights and permissions

[Reprints and Permissions](#)

About this article



Check for
updates

Cite this article

Gao, A., Liu, YF., Hu, C. *et al.* Layer Hall effect in a 2D topological axion antiferromagnet. *Nature* **595**, 521–525 (2021).

<https://doi.org/10.1038/s41586-021-03679-w>

[Download citation](#)

- Received: 21 December 2020
- Accepted: 27 May 2021
- Published: 21 July 2021
- Issue Date: 22 July 2021
- DOI: <https://doi.org/10.1038/s41586-021-03679-w>

Comments

By submitting a comment you agree to abide by our [Terms](#) and [Community Guidelines](#). If you find something abusive or that does not comply with our terms or guidelines please flag it as inappropriate.

[Access through your institution](#)

[Change institution](#)

[Buy or subscribe](#)

Advertisement

This article was downloaded by **calibre** from <https://www.nature.com/articles/s41586-021-03679-w>

| [Section menu](#) | [Main menu](#) |

- Article
- [Published: 21 July 2021](#)

Pauli-limit violation and re-entrant superconductivity in moiré graphene

- [Yuan Cao](#) ORCID: [orcid.org/0000-0002-9000-4501^{1 na1}](https://orcid.org/0000-0002-9000-4501),
- [Jeong Min Park](#) ORCID: [orcid.org/0000-0001-8905-3640^{1 na1}](https://orcid.org/0000-0001-8905-3640),
- [Kenji Watanabe](#) ORCID: [orcid.org/0000-0003-3701-8119²](https://orcid.org/0000-0003-3701-8119),
- [Takashi Taniguchi](#) ORCID: [orcid.org/0000-0002-1467-3105³](https://orcid.org/0000-0002-1467-3105) &
- [Pablo Jarillo-Herrero](#) ORCID: [orcid.org/0000-0001-8217-8213¹](https://orcid.org/0000-0001-8217-8213)

Nature volume **595**, pages 526–531 (2021) [Cite this article](#)

- 3720 Accesses
- 220 Altmetric
- [Metrics details](#)

Subjects

- [Phase transitions and critical phenomena](#)
- [Superconducting properties and materials](#)
- [Two-dimensional materials](#)

Abstract

Moiré quantum matter has emerged as a materials platform in which correlated and topological phases can be explored with unprecedented

control. Among them, magic-angle systems constructed from two or three layers of graphene have shown robust superconducting phases with unconventional characteristics^{1,2,3,4,5}. However, direct evidence of unconventional pairing remains to be experimentally demonstrated. Here we show that magic-angle twisted trilayer graphene exhibits superconductivity up to in-plane magnetic fields in excess of 10 T, which represents a large (2–3 times) violation of the Pauli limit for conventional spin-singlet superconductors^{6,7}. This is an unexpected observation for a system that is not predicted to have strong spin–orbit coupling. The Pauli-limit violation is observed over the entire superconducting phase, which indicates that it is not related to a possible pseudogap phase with large superconducting amplitude pairing. Notably, we observe re-entrant superconductivity at large magnetic fields, which is present over a narrower range of carrier densities and displacement fields. These findings suggest that the superconductivity in magic-angle twisted trilayer graphene is likely to be driven by a mechanism that results in non-spin-singlet Cooper pairs, and that the external magnetic field can cause transitions between phases with potentially different order parameters. Our results demonstrate the richness of moiré superconductivity and could lead to the design of next-generation exotic quantum matter.

Access options

Subscribe to Journal

Get full journal access for 1 year

\$199.00

only \$3.90 per issue

[Subscribe](#)

All prices are NET prices.

VAT will be added later in the checkout.

Tax calculation will be finalised during checkout.

Rent or Buy article

Get time limited or full article access on ReadCube.

from \$8.99

[Rent or Buy](#)

All prices are NET prices.

Additional access options:

- [Log in](#)
- [Access through your institution](#)
- [Learn about institutional subscriptions](#)

Fig. 1: Superconductivity in MATTG at high in-plane magnetic fields.

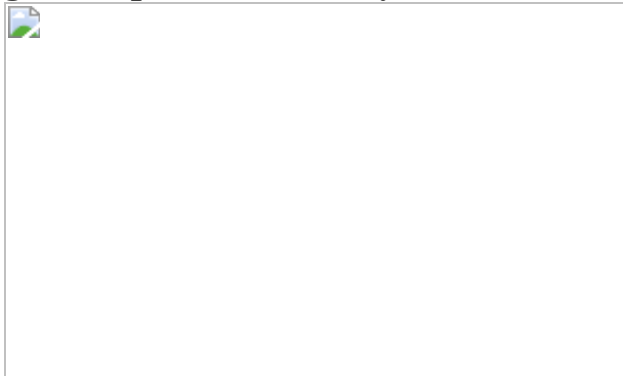


Fig. 2: Large Pauli-limit violation in MATTG.

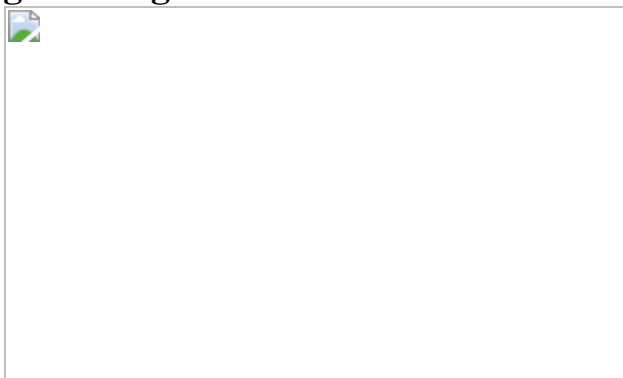


Fig. 3: Re-entrant superconductivity.

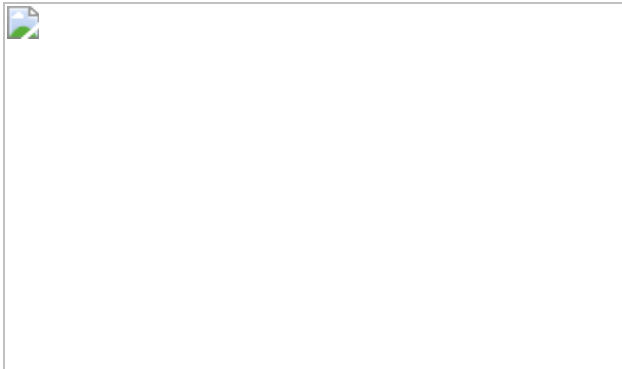
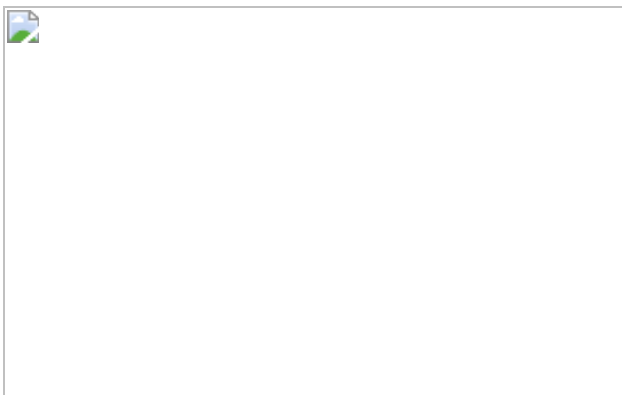


Fig. 4: Field-induced transition between superconducting phases in MATTG.



References

1. 1.

Cao, Y. et al. Unconventional superconductivity in magic-angle graphene superlattices. *Nature* **556**, 43–50 (2018).

[ADS](#) [CAS](#) [Google Scholar](#)

2. 2.

Yankowitz, M. et al. Tuning superconductivity in twisted bilayer graphene. *Science* **363**, 1059–1064 (2019).

[ADS](#) [CAS](#) [Google Scholar](#)

3. 3.

Lu, X. et al. Superconductors, orbital magnets and correlated states in magic-angle bilayer graphene. *Nature* **574**, 653–657 (2019).

[ADS](#) [CAS](#) [Google Scholar](#)

4. 4.

Park, J. M., Cao, Y., Watanabe, K., Taniguchi, T. & Jarillo-Herrero, P. Tunable strongly coupled superconductivity in magic-angle twisted trilayer graphene. *Nature* **590**, 249–255 (2021).

[ADS](#) [CAS](#) [Google Scholar](#)

5. 5.

Hao, Z. et al. Electric field-tunable superconductivity in alternating-twist magic-angle trilayer graphene. *Science* **371**, 1133–1138 (2021).

[ADS](#) [CAS](#) [Google Scholar](#)

6. 6.

Chandrasekhar, B. S. A note on the maximum critical field of high-field superconductors. *Appl. Phys. Lett.* **1**, 7–8 (1962).

[ADS](#) [CAS](#) [Google Scholar](#)

7. 7.

Clogston, A. M. Upper limit for the critical field in hard superconductors. *Phys. Rev. Lett.* **9**, 266–267 (1962).

[ADS](#) [Google Scholar](#)

8. 8.

Cao, Y. et al. Correlated insulator behaviour at half-filling in magic-angle graphene superlattices. *Nature* **556**, 80–84 (2018).

[ADS](#) [CAS](#) [Google Scholar](#)

9. 9.

Sharpe, A. L. et al. Emergent ferromagnetism near three-quarters filling in twisted bilayer graphene. *Science* **365**, 605–608 (2019).

[ADS](#) [CAS](#) [Google Scholar](#)

10. 10.

Serlin, M. et al. Intrinsic quantized anomalous Hall effect in a moiré heterostructure. *Science* **367**, 900–903 (2020).

[ADS](#) [CAS](#) [Google Scholar](#)

11. 11.

Chen, G. et al. Evidence of a gate-tunable Mott insulator in a trilayer graphene moiré superlattice. *Nat. Phys.* **15**, 237 (2019).

[CAS](#) [Google Scholar](#)

12. 12.

Regan, E. C. et al. Mott and generalized Wigner crystal states in WSe₂/WS₂ moiré superlattices. *Nature* **579**, 359–363 (2020).

[ADS](#) [CAS](#) [Google Scholar](#)

13. 13.

Tang, Y. et al. Simulation of Hubbard model physics in WSe₂/WS₂ moiré superlattices. *Nature* **579**, 353–358 (2020).

[ADS](#) [CAS](#) [Google Scholar](#)

14. 14.

Wang, L. et al. Correlated electronic phases in twisted bilayer transition metal dichalcogenides. *Nat. Mater.* **19**, 861–866 (2020).

[CAS](#) [Google Scholar](#)

15. 15.

Lee, P. A., Nagaosa, N. & Wen, X.-G. Doping a Mott insulator: physics of high-temperature superconductivity. *Rev. Mod. Phys.* **78**, 17–85 (2006).

[ADS](#) [CAS](#) [Google Scholar](#)

16. 16.

Strand, J. D. et al. The transition between real and complex superconducting order parameter phases in UPt₃. *Science* **328**, 1368–1369 (2010).

[ADS](#) [CAS](#) [Google Scholar](#)

17. 17.

Ran, S. et al. Nearly ferromagnetic spin-triplet superconductivity. *Science* **365**, 684–687 (2019).

[ADS](#) [CAS](#) [Google Scholar](#)

18. 18.

Leggett, A. J. A theoretical description of the new phases of liquid ³He. *Rev. Mod. Phys.* **47**, 331–414 (1975).

[ADS](#) [CAS](#) [Google Scholar](#)

19. 19.

Kitaev, A. Y. Unpaired Majorana fermions in quantum wires. *Phys. Uspekhi* **44**, 131–136 (2001).

[ADS](#) [Google Scholar](#)

20. 20.

Khalaf, E., Ledwith, P. & Vishwanath, A. Symmetry constraints on superconductivity in twisted bilayer graphene: Fractional vortices, $4e$ condensates or non-unitary pairing. Preprint at <https://arxiv.org/abs/2012.05915> (2020).

21. 21.

Christos, M., Sachdev, S. & Scheurer, M. S. Superconductivity, correlated insulators, and Wess–Zumino–Witten terms in twisted bilayer graphene. *Proc. Natl Acad. Sci. USA* **117**, 29543–29554 (2020).

[ADS](#) [MathSciNet](#) [CAS](#) [PubMed](#) [PubMed Central](#) [Google Scholar](#)

22. 22.

Cea, T. & Guinea, F. Coulomb interaction, phonons, and superconductivity in twisted bilayer graphene. Preprint at <https://arxiv.org/abs/2103.01815> (2021).

23. 23.

Khalaf, E., Kruchkov, A. J., Tarnopolsky, G. & Vishwanath, A. Magic angle hierarchy in twisted graphene multilayers. *Phys. Rev. B* **100**, 085109 (2019).

[ADS](#) [CAS](#) [Google Scholar](#)

24. 24.

Carr, S. et al. Ultraheavy and ultrarelativistic Dirac quasiparticles in sandwiched graphenes. *Nano Lett.* **20**, 3030–3038 (2020).

[ADS](#) [CAS](#) [Google Scholar](#)

25. 25.

Lei, C., Linhart, L., Qin, W., Libisch, F. & MacDonald, A. H. Mirror symmetry breaking and stacking-shift dependence in twisted trilayer graphene. Preprint at <https://arxiv.org/abs/2010.05787> (2020).

26. 26.

Călugăru, D. et al. Twisted symmetric trilayer graphene: single-particle and many-body Hamiltonians and hidden nonlocal symmetries of trilayer moiré systems with and without displacement field. *Phys. Rev. B* **103**, 195411 (2021).

[ADS](#) [Google Scholar](#)

27. 27.

Cao, Y. et al. Nematicity and competing orders in superconducting magic-angle graphene. *Science* **372**, 264–271 (2021).

[ADS](#) [CAS](#) [Google Scholar](#)

28. 28.

Fulde, P. & Ferrell, R. A. Superconductivity in a strong spin-exchange field. *Phys. Rev.* **135**, A550–A563 (1964).

[ADS](#) [Google Scholar](#)

29. 29.

Larkin, A. I. & Ovchinnikov, Y. N. Nonuniform state of superconductors. *Sov. Phys. JETP* **20**, 762–770 (1965).

[Google Scholar](#)

30. 30.

Burkhardt, H. & Rainer, D. Fulde–Ferrell–Larkin–Ovchinnikov state in layered superconductors. *Ann. Phys.* **506**, 181–194 (1994).

[Google Scholar](#)

31. 31.

Lu, J. M. et al. Evidence for two-dimensional Ising superconductivity in gated MoS₂. *Science* **350**, 1353–1357 (2015).

[ADS](#) [MathSciNet](#) [CAS](#) [MATH](#) [Google Scholar](#)

32. 32.

Saito, Y. et al. Superconductivity protected by spin–valley locking in ion-gated MoS₂. *Nat. Phys.* **12**, 144–149 (2016).

[CAS](#) [Google Scholar](#)

33. 33.

Xi, X. et al. Ising pairing in superconducting NbSe 2 atomic layers. *Nat. Phys.* **12**, 139–143 (2016).

[CAS](#) [Google Scholar](#)

34. 34.

Sichau, J. et al. Resonance microwave measurements of an intrinsic spin–orbit coupling gap in graphene: a possible indication of a topological state. *Phys. Rev. Lett.* **122**, 046403 (2019).

[ADS](#) [CAS](#) [Google Scholar](#)

35. 35.

Banszerus, L. et al. Observation of the spin–orbit gap in bilayer graphene by one-dimensional ballistic transport. *Phys. Rev. Lett.* **124**, 177701 (2020).

[ADS](#) [CAS](#) [Google Scholar](#)

36. 36.

Avsar, A. et al. Colloquium: Spintronics in graphene and other two-dimensional materials. *Rev. Mod. Phys.* **92**, 021003 (2020).

[ADS](#) [CAS](#) [Google Scholar](#)

37. 37.

Bauer, E. & Sigrist, M. (eds) *Non-Centrosymmetric Superconductors: Introduction and Overview* (Springer, 2012).

38. 38.

Uji, S. et al. Magnetic-field-induced superconductivity in a two-dimensional organic conductor. *Nature* **410**, 908–910 (2001).

[ADS](#) [CAS](#) [Google Scholar](#)

39. 39.

Balicas, L. et al. Superconductivity in an organic insulator at very high magnetic fields. *Phys. Rev. Lett.* **87**, 067002 (2001).

[ADS](#) [CAS](#) [Google Scholar](#)

40. 40.

Schemm, E. R., Gannon, W. J., Wishne, C. M., Halperin, W. P. & Kapitulnik, A. Observation of broken time-reversal symmetry in the heavy-fermion superconductor UPt₃. *Science* **345**, 190–193 (2014).

[ADS](#) [CAS](#) [Google Scholar](#)

41. 41.

Aoki, D., Ishida, K. & Flouquet, J. Review of U-based ferromagnetic superconductors: comparison between UGe_2 , URhGe , and UCoGe . *J. Phys. Soc. Jpn* **88**, 022001 (2019).

[ADS](#) [Google Scholar](#)

42. 42.

Zondiner, U. et al. Cascade of phase transitions and Dirac revivals in magic-angle graphene. *Nature* **582**, 203–208 (2020).

[ADS](#) [CAS](#) [Google Scholar](#)

43. 43.

Wong, D. et al. Cascade of electronic transitions in magic-angle twisted bilayer graphene. *Nature* **582**, 198–202 (2020).

[ADS](#) [CAS](#) [Google Scholar](#)

44. 44.

Park, J. M., Cao, Y., Watanabe, K., Taniguchi, T. & Jarillo-Herrero, P. Flavour Hund's coupling, Chern gaps and charge diffusivity in moiré graphene. *Nature* **592**, 43–48 (2021).

[CAS](#) [Google Scholar](#)

45. 45.

Bultinck, N. et al. Ground state and hidden symmetry of magic-angle graphene at even integer filling. *Phys. Rev. X* **10**, 031034 (2020).

[CAS](#) [Google Scholar](#)

46. 46.

Park, J. M. Replication data for: Pauli limit violation and reentrant superconductivity in moiré graphene. *Harvard Dataverse*

<https://doi.org/10.7910/DVN/CYON7L> (2021).

47. 47.

Xu, C. & Balents, L. Topological superconductivity in twisted multilayer graphene. *Phys. Rev. Lett.* **121**, 087001 (2018).

[ADS](#) [CAS](#) [Google Scholar](#)

48. 48.

Uykur, E., Li, W., Kuntscher, C. A. & Dressel, M. Optical signatures of energy gap in correlated Dirac fermions. *npjQuantum Mater.* **4**, 19 (2019).

[ADS](#) [Google Scholar](#)

49. 49.

Scheurer, M. S. & Samajdar, R. Pairing in graphene-based moiré superlattices. *Phys. Rev. Res.* **2**, 033062 (2020).

[CAS](#) [Google Scholar](#)

50. 50.

Frigeri, P. A., Agterberg, D. F. & Sigrist, M. Spin susceptibility in superconductors without inversion symmetry. *New J. Phys.* **6**, 115 (2004).

[ADS](#) [Google Scholar](#)

51. 51.

Frigeri, P. A., Agterberg, D. F., Koga, A. & Sigrist, M. Superconductivity without inversion symmetry: MnSi versus CePt₃Si. *Phys. Rev. Lett.* **92**, 097001 (2004).

[ADS](#) [CAS](#) [Google Scholar](#)

52. 52.

Goh, S. K. et al. Anomalous upper critical field in CeCoIn₅/YbCoIn₅ superlattices with a Rashba-type heavy Fermion interface. *Phys. Rev. Lett.* **109**, 157006 (2012).

[ADS](#) [CAS](#) [Google Scholar](#)

53. 53.

Werthamer, N. R., Helfand, E. & Hohenberg, P. C. Temperature and purity dependence of the superconducting critical field, H_{c2}. III. Electron spin and spin-orbit effects. *Phys. Rev.* **147**, 295–302 (1966).

[ADS](#) [CAS](#) [Google Scholar](#)

54. 54.

Alicea, J. New directions in the pursuit of Majorana fermions in solid state systems. *Rep. Prog. Phys.* **75**, 076501 (2012).

[ADS](#) [Google Scholar](#)

55. 55.

Alicea, J. Majorana fermions in a tunable semiconductor device. *Phys. Rev. B* **81**, 125318 (2010).

[ADS](#) [Google Scholar](#)

56. 56.

Lyon, T. J. et al. Probing electron spin resonance in monolayer graphene. *Phys. Rev. Lett.* **119**, 066802 (2017).

[ADS](#) [CAS](#) [Google Scholar](#)

57. 57.

Nicholas, R. J., Haug, R. J., Klitzing, K. & Weimann, G. Exchange enhancement of the spin splitting in a GaAs–Ga_xAl_{1-x}As heterojunction. *Phys. Rev. B* **37**, 1294–1302 (1988).

[ADS](#) [CAS](#) [Google Scholar](#)

58. 58.

Tutuc, E., Melinte, S. & Shayegan, M. Spin polarization and *g* factor of a dilute GaAs two-dimensional electron system. *Phys. Rev. Lett.* **88**, 036805 (2002).

[ADS](#) [CAS](#) [Google Scholar](#)

59. 59.

Xu, S. et al. Odd-integer quantum hall states and giant spin susceptibility in p-type few-layer WSe₂. *Phys. Rev. Lett.* **118**, 067702 (2017).

[ADS](#) [Google Scholar](#)

60. 60.

Rodan-Legrain, D. et al. Highly tunable junctions and non-local Josephson effect in magic-angle graphene tunnelling devices. *Nat. Nanotechnol.* <https://doi.org/10.1038/s41565-021-00894-4> (2021).

61. 61.

Fatemi, V. et al. Electrically tunable low-density superconductivity in a monolayer topological insulator. *Science* **362**, 926–929 (2018).

[ADS](#) [MathSciNet](#) [CAS](#) [Google Scholar](#)

62. 62.

Saito, Y., Itahashi, Y. M., Nojima, T. & Iwasa, Y. Dynamical vortex phase diagram of two-dimensional superconductivity in gated MoS₂. *Phys. Rev. Mater.* **4**, 074003 (2020).

[CAS](#) [Google Scholar](#)

[Download references](#)

Acknowledgements

We thank L. Fu, F. Guinea, S. Kivelson, P. Lee, A. MacDonald, M. Sigrist, S. Todadri and A. Vishwanath for discussions. This work has been primarily supported by the US Department of Energy (DOE), Office of Basic Energy Sciences (BES), Division of Materials Sciences and Engineering under Award DE-SC0001819 (J.M.P.). Help with transport measurements and data analysis were supported by the National Science Foundation (DMR-1809802), and the STC Center for Integrated Quantum Materials (NSF grant no. DMR-1231319) (Y.C.). P.J.-H. acknowledges support from the Gordon and Betty Moore Foundation's EPiQS Initiative through grant GBMF9643. P.J.-H. acknowledges partial support by the Fundación Ramon Areces and the CIFAR Quantum Materials program. The development of new nanofabrication and characterization techniques enabling this work has been supported by the US DOE Office of Science, BES, under award DE-SC0019300. K.W. and T.T. acknowledge support from the Elemental Strategy Initiative conducted by the MEXT, Japan, grant number JPMXP0112101001, JSPS KAKENHI grant numbers JP20H00354 and the CREST(JPMJCR15F3), JST. This work made use of the Materials Research Science and Engineering Center Shared Experimental Facilities supported by the National Science Foundation (DMR-0819762) and of Harvard's Center for Nanoscale Systems, supported by the NSF (ECS-0335765).

Author information

Author notes

1. These authors contributed equally: Yuan Cao, Jeong Min Park

Affiliations

1. Department of Physics, Massachusetts Institute of Technology, Cambridge, MA, USA

Yuan Cao, Jeong Min Park & Pablo Jarillo-Herrero

2. Research Center for Functional Materials, National Institute for Materials Science, Tsukuba, Japan

Kenji Watanabe

3. International Center for Materials Nanoarchitectonics, National Institute for Materials Science, Tsukuba, Japan

Takashi Taniguchi

Authors

1. Yuan Cao

[View author publications](#)

You can also search for this author in [PubMed](#) [Google Scholar](#)

2. Jeong Min Park

[View author publications](#)

You can also search for this author in [PubMed](#) [Google Scholar](#)

3. Kenji Watanabe

[View author publications](#)

You can also search for this author in [PubMed](#) [Google Scholar](#)

4. Takashi Taniguchi

[View author publications](#)

You can also search for this author in [PubMed](#) [Google Scholar](#)

5. Pablo Jarillo-Herrero
[View author publications](#)

You can also search for this author in [PubMed](#) [Google Scholar](#)

Contributions

J.M.P. and Y.C. fabricated the samples and performed transport measurements. K.W. and T.T. provided hBN samples. J.M.P., Y.C. and P.J.-H. performed data analysis, discussed the results and wrote the manuscript with input from all co-authors.

Corresponding authors

Correspondence to [Yuan Cao](#) or [Jeong Min Park](#) or [Pablo Jarillo-Herrero](#).

Ethics declarations

Competing interests

The authors declare no competing interests.

Additional information

Peer review information *Nature* thanks Folkert de Vries, Yi-Ting Hsu and the other, anonymous, reviewer(s) for their contribution to the peer review of this work.

Publisher's note Springer Nature remains neutral with regard to jurisdictional claims in published maps and institutional affiliations.

Extended data figures and tables

[**Extended Data Fig. 1 Pauli-limit violation for electron doping.**](#)

a, $B_{\parallel}-T$ phase diagram at the stated density in the $+2 - \delta$ superconducting dome. The extracted Pauli-limit violation ratios using 10%, 20% and 30% of normal resistance as the threshold are 3.44, 2.98 and 2.83, respectively. **b**, $B_{\parallel}-T$ phase diagram at a density in the $+2 + \delta$ superconducting dome. The extracted Pauli-limit violation ratios using 10%, 20% and 30% of normal resistance as the threshold are 2.49, 2.37 and 2.65 respectively. The solid lines show the fit to the Ginzburg–Landau expression $\propto T^{\alpha(B_{\parallel})}$, and the colour tick marks at $T = 0$ show the corresponding Pauli limit, the same as in Fig. 2.

Extended Data Fig. 2 Pauli-limit violation in other devices.

a, $B_{\parallel}-T$ phase diagram of device B with twist angle $\theta \approx 1.44^\circ$. The extracted Pauli-limit violation ratios using 10%, 20% and 30% of the normal-state resistance as the threshold are 2.13, 2.00 and 2.00, respectively. **b**, $B_{\parallel}-T$ phase diagram of device C with twist angle $\theta \approx 1.4^\circ$. The extracted Pauli-limit violation ratios using 10%, 20% and 30% of the normal state resistance as the threshold are 2.29, 2.23 and 2.19, respectively. The solid lines show the fit to the Ginzburg–Landau expression $\propto T^{\alpha(B_{\parallel})}$, and the colour tick marks at $T = 0$ show the corresponding Pauli limit, the same as in Fig. 2.

Extended Data Fig. 3 Additional data on the high-field phases.

a, $B_{\parallel}-D$ map of resistance at a lower temperature $T = 0.3$ K (see Fig. 4a for comparison). The filament-like transition between SC-I and SC-II is much less pronounced. **b**, **c**, Bidirectional sweeps in B_{\parallel} at fixed D indicated by the white dashed line in a. The only change in measurement conditions between the two scans is a different arrangement of the BNC cables connecting to the lock-in amplifiers. Both scans are performed at 0.3 K. **d**, $B_{\parallel}-D$ map of resistance on the positive D side measured at $T = 0.4$ K (see Fig. 4a for comparison).

Extended Data Fig. 4 Extracted PVR as a function of displacement field at $\nu = -2.4$.

Values of 10%, 20% and 30% normal-state resistance were used as the threshold.

Extended Data Fig. 5 Schematic of measurement setup and images of the main MATTG device from optical microscopy and atomic force microscopy.

The microscopy image shows that the core region of the device (inside the dashed rectangle) is clean and free of bubbles. The blue lines are the outlines of the Hall bar that were subsequently etched out.

Extended Data Fig. 6 Calibration of the perpendicular component using the X axis magnetic field B_x .

Calibration curves are shown for $B_{\parallel} = 0$ T, 5 T and 10 T. The dashed lines indicate the calibrated zero perpendicular field condition at each B_{\parallel} . The grey bar spans ± 5 mT from the centre of the curves, showing that the minimum can be determined well within the bars. See [Methods](#) for more details.

Extended Data Fig. 7 Superconducting phases in a perpendicular magnetic field.

All measurements are taken at $v = -2.4$, $D/\varepsilon_0 = -0.31$ V nm⁻¹. **a**, The suppression of SC-I and SC-II phases by a perpendicular field B_{\perp} at $T = 0.4$ K. The white dashed line denotes zero B_{\perp} . This rules out the possibility that the SC-II phase is due to imperfect sample alignment with the axis of B_{\parallel} . **b–e**, Map of dV_{xx}/dI versus I and B_{\perp} at four different in-plane fields, measured at $T = 0.25$ K.

Extended Data Fig. 8 Depairing energy for a spin-singlet inter-valley pairing state, calculated for a simple toy model.

The orange curve shows the total depairing energy averaged over the Fermi surface $\langle \bar{\varepsilon} \rangle_{\text{depair}}$, versus the valley depairing energy amplitude ε_V . Both quantities are normalized by the Zeeman depairing energy ε_Z . For comparison, the dashed lines show the cases when the Zeeman effect is omitted (blue dashed line) and when the valley depairing effect is omitted (purple dashed line). Regardless of $\varepsilon_V/\varepsilon_Z$, the total depairing effect is always stronger than the valley-only or the Zeeman-only case, which means that the critical magnetic field will be reduced from the Pauli limit (corresponding to the Zeeman-only case). Therefore it is unlikely that a spin-singlet inter-valley pairing state accounts for our experimental results.

Rights and permissions

[Reprints and Permissions](#)

About this article



Check for
updates

Cite this article

Cao, Y., Park, J.M., Watanabe, K. *et al.* Pauli-limit violation and re-entrant superconductivity in moiré graphene. *Nature* **595**, 526–531 (2021).
<https://doi.org/10.1038/s41586-021-03685-y>

[Download citation](#)

- Received: 04 March 2021
- Accepted: 28 May 2021
- Published: 21 July 2021

- Issue Date: 22 July 2021
- DOI: <https://doi.org/10.1038/s41586-021-03685-y>

Comments

By submitting a comment you agree to abide by our [Terms](#) and [Community Guidelines](#). If you find something abusive or that does not comply with our terms or guidelines please flag it as inappropriate.

[Access through your institution](#)

[Change institution](#)

[Buy or subscribe](#)

Associated Content

[Superconductivity in a graphene system survives a strong magnetic field](#)

- Yi-Ting Hsu

Advertisement

This article was downloaded by **calibre** from <https://www.nature.com/articles/s41586-021-03685-y>.

A natively flexible 32-bit Arm microprocessor

[Download PDF](#)

- Article
- [Published: 21 July 2021](#)

A natively flexible 32-bit Arm microprocessor

- [John Biggs¹](#),
- [James Myers¹](#),
- [Jedrzej Kufel¹](#),
- [Emre Ozer](#) [ORCID: orcid.org/0000-0001-8285-1551¹](#),
- [Simon Craske¹](#),
- [Antony Sou²](#),
- [Catherine Ramsdale²](#),
- [Ken Williamson²](#),
- [Richard Price²](#) &
- [Scott White²](#)

Nature volume **595**, pages 532–536 (2021) [Cite this article](#)

- 12k Accesses
- 275 Altmetric
- [Metrics details](#)

Subjects

- [Electrical and electronic engineering](#)
- [Electronic and spintronic devices](#)
- [Electronic devices](#)

Abstract

Nearly 50 years ago, Intel created the world's first commercially produced microprocessor—the 4004 (ref. ¹), a modest 4-bit CPU (central processing unit) with

2,300 transistors fabricated using 10 µm process technology in silicon and capable only of simple arithmetic calculations. Since this ground-breaking achievement, there has been continuous technological development with increasing sophistication to the stage where state-of-the-art silicon 64-bit microprocessors now have 30 billion transistors (for example, the AWS Graviton2 (ref. 2) microprocessor, fabricated using 7 nm process technology). The microprocessor is now so embedded within our culture that it has become a meta-invention—that is, it is a tool that allows other inventions to be realized, most recently enabling the big data analysis needed for a COVID-19 vaccine to be developed in record time. Here we report a 32-bit Arm (a reduced instruction set computing (RISC) architecture) microprocessor developed with metal-oxide thin-film transistor technology on a flexible substrate (which we call the PlasticARM). Separate from the mainstream semiconductor industry, flexible electronics operate within a domain that seamlessly integrates with everyday objects through a combination of ultrathin form factor, conformability, extreme low cost and potential for mass-scale production. PlasticARM pioneers the embedding of billions of low-cost, ultrathin microprocessors into everyday objects.

[Download PDF](#)

Main

Unlike conventional semiconductor devices, flexible electronic devices are built on substrates such as paper, plastic or metal foil, and use active thin-film semiconductor materials such as organics or metal oxides or amorphous silicon. They offer a number of advantages over crystalline silicon, including thinness, conformability and low manufacturing costs. Thin-film transistors (TFTs) can be fabricated on flexible substrates at a much lower processing cost than metal–oxide–semiconductor field-effect transistors (MOSFETs) fabricated on crystalline silicon wafers. The aim of the TFT technology is not to replace silicon. As both technologies continue to evolve, it is likely that silicon will maintain advantages in terms of performance, density and power efficiency. However, TFTs enable electronic products with novel form factors and at cost points unachievable with silicon, thereby vastly expanding the range of potential applications.

Microprocessors are at the heart of every electronic device, including smartphones, tablets, laptops, routers, servers, cars and, more recently, smart objects that make up the Internet of Things. Although conventional silicon technology has embedded at least one microprocessor into every ‘smart’ device on Earth, it faces key challenges to make everyday objects smarter, such as bottles (milk, juice, alcohol or perfume), food packages, garments, wearable patches, bandages, and so on. Cost is the most important factor preventing conventional silicon technology from being viable in these everyday objects. Although economies of scale in silicon fabrication have helped to reduce unit

costs dramatically, the unit cost of a microprocessor is still prohibitively high. In addition, silicon chips are not naturally thin, flexible and conformable, all of which are highly desirable characteristics for embedded electronics in these everyday objects.

Flexible electronics, on the other hand, does offer these desirable characteristics. Over the past two decades, flexible electronics have progressed to offer mature low-cost, thin, flexible and conformable devices, including sensors, memories, batteries, light-emitting diodes, energy harvesters, near-field communication/radio frequency identification and printed circuitry such as antennas. These are the essential electronic components to build any smart integrated electronic device. The missing piece is the flexible microprocessor. The main reason why no viable flexible microprocessor yet exists is that a relatively large number of TFTs need to be integrated on a flexible substrate in order to perform any meaningful computation. This has not previously been possible with the emerging flexible TFT technology, in which a certain level of technology maturity is required before a large-scale integration can be done.

A midway approach has been to integrate silicon-based microprocessor dies onto flexible substrates—also called hybrid integration^{3,4,5}—where the silicon wafer is thinned and dies from the wafer are integrated onto a flexible substrate. Although thin silicon die integration offers a short-term solution, the approach still relies on conventional high-cost manufacturing processes. It is, therefore, not a viable long-term solution for enabling the production of the billions of everyday smart objects expected over the next decade and beyond⁶.

Our approach is to develop the microprocessor natively using flexible electronic fabrication techniques, also termed a natively flexible processing engine⁷. The flexible electronics technology we used to build the natively flexible microprocessor described here consists of metal-oxide TFTs on polyimide substrates. Metal-oxide TFTs are low cost and can also be scaled down to the smaller geometries required for large-scale integration⁸.

Early natively flexible processor works were based on developing 8-bit CPUs (refs. 9,10,11,12) using low-temperature poly-silicon TFT technology, which has a high manufacturing cost and poor lateral scalability⁸. Recently, two-dimensional material-based transistors have been used to develop processors such as a 1-bit CPU using molybdenum disulfide (MoS_2) transistors¹³, and a 16-bit RISC-V CPU¹⁴ built from complementary carbon nanotube transistors. However, both works were demonstrated on a conventional silicon wafer rather than on a flexible substrate.

The first attempt to build a metal-oxide TFT-based processing element is an 8-bit arithmetic logic unit, which is a part of the CPU, coupled with a print-programmable ROM fabricated on polyimide^{15,16}. Very recently, Ozer et al.^{7,17,18} presented natively

flexible dedicated machine learning hardware in metal-oxide TFTs. Although the machine learning hardware¹⁸ had the most complex flexible integrated circuit (the FlexIC) built with metal-oxide TFTs at around 1,400 gates, the FlexIC was not a microprocessor. A programmable processor approach is more generic than machine learning hardware, and supports a rich set of instructions that can be used to program a wide variety of applications from control codes to data-intensive applications including machine learning algorithms.

There are three major components of the natively flexible microprocessor—(1) a 32-bit CPU, (2) a 32-bit processor containing a CPU and CPU peripherals, and (3) a system-on-a-chip (SoC) containing the processor, memories and bus interfaces—all fabricated with metal-oxide TFTs on a flexible substrate. The natively flexible 32-bit processor is derived from the Arm Cortex-M0+ processor supporting the Armv6-M architecture¹⁹ (a rich set of 80+ instructions) and existing toolchain for software development (for example, compilers, debuggers, linkers, integrated development environments and so on). The entire natively flexible SoC, called PlasticARM, is capable of running programs from its internal memory. PlasticARM contains 18,334 NAND2 equivalent gates, which makes it the most complex FlexIC (at least 12× more complex than previous integrated circuits) that has been ever built with metal-oxide TFTs on a flexible substrate.

PlasticARM system architecture

The chip architecture of PlasticARM is shown in Fig. 1a. It is a SoC comprising a 32-bit processor derived from the 32-bit Arm Cortex-M0+ processor product²⁰, memories, system interconnect fabric and interface blocks, and an external bus interface.

Fig. 1: PlasticARM architecture and features.

 **figure1**

a, The SoC architecture, showing the internal structure, the processor and system peripherals. The processor contains a 32-bit Arm Cortex-M CPU and a Nested Vector Interrupt Controller (NVIC), and is connected to its memory through the interconnect fabric (AHB-LITE). Finally, the external bus interface provides a General-Purpose Input-Output (GPIO) interface to communicate off-chip with the test framework. **b**, Features of the CPU used in PlasticARM compared to those of the Arm Cortex-M0+ CPU. Both CPUs fully support Armv6-M architecture with 32-bit address and data capabilities and a total of 86 instructions from the entire 16-bit Thumb and a subset of 32-bit Thumb instruction set architecture. The CPU microarchitecture has a two-stage pipeline. The registers are in the CPU of the Cortex-M0+, but in the PlasticARM the registers are moved to the latch-based RAM in the SoC to save the CPU area of the Cortex-M. Finally, both CPUs are binary compatible with each other and to other CPUs in the same architecture family. **c**, The die layout of PlasticARM, denoting the

key blocks in white boxes such as the Cortex-M processor, ROM and RAM. **d**, The die micrograph of PlasticARM, showing the dimensions of the die and core areas.

[Full size image](#)

This processor fully supports the Armv6-M instruction set architecture, which means that the code generated for a Cortex-M0+ processor will also run on the processor derived from it. The processor comprises the CPU and a Nested Vector Interrupt Controller (NVIC) tightly coupled to the CPU, handling interrupts from external devices.

The rest of the SoC consists of memories (ROM/RAM), the AHB-LITE interconnect fabric (a subset of the advanced high-performance bus (AHB) specification) and interface logic to connect the memories to the processor, and finally an external bus interface that is used to control two General-Purpose Input-Output (GPIO) pins to communicate off-chip. The ROM contains 456 bytes of system code and test programs, and has been implemented as combinational logic. The 128 bytes of RAM has been implemented as a latch-based register file and is mainly used as a stack.

Figure [1b](#) shows the comparison of the Cortex-M used in PlasticARM and the Arm Cortex-M0+. Although the Cortex-M processor in PlasticARM is not a standard product, it implements the Armv6-M architecture supporting the 16-bit Thumb and a subset of the 32-bit Thumb instruction set architectures, and so it is binary compatible with all Cortex-M class processors, including Cortex-M0+, in the same architecture family. The key difference between the Cortex-M in PlasticARM and Cortex-M0+ is that we allocated a specific portion of the RAM in the SoC to the CPU registers (about 64 bytes), and moved them from the CPU to the RAM in Cortex-M in PlasticARM, whereas in Cortex-M0+ the registers remain within its CPU. A large reduction (about 3×) in CPU area is achieved by eliminating the registers from the CPU and using the existing RAM for register space, at the cost of slower register access.

Results

PlasticARM is implemented with PragmatIC's 0.8- μm process using industry-standard chip implementation tools. We have developed a process design kit, a standard cell library and device/circuit simulations for this technology in order to implement the PlasticARM FlexIC. Figure [1c](#) shows the FlexIC layout, where the Cortex-M processor, RAM and ROM are demarcated. The details of the implementation methodology can be found in the Methods.

PlasticARM is fabricated using a commercial ‘fab-in-a-box’ manufacturing line, FlexLogIC²¹, and its die micrograph is shown in Fig. [1d](#). The process uses an n-type

metal-oxide TFT technology based on indium–gallium–zinc oxide (IGZO) and generates the FlexIC design on a 200-mm-diameter polyimide wafer. The IGZO TFT circuits are made using conventional semiconductor processing equipment adapted and configured to produce devices on a flexible (polyimide) substrate with a thickness of less than 30 μm . They have a channel length of 0.8 μm , and a minimum supply voltage of 3 V.

Design in n-type metal-oxide thin-film technology is facing many of the same challenges that affected the complexity and yield of the first silicon (negative channel metal–oxide–semiconductor, NMOS) technology during the 1970s and early 1980s, in particular poor noise margin, high power consumption, and large process variation (for example, V_t). The details of the fabrication methodology can be found in the Methods.

We report a fully functional PlasticARM FlexIC. This has been demonstrated by running the three test programs pre-programmed (hardwired) into the ROM before fabrication. Although the test programs are executed from the ROM, this is not a requirement for the system; it simply facilitates the test setup of PlasticARM. The current ROM implementation does not allow changing or updating of the program code after fabrication, although this would be possible in future implementations (for example, via programmable ROM). The test programs are written in such a way that the instructions exercise all functional units inside the CPU such as arithmetic logic units, load/store units and branch units, and are compiled with the *armcc* compiler using the CPU flag set to ‘cortex-m0plus’. The flow chart and detailed description of the test programs are shown in Fig. 2. When each test program completes its execution, the result of the test program is transmitted over the output GPIO pin off-chip to the test framework.

Fig. 2: Test programs.



a, A simple accumulation program reads values from the ROM and sums them up. If the sum matches the expected value, a confirmation signal is sent to the GPIO output pin that will be read by the tester. The test uses load, add, compare and branch instructions. **b**, A set of 32-bit integer values are written into the RAM on the fly and reads them back while checking the read values against expected values. If all written values are read correctly, a confirmation signal is sent to the GPIO output pin. The test uses load, store, add, shift, logic, compare and branch instructions. **c**, A value is read continuously through the GPIO input pin from the tester. The value is masked with a constant value. If the masked result is 1, then a counter is incremented. If it is 0, then the counter is reset. If the counter value is equal to an expected value, then a confirmation signal is sent to the GPIO output pin. The test uses load, store, add, logic, compare and branch instructions. Terms in italics represent variables in the test programs; terms in bold and uppercase are pins and memories.

[Full size image](#)

IGZO TFTs are known to be bent to a radius of curvature of 3 mm without damage²², which PragmatIC has also verified through repeated bending of its own circuitry to this radius of curvature. However, all PlasticARM measurements are performed while the flexible wafer remains on its glass carrier, using standard wafer test equipment located at Arm Ltd, at room temperature. The measured results of PlasticARM are validated against its simulated results. The details of the measurement setup, results and its validation against simulation can be found in the Methods.

The implementation and measured circuit characteristics of PlasticARM are shown in Table 1, and are compared to the best previous natively flexible integrated circuits built with metal-oxide TFTs^{7,16,18}. PlasticARM has an area of 59.2 mm² (without pads), and contains 56,340 devices (n-type TFTs plus resistors) or 18,334 NAND2-equivalent gates, which is at least 12 times higher than the best previous integrated circuit (that is, binary neural network (BNN) FlexIC). The microprocessor can be clocked at up to 29 kHz and consumes only 21 mW, which is predominantly (>99%) static power, with the processor accounting for 45%, memories 33% and peripherals 22%. The SoC uses 28 pins, which include clock, reset, GPIO, power and other debug pins. There are no dedicated electrostatic discharge mitigation techniques used in this design. Instead, all inputs contain 140-pF capacitors, whereas all outputs are driven by output drivers with active pull-up transistors.

Table 1 Advantages of flexible integrated circuits built with metal-oxide TFTs
[Full size table](#)

A key challenge of any resistive load technology is the power consumption. We anticipate that the lower-power cell libraries we are developing will support increased complexity, up to about 100,000 gates. Moving to more than 1,000,000 gates will probably require complementary metal–oxide–semiconductor (CMOS) technology.

Conclusions

We have reported a natively flexible 32-bit microprocessor, PlasticARM, fabricated with 0.8-μm metal-oxide TFT technology. We have demonstrated the functionality of a SoC that has a 32-bit Arm processor fabricated on a flexible substrate. It can piggyback on existing software/tool support (such as compilers) because of its compatibility with the Arm Cortex-M class processors in the Armv6-M architecture, so there is no need to develop a software toolchain. Finally, to our knowledge, so far it is the most complex flexible integrated circuit built with metal-oxide TFTs, comprising over 18,000 gates, which is at least 12× higher than the best previous integrated circuit.

We envisage that PlasticARM will pioneer the development of low-cost, fully flexible smart integrated systems to enable an ‘internet of everything’ consisting of the integration of more than a trillion inanimate objects over the next decade into the digital world. Having an ultrathin, conformable, low-cost, natively flexible microprocessor for everyday objects will unravel innovations leading to a variety of research and business opportunities.

Methods

Implementation

To take full advantage of the highly automated, fast turn-around implementation and verification offered by modern silicon integrated circuit design flows, we developed a small standard cell library. A standard cell library is a collection of small pre-verified building blocks from which much larger and more complex designs can be quickly and easily built using sophisticated electronic design automation tools such as synthesis, place and route.

Before the implementation of the standard cell library could begin, some preliminary investigations were done to determine the most suitable standard cell architecture for the library given the constraints of the target technology. The cell architecture is the set of features that are common to every cell in the library, such as cell height, power strap sizing, routeing grid and so on, which allow the cells to be snapped together in a standard way to form larger structures. These common features are largely governed by the design rules of the manufacturing process but are also influenced by the performance and area requirements of the final design.

Once the cell architecture was established, the next step was to determine the content of the cell library not only in terms of variety of logic functions but also the number of drive strength variants of each logic function. Because the effort involved to design, implement and characterize each standard cell is substantial, it was decided to run some trials with a small prototype library and then to expand the library as required. To evaluate the performance of this small prototype standard cell library some simple representative circuits (such as ring oscillators, counters and shift arrays) were implemented, manufactured and tested.

We migrated from 1.0- μm design rules to the new FlexIC 0.8- μm design rules to reduce area and, hence, increase yield. As this meant redrawing each cell in the library with smaller transistors, we took the opportunity also to change the standard cell architecture to include MT1 (metal-tracking 1) pins to make it easier for the router to hook up the cells. Improvements to the resistive material (higher sheet resistance, R_s) also enabled a 3 \times reduction in the size of the resistors.

This dramatic reduction in both transistor and resistor size reduced the area of most cells by about 50% (see Extended Data Fig. 1), which in turn improved the manufacturing yield by bringing down the overall size of the design. However, as there were still manufacturing yield issues that we could further mitigate by changes to the standard cell architecture, the library was redrawn again. This time we focused on things that would improve the overall yield of the final design, such as the inclusion of redundant vias and contacts, reducing the number of vertices in the source–drain polygons (where possible) and keeping the size of stacked transistors to a minimum. In addition, we reverted to a lower sheet resistance in order to improve the process spread but we were able to maintain the area savings by using narrower resistors. To improve the overall quality of the logic synthesis a number of complex AND-OR-INVERT and OR-AND-INVERT logic gates were added to the library as well as some high-drive-strength simple logic gates, such as NAND2_X2 and NOR2_X2.

The FlexLogIC process is an NMOS process and so relies on a resistive load to pull the cell output towards the power supply to drive a logic 1. As a consequence of this, the cell output rise times are much slower than the fall times and this asymmetry can affect performance, especially for heavily loaded nets. To improve the timing on critical nets, such as the clock, we added buffers with an active transistor pull-up. Although these active pull-ups increase the area by a small amount, they do have the added benefit of reducing the static power consumption. Layouts and simulated transfer characteristics of buffers with resistive pull-up and active transistor pull-up are shown in Extended Data Fig. 2.

This simple standard cell library was then successfully used as the target technology to implement the PlasticARM SoC using a typical silicon integrated circuit design flow based on industry standard electronic design automation tools. The standard cell library contents and cell usage information are shown in Extended Data Table 1.

As we do not yet have a dedicated static random access memory FlexIC, we created a simple register file by carefully placing some modified standard cells in a tiled array that connected by abutment to form a 32×32 bit memory (this block can be seen in the chip layout in Fig. 1c).

The FlexLogIC technology (see Extended Data Table 2) has four routable metal layers of which only the lower two were used inside the standard cells. This left the top two metal layers free to be used for the interconnect between the standard cells, which could then be routed over the top of any neighbouring cells leading to a much-improved overall gate density of about 300 gates per mm^2 .

Fabrication

Process parameters and statistical variations of TFT parameters are summarized in Extended Data Table 2. FlexLogIC is a proprietary 200-mm wafer semiconductor manufacturing process that creates patterned layers of metal-oxide thin-film transistors and resistors, with four routable (gold-free) metal layers deposited onto a flexible polyimide substrate according to the FlexIC design. Repeated instances of the FlexIC design are realized by running multiple sequences of thin-film material deposition, patterning and etching. For ease of handling and to allow industry standard process tools to be used and sub-micrometre patterned features to be achieved (down to 0.8 µm), the flexible polyimide substrate is spin-coated onto glass at the outset of production. The process has been optimized to ensure that the thickness variation is substantially less than 3% over a lateral distance of 20 mm. Thin-film material deposition is achieved through a combination of physical-vapour deposition, atomic-layer deposition and solution-processing (for example, spin-coating). Substrate processing conditions have been carefully optimized to minimise film stress and substrate bow. Feature patterning is achieved using a photolithographic 5× stepper tool, which images a shot that is repeated at multiple instances across the 200-mm-diameter wafer. Each shot is focused individually, which further compensates for any thickness variation within the spun-cast film. The technology measurements were carried out using process control monitoring structures.

Simulation, test and validation

We captured the timing characteristics of the functional PlasticARM FlexIC using a test measurement setup, and compared the measured results with the results of its register-transfer level (RTL) simulation in order to validate the functionality.

The RTL simulation is shown in Extended Data Fig. 3. It starts by resetting the PlasticARM to a known state by setting a RESET input to ‘0’. Then, RESET is set to ‘1’, the processor is released from its reset state and starts executing the code from ROM. At first, the GPIO[0] output pin is toggled once before the three tests described in Fig. 2 are executed. In the first test, data are read and added to an accumulator from the ROM, and the sum is compared against an expected value (see Fig. 2a). If values match, a short burst of two pulses is sent to GPIO[0] as shown in Extended Data Fig. 3a. If values are different, the period and duty cycle of pulses on GPIO[0] is increased in Extended Data Fig. 3b. In the second test (Fig. 2b), data are written to RAM, read back and compared. If data has not been corrupted while writing or reading from the RAM, a short burst of three pulses is sent to GPIO[0] as shown in Extended Data Fig. 3a. If data was corrupted, the period and duty cycle of pulses on GPIO[0] is increased as before. In the final test (Fig. 2c), the processor enters an infinite loop and measures the time a ‘1’ is applied on the GPIO[1] input pin. If GPIO[1] is held at ‘1’ without any glitches for long enough, GPIO[0] changes from ‘0’ to ‘1’. PlasticARM was implemented with a clock frequency of 20 kHz. Since it does not use any timers, a

value was chosen in software to represent the GPIO[1] signal being held at ‘1’ for approximately 1 s when operating at 20 kHz. In our simulations in Extended Data Fig. 3a, that value corresponds to 20,459 clock cycles, which at 20 kHz yields 1.02295 s.

After fabrication, PlasticARM was tested on a wafer probe station while still attached to a glass carrier. The input signals including a clock signal were generated externally with a ZC702 FPGA Evaluation Board from Xilinx. Both input and output signals were captured using a Saleae Logic Pro 16 logic analyser. Measurements were carried out at 3 V and 4.5 V, with various clock frequencies. An experiment with power supply set to 3 V and clock frequency of 20 kHz is shown in Extended Data Fig. 4. The ZC702 I/O voltage caps the inputs and outputs to 2.5 V. The measured data waveform is shown in Extended Data Fig. 4a, and matches the waveform in the RTL simulation of all three tests in Extended Data Fig. 3a. PlasticARM is fully functional up to 29 kHz at 3 V and 40 kHz at 4.5 V.

Data availability

The data that generated the waveforms in the test and validation is available from the corresponding author upon request.

Code availability

The code of the three test programs to validate PlasticARM is available from the corresponding author upon request.

References

1. 1.

The Story of the Intel 4004 (Intel, 2021);
<https://www.intel.com/content/www/us/en/history/museum-story-of-intel-4004.html>

2. 2.

AWS Graviton2-Powered EC2 Instances Now Available (HPC Wire, 2020);
<https://www.hpcwire.com/2020/06/12/aws-graviton2-powered-ec2-instances/>

3. 3.

Flex-ICs: Silicon-on-Polymer Products (American Semiconductor, 2020);
<https://www.americansemi.com/flex-ics.html>

4. 4.

Gupta, S., Navaraj, W.T., Lorenzelli, L. & Dahiya, R. Ultra-thin chips for high-performance flexible electronics. *npjFlexible Electron.* **2**, 8 (2018).

[Article](#) [Google Scholar](#)

5. 5.

Harendt, C. et al. Hybrid Systems in Foil (HySiF) exploiting ultra-thin flexible chips. In *44th European Solid-State Device Research Conference (ESSDERC)* 210–213 (2014).

6. 6.

Growing Opportunities in the Internet of Things (McKinsey, 2019);
<https://www.mckinsey.com/industries/private-equity-and-principal-investors/our-insights/growing-opportunities-in-the-internet-of-things>

7. 7.

Ozer, E. et al. A hardwired machine learning processing engine fabricated with submicron metal-oxide thin-film transistors on a flexible substrate. *Nat. Electron.* **3**, 419–425 (2020).

[Article](#) [Google Scholar](#)

8. 8.

Myny, K. The development of flexible integrated circuits based on thin-film transistors. *Nat. Electron.* **1**, 30–39 (2018).

[CAS](#) [Article](#) [Google Scholar](#)

9. 9.

Takayama, T. et al. A CPU on a plastic film substrate. *Symposium on VLSI Technology* 230–231 (IEEE, 2004).

10. 10.

Dembo, H. et al. RFCPUs on glass and plastic substrates fabricated by TFT transfer technology. In *IEEE International Electron Devices Meeting (IEDM)* 125–127 (IEEE, 2005).

11. 11.

Karaki, N. et al. A flexible 8b asynchronous microprocessor based on low-temperature poly-silicon TFT technology. In *IEEE International Solid-State Circuits Conference (ISSCC)* 272–273 (IEEE, 2005).

12. 12.

Kurokawa, Y. et al. UHF RFCPUs on flexible and glass substrates for secure RFID systems. *IEEE J. Solid-State Circuits* **43**, 292–299 (2008).

[ADS](#) [Article](#) [Google Scholar](#)

13. 13.

Wachter, S., Polyushkin, D. K., Bethge, O. & Mueller, T. A microprocessor based on a two-dimensional semiconductor. *Nat. Commun.* **8**, 14948 (2017).

[ADS](#) [CAS](#) [Article](#) [Google Scholar](#)

14. 14.

Hills, G. et al. Modern microprocessor built from complementary carbon nanotube transistors. *Nature* **572**, 595–602 (2019).

[ADS](#) [CAS](#) [Article](#) [Google Scholar](#)

15. 15.

Myny, K., van Veenendaal, E., Gelinck, G. H., Genoe, J. & Dehaene, W. An 8-bit, 40-instructions-per-second organic microprocessor on plastic foil. *IEEE J. Solid-State Circuits* **47**, 284–291 (2012).

[ADS](#) [Article](#) [Google Scholar](#)

16. 16.

Myny, K. et al. 8b thin-film microprocessor using a hybrid oxide-organic complementary technology with inkjet-printed P²ROM memory. In *IEEE International Solid-State Circuits Conference (ISSCC)* 486–487 (IEEE, 2014).

17. 17.

Ozer, E. et al. Bespoke machine learning processor development framework on flexible substrates. In *IEEE International Conference on Flexible and Printable Sensors and Systems (FLEPS)* 1–3 (IEEE, 2019).

18. 18.

Ozer, E. et al. Binary neural network as a flexible integrated circuit for odour classification. In *IEEE International Conference on Flexible and Printable Sensors and Systems (FLEPS)* 1–4 (IEEE, 2020).

19. 19.

Armv6-M. Architecture Reference Manual (Arm, 2018).

20. 20.

Arm Cortex-M0+ Revision: r0p1 Technical Reference Manual (Arm, 2012).

21. 21.

FlexLogIC (PragmatIC, 2020); <https://www.pragmaticsemi.com/technology>

22. 22.

Jang, H.-W., Kim, G.-H. & Yoon, S.-M. Analysis of mechanical and electrical origins of degradations in device durability of flexible InGaZnO thin-film transistors. *ACS Appl. Electron. Mater.* **2**, 2113–2122 (2020).

[CAS Article](#) [Google Scholar](#)

[Download references](#)

Author information

Affiliations

1. Arm Ltd, Cambridge, UK

John Biggs, James Myers, Jedrzej Kufel, Emre Ozer & Simon Craske

2. PragmatIC Semiconductor Ltd, Cambridge, UK

Antony Sou, Catherine Ramsdale, Ken Williamson, Richard Price & Scott White

Authors

1. John Biggs

[View author publications](#)

You can also search for this author in [PubMed](#) [Google Scholar](#)

2. James Myers

[View author publications](#)

You can also search for this author in [PubMed](#) [Google Scholar](#)

3. Jędrzej Kufel

[View author publications](#)

You can also search for this author in [PubMed](#) [Google Scholar](#)

4. Emre Ozer

[View author publications](#)

You can also search for this author in [PubMed](#) [Google Scholar](#)

5. Simon Craske

[View author publications](#)

You can also search for this author in [PubMed](#) [Google Scholar](#)

6. Antony Sou

[View author publications](#)

You can also search for this author in [PubMed](#) [Google Scholar](#)

7. Catherine Ramsdale

[View author publications](#)

You can also search for this author in [PubMed](#) [Google Scholar](#)

8. Ken Williamson

[View author publications](#)

You can also search for this author in [PubMed](#) [Google Scholar](#)

9. Richard Price

[View author publications](#)

You can also search for this author in [PubMed](#) [Google Scholar](#)

10. Scott White

[View author publications](#)

You can also search for this author in [PubMed](#) [Google Scholar](#)

Contributions

J.B. and J.M. conceived the PlasticARM concept. S.C. designed the Cortex-M processor and J.B., J.M. and J.K. implemented the SoC. J.K. developed the PlasticARM test framework. A.S., C.R., K.W., R.P. and S.W. developed the fabrication process and methodology for the PlasticARM FlexIC. All authors contributed to analysis of the data generated in the development of PlasticARM. E.O., J.B., J.K., J.M., C.R., R.P. and S.W. wrote the paper.

Corresponding author

Correspondence to [Emre Ozer](#).

Ethics declarations

Competing interests

The authors declare no competing interests.

Additional information

Peer review information *Nature* thanks Zili Yu and the other, anonymous, reviewer(s) for their contribution to the peer review of this work.

Publisher's note Springer Nature remains neutral with regard to jurisdictional claims in published maps and institutional affiliations.

Extended data figures and tables

[Extended Data Fig. 1 Evolution of the standard cell architecture.](#)

The figure shows the evolution of the standard cell library from left to right. It starts with a 1- μm channel length library, and then moves to an 0.8 μm channel length with different sheet resistances. The far right panel shows the final library that is used to

implement the PlasticARM FlexIC. VDD, supply voltage; VSS, ground; CONT, electrical contact between the source–drain layer and the next metal layer; VIA, electrical contact between routing layers.

Extended Data Fig. 2 Layouts and transfer characteristics of buffers.

a, Layouts of X4 buffers with resistive pull-up (BUF_X4) are shown on the left and layouts of X4 buffers with active transistor pull-up (BUF_X4M) are shown on the right. **b**, Simulated responses including parasitic capacitance and resistance extracted from the layout. The maximum capacitive load of BUF_X4 is 4.8 pF, based on the data from the liberty file at the typical corner. Buffers with active pull-up can drive much higher loads and consume less static power than their resistive load counterparts at the expense of area increase and reduced output voltage range due to a drop in V_{DS} (the voltage between the drain and source electrodes) across the pull-up transistor. For X4 cells the average static power consumption reduces by 60%, area increases by 43% and the V_{DS} drop is 0.2 V.

Extended Data Fig. 3 Simulation of the PlasticARM RTL.

a, GPIO toggles are shown when data are correct in all three tests. **b**, GPIO toggles are shown when data read from the ROM is incorrect. The simulation was run with a 20-kHz clock frequency.

Extended Data Fig. 4 PlasticARM timing measurements of all three tests.

a, Waveform showing the functionality of PlasticARM that correctly matches the RTL simulation. **b**, Magnified views of GPIO input pin (I_GPIO[1]) changing from logic 0 to logic 1. **c**, GPIO output pin (O_GPIO[0]) changing from logic 0 to logic 1, marking an input that was held HIGH for about 1 s. The experiment was carried out with a 20-kHz clock frequency.

Extended Data Table 1 Standard cell library contents and usage

[Full size table](#)

Extended Data Table 2 Process technology parameters

[Full size table](#)

Rights and permissions

[Reprints and Permissions](#)

About this article



Check for
updates

Cite this article

Biggs, J., Myers, J., Kufel, J. *et al.* A natively flexible 32-bit Arm microprocessor. *Nature* **595**, 532–536 (2021). <https://doi.org/10.1038/s41586-021-03625-w>

[Download citation](#)

- Received: 05 January 2021
- Accepted: 10 May 2021
- Published: 21 July 2021
- Issue Date: 22 July 2021
- DOI: <https://doi.org/10.1038/s41586-021-03625-w>

Comments

By submitting a comment you agree to abide by our [Terms](#) and [Community Guidelines](#). If you find something abusive or that does not comply with our terms or guidelines please flag it as inappropriate.

[Download PDF](#)

Advertisement

This article was downloaded by **calibre** from <https://www.nature.com/articles/s41586-021-03625-w>

- Article
- [Published: 21 July 2021](#)

Extreme flow simulations reveal skeletal adaptations of deep-sea sponges

- [Giacomo Falcucci](#) [ORCID: orcid.org/0000-0001-6446-4697^{1,2}](#),
- [Giorgio Amati³](#),
- [Pierluigi Fanelli⁴](#),
- [Vesselin K. Krastev¹](#),
- [Giovanni Polverino](#) [ORCID: orcid.org/0000-0001-9737-7995⁵](#),
- [Maurizio Porfiri](#) [ORCID: orcid.org/0000-0002-1480-3539^{6,7,8 na1}](#) &
- [Sauro Succi^{2,9,10 na1}](#)

[Nature](#) volume 595, pages 537–541 (2021) [Cite this article](#)

- 1071 Accesses
- 129 Altmetric
- [Metrics details](#)

Subjects

- [Computational models](#)
- [Fluid dynamics](#)
- [Mechanical properties](#)

Abstract

Since its discovery^{1,2}, the deep-sea glass sponge *Euplectella aspergillum* has attracted interest in its mechanical properties and beauty. Its skeletal system is composed of amorphous hydrated silica and is arranged in a highly regular and hierarchical cylindrical lattice that begets exceptional flexibility and resilience to damage^{3,4,5,6}. Structural analyses dominate the literature, but hydrodynamic fields that surround and penetrate the sponge have remained largely unexplored. Here we address an unanswered question: whether, besides improving its mechanical properties, the skeletal motifs of *E. aspergillum* underlie the optimization of the flow physics within and beyond its body cavity. We use extreme flow simulations based on the ‘lattice Boltzmann’ method⁷, featuring over fifty billion grid points and spanning four spatial decades. These *in silico* experiments reproduce the hydrodynamic conditions on the deep-sea floor where *E. aspergillum* lives^{8,9,10}. Our results indicate that the skeletal motifs reduce the overall hydrodynamic stress and support coherent internal recirculation patterns at low flow velocity. These patterns are arguably beneficial to the organism for selective filter feeding and sexual reproduction^{11,12}. The present study reveals mechanisms of extraordinary adaptation to live in the abyss, paving the way towards further studies of this type at the intersection between fluid mechanics, organism biology and functional ecology.

Access options

Subscribe to Journal

Get full journal access for 1 year

\$199.00

only \$3.90 per issue

[Subscribe](#)

All prices are NET prices.

VAT will be added later in the checkout.

Tax calculation will be finalised during checkout.

Rent or Buy article

Get time limited or full article access on ReadCube.

from \$8.99

[Rent or Buy](#)

All prices are NET prices.

Additional access options:

- [Log in](#)
- [Access through your institution](#)
- [Learn about institutional subscriptions](#)

Fig. 1: Skeletal motifs of *E. aspergillum* and associated flow physics.



Fig. 2: Effect of manipulations of the morphology of *E. aspergillum* on the flow downstream.

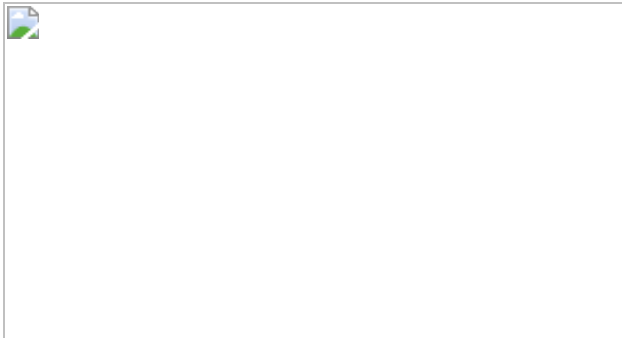
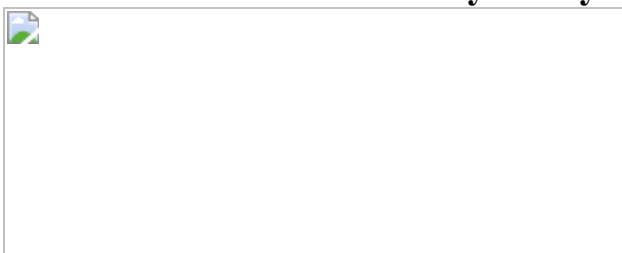


Fig. 3: Effect of manipulations of the morphology of *E. aspergillum* on helicity, enstrophy and drag coefficient.



Fig. 4: Role of the ridges in flow speed, vorticity, Q -structures and residence time within the body cavity.



Data availability

STL files for all of the models, raw data for the plots, and scripts to reproduce the figures are available on GitHub at https://github.com/giacomofalcucci/Euplectella_HPC. Additional data that

support the findings of this study are available from the corresponding author on request.

Code availability

All codes necessary to reproduce results in main paper are available on GitHub at https://github.com/giacomofalcucci/Euplectella_HPC.

References

1. 1.

Owen, R. Description of a new genus and species of sponge (*Euplectella aspergillum*, O.). *Trans. Zool. Soc. Lond.* **3**, 203–215 (1849).

[Google Scholar](#)

2. 2.

Report on the Scientific Results of the Voyage of H.M.S. Challenger During the Years 1873–76 — Under the Command of Captain George S. Nares, R.N., F.R.S. and Captain Frank Turle Thomson, R.N. Vol. XXI, Zoology, Plates (Neill, 1887);
<https://archive.org/details/reportonscientif21grea/page/n13/mode/2up> (2008).

3. 3.

Weaver, J. C. et al. Hierarchical assembly of the siliceous skeletal lattice of the hexactinellid sponge *Euplectella aspergillum*. *J. Struct. Biol.* **158**, 93–106 (2007).

[CAS Article](#) [Google Scholar](#)

4. 4.

Aizenberg, J. et al. Skeleton of *Euplectella* sp.: structural hierarchy from the nanoscale to the macroscale. *Science* **309**, 275–278 (2005).

[ADS](#) [CAS](#) [Article](#) [Google Scholar](#)

5. 5.

Monn, M. A., Weaver, J. C., Zhang, T., Aizenberg, J. & Kesari, H. New functional insights into the internal architecture of the laminated anchor spicules of *Euplectella aspergillum*. *Proc. Natl Acad. Sci. USA* **112**, 4976–4981 (2015).

[ADS](#) [CAS](#) [Article](#) [Google Scholar](#)

6. 6.

Fernandes, M. C., Aizenberg, J., Weaver, J. C. & Bertoldi, K. Mechanically robust lattices inspired by deep-sea sponges. *Nat. Mater.* **20**, 237–241 (2020).

[ADS](#) [Article](#) [Google Scholar](#)

7. 7.

Succi, S. *The Lattice Boltzmann Equation: For Complex States of Flowing Matter* (Oxford Univ. Press, 2018).

8. 8.

Kanari, S.-I., Kobayashi, C. & Ishikawa, T. An estimate of the velocity and stress in the deep ocean bottom boundary layer. *J. Fac. Sci. Hokkaido Univ. Ser. 7 Geophys.* **9**, 1–16 (1991).

[Google Scholar](#)

9. 9.

Doron, P., Bertuccioli, L., Katz, J. & Osborn, T. R. Turbulence characteristics and dissipation estimates in the coastal ocean bottom

boundary layer from PIV data. *J. Phys. Oceanogr.* **31**, 2108–2134 (2001).

[ADS](#) [Article](#) [Google Scholar](#)

10. 10.

26th ITTC Specialist Committee on Uncertainty Analysis (eds). In *Proc. International Towing Tank Conf.* Paper 7.5-02-01-03 <https://ittc.info/media/4048/75-02-01-03.pdf> (ITTC, 2011).

11. 11.

Yahel, G., Eerkes-Medrano, D. I. & Leys, S. P. Size independent selective filtration of ultraplankton by hexactinellid glass sponges. *Aquat. Microb. Ecol.* **45**, 181–194 (2006).

[Article](#) [Google Scholar](#)

12. 12.

Schulze, F. E. XXIV.—On the structure and arrangement of the soft parts in *Euplectella aspergillum*. *Earth Environ. Sci. Trans. R. Soc. Edinb.* **29**, 661–673 (1880).

[Article](#) [Google Scholar](#)

13. 13.

Kitano, H. Computational systems biology. *Nature* **420**, 206–210 (2002).

[ADS](#) [CAS](#) [Article](#) [Google Scholar](#)

14. 14.

Coveney, P. V., Boon, J. P. & Succi, S. Bridging the gaps at the physics-chemistry-biology interface. *Phil. Trans. R. Soc. A* **374**, 20160335 (2016).

[ADS](#) [Article](#) [Google Scholar](#)

15. 15.

Succi, S. et al. Towards exascale lattice Boltzmann computing. *Comput. Fluids* **181**, 107–115 (2019).

[MathSciNet](#) [Article](#) [Google Scholar](#)

16. 16.

Fung, Y. C. *Biomechanics: Mechanical Properties of Living Tissues* (Springer Science and Business Media, 2013).

17. 17.

Marconi100, the new accelerated system.

<https://www.hpc.cineca.it/hardware/marconi100> (SuperComputing Applications and Innovation, 2020).

18. 18.

Reitner, J. & Mehl, D. Early Paleozoic diversification of sponges; new data and evidences. *Geol.-paläontol. Mitt. Innsbruck* **20**, 335–347 (1995).

[Google Scholar](#)

19. 19.

Moore, T. J. XXVIII.—On the habitat of the Regadera (watering-pot) or Venus's flower-basket (*Euplectella aspergillum*, Owen). *J. Nat. Hist.* **3**, 196–199 (1869).

[Google Scholar](#)

20. 20.

Leys, S. P., Mackie, G. O. & Reiswig, H. M. The biology of glass sponges. *Adv. Mar. Biol.* **52**, 1–145 (2007).

[CAS](#) [Article](#) [Google Scholar](#)

21. 21.

Gray, J. E. LXIV.—Venus's flower-basket (*Euplectella speciosa*). *Ann. Mag. Nat. Hist.* **18**, 487–490 (1866).

[Article](#) [Google Scholar](#)

22. 22.

Saito, T., Uchida, I. & Takeda, M. Skeletal growth of the deep-sea hexactinellid sponge *Euplectella oweni*, and host selection by the symbiotic shrimp *Spongicola japonica* (Crustacea: Decapoda: Spongicolidae). *J. Zool.* **258**, 521–529 (2002).

[Article](#) [Google Scholar](#)

23. 23.

Chree, C. Recent advances in our knowledge of silicon and of its relations to organised structures. *Nature* **81**, 206–208 (1909).

[ADS](#) [Article](#) [Google Scholar](#)

24. 24.

Woesz, A. et al. Micromechanical properties of biological silica in skeletons of deep-sea sponges. *J. Mater. Res.* **21**, 2068–2078 (2006).

[ADS](#) [CAS](#) [Article](#) [Google Scholar](#)

25. 25.

Monn, M. A., Vijaykumar, K., Kochiyama, S. & Kesari, H. Lamellar architectures in stiff biomaterials may not always be templates for

enhancing toughness in composites. *Nat. Commun.* **11**, 373 (2020).

[ADS](#) [CAS](#) [Article](#) [Google Scholar](#)

26. 26.

Nayar, K. G., Sharqawy, M. H. & Banchik, L. D. Thermophysical properties of seawater: a review and new correlations that include pressure dependence. *Desalination* **390**, 1–24 (2016).

[CAS](#) [Article](#) [Google Scholar](#)

27. 27.

Vogel, S. Current-induced flow through living sponges in nature. *Proc. Natl Acad. Sci. USA* **74**, 2069–2071 (1977).

[ADS](#) [CAS](#) [Article](#) [Google Scholar](#)

28. 28.

Prandtl, L. & Tietjens, O. G. *Applied Hydro- and Aeromechanics* (transl. Den Hartog, J. P.) (Dover Publications, 1957).

29. 29.

Tritton, D. J. *Physical Fluid Dynamics* 2nd edn Ch. 21 (Clarendon, 1988).

30. 30.

Gualtieri, P., Casciola, C. M., Benzi, R., Amati, G. & Piva, R. Scaling laws and intermittency in homogeneous shear flow. *Phys. Fluids* **14**, 583–596 (2002).

[ADS](#) [CAS](#) [Article](#) [Google Scholar](#)

31. 31.

Koehl, M. A. R. How do benthic organisms withstand moving water? *Am. Zool.* **24**, 57–70 (1984).

[Article](#) [Google Scholar](#)

32. 32.

Yahel, G., Whitney, F., Reiswig, H. M., Eerkes-Medrano, D. I. & Leys, S. P. In situ feeding and metabolism of glass sponges (Hexactinellida, Porifera) studied in a deep temperate fjord with a remotely operated submersible. *Limnol. Oceanogr.* **52**, 428–440 (2007).

[ADS](#) [CAS](#) [Article](#) [Google Scholar](#)

33. 33.

Hunt, J. C. R., Wray, A. & Moin, P. *Eddies, Stream, and Convergence Zones in Turbulent Flows*. Report CTR-S88 (Center for Turbulence Research, 1988).

34. 34.

Haller, G. An objective definition of a vortex. *J. Fluid Mech.* **525**, 1–26 (2005).

[ADS](#) [MathSciNet](#) [Article](#) [Google Scholar](#)

35. 35.

Krastev, V. K., Amati, G., Succi, S. & Falcucci, G. On the effects of surface corrugation on the hydrodynamic performance of cylindrical rigid structures. *Eur. Phys. J. E* **41**, 95 (2018).

[Article](#) [Google Scholar](#)

36. 36.

Kawamura, T., Takami, H. & Kuwahara, K. Computation of high Reynolds number flow around a circular cylinder with surface

roughness. *Fluid Dyn. Res.* **1**, 145 (1986).

[ADS](#) [Article](#) [Google Scholar](#)

37. 37.

Hanchi, S., Askovic, R. & Ta Phuoc, L. Numerical simulation of a flow around an impulsively started radially deforming circular cylinder. *Int. J. Numer. Methods Fluids* **29**, 555–573 (1999).

[ADS](#) [CAS](#) [Article](#) [Google Scholar](#)

38. 38.

Sahin, M. & Owens, R. G. A numerical investigation of wall effects up to high blockage ratios on two-dimensional flow past a confined circular cylinder. *Phys. Fluids* **16**, 1305–1320 (2004).

[ADS](#) [CAS](#) [Article](#) [Google Scholar](#)

39. 39.

Fujisawa, N., Tanahashi, S. & Srinivas, K. Evaluation of pressure field and fluid forces on a circular cylinder with and without rotational oscillation using velocity data from PIV measurement. *Meas. Sci. Technol.* **16**, 989–996 (2005).

[ADS](#) [CAS](#) [Article](#) [Google Scholar](#)

40. 40.

Henderson, R. D. Detail of the drag curve near the onset of vortex shedding. *Phys. Fluids* **7**, 2102–2104 (1995).

[ADS](#) [Article](#) [Google Scholar](#)

41. 41.

Posdziech, O. & Grundmann, R. Numerical simulation of the flow around an infinitely long circular cylinder in the transition regime. *Theor. Comput. Fluid Dyn.* **15**, 121–141 (2001).

[CAS](#) [Article](#) [Google Scholar](#)

42. 42.

Succi, S. *The Lattice Boltzmann Equation: For Fluid Dynamics and Beyond* (Oxford Univ. Press, 2001).

43. 43.

Norberg, C. An experimental investigation of the flow around a circular cylinder: influence of aspect ratio. *J. Fluid Mech.* **258**, 287–316 (1994).

[ADS](#) [CAS](#) [Article](#) [Google Scholar](#)

44. 44.

Krüger, T. et al. *The Lattice Boltzmann Method* (Springer International, 2017).

45. 45.

Montessori, A. & Falcucci, G. *Lattice Boltzmann Modeling of Complex Flows for Engineering Applications* (Morgan and Claypool, 2018).

46. 46.

Falcucci, G. et al. Lattice Boltzmann methods for multiphase flow simulations across scales. *Commun. Comput. Phys.* **9**, 269–296 (2011).

[Article](#) [Google Scholar](#)

47. 47.

Johnson, R. W. (ed.) *Handbook of Fluid Dynamics* (CRC, 2016).

[Download references](#)

Acknowledgements

G.F. acknowledges CINECA computational grant ISCRA-B IsB17–SPONGES, no. HP10B9ZOKQ and, partially, the support of PRIN projects CUP E82F16003010006 (principal investigator, G.F. for the Tor Vergata Research Unit) and CUP E84I19001020006 (principal investigator, G. Bella). G.P. acknowledges the support of the Forrest Research Foundation, under a postdoctoral research fellowship. M.P. acknowledges the support of the National Science Foundation under grant no. CMMI 1901697. S.S. acknowledges financial support from the European Research Council under the Horizon 2020 Programme advanced grant agreement no. 739964 ('COPMAT'). G.F. and S.S. acknowledge K. Bertoldi, M. C. Fernandes and J. C. Weaver (Harvard University) for introducing them to *E. aspergillum* and for early discussions on the subject. A. L. Facci (Tuscia University) is acknowledged for discussions on graphics realization. M. Bernaschi (IAC-CNR) is acknowledged for discussions on extreme computing. V. Villani is acknowledged for his support with Japanese language and culture. E. Kaxiras (Harvard University) is acknowledged for early discussions that proved fruitful for the development of the present code.

Author information

Author notes

1. These authors contributed equally: Maurizio Porfiri, Sauro Succi

Affiliations

1. Department of Enterprise Engineering “Mario Lucertini”, University of Rome “Tor Vergata”, Rome, Italy

Giacomo Falcucci & Vesselin K. Krastev

2. Department of Physics, Harvard University, Cambridge, MA, USA

Giacomo Falcucci & Sauro Succi

3. High Performance Computing Department, CINECA Rome Section, Rome, Italy

Giorgio Amati

4. DEIM, School of Engineering, University of Tuscany, Viterbo, Italy

Pierluigi Fanelli

5. Centre for Evolutionary Biology, School of Biological Sciences, University of Western Australia, Perth, Western Australia, Australia

Giovanni Polverino

6. Department of Biomedical Engineering, Tandon School of Engineering, New York University, New York, NY, USA

Maurizio Porfiri

7. Department of Mechanical and Aerospace Engineering, Tandon School of Engineering, New York University, New York, NY, USA

Maurizio Porfiri

8. Center for Urban Science and Progress, Tandon School of Engineering, New York University, New York, NY, USA

Maurizio Porfiri

9. Italian Institute of Technology, Center for Life Nano- and Neuro-Science, Rome, Italy

Sauro Succi

10. National Research Council of Italy – Institute for Applied Computing (IAC), Rome, Italy

Sauro Succi

Authors

1. Giacomo Falcucci

[View author publications](#)

You can also search for this author in [PubMed](#) [Google Scholar](#)

2. Giorgio Amati

[View author publications](#)

You can also search for this author in [PubMed](#) [Google Scholar](#)

3. Pierluigi Fanelli

[View author publications](#)

You can also search for this author in [PubMed](#) [Google Scholar](#)

4. Vesselin K. Krastev

[View author publications](#)

You can also search for this author in [PubMed](#) [Google Scholar](#)

5. Giovanni Polverino

[View author publications](#)

You can also search for this author in [PubMed](#) [Google Scholar](#)

6. Maurizio Porfiri

[View author publications](#)

You can also search for this author in [PubMed](#) [Google Scholar](#)

7. Sauro Succi

[View author publications](#)

You can also search for this author in [PubMed](#) [Google Scholar](#)

Contributions

G.F. designed the research; G.F. and G.A. wrote the original lattice Boltzmann method code; G.A. extended the code for massively parallel computation, developed the GPU version for Marconi100, and helped collect and post-process the data; P.F. realized all of the models; V.K.K. ran the validation tests and helped in post-processing and data interpretation; G.F. created the figures; G.P. and M.P. led the biological framing of the results; G.F., M.P. and S.S. supervised the research and the interpretation of the results; G.F., G.P., M.P. and S.S. wrote the manuscript. All authors contributed to analysing the results of the simulations and revising the manuscript.

Corresponding author

Correspondence to [Giacomo Falcucci](#).

Ethics declarations

Competing interests

The authors declare no competing interests.

Additional information

Peer review information *Nature* thanks Carlo Massimo Casciola and the other, anonymous, reviewer(s) for their contribution to the peer review of this work.

Publisher's note Springer Nature remains neutral with regard to jurisdictional claims in published maps and institutional affiliations.

Extended data figures and tables

Extended Data Fig. 1 Detail of the grid resolution.

The grid resolution within the small fenestrae of *E. aspergillum* models is 5.33 lattice spacings.

Extended Data Fig. 2 Details of the flow field.

a, Tilted view of main text Fig. 1c, detailing the flow field downstream and within the body cavity of the complete model of *E. aspergillum* at $Re = 2,000$. Colour intensity indicates the helicity magnitude, and the streak lines are coloured according to the velocity magnitude. **b**, Stereo view of a.

Extended Data Fig. 3 Details of the vorticity field.

a, Visualization of the vorticity magnitude, complementing Extended Data Fig. 2a, such that colour intensity indicates the helicity magnitude, and the streak lines are coloured in green, based on the vorticity magnitude. **b**, Stereo view of a.

Extended Data Fig. 4 Morphological manipulations of the *E. aspergillum* model.

a–i, Details of the nine variations of the hollow cylindrical lattice with helical ridges (P2), obtained by including random defects simulating wounds and scars. The nine morphological manipulations are identified as Mark01, Mark02, …, Mark09.

Extended Data Fig. 5 Details of the vorticity magnitude fields.

a–e, Comparison between the vorticity magnitudes (colour scale) for the plain cylinder (S1, left panels) and for the hollow cylindrical lattice with helical ridges (P2, right panels) at statistical steady states, for all Re simulated in the present work. Panels a–e show data for $Re = 100, 500, 1,000, 1,500$ and $2,000$, respectively.

Extended Data Fig. 6 Details of the drag coefficient.

Zoomed-out view of main text Fig. 3c, with error bars identifying the range of predicted values of the drag coefficient C_D due to random morphological manipulations. These variations lead to a modest decrease, from 2.5% to 3.5% in the drag coefficient with respect to the pristine model.

Extended Data Fig. 7 Views of the skeletal system of *E. aspergillum*.

The model is reconstructed according to ref. 3: left, side view; right, AA and BB cross-sections from the left panel, detailing the osculum and the body cavity, respectively.

Extended Data Fig. 8 Details of the *E. aspergillum* complete model.

a, Front (centre panel) and side (leftmost and rightmost) views of the complete model of *E. aspergillum*; **b**, stereo views of the complete model of *E. aspergillum* realized with the Anaglyph algorithm.

Extended Data Fig. 9 Lift coefficient C_L .

Left, time trace at statistical steady state of the lift coefficient C_L for the different models (see key at right) of *E. aspergillum* at $Re = 2,000$. The range of the oscillations in the porous models is two orders of magnitude less than that of the plain cylinder S1. Right, magnified view of boxed region.

Extended Data Table 1 Accuracy assessment

[Full size table](#)

Extended Data Table 2 Main physical parameters at $Re = 2,000$

[Full size table](#)

Extended Data Table 3 Details of resource allocation

[Full size table](#)

Supplementary information

Supplementary Data

This zipped file contains the STL geometry of the complete *E. aspergillum*, as well as the STL files to realize models S2, P1 and P2. The simple cylinder model S1 is not provided.

Video 1 Comparison of the Vorticity Field generated by S1 and P2 models.

The Video shows the vorticity field generated by S1 (left) and P2 (right) models for Re=100, 500, 1,000, 1,500 and 2,000. The video highlights the formation of a nearly quiescent region downstream the porous model, as well as the vortical patterns within the body cavity.

Video 2 Comparison of the Vorticity Field for all models at Re=2,000

The video shows the vorticity field generated by S1 (top left), P1 (top right), S2 (bottom left) and P2 (bottom right) at Re=2,000. The two porous models are characterised by a nearly quiescent region extending several diameters downstream the structure.

Video 3 Detail pf the vorticity field generated by S1 and P2 at Re=2,000.

The video highlights the vorticity field downstream S1 (top) and P2 (bottom) models, as well as within the body cavity of P2.

Rights and permissions

Reprints and Permissions

About this article



Cite this article

Falcucci, G., Amati, G., Fanelli, P. *et al.* Extreme flow simulations reveal skeletal adaptations of deep-sea sponges. *Nature* **595**, 537–541 (2021).
<https://doi.org/10.1038/s41586-021-03658-1>

[Download citation](#)

- Received: 30 October 2020
- Accepted: 20 May 2021
- Published: 21 July 2021
- Issue Date: 22 July 2021
- DOI: <https://doi.org/10.1038/s41586-021-03658-1>

Comments

By submitting a comment you agree to abide by our [Terms](#) and [Community Guidelines](#). If you find something abusive or that does not comply with our terms or guidelines please flag it as inappropriate.

[Access through your institution](#)

[Change institution](#)

[Buy or subscribe](#)

Associated Content

Fluid flow through a deep-sea sponge could inspire engineering designs

- Laura A. Miller

Advertisement

This article was downloaded by **calibre** from <https://www.nature.com/articles/s41586-021-03658-1>

| [Section menu](#) | [Main menu](#) |

- Article
- [Published: 21 July 2021](#)

Orthogonal-array dynamic molecular sieving of propylene/propane mixtures

- [Heng Zeng](#) [ORCID: orcid.org/0000-0003-2298-7347](#)^{1,2},
- [Mo Xie](#)^{1,2},
- [Ting Wang](#)^{1,2},
- [Rong-Jia Wei](#) [ORCID: orcid.org/0000-0001-7898-567X](#)^{1,2},
- [Xiao-Jing Xie](#)^{1,2},
- [Yifang Zhao](#)^{1,2},
- [Weigang Lu](#) [ORCID: orcid.org/0000-0001-9751-8241](#)^{1,2} &
- [Dan Li](#) [ORCID: orcid.org/0000-0002-4936-4599](#)^{1,2}

[Nature](#) volume 595, pages 542–548 (2021) [Cite this article](#)

- 2059 Accesses
- 15 Altmetric
- [Metrics details](#)

Subjects

- [Crystal engineering](#)
- [Metal–organic frameworks](#)

Abstract

Rigid molecular sieving materials work well for small molecules with the complete exclusion of large ones^{1,2,3}, and molecules with matching physiochemical properties may be separated using dynamic molecular sieving materials^{4,5,6}. Metal–organic frameworks (MOFs)^{7,8,9} are known for their precise control of structures and functions on a molecular level^{10,11,12,13,14,15}. However, the rational design of local flexibility in the MOF framework for dynamic molecular sieving remains difficult and challenging. Here we report a MOF material (JNU-3a) featuring one-dimension channels with embedded molecular pockets opening to propylene (C_3H_6) and propane (C_3H_8) at substantially different pressures. The dynamic nature of the pockets is revealed by single-crystal-to-single-crystal transformation upon exposure of JNU-3a to an atmosphere of C_3H_6 or C_3H_8 . Breakthrough experiments demonstrate that JNU-3a can realize high-purity C_3H_6 ($\geq 99.5\%$) in a single adsorption–desorption cycle from an equimolar C_3H_6/C_3H_8 mixture over a broad range of flow rates, with a maximum C_3H_6 productivity of 53.5 litres per kilogram. The underlying separation mechanism—orthogonal-array dynamic molecular sieving—enables both large separation capacity and fast adsorption–desorption kinetics. This work presents a next-generation sieving material design that has potential for applications in adsorptive separation.

Access options

Subscribe to Journal

Get full journal access for 1 year

\$199.00

only \$3.90 per issue

[Subscribe](#)

All prices are NET prices.

VAT will be added later in the checkout.

Tax calculation will be finalised during checkout.

Rent or Buy article

Get time limited or full article access on ReadCube.

from \$8.99

[Rent or Buy](#)

All prices are NET prices.

Additional access options:

- [Log in](#)
- [Access through your institution](#)
- [Learn about institutional subscriptions](#)

Fig. 1: Molecular sieving.

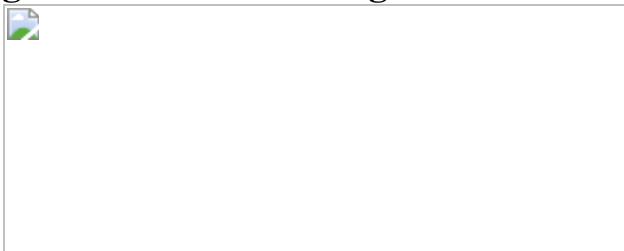


Fig. 2: Crystal structure of JNU-3.

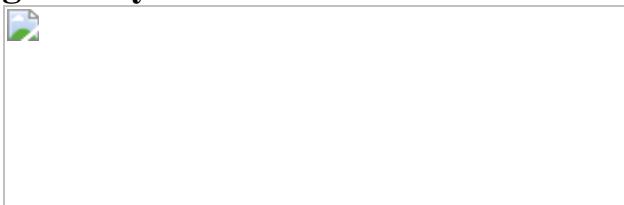


Fig. 3: Gas sorption properties and DSC profiles.

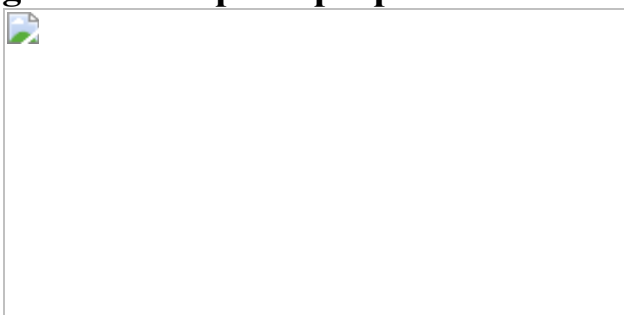


Fig. 4: Binding sites and dynamic gate-opening.

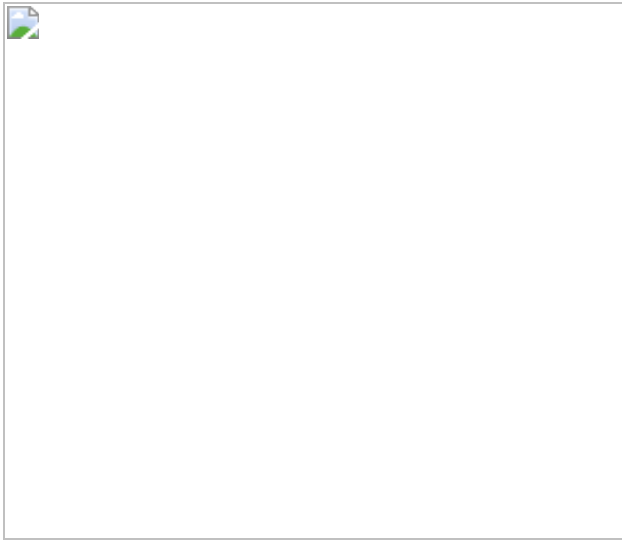
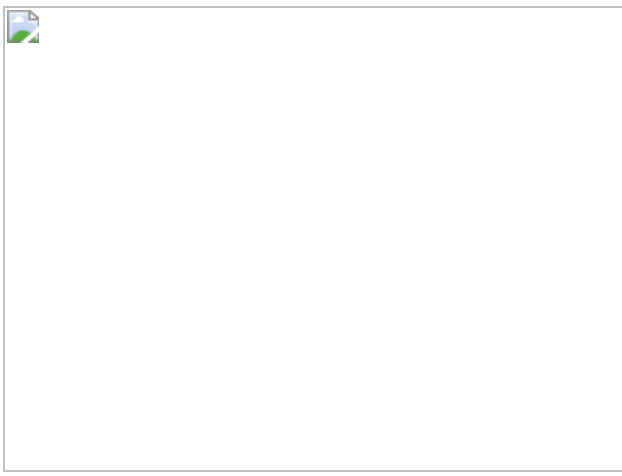


Fig. 5: Breakthrough experiments.



Fig. 6: Recyclability and breakthrough experiment under humid conditions.



Data availability

The data that support the plots within this paper and other finding of this study are available from the corresponding authors upon reasonable request. The X-ray crystallographic coordinates for structures reported in this

Article have been deposited at the Cambridge Crystallographic Data Centre (CCDC), under deposition numbers CCDC 2018163–2018167. These data can be obtained free of charge from the Cambridge Crystallographic Data Centre via https://www.ccdc.cam.ac.uk/data_request/cif.

References

1. 1.

Yang, R. T. *Gas Separation by Adsorption Processes* (Imperial College Press, 1997).

2. 2.

Lin, R. et al. Molecular sieving of ethylene from ethane using a rigid metal–organic framework. *Nat. Mater.* **17**, 1128–1133 (2018).

[ADS](#) [CAS](#) [Article](#) [Google Scholar](#)

3. 3.

Lin, J. Y. S. Molecular sieves for gas separation. *Science* **353**, 121–122 (2016).

[ADS](#) [CAS](#) [Article](#) [Google Scholar](#)

4. 4.

Zhou, D. et al. Intermediate-sized molecular sieving of styrene from larger and smaller analogues. *Nat. Mater.* **18**, 994–998 (2019).

[ADS](#) [CAS](#) [Article](#) [Google Scholar](#)

5. 5.

Shimomura, S. et al. Selective sorption of oxygen and nitric oxide by an electron-donating flexible porous coordination polymer. *Nat. Chem.* **2**, 633–637 (2010).

[CAS](#) [Article](#) [Google Scholar](#)

6. 6.

Zhang, X.-W. et al. Tuning the gating energy barrier of metal–organic framework for molecular sieving. *Chem.* **7**, 1006–1019 (2021).

[CAS](#) [Article](#) [Google Scholar](#)

7. 7.

Zhou, H. C., Long, J. R. & Yaghi, O. M. Introduction to metal organic frameworks. *Chem. Rev.* **112**, 673–674 (2012).

[CAS](#) [Article](#) [Google Scholar](#)

8. 8.

Zhou, H. C. & Kitagawa, S. Metal–organic frameworks (MOFs). *Chem. Soc. Rev.* **43**, 5415–5418 (2014).

[CAS](#) [Article](#) [Google Scholar](#)

9. 9.

Furukawa, H., Cordova, K. E., O’Keeffe, M. & Yaghi, O. M. The chemistry and applications of metal–organic frameworks. *Science* **341**, 1230444 (2013).

[Article](#) [Google Scholar](#)

10. 10.

Chen, B., Xiang, S. C. & Qian, G. D. Metal–organic frameworks with functional pores for recognition of small molecules. *Acc. Chem. Res.* **43**, 1115–1124 (2010).

[CAS](#) [Article](#) [Google Scholar](#)

11. 11.

Yaghi, O. M., Kalmutzki, M. J. & Diercks, C. S. *Introduction to Reticular Chemistry: Metal–Organic Frameworks and Covalent Organic Frameworks* (Wiley-VCH, 2019).

12. 12.

Bloch, E. D. et al. Hydrocarbon separations in a metal–organic framework with open iron(II) coordination sites. *Science* **335**, 1606–1610 (2012).

[ADS](#) [CAS](#) [Article](#) [Google Scholar](#)

13. 13.

Chen, K.-J. et al. Synergistic sorbent separation for one-step ethylene purification from a four-component mixture. *Science* **366**, 241–246 (2019).

[ADS](#) [CAS](#) [Article](#) [Google Scholar](#)

14. 14.

Cadiau, A., Adil, K., Bhatt, P. M., Belmabkhout, Y. & Eddaoudi, M. A metal–organic framework-based splitter for separating propylene from propane. *Science* **353**, 137–140 (2016).

[ADS](#) [CAS](#) [Article](#) [Google Scholar](#)

15. 15.

Wang, H. et al. Tailor-made microporous metal–organic frameworks for the full separation of propane from propylene through selective size exclusion. *Adv. Mater.* **30**, 1805088 (2018).

[Article](#) [Google Scholar](#)

16. 16.

IHS. Natural gas liquids challenging oil as petrochemical feedstock in North America, increasing global demand for on-purpose production of propylene, IHS says. *Business Wire*
<https://www.businesswire.com/news/home/20140827005068/en/Natural-Gas-Liquids-Challenging-Oil-as-Petrochemical-Feedstock-in-North-America-Increasing-Global-Demand-for-On-purpose-Production-of-Propylene-IHS-Says> (2014).

17. 17.

Eldridge, R. B. Olefin/paraffin separation technology: a review. *Ind. Eng. Chem. Res.* **32**, 2208–2212 (1993).

[Article](#) [Google Scholar](#)

18. 18.

Sholl, D. S. & Lively, R. P. Seven chemical separations to change the world. *Nature* **532**, 435–437 (2016).

[ADS](#) [Article](#) [Google Scholar](#)

19. 19.

Li, J.-R., Kuppler, R. J. & Zhou, H.-C. Selective gas adsorption and separation in metal–organic frameworks. *Chem. Soc. Rev.* **38**, 1477–1504 (2009).

[CAS](#) [Article](#) [Google Scholar](#)

20. 20.

Rege, S. U. & Yang, R. T. Propane/propylene separation by pressure swing adsorption: sorbent comparison and multiplicity of cyclic steady states. *Chem. Eng. Sci.* **57**, 1139–1149 (2002).

[CAS](#) [Article](#) [Google Scholar](#)

21. 21.

Papastathopoulou, H. S. & Luyben, W. L. Control of a binary sidestream distillation column. *Ind. Eng. Chem. Res.* **30**, 705–713 (1991).

[CAS Article](#) [Google Scholar](#)

22. 22.

Martins, V. F. D. et al. Development of gas phase SMB technology for light olefin/paraffin separations. *AIChE J.* **62**, 2490–2500 (2016).

[CAS Article](#) [Google Scholar](#)

23. 23.

Narin, G. et al. Light olefins/paraffins separation with 13X zeolite binderless beads. *Separ. Purif. Tech.* **133**, 452–475 (2014).

[CAS Article](#) [Google Scholar](#)

24. 24.

Chai, Y. et al. Control of zeolite pore interior for chemoselective alkyne/olefin separations. *Science* **368**, 1002–1006 (2020).

[CAS Article](#) [Google Scholar](#)

25. 25.

Mohanty, S. & McCormick, A. V. Prospects for principles of size and shape selective separations using zeolites. *Chem. Eng. J.* **74**, 1–14 (1999).

[CAS Article](#) [Google Scholar](#)

26. 26.

Nugent, P. et al. Porous materials with optimal adsorption thermodynamics and kinetics for CO₂ separation. *Nature* **495**, 80–84

(2013).

[ADS](#) [CAS](#) [Article](#) [Google Scholar](#)

27. 27.

Li, B. et al. An ideal molecular sieve for acetylene removal from ethylene with record selectivity and productivity. *Adv. Mater.* **29**, 1704210 (2017).

[Article](#) [Google Scholar](#)

28. 28.

Hu, T. et al. Microporous metal–organic framework with dual functionalities for highly efficient removal of acetylene from ethylene/acetylene mixtures. *Nat. Commun.* **6**, 7328 (2015).

[ADS](#) [CAS](#) [Article](#) [Google Scholar](#)

29. 29.

Ma, S., Sun, D., Wang, X.-S. & Zhou, H.-C. A mesh-adjustable molecular sieve for general use in gas separation. *Angew. Chem. Int. Ed.* **46**, 2458–2462 (2007).

[CAS](#) [Article](#) [Google Scholar](#)

30. 30.

Katsoulidis, A. P. et al. Chemical control of structure and guest uptake by a conformationally mobile porous material. *Nature* **565**, 213–217 (2019).

[ADS](#) [CAS](#) [Article](#) [Google Scholar](#)

31. 31.

Gu, C. et al. Design and control of gas diffusion process in a nanoporous soft crystal. *Science* **363**, 387–391 (2019).

[ADS](#) [CAS](#) [Article](#) [Google Scholar](#)

32. 32.

Krokidas, P. et al. Molecular simulation studies of the diffusion of methane, ethane, propane, and propylene in ZIF-8. *J. Phys. Chem. C* **119**, 27028–27037 (2015).

[CAS](#) [Article](#) [Google Scholar](#)

33. 33.

Férey, G. & Serre, C. Large breathing effects in three-dimensional porous hybrid matter: facts, analyses, rules and consequences. *Chem. Soc. Rev.* **38**, 1380–1399 (2009).

[Article](#) [Google Scholar](#)

34. 34.

Lin, R. B. et al. Optimized separation of acetylene from carbon dioxide and ethylene in a microporous material. *J. Am. Chem. Soc.* **139**, 8022–8028 (2017).

[CAS](#) [Article](#) [Google Scholar](#)

35. 35.

Li, L. et al. Flexible robust metal–organic framework for efficient removal of propyne from propylene. *J. Am. Chem. Soc.* **139**, 7733–7736 (2017).

[CAS](#) [Article](#) [Google Scholar](#)

36. 36.

Wang, X. et al. Guest-dependent pressure induced gate-opening effect enables effective separation of propene and propane in a flexible MOF. *Chem. Eng. J.* **346**, 489–496 (2018).

[CAS](#) [Article](#) [Google Scholar](#)

37. 37.

Grande, C. A. & Rodrigues, A. E. Adsorption kinetics of propane and propylene in zeolite 4A. *Chem. Eng. Res. Des.* **82**, 1604–1612 (2004).

[CAS](#) [Article](#) [Google Scholar](#)

38. 38.

Khalighi, M., Karimi, I. A. & Farooq, S. Comparing SiCHA and 4A zeolite for propylene/propane separation using a surrogate-based simulation/optimization approach. *Ind. Eng. Chem. Res.* **53**, 16973–16983 (2014).

[CAS](#) [Article](#) [Google Scholar](#)

39. 39.

Liang, B. et al. An ultramicroporous metal–organic framework for high sieving separation of propylene from propane. *J. Am. Chem. Soc.* **142**, 17795–17801 (2020).

[CAS](#) [Article](#) [Google Scholar](#)

40. 40.

Myers, A. L. & Prausnitz, J. M. Thermodynamics of mixed-gas adsorption. *AIChE J.* **11**, 121–127 (1965).

[CAS](#) [Article](#) [Google Scholar](#)

41. 41.

Lee, C. Y. et al. Kinetic separation of propene and propane in metal organic frameworks: controlling diffusion rates in plate-shaped crystals via tuning of pore apertures and crystallite aspect ratios. *J. Am. Chem. Soc.* **133**, 5228–5231 (2011).

[CAS Article](#) [Google Scholar](#)

42. 42.

Meyers, R. A. *Handbook of Petrochemicals Production Processes* (McGraw-Hill, 2005).

[Download references](#)

Acknowledgements

We thank W. Chen and A. Zheng from the Wuhan Institute of Physics and Mathematics (WIPM) of Chinese Academy of Sciences for their advice on computational studies. This work was financially supported by the National Natural Science Foundation of China (nos 21731002 and 21975104), the Guangdong Major Project of Basic and Applied Research (no. 2019B030302009), and Guangdong Basic and Applied Basic Research Foundation (no. 2020A1515011005).

Author information

Affiliations

1. College of Chemistry and Materials Science, Jinan University, Guangzhou, P. R. China

Heng Zeng, Mo Xie, Ting Wang, Rong-Jia Wei, Xiao-Jing Xie, Yifang Zhao, Weigang Lu & Dan Li

2. Guangdong Provincial Key Laboratory of Functional Supramolecular Coordination Materials and Applications, Jinan University, Guangzhou, P. R. China

Heng Zeng, Mo Xie, Ting Wang, Rong-Jia Wei, Xiao-Jing Xie, Yifang Zhao, Weigang Lu & Dan Li

Authors

1. Heng Zeng

[View author publications](#)

You can also search for this author in [PubMed](#) [Google Scholar](#)

2. Mo Xie

[View author publications](#)

You can also search for this author in [PubMed](#) [Google Scholar](#)

3. Ting Wang

[View author publications](#)

You can also search for this author in [PubMed](#) [Google Scholar](#)

4. Rong-Jia Wei

[View author publications](#)

You can also search for this author in [PubMed](#) [Google Scholar](#)

5. Xiao-Jing Xie

[View author publications](#)

You can also search for this author in [PubMed](#) [Google Scholar](#)

6. Yifang Zhao

[View author publications](#)

You can also search for this author in [PubMed](#) [Google Scholar](#)

7. Weigang Lu

[View author publications](#)

You can also search for this author in [PubMed](#) [Google Scholar](#)

8. Dan Li

[View author publications](#)

You can also search for this author in [PubMed](#) [Google Scholar](#)

Contributions

W.L. and D.L. conceived and designed the research. H.Z., T.W. and X.-J.X. synthesized the compounds. H.Z. collected and analysed the gas adsorption and separation data. H.Z. collected the X-ray diffraction data. R.-J.W. and Y.Z. analysed the X-ray diffraction data. M.X. performed the theoretical calculations. H.Z., W.L. and D.L. prepared the first version of the manuscript, and all authors participated in and contributed to the final version.

Corresponding authors

Correspondence to [Weigang Lu](#) or [Dan Li](#).

Ethics declarations

Competing interests

The authors declare no competing interests.

Additional information

Peer review information *Nature* thanks the anonymous reviewers for their contribution to the peer review of this work. Peer reviewer reports are available.

Publisher's note Springer Nature remains neutral with regard to jurisdictional claims in published maps and institutional affiliations.

Extended data figures and tables

Extended Data Fig. 1 Coordination environment.

Local coordination environment of Co^{2+} . Co, light blue; C, dark grey; N, blue; O, red; H, white.

Extended Data Fig. 2 Pore structure of JNU-3a.

Connolly surface representation of JNU-3a viewed along the a axis (yellow/grey curved surface).

Extended Data Fig. 3 DSC profiles.

a–d, Differential scanning calorimetry of 50/50 mixed-component of $\text{C}_3\text{H}_6/\text{He}$ (**a**), $\text{C}_3\text{H}_8/\text{He}$ (**b**), $\text{C}_3\text{H}_6/\text{C}_3\text{H}_8$ (**c**), and helium (**d**) on JNU-3a at 303 K. The flow rate is 5.0 ml min^{-1} .

Extended Data Fig. 4 IAST selectivity.

Calculated IAST adsorption selectivity of C_3H_6 over C_3H_8 on JNU-3a for an equimolar mixture of $\text{C}_3\text{H}_6/\text{C}_3\text{H}_8$ at 303 K. P , pressure.

Extended Data Fig. 5 Kinetic profiles.

a, C_3H_6 kinetic adsorption on JNU-3a, Y-abtc and KAUST-7 at 303 K. **b**, C_3H_6 kinetic desorption on JNU-3a, Y-abtc and KAUST-7 at 303 K.

Extended Data Fig. 6 Diffusion rate constants.

a–c, The calculated C_3H_6 diffusion rate constants on JNU-3a (**a**), KAUST-7 (**b**), and Y-abtc (**c**), fitted automatically with BEL-Master software according to the Crank theory. C , concentration; C_0 , initial concentration; C_e , concentration at equilibrium.

Extended Data Fig. 7 DFT calculations.

a, Geometry optimization by DFT for (i) JNU-3a@ $2\text{C}_3\text{H}_6$ with fully relaxed geometry and cell parameters; and (ii) JNU-3a@ $2\text{C}_3\text{H}_6'$ (the prime symbol is used here to differentiate it from scenario (i)) with fixed geometry and cell parameters. **b**, The rotation of the dihedral angle of the pyridine plane and triazole plane. Light blue, red, blue, white and grey represent Co, O, N, H and C atoms, respectively. H atoms are omitted in **a** for clarity.

Extended Data Fig. 8 C_3H_6 .productivity and purity.

Comparison of C_3H_6 productivity and purity estimated from the experimental breakthrough data of an equimolar $\text{C}_3\text{H}_6/\text{C}_3\text{H}_8$ mixture on JNU-3a, KAUST-7 and Y-abtc at different flow rates.

Supplementary information

Supplementary Information

This file contains supplementary text, supplementary tables 1 – 5, supplementary figures 1 – 54 and supplementary references.

Supplementary Data.

Rights and permissions

Reprints and Permissions

About this article



Check for
updates

Cite this article

Zeng, H., Xie, M., Wang, T. *et al.* Orthogonal-array dynamic molecular sieving of propylene/propane mixtures. *Nature* **595**, 542–548 (2021). <https://doi.org/10.1038/s41586-021-03627-8>

[Download citation](#)

- Received: 26 July 2020
- Accepted: 10 May 2021
- Published: 21 July 2021
- Issue Date: 22 July 2021
- DOI: <https://doi.org/10.1038/s41586-021-03627-8>

Comments

By submitting a comment you agree to abide by our [Terms](#) and [Community Guidelines](#). If you find something abusive or that does not comply with our terms or guidelines please flag it as inappropriate.

[Access through your institution](#)

[Change institution](#)

[Buy or subscribe](#)

Advertisement

This article was downloaded by **calibre** from <https://www.nature.com/articles/s41586-021-03627-8>

- Article
- [Published: 07 July 2021](#)

Sexual arousal gates visual processing during *Drosophila* courtship

- [Tom Hindmarsh Sten¹](#),
- [Rufei Li ORCID: orcid.org/0000-0001-8742-6933¹](#),
- [Adriane Otopalik¹](#) &
- [Vanessa Ruta ORCID: orcid.org/0000-0002-4963-2768¹](#)

Nature volume **595**, pages 549–553 (2021) [Cite this article](#)

- 4207 Accesses
- 69 Altmetric
- [Metrics details](#)

Subjects

- [Motivation](#)
- [Neural circuits](#)
- [Sensory processing](#)
- [Social behaviour](#)

Abstract

Long-lasting internal arousal states motivate and pattern ongoing behaviour, enabling the temporary emergence of innate behavioural programs that

serve the needs of an animal, such as fighting, feeding, and mating. However, how internal states shape sensory processing or behaviour remains unclear. In *Drosophila*, male flies perform a lengthy and elaborate courtship ritual that is triggered by the activation of sexually dimorphic P1 neurons^{[1,2,3,4,5](#)}, during which they faithfully follow and sing to a female^{[6,7](#)}. Here, by recording from males as they court a virtual ‘female’, we gain insight into how the salience of visual cues is transformed by a male’s internal arousal state to give rise to persistent courtship pursuit. The gain of LC10a visual projection neurons is selectively increased during courtship, enhancing their sensitivity to moving targets. A concise network model indicates that visual signalling through the LC10a circuit, once amplified by P1-mediated arousal, almost fully specifies a male’s tracking of a female. Furthermore, P1 neuron activity correlates with ongoing fluctuations in the intensity of a male’s pursuit to continuously tune the gain of the LC10a pathway. Together, these results reveal how a male’s internal state can dynamically modulate the propagation of visual signals through a high-fidelity visuomotor circuit to guide his moment-to-moment performance of courtship.

Access options

Subscribe to Journal

Get full journal access for 1 year

\$199.00

only \$3.90 per issue

[Subscribe](#)

All prices are NET prices.

VAT will be added later in the checkout.

Tax calculation will be finalised during checkout.

Rent or Buy article

Get time limited or full article access on ReadCube.

from \$8.99

[Rent or Buy](#)

All prices are NET prices.

Additional access options:

- [Log in](#)
- [Access through your institution](#)
- [Learn about institutional subscriptions](#)

Fig. 1: P1 neurons release and reflect a dynamic state of sexual arousal.

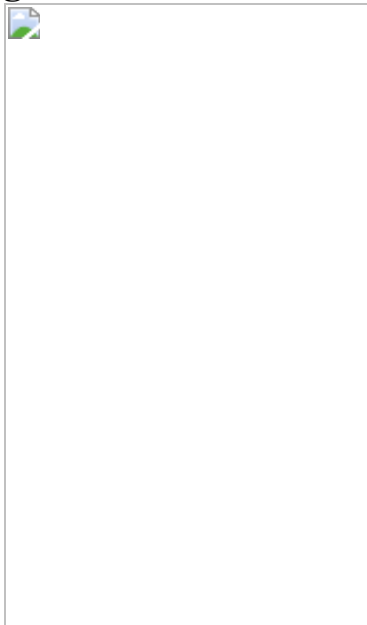


Fig. 2: Modulation of LC10a neurons during courtship.

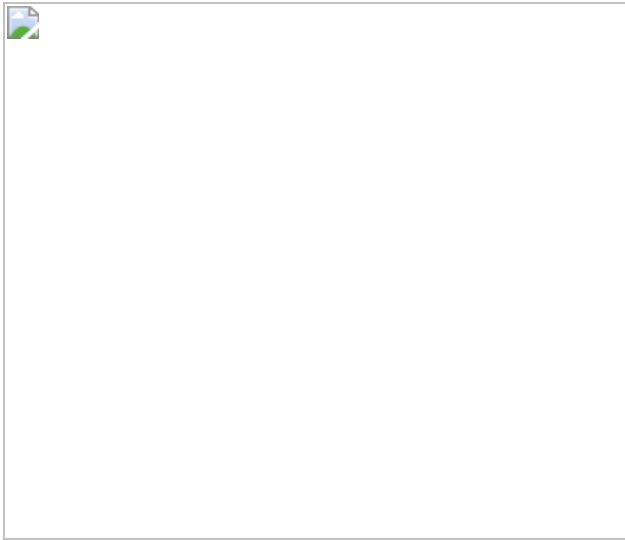


Fig. 3: P1 neurons represent intensity of courtship and acutely regulate pursuit.

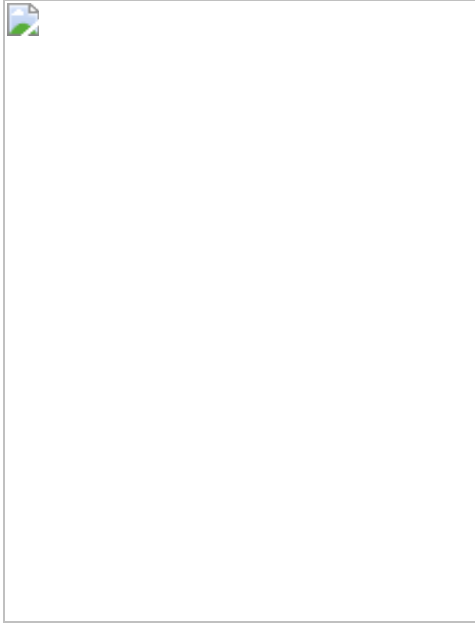
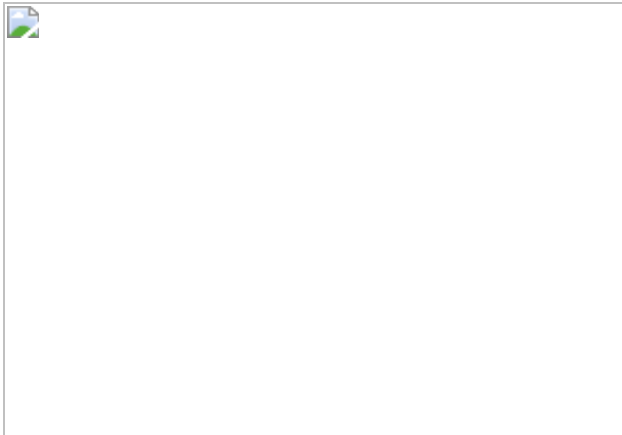


Fig. 4: A network model of LC10a neurons recapitulates male pursuit.



Data availability

All data underlying this study are available upon request from the corresponding author. [Source data](#) are provided with this paper.

Code availability

Code underlying the network model is available at
<https://github.com/rutalaboratory/LC10NetworkModel>.

References

1. 1.

Kimura, K., Hachiya, T., Koganezawa, M., Tazawa, T. & Yamamoto, D. Fruitless and doublesex coordinate to generate male-specific neurons that can initiate courtship. *Neuron* **59**, 759–769 (2008).

[CAS](#) [PubMed](#) [Article](#) [PubMed Central](#) [Google Scholar](#)

2. 2.

von Philipsborn, A. C. et al. Neuronal control of *Drosophila* courtship song. *Neuron* **69**, 509–522 (2011).

[Article](#) [CAS](#) [Google Scholar](#)

3. 3.

Yamamoto, D. & Koganezawa, M. Genes and circuits of courtship behaviour in *Drosophila* males. *Nat. Rev. Neurosci.* **14**, 681–692 (2013).

[CAS](#) [PubMed](#) [Article](#) [PubMed Central](#) [Google Scholar](#)

4. 4.

Yu, J. Y., Kanai, M. I., Demir, E., Jefferis, G. S. X. E. & Dickson, B. J. Cellular organization of the neural circuit that drives *Drosophila* courtship behavior. *Curr. Biol.* **20**, 1602–1614 (2010).

[CAS](#) [PubMed](#) [Article](#) [PubMed Central](#) [Google Scholar](#)

5. 5.

Pan, Y., Meissner, G. W. & Baker, B. S. Joint control of *Drosophila* male courtship behavior by motion cues and activation of male-specific P1 neurons. *Proc. Natl Acad. Sci. USA* **109**, 10065–10070 (2012).

[CAS](#) [PubMed](#) [PubMed Central](#) [Article](#) [ADS](#) [Google Scholar](#)

6. 6.

Bastock, M. & Manning, A. The courtship of *Drosophila melanogaster*. *Behaviour* **8**, 85–111 (1955).

[Article](#) [Google Scholar](#)

7. 7.

Spieth, H. T. Courtship behavior in *Drosophila*. *Annu. Rev. Entomol.* **19**, 385–405 (1974).

[CAS](#) [PubMed](#) [Article](#) [PubMed Central](#) [Google Scholar](#)

8. 8.

Kohatsu, S. & Yamamoto, D. Visually induced initiation of *Drosophila* innate courtship-like following pursuit is mediated by central excitatory state. *Nat. Commun.* **6**, 6457 (2015).

[CAS](#) [PubMed](#) [Article](#) [ADS](#) [PubMed Central](#) [Google Scholar](#)

9. 9.

Seeholzer, L. F., Seppo, M., Stern, D. L. & Ruta, V. Evolution of a central neural circuit underlies *Drosophila* mate preferences. *Nature* **559**, 564–569 (2018).

[CAS](#) [PubMed](#) [PubMed Central](#) [Article](#) [ADS](#) [Google Scholar](#)

10. 10.

Clowney, E. J., Iguchi, S., Bussell, J. J., Scheer, E. & Ruta, V. Multimodal chemosensory circuits controlling male courtship in *Drosophila*. *Neuron* **87**, 1036–1049 (2015).

[CAS](#) [PubMed](#) [PubMed Central](#) [Article](#) [Google Scholar](#)

11. 11.

Kallman, B. R., Kim, H. & Scott, K. Excitation and inhibition onto central courtship neurons biases *Drosophila* mate choice. *eLife* **4**, e11188 (2015).

[PubMed](#) [PubMed Central](#) [Article](#) [Google Scholar](#)

12. 12.

Zhang, S. X., Miner, L. E., Boutros, C. L., Rogulja, D. & Crickmore, M. A. Motivation, perception, and chance converge to make a binary decision. *Neuron* **99**, 376–388.e6 (2018).

[CAS](#) [PubMed](#) [PubMed Central](#) [Article](#) [Google Scholar](#)

13. 13.

Bath, D. E. et al. FlyMAD: rapid thermogenetic control of neuronal activity in freely walking *Drosophila*. *Nat. Methods* **11**, 756–762 (2014).

[CAS](#) [PubMed](#) [Article](#) [PubMed Central](#) [Google Scholar](#)

14. 14.

Inagaki, H. K. et al. Optogenetic control of *Drosophila* using a red-shifted channelrhodopsin reveals experience-dependent influences on courtship. *Nat. Methods* **11**, 325–332 (2014).

[CAS](#) [PubMed](#) [Article](#) [PubMed Central](#) [Google Scholar](#)

15. 15.

Hoopfer, E. D., Jung, Y., Inagaki, H. K., Rubin, G. M. & Anderson, D. J. P1 interneurons promote a persistent internal state that enhances inter-male aggression in *Drosophila*. *eLife* **4**, e11346 (2015).

[PubMed](#) [PubMed Central](#) [Article](#) [Google Scholar](#)

16. 16.

Götz, K. G. & Wenking, H. Visual control of locomotion in the walking fruitfly *Drosophila*. *J. Comp. Physiol.* **85**, 235–266 (1973).

[Article](#) [Google Scholar](#)

17. 17.

Agrawal, S., Safarik, S. & Dickinson, M. The relative roles of vision and chemosensation in mate recognition of *Drosophila melanogaster*. *J. Exp. Biol.* **217**, 2796–2805 (2014).

[PubMed](#) [PubMed Central](#) [Google Scholar](#)

18. 18.

Billeter, J.-C., Atallah, J., Krupp, J. J., Millar, J. G. & Levine, J. D. Specialized cells tag sexual and species identity in *Drosophila melanogaster*. *Nature* **461**, 987–991 (2009).

[CAS](#) [PubMed](#) [Article](#) [ADS](#) [PubMed Central](#) [Google Scholar](#)

19. 19.

Zhang, S. X., Rogulja, D. & Crickmore, M. A. Dopaminergic circuitry underlying mating drive. *Neuron* **91**, 168–181 (2016).

[CAS](#) [PubMed](#) [Article](#) [PubMed Central](#) [Google Scholar](#)

20. 20.

Ribeiro, I. M. A. et al. Visual projection neurons mediating directed courtship in *Drosophila*. *Cell* **174**, 607–621.e18 (2018).

[CAS](#) [PubMed](#) [Article](#) [PubMed Central](#) [Google Scholar](#)

21. 21.

Wu, M. et al. Visual projection neurons in the *Drosophila* lobula link feature detection to distinct behavioral programs. *eLife* **5**, e21022 (2016).

[PubMed](#) [PubMed Central](#) [Article](#) [Google Scholar](#)

22. 22.

Otsuna, H. & Ito, K. Systematic analysis of the visual projection neurons of *Drosophila melanogaster*. I. Lobula-specific pathways. *J. Comp. Neurol.* **497**, 928–958 (2006).

[PubMed](#) [Article](#) [PubMed Central](#) [Google Scholar](#)

23. 23.

Scheffer, L. K. et al. A connectome and analysis of the adult *Drosophila* central brain. *eLife* **9**, e57443 (2020).

[CAS](#) [PubMed](#) [PubMed Central](#) [Article](#) [Google Scholar](#)

24. 24.

Talay, M. et al. Transsynaptic mapping of second-order taste neurons in flies by trans-Tango. *Neuron* **96**, 783–795.e4 (2017).

[CAS](#) [PubMed](#) [PubMed Central](#) [Article](#) [Google Scholar](#)

25. 25.

Namiki, S., Dickinson, M. H., Wong, A. M., Korff, W. & Card, G. M. The functional organization of descending sensory-motor pathways in *Drosophila*. *eLife* **7**, e34272 (2018).

[PubMed](#) [PubMed Central](#) [Article](#) [Google Scholar](#)

26. 26.

Schretter, C. E. et al. Cell types and neuronal circuitry underlying female aggression in *Drosophila*. *eLife* **9**, e58942 (2020).

[CAS](#) [PubMed](#) [PubMed Central](#) [Article](#) [Google Scholar](#)

27. 27.

Rayshubskiy, A. et al. Neural circuit mechanisms for steering control in walking *Drosophila*. Preprint at <https://doi.org/10.1101/2020.04.04.204703> (2020).

28. 28.

Heisenberg, M. & Wolf, R. *Vision in Drosophila: Genetics of Microbehavior* (Springer, 1984).

29. 29.

Land, M. F. & Collett, T. S. Chasing behaviour of houseflies (*Fannia canicularis*): a description and analysis. *J. Comp. Physiol.* **89**, 331–357 (1974).

[Article](#) [Google Scholar](#)

30. 30.

Wehrhahn, C., Poggio, T. & Bülthoff, H. Tracking and chasing in houseflies (*Musca*): an analysis of 3-D flight trajectories. *Biol. Cybern.* **45**, 123–130 (1982).

[Article](#) [Google Scholar](#)

31. 31.

Soto-Yéber, L., Soto-Ortiz, J., Godoy, P. & Godoy-Herrera, R. The behavior of adult *Drosophila* in the wild. *PLoS ONE* **13**, e0209917 (2018).

[PubMed](#) [PubMed Central](#) [Article](#) [Google Scholar](#)

32. 32.

Trivers, R. in *Sexual Selection and the Descent of Man, 1871–1971* (Aldine, 1972).

33. 33.

Kohatsu, S., Koganezawa, M. & Yamamoto, D. Female contact activates male-specific interneurons that trigger stereotypic courtship behavior in *Drosophila*. *Neuron* **69**, 498–508 (2011).

[CAS](#) [PubMed](#) [Article](#) [PubMed Central](#) [Google Scholar](#)

34. 34.

Tinbergen, N. *The Study of Instinct* (Clarendon, 1951).

35. 35.

Klapoetke, N. C. et al. Independent optical excitation of distinct neural populations. *Nat. Methods* **11**, 338–346 (2014).

[CAS](#) [PubMed](#) [PubMed Central](#) [Article](#) [Google Scholar](#)

36. 36.

Chen, T.-W. et al. Ultrasensitive fluorescent proteins for imaging neuronal activity. *Nature* **499**, 295–300 (2013).

[CAS](#) [PubMed](#) [PubMed Central](#) [Article](#) [ADS](#) [Google Scholar](#)

37. 37.

Mohammad, F. et al. Optogenetic inhibition of behavior with anion channelrhodopsins. *Nat. Methods* **14**, 271–274 (2017).

[CAS](#) [Article](#) [Google Scholar](#)

38. 38.

Dana, H. et al. High-performance calcium sensors for imaging activity in neuronal populations and microcompartments. *Nat. Methods* **16**, 649–657 (2019).

[CAS](#) [PubMed](#) [Article](#) [PubMed Central](#) [Google Scholar](#)

39. 39.

Eyjolfsdottir, E. et al. Detecting social actions of fruit flies. In *Computer Vision — ECCV 2014* (eds. Fleet, D., Pajdla, T., Schiele, B. & Tuytelaars, T.) vol. 8690, 772–787 (Springer, 2014).

40. 40.

Maimon, G., Straw, A. D. & Dickinson, M. H. Active flight increases the gain of visual motion processing in *Drosophila*. *Nat. Neurosci.* **13**,

393–399 (2010).

[CAS](#) [PubMed](#) [Article](#) [PubMed Central](#) [Google Scholar](#)

41. 41.

Green, J. et al. A neural circuit architecture for angular integration in *Drosophila*. *Nature* **546**, 101–106 (2017).

[CAS](#) [PubMed](#) [PubMed Central](#) [Article](#) [ADS](#) [Google Scholar](#)

42. 42.

Seelig, J. D. & Jayaraman, V. Neural dynamics for landmark orientation and angular path integration. *Nature* **521**, 186–191 (2015).

[CAS](#) [PubMed](#) [PubMed Central](#) [Article](#) [ADS](#) [Google Scholar](#)

43. 43.

Moore, R. J. D. et al. FicTrac: a visual method for tracking spherical motion and generating fictive animal paths. *J. Neurosci. Methods* **225**, 106–119 (2014).

[PubMed](#) [Article](#) [PubMed Central](#) [Google Scholar](#)

44. 44.

Aronov, D. & Tank, D. W. Engagement of neural circuits underlying 2D spatial navigation in a rodent virtual reality system. *Neuron* **84**, 442–456 (2014).

[CAS](#) [PubMed](#) [PubMed Central](#) [Article](#) [Google Scholar](#)

45. 45.

Berens, P. CircStat: a Matlab toolbox for circular statistics. *J. Stat. Softw.* **31**, 1–21 (2009).

[Article](#) [Google Scholar](#)

46. 46.

Nojima, T. et al. A sex-specific switch between visual and olfactory inputs underlies adaptive sex differences in behavior. *Curr. Biol.* **31**, 1175–1191.e6 (2021).

[CAS](#) [PubMed](#) [PubMed Central](#) [Article](#) [Google Scholar](#)

47. 47.

Pnevmatikakis, E. A. & Giovannucci, A. NoRMCorre: an online algorithm for piecewise rigid motion correction of calcium imaging data. *J. Neurosci. Methods* **291**, 83–94 (2017).

[CAS](#) [PubMed](#) [Article](#) [PubMed Central](#) [Google Scholar](#)

48. 48.

Giovannucci, A. et al. CaImAn an open source tool for scalable calcium imaging data analysis. *eLife* **8**, e38173 (2019).

[PubMed](#) [PubMed Central](#) [Article](#) [Google Scholar](#)

49. 49.

Dayan, P. & Abbott, L. F. *Theoretical Neuroscience: Computational and Mathematical Modeling of Neural Systems* (Massachusetts Institute of Technology Press, 2001).

50. 50.

Friedrich, J. & Paninski, L. Fast active set methods for online spike inference from calcium imaging. In *Advances in Neural Information Processing Systems* 29 (eds. Lee, D. D., Sugiyama, M., Luxburg, U. V., Guyon, I. & Garnett, R.) 1984–1992 (2016).

51. 51.

Clements, J. et al. neuPrint: analysis tools for EM connectomics. Preprint at <https://doi.org/10.1101/2020.01.16.909465> (2020).

[Download references](#)

Acknowledgements

We thank K. Kuchibhotla, B. Noro, L. Abbott, S. R. Datta, R. Coleman, and P. Brand for comments on the manuscript; I. Ribeiro for discussions and sharing the LC10a split-GAL4 and LC10a-LexA driver lines; Y. Aso for LexAop-GCaMP6s/UAS-CsChrimson flies; J. Weisman and G. Maimon for sharing their designs for an integrated, projector-based system for presenting tethered, walking flies with visual stimuli in advance of publication; R. Coleman, I. Morantte, A. Siliciano, J. Petrillo, and Rockefeller Precision Instrumentation Technologies for technical advice; and G. Maimon, C. Bargmann, L. Abbott, and members of the Ruta laboratory for discussion. Stocks obtained from the Bloomington *Drosophila* Stock Center, NIH P40OD018537 were used in this study. This work was supported by the Simons Collaboration on the Global Brain, a Reem-Kayden Award, grant 5R35NS111611 from the National Institute of Health to V.R., a David Rockefeller Fellowship and National Science Foundation Graduate Research Fellowship Program to T.H.S., and an HHMI Hanna H. Gray Fellowship to A.O.

Author information

Affiliations

1. Laboratory of Neurophysiology and Behavior, The Rockefeller University, New York, NY, USA

Tom Hindmarsh Sten, Rufei Li, Adriane Otopalik & Vanessa Ruta

Authors

1. Tom Hindmarsh Sten

[View author publications](#)

You can also search for this author in [PubMed](#) [Google Scholar](#)

2. Rufei Li

[View author publications](#)

You can also search for this author in [PubMed](#) [Google Scholar](#)

3. Adriane Otopalik

[View author publications](#)

You can also search for this author in [PubMed](#) [Google Scholar](#)

4. Vanessa Ruta

[View author publications](#)

You can also search for this author in [PubMed](#) [Google Scholar](#)

Contributions

T.H.S. and V.R. conceived of and designed the study. T.H.S. and R.L. performed tethered behavioural experiments. A.O. carried out the free courtship assays in Fig. 4. T.H.S. performed and analysed functional imaging experiments. T.H.S. designed and implemented the model. T.H.S. and V.R. analysed data and wrote the manuscript with input from R.L and A.O.

Corresponding author

Correspondence to [Vanessa Ruta](#).

Ethics declarations

Competing interests

The authors declare no competing interests.

Additional information

Peer review information *Nature* thanks Michael Reiser and the other, anonymous, reviewer(s) for their contribution to the peer review of this work. Peer reviewer reports are available.

Publisher's note Springer Nature remains neutral with regard to jurisdictional claims in published maps and institutional affiliations.

Extended data figures and tables

[Extended Data Fig. 1 A virtual reality preparation for tethered courtship.](#)

a, Schematic of virtual reality preparation. Tethered male flies are placed on an air-cushioned foam ball, whose rotational velocity along all three axes is read out by a single camera via the FicTrac software. During closed-loop experiments, the male's position in the virtual world is updated on the basis of these rotations, as is the position of the target stimulus on the screen. Changes in the 2D world are mapped to a conical screen and projected by way of a mirror from above. Hardware design by J. Weisman and G. Maimon. **b**, Schematic of the stimulus presentation during two-photon imaging. Owing to the sterics of the objective, the stimulus is rear-projected onto the screen instead of being projected from above as in **a**.

[Extended Data Fig. 2 Tethered courtship in an open 2D virtual world.](#)

a, Pseudocolour images of a courting male fly during activation of P1 neurons when the visual target is on his left (top), on his right (bottom), or in front of him (middle) showing ipsilateral wing extensions characteristic of courtship song. **b**, Top, position of the male and autonomously moving fictive female in the 2D world during P1 activation over the course of 200 s. Bottom, histogram of the distance between the male and female target during closed-loop courtship. Note that the male is prevented from bringing the stimulus closer than about 10 mm from his position in the virtual world.

c, As in **b** but for a wild-type male. The increased jitter in the ‘female’ trajectory results from the target frequently reaching the maximum distance from the male and subsequently approaching him along a straight path. **d**, Top, representative example of the 2D positions of the male and female in a freely courting pair of animals. Bottom, histogram of the distance between the male and female fly. **e**, Density plot of the relative position of fictive females with respect to the courting male during P1 activation. **f**, As in **e** but for a wild-type male. **g**, Density plot of the location of the female relative to the male in freely courting pairs of animals. Details of statistical analyses and sample sizes are given in Supplementary Table 1.

Source data

Extended Data Fig. 3 The behaviour of aroused animals.

a, Schematic illustrating our definition of the vigour and fidelity of a male’s courtship pursuit. Vigour is quantified as the total turning in the direction of the visual target (normalized within-animal), while fidelity is the correlation between the visual target and the male’s turning. **b**, Representative example of the vigour, fidelity, and tracking index over the course of a courtship trial. P1 activation is denoted by red line. The male is classified as courting when $TI > 0.3$, and as disengaged when $TI < 0.3$ but he remains primed to reinitiate courtship pursuit. **c**, Comparison of the tracking fidelity, tracking vigour, and tracking index across animals. Each dot represents one frame; black lines indicate zero on axes. **d**, Distribution of tracking fidelity, tracking vigour, and tracking indices across animals, before (black) and after (red) brief activation of P1 neurons. $TI > 0.3$ was used as a cut-off to indicate courting males. **e**, **f**, Distribution of linear speeds (**e**) and angular speeds (**f**) during courtship trials. Lines indicate the thresholds used for denoting animals as ‘moving’ (for example, Fig. 3d,e). **g**, Distribution of the duration of bouts of courtship (black) and bouts of disengagement (grey) after transient P1 activation. **h**, Distributions of the angular velocity exhibited by animals that are actively courting (black), that are disengaged (dark grey), or that are passively watching the visual stimulus before P1 activation (light grey). **i**, As in **h** but for linear speeds. **j**, Probability that an animal that is currently courting will transition to disengagement in any given second, plotted over the course of a trial in 10-s bins (red line denotes

P1 activation). **k**, Probability that an animal that is disengaged will transition to courtship in any given second, plotted over the course of a trial in 10-s bins (red line denotes P1 activation). Details of statistical analyses and sample sizes are given in Supplementary Table 1.

[Source data](#)

[Extended Data Fig. 4 Acute and enduring regulation of courtship arousal.](#)

a, Heading of a courting male before, during, and after the visual target was transiently removed from the screen (30 s). Courtship arousal was induced by a 3-s optogenetic activation of P1 neurons expressing CsChrimson 60 s before stimulus removal. **b**, Average tracking index of males during trials where stimulus was removed (mean \pm s.e.m.). P1 neurons were transiently activated for 3 s, 1 min after the visual target began to oscillate, and target was temporarily removed from the screen for 30 s 1 min after P1 activation. **c**, Schematic of the preparation allowing male to sample gustatory pheromones to trigger courtship. The male fly was provided with the abdomen of a virgin female to taste with his foreleg while the visual target oscillated on the screen in front of him. **d**, Example of a male's heading during a courtship trial, before and after the male tapped the female abdomen with his foreleg (black line indicates tap). Each row consists of three stimulus cycles. **e**, Pseudocolour image of a male fly sampling the pheromones on a female abdomen. **f**, Maximal tracking index (right) and duration between the first and last detected bouts of courtship (left) during tapping-induced courtship trials. **g**, Representative example of male turning during interleaved presentations of either a female target (black line) or a wide-field grating turning in the clockwise (CW, grey) or anticlockwise (counterclockwise; CCW, burgundy) before (left) or during (right) optogenetic activation of P1 neurons. **h**, Average male turning in response to three cycles of the oscillating female target before (black) or during (red) activation of P1 neurons. **i**, Average male turning in response to the wide-field grating rotating in the clockwise (grey) or anticlockwise (burgundy) direction before (black) or during (red) activation of P1 neurons. Note that unlike responses to the 'female' target in (**h**), optomotor responses were not enhanced during P1 activation. **j**, Two-dimensional path of the dynamic

visual target used for inducing spontaneous courtship. **k**, **l**, Angular position (**k**) and angular size (**l**) of the dynamic visual target subtended on the male retina over the course of a 10 min trial. **m**, Duration between the first and last detected bouts of courtship for trials induced by optogenetic activation of P1 neurons or spontaneously initiated (left), and the maximum tracking fidelity (middle) and vigour (right) displayed by animals in the two conditions. **n**, Average turning response during courtship in trials where courtship was induced by activation of P1 neurons (left) or spontaneously initiated (right). **o**, Fraction of males actively engaged in courtship (TI > 0.3) over the course of a 10-min trial in P1-induced trials (left) and spontaneously initiated trials (right). Dashed lines indicate LED onset (red) or the onset of visual motion (right). All shaded line plots are mean ± s.e.m.; * $P < 0.05$; n.s., $P > 0.05$; details of statistical analyses and sample sizes are given in Supplementary Table 1.

Source data

Extended Data Fig. 5 P1 neurons are dynamic but strongly correlated to the intensity of courtship pursuit.

a, The average activity of P1 neurons ($\Delta F/F_0$) plotted against the position of the ‘female’ visual target. Thin grey lines are individual animals, black line is the average across animals. **b**, Correlation between P1 activity ($\Delta F/F_0$) and the tracking fidelity, tracking vigour, and tracking index (T.I.) of males. Individual data points are individual animals. **c**, P1 activity ($\Delta F/F_0$) plotted against tracking index at the onset of courtship (first 60 s; left) and for the remainder of the trial (right). **d**, Top, average response of P1 neurons aligned to the onset of courtship. Bottom, average tracking index aligned to the onset of courtship. Note that P1 activity is disproportionately elevated in the first few seconds, indicating that it may reflect additional aspects of the male’s internal state or behaviour that we are not measuring. **e**, Maximum P1 activity observed across animals as a function of time since courtship initiation. **f**, Maximum tracking index observed across animals as a function of time since courtship initiation. **g**, Average correlation between P1 activity ($\Delta F/F_0$) and the tracking index across animals as a function of time since courtship initiation. All shaded line plots are mean ± s.e.m.;

**** $P < 0.0001$, * $P < 0.05$; details of statistical analyses and sample sizes are given in Supplementary Table 1.

[Source data](#)

Extended Data Fig. 6 P1 neuron activity is uncorrelated with the motor implementation of courtship.

a, Schematic of preparation for evoking optomotor responses using wide-field motion (top), and the turning responses of animals presented with alternating-direction wide-field motion. **b**, Example of a male's turning during an optomotor trial. Each row consists of three stimulus cycles. Purple bars indicate when the grating is rotating. **c**, Example of the functional response ($\Delta F/F_0$) of P1 neurons during an optomotor trial, before and during periods when the grating turned, as well as the angular velocity and linear speed of the animal. **d**, Histogram of angular velocities observed during courtship trials (grey) and during optomotor trials (purple). **e**, Histogram of linear speeds observed during courtship trials (grey) and during optomotor trials (purple). **f–i**, Scatter plots of P1 activity against the tracking index (**f**), stimulus position (**g**), linear speed (**h**) and angular velocity (**i**) of all animals during courtship trials. **j**, Correlation between P1 activity and the parameters explored in **f–i** during courtship trials. Individual data points are animals. **k–n**, Scatter plots of P1 activity against the optomotor tracking index (**k**), velocity of the grating (**l**), linear speed (**m**) and angular velocity (**n**) of all animals during optomotor trials. **o**, Correlation between P1 activity and the parameters explored in **k–n** during optomotor trials. Individual data points are animals. All shaded line plots are mean \pm s.e.m.; * $P < 0.05$, ** $P < 0.01$, *** $P < 0.001$, **** $P < 0.0001$. Details of statistical analyses and group sizes are given in Supplementary Table 1.

[Source data](#)

Extended Data Fig. 7 LC10a signalling is necessary and amplified during courtship.

a, Schematic of LC10a neurons expressing GtACR1 with approximate ROIs used for silencing (or sham-silencing) in a single hemisphere. **b**, Average turning of one male to the visual stimulus during silencing of LC10a neurons in the right hemisphere versus sham trials. Note that male fails to execute turns in the direction ipsilateral to silencing. **c**, Average turning in the directions ipsilateral and contralateral to the hemisphere where LC10a was silenced, compared to sham trials. **d**, Image of LC10a axon terminals expressing jGCaMP7f in the AOTu. **e**, Example of functional response ($\Delta F/F_0$) of LC10a neurons expressing jGCaMP7f during a courtship. Note that, in contrast to recordings made using GCaMP6s (Fig. 2b), calcium transients return to baseline in between responses with this faster indicator. **f**, Average evoked LC10a responses ($\Delta F/F_0$) to one stimulus cycle for animals expressing GCaMP6s versus jGCaMP7f. **g**, Average change in LC10a gain (distance between peak and trough of evoked responses) for animals expressing GCaMP6s versus jGCaMP7f. **h**, Example of LC10a functional responses during courtship versus during a later period of undirected running with similar linear speed. All shaded line plots are mean \pm s.e.m.; n.s., $P > 0.05$; ** $P < 0.01$. Details of statistical analyses and group sizes are given in Supplementary Table 1.

Source data

Extended Data Fig. 8 LC10a gain can be dissociated from the motor implementation of courtship pursuit.

a, b, Histograms of the linear speeds (a) and angular velocities (b) exhibited by animals in periods classified as courtship versus periods classified as ‘moving’. **c**, Average evoked LC10a activity ($\Delta F/F_0$) when the stimulus swept across the ipsilateral hemifield versus the average linear speed of animals in the same time period, colour coded by the average tracking index during the sweep. Red line is the linear fit. **d, e**, As in c but plotted against the average angular speed (d) or average tracking index (e) exhibited by animals. **f**, Correlations between LC10a activity and the linear speed, angular speed, and tracking index exhibited by animals. Individual data points denote individual animals. **g**, Left, schematic of animal being presented with two identical ‘female’ targets, moving in opposition and thus

yielding identical stimulation to both eyes. Middle, example of LC10a functional responses plotted against the position of a single target (top) and animal turning responses (bottom). Right: as for middle, but later in the trial when the animal was presented with two opposing targets. P1 neurons were activated continuously. Note that LC10a neurons responded even when the male failed to turn ipsilaterally when two targets were present. **h**, Average LC10a activity during presentation of two opposing visual targets (top). **i**, Left, average evoked LC10a activity during ipsilateral sweeps of the visual target versus the total turning exhibited in the direction of the visual target during the same period. Right, average evoked LC10a activity during ipsilateral sweeps of either of the two visual targets versus the total turning exhibited in the direction of the visual target during the same period. **j**, Correlation between LC10a evoked responses and ipsilateral turning. Individual data points denote individual animals. **k**, Average peak-normalized responses ($\Delta F/F_0$) of LC10b/c neurons during courtship versus during locomotion. **l**, As in **k** but for LC10d neurons. **m**, **n**, Average evoked LC10a functional response ($\Delta F/F_0$, **k**) and average evoked ipsiversive turning (**n**) as a function of the average angular size of the visual target on each stimulus cycle. All shaded line plots are mean \pm s.e.m.; n.s., $P > 0.05$; * $P < 0.05$, ** $P < 0.01$, *** $P < 0.001$. Details of statistical analyses and group sizes are given in Supplementary Table 1.

Source data

Extended Data Fig. 9 LC10a neurons exhibit sparse and selective connectivity in the central brain.

a, Examples of identified LC10a, LC10b, LC10c, and LC10d neurons in the female hemi-brain connectome²³. **b**, Morphology of all identified LC10a-d neurons ($n = 248$). **c**, Correlation matrix of the outputs from all LC10 neurons, sorted by their assigned subtype. Note that individual subtypes have strongly correlated outputs that are largely distinct from the output patterns of other subtypes. **d**, t-SNE plot of the output connectivity matrix of all identified LC10 neurons, labelled according to the manually assigned subtype. The output connectivity naturally segregates LC10 neurons into four groups. **e**, **f**, Same as **c**, **d** but based on the input connections to LC10

neurons in the AOTu. **g**, Morphology of all non-visual output neurons from LC10a neurons with at least 10 synaptic connections, grouped by projections to the LALs (left) versus to the inferior bridge (IB; right). **h**, As in **g** but for non-visual input neurons to LC10a neurons in the AOTu. **i**, Representative example of trans-synaptic tracing of LC10a neurons in the male using trans-Tango²⁴. Magenta denotes labelled LC10a neurons, and cyan the labelled postsynaptic partners. Similar results were obtained across four male brains. **j**, Histogram of synaptic weights between all LC10a neurons and their postsynaptic partners. **k**, Number of input and output synapses to and from LC10a neurons from the 10 most common brain regions (superior intermediate protocerebrum (SIP), lateral accessory lobe (LAL), superior medial protocerebrum (SMP), inferior bridge (IB), superior posterior slope (SPS), posterior ventrolateral protocerebrum (PVLP), posteriolateral protocerebrum (PLP), superior medial protocerebrum (SMP), wedge (WED)). R and L indicate the right and left hemisphere, respectively.

[Source data](#)

[**Extended Data Fig. 10 P1 neurons enhance the gain of LC10a neurons.**](#)

a, Left, schematic of synchronous recordings from P1 neurons in the LPC and LC10a neurons in the AOTu. Middle, cross-covariance of P1 neuron activity and LC10a activity during spontaneous courtship trial. Right, as for middle, but zoomed in to highlight that P1 neuron activity leads LC10a activity. Maximum covariance occurred at lag of -500 ms. **b**, LC10a responses to presentation of a 10° sweeping dot in the progressive or regressive direction before and during activation of P1 neurons. Top, average LC10a response during presentation of a regressively (orange) or progressively (blue) moving stimulus in the absence of P1 activation. Bottom, average LC10a response during presentation of a regressively (orange) or progressively (blue) moving stimulus in the presence of P1 activation. **c–e**, As in **b** but for a sweeping 25° sphere (**c**), a sweeping 10° wide tall bar (**d**), or an approaching sphere expanding from 10° at $20^\circ/\text{s}$ (**e**). Red indicates P1 stimulation and black indicates pre-stimulation baseline throughout. **f**, Response modulation index (see [Methods](#)) for each stimulus

presented before and during P1 activation, indicating that responses to the distinct visual stimuli are near-uniformly enhanced. **g**, Average evoked ipsilateral turning in response to progressive motion of the different targets during P1 activation, plotted against the average evoked LC10a response in the same period. Note that turning responses evoked by the motion of these diverse stimuli were proportional to the magnitude of LC10a evoked calcium transients: sweeping dots evoked the strongest turns, bars evoked much weaker turns, and slowly looming spheres did not elicit any turning on average, presumably because both eyes were stimulated equally. **h**, Average evoked linear speed in response to progressive motion of the different targets during P1 activation, plotted against the average evoked LC10a response in the same period. **i**, Direction selectivity index (see [Methods](#)) for sweeping stimuli presented during baseline recordings or during continuous P1 activation. Positive values indicate a preference for progressive motion, negative values indicate preference for regressive motion. All shaded line plots are mean \pm s.e.m.; n.s., $P > 0.05$. Details of statistical analyses and sample sizes are given in Supplementary Table [1](#).

[Source data](#)

[**Extended Data Fig. 11 Motion-direction selectivity during courtship pursuit.**](#)

a, Left, example image of LC10a–LexA axon terminals in the AOTu, with 48 ROIs of strongly correlated pixels automatically selected using the CaImAn-CNMF framework⁴⁸ overlayed. Right, as for left, but with ROIs colour-coded according to their exhibited direction selectivity index (positive values indicate a preference for progressive motion, negative values indicate preference for regressive motion). **b**, Heat map of the average evoked responses to progressive (right) and regressive (left) sweeps of the 25° sphere during P1 activation for the 48 ROIs shown in **a**. Each row represents the average evoked fluorescence across 10 trials for each ROI. **c**, Average evoked responses to a progressively versus regressively moving 25° dot across all ROIs from all animals (300 ROIs across 7 males). **d**, Direction selectivity index for all ROIs across animals (see [Methods](#)). Black line denotes zero; positive values indicate a selectivity for progressive motion, negative values indicate a selectivity for regressive

motion. **e**, Top, schematic of monocular stimulation. ‘Female’ targets were presented to one eye alone, and moved in either the regressive or progressive direction with respect to that eye with a 5-s ISI. Bottom, average turning of males in response to monocular stimuli moving regressively (left) or progressively (right). **f**, Turning responses of LC10a circuit model without motion-direction selectivity, with regressive-motion selectivity, and with progressive-motion selectivity. **g**, Left, normalized LC10a receptive fields with varying rise-times (κ , see [Methods](#)). Right, correlation between predicted and actual responses to the simple stimulus in **f** for the receptive fields shown to the left. **h**, From left: average turning response to a single stimulus cycle; predicted response from full model to a single stimulus cycle; predicted response of a model with no binocular overlap; predicted response of a model not selective for progressive versus regressive motion. **i**, Example of predicted versus actual turning response to two targets with a drifting phase-offset (as in Fig. [4d](#)) across the courtship trial. Black line indicates when first target is present, grey line indicates when the second target is present. **j**, Left, average correlation between stimulus 1 and predicted turning (cyan) during dual dot presentations. Right, average correlation between stimulus 1 and the turning of males during dual dot presentations. In grey is what the correlation to stimulus 1 would be if the animal perfectly tracked stimulus 2. Positive x -values indicate that the first stimulus leads in phase. All shaded line plots are mean \pm s.e.m.; ** P < 0.01, *** P < 0.0001. Details of statistical analyses and sample sizes are given in Supplementary Table [1](#).

[Source data](#)

[**Extended Data Fig. 12 Network model predicts turning dynamics of freely courting males.**](#)

a, Examples of predicted versus actual turning of freely courting males over the first 100 s of courtship. **b**, Frame-by-frame predicted versus actual male turning over the course of the full courtship trials for the pairs shown in **a** (5–10 min); red line shows the linear fit. Details of statistical analyses and sample sizes are given in Supplementary Table [1](#).

[Source data](#)

Extended Data Fig. 13 Incorporating P1 neural activity improves model performance.

a, Hit rate (fraction of predicted turns accompanied by a real turn; true positive rate) and false-alarm rate (fraction of predicted turns not accompanied by a real turn; false positive rate) of the naive model (lacking P1 input) versus when input current to LC10a neurons is scaled by the functional responses of P1 neurons. **b**, Example of the predicted turning over a courtship trial by a model lacking P1 input (as in Fig. 4a) in which input current to LC10a neurons is consistently high. **c, d**, Two examples of actual (left) versus predicted (middle) turning responses when the activity of P1 neurons (right) is incorporated into the model. Compare to model without P1 input in **b**. Black lines indicate when stimulus is oscillating. Details of statistical analyses and sample sizes are given in Supplementary Table 1.

[Source data](#)

Supplementary information

Supplementary Tables

This file contains Supplementary Tables 1-2.

Reporting Summary

Video 1

Tethered males court a fictive female target. Representative example of a male courting a virtual ‘female’ target in closed loop during continuous optogenetic activation of P1 neurons. Note frequent unilateral wing-extensions, indicating production of courtship song.

Video 2

Males effectively pursue the female target in closed-loop. Representative example of the visual stimulus presented to a male courting a virtual ‘female’ target in closed loop during continuous optogenetic activation of P1 neurons. Female moves autonomously from the male in the virtual world. Note that the male efficiently centers the ‘female’ target in his field-of-view, and actively brings it closer to him in the virtual world.

Video 3

Transient activation of P1 neurons drives sustained courtship. Representative example of a male presented with a simple, repeating visual target before and after P1 neurons are optogenetically activated. Blue line indicates the integrated path of the male. Note the stimulus can be observed as a dark target in the background, and that the male readily exhibits unilateral wing-extensions in the direction ipsilateral to the target after P1 neurons have been activated.

Video 4

A dynamic visual target for evoking spontaneous courtship. Example of the translating visual stimulus used to drive males to spontaneously initiate courtship. The target traverses a steady arc but appears to advance and recede.

Video 5

Males spontaneously initiate courtship towards a dynamic visual target. Representative example of a male spontaneously initiating courtship towards the translating visual stimulus shown in Supplementary Video 4, with his trajectory and unilateral wing extensions shown. Note that the male does not exhibit any structured turning before the visual stimulus is presented, and the performance of alternating unilateral wing-extensions, early during the courtship bout. Faithful tracking persists after the male stops performing wing-extensions.

Video 6

Two visual targets with a drifting phase relationship. Example of the two-target stimulus presented to males, with one target moving slightly slower than the other, causing the phase-relationship between the two to drift over time. 2x playback.

[Video 7](#)

An LC10a network model predicts the behaviour of freely courting males. Three examples of the actual versus predicted paths of how a male pursues a female target in two dimensions. Pink dot is the trajectory of the real female fly; blue dot is the trajectory of the real male fly; green is the trajectory of a simulated fly. The simulated fly is initialized at the same position as the real male fly and matches its linear velocity to that of the real female fly.

[Peer Review File](#)

Source data

[Source Data Fig. 1](#)

[Source Data Fig. 2](#)

[Source Data Fig. 3](#)

[Source Data Fig. 4](#)

[Source Data Extended Data Fig. 2](#)

[Source Data Extended Data Fig. 3](#)

[Source Data Extended Data Fig. 4](#)

[Source Data Extended Data Fig. 5](#)

[**Source Data Extended Data Fig. 6**](#)

[**Source Data Extended Data Fig. 7**](#)

[**Source Data Extended Data Fig. 8**](#)

[**Source Data Extended Data Fig. 9**](#)

[**Source Data Extended Data Fig. 10**](#)

[**Source Data Extended Data Fig. 11**](#)

[**Source Data Extended Data Fig. 12**](#)

[**Source Data Extended Data Fig. 13**](#)

Rights and permissions

[Reprints and Permissions](#)

About this article



Check for
updates

Cite this article

Hindmarsh Sten, T., Li, R., Otopalik, A. *et al.* Sexual arousal gates visual processing during *Drosophila* courtship. *Nature* **595**, 549–553 (2021).
<https://doi.org/10.1038/s41586-021-03714-w>

[Download citation](#)

- Received: 04 September 2020
- Accepted: 09 June 2021
- Published: 07 July 2021
- Issue Date: 22 July 2021
- DOI: <https://doi.org/10.1038/s41586-021-03714-w>

Comments

By submitting a comment you agree to abide by our [Terms](#) and [Community Guidelines](#). If you find something abusive or that does not comply with our terms or guidelines please flag it as inappropriate.

[Access through your institution](#)

[Change institution](#)

[Buy or subscribe](#)

Advertisement

This article was downloaded by **calibre** from <https://www.nature.com/articles/s41586-021-03714-w>

| [Section menu](#) | [Main menu](#) |

- Article
- [Published: 23 June 2021](#)

Molecular logic of cellular diversification in the mouse cerebral cortex

- [Daniela J. Di Bella](#) ORCID: [orcid.org/0000-0001-6141-3704^{1,2 na1}](https://orcid.org/0000-0001-6141-3704),
- [Ehsan Habibi](#) ORCID: [orcid.org/0000-0002-7208-7999^{1,3 na1}](https://orcid.org/0000-0002-7208-7999),
- [Robert R. Stickels](#) ORCID: [orcid.org/0000-0003-4326-4084²](https://orcid.org/0000-0003-4326-4084),
- [Gabriele Scalia](#) ORCID: [orcid.org/0000-0003-3305-9220³](https://orcid.org/0000-0003-3305-9220),
- [Juliana Brown^{1,2}](#),
- [Payman Yadollahpour](#) ORCID: [orcid.org/0000-0003-1984-5014³](https://orcid.org/0000-0003-1984-5014),
- [Sung Min Yang](#) ORCID: [orcid.org/0000-0003-4318-2011^{1,2}](https://orcid.org/0000-0003-4318-2011),
- [Catherine Abbate^{1,2}](#),
- [Tommaso Biancalani](#) ORCID: [orcid.org/0000-0001-9104-9755^{3 nAff5}](https://orcid.org/0000-0001-9104-9755),
- [Evan Z. Macosko](#) ORCID: [orcid.org/0000-0002-2794-5165²](https://orcid.org/0000-0002-2794-5165),
- [Fei Chen^{1,2}](#),
- [Aviv Regev](#) ORCID: [orcid.org/0000-0003-3293-3158^{3,4 na2 nAff5}](https://orcid.org/0000-0003-3293-3158) &
- [Paola Arlotta](#) ^{1,2 na2}

Nature volume **595**, pages 554–559 (2021) [Cite this article](#)

- 14k Accesses
- 230 Altmetric
- [Metrics details](#)

Subjects

- [Cell fate and cell lineage](#)
- [Developmental neurogenesis](#)

Abstract

The mammalian cerebral cortex has an unparalleled diversity of cell types, which are generated during development through a series of temporally orchestrated events that are under tight evolutionary constraint and are critical for proper cortical assembly and function^{1,2}. However, the molecular logic that governs the establishment and organization of cortical cell types remains unknown, largely due to the large number of cell classes that undergo dynamic cell-state transitions over extended developmental timelines. Here we generate a comprehensive atlas of the developing mouse neocortex, using single-cell RNA sequencing and single-cell assay for transposase-accessible chromatin using sequencing. We sampled the neocortex every day throughout embryonic corticogenesis and at early postnatal ages, and complemented the sequencing data with a spatial transcriptomics time course. We computationally reconstruct developmental trajectories across the diversity of cortical cell classes, and infer their spatial organization and the gene regulatory programs that accompany their lineage bifurcation decisions and differentiation trajectories. Finally, we demonstrate how this developmental map pinpoints the origin of lineage-specific developmental abnormalities that are linked to aberrant corticogenesis in mutant mice. The data provide a global picture of the regulatory mechanisms that govern cellular diversification in the neocortex.

Access options

Subscribe to Journal

Get full journal access for 1 year

\$199.00

only \$3.90 per issue

[Subscribe](#)

All prices are NET prices.
VAT will be added later in the checkout.
Tax calculation will be finalised during checkout.

Rent or Buy article

Get time limited or full article access on ReadCube.

from \$8.99

[Rent or Buy](#)

All prices are NET prices.

Additional access options:

- [Log in](#)
- [Access through your institution](#)
- [Learn about institutional subscriptions](#)

Fig. 1: Comprehensive atlas of mouse cortical development.

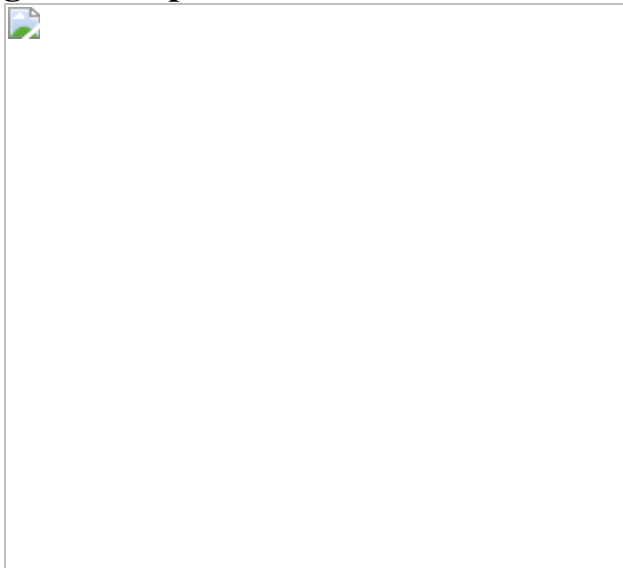


Fig. 2: Spatial distribution of cell types in the developing cortex.

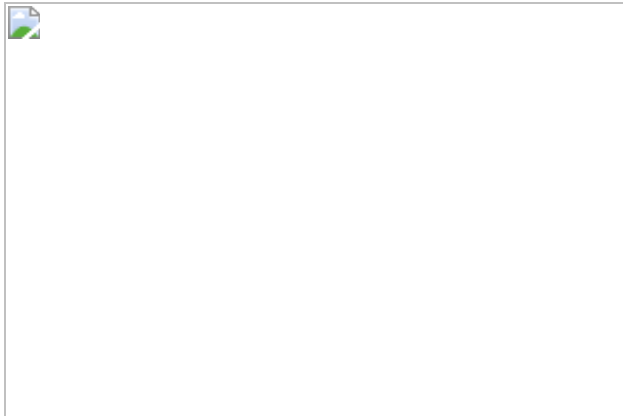


Fig. 3: Molecular developmental trajectories of neocortical cell types.

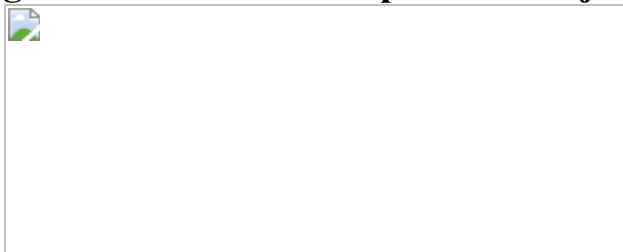


Fig. 4: scATAC-seq landscape of the developing neocortex.



Fig. 5: FEZF2 prevents the acquisition of callosal identity in CFuPN.

Data availability

The datasets generated during the current study are available in the Gene Expression Omnibus (GEO SuperSeries [GSE153164](#)) and at the Single Cell Portal:

https://singlecell.broadinstitute.org/single_cell/study/SCP1290/molecular-logic-of-cellular-diversification-in-the-mammalian-cerebral-cortex.

Code availability

R markdown scripts enabling the main steps of analysis are available on a GitHub repository

<https://github.com/ehsanhabibi/MolecularLogicMouseNeoCortex>.

References

1. 1.

Lodato, S. & Arlotta, P. Generating neuronal diversity in the mammalian cerebral cortex. *Annu. Rev. Cell Dev. Biol.* **31**, 699–720 (2015).

[CAS](#) [PubMed](#) [PubMed Central](#) [Article](#) [Google Scholar](#)

2. 2.

Greig, L. C., Woodworth, M. B., Galazo, M. J., Padmanabhan, H. & Macklis, J. D. Molecular logic of neocortical projection neuron specification, development and diversity. *Nat. Rev. Neurosci.* **14**, 755–769 (2013).

[CAS](#) [PubMed](#) [Article](#) [Google Scholar](#)

3. 3.

Yuzwa, S. A. et al. Developmental emergence of adult neural stem cells as revealed by single-cell transcriptional profiling. *Cell Rep.* **21**,

3970–3986 (2017).

[CAS](#) [PubMed](#) [Article](#) [Google Scholar](#)

4. 4.

Frazer, S. et al. Transcriptomic and anatomic parcellation of 5-HT_{3A}R expressing cortical interneuron subtypes revealed by single-cell RNA sequencing. *Nat. Commun.* **8**, 14219 (2017).

[CAS](#) [PubMed](#) [PubMed Central](#) [Article](#) [ADS](#) [Google Scholar](#)

5. 5.

Mayer, C. et al. Developmental diversification of cortical inhibitory interneurons. *Nature* **555**, 457–462 (2018).

[CAS](#) [PubMed](#) [PubMed Central](#) [Article](#) [ADS](#) [Google Scholar](#)

6. 6.

Bielle, F. et al. Multiple origins of Cajal–Retzius cells at the borders of the developing pallium. *Nat. Neurosci.* **8**, 1002–1012 (2005).

[CAS](#) [PubMed](#) [Article](#) [Google Scholar](#)

7. 7.

Stickels, R. R. et al. Highly sensitive spatial transcriptomics at near-cellular resolution with Slide-seqV2. *Nat. Biotechnol.* **39**, 313–319 (2021).

[CAS](#) [PubMed](#) [Article](#) [Google Scholar](#)

8. 8.

Biancalani, T. et al. Deep learning and alignment of spatially-resolved whole transcriptomes of single cells in the mouse brain with Tangram. Preprint at <https://doi.org/10.1101/2020.08.29.272831> (2020).

9. 9.

Kim, E. J., Juavinett, A. L., Kyubwa, E. M., Jacobs, M. W. & Callaway, E. M. Three types of cortical layer 5 neurons that differ in brain-wide connectivity and function. *Neuron* **88**, 1253–1267 (2015).

[CAS](#) [PubMed](#) [PubMed Central](#) [Article](#) [Google Scholar](#)

10. 10.

Tasic, B. et al. Shared and distinct transcriptomic cell types across neocortical areas. *Nature* **563**, 72–78 (2018).

[CAS](#) [PubMed](#) [PubMed Central](#) [Article](#) [ADS](#) [Google Scholar](#)

11. 11.

Allen Cell Types Database. http://celltypes.brain-map.org/rnaseq/mouse_ctx-hip_smart-seq (Allen Institute for Brain Science, 2015).

12. 12.

Farrell, J. A. et al. Single-cell reconstruction of developmental trajectories during zebrafish embryogenesis. *Science* **360**, eaar3131 (2018).

[PubMed](#) [PubMed Central](#) [Article](#) [CAS](#) [Google Scholar](#)

13. 13.

Arlotta, P. et al. Neuronal subtype-specific genes that control corticospinal motor neuron development in vivo. *Neuron* **45**, 207–221 (2005).

[CAS](#) [PubMed](#) [Article](#) [Google Scholar](#)

14. 14.

Florio, M. & Huttner, W. B. Neural progenitors, neurogenesis and the evolution of the neocortex. *Development* **141**, 2182–2194 (2014).

[CAS](#) [Article](#) [PubMed](#) [Google Scholar](#)

15. 15.

Jhas, S. et al. Hes6 inhibits astrocyte differentiation and promotes neurogenesis through different mechanisms. *J. Neurosci.* **26**, 11061–11071 (2006).

[CAS](#) [PubMed](#) [PubMed Central](#) [Article](#) [Google Scholar](#)

16. 16.

Malatesta, P. & Götz, M. Radial glia – from boring cables to stem cell stars. *Development* **140**, 483–486 (2013).

[CAS](#) [PubMed](#) [Article](#) [Google Scholar](#)

17. 17.

Telley, L. et al. Temporal patterning of apical progenitors and their daughter neurons in the developing neocortex. *Science* **364**, eaav2522 (2019).

[CAS](#) [Article](#) [PubMed](#) [Google Scholar](#)

18. 18.

Llorca, A. et al. A stochastic framework of neurogenesis underlies the assembly of neocortical cytoarchitecture. *eLife* **8**, e51381 (2019).

[CAS](#) [PubMed](#) [PubMed Central](#) [Article](#) [Google Scholar](#)

19. 19.

Guo, C. et al. Fezf2 expression identifies a multipotent progenitor for neocortical projection neurons, astrocytes, and oligodendrocytes.

Neuron **80**, 1167–1174 (2013).

[CAS](#) [PubMed](#) [Article](#) [Google Scholar](#)

20. 20.

Gao, P. et al. Deterministic progenitor behavior and unitary production of neurons in the neocortex. *Cell* **159**, 775–788 (2014).

[CAS](#) [PubMed](#) [PubMed Central](#) [Article](#) [Google Scholar](#)

21. 21.

Franco, S. J. et al. Fate-restricted neural progenitors in the mammalian cerebral cortex. *Science* **337**, 746–749 (2012).

[CAS](#) [PubMed](#) [PubMed Central](#) [Article](#) [ADS](#) [Google Scholar](#)

22. 22.

Zahr, S. K. et al. A translational repression complex in developing mammalian neural stem cells that regulates neuronal specification. *Neuron* **97**, 520–537.e6 (2018).

[CAS](#) [PubMed](#) [Article](#) [Google Scholar](#)

23. 23.

Thompson, C. L. et al. A high-resolution spatiotemporal atlas of gene expression of the developing mouse brain. *Neuron* **83**, 309–323 (2014).

[CAS](#) [PubMed](#) [PubMed Central](#) [Article](#) [Google Scholar](#)

24. 24.

Molyneaux, B. J. et al. DeCoN: genome-wide analysis of in vivo transcriptional dynamics during pyramidal neuron fate selection in neocortex. *Neuron* **85**, 275–288 (2015).

[CAS](#) [PubMed](#) [Article](#) [Google Scholar](#)

25. 25.

Dixit, A. et al. Perturb-seq: dissecting molecular circuits with scalable single-cell RNA profiling of pooled genetic screens. *Cell* **167**, 1853–1866 (2016).

[CAS](#) [PubMed](#) [PubMed Central](#) [Article](#) [Google Scholar](#)

26. 26.

Preissl, S. et al. Single-nucleus analysis of accessible chromatin in developing mouse forebrain reveals cell-type-specific transcriptional regulation. *Nat. Neurosci.* **21**, 432–439 (2018).

[CAS](#) [PubMed](#) [PubMed Central](#) [Article](#) [Google Scholar](#)

27. 27.

Ma, S. et al. Chromatin potential identified by shared single-cell profiling of RNA and chromatin. *Cell* **183**, 1103–1116 (2020).

[CAS](#) [Article](#) [Google Scholar](#)

28. 28.

Urquhart, J. E. et al. DMRTA2 (*DMRT5*) is mutated in a novel cortical brain malformation. *Clin. Genet.* **89**, 724–727 (2016).

[CAS](#) [PubMed](#) [Article](#) [Google Scholar](#)

29. 29.

Cubelos, B. et al. *Cux1* and *Cux2* regulate dendritic branching, spine morphology, and synapses of the upper layer neurons of the cortex. *Neuron* **66**, 523–535 (2010).

[CAS](#) [PubMed](#) [PubMed Central](#) [Article](#) [Google Scholar](#)

30. 30.

Lodato, S. et al. Excitatory projection neuron subtypes control the distribution of local inhibitory interneurons in the cerebral cortex. *Neuron* **69**, 763–779 (2011).

[CAS](#) [PubMed](#) [PubMed Central](#) [Article](#) [Google Scholar](#)

31. 31.

Molyneaux, B. J., Arlotta, P., Hirata, T., Hibi, M. & Macklis, J. D. *Fezl* is required for the birth and specification of corticospinal motor neurons. *Neuron* **47**, 817–831 (2005).

[CAS](#) [PubMed](#) [Article](#) [Google Scholar](#)

32. 32.

Chen, B., Schaevitz, L. R. & McConnell, S. K. *Fezl* regulates the differentiation and axon targeting of layer 5 subcortical projection neurons in cerebral cortex. *Proc. Natl Acad. Sci. USA* **102**, 17184–17189 (2005).

[CAS](#) [PubMed](#) [PubMed Central](#) [Article](#) [ADS](#) [Google Scholar](#)

33. 33.

Lodato, S. et al. Gene co-regulation by *Fezf2* selects neurotransmitter identity and connectivity of corticospinal neurons. *Nat. Neurosci.* **17**, 1046–1054 (2014).

[CAS](#) [PubMed](#) [PubMed Central](#) [Article](#) [Google Scholar](#)

34. 34.

Hirata, T. et al. Zinc finger gene *fez-like* functions in the formation of subplate neurons and thalamocortical axons. *Dev. Dyn.* **230**, 546–556 (2004).

[CAS](#) [PubMed](#) [Article](#) [Google Scholar](#)

35. 35.

Loo, L. et al. Single-cell transcriptomic analysis of mouse neocortical development. *Nat. Commun.* **10**, 134 (2019).

[PubMed](#) [PubMed Central](#) [Article](#) [ADS](#) [CAS](#) [Google Scholar](#)

36. 36.

10x Genomics. *Nuclei Isolation for Single Cell ATAC Sequencing*. Demonstrated Protocol CG000169 (10x Genomics, 2019).

37. 37.

Fleming, S. J., Marioni, J. C. & Babadi, M. CellBender remove-background: a deep generative model for unsupervised removal of background noise from scRNA-seq datasets. Preprint at <https://doi.org/10.1101/791699> (2019).

38. 38.

Stuart, T. et al. Comprehensive integration of single-cell data. *Cell* **177**, 1888–1902 (2019).

[CAS](#) [PubMed](#) [PubMed Central](#) [Article](#) [Google Scholar](#)

39. 39.

Kowalczyk, M. S. et al. Single-cell RNA-seq reveals changes in cell cycle and differentiation programs upon aging of hematopoietic stem cells. *Genome Res.* **25**, 1860–1872 (2015).

[CAS](#) [PubMed](#) [PubMed Central](#) [Article](#) [Google Scholar](#)

40. 40.

Blondel, V. D., Guillaume, J.-L., Lambiotte, R., Lefebvre, E. Fast unfolding of communities in large networks. *J. Stat. Mech.* P10008 (2008).

41. 41.

McGinnis, C. S., Murrow, L. M. & Gartner, Z. J. DoubletFinder: doublet detection in single-cell RNA sequencing data using artificial nearest neighbors. *Cell Syst.* **8**, 329–337 (2019).

[CAS](#) [PubMed](#) [PubMed Central](#) [Article](#) [Google Scholar](#)

42. 42.

Wolock, S. L., Lopez, R. & Klein, A. M. Scrublet: computational identification of cell doublets in single-cell transcriptomic data. *Cell Syst.* **8**, 281–291 (2019).

[CAS](#) [PubMed](#) [PubMed Central](#) [Article](#) [Google Scholar](#)

43. 43.

Dobin, A. et al. STAR: ultrafast universal RNA-seq aligner. *Bioinformatics* **29**, 15–21 (2013).

[CAS](#) [PubMed](#) [Article](#) [Google Scholar](#)

44. 44.

Angerer, P. et al. destiny: diffusion maps for large-scale single-cell data in R. *Bioinformatics* **32**, 1241–1243 (2016).

[CAS](#) [PubMed](#) [Article](#) [Google Scholar](#)

45. 45.

Bergen, V., Lange, M., Peidli, S., Wolf, F. A. & Theis, F. J. Generalizing RNA velocity to transient cell states through dynamical modeling. *Nat. Biotechnol.* **38**, 1408–1414 (2020).

[PubMed](#) [Article](#) [CAS](#) [Google Scholar](#)

46. 46.

Haghverdi, L., Büttner, M., Wolf, F. A., Buettner, F. & Theis, F. J. Diffusion pseudotime robustly reconstructs lineage branching. *Nat. Methods* **13**, 845–848 (2016).

[CAS](#) [PubMed](#) [Article](#) [Google Scholar](#)

47. 47.

Cao, J. et al. The single-cell transcriptional landscape of mammalian organogenesis. *Nature* **566**, 496–502 (2019).

[CAS](#) [PubMed](#) [PubMed Central](#) [Article](#) [ADS](#) [Google Scholar](#)

48. 48.

Stuart, T., Srivastava, A., Lareau, C. & Satija, R. Multimodal single-cell chromatin analysis with Signac. Preprint at <https://doi.org/10.1101/2020.11.09.373613> (2020).

49. 49.

Dong, M. et al. SCDC: bulk gene expression deconvolution by multiple single-cell RNA sequencing references. *Brief. Bioinform.* **22**, 416–427 (2021).

[PubMed](#) [Article](#) [Google Scholar](#)

50. 50.

Tan, Y. & Cahan, P. SingleCellNet: a computational tool to classify single cell RNA-seq data across platforms and across species. *Cell Syst.* **9**, 207–213 (2019).

[CAS](#) [PubMed](#) [PubMed Central](#) [Article](#) [Google Scholar](#)

51. 51.

Yu, G., Wang, L. G., Han, Y. & He, Q. Y. clusterProfiler: an R package for comparing biological themes among gene clusters. *OMICS* **16**, 284–287 (2012).

[CAS](#) [PubMed](#) [PubMed Central](#) [Article](#) [Google Scholar](#)

52. 52.

DeCoN. <http://decon.fas.harvard.edu/pyramidal/> (2014).

53. 53.

Allen Developing Mouse Brain Atlas. <http://developingmouse.brain-map.org/> (Allen Institute for Brain Science, 2008).

[Download references](#)

Acknowledgements

We thank former and present members of the Arlotta and Regev laboratories for discussions and editing of the manuscript. This work was supported by grants from the Stanley Center for Psychiatric Research, the Broad Institute of MIT and Harvard to P.A., grants from the National Institutes of Health (P50MH094271, U19MH114821 and R01NS103758 to P.A., and DP5OD024583 to F.C.), and grants from The Klarman Cell Observatory, HHMI and NHGRI Center for Cell Circuits CEGS to A.R. D.J.D. was supported by the Pew Latin American Postdoctoral Fellowship.

Author information

Author notes

1. Tommasso Biancalani & Aviv Regev

Present address: Genentech, South San Francisco, CA, USA

2. These authors contributed equally: Daniela J. Di Bella, Ehsan Habibi
3. These authors jointly supervised this work: Aviv Regev, Paola Arlotta

Affiliations

1. Department of Stem Cell and Regenerative Biology, Harvard University, Cambridge, MA, USA

Daniela J. Di Bella, Ehsan Habibi, Juliana Brown, Sung Min Yang, Catherine Abbate, Fei Chen & Paola Arlotta

2. Stanley Center for Psychiatric Research, Broad Institute of MIT and Harvard, Cambridge, MA, USA

Daniela J. Di Bella, Robert R. Stickels, Juliana Brown, Sung Min Yang, Catherine Abbate, Evan Z. Macosko, Fei Chen & Paola Arlotta

3. Klarman Cell Observatory, Broad Institute of MIT and Harvard, Cambridge, MA, USA

Ehsan Habibi, Gabriele Scalia, Payman Yadollahpour, Tommasso Biancalani & Aviv Regev

4. Howard Hughes Medical Institute, Koch Institute of Integrative Cancer Research, Department of Biology, Massachusetts Institute of Technology, Cambridge, MA, USA

Aviv Regev

Authors

1. Daniela J. Di Bella
[View author publications](#)

You can also search for this author in [PubMed](#) [Google Scholar](#)

2. Ehsan Habibi
[View author publications](#)

You can also search for this author in [PubMed](#) [Google Scholar](#)

3. Robert R. Stickels

[View author publications](#)

You can also search for this author in [PubMed](#) [Google Scholar](#)

4. Gabriele Scalia

[View author publications](#)

You can also search for this author in [PubMed](#) [Google Scholar](#)

5. Juliana Brown

[View author publications](#)

You can also search for this author in [PubMed](#) [Google Scholar](#)

6. Payman Yadollahpour

[View author publications](#)

You can also search for this author in [PubMed](#) [Google Scholar](#)

7. Sung Min Yang

[View author publications](#)

You can also search for this author in [PubMed](#) [Google Scholar](#)

8. Catherine Abbate

[View author publications](#)

You can also search for this author in [PubMed](#) [Google Scholar](#)

9. Tommasso Biancalani

[View author publications](#)

You can also search for this author in [PubMed](#) [Google Scholar](#)

10. Evan Z. Macosko

[View author publications](#)

You can also search for this author in [PubMed](#) [Google Scholar](#)

11. Fei Chen

[View author publications](#)

You can also search for this author in [PubMed](#) [Google Scholar](#)

12. Aviv Regev

[View author publications](#)

You can also search for this author in [PubMed](#) [Google Scholar](#)

13. Paola Arlotta

[View author publications](#)

You can also search for this author in [PubMed](#) [Google Scholar](#)

Contributions

P.A., D.J.D., E.H. and A.R. conceived the experiments. D.J.D. and E.H. performed all the experiments and analysed data with help from P.Y. and S.M.Y. D.J.D. performed and analysed *in situ* hybridizations with help from C.A. R.R.S. performed Slide-seq experiments with help from D.J.D., F.C. and E.Z.M. G.S. and T.B. performed all Tangram analyses. P.A., D.J.D., E.H., J.B. and A.R. wrote the manuscript with contributions from all authors. All authors read and approved the final manuscript.

Corresponding authors

Correspondence to [Aviv Regev](#) or [Paola Arlotta](#).

Ethics declarations

Competing interests

P.A. is a scientific advisory board member for System 1 Biosciences and Foresite Labs and is a co-founder of Serqet Therapeutics. A.R. is a co-

founder of and an equity holder in Celsius Therapeutics, an equity holder in Immunitas, and until 31 July 2020 was a scientific advisory board member of Thermo Fisher Scientific, Syros Pharmaceuticals, Asimov and Neogene Therapeutics. Since 1 August 2020, A.R. has been an employee of Genentech/Roche. Since 1 February 2021, T.B. has been an employee of Genentech. Since 1 January 2021, G.S. has been an employee of Roche.

Additional information

Peer review information *Nature* thanks Debra Silver, Fabian Theis and the other, anonymous, reviewer(s) for their contribution to the peer review of this work.

Publisher's note Springer Nature remains neutral with regard to jurisdictional claims in published maps and institutional affiliations.

Extended data figures and tables

[Extended Data Fig. 1 Classification of cell types in scRNA-seq data from individual time points.](#)

Related to Fig. 1. **a**, Number of replicates, total number of embryos, sex of mice and number of cells analysed per time point. **b**, Number of genes, number of mRNA molecules (counts) and percentage of mitochondrial counts per cell in each time point. **c**, Proportion of cells corresponding to the different cell types present in each time point. 85–98% of cells were successfully identified for each time point. The earliest stages were primarily composed of apical and intermediate progenitors: AP + IP = 77% at E10.5, 80% at E11.5, 69% at E12.5, 66% at E13.5. **d**, Correlation between male (M, *Xist* expression < 1) and female (F, *Xist* expression > 1) cells at E12.5 and E18.5 in selected cell types. Pearson correlation coefficients are indicated. Distinct genes include X-chromosome genes *Xist* and *Tsix* and Y-chromosome genes *Ddx3y* and *Eif2s3y*. Some haemoglobin genes also appear distinct, but, as shown in **e** they constitute few outlier cells. **e**, Normalized expression levels of some of distinct genes between male and female cells at E18.5. Only two cell types are shown for clarity. **f**,

UMAP visualization of cells collected at each time point, showing expression levels (normalized) of marker genes for dorsal derivatives (*Emx1*), apical progenitors (*Sox2*), intermediate progenitors (*Eomes*), excitatory neurons (*Neurod2*, *Fezf2*, *Satb2*), inhibitory interneurons (*Dlx2*) and glial cells (*Apoe*).

Extended Data Fig. 2 Molecular signatures and interneuron heterogeneity in the developing cerebral cortex.

Related to Fig. 1. **a**, Selective expression (normalized) of marker genes per cell type in the combined scRNA-seq dataset. Cell types are grouped on the basis of their identity and shared marker genes. **b**, Gene signatures for all cell types identified in the combined time points. Top 20 differentially expressed genes for each cell type are presented. Cells were down-sampled to a maximum of 500 cells per cell type. **c**, Expression of canonical marker genes for selected cell types in the UMAP visualization of the combined scRNA-seq time course. **d**, Different subtypes of interneuron integrate into the developing cortex through time. Left, clustering of interneurons collected at all time points, visualized via UMAP. Middle, interneuron UMAP plots show the expression of the inhibitory markers *Dlx2* and *Gad2*, as well as a marker of dorsally-derived cell types (*Emx1*), not expressed by interneurons. Right, proportion of cells corresponding to each cluster in each time point. **e**, Expression of genes characteristic of interneurons of different embryonic origins. Medial ganglionic eminence (MGE)-derived interneurons express *Npy*, *Sst*, *Lhx6* and *Nxph1*. Interneurons originating in the CGE (caudal ganglionic eminence) are positive for *Htr3a*, *Prox1*, *Cxcl14* and *Sp8*. A second population of *Htr3a*⁺ interneurons express *Meis2*, *Etv1* and *Sp8*, putatively from the pallial–subpallial (P–SP) boundary.

Extended Data Fig. 3 Spatial mappings of cell types in the developing cerebral cortex.

Related to Fig. 2. **a**, Scheme summarizing the approach to map cell types from the scRNA-seq developmental atlas onto matching tissue spatial transcriptomes (Slide-seq v2) using Tangram⁸. **b**, Mapping of extended cell

types from the scRNA-seq data onto the matching Slide-seq section. Beads are coloured according to the probability of the cell type being mapped in that position. **c**, Gene expression of characteristic genes validating cell types matched for each time point. **d**, Cell-type assignment in the deep layers of P1 cortex shows accurate distribution. Beads are coloured according to the cell type with highest mapping probability. Right, summed probabilities across bins parallel to the ventricular surface (normalized to maximum value). **e**, Mapping probabilities for the deep layer cell types grouped by the cell type assigned (cell type with highest probability) corresponding to **d**. In box plots the middle line is the median, the lower and upper hinges correspond to the 25% and 75% quantiles, the upper whisker corresponds to the largest value no larger than $1.5 \times \text{IQR}$ from the hinge (where IQR is the interquartile range) and the lower whisker corresponds to the smallest value at most $1.5 \times \text{IQR}$ of the lower hinge. Total number of beads = 812. **f**, Gene expression in E15.5 scRNA-seq data of genes associated with the migrating neuron substates identified in Fig. [2b](#).

[Extended Data Fig. 4 Consistent ordering of cells in developmental trajectories and characterization of branching tree of cortical development.](#)

Related to Fig. [3](#). **a**, UMAP visualizations of the scRNA-seq data from combined time points, with cells coloured by pseudotime inferred by different methods. Left to right: URD pseudotime, Monocle3 pseudotime^{[47](#)}, Latent time from sc-Velo^{[45](#)}, Diffusion pseudotime (DPT)^{[46](#)}, and Velocity pseudotime^{[45](#)}. Purple represents earlier cells in the trajectory, while yellow labels later cells. Grey indicates cells that were excluded from the trajectory. **b**, Correlation (red, low; white, high) for all cells between URD pseudotime values and pseudotime calculated by the specified method. R coefficient and P value of the Pearson correlation is stated. **c**, UMAP visualization of the cells used for trajectory building (same as cells used for Fig. [3a](#) and related figures) coloured by cell type (left) and pseudotime (right), on which a developmental trajectory was calculated using Monocle3. A similar branching structure was found. Although it did not allow for finer segregation of the terminal neuronal types, Monocle3

ascribed a unique trajectory going from progenitors to all classes of neurons, with a post-mitotic branching into CPN and CFuPN branches (arrows, similar to URD). **d**, Gene expression along trajectories calculated with URD (right) or Monocle3 (left). **e**, URD trajectory branching tree of the developing cortex. Cells are coloured according to their developmental time of collection. **f, g**, Normalized fraction of cells corresponding to each time point of collection (**f**) and to each cell type (**g**) across binned pseudotime, showing that pseudotime is aligned with age and cell type (compare with Fig. [1c](#)).

[Extended Data Fig. 5 Neuronal cell types diverge post-mitotically.](#)

Related to Fig. [3](#). **a**, Branching trees showing the expression of marker genes of apical progenitors (*Sox2*, *Hes5*), intermediate progenitors (*Eomes*) and excitatory neurons (*Neurod2*), as well as genes characteristic of the dorsally-derived cortical cell types, including callosal neurons (*Satb2*, *Cux2*), layer 4 stellate neurons (*Rorb*), corticofugal neurons (*Fezf2*, *Tle4*, *Pcp4*, *Tcerg1l*), putative near-projecting neurons (*Tshz2*), astrocytes (*Slc1a3*, *Aqp4*, *Aldh1l1*), and ependymocytes (*Foxj1*). There is a sequential progression of apical progenitors, intermediate progenitors and excitatory neurons, followed by neuronal subtypes, astrocytes and ependymocytes. **b, c**, Force-directed layout embedding representation of the developmental branching tree, showing the initial part of the tree. Cells are coloured according to their pseudotime value (left), age of collection (middle), or cell type (right). Differentially expressed genes between AP in each branch are highlighted and their expression levels are shown in **c** (see also Supplementary Table [2](#)). AP corresponding to the astrocytic and neuronal branches form a continuum of cells. **d**, Tangram mapping probabilities of E13.5 AP from each branch onto matching Slide-seq section show that both states coexist in the ventricular zone. Arrowheads and arrows in the inset show probabilities in individual beads. **e**, Top, apical progenitors from different ages form a continuum of cells and do not segregate into distinct clusters. AP from all time points were sub-clustered separately, coloured by age (left) and clusters identified by Seurat (right). Bottom, a similar effect is observed when both apical and intermediate progenitors were sub-clustered, cells first separate mostly by cell type (right), and then continuously by time

point (left). **f**, Expression of CPN markers (*Satb2*, *Pou3f3* and *Cux1*, left), and CFuPN markers (*Fezf2*, *Tle4* and *Bcl11b*, right) in both early (E12.5) and late (E15.5) AP, as well as in the combined AP populations (all time points), when AP were co-embedded using the top 100 differentially expressed genes between CFuPN and CPN as input for principal component analysis and downstream clustering and visualization. Cell-type marker genes are expressed in progenitors but do not drive clustering of the cells. **g**, Separation in different classes of neurons occurs post-mitotically. Branching tree and UMAP representation of the full developmental atlas coloured by cell-cycle phase, as predicted by gene expression. **h**, Tangram mapping of layer 5 and 6 CPN on P1 Slide-seq section. P1 cells allocated to each of the two terminal branches broadly labelled as layer 5&6 CPN were mapped onto the Slide-seq P1 section to find their distribution in the developing cortex. Mapping probabilities (top) indicated that cells from branch 1 were more likely to be mapped to layer 5, while cells from branch 2 mapped with enrichment to layer 6. Genes differentially expressed between both populations, layer 5- (*Rorb*, *Fam19a2*) and layer 6-CPN markers (*Cdh13*, *Igsf21*, *Gnb4*) show matching distribution (bottom).

Extended Data Fig. 6 Novel expression pattern of selected genes and NMF gene modules.

Related to Fig. 3. **a–d**, New expression patterns emerging from the inferred tree. Expression levels overlaid on the tree (left), UMAP of full scRNA-seq developmental data (middle), and Slide-seq counts on an E15.5 or P1 section of cortex (right) for each gene. **a**, *Rorb* is expressed in developing CFuPN, astrocytes and layer 4 stellate neurons and present in the deep cortical plate (CP). **b**, *Pcp4* is expressed in migrating and immature neurons that contribute to both CPN and CFuPN, as well as in SCPN, layer 6b, NP and Cajal–Retzius cells (CR), and is found in the intermediate zone (IZ) and CP. **c**, *Npy* is expressed in CFuPN and highly in CPN of layers 5 and 6. A positive *Npy* signal is evident in the deep CP through Slide-seq. **d**, *Cck* was also detected in CFuPN and at higher levels in CPN of layers 5 and 6. Low levels of expression in the CP were detected via Slide-seq. VZ, ventricular zone. **e**, Validation of expression of novel cell-type-specific genes emerging from the cascade analysis. Expression levels overlaid on the tree (left), time course expression on purified subtypes of PN from DeCoN transcriptomic

resource^{24,52} (middle), and in situ hybridization from the Allen Developing Mouse Brain Atlas^{23,53} (right, age indicated in figure). **f**, Complete set of gene programs of connected modules found by NMF. Each circular node represents a module. Modules are horizontally aligned to the developmental stage that the module was computed from, and coloured by the annotated function (see also Supplementary Table 3). **g**, Scaled expression overlaid on branching tree of modules corresponding to broad neuronal differentiation programs, coloured according to program identity. **h**, Selected NMF modules expression from scRNA-seq data mapped onto time-matched Slide-seq section using Tangram (Methods).

Extended Data Fig. 7 Genetic cascades accompanying the development of cortical cell types.

Related to Fig. 3. Gene cascades for projection neuron subtypes, astrocytes and ependymocytes differentiation. The *x* axis represents pseudotime across the tree. Each row is a gene in which gene expression is scaled to the maximum observed expression and then smoothed. Genes are ordered by the pseudotime value at which they enter and then leave ‘peak’ expression (expression 50% higher than minimum value), and start and then leave ‘expression’ (expression 20% higher than minimum value), in that order. Smoothing of expression values was performed using spline fitting from URD for expression dynamics (Methods). Known marker genes for the cell type are labelled; see Supplementary Table 3 for the full list of genes.

Extended Data Fig. 8 Extended analysis of genes distinguishing between branches in URD tree.

Related to Fig. 3. **a**, Feature importance (0.5 power transformed, dot size) and average expression of genes predicted to be involved in cell-type divergence (row-scaled, colour). Top 10 genes per branch, ranked by their Friedman MSE score (importance) for distinguishing between cells in one branch versus cells in sibling and parent branch. The colour bar at the top indicates branch-points marked on the tree to the left. Genes in red correspond to TFs. Expression in parent branch not shown. **b**, Gene Ontology analysis showing molecular function enrichment among genes

involved in branch-points as determined in **a**. **c**, Simplified URD branching trees on which average gene expression within a segment and a pseudotime bin is overlaid on the tree structure, showing restricted expression patterns of genes identified in **a**.

Extended Data Fig. 9 Characterization of scATAC-seq atlas and developmental trajectories of accessible elements through cortical development.

Related to Fig. 4. **a**, scATAC-seq data per time point. UMAP visualization of the single cells coloured by their predicted identity from integration with scRNA-seq datasets (left). Gene accessibility of selected markers for main cell types present in each time point (middle). Maximum prediction score for each cell based on labels transferred from scRNA-seq data (right). **b**, URD chromatin accessibility trajectories during cortical development. Cells are coloured according to their age of collection. **c**, ATAC trees highlighting the accessibility of marker genes characteristic of the different cortical cell types, including apical and intermediate progenitors, astrocytes, callosal and corticofugal neurons. **d**, RNA-based tree generated from only the E13.5, E15.5 and E18.5 time points, corresponding to the scATAC-seq data. Trees are coloured by cell type (left) and time of collection (right). **e**, Chromatin accessibility and gene expression cascades for layers 2&3 CPN and SCPN. Same genes are plotted for both modalities, in the same order. **f**, Chromatin accessibility and gene expression across pseudotime for illustrative genes from the SCPN cascade, CPN markers, or general neuronal markers plotted on the SCPN cascade. In many cases accessibility rises before gene expression.

Extended Data Fig. 10 Transcription factors with binding sites enriched along cortical development.

Related to Fig. 4. **a**, Total number of accessible sites identified per time point and fraction that is dynamic across cell types (that is, is enriched in at least one cell type). **b**, Left, schematic of the approach used to identify candidate cell-type-specific enhancers. Differential expression analysis identified cell-type-specific genes, for which we calculated co-accessibility

(correlation higher than 25%) between distal elements (within a 100 kb region) and target gene promoters using Cicero, within each cell type. **c**, Distal elements co-accessible with the *Pcp4* promoter region in E18.5 SCPN and migrating neurons. Cicero co-accessibility is shown in blue curves, detected peaks in each cell type are shown as coloured bars. Black bars correspond to promoter peak, blue bars are peaks selectively co-accessible in CFuPN, and purple bars are peaks only co-accessible in migrating neurons. Boxes indicate TFs for which motifs are present in indicated peaks. Peaks are aligned to coverage plots (bottom) showing combined ATAC reads for the indicated cell types. Chromosome coordinates and genes are indicated at bottom. **d**, TF binding sites enrichment on accessible sites of cells in the CPN vs CFuPN branch-point (see Fig. 3d) shows significant enrichment of some of the TF detected in Fig. 3d, suggesting an actual role in this step. **e**, Left, in situ hybridization against *Eomes* (IP marker), *Ube2c* (mitotic marker) and *Dmrt2* showing expression of the latter in the dorsal ventricular zone (VZ) of E12.5 developing cortex. Right, in situ hybridization against *Satb2* and *Myt1l* showing expression of the latter in newborn neurons, co-expressed with *Satb2*. Slide-seq gene expression at the indicated ages show similar expression patterns. Scale bars, 30 µm. Representative images from in situ hybridizations repeated in 2 different embryos. ML and DV indicate dorso-ventral and medio-lateral orientations. **f**, Slide-seq gene expression of several TFs whose binding sites were found to be enriched within the accessible regions of the indicated trajectories (or portion of). Confirmation of gene expression in target cell type supports TF activity.

Extended Data Fig. 11 Use of developmental atlas to investigate *Fezf2*-knockout cortex.

Related to Fig. 5. **a**, Violin plots of number of genes (left), number of mRNA molecules (counts; middle), and percentage of mitochondrial counts (right) per cell in control (Het) and *Fezf2* knockout, and UMAP visualizations of merged scRNA-seq datasets at E15.5 (top) and P1 (bottom). UMAP visualizations are coloured by genotype or assigned cell type. **b**, UMAP visualization of single-cell transcriptomes from the excitatory lineage of control and KO cortices at P1 (as shown in Fig. 5c for E15.5), coloured by genotype (left) and cell type (right). Proportion of cells

of each cell type by genotype (bottom). **c**, Heat map showing the overlapping scores between NMF modules identified in the E15.5 *Fezf2* datasets and the original E15.5 wild-type modules. All modules were identified with an overlapping score of 40% or higher. **d**, Left, scaled module expression of significant modules in all cells (two-sided Wilcoxon Sum Rank test, Bonferroni correction). Right, average expression of the top 30 genes from selected modules, in apical and intermediate progenitors, and excitatory neurons, by genotype. Differential expression between control (*Fezf2* Het) and knockout neurons, at the single-cell level (two-sided Wilcoxon rank-sum test, Bonferroni correction). **e**, Gene Ontology terms enriched in the *Fezf2*-knockout-specific module. **f**, Confusion matrix for random forest classifier calculated using 1,000 cells per cluster of the wild-type developmental atlas. The remaining held-out cells were used to test accuracy. **g**, Classification of control (*Fezf2* Het) and *Fezf2* knockout excitatory neurons by the classifier presented in **f**, for P1 (left) or E15.5 (right) datasets. Cells are grouped according to their manually assigned identity on the basis of the expression of marker genes. Box plots to the right show the corresponding classification scores in which the middle line is the median, the lower and upper hinges correspond to the 25% and 75% quantiles, the upper whisker corresponds to the largest value no larger than $1.5 \times \text{IQR}$ from the hinge and the lower whisker corresponds to the smallest value at most $1.5 \times \text{IQR}$ of the lower hinge. Lines in magenta, cyan and green indicate 1, 0.5 and 0 values, respectively. Total number of cells: *Fezf2* Het E15.5 = 6,092, *Fezf2* knockout E15.5 = 6,110, *Fezf2* Het P1 = 5,101, *Fezf2* knockout P1 = 4,235.

Extended Data Fig. 12 CFuPN acquire CThPN-like and layers 5&6 CPN-like identities in the absence of Fezf2.

Related to Fig. 5. **a–f**, Two subtypes of deep-layers knockout cells were identified at E15.5. Sub-clustering of deep-layers knockout-exclusive cells alone at E15.5 (**a**) shows a *Satb2*^{low}, *Bcl11b*^{high} cluster (cluster 0), and a *Satb2*^{high} cluster expressing also CPN markers *Cux1* and *Pou3f2* (cluster 1), as indicated in the violin plots (**b**). Differential expression analysis between both subtypes indicates enrichment of CFuPN genes in cluster 0 and CPN genes in cluster 1 (**c**). **d**, Comparison to neurons in E15.5 wild-type data showing overlap between differentially expressed genes and markers from

E15.5 neuronal subtypes. Bars indicate the number of overlapping genes and are coloured by the adjusted *P* value calculated by hypergeometric test for significant enrichment. **e**, Classification of cells from both E15.5 knockout-specific clusters according to random forest classifier shows good agreement between both annotations. **f**, NMF module expression (as in Extended Data Fig. 11d) in the knockout-specific cells, grouped according to the cell type assigned by the random forest classifier. **g, h**, Sub-clustering (**g**) and differential expression analysis (**h**) of deep-layers knockout-exclusive cells alone at P1 reveals two subpopulations that correspond to CThPN-like and layers 5&6 CPN-like populations. **i**, Classification of cells from both P1 knockout-specific clusters according to random forest classifier shows good agreement between both annotations. **j**, Differential expression analysis of the aberrant layer 5&6 CPN-like cells from the knockout-exclusive populations at P1 compared to layers 5&6 CPN (left) or SCPN (right) populations in the control. **k**, Differential expression analysis of the aberrant CThPN-like cells from the knockout-exclusive populations at P1 compared to CThPN in the control. **l, m**, In situ hybridization against *Bcl11b* and *Lpl* (**l**) or *Ptn* (**m**), in P1 control (wild type) and *Fezf2* knockout coronal sections, showing higher levels of expression of *Lpl* and *Ptn* on layers 5 and 6 and reduced *Bcl11b* in layer 5 (insets to the right correspond to boxes in left panels). Note cells expressing both *Bcl11b* and *Lpl* in magnification from layer 6, reflecting an aberrant CThPN identity. Number of positive speckles per $10^4 \mu\text{m}^2$. Quantification was calculated with a modified pipeline from CellProfiler from an area of ~ 200 by $150 \mu\text{m}$ or ~ 200 by $100 \mu\text{m}$ centred in layers 6 or 5, respectively. Data correspond to mean \pm s.e.m., from $n = 3$ mice, > 3 sections each. Unpaired *t*-test, exact *P* values indicated. Scale bars, $30 \mu\text{m}$; except in higher magnification in **l**, $15 \mu\text{m}$. **n**, Summary of phenotypes in the *Fezf2* KO. CThPN acquire an aberrant identity and upregulate CPN genes, while SCPN convert to layers 5&6 CPN-like neurons, which project through the anterior commissure (ac) to the contralateral cortex. th: thalamus, sc: spinal cord, bs: brain stem. **o**, Violin plots of number of genes (left) and mRNA molecules (counts; middle), and percentage of mitochondrial counts (right) per cell in control and KO *Fezf2* E13.5 single cell transcriptomes, and UMAP visualizations of combined control and KO complete datasets, coloured by genotype or assigned cell type. **p**, Dorsally-derived cells in *Fezf2* control and KO E13.5 scRNA-seq, visualized via UMAP and coloured by genotype (left) or cell

types (right). Proportion of cells in each cell type, according to their genotype. **q**, Differential expression analysis between control and KO migrating or immature neurons shows upregulation of a subset of CPN marker genes and downregulation of CFuPN-specific genes.

Supplementary information

[Reporting Summary](#)

[Supplementary Table 1](#)

Marker genes used for mapping scRNA-seq data onto Slide-seq using Tangram.

[Supplementary Table 2](#)

Differentially expressed genes between apical progenitors of all ages in the neuronal vs. glial branch of the inferred tree.

[Supplementary Table 3](#)

Genes that constitute the cascades plotted in Extended Data Fig. 7, in the same order as plotted.

[Supplementary Table 4](#)

Genes and gene scores in NMF modules calculated at each time point of the developmental wild-type atlas.

Rights and permissions

[Reprints and Permissions](#)

About this article



Check for
updates

Cite this article

Di Bella, D.J., Habibi, E., Stickels, R.R. *et al.* Molecular logic of cellular diversification in the mouse cerebral cortex. *Nature* **595**, 554–559 (2021). <https://doi.org/10.1038/s41586-021-03670-5>

[Download citation](#)

- Received: 29 June 2020
- Accepted: 24 May 2021
- Published: 23 June 2021
- Issue Date: 22 July 2021
- DOI: <https://doi.org/10.1038/s41586-021-03670-5>

Comments

By submitting a comment you agree to abide by our [Terms](#) and [Community Guidelines](#). If you find something abusive or that does not comply with our terms or guidelines please flag it as inappropriate.

[Access through your institution](#)

[Change institution](#)

[Buy or subscribe](#)

Advertisement

| [Section menu](#) | [Main menu](#) |

- Article
- [Published: 14 July 2021](#)

Acetate differentially regulates IgA reactivity to commensal bacteria

- [Tadashi Takeuchi](#)^{1,2},
- [Eiji Miyauchi](#) ORCID: [orcid.org/0000-0002-8202-684X](#)¹,
- [Takashi Kanaya](#)^{1,3},
- [Tamotsu Kato](#)^{1,3},
- [Yumiko Nakanishi](#)^{1,3,4},
- [Takashi Watanabe](#)⁵,
- [Toshimori Kitami](#)⁶,
- [Takashi Taida](#)¹,
- [Takaharu Sasaki](#)¹,
- [Hiroki Negishi](#)^{1,3},
- [Shu Shimamoto](#) ORCID: [orcid.org/0000-0001-5851-3464](#)⁷,
- [Akinobu Matsuyama](#)⁷,
- [Ikuo Kimura](#) ORCID: [orcid.org/0000-0001-8778-145X](#)^{8,9},
- [Ifor R. Williams](#) ORCID: [orcid.org/0000-0002-8810-2911](#)¹⁰,
- [Osamu Ohara](#)^{5,11} &
- [Hiroshi Ohno](#) ORCID: [orcid.org/0000-0001-8776-9661](#)^{1,3,4}

[Nature](#) volume 595, pages 560–564 (2021) [Cite this article](#)

- 4066 Accesses
- 113 Altmetric
- [Metrics details](#)

Subjects

- [Microbiome](#)
- [Mucosal immunology](#)

Abstract

The balance between bacterial colonization and its containment in the intestine is indispensable for the symbiotic relationship between humans and their bacteria. One component to maintain homeostasis at the mucosal surfaces is immunoglobulin A (IgA), the most abundant immunoglobulin in mammals^{1,2}. Several studies have revealed important characteristics of poly-reactive IgA^{3,4}, which is produced naturally without commensal bacteria. Considering the dynamic changes within the gut environment, however, it remains uncertain how the commensal-reactive IgA pool is shaped and how such IgA affects the microbial community. Here we show that acetate—one of the major gut microbial metabolites—not only increases the production of IgA in the colon, but also alters the capacity of the IgA pool to bind to specific microorganisms including Enterobacterales. Induction of commensal-reactive IgA and changes in the IgA repertoire by acetate were observed in mice monocolonized with *Escherichia coli*, which belongs to Enterobacterales, but not with the major commensal *Bacteroides thetaiotaomicron*, which suggests that acetate directs selective IgA binding to certain microorganisms. Mechanistically, acetate orchestrated the interactions between epithelial and immune cells, induced microbially stimulated CD4 T cells to support T-cell-dependent IgA production and, as a consequence, altered the localization of these bacteria within the colon. Collectively, we identified a role for gut microbial metabolites in the regulation of differential IgA production to maintain mucosal homeostasis.

Access options

Subscribe to Journal

Get full journal access for 1 year

\$199.00

only \$3.90 per issue

[Subscribe](#)

All prices are NET prices.

VAT will be added later in the checkout.

Tax calculation will be finalised during checkout.

Rent or Buy article

Get time limited or full article access on ReadCube.

from \$8.99

[Rent or Buy](#)

All prices are NET prices.

Additional access options:

- [Log in](#)
- [Access through your institution](#)
- [Learn about institutional subscriptions](#)

Fig. 1: Acetate increases large intestinal IgA production and alters the reactivity towards commensal bacteria.

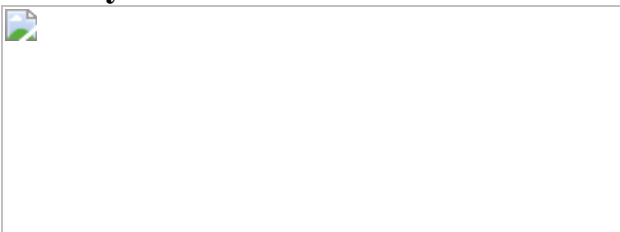


Fig. 2: Acetate affects the community of mucosa-associated bacteria in an IgA-dependent manner.

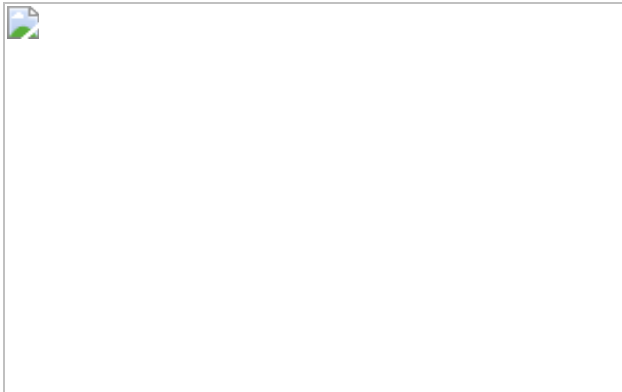
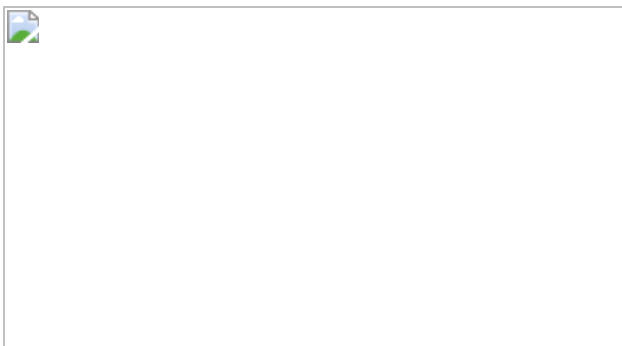


Fig. 3: Acetate orchestrates epithelial–immune cell interactions and induces differential IgA production with microbially stimulated CD4 T cells.



Data availability

The raw 16S rRNA gene sequencing and IgA repertoire sequencing data are deposited in the DNA Data Bank of Japan, under NCBI BioProject accession numbers [PRJDB7422](#) and [PRJDB7423](#). Taxonomic assignment of 16S rRNA gene sequencing data was determined with the Greengenes database v.13.5 (<http://greengenes.secondgenome.com/>)³⁶. IgA repertoire was analysed using the IMGT database (<http://www.imgt.org/>)⁴³. [Source data](#) are provided with this paper.

References

1. 1.

Lycke, N. Y. & Bemark, M. The regulation of gut mucosal IgA B-cell responses: recent developments. *Mucosal Immunol.* **10**, 1361–1374

(2017).

[CAS](#) [PubMed](#) [Article](#) [Google Scholar](#)

2. 2.

Pabst, O., Cerovic, V. & Hornef, M. Secretory IgA in the coordination of establishment and maintenance of the microbiota. *Trends Immunol.* **37**, 287–296 (2016).

[CAS](#) [PubMed](#) [Article](#) [Google Scholar](#)

3. 3.

Okai, S. et al. High-affinity monoclonal IgA regulates gut microbiota and prevents colitis in mice. *Nat. Microbiol.* **1**, 16103 (2016).

[CAS](#) [PubMed](#) [Article](#) [Google Scholar](#)

4. 4.

Bunker, J. J. et al. Natural polyreactive IgA antibodies coat the intestinal microbiota. *Science* **358**, eaan6619 (2017).

[PubMed](#) [PubMed Central](#) [Article](#) [CAS](#) [Google Scholar](#)

5. 5.

Kim, M., Qie, Y., Park, J. & Kim, C. H. Gut microbial metabolites fuel host antibody responses. *Cell Host Microbe* **20**, 202–214 (2016).

[CAS](#) [PubMed](#) [PubMed Central](#) [Article](#) [Google Scholar](#)

6. 6.

Wu, W. et al. Microbiota metabolite short-chain fatty acid acetate promotes intestinal IgA response to microbiota which is mediated by GPR43. *Mucosal Immunol.* **10**, 946–956 (2017).

[CAS](#) [PubMed](#) [Article](#) [Google Scholar](#)

7. 7.

Goverse, G. et al. Diet-derived short chain fatty acids stimulate intestinal epithelial cells to induce mucosal tolerogenic dendritic cells. *J. Immunol.* **198**, 2172–2181 (2017).

[CAS](#) [PubMed](#) [Article](#) [Google Scholar](#)

8. 8.

Kato, T. et al. Multiple omics uncovers host-gut microbial mutualism during prebiotic fructooligosaccharide supplementation. *DNA Res.* **21**, 469–480 (2014).

[CAS](#) [PubMed](#) [PubMed Central](#) [Article](#) [Google Scholar](#)

9. 9.

Hara, S. et al. Dietary antigens induce germinal center responses in Peyer's patches and antigen-specific IgA production. *Front. Immunol.* **10**, 2432 (2019).

[CAS](#) [PubMed](#) [PubMed Central](#) [Article](#) [Google Scholar](#)

10. 10.

Palm, N. W. et al. Immunoglobulin A coating identifies colitogenic bacteria in inflammatory bowel disease. *Cell* **158**, 1000–1010 (2014).

[CAS](#) [PubMed](#) [PubMed Central](#) [Article](#) [Google Scholar](#)

11. 11.

Hapfelmeier, S. et al. Reversible microbial colonization of germ-free mice reveals the dynamics of IgA immune responses. *Science* **328**, 1705–1709 (2010).

[ADS](#) [CAS](#) [PubMed](#) [PubMed Central](#) [Article](#) [Google Scholar](#)

12. 12.

Rosner, K. et al. Third complementarity-determining region of mutated V_H immunoglobulin genes contains shorter V, D, J, P, and N components than non-mutated genes. *Immunology* **103**, 179–187 (2001).

[CAS](#) [PubMed](#) [PubMed Central](#) [Article](#) [Google Scholar](#)

13. 13.

Yasuda, K. et al. Biogeography of the intestinal mucosal and luminal microbiome in the rhesus macaque. *Cell Host Microbe* **17**, 385–391 (2015).

[CAS](#) [PubMed](#) [PubMed Central](#) [Article](#) [Google Scholar](#)

14. 14.

Reboldi, A. et al. IgA production requires B cell interaction with subepithelial dendritic cells in Peyer's patches. *Science* **352**, aaf4822 (2016).

[PubMed](#) [PubMed Central](#) [Article](#) [CAS](#) [Google Scholar](#)

15. 15.

Lin, Y. L., Ip, P. P. & Liao, F. CCR6 deficiency impairs IgA production and dysregulates antimicrobial peptide production, altering the intestinal flora. *Front. Immunol.* **8**, 805 (2017).

[PubMed](#) [PubMed Central](#) [Article](#) [CAS](#) [Google Scholar](#)

16. 16.

Baptista, A. P. et al. Colonic patch and colonic SILT development are independent and differentially regulated events. *Mucosal Immunol.* **6**,

511–521 (2013).

[CAS](#) [PubMed](#) [Article](#) [Google Scholar](#)

17. 17.

Lee, A. Y. S. et al. Expression of membrane-bound CC Chemokine ligand 20 on follicular T helper cells in T–B-cell conjugates. *Front. Immunol.* **8**, 1871 (2017).

[PubMed](#) [PubMed Central](#) [Article](#) [CAS](#) [Google Scholar](#)

18. 18.

Kubinak, J. L. et al. MyD88 signaling in T cells directs IgA-mediated control of the microbiota to promote health. *Cell Host Microbe* **17**, 153–163 (2015).

[CAS](#) [PubMed](#) [PubMed Central](#) [Article](#) [Google Scholar](#)

19. 19.

Vatanen, T. et al. Variation in microbiome LPS immunogenicity contributes to autoimmunity in humans. *Cell* **165**, 842–853 (2016).

[CAS](#) [PubMed](#) [PubMed Central](#) [Article](#) [Google Scholar](#)

20. 20.

Preite, S. et al. Somatic mutations and affinity maturation are impaired by excessive numbers of T follicular helper cells and restored by Treg cells or memory T cells. *Eur. J. Immunol.* **45**, 3010–3021 (2015).

[CAS](#) [PubMed](#) [PubMed Central](#) [Article](#) [Google Scholar](#)

21. 21.

Kau, A. L. et al. Functional characterization of IgA-targeted bacterial taxa from undernourished Malawian children that produce diet-

dependent enteropathy. *Sci. Transl. Med.* **7**, 276ra24 (2015).

[CAS](#) [PubMed](#) [PubMed Central](#) [Article](#) [Google Scholar](#)

22. 22.

Sugahara, H. et al. Decreased taxon-specific IgA response in relation to the changes of gut microbiota composition in the elderly. *Front. Microbiol.* **8**, 1757 (2017).

[PubMed](#) [PubMed Central](#) [Article](#) [Google Scholar](#)

23. 23.

Ragonnaud, E. & Biragyn, A. Gut microbiota as the key controllers of “healthy” aging of elderly people. *Immun. Ageing* **18**, 2 (2021).

[PubMed](#) [PubMed Central](#) [Article](#) [Google Scholar](#)

24. 24.

Kono, H., Hashimoto, H. & Shimizu, Y. NMR characterization of cellulose acetate: chemical shift assignments, substituent effects, and chemical shift additivity. *Carbohydr. Polym.* **118**, 91–100 (2015).

[CAS](#) [PubMed](#) [Article](#) [Google Scholar](#)

25. 25.

Kamide, K., Saito, M. & Abe, T. Dilute solution properties of water-soluble incompletely substituted cellulose acetate. *Polym. J.* **13**, 421–431 (1981).

[CAS](#) [Article](#) [Google Scholar](#)

26. 26.

Shimamoto, S., Kohmoto, T. & Shibata, T. in *Cellulose Derivatives: Modification, Characterization, and Nanostructures* ACS Symposium

Series Vol. 688, Ch. 14, 194–200 (ASC Publications, 1998).

27. 27.

Tezuka, Y. & Tsuchiya, Y. Determination of substituent distribution in cellulose acetate by means of a ^{13}C NMR study on its propanoated derivative. *Carbohydr. Res.* **273**, 83–91 (1995).

[CAS](#) [Article](#) [Google Scholar](#)

28. 28.

Clausen, M. R., Bonnén, H., Tvede, M. & Mortensen, P. B. Colonic fermentation to short-chain fatty acids is decreased in antibiotic-associated diarrhea. *Gastroenterology* **101**, 1497–1504 (1991).

[CAS](#) [PubMed](#) [Article](#) [Google Scholar](#)

29. 29.

Kucharzik, T., Hudson, J. T. III, Waikel, R. L., Martin, W. D. & Williams, I. R. CCR6 expression distinguishes mouse myeloid and lymphoid dendritic cell subsets: demonstration using a CCR6 EGFP knock-in mouse. *Eur. J. Immunol.* **32**, 104–112 (2002).

[CAS](#) [PubMed](#) [Article](#) [Google Scholar](#)

30. 30.

Kimura, I. et al. The gut microbiota suppresses insulin-mediated fat accumulation via the short-chain fatty acid receptor GPR43. *Nat. Commun.* **4**, 1829 (2013).

[ADS](#) [PubMed](#) [Article](#) [CAS](#) [Google Scholar](#)

31. 31.

Malissen, M. et al. Altered T cell development in mice with a targeted mutation of the CD3-epsilon gene. *EMBO J.* **14**, 4641–4653 (1995).

[CAS](#) [PubMed](#) [PubMed Central](#) [Article](#) [Google Scholar](#)

32. 32.

Muramatsu, M. et al. Class switch recombination and hypermutation require activation-induced cytidine deaminase (AID), a potential RNA editing enzyme. *Cell* **102**, 553–563 (2000).

[CAS](#) [PubMed](#) [Article](#) [Google Scholar](#)

33. 33.

Hase, K. et al. Uptake through glycoprotein 2 of FimH⁺ bacteria by M cells initiates mucosal immune response. *Nature* **462**, 226–230 (2009).

[ADS](#) [CAS](#) [PubMed](#) [Article](#) [Google Scholar](#)

34. 34.

Kozich, J. J., Westcott, S. L., Baxter, N. T., Highlander, S. K. & Schloss, P. D. Development of a dual-index sequencing strategy and curation pipeline for analyzing amplicon sequence data on the MiSeq Illumina sequencing platform. *Appl. Environ. Microbiol.* **79**, 5112–5120 (2013).

[ADS](#) [CAS](#) [PubMed](#) [PubMed Central](#) [Article](#) [Google Scholar](#)

35. 35.

Caporaso, J. G. et al. QIIME allows analysis of high-throughput community sequencing data. *Nat. Methods* **7**, 335–336 (2010).

[CAS](#) [PubMed](#) [PubMed Central](#) [Article](#) [Google Scholar](#)

36. 36.

DeSantis, T. Z. et al. Greengenes, a chimera-checked 16S rRNA gene database and workbench compatible with ARB. *Appl. Environ. Microbiol.* **72**, 5069–5072 (2006).

[ADS](#) [CAS](#) [PubMed](#) [PubMed Central](#) [Article](#) [Google Scholar](#)

37. 37.

Osman, N., Adawi, D., Ahrné, S., Jeppsson, B. & Molin, G. Probiotics and blueberry attenuate the severity of dextran sulfate sodium (DSS)-induced colitis. *Dig. Dis. Sci.* **53**, 2464–2473 (2008).

[PubMed](#) [Article](#) [Google Scholar](#)

38. 38.

Furusawa, Y. et al. Commensal microbe-derived butyrate induces the differentiation of colonic regulatory T cells. *Nature* **504**, 446–450 (2013).

[ADS](#) [CAS](#) [PubMed](#) [PubMed Central](#) [Article](#) [Google Scholar](#)

39. 39.

Gong, J. et al. Diversity and phylogenetic analysis of bacteria in the mucosa of chicken ceca and comparison with bacteria in the cecal lumen. *FEMS Microbiol. Lett.* **208**, 1–7 (2002).

[CAS](#) [PubMed](#) [Article](#) [Google Scholar](#)

40. 40.

Schindelin, J. et al. Fiji: an open-source platform for biological-image analysis. *Nat. Methods* **9**, 676–682 (2012).

[CAS](#) [PubMed](#) [PubMed Central](#) [Article](#) [Google Scholar](#)

41. 41.

Vicente-Suarez, I. et al. Unique lamina propria stromal cells imprint the functional phenotype of mucosal dendritic cells. *Mucosal Immunol.* **8**, 141–151 (2015).

[CAS](#) [PubMed](#) [Article](#) [Google Scholar](#)

42. 42.

Kanaya, T. et al. Development of intestinal M cells and follicle-associated epithelium is regulated by TRAF6-mediated NF-κB signaling. *J. Exp. Med.* **215**, 501–519 (2018).

[CAS](#) [PubMed](#) [PubMed Central](#) [Article](#) [Google Scholar](#)

43. 43.

Lefranc, M. P. et al. IMGT, the international ImMunoGeneTics information system. *Nucleic Acids Res.* **37**, D1006–D1012 (2009).

[CAS](#) [PubMed](#) [Article](#) [Google Scholar](#)

44. 44.

Sato, T. et al. Single Lgr5 stem cells build crypt-villus structures in vitro without a mesenchymal niche. *Nature* **459**, 262–265 (2009).

[ADS](#) [CAS](#) [PubMed](#) [Article](#) [Google Scholar](#)

45. 45.

Ootani, A. et al. Sustained in vitro intestinal epithelial culture within a Wnt-dependent stem cell niche. *Nat. Med.* **15**, 701–706 (2009).

[CAS](#) [PubMed](#) [PubMed Central](#) [Article](#) [Google Scholar](#)

46. 46.

Moon, C., VanDussen, K. L., Miyoshi, H. & Stappenbeck, T. S. Development of a primary mouse intestinal epithelial cell monolayer culture system to evaluate factors that modulate IgA transcytosis. *Mucosal Immunol.* **7**, 818–828 (2014).

[CAS](#) [PubMed](#) [Article](#) [Google Scholar](#)

47. 47.

Ettayebi, K. et al. Replication of human noroviruses in stem cell-derived human enteroids. *Science* **353**, 1387–1393 (2016).

[ADS](#) [PubMed](#) [PubMed Central](#) [Article](#) [Google Scholar](#)

[Download references](#)

Acknowledgements

We thank N. Atarashi, M. Kawasumi, S. Onawa, N. Tachibana and A. Ito for their technical support; B. Malissen and T. Honjo for providing *Cd3e*^{-/+} and *Aicda*^{-/+} mice, respectively; C. Kuo for providing the R-spondin-1-producing cell line; and S. Koyasu and P. D. Burrows for critical reading and English editing of the manuscript. This study was supported in part by research grants from RIKEN Interdisciplinary Research Program ‘Integrated Symbiology’, RIKEN Pioneering Project ‘Biology of Symbiosis’, Grants-in-Aid for Young Scientists (B) (26850090 to E.M.), AMED-CREST (JP19gm0710009 to H.O.) and Daicel Corporation. T. Takeuchi was supported by RIKEN Junior Research Associate Program.

Author information

Affiliations

1. Laboratory for Intestinal Ecosystem, RIKEN Center for Integrative Medical Sciences, Kanagawa, Japan

Tadashi Takeuchi, Eiji Miyauchi, Takashi Kanaya, Tamotsu Kato, Yumiko Nakanishi, Takashi Taida, Takaharu Sasaki, Hiroki Negishi & Hiroshi Ohno

2. Department of Microbiology and Immunology, Keio University School of Medicine, Tokyo, Japan

Tadashi Takeuchi

3. Graduate School of Medical Life Science, Yokohama City University, Kanagawa, Japan

Takashi Kanaya, Tamotsu Kato, Yumiko Nakanishi, Hiroki Negishi & Hiroshi Ohno

4. Intestinal Microbiota Project, Kanagawa Institute of Industrial Science and Technology, Kanagawa, Japan

Yumiko Nakanishi & Hiroshi Ohno

5. Laboratory for Integrative Genomics, RIKEN Center for Integrative Medical Sciences, Kanagawa, Japan

Takashi Watanabe & Osamu Ohara

6. YCI Laboratory for Cellular Bioenergetic Network, RIKEN Center for Integrative Medical Sciences, Kanagawa, Japan

Toshimori Kitami

7. Tokyo Headquarters, Daicel Corporation, Tokyo, Japan

Shu Shimamoto & Akinobu Matsuyama

8. Department of Signal Transductions, Graduate School of Biostudies, Kyoto University, Kyoto, Japan

Ikuo Kimura

9. Department of Applied Biological Science, Graduate School of Agriculture, Tokyo University of Agriculture and Technology, Tokyo, Japan

Ikuo Kimura

10. Department of Pathology, Emory University School of Medicine, Atlanta, GA, USA

Ifor R. Williams

11. Department of Applied Genomics, Kazusa DNA Research Institute,
Chiba, Japan

Osamu Ohara

Authors

1. Tadashi Takeuchi

[View author publications](#)

You can also search for this author in [PubMed](#) [Google Scholar](#)

2. Eiji Miyauchi

[View author publications](#)

You can also search for this author in [PubMed](#) [Google Scholar](#)

3. Takashi Kanaya

[View author publications](#)

You can also search for this author in [PubMed](#) [Google Scholar](#)

4. Tamotsu Kato

[View author publications](#)

You can also search for this author in [PubMed](#) [Google Scholar](#)

5. Yumiko Nakanishi

[View author publications](#)

You can also search for this author in [PubMed](#) [Google Scholar](#)

6. Takashi Watanabe

[View author publications](#)

You can also search for this author in [PubMed](#) [Google Scholar](#)

7. Toshimori Kitami

[View author publications](#)

You can also search for this author in [PubMed](#) [Google Scholar](#)

8. Takashi Taida

[View author publications](#)

You can also search for this author in [PubMed](#) [Google Scholar](#)

9. Takaharu Sasaki

[View author publications](#)

You can also search for this author in [PubMed](#) [Google Scholar](#)

10. Hiroki Negishi

[View author publications](#)

You can also search for this author in [PubMed](#) [Google Scholar](#)

11. Shu Shimamoto

[View author publications](#)

You can also search for this author in [PubMed](#) [Google Scholar](#)

12. Akinobu Matsuyama

[View author publications](#)

You can also search for this author in [PubMed](#) [Google Scholar](#)

13. Ikuo Kimura

[View author publications](#)

You can also search for this author in [PubMed](#) [Google Scholar](#)

14. Ifor R. Williams

[View author publications](#)

You can also search for this author in [PubMed](#) [Google Scholar](#)

15. Osamu Ohara

[View author publications](#)

You can also search for this author in [PubMed](#) [Google Scholar](#)

16. Hiroshi Ohno

[View author publications](#)

You can also search for this author in [PubMed](#) [Google Scholar](#)

Contributions

T. Takeuchi and H.O. conceived the study. T. Takeuchi designed and performed the experiments and analyses and co-wrote the manuscript. E.M. contributed to the data analyses and discussions and co-wrote the manuscript. T. Kanaya contributed to fluorescence immunohistochemistry and in vitro experiments. T. Kato analysed the human faecal data and performed 16S rRNA gene sequencing. Y.N. quantified the SCFA concentration in the intestines using gas chromatography–tandem mass spectrometry. T.W., T.S. and O.O. contributed to the analyses of the IgA repertoire. T. Taida and H.N. contributed to the animal experiments and FACS analyses. T. Kitami contributed to the immune cell metabolism measurements. S.S. and A.M. developed SCFA-conjugated cellulose. I.K. and I.R.W. provided essential materials and helped to interpret the data. H.O. directed the research, provided essential materials and co-wrote the manuscript.

Corresponding author

Correspondence to [Hiroshi Ohno](#).

Ethics declarations

Competing interests

S.S. and A.M. are employees of Daicel Corporation; T. Takeuchi, E.M., S.S., A.M. and H.O. have applied for a patent regarding SCFA-conjugated

cellulose; and H.O. received research funds from Daicel Corporation. Otherwise the authors have no competing interests.

Additional information

Peer review information *Nature* thanks Andrea Cerutti and the other, anonymous, reviewer(s) for their contribution to the peer review of this work.

Publisher's note Springer Nature remains neutral with regard to jurisdictional claims in published maps and institutional affiliations.

Extended data figures and tables

Extended Data Fig. 1 Faecal SCFAs are associated with IgA levels in mice and humans.

a, Correlation of total major SCFAs, acetate, propionate and butyrate with SIgA concentration in faeces of antibiotic-treated mice. Mice were administered the following antibiotics via ad libitum drinking water: vancomycin (orange), neomycin (red), ampicillin (aqua), metronidazole (purple) and distilled water (grey) for 2 weeks ($n = 4$ per group). Faecal samples were sequentially collected at weeks 1 and 2. Total major SCFAs is the sum of acetate, propionate and butyrate. **b**, Association of human faecal metabolites with SIgA concentration ($n = 17$ per group). All faecal samples were dichotomized according to the IgA concentration and the relative intensity of specified metabolites was compared between the IgA-low and IgA-high groups. **c**, Relative intensity of faecal acetate, propionate and butyrate was compared between the IgA-low and high-groups. **d–f**, Ileal, caecal and colonic concentrations of acetate (**d**), propionate (**e**) and butyrate (**f**) in mice fed the fibre-deprived cWSCA (control)-containing or WSCA-containing diet ($n = 4$ per group (**d**), $n = 4$ per group (**e**) and $n = 4$ versus 3 (**f**)). **g, h**, Faecal concentration of SCFAs in mice fed the cWSCP (control) or WSCP diet (**g**), and cWSCB (control) or WSCB diet (**h**) ($n = 4$ per group). **i**, Faecal concentration of SCFAs in mice fed a standard chow diet (CE2, CLEA Japan) ($n = 8$). **c**, Box plots indicate the median, upper and

lower quartiles, and upper and lower extremes except for outliers. **d–i**, Data are mean and s.d. $*P < 0.05$, $**P < 0.01$, $***P < 0.001$; Spearman's rank-order correlation (**a**), two-sided Wilcoxon rank-sum test (**c**) and Kruskal–Wallis test with Dunn's test (**d–i**). Exact P values are provided in the Source Data.

[Source data](#)

[Extended Data Fig. 2 Acetate, but not other SCFAs, increases colonic IgA production and SIgA binding of commensal bacteria.](#)

a, Representative histograms showing the patterns of faecal SIgA binding to faecal DAPI⁺ bacteria. **b**, The IgA concentration in different parts of the intestine was analysed using ELISA ($n = 4$ per group). Small intestines were divided into duodenum, jejunum and ileum, and large intestines were divided into caecum, proximal and distal colon. **c**, **d**, Representative flow cytometry plots of colonic IgA-producing plasma cells (defined as IgA⁺B220[−]CD3ε[−] cells, gated on CD3ε[−] lymphocytes) (**c**) and the frequency among colonic lymphocytes and the absolute number (**d**) ($n = 10$ per group). **e**, The frequency of IgA-producing plasma cells among small intestinal lymphocytes and the absolute number ($n = 5$ per group). **f–h**, Faecal SIgA concentration at week 4 after the start of the modified diet (**f**), colonic IgA-producing plasma cells (**g**) and faecal SIgA-coated (SIgA⁺) bacteria (**h**) in mice fed cWSCP (control) or WSCP ($n = 4$ per group). **i–k**, Faecal SIgA concentration at week 4 (**i**), colonic IgA-producing plasma cells (**j**) and faecal SIgA⁺ bacteria (**k**) in mice fed cWSCB (control) or WSCB ($n = 4$ per group (**i**, **j**); $n = 3$ versus 4 (**k**)). **l**, Weighted UniFrac distances between faecal SIgA[−] and SIgA⁺ bacteria in the cWSCA (control) or WSCA groups. The distances between all samples within groups are indicated as a reference ($n = 4$ versus 5). **m**, The relative abundance of faecal SIgA[−] and SIgA⁺ bacteria at the phylum level ($n = 4$ per group). **n**, The relative abundance of faecal SIgA[−] and SIgA⁺ Bifidobacteriales, Bacteroidales, Erysipelotrichales and Enterobacteriales ($n = 4$ per group). Data are mean and s.d. $*P < 0.05$, $**P < 0.01$, $***P < 0.001$; Kruskal–Wallis test with Dunn's test (**b**, **l**, **n**) and two-sided Wilcoxon rank-sum test

(d–k). Pooled data from two independent experiments (d). Exact *P* values are provided in the Source Data.

[Source data](#)

Extended Data Fig. 3 Acetate increases IgA production in *E. coli*-monocolonized mice and germ-free mice orally administered heat-killed *E. coli*.

a, Representative flow cytometry plots (gated on DAPI⁺ population) and summary data of caecal SIgA⁺ bacteria in control-diet-fed and WSCA-diet-fed mice monocolonized with *B. thetaiotaomicron* (*n* = 9 per group) or *E. coli* (*n* = 9 versus 10, respectively). **b**, Representative flow cytometry plots (gated on lymphocytes) and summary data of colonic IgA⁺B220[−] plasma cells (PC) and IgA⁺B220⁺ B cells (BC) in mice monocolonized with *B. thetaiotaomicron* (*n* = 9 per group) or *E. coli* (*n* = 9 versus 10). **c**, Abundance of *E. coli* in *E. coli*-monocolonized mice measured as CFU per gram (CFU/g) of colonic contents (*n* = 5 per group). **d**, **e**, Representative flow cytometry plots (gated on CD3ε[−] lymphocytes) depicting colonic IgA⁺ plasma cells and B cells in germ-free mice (**d**) and the absolute number (**e**) (*n* = 3 versus 4). **f**, Faecal SIgA concentration at week 4 in germ-free mice (*n* = 8 per group). **g**, Microorganism-reactive SIgA in the caecal contents from control-diet-fed and WSCA-diet-fed germ-free mice orally administered heat-killed *B. thetaiotaomicron* (*n* = 4 versus 5, respectively) or *E. coli* (*n* = 9 per group). The OD₄₅₀ in the WSCA diet groups was normalized to that of the cWSCA (control) diet groups. **h**, The frequency among colonic lymphocytes and the absolute number of colonic IgA-producing plasma cells in control-diet-fed and WSCA-diet-fed germ-free mice orally administered heat-killed *B. thetaiotaomicron* (*n* = 4 versus 5, respectively) or *E. coli* (*n* = 4 per group). **i–k**, Skewness (**i**), kurtosis (**j**) and inverse Simpson's index (**k**) of HCDR3 amino acid length distribution in colonic IgA-producing B cells of control-diet-fed and WSCA-diet-fed mice monocolonized with *B. thetaiotaomicron* (*n* = 5 per group) or *E. coli* (*n* = 4 versus 5, respectively). **l**, HCDR3 amino acid sequence distribution in control-diet-fed and WSCA-diet-fed mice monocolonized with *B. thetaiotaomicron* (*n* = 5 per group) or *E. coli* (*n* = 4 versus 5, respectively).

Each column corresponds to the sequencing results from a single mouse and the colour corresponds to the order of frequency. **m**, The frequency of IgA⁺ B cell clones expressing the most-dominant HCDR3 amino acid sequence in control-diet-fed and WSCA-diet-fed mice monocolonized with *B. thetaiotaomicron* ($n = 5$ per group) or *E. coli* ($n = 4$ versus 5, respectively). **n**, Mode (that is, the value that appears the most frequently in a sample) of HCDR3 amino acid length in control-diet-fed and WSCA-diet-fed mice monocolonized with *B. thetaiotaomicron* ($n = 5$ per group) or *E. coli* ($n = 4$ versus 5, respectively). **b, c, e, f**, Data are mean and s.d. **a, g–k, m, n**, Box plots indicate median, upper and lower quartiles, and upper and lower extremes except for outliers. * $P < 0.05$, ** $P < 0.01$; two-sided Wilcoxon rank-sum test (**a–c, e–g, i–k, m, n**) and Kruskal–Wallis test with Dunn’s test (**h**). **a, b, f, g**, Pooled data from two independent experiments. Exact P values are provided in the Source Data.

[Source data](#)

Extended Data Fig. 4 Acetate alters the composition of mucosa-associated bacteria in an IgA-dependent manner.

a, Ratio of mucosa-associated to luminal bacteria at the order level in wild-type mice and *Aicda*^{-/-} mice depicted on a log₁₀ scale. Each row represents the sequencing results from a single mouse. Results of unsupervised clustering based on Ward’s method are also shown. The taxa in bold font were significantly altered in terms of their localization upon WSCA diet administration. **b**, The relative abundance of gut bacteria at the phylum level in the colonic luminal contents and mucus layer of wild-type and *Aicda*^{-/-} mice. **c**, Schematic of the experimental protocol. Mice fed cWSCA (control) or WSCA were orally administered 1×10^9 CFU of *E. coli* to enhance IgA production. On the day of assessment, 1×10^9 CFU of GFP-expressing *E. coli* were orally administered and, 3 h later, the colonic tissues and contents were sampled. **d–g**, The frequency of total GFP-expressing *E. coli* (**d**), SIgA⁻ (**e**) and SIgA⁺ (**f**) GFP-expressing *E. coli*, and SIgA⁺ GFP-negative bacteria (**g**) in the colonic contents ($n = 5$ versus 6). **d–g**, Data are mean and s.d. * $P < 0.05$; two-sided Wilcoxon rank-sum test (**a, d–g**). P values were corrected by FDR (**a**). N.S., not significant. $n = 4$

per group for wild-type mice and $n = 5$ per group for $Aicda^{-/-}$ mice (**a, b**). Exact P values are provided in the Source Data.

[Source data](#)

Extended Data Fig. 5 Acetate increases germinal-centre B cells in MLNs and the colon.

a, Representative flow cytometry plots (gated on $B220^+$ lymphocytes) depicting $GL7^+Fas^+$ germinal-centre B cells in MLNs. **b**, Frequency among $B220^+$ B cells and the absolute number of $GL7^+Fas^+$ germinal-centre B cells ($n = 5$ per group). **c**, Representative flow cytometry plots (gated on $B220^+$ lymphocytes) depicting $GL7^+Fas^+$ germinal-centre B cells in the colon. **d**, Frequency among $B220^+$ B cells and the absolute number of $GL7^+Fas^+$ germinal-centre B cells ($n = 15$ per group). **b, d**, Data are mean and s.d. $*P < 0.05$, $**P < 0.01$; two-sided Wilcoxon rank-sum test (**b, d**). Pooled data from three independent experiments (**d**). Exact P values are provided in the Source Data.

[Source data](#)

Extended Data Fig. 6 Acetate increases colonic IgA production and alters IgA reactivity in a CCR6–CCL20-axis-dependent manner.

a, The frequency among colonic lymphocytes of IgA-producing plasma cells and faecal SIgA concentration in $Ccr6^{GFP/+}$ (hetero) and $Ccr6^{GFP/GFP}$ (KO) mice. **b**, Faecal SIgA reactive to *B. thetaiotaomicron* and to *E. coli* in $Ccr6^{GFP/+}$ and $Ccr6^{GFP/GFP}$ mice. **c**, A principal coordinate analysis plot of weighted UniFrac distances for faecal SIgA^- and SIgA^+ bacteria in $Ccr6^{GFP/GFP}$ mice ($n = 4$ per group). The dashed and solid lines indicate 90% confidence levels for the SIgA^- and SIgA^+ bacteria groups, respectively. **d**, The relative abundance of faecal SIgA^- and SIgA^+ bacteria at the phylum level in $Ccr6^{GFP/GFP}$ mice ($n = 4$ per group). **e**, The relative abundance of faecal SIgA^- and SIgA^+ Bacteroidales, Erysipelotrichales and

Proteobacteria in *Ccr6*^{GFP/GFP} mice ($n = 4$ per group). **f**, The frequency of faecal SIgA⁺ bacteria in *Ccr6*^{GFP/GFP} mice monocolonized with *E. coli* ($n = 8$ per group). **g**, *Ccl20* mRNA expression in colonic epithelial cells of wild-type mice ($n = 5$ versus 6). **h**, *Ccl20* mRNA expression in a monolayer form of mouse colonic organoids stimulated with or without sodium acetate ($n = 5$ per group). **a, b, e–h**, Data are mean and s.d. * $P < 0.05$, ** $P < 0.01$; Kruskal–Wallis test with Dunn’s test (**a, b, e**) or two-sided Wilcoxon rank-sum test (**f–h**). $n = 6$ per group for *Ccr6*^{GFP/+} mice and $n = 5$ versus 4 for *Ccr6*^{GFP/GFP} mice (**a, b**). Pooled data from two independent experiments (**f**). Exact P values are provided in the Source Data.

[Source data](#)

Extended Data Fig. 7 Acetate increases CCR6-expressing T_{FH}-like cells in the colon.

a, Representative flow cytometry plots (gated on CD3ε⁺CD4⁺ lymphocytes) depicting CCR6⁺ T cells and CCR6⁺CXCR5⁺ T_{FH}-like cells in the colon of *Ccr6*^{GFP/+} mice. **b, c**, The frequency among CD3ε⁺CD4⁺ T cells and the absolute number of CCR6⁺ T cells (**b**) and CCR6⁺CXCR5⁺ T_{FH}-like cells (**c**) in the colon of *Ccr6*^{GFP/+} mice ($n = 6$ per group). **d**, Representative flow cytometry plots (gated on CD19[−]CD3ε⁺CD4⁺ lymphocytes) depicting CXCR5⁺PD-1⁺ T_{FH}-like cells in the colon of wild-type mice. **e, f**, The frequency among CD3ε⁺CD4⁺ T cells and the absolute number of CXCR5⁺PD-1⁺ T_{FH}-like cells (**e**) and RORyt⁺ T_H17 cells (**f**) in the colon of wild-type mice ($n = 5$ per group). **g**, The frequency among CD3ε[−]CD19[−] lineage marker (lin) negative cells and the absolute number of RORyt⁺ innate lymphoid cells (ILCs) in the colon of wild-type mice ($n = 5$ per group). Data are mean and s.d. (**b, c, e–g**). * $P < 0.05$, ** $P < 0.01$; two-sided Wilcoxon rank-sum test (**b, c, e–g**). Exact P values are provided in the Source Data.

[Source data](#)

Extended Data Fig. 8 Acetate and *E. coli* synergistically regulate T cell functions to facilitate IgA production ex vivo and in vitro.

a, *Bcl6* mRNA expression in CD4 T cells sorted from MLN cells co-stimulated ex vivo with heat-killed bacteria and 5 mM sodium acetate for 4 h ($n = 3$ per group). **b**, IgA concentrations in culture supernatants of B cells with CD11c⁺ cells and with ($n = 5$ per group) or without ($n = 3$ versus 4) CD4 T cells, and co-stimulated with heat-killed bacteria and sodium acetate for 7 days. **c**, IgA concentrations in culture supernatants of CD19⁺IgD⁺ B cells and CD11c⁺ cells with CD4 T cells from wild-type mice, and co-stimulated with 0.1 μ g ml⁻¹ of LPS and sodium acetate for 7 days ($n = 10$ per group). **d**, IgA concentrations in culture supernatants of CD19⁺IgD⁺ B cells and CD11c⁺ cells with CD4 T cells from *Myd88*^{-/-} *Ticam1*^{-/-} mice, and co-stimulated with 0.1 μ g ml⁻¹ of LPS and sodium acetate for 7 days ($n = 5$ per group). **e**, *Aldh1a2* mRNA expression in CD11c⁺ cells sorted from MLN cells co-stimulated ex vivo with heat-killed bacteria and 5 mM sodium acetate for 4 h ($n = 3$ per group). **a–e**, Data are mean and s.d. * $P < 0.05$, ** $P < 0.01$, *** $P < 0.001$; two-way ANOVA with Tukey's test (**a, e**) and Kruskal–Wallis test with Dunn's test (**b–d**). Pooled data from two independent experiments (**c**). Exact P values are provided in the Source Data.

[Source data](#)

Extended Data Fig. 9 Acetate does not increase colonic IgA production or SIgA binding of Enterobacteriales in T-cell-deficient mice.

a, b, Representative flow cytometry plots (gated on DAPI⁺ population) illustrating faecal SIgA⁺ bacteria in *Cd3e*^{-/-} mice (**a**) and summary data (**b**) ($n = 4$ per group). **c**, Faecal SIgA concentration in *Cd3e*^{-/-} mice ($n = 6$ per group). **d**, Representative flow cytometry plots (gated on lymphocytes) depicting colonic IgA⁺B220⁻ plasma cells in *Cd3e*^{-/-} mice. **e, f**, The frequency among colonic lymphocytes (**e**) and the absolute number (**f**) of

IgA-producing plasma cells ($n = 6$ per group). **g**, Representative flow cytometry plots (gated on $B220^+$ lymphocytes) depicting $GL7^+Fas^+$ germinal-centre B cells in MLNs of $Cd3e^{-/-}$ mice. **h, i**, The frequency of germinal-centre B cells among MLN lymphocytes (**h**) and the absolute number in $Cd3e^{-/-}$ mice (**i**) ($n = 5$ per group). **j**, A principal coordinate analysis (PCoA) plot of weighted UniFrac distances for faecal SIgA⁻ and SIgA⁺ bacteria in $Cd3e^{-/-}$ mice ($n = 6$ per group). The dashed and solid lines indicate 90% confidence levels for the SIgA⁻ and SIgA⁺ bacteria groups, respectively. **k**, The relative abundance of faecal SIgA⁻ and SIgA⁺ bacteria at the phylum level in $Cd3e^{-/-}$ mice ($n = 6$ per group). **l–n**, The relative abundance of faecal SIgA⁻ and SIgA⁺ Bacteroidales (**l**), Erysipelotrichales (**m**) and Enterobacterales (**n**) in $Cd3e^{-/-}$ mice ($n = 6$ per group). **o**, A principal coordinate analysis plot of weighted UniFrac distances for luminal and mucosa-associated bacteria in $Cd3e^{-/-}$ mice ($n = 6$ per group). The dashed and solid lines indicate 90% confidence levels for the luminal and mucosa-associated bacteria groups, respectively. **p**, The relative abundance of gut bacteria at the phylum level in the colonic luminal contents and mucus layer of $Cd3e^{-/-}$ mice ($n = 6$ per group). **q**, Ratio of mucosa-associated to luminal bacteria at the order level in $Cd3e^{-/-}$ mice depicted on a \log_{10} scale, with unsupervised clustering based on Ward's method ($n = 6$ per group). The taxa highlighted in bold were significantly altered in terms of their localization upon WSCA diet administration. **b, c, e, f, h, i, l–n**, Data are mean and s.d. * $P < 0.05$, *** $P < 0.001$; two-sided Wilcoxon rank-sum test (**b, e, f, h, i, q**), two-way ANOVA with Tukey's test (**c**) and Kruskal–Wallis test with Dunn's test (**l–n**). P values were corrected by FDR (**q**). Exact P values are provided in the Source Data.

[Source data](#)

[Extended Data Fig. 10 Toll-like receptor signalling in CD4 T cells is necessary for acetate to increase colonic IgA production.](#)

a, Microorganism-reactive SIgA in the caecal contents from $Cd3e^{-/-}$ mice transferred with wild-type ($n = 9$ per group) or $Myd88^{-/-}Ticam1^{-/-}$ (DKO;

n = 8 versus 9) CD4 T cells. **b**, The absolute number of colonic CD4 T cells in *Cd3e*^{-/-} mice transferred with wild-type (*n* = 9 per group) or *Myd88*^{-/-} *Ticam1*^{-/-} (*n* = 8 versus 9) CD4 T cells. **c, d**, The frequency of caecal SIgA⁺ bacteria (**c**) and the absolute number of colonic IgA-producing plasma cells (**d**) in *Cd3e*^{-/-} mice monocolonized with *E. coli*. The mice were transferred with CD4 T cells from either wild-type (*n* = 4 versus 6) or *Myd88*^{-/-} *Ticam1*^{-/-} (*n* = 4 per group) mice two to three weeks before the dietary intervention. **e, f**, The frequency of faecal SIgA⁺ bacteria (**e**) and the absolute number of colonic IgA-producing plasma cells (**f**) in *Gpr43*^{+/-} (*n* = 5 per group) and *Gpr43*^{-/-} (*n* = 5 versus 6) mice. Data are mean and s.d. (**a–f**). **P* < 0.05, ***P* < 0.01, ****P* < 0.001; Kruskal–Wallis test with Dunn’s test (**a–f**). Pooled data from two independent experiments (**a, c, d**). Exact *P* values are provided in the Source Data.

[Source data](#)

Supplementary information

[Supplementary Figure 1](#)

This file contains Supplementary Figure 1 and the accompanying legend for Supplementary Figure 1.

[Reporting Summary](#)

Source data

[Source Data Fig. 1](#)

[Source Data Fig. 2](#)

[Source Data Fig. 3](#)

[Source Data Extended Data Fig. 1](#)

[Source Data Extended Data Fig. 2](#)

[Source Data Extended Data Fig. 3](#)

[Source Data Extended Data Fig. 4](#)

[Source Data Extended Data Fig. 5](#)

[Source Data Extended Data Fig. 6](#)

[Source Data Extended Data Fig. 7](#)

[Source Data Extended Data Fig. 8](#)

[Source Data Extended Data Fig. 9](#)

[Source Data Extended Data Fig. 10](#)

Rights and permissions

[Reprints and Permissions](#)

About this article



Check for
updates

Cite this article

Takeuchi, T., Miyauchi, E., Kanaya, T. *et al.* Acetate differentially regulates IgA reactivity to commensal bacteria. *Nature* **595**, 560–564 (2021).
<https://doi.org/10.1038/s41586-021-03727-5>

Download citation

- Received: 11 April 2019
- Accepted: 15 June 2021
- Published: 14 July 2021
- Issue Date: 22 July 2021
- DOI: <https://doi.org/10.1038/s41586-021-03727-5>

Comments

By submitting a comment you agree to abide by our [Terms](#) and [Community Guidelines](#). If you find something abusive or that does not comply with our terms or guidelines please flag it as inappropriate.

[Access through your institution](#)

[Change institution](#)

[Buy or subscribe](#)

Advertisement

This article was downloaded by **calibre** from <https://www.nature.com/articles/s41586-021-03727-5>

Dysregulation of brain and choroid plexus cell types in severe COVID-19

[Download PDF](#)

- Article
- [Published: 21 June 2021](#)

Dysregulation of brain and choroid plexus cell types in severe COVID-19

- [Andrew C. Yang](#) [ORCID: orcid.org/0000-0002-6756-4746](#)^{1,2,3 na1},
- [Fabian Kern](#) [ORCID: orcid.org/0000-0002-8223-3750](#)^{4 na1},
- [Patricia M. Losada](#)³,
- [Maayan R. Agam](#)³,
- [Christina A. Maat](#)³,
- [Georges P. Schmartz](#)⁴,
- [Tobias Fehlmann](#) [ORCID: orcid.org/0000-0003-1967-2918](#)⁴,
- [Julian A. Stein](#)⁵,
- [Nicholas Schaum](#)³,
- [Davis P. Lee](#)³,
- [Kruti Calcuttawala](#)³,
- [Ryan T. Vest](#)³,
- [Daniela Berdnik](#)³,
- [Nannan Lu](#)³,
- [Oliver Hahn](#)³,
- [David Gate](#) [ORCID: orcid.org/0000-0003-0481-9657](#)³,
- [M. Windy McNerney](#)⁶,
- [Divya Channappa](#)³,
- [Inma Cobos](#)^{3,7},
- [Nicole Ludwig](#)⁸,
- [Walter J. Schulz-Schaeffer](#) [ORCID: orcid.org/0000-0001-5886-2322](#)⁵,
- [Andreas Keller](#) [ORCID: orcid.org/0000-0002-5361-0895](#)^{3,4 na2} &
- [Tony Wyss-Coray](#) [ORCID: orcid.org/0000-0001-5893-0831](#)^{2,3,9,10 na2}

[Nature](#) volume 595, pages 565–571 (2021) [Cite this article](#)

- 37k Accesses

- 1486 Altmetric
- [Metrics details](#)

Subjects

- [Cellular neuroscience](#)
- [Immunohistochemistry](#)
- [Infection](#)
- [Neuroimmunology](#)
- [SARS-CoV-2](#)
- [Transcriptomics](#)

Abstract

Although SARS-CoV-2 primarily targets the respiratory system, patients with and survivors of COVID-19 can suffer neurological symptoms^{1,2,3}. However, an unbiased understanding of the cellular and molecular processes that are affected in the brains of patients with COVID-19 is missing. Here we profile 65,309 single-nucleus transcriptomes from 30 frontal cortex and choroid plexus samples across 14 control individuals (including 1 patient with terminal influenza) and 8 patients with COVID-19. Although our systematic analysis yields no molecular traces of SARS-CoV-2 in the brain, we observe broad cellular perturbations indicating that barrier cells of the choroid plexus sense and relay peripheral inflammation into the brain and show that peripheral T cells infiltrate the parenchyma. We discover microglia and astrocyte subpopulations associated with COVID-19 that share features with pathological cell states that have previously been reported in human neurodegenerative disease^{4,5,6}. Synaptic signalling of upper-layer excitatory neurons—which are evolutionarily expanded in humans⁷ and linked to cognitive function⁸—is preferentially affected in COVID-19. Across cell types, perturbations associated with COVID-19 overlap with those found in chronic brain disorders and reside in genetic variants associated with cognition, schizophrenia and depression. Our findings and public dataset provide a molecular framework to understand current observations of COVID-19-related neurological disease, and any such disease that may emerge at a later date.

[Download PDF](#)

Main

Patients with COVID-19 can suffer neurological and psychiatric symptoms that range from loss of smell and headache to encephalitis and stroke^{1,2,3,9,10,11}. These symptoms

are more prevalent in patients who are hospitalized^{1,12,13} and may persist as ‘long COVID’, which consists of ‘brain fog’, difficulty in concentrating and fatigue^{14,15}.

Cellular and molecular approaches are required to understand the neurological changes that may contribute to symptoms reported in patients with COVID-19.

Neuropathology may arise from direct virus neuroinvasion or indirectly from peripheral infection and its attendant immune response¹⁶. Thus, much attention has been paid to whether SARS-CoV-2 can be detected in the brain, which has yielded inconsistent results^{9,17,18,19,20,21}. Critically, a comprehensive assessment across specific cell types in the brain affected by severe COVID-19 is missing. This is in part because the high-quality, fresh-frozen human brain tissue from patients with COVID-19 needed for single-cell transcriptomic studies is largely inaccessible, and methods to isolate human brain barrier cells have only recently emerged^{22,23}.

Here we characterized the transcriptomes of 65,309 nuclei isolated from the brains of 14 control individuals and 8 patients with COVID-19 (Fig. 1a, Supplementary Table 1). We created an interactive data browser (https://tvc-stanford.shinyapps.io/scRNA_Brain_COVID19) to provide researchers with a comprehensive resource to further investigate the molecular mechanisms of the effects of SARS-CoV-2 on the brain.

Fig. 1: Overview of diverse brain and choroid plexus cell types captured from post-mortem tissue from patients with COVID-19.

 **figure1**

a, Study design. Coloured triangles denote the brain regions that were studied for each patient. IHC, immunohistochemistry. **b**, Uniform manifold approximation and projection (UMAP) of 38,217 nuclei from the medial frontal cortex of 8 control individuals (including 1 patient with influenza) and 8 patients with COVID-19. As in

previous reports^{5,25,46}, the ‘endothelial’ cluster also exhibits vascular mural cell markers and perivascular cells (perivascular fibroblast-like cells and perivascular macrophages) are not efficiently captured. exc., excitatory; in., inhibitory; OPC, oligodendrocyte precursor cell. **c**, Examples of DEGs in COVID-19 ($n = 7$ control individuals (without viral infection); $n = 8$ patients with COVID-19; MAST with default settings): excitatory neurons (exc. n.), inhibitory neurons (in. n.), astrocytes (ast.), oligodendrocytes (oli.), OPCs, and microglia and macrophages (mic./mac.). DEGs defined as log-transformed fold change > 0.25 (absolute value) and adjusted P value < 0.05 (Bonferroni correction). **d**, Cell-type specificity of cortical DEGs. UpSet plot showing a matrix layout of DEGs shared across and specific to each cell type. Each matrix column represents either DEGs specific to a cell type (single circle with no vertical lines) or DEGs shared between cell types, with the vertical line indicating the cell types that share that given DEG. Top, bar graph displays the number of DEGs in each combination of cell types. Right, bar graph displays the total number of DEGs for a given cell type. **e**, UMAP of 27,092 nuclei from the lateral choroid plexus of 14 individuals ($n = 7$ control individuals (including 1 patient with influenza); $n = 7$ patients with COVID-19; MAST with default settings). **f**, Expression profiles (counts per million reads mapped (CPM)) (circle size) and differential expression in patients with COVID-19 (average log-transformed fold change (avg log FC)) (colour) for genes relevant to SARS-CoV-2 entry into the brain¹⁶. The highlighted region indicates the consistent upregulation of the antiviral defence gene *IFITM3* in choroid and glia limitans brain-barrier cells.

[Full size image](#)

Cortex and choroid plexus cell types

We generated 38,217 single-nucleus gene-expression profiles from the medial frontal cortex (8 control individuals and 8 patients with COVID-19) and detected a median of 1,918 genes per nucleus, consistent with recent studies^{5,8,24,25} (Fig. 1b, Extended Data Fig. 1a). Our sample sizes were similar to or greater than those reported in previous COVID-19 or brain single-nucleus RNA-sequencing (snRNA-seq) studies^{24,25,26}. The samples in the control and COVID-19 groups were from individuals between 55 and 91 years of age and matched for tissue dissection area, tissue and RNA quality (Extended Data Fig. 1b,c, Supplementary Table 1). The cause of death for nearly all patients with COVID-19 or influenza was interstitial pneumonia after more than two weeks of mechanical ventilation. Samples were not confounded by technical or batch artefacts (Extended Data Fig. 2).

Our unsupervised clustering of nuclear transcriptomes yielded 14 cell types, including subtypes of excitatory neurons and interneurons that express previously established

marker genes (Extended Data Fig. 3) and proportional to previous snRNA-seq data from adult human cortex^{5,8,24,25} (Extended Data Figs. 1–3, Supplementary Table 2).

We collapsed nuclei into 6 broad cell types, and identified 786 unique differentially expressed genes (DEGs) that implicated all major cell types (Fig. 1c, Extended Data Fig. 4). DEGs strongly correlated with alternative pseudobulk methods (but with greater statistical power (Extended Data Fig. 5)); and showed no significant overlap with genes affected by post-mortem delay to autopsy²⁷ (Extended Data Fig. 6). Broadly, the strongest effects were seen in astrocytes and other glia, marked by inflammatory and dysregulated homeostatic pathways (Fig. 1c, Extended Data Fig. 4). The majority of DEGs were perturbed in only a single cell type (about 80%) (Fig. 1d). Several DEGs upregulated in one cell type were downregulated in others (Supplementary Tables 3, 5). Overall, these data demonstrate that all major brain parenchymal cell types are affected in COVID-19.

Recent reports have found SARS-CoV-2 infection of cultured choroid plexus organoids^{20,21} but to our knowledge no snRNA-seq study exists on the human choroid plexus, in health or disease²². We thus developed a method (Methods) that yielded 27,092 nuclei across 7 major epithelial, mesenchymal, immune, ependymal and glial cell types (7 control individuals and 7 patients with COVID-19) (Fig. 1e, Extended Data Fig. 3b, Supplementary Table 4). With capture of both brain parenchymal and barrier cell types, we assessed the expression and disease perturbation of genes related to SARS-CoV-2 entry, docking and defence¹⁶. Similar to brain vascular cells, choroid barrier cells robustly expressed several genes that are relevant to SARS-CoV-2 brain entry (Fig. 1f, Extended Data Fig. 7). We observed a broad upregulation of the antiviral defence gene *IFITM3* across choroid and glia limitans barrier cells in patients with COVID-19, consistent with potential SARS-CoV-2 infection. *IFITM3* serves as the first line of defence against viral infection²⁸ and its upregulation is a marker of SARS-CoV-2 infection across public datasets²⁹.

Brain barriers relay inflammation

We observed a broad upregulation of inflammatory genes across various interferon (*IFITM3* and *STAT3*), complement (*C1S*, *C3* and so on) and related pathways across choroid plexus cell types (Fig. 2a). Quantitative PCR with reverse transcription (RT-qPCR) corroborated significant differential expression of tested inflammatory genes as well as other genes predicted to be upregulated by a similar magnitude in COVID-19 (for example, *NQO1* and *ZFP36*) (Fig. 2b). Immunohistochemical staining also confirmed choroid plexus inflammation (Extended Data Fig. 8). Together, these data reveal substantial brain barrier inflammation in COVID-19 and validate the reliability of the DEGs that we identified in our snRNA-seq analysis.

Fig. 2: Brain-barrier inflammation in patients with COVID-19 does not require direct replicative infection.

 figure2

a, Examples of inflammation-related DEGs in the choroid plexus of patients with COVID-19 ($n = 6$ control individuals (without viral infection); $n = 7$ patients with COVID-19; MAST with default settings). DEGs defined as log-transformed fold change > 0.25 (absolute value) and adjusted P value < 0.05 (Bonferroni correction). **b**, Validation of predicted choroid plexus DEGs by RT-qPCR ($n = 6$ control individuals (without viral infection), $n = 7$ patients with COVID-19; two-sided Mann–Whitney t -test; mean \pm s.e.m.). Genes chosen for validation are either immediately related to SARS-CoV-2 (*IFITM3*) or genes with log-transformed fold changes similar to those of *IFITM3* (*NQO1*), to assess the robustness of snRNA-seq thresholds. P values $P = 0.0023$ (*IFITM3*), 0.0484 (*C7*), 0.0350 (*STAT3*), 0.0140 (*NQO1*), 0.0082 (*ZFP36*) and 0.0734 (*SDC4*). **c**, snRNA-seq (left) or bulk RNA-seq (right) of choroid plexus and cortex from control individuals or patients with COVID-19 (no reads). snRNA-seq, $n = 7$ control, $n = 7$ COVID-19 (choroid plexus); $n = 7$ control, $n = 7$ COVID-19 (cortex). Bulk RNA-seq (after viral RNA isolation): $n = 7$ control, $n = 4$ COVID-19 (choroid plexus); $n = 5$ control, $n = 4$ COVID-19 (cortex). **d**, Circle plot showing the

number of statistically significant intercellular signalling interactions for the CXCL and CCL pathway family of molecules in control individuals compared to patients with COVID-19 (permutation test, CellChat³²; $n = 8$ control individuals (including patients with influenza); $n = 8$ patients with COVID-19 (cortex); and $n = 7$ control individuals (including patients with influenza); $n = 7$ patients with COVID-19 (choroid plexus)). Each circle (colour) represents one cell type; edges connecting circles represent significant intercellular signalling inferred between those cell types. Circles and edges are normalized to the number of cells for a given cell type and inferred strength of signalling, respectively. Cell types labelled on the right correspond to signalling pathways increased in COVID-19. Endo., endothelial; epen., ependymal; epi., epithelial; mes., mesenchymal.

[Source data](#)

[Full size image](#)

Brain and choroid cell types express several SARS-CoV-2 entry genes (Fig. 1f, Extended Data Fig. 7) but claims of neuroinvasion in the literature have thus far been inconsistent^{9,17,18,19,20}. To detect molecular evidence of SARS-CoV-2, we systematically performed four RNA-based and four antibody-based assays across our samples. RNA assays included searching for virus-specific reads (Methods) in our snRNA-seq dataset as well as in custom-generated bulk RNA-seq datasets with and without viral RNA enrichment. In no case did we detect SARS-CoV-2-specific RNA in the brain (Fig. 2c, Extended Data Fig. 9a). We confirmed this via qPCR using US Centers for Disease Control and Prevention Emergency Use Authorization primers against the *N1* and *N2* genes of the virus, again finding no enrichment in the brains of individuals with COVID-19 (Extended Data Fig. 9b). Some of the samples from the control individuals without viral infection have high cycle counts (between 37 and 40), which in previous work (without such controls) has been interpreted as evidence of neuroinvasion^{9,18}. Finally, with the anti-SARS-CoV-2 spike (3A2) antibody used for immunohistochemistry (as in previous publications^{17,18}), we observed signal across the barrier-forming cortical vasculature, meninges and choroid plexus (Extended Data Fig. 9c,d). Specific signal was retained across secondary detection methods (Extended Data Fig. 9e, Methods). However, no other antibody—including those also used in recent publications^{9,30}—yielded specific signal over controls. Therefore, the 3A2 antibody may bind a specific, but non-SARS-CoV-2, antigen.

The inflamed choroid plexus has previously been shown to send inflammatory signals into the brain, thereby activating parenchymal glia and impairing cognitive function³¹. To assess whether similar pro-inflammatory relay mechanisms occur in the brains of patients with COVID-19, we performed cell–cell communication analysis³². We observed a strong increase in the choroid-to-cortex network across key inflammatory

pathways, such as the CCL and CXCL family of chemokines from the choroid plexus epithelium to brain astrocytes, oligodendrocytes, microglia and layer (L) 2/3 and L4 excitatory neurons (Fig. 2d, Extended Data Fig. 10). Complement pathway signalling from the choroid plexus to brain microglia (the resident immune cells of the brain) was also predicted to increase in the brains of patients with COVID-19. Excessive complement signalling in microglia has previously been linked to premature neuronal synapse pruning in neurodegenerative disease³³. Together, although we could not specifically detect virus RNA or protein in our brain samples, these results suggest that peripheral SARS-CoV-2 infection inflames brain-barrier cells such as those of the choroid plexus; and that this inflammation is then relayed into the brain parenchyma.

Disease-associated microglia and astrocytes

We thus sought to evaluate the immune landscape of the brain in individuals with COVID-19. We first analysed cortical immune cells, which contain mostly microglia but also lesser fractions of perivascular macrophages (*MRC1*⁺, which encodes macrophage-specific mannose receptor CD206³⁴) and T cells (*CD247*⁺, which encodes the T cell receptor CD3ζ protein). Our unsupervised clustering revealed the presence of a subpopulation of immune cells associated with COVID-19 (Fig. 3a), which was significantly enriched at both the per-nucleus and per-patient level (Fig. 3b). The emergence of disease-associated clusters reflects strong perturbations across the transcriptome. Similarly, although we did not find cortical T cells in any of our samples from control individuals (without viral infection or with terminal influenza), we detected them in all but one of the patients with COVID-19 (Fig. 3c). Aberrant T cell infiltration into the mouse brain has previously been reported to be sufficient to promote neuroinflammation and impair neurogenesis³⁵.

Fig. 3: A neuroinflammatory COVID-19 milieu marked by disease-associated microglia.

 **figure3**

a, UMAP of immune cells captured in the human frontal cortex, split by control individuals (including a patient with influenza) ($n = 8$) (red) and patients with COVID-19 ($n = 8$) (light blue). Cells are coloured by cell-type subcluster (red cluster defined by homeostatic markers; light blue cluster defined by activation markers). **b**, Quantification of immune cell cluster 1 as a proportion of total immune cells ($n = 8$ control individuals (including a patient with influenza (circle marked as ‘flu’)); $n = 8$ patients with COVID-19, two-sided Mann–Whitney t -test $P = 0.0098$; mean \pm s.e.m.). **c**, As in **b**, but for T cells. $P = 0.0003$. **d**, **e**, As in **a**, **b**, respectively, but for MRC1[−] parenchymal microglia. $P = 0.0343$. Unlike macrophages, microglia express low levels of *MRC1* (CD206)³⁴. Examples of genes that are upregulated in the microglial cluster associated with COVID-19 are shown in light blue. **f**, Pseudotime trajectory (Methods) indicated in graded purple (low) to yellow (high), plotting the emergence of the microglial cluster associated with COVID-19. Numbers indicate original source population (1) and the newly emerged population in COVID-19 (2). **g**,

Immunohistochemical staining for the microglial activation marker CD68 (brown) in the frontal medial cortex of a patient with COVID-19, immediately adjacent to that used for snRNA-seq. Haematoxylin counterstain (blue). Scale bars, 20 µm.

Immunohistochemical stains are representative of at least two independent experiments. **h**, Overlap (hypergeometric test) between marker genes of Alzheimer's-disease-associated microglia (DAM, ARM and Mic1)^{4,5,6} and genes that are upregulated in the microglial cluster associated with COVID-19.

[Source data](#)

[Full size image](#)

To study microglia, we focused on the *MRC1*⁻*CD247*⁻ immune cell subset to eliminate confounds from perivascular macrophages and T cells. Library quality was not affected upon restricting analyses to the *MRC1*⁻ subset of microglia (Methods). We clustered 1,814 *MRC1*⁻ microglia, which revealed a distinct microglial subpopulation associated with COVID-19 (Fig. 3d) that was significant at both the per-nucleus and per-patient level (Fig. 3e). This subpopulation was marked by expression of microglial activation genes previously associated with human disease^{4,5}, such as complement *C1QC*, *CD74*, *FTL* and *FTH1*, and downregulation of the homeostatic markers including *P2RY12* (Fig. 3d, Supplementary Table 6). Trajectory analysis revealed that the microglia cluster associated with COVID-19 emerged from the parent homeostatic population (Fig. 3f), which further suggests that these microglia emerge in response to an increasingly inflamed central nervous system (CNS) environment. Our *in situ* staining confirmed the enriched presence of activated CD68⁺ parenchymal microglia in the brains of patients with COVID-19 as compared to those of control individuals (Fig. 3g, Extended Data Fig. 11); at times, these microglia form nodules that have previously been linked to viral encephalitis³⁶ and myelin degeneration in ageing mice³⁷.

Microglial subclusters that are associated with disease have been identified for various neurodegenerative diseases^{4,5}. A fraction of the genes enriched in the COVID-19-associated microglia cluster overlap ($P = 2.3 \times 10^{-15}$, hypergeometric test) with those enriched in neurodegenerative-disease-associated microglia (Fig. 3h), including *C1QC* and *CD14* (which mark microglia associated with Alzheimer's disease). Yet, several genes that have been implicated in neuroinflammation³⁸ (such as *RIPK1*) were seen specifically in microglial states associated with COVID-19. Our observations suggest that the microglial subpopulation enriched in patients with COVID-19 represents a distinct microglial state that shares features with—but is ultimately different from—microglial cell states that have previously been reported in human neurodegenerative disease.

In addition to abnormally activated microglia, we uncovered an astrocyte cluster associated with COVID-19 that is marked by established inflammation and astrogliosis genes (such as *IFITM3* and *GFAP*) and upregulated expression of the secreted neurotoxic factor chitinase 3-like 1 (*CHI3L1*)³⁹ (Extended Data Fig. 12a–c). Within this astrocyte cluster, we also observed significant dysregulation of genes that support neurotransmission and synaptic organization. By contrast, we did not observe any new subpopulations for oligodendrocyte lineage cells (Extended Data Fig. 12d–g). Together, we identify the robust emergence of disease-associated microglia and astrocyte subpopulations with distinct transcriptional profiles in the brains of individuals with COVID-19.

Links to long-term CNS dysfunction

Given the predicted astrocytic impairments in supporting neurotransmission, we next sought to identify the neuronal subtypes that are most affected in COVID-19.

Although we captured neurons from all cortical layers, we found gene-expression changes linked to synaptic deficits particularly in L2/3 excitatory neurons and L2/3-residing VIP interneurons⁴⁰ (Fig. 4a, b). Specifically, the downregulation of synaptic genes that mediate neurotransmission (for example, *VAMP2*, *SNAP25* and *ATP6V0C*) in L2/3 excitatory neurons alongside a concomitant upregulation in proximal VIP inhibitory neurons suggests dysfunction in upper-layer cortical circuitry. Such a pattern of dysfunction has previously been reported in an snRNA-seq study of autism and correlated with cognitive deficits⁸. L2/3 excitatory neurons are cortico-cortical projecting and already exhibit sparse action potential firing to generate a simple and reliable neural code for associative learning⁴¹. Thus, this neuronal population may be particularly sensitive to deficits in neurotransmission by COVID-19.

Fig. 4: Molecular dysfunction in upper-layer neurons and links to long-term symptoms.

 **figure4**

a, Dot plot showing downregulation of synaptic vesicle components, especially in L2/3 excitatory neurons in patients with COVID-19 ($n = 7$ control individuals (without viral infection); $n = 8$ patients with COVID-19; MAST with default settings). FC, fold change. **b**, Diagram of cortical neurons captured in this study that have known layer localization. Neuron labels are colour-coded by layer localization as shaded in **a**. Figure layout adapted with permission from ref. [8](#). **c**, Overlap between COVID-19

DEGs and those in chronic CNS diseases (Methods). Dotted line indicates statistical significance (adjusted P value < 0.05 , false-discovery rate (FDR) correction, cumulative hypergeometric test). **d**, Heat map showing the number of DEGs per cell type that overlap as GWAS risk variants across psychiatric and neurological diseases and traits from the GWAS catalogue (NHGRI-EBI)⁴³. Significance of overlap is based on FDR-corrected cumulative hypergeometric P values (Benjamini–Hochberg correction) < 0.05 ; MAST with default thresholds). AD, Alzheimer’s disease; ADHD, attention deficit hyperactivity disorder; ALS, amyotrophic lateral sclerosis; MS, multiple sclerosis; MSA, multiple system atrophy; PD, Parkinson’s disease; PTSD, post-traumatic stress disorder.

[Full size image](#)

To investigate the potential pathologies that underlie reported neurological symptoms of long COVID, we analysed the intersection between COVID-19 DEGs across brain cell types with those that have previously been described in chronic CNS diseases, such as Alzheimer’s disease⁵, multiple sclerosis²⁶, Huntington’s disease⁴² and autism spectrum disorder⁸. Although neuronal perturbations in COVID-19 were unique compared to those in chronic CNS diseases, the overlap in glial cells was particularly strong (Fig. 4c, Supplementary Table 7).

To further determine the enrichment of COVID-19 DEGs within genetic variants associated with complex traits and diseases in a cell-type-specific fashion, we obtained genome-wide association study (GWAS) summary statistics for neurological and psychiatric disorders and neurobehavioural traits⁴³ (Supplementary Table 8). We found a strong enrichment of DEGs residing within GWAS hits of neurological disorders and traits, especially in cognition, schizophrenia and depression (Fig. 4d). Together, these data suggest that COVID-19 may partially recapitulate the pathological processes of various CNS diseases.

Discussion

Previous snRNA-seq studies have begun to elucidate the cell-type-specific perturbations and interactions involved in several CNS disorders^{5,8,25,26,42}. Here, by combining sequencing of 65,309 nuclei in both the frontal cortex and choroid plexus, along with confirmatory immunohistochemistry and RT-qPCR, we reveal several major neuropathological mechanisms in severe COVID-19. However, there are limitations to consider. Most post-mortem brain tissue from individuals with COVID-19 is inadequately preserved or immediately fixed for safety and regulatory reasons, so there is a scarcity of high-quality tissue available for molecular studies. Also, although we did not detect SARS-CoV-2 in the choroid plexus or cortex, we cannot exclude the possibility of earlier neuroinvasion that had subsequently been cleared. Indeed, the

mouse choroid plexus has recently been reported to express several SARS-CoV-2 entry factors²², which we corroborate in humans ([Supplementary Discussion](#)).

There is a precedent for acute viral infections causing long-term inflammation and dysfunction that predisposes individuals to neurodegenerative disease^{44,45}, although not at the scale of the COVID-19 pandemic. It will be important to study how the molecular processes elucidated here contribute to the COVID-19 neurological symptoms and deficits of which we are aware now, and to those that may emerge in the years to come.

Methods

No statistical methods were used to predetermine sample size. The experiments were not randomized, and investigators were not blinded to allocation during experiments and outcome assessment.

Isolation of nuclei from frozen post-mortem medial frontal gyrus

Frozen medial frontal cortex tissue from post-mortem control individuals and patients with COVID-19 was obtained from the Stanford/VA/NIA Ageing Clinical Research Center (ACRC) and the Saarland University Hospital Institute for Neuropathology, with approval from local ethics committees. Group characteristics are presented in Supplementary Table 1. The protocol for the isolation of nuclei was adapted from previous studies^{5,25,46,47,48}, and performed in a BSL2+ biosafety cabinet wearing personal protective equipment (PPE). All procedures were carried out on ice or at 4 °C. In brief, 50 mg of post-mortem brain tissue was dounce-homogenized in 2 ml of Nuclei EZ Prep Lysis Buffer (Sigma, NUC101) spiked with 0.2 U μl^{-1} RNase inhibitor (Takara, 2313A) and EDTA-free protease inhibitor Cocktail (Roche, 11873580001) before incubating on ice for 5 min in a final volume of 5 ml.

Homogenized tissue was filtered through a 100- μm cell strainer (Falcon, 352360), mixed with an equal volume of 50% iodixanol density gradient medium in PBS (OptiPrep, Sigma-Aldrich, D1556) to make a final concentration of 25% iodixanol. Thirty per cent iodixanol was layered underneath the 25% mixture. Similarly, 40% iodixanol was layered underneath the 30% iodixanol. In a swinging-bucket centrifuge, nuclei were centrifuged for 20 min at 3,000 r.c.f. After centrifugation, the nuclei were present at the interface of the 30% and 40% iodixanol solutions. Isolated nuclei were resuspended in 1% BSA with 0.2 U μl^{-1} RNase inhibitor, filtered twice through a 40- μm strainer (Flowmi) and counted on an TC20 automated cell counter (Bio-Rad) after the addition of Trypan blue. We did not use statistical methods to predetermine sample sizes, but our sample sizes are similar to those reported in previous publications^{24,25,49}.

Isolation of nuclei from frozen post-mortem choroid plexus

Frozen choroid plexus tissue was extracted from the lateral ventricles of post-mortem tissue obtained from the Stanford University Pathology department and the Saarland University Hospital Institute for Neuropathology, with approval from local ethics committees. Group characteristics are presented in Supplementary Table 1. All procedures were carried out on ice or at 4 °C, and in a BSL2+ biosafety cabinet while wearing PPE. Dounce homogenization or enzymatic dissociation resulted in loss of nuclei integrity and low nuclei complexity (<50 median genes per nuclei). We hypothesized that, similar to shaking an apple tree, gentle pipetting of choroid plexi tissue in lysis buffer could liberate nuclei without needing to physically disintegrate the fibrous choroid matrix—and thus avoid collateral physical damage to nuclei. Specifically, 40 mg of choroid plexus tissue was thawed in 250 µl of 1% BSA with 0.2 U µl⁻¹ RNase inhibitor until the tissue settled. Five ml of lysis buffer (10 mM Tris, 10 mM NaCl, 3 mM MgCl₂, 0.1% Nonidet P40 substitute (Roche/Sigma, 11754599001), 0.2 U µl⁻¹ RNase inhibitor, and protease inhibitor) was added and tissue incubated on ice for 10 min with gentle swirling every 2 min. Five ml of 1% BSA was added and the tissue triturated 10 times with a 5-ml serological pipette. After centrifugation (500g, 5 min), pelleted nuclei were resuspended in 1% BSA with 0.2 U µl⁻¹ RNase inhibitor, gently triturated 10 times with a 1-ml regular-bore pipette tip and filtered twice through a 70-µm and then a 40-µm strainer (Flowmi). Debris was inspected on a brightfield microscope and nuclei were counted on an TC20 automated cell counter (Bio-Rad) after the addition of Trypan blue.

Droplet-based snRNA-seq

For droplet-based snRNA-seq, libraries were prepared using the Chromium Next GEM Single Cell 3' v.3.1 according to the manufacturer's protocol (10x Genomics), targeting 10,000 nuclei per sample after counting with a TC20 Automated Cell Counter (Bio-Rad). Thirteen cycles were applied to brain parenchyma samples to generate cDNA, and 15 for choroid plexus samples. All samples underwent 15 or 16 cycles for final library generation. Generated snRNA-seq libraries were sequenced across two S4 lanes on a NovaSeq 6000 (150 cycles, Novogene).

snRNA-seq quality control

Raw gene counts were obtained by aligning reads to the hg38 genome (refdata-gex-GRCh38-2020-A) using CellRanger software (v.4.0.0) (10x Genomics). To account for unspliced nuclear transcripts, reads mapping to pre-mRNA were also counted. As previously published, a cut-off value of 200 unique molecular identifiers was used to select nuclei of sufficient complexity for further analysis⁵. As initial reference, the

entire dataset was projected onto two-dimensional space using UMAP on the top 20 principal components⁵⁰. Three approaches were combined for quality control: (1) ambient cell free mRNA contamination was removed using SoupX⁵¹ for each individual sample; (2) outliers with a high ratio of mitochondrial (>5%, <200 features) relative to endogenous RNAs and homotypic doublets (>5,000 features) were removed in Seurat 3.2.1⁵²; and (3) after scTransform normalization and integration, doublets and multiplets were filtered out using DoubletFinder with subsequent manual inspection and filtering on the basis of cell-type-specific marker genes⁵³. Similarly, genes detected in fewer than four cells were excluded from the analysis. The core statistical parameters of DoubletFinder (nExp and pK) used to build artificial doublets for true doublet classification were determined automatically using recommended settings. The computed nExp and pK values for each sample are provided in Supplementary Table 1. After applying these filtering steps, the dataset contained 65,309 high-quality nuclei.

Cell annotations

The SCTransform-based integration workflow of Seurat⁵⁴ was used to align data, using default settings. In brief, the integration workflow searches for common gene modules (anchors) in cells with similar transcriptomes. Individual samples after undergoing quality control (described in ‘snRNA-seq quality control’) are integrated in a step-wise fashion, using cellular sequencing depth as a covariate to mitigate technical artefacts. After combining the samples into a single dataset or Seurat object, genes were projected into principal component space using the principal component analysis (RunPCA). The first 80 (for global object), 30 (choroid plexus) or 25 (specific cell types) dimensions were used as inputs into the FindNeighbours, FindClusters (at 0.2 resolution) and RunUMAP functions of Seurat. In brief, a shared-nearest-neighbour graph was constructed on the basis of the Euclidean distance metric in principal component space, and cells were clustered using the Louvain method. RunUMAP functions with default settings was used to calculate 2D UMAP coordinates and search for distinct cell populations. The positive differential expression of each cluster against all other clusters (MAST) was used to identify marker genes for each cluster⁵⁵. We annotated cell types using previously published marker genes^{5,8,24,46}. To distinguish between confounding (perivascular) macrophages and T cells and pure microglia in the larger cortex immune population, we subset the cluster and repeated the standard steps of Seurat for dimension reduction and unsupervised clustering. Then, to yield pure microglia by requiring the normalized expression of the specific cell-type markers MRC1 and CD247 to be strictly less than 1. As choosing a threshold involves a sensitivity–specificity trade-off, we sought to set strict cut-offs as to yield pure microglia at a high specificity. The MRC1⁺ cell population did not form separate clusters in an unsupervised clustering of the larger

immune population and was not associated with better or lower library quality scores, as assessed through the number of detected unique molecular identifiers, number of detected RNAs (genes) and percentage of mitochondrial reads.

Differential gene expression and subcluster analysis

Differential gene expression of genes comparing control individuals and patients with COVID-19—or comparing cell-type subcluster markers—was done using the MAST⁵⁵ algorithm (v.1.12.0), which implements a two-part hurdle model, and has demonstrated superior type-I error control without significantly sacrificing sensitivity^{56,57,58,59}. First, we ensured that our data did not exhibit signs of confounding effects (Extended Data Fig. 2). For example, although sex imbalance of patient cohorts can influence some genes in single-cell analysis and is a general issue in the field, we balanced genders by group, mitigating variance due to sex (Extended Data Fig. 2a, Supplementary Tables 3, 5). Default Seurat thresholds of log-transformed fold change > 0.25 (absolute value), adjusted P value (Bonferroni correction) < 0.05 and expression in greater than 10% of cells were required to consider a gene differentially expressed, as similarly done in previous studies of the brain^{5,8,25,26,46,60,61,62,63} and COVID-19^{64,65,66,67,68,69,70}. Sex and batch were set as latent variables. Our sensitivity to detect DEGs for a given cell type was not driven by the number of nuclei isolated (Extended Data Fig. 4c).

Cell-quality-associated markers were removed and biological pathway and gene ontology enrichment analysis were performed using Enrichr⁷¹, Metascape⁷² or GeneTrail 3⁷³ with input species set to *Homo sapiens* and using standard parameters. Docking, processing and viral defence genes relevant to SARS-CoV-2 were chosen on the basis of a previous publication¹⁶. To identify microglia subcluster markers, differential expression analysis of cells grouped in each subcluster was performed against the remaining cells within the given cell-type. Markers were defined based on the MAST algorithm using only positive values with log-transformed fold change > 0.25 (absolute value) and adjusted P value (Bonferroni correction) < 0.05 . Enrichment or over-representation of the overlap between markers defining the COVID-19 microglia 2 cluster and the Mathys⁵ Alzheimer’s disease Mic1 cluster followed the hypergeometric probability, using the set of 17,926 protein-coding genes as background. To assess alternative differential expression approaches, raw gene counts were aggregated for each sample and cell-type cluster separately. For the subsequent pseudobulk analysis, we used the pbDS function of the muscat package⁷⁴ with limma-voom⁷⁵ selected as differential state method, and the parameters min_cells, and filter set to 20 and gene, respectively, where we configured sample sex and batch as latent variables in the design matrix. All other parameters were kept as default.

RT-qPCR validation of snRNA-seq differential gene expression

For RT-qPCR validation of our snRNA-seq DEG analysis, we focused on choroid plexus tissue because of its relative homogeneity compared to cortex: epithelium and mesenchymal cells form over 90% of all nuclei and, hence, DEGs in those cell types can be assessed even in bulk choroid plexus mRNA samples with only an approximately 10% potential confound from other cell types. This is not the case with cortex samples consisting of various cell types and subtypes (for example, neuronal subtypes). In brief, choroid plexus nuclei were isolated as in ‘Isolation of nuclei from frozen post-mortem choroid plexus’, and bulk mRNA isolated using the RNeasy Micro Kit (Qiagen). cDNA was generated using the qScript cDNA SuperMix (Quantabio) and then mixed with SYBR green master mix before loading as technical duplicates on a LightCycler 480 (Roche). $\Delta\Delta C_T$ values normalized to *ACTB* were used to assess relative gene expression between samples. The following validated primer pairs were used (PrimerBank, human)⁷⁶ to assess major inflammatory genes predicted upregulated in COVID-19 as well as other genes predicted upregulated at a similar log-transformed fold change to confirm the validity of default snRNA-seq DEG MAST thresholds: *IFITM3*: 5'-CTGGGCTTC ATAGCATTGCCT-3' (forward) and 5'-AGATGTTCAAGCACTTGGCGGT-3' (reverse); *STAT3*: 5'-CAGCAGCTTGACACACGGTA-3' (forward) and 5'-AAACACCAAAGTGGCATGTGA-3' (reverse); *C7*: 5'-AATGGCTGTACCAAGACTCAGA-3' (forward) and 5'-GCTGATGCACTGACCTGAAAA-3' (reverse); *NQO1*: 5'-GAAGAGCACTGATCGTACTGGC-3' (forward) and 5'-GGATACTGAAAGTTCGCAGGG-3' (reverse); *ZFP36*: 5'-GACTGAGCTATGTCGGACCTT-3' (forward) and 5'-GAGTTC CGTCTTGTATTGGGG-3' (reverse); *SDC4*: 5'-GGACCTCCTAGAAGGCCGATA-3' (forward) and 5'-AGGGCCGATCATGGAGTCTT-3' (reverse); *ACTB*: 5'-CACCATGGCAATGAGCGGTT-3' (forward) and 5'-AGGTCTTGCGGATGTCCACGT-3' (reverse); and (housekeeping performed in duplicate): 5'-GGAGAAGAGCTACGAGCTGCCTGAC-3' (forward) and 5'-AAGGTAGTTCGTGGATGCCACAGG-3' (reverse)

Monocle trajectory analysis

Monocle3 (v.0.2.1.) was used to generate the pseudotime trajectory analysis in microglia⁷⁷. Cells were reclustered as described in ‘Cell annotations’ and used as input into Monocle to infer cluster and lineage relationships within a given cell type. Specifically, UMAP embeddings and cell subclusters generated from Seurat were converted to a `cell_data_set` object using SeuratWrappers (v.0.2.0) and then used as input to perform trajectory graph learning and pseudotime measurement through reversed graph embedding with Monocle.

Viral transcript analysis

Four RNA-based approaches were applied to systematically probe for the presence of SARS-CoV-2 RNA in the brain: analysis by snRNA-seq, bulk RNA-seq after viral isolation (QIAamp Viral RNA Mini Kit, Qiagen, manufacturer’s instructions), bulk RNA-seq after whole transcriptome isolation and RT–PCR using US Centers of Disease Control and Prevention (CDC) Emergency Use Authorization primers against the SARS-CoV-2 *N1* and *N2* genes (IDT 10006770). Both bulk RNA-seq RNA underwent established cDNA and library generation: in brief, mRNA was transcribed into full-length cDNA by using the Smart-Seq v.4 Ultra-Low-Input RNA kit from Clontech according to the manufacturer’s instructions. Samples were validated with an Agilent 2100 Bioanalyzer. Full-length cDNA was processed with the Nextera XT kit from Illumina for library preparation according to the manufacturer’s protocol. Library quality was verified with an Agilent 2100 Bioanalyzer. Sequencing was carried out on a NovaSeq 6000 (150 cycles, Novogene). For RT–PCR analysis, bulk choroid whole transcriptome mRNA samples were diluted and mixed with SYBR green master mix before loading as technical duplicates on a LightCycler 480 (Roche) for 40 cycles.

To search for SARS-CoV-2 reads in either the snRNA-seq or bulk RNA-seq datasets, raw .fastq files were subjected to read alignment via Viral-Track⁷⁸, VIRTUS⁷⁹ or centrifuge⁸⁰ using the human (GRCh38) genome reference. For Viral-Track, both a collection of 12,163 consensus virus sequences

from Virusite⁸¹ (release 2020.3) and 17,133 curated SARS-CoV-2 genomes from NCBI (downloaded on 29 September 2020) were used. For centrifuge, a preprocessed virus index compiled by genexa containing among other viruses 138 SARS-CoV-2 genomes was used. We also adopted a complementary approach⁸² focusing on SARS-CoV-2 reads, in which barcoded but unmapped BAM reads were aligned using STAR to the SARS-CoV-2 reference genome, with a less stringent mapping parameter (outFilterMatchNmin 25-30) than the original Viral-Track pipeline.

Cell–cell communication

Cell–cell interactions based on the expression of known ligand–receptor pairs in different cell types were inferred using CellChat³² (v.0.02). To identify potential cell–cell communication networks perturbed or induced in brains of patients with COVID-19, we followed the official workflow and loaded the normalized counts into CellChat and applied the preprocessing functions identifyOverExpressedGenes, identifyOverExpressedInteractions and projectData with standard parameters set. As database, we selected the Secreted Signalling pathways and used the precompiled human Protein–protein-Interactions as a priori network information. For the main analyses the core functions computeCommunProb, computeCommunProbPathway and aggregateNet were applied using standard parameters and fixed randomization seeds. Finally, to determine the senders and receivers in the network, the function netAnalysis_signallingRole was applied on the netP data slot.

Overlap with GWAS hits

From the GWAS catalogue⁴³, we obtained GWAS risk genes for neurological disorders (Alzheimer’s disease, amyotrophic lateral sclerosis, brain ageing, multiple system atrophy, multiple sclerosis, Parkinson’s disease and narcolepsy), psychiatric disorders (attention deficit hyperactivity disorder, autism, bipolar disorder, depression, psychosis, post-traumatic stress disorder and schizophrenia) and neurobehaviour traits (anxiety, suicidality, insomnia, neuroticism, risk behaviour, intelligence and cognitive function). We removed gene duplicates and GWAS loci either not

reported or in intergenic regions, and used a $P < 9 \times 10^{-6}$ to identify significant associations²⁵. Then, as GWAS signals can point to multiple candidate genes within the same locus, we focused on the ‘Reported Gene(s)’ (genes reported as associated by the authors of each GWAS study). Disorders and traits exhibiting a significant number of genes that were also perturbed in patients with COVID-19 are highlighted. Following gene symbol extraction, we curated the gene set by (1) removing unknown or outdated gene names using the HGNChelper package (v.0.8.6), (2) converting remaining Ensembl gene identifiers to actual gene names using the packages ensemblldb (v.2.10.0) and EnsDb.Hsapiens.v86 (v.2.99.0) and (3) removing any remaining duplicates. We then calculated the overlap between each set of GWAS genes with the cell-type-specific DEGs. Finally, a statistical enrichment of each overlap against background was calculated using a hypergeometric test with the total background size set equal to the number of unique RNAs mapped in our dataset (29,431). Overlaps between GWAS DEGs and disease GWAS genes expressed were calculated separately for each cell type.

Comparison of DEGs in chronic CNS disease

We compiled cell type-specific DEGs reported in published datasets for Alzheimer’s disease⁵, autism spectrum disorder⁸, Huntington’s disease⁴² and multiple sclerosis²⁶. Lists of gene symbols were curated using the aforementioned approach. COVID-19 DEGs that overlap with those found across the selected CNS diseases were called shared, whereas those not previously reported were called unique to COVID-19. Statistical significance calculations of over-representation in DEG overlaps are based on cumulative hypergeometric P values analogous to the procedures described in ‘Differential gene expression and sub-cluster analysis’ and ‘Overlap with GWAS hits’, with the total background size set equal to the number of unique RNAs mapped in our dataset (29,431). Using the smaller set of 17,926 protein-coding genes as background does not change the qualitative statistical significance of the overlaps. Similar to the analysis of GWAS hits, we determined the overlap and tested its significance for each cell type separately.

Principal variance component and principal component analyses

In brief, to conduct the principal variance component analysis (PVCA), we aggregated the SoupX corrected raw counts for each gene and each biological sample using the aggregateData function of the muscat package (v.1.2.1)⁷⁴. The resulting matrix was normalized by dividing each feature of a sample by the total counts from that sample, multiplied by 100,000 and scaling the result using the function $\log(x + 1)$. As variables we considered the sample annotation fields ‘Sample-ID’, ‘Patient-ID’, ‘Sex’, ‘Brain-region’, ‘Disease’, ‘ageBin’, ‘nNucleiBin’ and ‘Batch’. As PVCA is designed to support factors, we assigned the values for numeric variables into ordered bins, more specifically, into six half-open (left-closed) intervals of size 1,000 starting at 1,000 for the number of nuclei and five similarly defined intervals of size 10 starting at 51 for the age. We set the cut-off for the minimal variance out of the total variance being explained to be 95%. For each single annotation variable, or first higher-order combinations of such, a cut-off of 0.005 was applied to consider them explanatory. All variables (or combinations of such) not passing the threshold were summarized as Other in the analysis. The residual was then defined as the remaining proportion of variance not being associated with any of the variables that are explanatory nor informative to a minor proportion. To conduct principal component analysis, we aggregated the log-normalized cell counts from Seurat for each gene and sample using the aggregateData function from muscat and centred the gene expression vectors before computing eigenvectors.

Computational analysis, statistics and schematics

Analysis of the data was performed with the statistical programming language R (v.3.6.3) using the following general-purpose package for loading, saving and manipulating data, as well as generating plots, and fitting statistical models: dplyr (v.1.0.0), ggplot2 (v.3.2.2.), patchwork (v.1.0.1), openxlsx (v.4.1.5), bioconductor-scater (v.1.14.6)⁸³, bioconductor-dropletutils (v1.6.1)^{84,85}, bioconductor-complexheatmap (v.2.2.0)⁸⁶, tidyverse (v.1.3.0)⁸⁷ and lsa (v.0.73.2). All other tasks were performed on

an x86_64-based Ubuntu (4.15.0-55-generic kernel) server cluster. We did not use statistical methods to predetermine sample sizes, but they are similar to those reported in previous publications^{24,25,49}. Data in graphs are always presented as mean \pm s.e.m. Statistical tests used for group or cluster comparisons in bulk or single-nucleus RNA-seq experiment analysis are specified in the respective sections in Methods. Schematic diagrams were created with BioRender.com.

Immunohistochemistry

Paraffin-embedded human brain tissue (medial frontal cortex, meninges and choroid plexus) adjacent to tissue processed for snRNA-seq was subjected to immunohistochemistry.

After deparaffinization and rehydration of 1–3- μ m sections, peroxidases were blocked by incubation in 1% H₂O₂ for 15 min at room temperature. Heat antigen retrieval was performed by steaming at 98 °C in target retrieval solution pH 6.1 (Dako, no. S1699) for 30 min. Sections were allowed to cool down at room temperature. Following antigen retrieval, sections were incubated for 45 min at room temperature with the anti-SARS spike glycoprotein antibody 3A2 (rabbit, Abcam ab272420, 1:100), which has been used in previous publications^{17,18}, anti-SARS-CoV-2 spike antibody (mouse, GeneTex GTX632604, 1A9 clone, 1:100) used in a previous publication¹⁹, anti-SARS-CoV-2 spike antibody (rabbit, Sino Biological 40150-T62-CoV2, 1:100), anti-SARS-CoV-2 nucleoprotein antibody (rabbit, Sino Biological 40143-T62, 1:100) used in a previous publication³⁰, and anti-human CD68 (mouse, Dako M0876, PG-M1 clone, 1:100) for determining microglial reactivity. Both antibodies were diluted in Dako REAL antibody diluent no. S2022. After three washes with wash buffer (Dako no. S3006), the Dako REAL EnVision HRP kit (no. K5007) or alkaline phosphatase/RED kit (no. K500511) was used for the visualization of the antibody reaction according to the manufacturer's instructions. Sections were counterstained with Mayer's haemalum (Sigma-Aldrich no. 1.09249). After dehydration, coverslips were mounted with Entellan (Merck no. 1.07961). Images were acquired with an Olympus BX 40 microscope, equipped with an Olympus SC30 digital microscope camera using the Olympus cellSens software. To assess disease-associated innate immune

activation in brains of individuals with COVID-19, slides were screened at low magnification and areas with the most pronounced changes were used for quantification. Spatial context was used to determine the myeloid cell type—for example, the meninges are evident in a brain slice, enabling confident identification of resident CD68⁺ cells as meningeal, and likewise for the brain vasculature. A semiquantitative categorization for activation, as typical in pathology, was used: mild = detectable microgliosis, atypical for healthy tissue; moderate = a pathological process typical of pathological changes; severe = a marked pathological process. Several clusters of microglia or macrophages were characterized as excessive beyond the severe category.

Reporting summary

Further information on research design is available in the [Nature Research Reporting Summary](#) linked to this paper.

Data availability

Raw sequencing data are deposited under NCBI Gene Expression Omnibus (GEO) [GSE159812](#). Normalized count data are also available for download at https://twc-stanford.shinyapps.io/scRNA_Brain_COVID19. Any other relevant data are available from the corresponding authors upon reasonable request. [Source data](#) are provided with this paper.

Code availability

All analyses have been carried out using freely available software packages. Custom code used to analyse the RNA-seq data and datasets generated and/or processed in the current study is available from the corresponding authors upon request.

References

1. 1.

Mao, L. et al. Neurologic manifestations of hospitalized patients with coronavirus disease 2019 in Wuhan, China. *JAMA Neurol.* **77**, 683–690 (2020).

[Article](#) [Google Scholar](#)

2. 2.

Yang, X. et al. Clinical course and outcomes of critically ill patients with SARS-CoV-2 pneumonia in Wuhan, China: a single-centered, retrospective, observational study. *Lancet Respir. Med.* **8**, 475–481 (2020).

[CAS](#) [PubMed](#) [PubMed Central](#) [Article](#) [Google Scholar](#)

3. 3.

Helms, J. et al. Neurologic features in severe SARS-CoV-2 infection. *N. Engl. J. Med.* **382**, 2268–2270 (2020).

[PubMed](#) [Article](#) [Google Scholar](#)

4. 4.

Keren-Shaul, H. et al. A unique microglia type associated with restricting development of Alzheimer’s disease. *Cell* **169**, 1276–1290 (2017).

[CAS](#) [PubMed](#) [Article](#) [Google Scholar](#)

5. 5.

Mathys, H. et al. Single-cell transcriptomic analysis of Alzheimer’s disease. *Nature* **570**, 332–337 (2019).

[ADS](#) [CAS](#) [PubMed](#) [PubMed Central](#) [Article](#) [Google Scholar](#)

6. 6.

Sala Frigerio, C. et al. The major risk factors for Alzheimer's disease: age, sex, and genes modulate the microglia response to A β plaques. *Cell Rep.* **27**, 1293–1306 (2019).

[CAS](#) [PubMed](#) [Article](#) [Google Scholar](#)

7. 7.

Gidon, A. et al. Dendritic action potentials and computation in human layer 2/3 cortical neurons. *Science* **367**, 83–87 (2020).

[ADS](#) [CAS](#) [PubMed](#) [Article](#) [Google Scholar](#)

8. 8.

Velmeshev, D. et al. Single-cell genomics identifies cell type-specific molecular changes in autism. *Science* **364**, 685–689 (2019).

[ADS](#) [CAS](#) [PubMed](#) [PubMed Central](#) [Article](#) [Google Scholar](#)

9. 9.

Matschke, J. et al. Neuropathology of patients with COVID-19 in Germany: a post-mortem case series. *Lancet Neurol.* **19**, 919–929 (2020).

[CAS](#) [PubMed](#) [PubMed Central](#) [Article](#) [Google Scholar](#)

10. 10.

Varatharaj, A. et al. Neurological and neuropsychiatric complications of COVID-19 in 153 patients: a UK-wide surveillance study. *Lancet Psychiatry* **7**, 875–882 (2020).

[PubMed](#) [PubMed Central](#) [Article](#) [Google Scholar](#)

11. 11.

Ellul, M. A. et al. Neurological associations of COVID-19. *Lancet Neurol.* **19**, 767–783 (2020).

[CAS](#) [PubMed](#) [PubMed Central](#) [Article](#) [Google Scholar](#)

12. 12.

Romero-Sánchez, C. M. et al. Neurologic manifestations in hospitalized patients with COVID-19: the ALBACOVID registry. *Neurology* **95**, e1060–e1070 (2020).

[PubMed](#) [Article](#) [CAS](#) [Google Scholar](#)

13. 13.

Liotta, E. M. et al. Frequent neurologic manifestations and encephalopathy-associated morbidity in Covid-19 patients. *Ann. Clin. Transl. Neurol.* **7**, 2221–2230 (2020).

[CAS](#) [PubMed](#) [PubMed Central](#) [Article](#) [Google Scholar](#)

14. 14.

Office for National Statistics. The prevalence of long COVID symptoms and COVID-19 complications, Office for National Statistics,

[https://www.ons.gov.uk/news/statementsandletters/the-prevalence-oflongcovidsymptomsandcovid19complications](https://www.ons.gov.uk/news/statementsandletters/the-prevalence-of-long-covid-symptoms-and-covid-19-complications) (2020).

15. 15.

Carfi, A., Bernabei, R. & Landi, F. Persistent symptoms in patients after acute COVID-19. *J. Am. Med. Assoc.* **324**, 603–605 (2020).

[Article](#) [CAS](#) [Google Scholar](#)

16. 16.

Iadecola, C., Anrather, J. & Kamel, H. Effects of COVID-19 on the nervous system. *Cell* **183**, 16–27 (2020).

[CAS](#) [PubMed](#) [PubMed Central](#) [Article](#) [Google Scholar](#)

17. 17.

Cantuti-Castelvetri, L. et al. Neuropilin-1 facilitates SARS-CoV-2 cell entry and infectivity. *Science* **370**, 856–860 (2020).

[ADS](#) [CAS](#) [PubMed](#) [PubMed Central](#) [Article](#) [Google Scholar](#)

18. 18.

Meinhardt, J. et al. Olfactory transmucosal SARS-CoV-2 invasion as a port of central nervous system entry in individuals with COVID-19. *Nat. Neurosci.* **24**, 168–175 (2021).

[CAS](#) [PubMed](#) [Article](#) [Google Scholar](#)

19. 19.

Song, E. et al. Neuroinvasion of SARS-CoV-2 in human and mouse brain. *J. Exp. Med.* **218**, e20202135 (2021).

[CAS](#) [PubMed](#) [PubMed Central](#) [Article](#) [Google Scholar](#)

20. 20.

Jacob, F. et al. Human pluripotent stem cell-derived neural cells and brain organoids reveal SARS-CoV-2 neurotropism predominates in choroid plexus epithelium. *Cell Stem Cell* **27**, 937–950 (2020).

[CAS](#) [PubMed](#) [PubMed Central](#) [Article](#) [Google Scholar](#)

21. 21.

Pellegrini, L. et al. SARS-CoV-2 infects the brain choroid plexus and disrupts the blood-CSF barrier in human brain organoids. *Cell Stem*

Cell **27**, 951–961 (2020).

[CAS](#) [PubMed](#) [PubMed Central](#) [Article](#) [Google Scholar](#)

22. 22.

Dani, N. et al. A cellular and spatial map of the choroid plexus across brain ventricles and ages. *Cell* **184**, 3056–3074 (2021).

[CAS](#) [PubMed](#) [Article](#) [Google Scholar](#)

23. 23.

Yang, A. C. et al. A human brain vascular atlas reveals diverse cell mediators of Alzheimer’s disease risk. Preprint at <https://doi.org/10.1101/2021.04.26.441262> (2021).

24. 24.

Lake, B. B. et al. Integrative single-cell analysis of transcriptional and epigenetic states in the human adult brain. *Nat. Biotechnol.* **36**, 70–80 (2018).

[CAS](#) [PubMed](#) [Article](#) [Google Scholar](#)

25. 25.

Grubman, A. et al. A single-cell atlas of entorhinal cortex from individuals with Alzheimer’s disease reveals cell-type-specific gene expression regulation. *Nat. Neurosci.* **22**, 2087–2097 (2019).

[CAS](#) [PubMed](#) [Article](#) [Google Scholar](#)

26. 26.

Jäkel, S. et al. Altered human oligodendrocyte heterogeneity in multiple sclerosis. *Nature* **566**, 543–547 (2019).

[ADS](#) [PubMed](#) [PubMed Central](#) [Article](#) [CAS](#) [Google Scholar](#)

27. 27.

Dachet, F. et al. Selective time-dependent changes in activity and cell-specific gene expression in human postmortem brain. *Sci. Rep.* **11**, 6078 (2021).

[ADS](#) [CAS](#) [PubMed](#) [PubMed Central](#) [Article](#) [Google Scholar](#)

28. 28.

Bailey, C. C., Zhong, G., Huang, I. C. & Farzan, M. IFITM-family proteins: the cell's first line of antiviral defense. *Annu. Rev. Virol.* **1**, 261–283 (2014).

[PubMed](#) [PubMed Central](#) [Article](#) [CAS](#) [Google Scholar](#)

29. 29.

Hachim, M. Y. et al. Interferon-induced transmembrane protein (IFITM3) is upregulated explicitly in SARS-CoV-2 infected lung epithelial cells. *Front. Immunol.* **11**, 1372 (2020).

[CAS](#) [PubMed](#) [PubMed Central](#) [Article](#) [Google Scholar](#)

30. 30.

Rockx, B. et al. Comparative pathogenesis of COVID-19, MERS, and SARS in a nonhuman primate model. *Science* **368**, 1012–1015 (2020).

[CAS](#) [PubMed](#) [PubMed Central](#) [Article](#) [Google Scholar](#)

31. 31.

Baruch, K. et al. Aging-induced type I interferon response at the choroid plexus negatively affects brain function. *Science* **346**, 89–93 (2014).

[ADS](#) [CAS](#) [PubMed](#) [PubMed Central](#) [Article](#) [Google Scholar](#)

32. 32.

Jin, S. et al. Inference and analysis of cell-cell communication using CellChat. *Nat. Commun.* **12**, 1088 (2021).

[ADS](#) [CAS](#) [PubMed](#) [PubMed Central](#) [Article](#) [Google Scholar](#)

33. 33.

Hong, S. et al. Complement and microglia mediate early synapse loss in Alzheimer mouse models. *Science* **352**, 712–716 (2016).

[ADS](#) [CAS](#) [PubMed](#) [PubMed Central](#) [Article](#) [Google Scholar](#)

34. 34.

Prinz, M., Erny, D. & Hagemeyer, N. Ontogeny and homeostasis of CNS myeloid cells. *Nat. Immunol.* **18**, 385–392 (2017).

[CAS](#) [PubMed](#) [Article](#) [Google Scholar](#)

35. 35.

Dulken, B. W. et al. Single-cell analysis reveals T cell infiltration in old neurogenic niches. *Nature* **571**, 205–210 (2019).

[CAS](#) [PubMed](#) [PubMed Central](#) [Article](#) [Google Scholar](#)

36. 36.

Tröscher, A. R. et al. Microglial nodules provide the environment for pathogenic T cells in human encephalitis. *Acta Neuropathol.* **137**, 619–635 (2019).

[PubMed](#) [PubMed Central](#) [Article](#) [CAS](#) [Google Scholar](#)

37. 37.

Safaiyan, S. et al. White matter aging drives microglial diversity. *Neuron* **109**, 1100–1117 (2021).

[CAS](#) [PubMed](#) [Article](#) [Google Scholar](#)

38. 38.

Yuan, J., Amin, P. & Ofengeim, D. Necroptosis and RIPK1-mediated neuroinflammation in CNS diseases. *Nat. Rev. Neurosci.* **20**, 19–33 (2019).

[CAS](#) [PubMed](#) [PubMed Central](#) [Article](#) [Google Scholar](#)

39. 39.

Matute-Blanch, C. et al. Chitinase 3-like 1 is neurotoxic in primary cultured neurons. *Sci. Rep.* **10**, 7118 (2020).

[ADS](#) [CAS](#) [PubMed](#) [PubMed Central](#) [Article](#) [Google Scholar](#)

40. 40.

Tremblay, R., Lee, S. & Rudy, B. GABAergic interneurons in the neocortex: from cellular properties to circuits. *Neuron* **91**, 260–292 (2016).

[CAS](#) [PubMed](#) [PubMed Central](#) [Article](#) [Google Scholar](#)

41. 41.

Petersen, C. C. H. & Crochet, S. Synaptic computation and sensory processing in neocortical layer 2/3. *Neuron* **78**, 28–48 (2013).

[CAS](#) [PubMed](#) [Article](#) [Google Scholar](#)

42. 42.

Al-Dalahmah, O. et al. Single-nucleus RNA-seq identifies Huntington disease astrocyte states. *Acta Neuropathol. Commun.* **8**, 19 (2020).

[CAS](#) [PubMed](#) [PubMed Central](#) [Article](#) [Google Scholar](#)

43. 43.

Buniello, A. et al. The NHGRI-EBI GWAS catalog of published genome-wide association studies, targeted arrays and summary statistics 2019. *Nucleic Acids Res.* **47**, D1005–D1012 (2019).

[CAS](#) [PubMed](#) [Article](#) [Google Scholar](#)

44. 44.

Hosseini, S. et al. Long-term neuroinflammation induced by influenza a virus infection and the impact on hippocampal neuron morphology and function. *J. Neurosci.* **38**, 3060–3080 (2018).

[CAS](#) [PubMed](#) [PubMed Central](#) [Article](#) [Google Scholar](#)

45. 45.

Deleidi, M. & Isacson, O. Viral and inflammatory triggers of neurodegenerative diseases. *Sci. Transl. Med.* **4**, 121ps3 (2012).

[PubMed](#) [PubMed Central](#) [Article](#) [CAS](#) [Google Scholar](#)

46. 46.

Zhou, Y. et al. Human and mouse single-nucleus transcriptomics reveal TREM2-dependent and TREM2-independent cellular responses in Alzheimer's disease. *Nat. Med.* **26**, 131–142 (2020).

[CAS](#) [PubMed](#) [PubMed Central](#) [Article](#) [Google Scholar](#)

47. 47.

Swiech, L. et al. In vivo interrogation of gene function in the mammalian brain using CRISPR-Cas9. *Nat. Biotechnol.* **33**, 102–106 (2015).

[CAS](#) [PubMed](#) [Article](#) [Google Scholar](#)

48. 48.

Corces, M. R. et al. An improved ATAC-seq protocol reduces background and enables interrogation of frozen tissues. *Nat. Methods* **14**, 959–962 (2017).

[CAS](#) [PubMed](#) [PubMed Central](#) [Article](#) [Google Scholar](#)

49. 49.

Zhong, S. et al. A single-cell RNA-seq survey of the developmental landscape of the human prefrontal cortex. *Nature* **555**, 524–528 (2018).

[ADS](#) [CAS](#) [PubMed](#) [Article](#) [Google Scholar](#)

50. 50.

McInnes, L., Healy, J., Saul, N. & Großberger, L. UMAP: uniform manifold approximation and projection. *J. Open Source Softw.* **3**, 861 (2018).

[Article](#) [Google Scholar](#)

51. 51.

Young, M. D. & Behjati, S. SoupX removes ambient RNA contamination from droplet-based single-cell RNA sequencing data. *Gigascience* **9**,giaa151 (2020).

[PubMed](#) [PubMed Central](#) [Article](#) [CAS](#) [Google Scholar](#)

52. 52.

Satija, R., Farrell, J. A., Gennert, D., Schier, A. F. & Regev, A. Spatial reconstruction of single-cell gene expression data. *Nat. Biotechnol.* **33**, 495–502 (2015).

[CAS](#) [PubMed](#) [PubMed Central](#) [Article](#) [Google Scholar](#)

53. 53.

McGinnis, C. S., Murrow, L. M. & Gartner, Z. J. DoubletFinder: doublet detection in single-cell RNA sequencing data using artificial nearest neighbors. *Cell Syst.* **8**, 329–337 (2019).

[CAS](#) [PubMed](#) [PubMed Central](#) [Article](#) [Google Scholar](#)

54. 54.

Hafemeister, C. & Satija, R. Normalization and variance stabilization of single-cell RNA-seq data using regularized negative binomial regression. *Genome Biol.* **20**, 296 (2019).

[CAS](#) [PubMed](#) [PubMed Central](#) [Article](#) [Google Scholar](#)

55. 55.

Finak, G. et al. MAST: a flexible statistical framework for assessing transcriptional changes and characterizing heterogeneity in single-cell RNA sequencing data. *Genome Biol.* **16**, 278 (2015).

[PubMed](#) [PubMed Central](#) [Article](#) [CAS](#) [Google Scholar](#)

56. 56.

Soneson, C. & Robinson, M. D. Bias, robustness and scalability in single-cell differential expression analysis. *Nat. Methods* **15**, 255–261 (2018).

[CAS](#) [PubMed](#) [Article](#) [Google Scholar](#)

57. 57.

Wang, T., Li, B., Nelson, C. E. & Nabavi, S. Comparative analysis of differential gene expression analysis tools for single-cell RNA sequencing data. *BMC Bioinformatics* **20**, 40 (2019).

[PubMed](#) [PubMed Central](#) [Article](#) [Google Scholar](#)

58. 58.

Mou, T., Deng, W., Gu, F., Pawitan, Y. & Vu, T. N. Reproducibility of methods to detect differentially expressed genes from single-cell RNA sequencing. *Front. Genet.* **10**, 1331 (2020).

[PubMed](#) [PubMed Central](#) [Article](#) [CAS](#) [Google Scholar](#)

59. 59.

Dal Molin, A., Baruzzo, G. & Di Camillo, B. Single-cell RNA-sequencing: assessment of differential expression analysis methods. *Front. Genet.* **8**, 62 (2017).

[PubMed](#) [PubMed Central](#) [Article](#) [CAS](#) [Google Scholar](#)

60. 60.

Ximerakis, M. et al. Single-cell transcriptomic profiling of the aging mouse brain. *Nat. Neurosci.* **22**, 1696–1708 (2019).

[CAS](#) [PubMed](#) [Article](#) [Google Scholar](#)

61. 61.

The Tabula Muris Consortium. A single-cell transcriptomic atlas characterizes ageing tissues in the mouse. *Nature* **583**, 590–595 (2020).

[PubMed Central](#) [Article](#) [CAS](#) [PubMed](#) [Google Scholar](#)

62. 62.

Yang, A. C. et al. Physiological blood–brain transport is impaired with age by a shift in transcytosis. *Nature* **583**, 425–430 (2020).

[ADS](#) [CAS](#) [PubMed](#) [Article](#) [Google Scholar](#)

63. 63.

Chen, M. B. et al. Brain endothelial cells are exquisite sensors of age-related circulatory cues. *Cell Rep.* **30**, 4418–4432 (2020).

[CAS](#) [PubMed](#) [PubMed Central](#) [Article](#) [Google Scholar](#)

64. 64.

Wilk, A. J. et al. A single-cell atlas of the peripheral immune response in patients with severe COVID-19. *Nat. Med.* **26**, 1070–1076 (2020).

[CAS](#) [PubMed](#) [PubMed Central](#) [Article](#) [Google Scholar](#)

65. 65.

Xu, G. et al. The differential immune responses to COVID-19 in peripheral and lung revealed by single-cell RNA sequencing. *Cell Discov.* **6**, 73 (2020).

[CAS](#) [PubMed](#) [PubMed Central](#) [Article](#) [Google Scholar](#)

66. 66.

Schulte-Schrepping, J. et al. Severe COVID-19 is marked by a dysregulated myeloid cell compartment. *Cell* **182**, 1419–1440 (2020).

[CAS](#) [PubMed](#) [PubMed Central](#) [Article](#) [Google Scholar](#)

67. 67.

Guo, C. et al. Single-cell analysis of two severe COVID-19 patients reveals a monocyte-associated and tocilizumab-responding cytokine storm. *Nat. Commun.* **11**, 3924 (2020).

[ADS](#) [CAS](#) [PubMed](#) [PubMed Central](#) [Article](#) [Google Scholar](#)

68. 68.

Meckiff, B. J. et al. Imbalance of regulatory and cytotoxic SARS-CoV-2-reactive CD4⁺ T cells in COVID-19. *Cell* **183**, 1340–1353 (2020).

[CAS](#) [PubMed](#) [PubMed Central](#) [Article](#) [Google Scholar](#)

69. 69.

Lee, J. S. et al. Immunophenotyping of COVID-19 and influenza highlights the role of type I interferons in development of severe COVID-19. *Sci. Immunol.* **5**, eabd1554 (2020).

[CAS](#) [PubMed](#) [PubMed Central](#) [Article](#) [Google Scholar](#)

70. 70.

Su, Y. et al. Multi-omics resolves a sharp disease-state shift between mild and moderate COVID-19. *Cell* **183**, 1479–1495 (2020).

[CAS](#) [PubMed](#) [PubMed Central](#) [Article](#) [Google Scholar](#)

71. 71.

Chen, E. Y. et al. Enrichr: interactive and collaborative HTML5 gene list enrichment analysis tool. *BMC Bioinformatics* **14**, 128 (2013).

[PubMed](#) [PubMed Central](#) [Article](#) [Google Scholar](#)

72. 72.

Zhou, Y. et al. Metascape provides a biologist-oriented resource for the analysis of systems-level datasets. *Nat. Commun.* **10**, 1523 (2019).

[ADS](#) [PubMed](#) [PubMed Central](#) [Article](#) [CAS](#) [Google Scholar](#)

73. 73.

Gerstner, N. et al. GeneTrail 3: advanced high-throughput enrichment analysis. *Nucleic Acids Res.* **48**, W515–W520 (2020).

[CAS](#) [PubMed](#) [PubMed Central](#) [Article](#) [Google Scholar](#)

74. 74.

Crowell, H. L. et al. muscat detects subpopulation-specific state transitions from multi-sample multi-condition single-cell transcriptomics data. *Nat. Commun.* **11**, 6077 (2020).

[CAS](#) [PubMed](#) [PubMed Central](#) [Article](#) [Google Scholar](#)

75. 75.

Law, C. W., Chen, Y., Shi, W. & Smyth, G. K. voom: precision weights unlock linear model analysis tools for RNA-seq read counts. *Genome Biol.* **15**, R29 (2014).

[PubMed](#) [PubMed Central](#) [Article](#) [CAS](#) [Google Scholar](#)

76. 76.

Spandidos, A., Wang, X., Wang, H. & Seed, B. PrimerBank: a resource of human and mouse PCR primer pairs for gene expression detection and quantification. *Nucleic Acids Res.* **38**, D792–D799 (2010).

[CAS](#) [PubMed](#) [Article](#) [Google Scholar](#)

77. 77.

Trapnell, C. et al. The dynamics and regulators of cell fate decisions are revealed by pseudotemporal ordering of single cells. *Nat. Biotechnol.* **32**, 381–386 (2014).

[CAS](#) [PubMed](#) [PubMed Central](#) [Article](#) [Google Scholar](#)

78. 78.

Bost, P. et al. Host-viral infection maps reveal signatures of severe COVID-19 patients. *Cell* **181**, 1475–1488 (2020).

[CAS](#) [PubMed](#) [PubMed Central](#) [Article](#) [Google Scholar](#)

79. 79.

Yasumizu, Y., Hara, A., Sakaguchi, S. & Ohkura, N. VIRTUS: a pipeline for comprehensive virus analysis from conventional RNA-seq data. *Bioinformatics* btaa859 (2020).

80. 80.

Kim, D., Song, L., Breitwieser, F. P. & Salzberg, S. L. Centrifuge: rapid and sensitive classification of metagenomic sequences. *Genome Res.* **26**, 1721–1729 (2016).

[CAS](#) [PubMed](#) [PubMed Central](#) [Article](#) [Google Scholar](#)

81. 81.

Stano, M., Beke, G. & Klucar, L. viruSITE-integrated database for viral genomics. *Database* **2016**, baw162 (2016).

[PubMed](#) [PubMed Central](#) [Article](#) [Google Scholar](#)

82. 82.

Wauters, E. et al. Discriminating mild from critical COVID-19 by innate and adaptive immune single-cell profiling of bronchoalveolar lavages. *Cell Res.* **31**, 272–290 (2021).

[CAS](#) [PubMed](#) [PubMed Central](#) [Article](#) [Google Scholar](#)

83. 83.

McCarthy, D. J., Campbell, K. R., Lun, A. T. L. & Wills, Q. F. Scater: pre-processing, quality control, normalization and visualization of single-cell RNA-seq data in R. *Bioinformatics* **33**, 1179–1186 (2017).

[CAS](#) [PubMed](#) [PubMed Central](#) [Google Scholar](#)

84. 84.

Griffiths, J. A., Richard, A. C., Bach, K., Lun, A. T. L. & Marioni, J. C. Detection and removal of barcode swapping in single-cell RNA-seq data. *Nat. Commun.* **9**, 2667 (2018).

[ADS](#) [PubMed](#) [PubMed Central](#) [Article](#) [CAS](#) [Google Scholar](#)

85. 85.

Lun, A. T. L. et al. EmptyDrops: distinguishing cells from empty droplets in droplet-based single-cell RNA sequencing data. *Genome Biol.* **20**, 63 (2019).

[PubMed](#) [PubMed Central](#) [Article](#) [Google Scholar](#)

86. 86.

Gu, Z., Eils, R. & Schlesner, M. Complex heatmaps reveal patterns and correlations in multidimensional genomic data. *Bioinformatics* **32**, 2847–2849 (2016).

[CAS](#) [PubMed](#) [PubMed Central](#) [Article](#) [Google Scholar](#)

87. 87.

Wickham, H. et al. Welcome to the Tidyverse. *J. Open Source Softw.* **4**, 1686 (2019). <https://doi.org/10.21105/joss.01686>.

[ADS](#) [Article](#) [Google Scholar](#)

88. 88.

Lan, X., Han, X., Li, Q., Yang, Q. W. & Wang, J. Modulators of microglial activation and polarization after intracerebral haemorrhage. *Nat. Rev. Neurol.* **13**, 420–433 (2017).

[CAS](#) [PubMed](#) [PubMed Central](#) [Article](#) [Google Scholar](#)

[Download references](#)

Acknowledgements

We thank N. Khoury, T. Iram, E. Tapp and other members of the laboratories of T.W.-C. and A.K. for feedback and support, and H. Zhang and K. Dickey for laboratory management. This work was funded by the NOMIS Foundation (T.W.-C.), the National Institute on Aging (T32-AG0047126 to A.C.Y. and 1RF1AG059694 to T.W.-C.), Nan Fung Life Sciences (T.W.-C.), the Bertarelli Brain Rejuvenation Sequencing Cluster (an initiative of the Stanford Wu Tsai Neurosciences Institute) and the Stanford Alzheimer's Disease Research Center (P30 AG066515). A.C.Y. was supported by a Siebel Scholarship. F.K., G.P.S., T.F., W.J.S.-S. and A.K. are a part of the CORSAAR study supported by the State of Saarland, the Saarland University and the Rolf M. Schwiete Stiftung.

Author information

Author notes

1. These authors contributed equally: Andrew C. Yang, Fabian Kern
2. These authors jointly supervised this work: Andreas Keller, Tony Wyss-Coray

Affiliations

1. Department of Bioengineering, Stanford University School of Medicine, Stanford, CA, USA

Andrew C. Yang

2. ChEM-H, Stanford University, Stanford, CA, USA

Andrew C. Yang & Tony Wyss-Coray

3. Department of Neurology and Neurological Sciences, Stanford University School of Medicine, Stanford, CA, USA

Andrew C. Yang, Patricia M. Losada, Maayan R. Agam, Christina A. Maat, Nicholas Schaum, Davis P. Lee, Kruti Calcuttawala, Ryan T. Vest, Daniela Berdnik, Nannan Lu, Oliver Hahn, David Gate, Divya Channappa, Inma Cobos, Andreas Keller & Tony Wyss-Coray

4. Chair for Clinical Bioinformatics, Saarland University, Saarbrücken, Germany

Fabian Kern, Georges P. Schmartz, Tobias Fehlmann & Andreas Keller

5. Institute for Neuropathology, Saarland University Hospital and Medical Faculty of Saarland University, Homburg, Germany

Julian A. Stein & Walter J. Schulz-Schaeffer

6. Department of Psychiatry, Stanford University School of Medicine, Stanford, CA, USA

M. Windy McNerney

7. Department of Pathology, Stanford University School of Medicine, Stanford, CA, USA

Inma Cobos

8. Department of Human Genetics, Saarland University, Homburg, Germany

Nicole Ludwig

9. Wu Tsai Neurosciences Institute, Stanford University, Stanford, CA, USA

Tony Wyss-Coray

10. Paul F. Glenn Center for the Biology of Aging, Stanford University School of Medicine, Stanford, CA, USA

Tony Wyss-Coray

Authors

1. Andrew C. Yang

[View author publications](#)

You can also search for this author in [PubMed](#) [Google Scholar](#)

2. Fabian Kern

[View author publications](#)

You can also search for this author in [PubMed](#) [Google Scholar](#)

3. Patricia M. Losada

[View author publications](#)

You can also search for this author in [PubMed](#) [Google Scholar](#)

4. Maayan R. Agam

[View author publications](#)

You can also search for this author in [PubMed](#) [Google Scholar](#)

5. Christina A. Maat

[View author publications](#)

You can also search for this author in [PubMed](#) [Google Scholar](#)

6. Georges P. Schmartz

[View author publications](#)

You can also search for this author in [PubMed](#) [Google Scholar](#)

7. Tobias Fehlmann

[View author publications](#)

You can also search for this author in [PubMed](#) [Google Scholar](#)

8. Julian A. Stein

[View author publications](#)

You can also search for this author in [PubMed](#) [Google Scholar](#)

9. Nicholas Schaum

[View author publications](#)

You can also search for this author in [PubMed](#) [Google Scholar](#)

10. Davis P. Lee

[View author publications](#)

You can also search for this author in [PubMed](#) [Google Scholar](#)

11. Kruti Calcuttawala

[View author publications](#)

You can also search for this author in [PubMed](#) [Google Scholar](#)

12. Ryan T. Vest

[View author publications](#)

You can also search for this author in [PubMed](#) [Google Scholar](#)

13. Daniela Berdnik

[View author publications](#)

You can also search for this author in [PubMed](#) [Google Scholar](#)

14. Nannan Lu

[View author publications](#)

You can also search for this author in [PubMed](#) [Google Scholar](#)

15. Oliver Hahn

[View author publications](#)

You can also search for this author in [PubMed](#) [Google Scholar](#)

16. David Gate

[View author publications](#)

You can also search for this author in [PubMed](#) [Google Scholar](#)

17. M. Windy McNerney

[View author publications](#)

You can also search for this author in [PubMed](#) [Google Scholar](#)

18. Divya Channappa

[View author publications](#)

You can also search for this author in [PubMed](#) [Google Scholar](#)

19. Inma Cobos

[View author publications](#)

You can also search for this author in [PubMed](#) [Google Scholar](#)

20. Nicole Ludwig

[View author publications](#)

You can also search for this author in [PubMed](#) [Google Scholar](#)

21. Walter J. Schulz-Schaeffer

[View author publications](#)

You can also search for this author in [PubMed](#) [Google Scholar](#)

22. Andreas Keller

[View author publications](#)

You can also search for this author in [PubMed](#) [Google Scholar](#)

23. Tony Wyss-Coray

[View author publications](#)

You can also search for this author in [PubMed](#) [Google Scholar](#)

Contributions

A.C.Y., F.K., A.K. and T.W.-C. conceptualized the study. M.W.M., N. Ludwig, I.C., W.J.S.-S., N.S., D.C., D.B. and A.C.Y. provided and organized tissue samples. A.C.Y. performed tissue dissociations. A.C.Y., N.S., D.P.L., R.T.V., D.G., N. Lu, O.H. and K.C. prepared libraries for sequencing. A.C.Y. and M.R.A. performed RT-PCR. F.K., G.P.S., T.F. and A.C.Y. performed computational analysis, with F.K. leading advanced analysis and data management. P.M.L. developed the searchable web interface (Shiny app). J.A.S. and W.J.S.-S. performed immunohistochemical stains and antibody tests. A.C.Y., F.K. and C.A.M. assembled figures. A.C.Y. wrote the manuscript with input from all authors. F.K. and T.W.-C. edited the manuscript. T.W.-C. and A.K. supervised the study.

Corresponding authors

Correspondence to [Andreas Keller](#) or [Tony Wyss-Coray](#).

Ethics declarations

Competing interests

T.W.-C. is a co-founder and scientific advisor of Alkahest Inc.

Additional information

Peer review information *Nature* thanks the anonymous reviewers for their contribution to the peer review of this work.

Publisher's note Springer Nature remains neutral with regard to jurisdictional claims in published maps and institutional affiliations.

Extended data figures and tables

Extended Data Fig. 1 Characterization of human cortical and choroid plexi nuclei sequenced.

a, Total number of nuclei and median number of genes of each human sample sequenced in medial frontal cortex and choroid plexus. **b, c**, Quantification of the median number of genes detected per nuclei (**b**) and patient ages (**c**) in control (non-viral and influenza) and COVID-19 samples in medial frontal cortex ($n = 8$ control; $n = 8$ COVID-19, two-sided Mann-Whitey t -test; mean \pm s.e.m.) and choroid plexus ($n = 7$ control; $n = 7$ COVID-19, two-sided Mann-Whitey t -test; mean \pm s.e.m.). **d, e**, Bar graph presenting frequency of nuclei for control and COVID-19 medial frontal cortex (**d**) and choroid plexus (**e**) sample groups.

Extended Data Fig. 2 Gene expression variance analysis.

a, PVCA, displaying the gene expression variance explained by residuals (biological and technical noise) or experimental factors such as brain region, age, sex and respective combinations. $n = 30$ samples. **b**, Principal component (PC) analysis visualization of all samples, based on unscaled counts. **c**, UMAP projections of nuclei isolated from the medial frontal

cortex (top) or choroid plexus (bottom), and split by disease group, showing no systematic batch effects.

Extended Data Fig. 3 Human brain cell-type markers.

a, Top cell-type-specific genes across the types of cells captured in the human cortex. The colour bar indicates gene expression from low (blue) to high (yellow). **b**, Example of top cell-type-specific genes across the types of cells captured in the human choroid plexus. Violin plots are centred around the median, with their shape representing cell distribution.

Extended Data Fig. 4 Cell-type-specific changes in gene expression and intercellular signalling in the brain of individuals with COVID-19.

a, Heat map displaying the number of significant biological pathways among the set of DEGs in each cell type (FDR < 0.05, Benjamini–Hochberg adjustment, hypergeometric test). Number of significant pathways is indicated in graded black (low) to yellow (high). **b**, Example upregulation of inflammatory and dysregulation of homeostatic genes in COVID-19 astrocytes. **c**, Comparison of the number of nuclei isolated per cell type and the number of predicted DEGs. Two-sided *P*-value indicates the significance of the correlation (Pearson, not significant).

Extended Data Fig. 5 Overlap between alternative snRNA-seq differential expression analysis methods.

a, b, Scatter plots demonstrating the strong correlation between the calculated effect sizes of two differential gene expression analysis methods (MAST⁵⁵ (used here) and pseudobulk^{74,75}) across cell types in the human medial frontal cortex (**a**) and choroid plexus (**b**). Orange line denotes the trend line fitted with a generalized linear model, surrounded by a 95% confidence interval in purple. Spearman correlation is shown along with the significance by two-sided *P*-values.

Extended Data Fig. 6 DEGs in the brains of individuals with COVID-19 show no significant overlap with brain PMI-sensitive genes.

a, Comparison of post-mortem interval (PMI)-sensitive genes (left column, from a previous publication²⁷) and COVID-19 DEGs (all other columns). No statistically significant overlap is observed (Fisher's exact test). **b**, The previous study²⁷ categorized PMI-sensitive genes in two categories: glial genes upregulated and neural genes downregulated. Minimal overlap is seen with COVID-19 changes of the same category (for example, glial genes upregulated in COVID-19 versus glial genes upregulated with extended PMI). **c**, Heat map showing that PMI-sensitive genes are not the DEGs in COVID-19 and thus not driving the DEG-based findings of our study.

Extended Data Fig. 7 Expression of SARS-CoV-2 virus entry genes across cell types.

a, b, Expression of SARS-CoV-2 entry receptors, established and putative, across cell types in the human medial frontal cortex (**a**) and choroid plexus (**b**). Violin plots are centred around the median, with their shape representing cell distribution.

Extended Data Fig. 8 Choroid plexus inflammation in COVID-19.

Immunohistochemical staining for the macrophage activation marker CD68 (brown) in the choroid plexus of patients with COVID-19 and control individuals. Haematoxylin counterstain (blue). Scale bars, 20 µm.

Extended Data Fig. 9 No conclusive detection of SARS-CoV-2 neuroinvasion.

a, Summary of RNA-based assays to detect SARS-CoV-2 in the human cortex and choroid plexus. Aside from the 3A2 antibody, no other anti-

SARS-CoV-2 antibody detected viral protein antigen in the brain or choroid plexus. **b**, qPCR detection of the SARS-CoV-2 genes *N1* and *N2* via CDC Emergency Use Authorization primers on choroid plexus samples ($n = 6$ non-viral control, $n = 7$ COVID-19; two-sided Mann–Whitney *t*-test; mean \pm s.e.m.). **c**, Aberrant anti-SARS-CoV-2 spike (3A2) antibody reactivity (brown) in the frontal medial cortex of two patients with COVID-19 in tissue immediately adjacent to that used for snRNA-seq. Haematoxylin counterstain (purple). Scale bar, 20 μ m. **d**, As in **c**, but for the choroid plexus and meninges in two patients with COVID-19. Scale bar, 20 μ m. **e**, As in **c**, but using a different secondary antibody detection method (biotin–alkaline phosphatase (red)), recapitulating the specific vascular-localized signal. Scale bar, 20 μ m. Immunohistochemical stains are representative of at least two independent experiments.

Extended Data Fig. 10 Cell communication analysis results for integrated choroid plexus and brain parenchyma cell types.

Circle plot showing the number of statistically significant intercellular signalling interactions for total signalling (over 30 ligand–receptor pathways) and the complement family of molecules in control individuals (non-viral and influenza) compared to patients with COVID-19 (permutation test, CellChat³⁴; $n = 8$ control, including influenza; $n = 8$ COVID-19 for cortex; and $n = 7$ control, including influenza; $n = 7$ COVID-19 for choroid plexus). Each circle (colour) represents one cell type, and edges connecting circles represent significant intercellular signalling inferred between those cell types. Circles and edges were normalized and scaled to display relative sizes, with the former proportional to the number of cells from a given cell type and the latter according to the inferred strength of signalling. Cell type labels correspond to signalling pathway increased in COVID-19.

Extended Data Fig. 11 Activation of parenchymal microglia and perivascular macrophages in COVID-19.

Immunohistochemical staining of microglia and macrophages by an antibody against the pro-inflammatory marker CD68⁸⁸ (immunoreaction in

brown). Counterstained with haematoxylin for cell nuclei in blue. **a**, The frontal medial gyrus of patients with COVID-19 immediately adjacent to that used for snRNA-seq. A cluster of activated microglia up to single macrophages is immunostained in the parenchyma of the gyrus (subcortical white matter). Scale bar, 20 μ m. **b**, A vessel of the medial frontal gyrus is surrounded by activated perivascular macrophages. Scale bar, 20 μ m. **c**, The cortical surface is shown. The upper third of the figure contains the leptomeninges that cover the cortex. A dense infiltration by brown stained macrophages into the leptomeninges is visible. Scale bar, 20 μ m. **d**, Summary of innate immune reactivity across eight patients with COVID-19, typically not observed in healthy brains at these levels, colour-coded and labelled by severity. A semiquantitative categorization for changes, as usual in the field of pathology, is used: mild = detectable microgliosis, atypical for healthy tissue; moderate = a pathological process typical of pathological changes; severe = a marked pathological process. Several clusters of microglia or macrophages were characterized as excessive beyond the severe category. Immunohistochemical stains are representative of at least two independent experiments.

Extended Data Fig. 12 Evaluation of COVID-19-enriched subpopulations in other parenchymal glia.

a, UMAP of astrocytes captured in the human frontal cortex, split by control individuals (including influenza, $n = 8$) and patients with COVID-19 ($n = 8$). Cells are coloured by cell-type subcluster. Genes upregulated in the COVID-19-enriched astrocyte cluster are labelled in green. **b**, Quantification of astrocyte cluster 1 as a proportion of total astrocytes ($n = 8$ control, including influenza; $n = 8$ COVID-19, two-sided Mann-Whitney t -test $P = 0.0041$; mean \pm s.e.m.). Example genes upregulated in the COVID-19-associated astrocyte cluster are shown. **c**, Enriched biological pathways (Metascape⁵⁴) amongst upregulated gene markers of COVID-19 astrocytes. Enrichment is based on FDR-corrected cumulative hypergeometric P values (Bonferroni correction FDR < 0.05 ; MAST with default thresholds). **d**, UMAP projection of OPCs and trending but not significant emergence of a COVID-19-enriched subcluster. **e**, Quantification of the frequency of the COVID-19-enriched OPC subcluster as a proportion of all OPCs ($n = 8$ control, including 1 influenza and $n = 8$

COVID-19, two-sided Mann–Whitney *t*-test, $P = 0.083$; mean \pm s.e.m., not significant). **f, g**, As in **d, e**, respectively, but for mature oligodendrocytes with $P = 0.9591$.

[Source data](#)

Supplementary information

Supplementary Information

This file contains a further referenced Supplementary Discussion to explain possible reasons for our observations, to mention other limitations both in our study and the field and to name implications of the study.

Reporting Summary

Supplementary Table 1

Sample and patient characteristics of control and severe COVID-19 cases included in the study.

Supplementary Table 2

Significant cluster markers (genes) for human prefrontal cortex cell types derived from single-nucleus sequencing (alpha-level=0.05). Two-sided p-values were computed using Seurat with MAST at standard parameters but correcting for percentage of mitochondrial RNA in each cell using latent variables. Adjusted p-values were calculated using the Bonferroni correction for multiple hypothesis testing. For more details, consult manuscript methods.

Supplementary Table 3

Significant differentially expressed genes between non-viral controls and COVID-19 patients included in the study and per cortex cell-type (alpha-level=0.05). Two-sided p-values were computed using Seurat with MAST

at standard parameters but correcting for patient sex and batch by providing latent variables. Adjusted p-values were calculated using the Bonferroni correction for multiple hypothesis testing. For more details, consult manuscript methods.

Supplementary Table 4

Significant cluster markers (genes) for human choroid plexus cell types derived from single-nucleus sequencing (alpha-level=0.05). Two-sided p-values were computed using Seurat with MAST at standard parameters but correcting for percentage of mitochondrial RNA in each cell using latent variables. Adjusted p-values were calculated using the Bonferroni correction for multiple hypothesis testing.

Supplementary Table 5

Significant differentially expressed genes between non-viral controls and COVID-19 patients included in the study and per choroid plexus cell-type (alpha-level=0.05). Two-sided p-values were computed using Seurat with MAST at standard parameters but correcting for patient sex and batch by providing latent variables. Adjusted p-values were calculated using the Bonferroni correction for multiple hypothesis testing.

Supplementary Table 6

Significant marker genes for the COVID-19 associated microglia subcluster based on differentially expressed genes (DEGs) between the subcluster and homeostatic cortex microglia (alpha-level=0.05). Microglia subclusters were defined by subsetting for the immune cell population, removing confounding (perivascular) macrophages and T cells, recomputing variable features and re-clustering using Seurat. Two-sided p-values were computed using Seurat with MAST at standard parameters using only positive values to define subcluster marker genes. Adjusted p-values were calculated using the Bonferroni correction for multiple hypothesis testing. For more details, consult manuscript methods.

Supplementary Table 7

Overlap of genes expressed in major human cortex and choroid plexus cell types with DEGs as previously reported for four neurodegenerative diseases.

Supplementary Table 8

List of GWAS hits curated from the literature for seven neurological diseases, seven psychiatric disorders, and seven neurological traits, used to calculate the similarity to disease signatures in cortex and choroid plexus cell types as observed in COVID-19 post-mortem samples.

Source data

Source Data Fig. 2

Source Data Fig. 3

Source Data Extended Data Fig. 12

Rights and permissions

Reprints and Permissions

About this article



Check for
updates

Cite this article

Yang, A.C., Kern, F., Losada, P.M. *et al.* Dysregulation of brain and choroid plexus cell types in severe COVID-19. *Nature* **595**, 565–571 (2021).
<https://doi.org/10.1038/s41586-021-03710-0>

[Download citation](#)

- Received: 20 October 2020
- Accepted: 07 June 2021
- Published: 21 June 2021
- Issue Date: 22 July 2021
- DOI: <https://doi.org/10.1038/s41586-021-03710-0>

Comments

By submitting a comment you agree to abide by our [Terms](#) and [Community Guidelines](#). If you find something abusive or that does not comply with our terms or guidelines please flag it as inappropriate.

[Download PDF](#)

Associated Content

[Single-cell transcriptomics reveals neuroinflammation in severe COVID-19](#)

- Sarah Lemprière

Advertisement

This article was downloaded by **calibre** from <https://www.nature.com/articles/s41586-021-03710-0>

BNT162b2 vaccine induces neutralizing antibodies and poly-specific T cells in humans

[Download PDF](#)

- Article
- [Published: 27 May 2021](#)

BNT162b2 vaccine induces neutralizing antibodies and poly-specific T cells in humans

- [Ugur Sahin](#) [ORCID: orcid.org/0000-0003-0363-1564^{1,2}](#),
- [Alexander Muik](#) [ORCID: orcid.org/0000-0003-4561-2273¹](#),
- [Isabel Vogler](#) [ORCID: orcid.org/0000-0001-9757-9618¹](#),
- [Evelyna Derhovanessian¹](#),
- [Lena M. Kranz](#) [ORCID: orcid.org/0000-0003-1943-3431¹](#),
- [Mathias Vormehr](#) [ORCID: orcid.org/0000-0001-7788-3380¹](#),
- [Jasmin Quandt](#) [ORCID: orcid.org/0000-0001-9589-9941¹](#),
- [Nicole Bidmon¹](#),
- [Alexander Ulges¹](#),
- [Alina Baum²](#),
- [Kristen E. Pascal](#) [ORCID: orcid.org/0000-0003-4826-4606³](#),
- [Daniel Maurus](#) [ORCID: orcid.org/0000-0003-2989-264X¹](#),
- [Sebastian Brachtendorf¹](#),
- [Verena Lörks](#) [ORCID: orcid.org/0000-0003-0673-9386¹](#),
- [Julian Sikorski¹](#),
- [Peter Koch](#) [ORCID: orcid.org/0000-0002-0638-0433¹](#),
- [Rolf Hilker](#) [ORCID: orcid.org/0000-0002-8576-7731¹](#),
- [Dirk Becker](#) [ORCID: orcid.org/0000-0002-4786-9331¹](#),
- [Ann-Kathrin Eller¹](#),
- [Jan Grützner¹](#),
- [Manuel Tonigold¹](#),
- [Carsten Boesler¹](#),
- [Corinna Rosenbaum¹](#),
- [Ludwig Heesen¹](#),

- [Marie-Cristine Kühnle](#) [ORCID: orcid.org/0000-0003-0256-5542¹](#),
- [Asaf Poran](#) [ORCID: orcid.org/0000-0001-9118-1051⁴](#),
- [Jesse Z. Dong](#) [ORCID: orcid.org/0000-0002-4877-852X⁴](#),
- [Ulrich Luxemburger](#) [ORCID: orcid.org/0000-0003-3505-3236¹](#),
- [Alexandra Kemmer-Brück¹](#),
- [David Langer¹](#),
- [Martin Bexon](#) [ORCID: orcid.org/0000-0002-5361-4343⁵](#),
- [Stefanie Bolte¹](#),
- [Tania Palanche¹](#),
- [Armin Schultz⁶](#),
- [Sybille Baumann⁷](#),
- [Azita J. Mahiny](#) [ORCID: orcid.org/0000-0001-9331-5869¹](#),
- [Gábor Boros](#) [ORCID: orcid.org/0000-0002-8668-9800¹](#),
- [Jonas Reinholtz](#) [ORCID: orcid.org/0000-0003-2384-8541¹](#),
- [Gábor T. Szabó](#) [ORCID: orcid.org/0000-0001-9880-0425¹](#),
- [Katalin Karikó](#) [ORCID: orcid.org/0000-0002-1864-3851¹](#),
- [Pei-Yong Shi](#) [ORCID: orcid.org/0000-0001-5553-1616⁸](#),
- [Camila Fontes-Garfias](#) [ORCID: orcid.org/0000-0002-1912-8413⁸](#),
- [John L. Perez⁹](#),
- [Mark Cutler⁹](#),
- [David Cooper⁹](#),
- [Christos A. Kyriatsous](#) [ORCID: orcid.org/0000-0002-2596-2906³](#),
- [Philip R. Dormitzer](#) [ORCID: orcid.org/0000-0003-0671-6360⁹](#),
- [Kathrin U. Jansen⁹](#) &
- [Özlem Türeci¹](#)

[Nature](#) volume 595, pages 572–577 (2021) [Cite this article](#)

- 26k Accesses
- 652 Altmetric
- [Metrics details](#)

Subjects

- [Drug development](#)
- [Drug safety](#)
- [Nucleic-acid therapeutics](#)
- [Preventive medicine](#)

- [SARS-CoV-2](#)
- [Viral infection](#)

Abstract

BNT162b2, a nucleoside-modified mRNA formulated in lipid nanoparticles that encodes the SARS-CoV-2 spike glycoprotein (S) stabilized in its prefusion conformation, has demonstrated 95% efficacy in preventing COVID-19¹. Here we extend a previous phase-I/II trial report² by presenting data on the immune response induced by BNT162b2 prime–boost vaccination from an additional phase-I/II trial in healthy adults (18–55 years old). BNT162b2 elicited strong antibody responses: at one week after the boost, SARS-CoV-2 serum geometric mean 50% neutralizing titres were up to 3.3-fold above those observed in samples from individuals who had recovered from COVID-19. Sera elicited by BNT162b2 neutralized 22 pseudoviruses bearing the S of different SARS-CoV-2 variants. Most participants had a strong response of IFN γ ⁺ or IL-2⁺ CD8⁺ and CD4⁺ T helper type 1 cells, which was detectable throughout the full observation period of nine weeks following the boost. Using peptide–MHC multimer technology, we identified several BNT162b2-induced epitopes that were presented by frequent MHC alleles and conserved in mutant strains. One week after the boost, epitope-specific CD8⁺ T cells of the early-differentiated effector-memory phenotype comprised 0.02–2.92% of total circulating CD8⁺ T cells and were detectable (0.01–0.28%) eight weeks later. In summary, BNT162b2 elicits an adaptive humoral and poly-specific cellular immune response against epitopes that are conserved in a broad range of variants, at well-tolerated doses.

[Download PDF](#)

Main

The effect of the SARS-CoV-2 pandemic has necessitated the rapid development of safe and effective prophylactic vaccines. Eleven months after starting ‘Project Lightspeed’ (the joint BioNTech–Pfizer programme for the development of an RNA vaccine for COVID-19), BNT162b2 became the first vaccine to be authorized for emergency use. The vaccine showed 95% efficacy for protection against COVID-19 in a phase-II/III trial¹ and emerging real-world data confirm that BNT162b2 is highly effective in preventing COVID-19 and hospitalization and death associated with SARS-CoV-2 infection^{3,4,5}. The observational data also demonstrate that BNT162b2 reduces laboratory-confirmed infection, as well as viral load in individuals who are infected^{3,4,5,6}.

BNT162b2 is based on lipid-nanoparticle-formulated mRNA vaccine technology, which delivers precise genetic information of the immunogen to antigen-presenting cells and elicits potent immune responses⁷. mRNA is transiently expressed, does not integrate into the genome and is degraded by physiological pathways. mRNA vaccines are molecularly well-defined and synthesized efficiently from DNA templates by in vitro transcription^{8,9,10}. mRNA production and lipid nanoparticle formulation are fast and highly scalable, which renders this technology suitable for the rapid development and supply of vaccines during pandemic scenarios^{11,12}.

Two phase-I/II umbrella trials, one in Germany and one in the USA, investigated four candidate RNA–lipid nanoparticle vaccines. Preliminary clinical data from these studies on two candidates, BNT162b1^{13,14} and BNT162b2², have previously been reported. Both of the candidates are pharmacologically optimized^{15,16}, *N*¹-methylpsudouridine nucleoside-modified mRNAs¹⁷ that are administered intramuscularly in a prime–boost regimen 21 days apart. BNT162b1 encodes a trimerized, secreted version of the receptor-binding domain (RBD) of S, whereas BNT162b2 encodes full-length SARS-CoV-2 S stabilized in the prefusion conformation¹⁸. BNT162b2 was selected as pivotal candidate on the basis of the totality of data obtained in the two phase-I/II trials and challenge studies in non-human primates^{2,18}.

In the phase-I/II trial in the USA (NCT04368728), immunization with BNT162b2 at dose levels of up to 30 µg was associated with generally mild-to-moderate local reactions at the injection site as well as systemic events, such as fatigue, headache and myalgia². Robust concentrations of S1-binding immunoglobulin G (IgG) and neutralizing titres against a SARS-CoV-2 strain with the wild-type (Wuhan-Hu-1) S sequence were elicited. Geometric mean 50% neutralizing titres (GMTs) of sera drawn from younger (18–55 years) and older (65–85 years) adults seven days after the booster dose of 30 µg BNT162b2 were 3.8-fold and 1.6-fold, respectively, the GMT of samples from individuals who had recovered from COVID-19. Here we provide data from the phase-I/II trial in Germany (NCT04380701, EudraCT: 2020-001038-36) that provide insights into vaccine-induced immune responses after prime–boost vaccination with 1, 10, 20 and 30 µg BNT162b2 in participants of 19–55 years of age. In addition to reporting neutralizing-antibody GMTs up to day 85 after dose 1 and cross-neutralizing-antibody GMTs against newly emerging SARS-CoV-2 strains, this study provides a characterization of the T cell responses elicited by BNT162b2, including the identification of epitopes that are recognized by the CD8⁺ T cells induced by a COVID-19 vaccine.

Study design and analysis sets

Participants ($n = 12$ per dose level) were assigned to a priming dose of 1, 10, 20 or 30 µg on day 1 and a booster dose on day 22 (Extended Data Fig. 1). The baseline characteristics and disposition of the participants are provided in Extended Data Tables 1, 2.

Safety and tolerability

We observed no related serious adverse events, no grade-4 reactions and no withdrawals owing to related adverse events. Local reactions (predominantly pain at the injection site) were mild-to-moderate (grades 1 and 2) and of similar frequency and severity after the priming and booster doses (Extended Data Fig. 2a, Extended Data Table 3a). The most common systemic adverse events were fatigue and headache, and only two participants reported mild fever (Extended Data Fig. 2b, Extended Data Table 3b). Transient chills were more common after the boost, were dose-dependent and were occasionally severe. Muscle pain and joint pain were also more common after the boost and showed dose-dependent severity. Reactions had their onset within 24 h of immunization, peaked on the day after immunization and mostly resolved within 2 or 3 days, and either did not require treatment or could be managed with simple measures (such as paracetamol).

No clinically relevant changes in routine clinical laboratory values occurred. We observed a mild drop in blood lymphocyte counts and an increase in C-reactive protein, which are known pharmacodynamic markers of mRNA vaccines^{19,20,21,22,23}, both of these were transient, dose-dependent and within, or close to, laboratory-normal levels (Extended Data Fig. 3).

Vaccine-induced antibody response

We assessed S1- and RBD-binding IgG concentrations and SARS-CoV-2 neutralizing titres on day 1 (pre-dose), day 8 and day 22 (1 and 3 weeks after the priming dose, respectively), and on day 29, day 43, day 50 and day 85 (1, 3, 4 and 9 weeks after the booster dose, respectively) (Fig. 1, Extended Data Fig. 4, Extended Data Table 2).

Fig. 1: BNT162b2-induced IgG concentrations and virus neutralization titres.

 **figure1**

Participants were immunized with BNT162b2 on days 1 and 22 ($n = 12$ per dose cohort; from day 22 onwards, $n = 11$ for the 1- μg and 10- μg dose cohorts).

Arrowheads indicate days of vaccination. Pre-dose responses (pre) across all dose levels were combined. Samples from individuals who had recovered from infection with SARS-CoV-2 or COVID-19 ('human convalescent samples' (HCS)) ($n = 38$) were obtained at least 14 days after PCR-confirmed diagnosis and at a time at which the donors were no longer symptomatic. Each serum was tested in duplicate and geometric mean 50% (pseudo)neutralizing titres (GMTs) were plotted. **a**, SARS-CoV-2 50% neutralization titres (VNT_{50}). For values below the lower limit of quantification (LLOQ; 20), LLOQ/2 values are plotted. Group GMTs (values above bars) with 95% confidence intervals. **b**, Pseudovirus 50% neutralization titres (pVNT_{50}) across a panel of pseudoviruses displaying SARS-CoV-2 S variants, including Wuhan-Hu-1 (wild type), B.1.1.298 with four point mutations (B.1.1.298 ($\Delta 4$)) and B.1.351 with all ten lineage-defining mutations (B.1.351 ($\Delta 10$)) or eight of those mutations (B.1.351 ($\Delta 8$)); 30- μg dose cohort, $n = 1$ for day 29, $n = 11$ for day 43.

[Full size image](#)

All participants who received dose levels greater than 1 μg had detectable antigen-binding antibody concentrations and virus neutralizing serum titres after the booster dose. On day 22, geometric mean concentrations (GMCs) of S1-binding IgG had increased in all dose cohorts and were in the range of 49 to 1,161 U ml^{-1} (Extended Data Fig. 4a). We observed a dose-level dependency only between the 1- and 10- μg dose levels. On day 29, S1-binding IgG GMCs showed a strong booster response that ranged from 691 to 8,279 U ml^{-1} . S1-binding antibody GMCs declined to a range of 1,384 to 2,991 U ml^{-1} at day 85, which is well above the level observed in individuals who had recovered from COVID-19 (631 U ml^{-1}). We made similar observations when using only the RBD as the target antigen (Extended Data Fig. 4a).

SARS-CoV-2 GMTs of sera increased modestly in a proportion of participants after the priming dose (day 22) (Fig. [1a](#)). After the booster dose (day 29), GMTs increased substantially to 169, 195 or 312 in participants immunized with 10 µg, 20 µg or 30 µg BNT162b2, respectively, but increased only minimally in participants immunized with 1 µg BNT162b2 (GMT of 25). GMTs initially decreased thereafter, and remained stable from day 43 up to day 85 for participants who were vaccinated with BNT162b2 dose levels of 10 to 30 µg. At day 85, GMTs ranged from 120 to 181, and were 1.3- to 1.9-fold those of individuals who had recovered from COVID-19 (GMT of 94). All participants immunized with 30 µg BNT162b2 remained well above a GMT of 40 throughout the entire follow-up period (until day 85) (Extended Data Fig. [4b](#)).

For dose levels of 10 µg and greater, the S1-binding IgG GMCs gradually declined from a peak on day 29, which is a typical response of B cells that are cognately activated by either natural infection or vaccination (reflecting an initial over-proliferation followed by contraction)[24,25](#). By contrast, GMTs initially decreased after their peak on day 29 and stabilized around day 43, which implies the selection and affinity maturation of functional antibodies. Neutralizing antibody GMTs correlated strongly with S1-binding IgG GMCs (Extended Data Fig. [4c](#)).

We investigated the breadth of inhibition of virus entry by BNT162b2-elicited antibodies using a vesicular stomatitis virus (VSV)-based SARS-CoV-2 pseudovirus neutralization assay (pVNT). We investigated 22 pseudoviruses: 19 of these contained SARS-CoV-2 S with a single mutation that has been identified in one of the common circulating virus strains[26,27](#), and 3 displayed S with sets of mutations that are found in either the mink-related SARS-CoV-2 variant B.1.1.298 that was first identified in Denmark[28](#) or the SARS-CoV-2 variant B.1.351 that was first identified in South Africa[29](#). We conducted the single- and multiple-mutant pVNTs using different protocols, and the resulting neutralization titres are not comparable. Sera collected from BNT162b2-vaccinated participants on day 29 had high neutralizing titres to each of the SARS-CoV-2 S variants with a single amino acid altered (Extended Data Fig. [4d](#)). Likewise, BNT162b2-immune sera collected on day 29 or 43 neutralized pseudovirus bearing the S of B.1.1.298 with four point mutations as efficiently as they did pseudovirus with the S of SARS-CoV-2 Wuhan-Hu-1 (wild type) (Fig. [1b](#)). Pseudoviruses with the S of B.1.351 with either ten mutations or a reduced set of eight mutations were neutralized at lower GMTs than the wild-type strain (33 and 30, respectively, as compared to 150). All of the BNT162b2-immune sera that we tested neutralized all the pseudoviruses, and no pseudovirus escaped neutralization.

Vaccine-induced T cell responses

We analysed the T cell responses of 37 participants immunized with BNT162b2 from the 1-, 10-, 20- and 30-µg dose cohorts on day 1 (pre-prime) and 29 (one week after

the boost) and from six 30- μ g-dosed participants on day 85 (nine weeks after the boost) using an ex vivo IFN γ enzyme-linked immunosorbent spot (ELISpot) assay (Extended Data Table 2). SARS-CoV-2 S is composed of a signal peptide (amino acids 1–13), the N-terminal S1 protease fragment (amino acids 14–685) containing the RBD (amino acids 319–541) and the C-terminal S2 protease fragment (amino acids 686–1273). We stimulated CD4 $^{+}$ or CD8 $^{+}$ T cell effectors overnight with overlapping pools of peptides representing the N-terminal ‘S pool 1’ (amino acids 1–643), the C-terminal ‘S pool 2’ (amino acids 633–1273) and the ‘RBD’ (amino acids 1–16 fused to amino acids 327–528 of S) of SARS-CoV-2 S.

After the booster dose (day 29), we detected robustly expanded SARS-CoV-2 S-specific CD4 $^{+}$ T cells in all 37 participants at all BNT162b2 dose levels (Fig. 2a, Extended Data Fig. 5a,b). Thirty of the 34 participants with available pre-vaccination peripheral blood mononuclear cells (PBMCs) (88.2%) had de novo CD4 $^{+}$ T cell responses against both of the S pools. One participant had a de novo response only against S pool 2. The remaining three participants had de novo responses against S pool 1 and low numbers of pre-existing S-pool-2-reactive CD4 $^{+}$ T cells. In these three participants, the pre-existing S-pool-2 responses were amplified by vaccination in the range of 3-, 5- or 13-fold. In conclusion, in 94.1% (32 out of 34) of participants, two doses of BNT162b2 induced poly-epitopic CD4 $^{+}$ T cell responses (de novo or amplified) directed against both N- and C-terminal portions of S.

Fig. 2: Magnitude and durability of BNT162b2-induced T cell responses.



a–c, PBMCs obtained on day 1 (pre), day 29 (dose cohorts of 1, 10 and 20 µg, $n = 9$ each; 30 µg, $n = 10$) and day 85 (30-µg dose cohort) were enriched for CD4⁺ or CD8⁺ T cells and separately stimulated overnight with overlapping peptide pools representing the wild-type sequence of SARS-CoV-2 S (S pool 1 and S pool 2), CMV, EBV, influenza virus and tetanus toxoid (CEFT) or CMV, EBV and influenza virus (CEF) pools for assessment by IFN γ ELISpot. Cumulative responses to both S pools are shown in **b**, **c**. Each data point represents the normalized mean spot count from duplicate wells for one study participant, after subtraction of the non-stimulated control. Numbers above each dataset in **a**, **c** represent the number of participants with a positive T cell response over the number of participants tested. **a**, S-specific CD4⁺ (top) and CD8⁺ (bottom) T cell responses for each dose cohort for S pool 1 (left panels) and S pool 2 (right panels). Spot count data from two participants from the 20-µg dose cohort could not be normalized and are not plotted. **b**, CD4⁺ (left) and CD8⁺ (right) T cell responses to S and recall antigens (CEF or CEFT) in all participants with a positive response on day 29 after initial vaccination. Horizontal bars indicate median values. **c**, Kinetics of CD4⁺ (left) and CD8⁺ (right) T cell responses in six participants from the 30-µg dose cohort. Vertical dotted lines indicate days of vaccination.

[Full size image](#)

At dose levels of 10 µg or higher, the magnitude of CD4⁺ T cell responses was not dose-dependent and varied between individuals. In the strongest-responding individuals, the S-specific CD4⁺ T cell responses were more than tenfold the individual memory responses to common viruses and recall antigens (cytomegalovirus (CMV), Epstein–Barr virus (EBV), influenza virus and tetanus toxoid) (Fig. [2b](#), Extended Data Fig. [5c](#)).

The majority of vaccine-induced S-specific CD8⁺ T cell responses that we detected in 34 of 37 participants (91.9%) were strong, with magnitudes comparable to individual memory responses against CMV, EBV and influenza virus (Fig. [2a](#), [b](#), Extended Data Fig. [5a–c](#)).

De novo S-specific CD8⁺ T cell responses were induced in 33 participants. These were directed against both (22 participants) or one of the S pools (S pool 1 in 10 participants and S pool 2 in 2 participants), indicating a poly-epitopic response that included non-RBD S-specific T cells (Extended Data Fig. [5d](#)). In seven participants, we detected pre-existing CD8⁺ T cell responses to S pool 2 that were not further augmented by vaccination. Six out of these seven participants had a concurrent de novo response to S pool 1, which did not differ in strength from those responses that we observed in individuals without pre-existing responses to S pool 2 (Extended Data Fig. [5e](#)). Of note, the strongest responses (higher than third quartile) against S pool 1 among the 34

participants with detectable CD8⁺ T cell responses were observed in those without pre-existing S-pool-2-specific responses.

Both the CD4⁺ and the CD8⁺ T cell responses contracted after day 29 in participants vaccinated with 30 µg BNT162b2, and were higher than or in the range of recall antigen memory responses on day 85 (Fig. 2c, Extended Data Fig. 5f).

The magnitude of S-specific CD4⁺ T cell responses correlated positively with S1-binding IgG (Extended Data Fig. 6a) and, consistent with the concept of intramolecular help³⁰, also with the strength of S-specific CD8⁺ T cell responses (Extended Data Fig. 6b). S-specific CD8⁺ T cell responses correlated with S1-binding IgG (Extended Data Fig. 6c), which implies a convergent development of the humoral and cellular adaptive immunity.

Polarization of T cell responses

We determined cytokine secretion in response to stimulation with S pool 1, S pool 2 and RBD pool by intracellular staining in PBMCs of 41 participants immunized with BNT162b2 (Extended Data Table 2). A considerable fraction of vaccine-induced, S-specific CD4⁺ T cells secreted IFN γ , IL-2 or both, whereas we barely detected T cells secreting the T helper 2 cell cytokine IL-4 (Fig. 3a, Extended Data Fig. 7a–c). S-specific CD8⁺ T cells secreted predominantly IFN γ , and lower levels of IL-2, in response to S pool 1 and S pool 2 stimulation. Fractions of IFN γ ⁺CD8⁺ T cells specific to S pool 1 constituted up to about 1% of total peripheral blood CD8⁺ T cells (Extended Data Fig. 7d). Confirming ELISpot findings, seven participants displayed pre-existing S-pool-2-specific CD8⁺ T cell responses, which were not further amplified by vaccination in six participants. We detected a strong pre-existing S-pool-2-specific IFN γ ⁺CD4⁺ T cell response in one participant (Extended Data Fig. 7b). The fraction of IFN γ and IL-2 cytokine-producing T cells induced by the vaccine strongly increased by day 29, declined until day 43 and stabilized towards day 85 (Fig. 3b, Extended Data Fig. 7e).

Fig. 3: Cytokine polarization of BNT162b2-induced T cells.

 **figure3**

a, b, PBMCs obtained on day 1 (pre), day 29 (dose cohorts 1 µg, $n = 8$; 10, 20 and 30 µg, $n = 11$ each), day 43 and day 85 (30-µg dose cohort, $n = 8$) were stimulated overnight with overlapping peptide pools representing the wild-type sequence of SARS-CoV-2 S (S pool 1 and S pool 2) for assessment by flow cytometry (gating strategy in Supplementary Fig. 1). Participant PBMCs were tested without replicates.

a, S-specific CD4⁺ T cells producing the indicated cytokine as a fraction of total cytokine-producing S-specific CD4⁺ T cells on day 29 after initial vaccination, for S pool 1 (top) and S pool 2 (bottom). CD4 non-responding individuals (<0.03% total cytokine-producing T cells: 1 µg, $n = 2$ (S pool 1) and $n = 1$ (S pool 2); 10 µg, $n = 1$) were excluded. Arithmetic means with 95% confidence intervals are shown. Pre-vaccination values from all analysed participants are plotted in Extended Data Fig. 7b.

b, Kinetics of S-pool-1-specific CD4⁺ (top) and CD8⁺ (bottom) T cell responses producing IFNγ (left) or IL-2 (right) as a fraction of total circulating T cells of the same subset. Vertical dotted lines indicate days of vaccination.

[Full size image](#)

In both assay systems, the cytokine production of CD4⁺ and CD8⁺ T cells in response to peptide pools comprising full SARS-CoV-2 S exceeded the responses against the RBD peptide pool, which further confirms the poly-specific nature of T cell responses elicited by BNT162b2. The mean fraction of S-specific IFNγ⁺ or IL-2⁺ CD4⁺ and CD8⁺ T cells induced by BNT162b2 within total circulating T cells was higher than that we detected in individuals who had recovered from COVID-19 (Extended Data Fig. 7b, d).

Specificity and phenotype of CD8⁺ T cells

We investigated epitope-specific CD8⁺ T cell responses in the PBMCs of three participants vaccinated with BNT162b2 with individual peptide–MHC (pMHC) multimer cocktails by flow cytometry analysis. Twenty-three (4 for *HLA-B*0702* and 19 for *HLA-A*2402*), 14 (all *HLA-B*3501*) and 23 (7 for *HLA-B*4401* and 16 for *HLA-A*0201*) pMHC allele pairs were used for participants 1, 2 and 3, respectively. We identified several epitopes for each participant, representing eight different epitope–MHC pairs that were recognized by de novo-induced CD8⁺ T cells and were spread across the full length of S (Fig. [4a, b](#)). All eight epitopes are fully conserved in the B.1.351, the B.1.1.7 (first identified in the UK) and P.1 (first identified in Brazil) lineages (Extended Data Fig. [7f](#)). In the B.1.1.298 lineage, one epitope was altered in a single amino acid.

Fig. 4: Characterization of BNT162b2-induced T cells on the single-epitope level.

 [figure4](#)

a, c, PBMCs obtained on day 1 (pre), day 29 and day 85 of three vaccinated participants (dose cohorts 10 µg, $n = 1$; 30 µg, $n = 2$) were analysed for CD8⁺ T cell

epitope specificity (**a**) and phenotype (**c**) by flow cytometry (gating strategy in Supplementary Fig. [2](#)). Peptide sequences above dot plots indicate pMHC class I multimer epitope specificity. Numbers above dot plots indicate the amino acid positions within S. **b**, Location of identified MHC class I-restricted epitopes within S.

[Full size image](#)

The magnitude of epitope-specific CD8⁺ T cell responses ranged from 0.02 to 2.92% of peripheral CD8⁺ T cells, with the most notable expansion for HLA-A*0201–YLQPRTFLL, HLA-A*2402–QYIKWPWYI and HLA-B*3501–QPTESIVRF, and contracted to 0.01 to 0.28% by day 85.

Compared to the pMHC multimer assay (which non-comprehensively samples discrete, predefined T cell reactivities), we found that the CD8⁺ responses determined by ELISpot and intracellular staining in bulk PBMCs underestimated the true magnitude of the poly-specific cellular immune response (Extended Data Fig. [7g](#)).

The pMHC multimer⁺ S-specific CD8⁺ T cells that we identified were of an early-differentiated, central or effector memory phenotype on day 29 (Fig. [4c](#)). On day 85, epitope-specific CD8⁺ T cells were unchanged in participants 1 and 2 and differentiated towards CD45RA re-expressing cells with CD27 and CD28 co-expression in participant 3, which suggests an early-differentiated state.

Discussion

Effectors of the adaptive immune system have complementary roles in virus defence. Antibodies neutralize free virus, whereas CD8⁺ cytotoxic T lymphocytes clear the intracellular virus compartment; CD4⁺ T cells exert various functions, including providing cognate help to B and T cells, promoting memory generation and indirect (for example, via IFN γ) or direct (against MHC-class-II-expressing target cells) cytotoxic activity.

The sufficiency of neutralizing antibodies alone for full and long-lasting protective immunity to SARS-CoV-2, and the contribution of SARS-CoV-2-specific T cells, remain unclear. An increasing amount of data supports a role of T cells^{[31,32,33](#)}, such as case reports of patients with critical COVID-19 who lack S1-reactive CD4⁺ T cells^{[34](#)} and of asymptomatic virus exposure being associated with cellular immune responses and without seroconversion^{[29](#)}.

We show that BNT162b2 induces a broad immune response with SARS-CoV-2 S-specific neutralizing antibodies and poly-specific CD4⁺ and CD8⁺ T cells. All

evaluable participants vaccinated with BNT162b2 mounted de novo S-specific CD4⁺ T cell responses, and almost 90% of participants mounted de novo CD8⁺ T cell responses. We observed potent memory T cell responses for the full observation period (of nine weeks after the booster dose). The magnitude of the T cell responses varied between individuals and, above a dose level of 1 µg, was independent of dose level. Robust expression of IFN γ and IL-2, and low levels of IL-4, in BNT162b2-induced CD4⁺ T cells indicated a T helper 1 cell profile.

Although CD8⁺ T cell responses against the S1 subunit were not detected at baseline, several individuals had pre-existing immune responses against the S2 subunit, most probably owing to the similarity of its sequence to corresponding seasonal-coronavirus sequences and pre-existing cross-reactive CD8⁺ T cells^{35,36}.

T cell recognition of epitopes spread across the entire length of S was one of the reasons to favour BNT162b2 over BNT162b1¹⁴. In three participants, we identified single S epitopes that were recognized by vaccine-induced CD8⁺ T cells and were highly conserved across various circulating SARS-CoV-2 variants. The set of single-epitope-reactive T cells for each individual was identified by a candidate approach that was not designed to capture the full spectrum of the vaccine-induced reactivities of that individual across all their restriction elements. Consequently, the pMHC multimers visualize only a fraction of the full vaccine-induced repertoire for each of the three participants. Nonetheless, in each participant the magnitude of the sum of the identified single-epitope T cell responses exceeded their overall T cell response measured by ELISpot and intracellular staining assay, as these assays stimulate with peptide pools in which the immunogenic epitopes compete with each other and thus yield lower T cell frequencies as compared to single-peptide analyses.

A high proportion of boosted CD8⁺ T cells were early-differentiated central effector and memory cells; the T cell population contracted and further differentiated towards an early-differentiated memory phenotype with co-expression of CD27 and CD28. This favourable phenotype has the potential to respond rapidly to infection, but has a limited capacity to produce IFN γ , and thus is less likely to be detected in functional T cell assays with PBMCs. Although SARS-CoV-2 S-derived CD8⁺ T cell epitopes after natural infection have previously been published (including the immunodominant HLA-A*0201-restricted peptide YLQPRTFLL that is also identified in this Article)^{37,38}, to our knowledge this is the first report of epitopes recognized by vaccine-induced T cells.

The breadth and poly-specific nature of CD8⁺ and CD4⁺ T cell responses, and the linear nature of T cell epitopes that make them less susceptible to the secondary conformation-driven effects of a single amino acid variation, may mitigate the risk of immune escape of new variant strains. All eight S epitopes recognized by BNT162b2-

elicited CD8⁺ T cells were shared by the vaccine-targeted SARS-CoV-2 isolate, and by B.1.1.7, P.1 and B.1.351 lineages. In the B.1.1.298 lineage, which has not demonstrated sustained human-to-human transmission, only one of the eight CD8⁺ T cell epitopes showed a single-point mutation (which may or may not affect its binding to the respective MHC molecule).

As reported for the phase-I/II trial in the USA², prime-boost vaccination with 10 to 30 µg of BNT162b2 elicited GMTs of sera that—after an initial decline—remained stable for the entire follow-up of nine weeks after the booster dose, in the range of or higher than GMTs in individuals who had recovered from COVID-19.

Of the 22 pseudotyped viruses with the S mutations of circulating SARS-CoV-2 variants, almost all were efficiently neutralized by BNT162b2-immune sera. Although neutralizing antibody GMTs against the two pseudoviruses representing B.1.351-lineage S proteins were neutralized at reduced GMTs, no escape from neutralization was noted. Together with recent reports of the preserved neutralization of SARS-CoV-2 with key S mutations found in the B.1.1.7 and the B.1.351 lineage^{39,40}, and neutralization of pseudovirus bearing the full set of mutations of B.1.1.7 S⁴¹, our data indicate broad BNT162b2-elicited immune recognition^{2,13,14}.

Phase-III trial data¹ and real-world data^{3,4,5} show that a single 30-µg dose of BNT162b2, although associated with low neutralizing antibody titres, confers partial disease protection. Potential explanations may be that S1-binding antibodies exert antiviral effects by other mechanisms, such as antibody-dependent cytotoxicity or phagocytosis, or by the contribution of vaccine-induced T cells.

The limitations of our clinical study include the small sample size, the lack of representation of populations of interest and limited availability of blood samples for a more in-depth T cell analysis. These are being addressed by the ongoing clinical programme and emerging real-world data.

Methods

The experiments were not randomized, and investigators were not blinded to allocation during experiments and outcome assessment.

Clinical trial design

Study BNT162-01 (NCT04380701) is an ongoing, umbrella-type first-in-human, phase-I/II, open-label, dose-ranging clinical trial to assesses the safety, tolerability and immunogenicity of ascending dose levels of various intramuscularly administered BNT162 mRNA vaccine candidates in healthy men and non-pregnant women of 18 to

55 years (amended to add 56–85 years) of age. The principal end points of the study are safety and immunogenicity. Key exclusion criteria include previous clinical or microbiological diagnosis of COVID-19; receipt of medications to prevent COVID-19; previous vaccination with any coronavirus vaccine; a positive serological test for SARS-CoV-2 IgM and/or IgG; and a SARS-CoV-2 nucleic acid amplification test-positive nasal swab; increased risk for severe COVID-19; and immunocompromised individuals.

The presented data are from the BNT162b2-immunized healthy adults 19 to 55 years of age exposed to dose levels 1, 10, 20 or 30 µg. The data are based on a preliminary analysis (data extraction date of 23 October 2020 for safety and antibody analysis, and 28 January 2021 and 17 February 2021 for T cell analysis (ELISpot and intracellular staining (ICS), respectively)) and are focused on the analysis of vaccine-induced immunogenicity descriptively summarized at the various time points, and on reactogenicity. All participants with data available were included in the immunogenicity analyses. This part of the study was performed at one site in Germany with 12 healthy participants per dose level in a dose-escalation and de-escalation design. Sentinel dosing was performed in each dose-escalation cohort. Progression in that cohort and dose escalation required data review by a safety review committee. Participants received a BNT162b2 priming dose on day 1, and a booster dose on day 22 ± 2 (on day 28 for one participant from the 10-µg dose cohort). Serum for antibody and neutralization assays was obtained on day 1 (pre-prime), 8 ± 1 (post-prime), 22 ± 2 (pre-boost), 29 ± 3 , 43 ± 4 , 50 ± 4 and 85 ± 7 (post-boost; for all dose levels except 1 µg). PBMCs for T cell studies were obtained on day 1 (pre-prime), 29 ± 3 , 43 ± 4 and 85 ± 7 (post-boost) (Extended Data Fig. 1). Follow-up of participants is ongoing and includes assessment of antibody and T cell responses at later time points. Reactogenicity was assessed by patient diary. One participant (1-µg dose cohort) withdrew before the booster dose for reasons unrelated to the study drug and was not available for further follow-up. Another participant (10-µg dose cohort) presented with concurrent moderate nasopharyngitis unrelated to the study drug when the booster dose was due; this participant did not receive the booster dose but remained on the study for follow-up. The trial was carried out in Germany in accordance with the Declaration of Helsinki and Good Clinical Practice Guidelines and with approval by an independent ethics committee (Ethik-Kommission of the Landesärztekammer Baden-Württemberg, Stuttgart, Germany) and the competent regulatory authority (Paul-Ehrlich Institute, Langen, Germany). All participants provided written informed consent.

mRNA vaccine manufacturing

BNT162b2 incorporates a Good Manufacturing Practice-grade, codon-optimized mRNA drug substance that encodes trimerized SARS-CoV-2 S derived from the

Wuhan-Hu-1 isolate (GenBank: QHD43416.1; amino acids 1–1273) and carrying mutations K986P and V987P (S stabilized in its prefusion conformation (P2 S)). The RNA is generated from a DNA template by in vitro transcription in the presence of 1-methylpseudouridine-5'-triphosphate (Thermo Fisher Scientific) instead of uridine-5'-triphosphate. Capping is performed co-transcriptionally using a trinucleotide cap 1 analogue ((m₂^{7,3'-O})Gppp(m^{2'-O})ApG) (TriLink). The antigen-encoding RNA contains sequence elements that increase RNA stability and translation efficiency in human dendritic cells^{15,16}. The mRNA is formulated with lipids (ALC-3015, ALC-0159, DSPC and cholesterol) in an aqueous solution of sucrose, NaCl, KCl, Na₂HPO₄ and KH₂PO₄ to obtain the RNA–lipid nanoparticle drug product. The vaccine was transported and supplied as a buffered-liquid solution for intramuscular injection and was stored at –80 °C.

Proteins and peptides

Two pools of 15-mer peptides overlapping by 11 amino acids and together covering the whole sequence of wild-type (no P2 S mutation) SARS-CoV-2 S (Wuhan-Hu-1, GenBank: QHD43416.1; S pool 1 featuring amino acids 1–643, S pool 2 featuring amino acids 633–1273) and one pool covering SARS-CoV-2 RBD (amino acids 327–528) with the signal peptide of S (amino acids 1–16) fused to its N terminus were used for ex vivo stimulation of PBMCs for flow cytometry and IFN γ ELISpot. CEF (CMV, EBV and influenza virus; HLA class I epitope peptide pool) and CEFT (CMV, EBV, influenza virus and tetanus toxoid; HLA class II epitope peptide pool) were used to benchmark the magnitude of memory T cell responses. All peptides were obtained from JPT Peptide Technologies. The 8–12-amino-acid-long peptides used in the easYmer assays were produced at BioNTech US.

Human convalescent serum and PBMC panel

Sera from individuals ($n = 38$) who had been infected with SARS-CoV-2 or recovered from COVID-19 were drawn from donors 18–83 years of age at least 14 days after PCR-confirmed diagnosis and at a time at which the participants were asymptomatic. The mean age of the donors was 45 years. GMTs in subgroups of the donors were as follows: symptomatic infections, 90 ($n = 35$); asymptomatic infections, 156 ($n = 3$); hospitalized, 618 ($n = 1$). Sera were obtained from Sanguine Biosciences, the MT Group and Pfizer Occupational Health and Wellness. The data presented for these sera have previously been reported^{2,13,14}. PBMC samples from individuals ($n = 18$) who had been infected with SARS-CoV-2 or recovered from COVID-19 were collected from donors 22–79 years of age 30–62 days after PCR-confirmed diagnosis, when donors were asymptomatic. PBMC donors had asymptomatic or mild infections

($n = 16$, clinical score 1 and 2) or had been hospitalized ($n = 2$, clinical score 4 and 5). Blood samples were obtained from the Frankfurt University Hospital.

Cell culture and primary cell isolation

HEK293T/17 cells (American Type Culture Collection (ATCC) CRL-11268), Vero cells (ATCC CCL-81), Vero E6 cells (ATCC CRL-1586) and Vero 76 cells (ATCC CRL-1587) were cultured in Dulbecco's modified Eagle's medium (DMEM) with GlutaMAX (Gibco) supplemented with 10% fetal bovine serum (FBS) (Sigma-Aldrich). Cell lines were tested for mycoplasma contamination after receipt and before expansion and cryopreservation. PBMCs were isolated by Ficoll-Paque PLUS (Cytiva) density gradient centrifugation and cryopreserved before analysis.

S1- and RBD-binding IgG assay

To enable the comparison of vaccine-induced S1- and RBD-binding IgG responses to previously reported data on the BioNTech–Pfizer RNA vaccines for COVID-19, sera were analysed as previously described^{2,13,14}. In brief, recombinant SARS-CoV-2 S1 or RBD containing a C-terminal Avitag (Acro Biosystems) were bound to streptavidin-coated Luminex microspheres. Heat-inactivated participant sera were diluted 1:500, 1:5,000 and 1:50,000. Following an overnight incubation at 2–8 °C while shaking, plates were washed in a solution containing 0.05% Tween-20. A secondary fluorescently labelled goat anti-human polyclonal antibody (Jackson Labs) was added for 90 min at room temperature while shaking, before plates were washed once more in a solution containing 0.05% Tween-20. Data were captured as median fluorescent intensities using a Bioplex200 system (Bio-Rad) and converted to U ml⁻¹ antibody concentrations using a reference standard curve with arbitrarily assigned concentrations of 100 U ml⁻¹ and accounting for the serum dilution factor. The reference standard was composed of a pool of 5 serum samples from individuals who had recovered from COVID-19 obtained >14 days after COVID-19 PCR diagnosis and was diluted sequentially in antibody-depleted human serum. Three dilutions were used to increase the likelihood that at least one result for any sample would fall within the useable range of the standard curve. Assay results were reported in U ml⁻¹ of IgG. The final assay results were expressed as the geometric mean concentration of all sample dilutions that produced a valid assay result within the assay range.

SARS-CoV-2 neutralization assay

To enable the comparison of vaccine-induced serum neutralizing titres to those previously reported for BioNTech–Pfizer RNA vaccines for COVID-19, sera were analysed as previously described^{2,13,14}. In brief, the neutralization assay used a

previously described strain of SARS-CoV-2 (USA_WA1/2020) that had been rescued by reverse genetics and engineered by the insertion of an mNeonGreen (mNG) gene into open reading frame 7 of the viral genome⁴². The USA_WA1/2020 strain S is identical in sequence to the wild-type SARS-CoV-2 S (Wuhan-Hu-1 isolate). The reporter virus generates similar plaque morphologies and indistinguishable growth curves from wild-type virus. Viral master stocks (2×10^7 plaque forming units (PFU) per ml) were grown in Vero E6 cells as previously described⁴². With sera from patients who had recovered from COVID-19, the fluorescent neutralization assay produced comparable results to the conventional plaque reduction neutralization assay⁴³. Serial dilutions of heat-inactivated sera were incubated with the reporter virus (2×10^4 PFU per well to yield a 10–30% infection rate of the Vero CCL81 monolayer) for 1 h at 37 °C before inoculating Vero CCL81 cell monolayers (targeted to have 8,000 to 15,000 cells in a central field of each well at the time of seeding, 24 h before infection) in 96-well plates to allow accurate quantification of infected cells. Total cell counts per well were enumerated by nuclear stain (Hoechst 33342) and fluorescent virally infected foci were detected 16–24 h after inoculation with a CytaCount 7 Cell Imaging Multi-Mode Reader (BioTek) with Gen5 Image Prime version 3.09. Titres were calculated in GraphPad Prism version 8.4.2 by generating a four-parameter logistical fit of the per cent neutralization at each serial serum dilution. The VNT₅₀ is reported as the interpolated reciprocal of the dilution yielding a 50% reduction in fluorescent viral foci.

VSV-SARS-CoV-2 S pseudovirus neutralization assay for single-amino-acid-exchange S

VSV-SARS-CoV-2-S pseudoparticle generation and neutralization assays were performed as previously described²⁶. In brief, human codon optimized SARS-CoV-2 S-encoding DNA (GenBank: MN908947.3) was synthesized (Genscript) and cloned into an expression plasmid. SARS-CoV-2 complete genome sequences representing circulating variants were downloaded from the GISAID nucleotide database (<https://www.gisaid.org>) late in the spring of 2020. Sequences were curated, and the genetic diversity of the S-encoding gene was assessed across high-quality genome sequences using custom pipelines. The most abundant amino acid substitutions identified were cloned into the S expression plasmid using site-directed mutagenesis. HEK293T cells (ATCC CRL-3216) were seeded (culture medium: DMEM high glucose (Life Technologies) supplemented with 10% heat-inactivated FBS (Life Technologies) and penicillin, streptomycin and l-glutamine (Life Technologies)), and transfected the following day with S expression plasmid using Lipofectamine LTX (Life Technologies) following the manufacturer's protocol. At 24 h after transfection at 37 °C, cells were infected with VSV glycoprotein (VSV-G) *trans*-complemented VSV encoding the mNeonGreen fluorescent reporter gene instead of the native viral

glycoprotein (VSV^{ΔG:mNeon}/VSV-G) diluted in Opti-MEM (Life Technologies) at a multiplicity of infection of 1. Cells were incubated 1 h at 37 °C, washed to remove residual input virus and overlaid with infection medium (DMEM high glucose supplemented with 0.7% low IgG bovine serum albumin (Sigma), sodium pyruvate (Life Technologies) and 0.5% gentamicin (Life Technologies)). After 24 h at 37 °C, the medium containing VSV-SARS-CoV-2-S pseudoparticles was collected, centrifuged at 3,000g for 5 min to clarify and stored at –80 °C until further use.

For pseudovirus neutralization assays, Vero cells (ATCC CCL-81) were seeded in 96-well plates in culture medium and allowed to reach approximately 85% confluence before use in the assay (24 h later). Sera were serially diluted 1:2 in infection medium starting with a 1:300 dilution. VSV-SARS-CoV-2-S pseudoparticles were diluted 1:1 in infection medium for a fluorescent focus unit count in the assay of about 1,000. Serum dilutions were mixed 1:1 with pseudoparticles for 30 min at room temperature before addition to Vero cells and incubation at 37 °C for 24 h. Supernatants were removed and replaced with PBS (Gibco), and fluorescent foci were quantified using the SpectraMax i3 plate reader with MiniMax imaging cytometer (Molecular Devices). Neutralization titres were calculated in GraphPad Prism version 8.4.2 by generating a four-parameter logistical fit of the per cent neutralization at each serial serum dilution. The pVNT₅₀ is reported as the interpolated reciprocal of the dilution yielding a 50% reduction in fluorescent viral foci.

VSV-SARS-CoV-2 S pseudovirus neutralization assay for multiple-site mutations

A recombinant replication-deficient VSV vector that encodes green fluorescent protein (GFP) and luciferase (Luc) instead of VSV-G was pseudotyped with Wuhan-Hu-1 isolate SARS-CoV-2 S (GenBank: QHD43416.1) variants according to published pseudotyping protocols⁴⁴. One variant had four mutations from S of the B.1.1.298 lineage (also referred to as SARS-CoV-2/hu/DK/CL-5/1) (Y453F/D614G/I692V/M1229I)²⁸. Two variants had either eight (D80A/D215G/Δ242–244/K417N/E484K/N501Y/D614G/A701V) or ten mutations (L18F/D80A/D215G/R246I/Δ242–244/K417N/E484K/N501Y/D614G/A701V) found in S of the B.1.351 lineage (also referred to as 20C/501Y.V2)⁴⁰. In brief, HEK293T/17 monolayers transfected to express SARS-CoV-2 S with the C-terminal cytoplasmic 19 amino acids (SARS-CoV-2-S(CΔ19)) truncated were inoculated with the VSVΔG-GFP/Luc vector. After incubation for 1 h at 37 °C, the inoculum was removed, and cells were washed with PBS before medium supplemented with anti-VSV-G antibody (clone 8G5F11, Kerafast) was added to neutralize residual input virus. VSV-SARS-CoV-2 pseudovirus-containing medium was collected 20 h after inoculation, 0.2-μm filtered and stored at –80 °C.

For pseudovirus neutralization assays, 40,000 Vero 76 cells were seeded per 96-well. Sera were serially diluted 1:2 in culture medium starting with a 1:10 dilution (dilution range of 1:10 to 1:2,560). VSV-SARS-CoV-2-S pseudoparticles were diluted in culture medium for a fluorescent focus unit count in the assay of about 1,000. Serum dilutions were mixed 1:1 with pseudovirus for 30 min at room temperature before addition to Vero 76 cell monolayers in 96-well plates and incubation at 37 °C for 24 h.

Supernatants were removed, and the cells were lysed with luciferase reagent (Promega). Luminescence was recorded, and neutralization titres were calculated by generating a four-parameter logistical fit of the per cent neutralization at each serial serum dilution. The pVNT₅₀ is reported as the interpolated reciprocal of the dilution yielding a 50% reduction in luminescence.

IFN γ ELISpot

IFN γ ELISpot analysis was performed ex vivo using PBMCs depleted of CD4 $^{+}$ and enriched for CD8 $^{+}$ T cells (CD8 $^{+}$ effectors) or depleted of CD8 $^{+}$ and enriched for CD4 $^{+}$ T cells (CD4 $^{+}$ effectors). Tests were performed in duplicate and with a positive control (anti-CD3 monoclonal antibody CD3-2 (1:1,000; Mabtech)). Multiscreen filter plates (Merck Millipore) pre-coated with IFN γ -specific antibodies (ELISpotPro kit, Mabtech) were washed with PBS and blocked with X-VIVO 15 medium (Lonza) containing 2% human serum albumin (CSL-Behring) for 1–5 h. Per well, 3.3×10^5 effector cells were stimulated for 16–20 h with overlapping peptide pools that are described in ‘Vaccine-induced T cell responses’. Bound IFN γ was visualized using a secondary antibody directly conjugated with alkaline phosphatase followed by incubation with 5-bromo-4-chloro-3'-indolyl phosphate and nitro blue tetrazolium substrate (ELISpotPro kit, Mabtech). Plates were scanned using an AID Classic Robot ELISPOT Reader and analysed by AID ELISPOT 7.0 software (AID Autoimmun Diagnostika). Spot counts were displayed as mean values of each duplicate.

Peptide-stimulated spot counts were compared to effectors incubated with medium only as negative control using an in-house ELISpot data analysis tool, based on two statistical tests (distribution-free resampling) according to previous publications^{45,46}.

To account for varying sample quality reflected in the number of spots in response to anti-CD3 antibody stimulation, we applied a normalization method that enabled direct comparison of spot counts and strength of response between individuals. This dependency was modelled in a log-linear fashion with a Bayesian model including a noise component (R.H., unpublished). For a robust normalization, each normalization was sampled 10,000 times from the model and the median taken as normalized spot count value. Likelihood of the model: $\log(\lambda_E) = \alpha \log(\lambda_P) + \log(\beta_j) + \sigma \varepsilon$, in which λ_E is the normalized spot count of the sample; α is a stable factor (normally distributed)

common among all positive controls, λ_p ; β_j is a sample- j -specific component (normally distributed); and $\sigma\varepsilon$ is the noise component, of which σ is Cauchy distributed and ε is Student's- t distributed. β_j ensures that each sample is treated as a different batch.

Intracellular cytokine staining by flow cytometry

Cytokine-producing T cells were identified by intracellular cytokine staining. PBMCs, thawed and rested for 4 h in OpTmizer medium supplemented with 2 $\mu\text{g ml}^{-1}$ DNase I (Roche), were restimulated with different portions of the wild-type sequence of SARS-CoV-2 S in peptide pools described in 'IFN γ ELISpot' (2 $\mu\text{g per ml per peptide}$) (JPT Peptide Technologies) in the presence of GolgiPlug (BD) for 18 h at 37 °C. Controls were treated with dimethyl sulfoxide (DMSO)-containing medium. Cells were stained for viability and surface markers (CD3 BV421, 1:250; CD4 BV480, 1:50; CD8 BB515, 1:100; all BD Biosciences) in flow buffer (DPBS (Gibco) supplemented with 2% FBS (Sigma), 2 mM EDTA (Sigma-Aldrich)) and Brilliant Staining Buffer Plus (BSB Plus, BD Horizon, according to the manufacturer's instructions) or in Brilliant Staining Buffer (BD Horizon) for 20 min at 4 °C. Afterwards, samples were fixed and permeabilized using the Cytofix/Cytoperm kit according to manufacturer's instructions (BD Biosciences). Intracellular staining (CD3 BV421, 1:250; CD4 BV480, 1:50; CD8 BB515, 1:100; IFN γ PE-Cy7, 1:50 (for samples from individuals who had recovered from COVID-19); IFN γ BB700, 1:250 (for participants in the trial); IL-2 PE, 1:10; IL-4 APC, 1:500; all BD Biosciences) was performed in Perm/Wash buffer supplemented with BSB Plus (BD Horizon, according to the manufacturer's instructions) for 30 min at 4 °C. Samples were acquired on a fluorescence-activated cell sorter (FACS) VERSE instrument (BD Biosciences) and analysed with FlowJo software version 10.6.2 (FlowJo, BD Biosciences). S- and RBD-specific cytokine production was corrected for background by subtraction of values obtained with DMSO-containing medium. Negative values were set to zero. Cytokine production in Fig. 3a was calculated by summing up the fractions of all CD4 $^+$ T cells positive for either IFN γ , IL-2 or IL-4, setting this sum to 100% and calculating the fraction of each specific cytokine-producing subset. Pseudocolor plot axes are in log₁₀ scale. Data presented here for 15 of the 18 individuals who had recovered from COVID-19 who donated PBMCs have previously been reported¹⁴.

pMHC multimer staining by flow cytometry

To select MHC-class-I epitopes for multimer analysis, we applied a mass-spectrometry-based binding and presentation predictor^{47,48} to 8–12-amino-acid-long peptide sequences from S derived from the GenBank reference sequence for SARS-CoV-2 (accession: NC_045512.2, https://www.ncbi.nlm.nih.gov/nuccore/NC_045512) and paired with 18 MHC-class-I alleles with >5% frequency in the European

population. Top predicted epitopes were identified by setting thresholds to the binding per cent rank ($\leq 1\%$) and presentation scores ($\geq 10^{-2.2}$). Peptides were manufactured at >90% purity. pMHC complexes were refolded with the easYmer technology (easYmer kit, ImmuneAware Aps), and complex formation was validated in a bead-based flow cytometry assay according to the manufacturer's instructions^{49,50}. Combinatorial labelling was used for investigating the antigen specificity of T cells using two-colour combinations of five different fluorescent labels to enable detection of up to ten different T cell populations per sample⁵¹. For tetramerization, streptavidin (ST)-fluorochrome conjugates were added: ST BV421, ST BV711, ST PE, STPE-Cy7, ST APC (all BD Biosciences). For three participants vaccinated with BNT162b2, individualized pMHC multimer staining cocktails contained up to ten pMHC complexes, with each pMHC complex encoded by a unique two-colour combination. PBMCs (2×10^6) were stained ex vivo for 20 min at room temperature with each pMHC multimer cocktail at a final concentration of 4 nM in BSB Plus (BD Horizon). Surface and viability staining was carried out in flow buffer (DPBS (Gibco) with 2% FBS (Sigma), 2 mM EDTA (Sigma-Aldrich)) supplemented with BSB Plus for 30 min at 4 °C (CD3 BUV395, 1:50; CD45RA BUV563, 1:200; CD27 BUV737, 1:200; CD8 BV480, 1:200; CD279 BV650, 1:20; CD197 BV786, 1:15; CD4 BB515, 1:50; CD28 BB700, 1:100; CD38 BUV805, 1:300; HLA-DR APC-R700, 1:150 (all BD Biosciences); CD57 BV605, 1:600 (Biolegend); DUMP channel: CD14 APC-eFluor780, 1:100; CD16 APC-eFluor780, 1:100; CD19 APC-eFluor780, 1:100; fixable viability dye eFluor780, 1:1,667 (all ThermoFisher Scientific)). Cells were fixed for 15 min at 4 °C in 1× stabilization fixative (BD), acquired on a FACSymphony A3 flow cytometer (BD Biosciences) and analysed with FlowJo software version 10.6.2 (FlowJo, BD Biosciences). CD8⁺ T cell reactivities were considered positive, when a clustered population was observed that was labelled with only two pMHC multimer colours.

Sequence alignment

To assess the conservation of the T cell epitopes assayed with pMHC multimers, multiple sequence alignment of four variants of concern (B.1.1.298, B.1.1.7, B.1.351 and P.1) and the BNT162b2 sequence was performed using the MAFFT online tool⁵².

Statistical analysis

The sample size for the reported part of the study was not based on statistical hypothesis testing. All participants with data available were included in the safety and immunogenicity analyses. The statistical method of aggregation used for the analysis of antibody concentrations and titres is the geometric mean and the corresponding 95% confidence interval. Using the geometric mean accounts for non-normal

distribution of antibody concentrations and titres that span several orders of magnitude. Spearman correlation was used to evaluate the monotonic relationship between non-normally distributed datasets. All statistical analyses were performed using GraphPad Prism software version 9.

Reporting summary

Further information on research design is available in the [Nature Research Reporting Summary](#) linked to this paper.

Data availability

The data that support the findings of this study are available from the corresponding author upon reasonable request. Upon completion of this clinical trial, summary-level results will be made public and shared in line with data-sharing guidelines.

References

1. 1.

Polack, F. P. et al. Safety and efficacy of the BNT162b2 mRNA Covid-19 vaccine. *N. Engl. J. Med.* **383**, 2603–2615 (2020).

[CAS](#) [Article](#) [Google Scholar](#)

2. 2.

Walsh, E. E. et al. Safety and immunogenicity of two RNA-based Covid-19 vaccine candidates. *N. Engl. J. Med.* **383**, 2439–2450 (2020).

[CAS](#) [PubMed](#) [Article](#) [Google Scholar](#)

3. 3.

Dagan, N. et al. BNT162b2 mRNA Covid-19 vaccine in a nationwide mass vaccination setting. *N. Engl. J. Med.* **384**, 1412–1423 (2021).

[CAS](#) [PubMed](#) [Article](#) [Google Scholar](#)

4. 4.

Amit, S., Regev-Yochay, G., Afek, A., Kreiss, Y. & Leshem, E. Early rate reductions of SARS-CoV-2 infection and COVID-19 in BNT162b2 vaccine recipients. *Lancet* **397**, 875–877 (2021).

[CAS](#) [PubMed](#) [PubMed Central](#) [Article](#) [Google Scholar](#)

5. 5.

Petter, E. et al. Initial real world evidence for lower viral load of individuals who have been vaccinated by BNT162b2. Preprint at <https://doi.org/10.1101/2021.02.08.21251329> (2021).

6. 6.

BioNTech SE. Real-world evidence confirms high effectiveness of Pfizer-BioNTech COVID-19 vaccine and profound public health impact of vaccination one year after pandemic declared, <https://investors.biontech.de/news-releases/news-release-details/real-world-evidence-confirms-high-effectiveness-pfizer-biontech> (2021).

7. 7.

Pardi, N. et al. Nucleoside-modified mRNA vaccines induce potent T follicular helper and germinal center B cell responses. *J. Exp. Med.* **215**, 1571–1588 (2018).

[CAS](#) [PubMed](#) [PubMed Central](#) [Article](#) [Google Scholar](#)

8. 8.

Rauch, S., Jasny, E., Schmidt, K. E. & Petsch, B. New vaccine technologies to combat outbreak situations. *Front. Immunol.* **9**, 1963 (2018).

[PubMed](#) [PubMed Central](#) [Article](#) [CAS](#) [Google Scholar](#)

9. 9.

Pardi, N. et al. Expression kinetics of nucleoside-modified mRNA delivered in lipid nanoparticles to mice by various routes. *J. Control. Release* **217**, 345–351 (2015).

[CAS](#) [PubMed](#) [PubMed Central](#) [Article](#) [Google Scholar](#)

10. 10.

Sahin, U., Karikó, K. & Türeci, Ö. mRNA-based therapeutics—developing a new class of drugs. *Nat. Rev. Drug Discov.* **13**, 759–780 (2014).

[CAS](#) [PubMed](#) [Article](#) [Google Scholar](#)

11. 11.

Pardi, N., Hogan, M. J., Porter, F. W. & Weissman, D. mRNA vaccines – a new era in vaccinology. *Nat. Rev. Drug Discov.* **17**, 261–279 (2018).

[CAS](#) [PubMed](#) [PubMed Central](#) [Article](#) [Google Scholar](#)

12. 12.

Maruggi, G., Zhang, C., Li, J., Ulmer, J. B. & Yu, D. mRNA as a transformative technology for vaccine development to control infectious diseases. *Mol. Ther.* **27**, 757–772 (2019).

[CAS](#) [PubMed](#) [PubMed Central](#) [Article](#) [Google Scholar](#)

13. 13.

Mulligan, M. J. et al. Phase I/II study of COVID-19 RNA vaccine BNT162b1 in adults. *Nature* **586**, 589–593 (2020).

[ADS](#) [CAS](#) [PubMed](#) [Article](#) [Google Scholar](#)

14. 14.

Sahin, U. et al. COVID-19 vaccine BNT162b1 elicits human antibody and T_H1 T cell responses. *Nature* **586**, 594–599 (2020).

[ADS](#) [CAS](#) [PubMed](#) [PubMed Central](#) [Article](#) [Google Scholar](#)

15. 15.

Holtkamp, S. et al. Modification of antigen-encoding RNA increases stability, translational efficacy, and T-cell stimulatory capacity of dendritic cells. *Blood* **108**, 4009–4017 (2006).

[CAS](#) [PubMed](#) [Article](#) [Google Scholar](#)

16. 16.

Orlandini von Niessen, A. G. et al. Improving mRNA-based therapeutic gene delivery by expression-augmenting 3' UTRs identified by cellular library screening. *Mol. Ther.* **27**, 824–836 (2019).

[CAS](#) [PubMed](#) [Article](#) [Google Scholar](#)

17. 17.

Karikó, K. et al. Incorporation of pseudouridine into mRNA yields superior nonimmunogenic vector with increased translational capacity and biological stability. *Mol. Ther.* **16**, 1833–1840 (2008).

[PubMed](#) [Article](#) [CAS](#) [Google Scholar](#)

18. 18.

Vogel, A. B. et al. BNT162b vaccines protect rhesus macaques from SARS-CoV-2. *Nature* **592**, 283–289 (2021).

[ADS](#) [CAS](#) [PubMed](#) [Article](#) [Google Scholar](#)

19. 19.

Kamphuis, E., Junt, T., Waibler, Z., Forster, R. & Kalinke, U. Type I interferons directly regulate lymphocyte recirculation and cause transient blood lymphopenia. *Blood* **108**, 3253–3261 (2006).

[CAS](#) [PubMed](#) [Article](#) [Google Scholar](#)

20. 20.

Tsai, M. Y. et al. Effect of influenza vaccine on markers of inflammation and lipid profile. *J. Lab. Clin. Med.* **145**, 323–327 (2005).

[CAS](#) [PubMed](#) [Article](#) [Google Scholar](#)

21. 21.

Taylor, D. N. et al. Development of VAX128, a recombinant hemagglutinin (HA) influenza-flagellin fusion vaccine with improved safety and immune response. *Vaccine* **30**, 5761–5769 (2012).

[CAS](#) [PubMed](#) [Article](#) [Google Scholar](#)

22. 22.

Doener, F. et al. RNA-based adjuvant CV8102 enhances the immunogenicity of a licensed rabies vaccine in a first-in-human trial. *Vaccine* **37**, 1819–1826 (2019).

[CAS](#) [PubMed](#) [Article](#) [Google Scholar](#)

23. 23.

Destexhe, E. et al. Evaluation of C-reactive protein as an inflammatory biomarker in rabbits for vaccine nonclinical safety studies. *J. Pharmacol. Toxicol. Methods* **68**, 367–373 (2013).

[CAS](#) [PubMed](#) [Article](#) [Google Scholar](#)

24. 24.

Kaech, S. M., Wherry, E. J. & Ahmed, R. Effector and memory T-cell differentiation: implications for vaccine development. *Nat. Rev. Immunol.* **2**, 251–262 (2002).

[CAS](#) [PubMed](#) [Article](#) [Google Scholar](#)

25. 25.

Pérez-Mazliah, D., Ndungu, F. M., Aye, R. & Langhorne, J. B-cell memory in malaria: myths and realities. *Immunol. Rev.* **293**, 57–69 (2020).

[PubMed](#) [Article](#) [CAS](#) [Google Scholar](#)

26. 26.

Baum, A. et al. Antibody cocktail to SARS-CoV-2 spike protein prevents rapid mutational escape seen with individual antibodies. *Science* **369**, 1014–1018 (2020).

[ADS](#) [CAS](#) [Article](#) [Google Scholar](#)

27. 27.

Zhang, L. et al. SARS-CoV-2 spike-protein D614G mutation increases virion spike density and infectivity. *Nat. Commun.* **11**, 6013 (2020).

[CAS](#) [PubMed](#) [PubMed Central](#) [Article](#) [Google Scholar](#)

28. 28.

Lassaunière, R. et al. Working paper on SARS-CoV-2 spike mutations arising in Danish mink, their 2 spread to humans and neutralization data, https://files.ssi.dk/Mink-cluster-5-short-report_AFO2 (2020).

29. 29.

Tegally, H. et al. Detection of a SARS-CoV-2 variant of concern in South Africa. *Nature* **592**, 438–443 (2021).

[ADS](#) [CAS](#) [PubMed](#) [Article](#) [Google Scholar](#)

30. 30.

Sette, A. et al. Selective CD4⁺ T cell help for antibody responses to a large viral pathogen: deterministic linkage of specificities. *Immunity* **28**, 847–858 (2008).

[CAS](#) [PubMed](#) [PubMed Central](#) [Article](#) [Google Scholar](#)

31. 31.

Ni, L. et al. Detection of SARS-CoV-2-specific humoral and cellular immunity in COVID-19 convalescent individuals. *Immunity* **52**, 971–977 (2020).

[CAS](#) [PubMed](#) [PubMed Central](#) [Article](#) [Google Scholar](#)

32. 32.

Grifoni, A. et al. Targets of T cell responses to SARS-CoV-2 coronavirus in humans with COVID-19 disease and unexposed individuals. *Cell* **181**, 1489–1501 (2020).

[CAS](#) [PubMed](#) [PubMed Central](#) [Article](#) [Google Scholar](#)

33. 33.

Giménez, E. et al. SARS-CoV-2-reactive interferon- γ -producing CD8⁺ T cells in patients hospitalized with coronavirus disease 2019. *J. Med. Virol.* **93**, 375–382 (2021).

[PubMed](#) [Article](#) [CAS](#) [Google Scholar](#)

34. 34.

Braun, J. et al. SARS-CoV-2-reactive T cells in healthy donors and patients with COVID-19. *Nature* **587**, 270–274 (2020).

[ADS](#) [CAS](#) [PubMed](#) [Article](#) [Google Scholar](#)

35. 35.

Liu, W. J. et al. T-cell immunity of SARS-CoV: implications for vaccine development against MERS-CoV. *Antiviral Res.* **137**, 82–92 (2017).

[CAS](#) [PubMed](#) [Article](#) [Google Scholar](#)

36. 36.

Lu, R. et al. Genomic characterisation and epidemiology of 2019 novel coronavirus: implications for virus origins and receptor binding. *Lancet* **395**, 565–574 (2020).

[CAS](#) [PubMed](#) [PubMed Central](#) [Article](#) [Google Scholar](#)

37. 37.

Shomuradova, A. S. et al. SARS-CoV-2 epitopes are recognized by a public and diverse repertoire of human T cell receptors. *Immunity* **53**, 1245–1257.e5 (2020).

[CAS](#) [PubMed](#) [PubMed Central](#) [Article](#) [Google Scholar](#)

38. 38.

Peng, Y. et al. Broad and strong memory CD4⁺ and CD8⁺ T cells induced by SARS-CoV-2 in UK convalescent individuals following COVID-19. *Nat. Immunol.* **21**, 1336–1345 (2020).

[CAS](#) [PubMed](#) [PubMed Central](#) [Article](#) [Google Scholar](#)

39. 39.

Xie, X. et al. Neutralization of SARS-CoV-2 spike 69/70 deletion, E484K and N501Y variants by BNT162b2 vaccine-elicited sera. *Nat. Med.* **27**, 620–621 (2021).

[CAS](#) [PubMed](#) [Article](#) [Google Scholar](#)

40. 40.

O'Toole, Á. et al. Tracking the international spread of SARS-CoV-2 lineages B.1.1.7 and B.1.351/501Y-V2,
<https://virological.org/t/tracking-the-international-spread-of-sars-cov-2-lineages-b-1-1-7-and-b-1-351-501y-v2/592> (2021).

41. 41.

Muik, A. et al. Neutralization of SARS-CoV-2 lineage B.1.1.7 pseudovirus by BNT162b2 vaccine-elicited human sera. *Science* **371**, 1152–1153 (2021).

[ADS](#) [CAS](#) [PubMed](#) [PubMed Central](#) [Article](#) [Google Scholar](#)

42. 42.

Xie, X. et al. An infectious cDNA clone of SARS-CoV-2. *Cell Host Microbe* **27**, 841–848 (2020).

[CAS](#) [PubMed](#) [PubMed Central](#) [Article](#) [Google Scholar](#)

43. 43.

Muruato, A. E. et al. A high-throughput neutralizing antibody assay for COVID-19 diagnosis and vaccine evaluation. *Nat. Commun.* **11**, 4059 (2020).

[ADS](#) [CAS](#) [PubMed](#) [PubMed Central](#) [Article](#) [Google Scholar](#)

44. 44.

Berger Rentsch, M. & Zimmer, G. A vesicular stomatitis virus replicon-based bioassay for the rapid and sensitive determination of multi-species type I interferon. *PLoS ONE* **6**, e25858 (2011).

[ADS](#) [PubMed](#) [PubMed Central](#) [Article](#) [CAS](#) [Google Scholar](#)

45. 45.

Moodie, Z., Huang, Y., Gu, L., Hural, J. & Self, S. G. Statistical positivity criteria for the analysis of ELISpot assay data in HIV-1 vaccine trials. *J. Immunol. Methods* **315**, 121–132 (2006).

[CAS](#) [PubMed](#) [Article](#) [Google Scholar](#)

46. 46.

Moodie, Z. et al. Response definition criteria for ELISPOT assays revisited. *Cancer Immunol. Immunother.* **59**, 1489–1501 (2010).

[CAS](#) [PubMed](#) [PubMed Central](#) [Article](#) [Google Scholar](#)

47. 47.

Abelin, J. G. et al. Mass spectrometry profiling of HLA-associated peptidomes in mono-allelic cells enables more accurate epitope prediction. *Immunity* **46**, 315–326 (2017).

[CAS](#) [PubMed](#) [PubMed Central](#) [Article](#) [Google Scholar](#)

48. 48.

Poran, A. et al. Sequence-based prediction of SARS-CoV-2 vaccine targets using a mass spectrometry-based bioinformatics predictor identifies immunogenic T cell epitopes. *Genome Med.* **12**, 70 (2020).

[CAS](#) [PubMed](#) [PubMed Central](#) [Article](#) [Google Scholar](#)

49. 49.

Svitek, N. et al. Use of “one-pot, mix-and-read” peptide-MHC class I tetramers and predictive algorithms to improve detection of cytotoxic T lymphocyte responses in cattle. *Vet. Res.* **45**, 50 (2014).

[PubMed](#) [PubMed Central](#) [Article](#) [Google Scholar](#)

50. 50.

Leisner, C. et al. One-pot, mix-and-read peptide-MHC tetramers. *PLoS ONE* **3**, e1678 (2008).

[ADS](#) [PubMed](#) [PubMed Central](#) [Article](#) [CAS](#) [Google Scholar](#)

51. 51.

Hadrup, S. R. et al. Parallel detection of antigen-specific T-cell responses by multidimensional encoding of MHC multimers. *Nat. Methods* **6**, 520–526 (2009).

[CAS](#) [PubMed](#) [Article](#) [Google Scholar](#)

52. 52.

Katoh, K., Rozewicki, J. & Yamada, K. D. MAFFT online service: multiple sequence alignment, interactive sequence choice and visualization. *Brief. Bioinform.* **20**, 1160–1166 (2019).

[CAS](#) [PubMed](#) [Article](#) [Google Scholar](#)

53. 53.

US Department of Health and Human Services, Food and Drug Administration & Centers for Biologics Evaluation and Research. Toxicity grading scale for healthy adult and adolescent volunteers enrolled in preventive vaccine clinical trials,
<https://www.fda.gov/regulatory-information/search-fda-guidance-documents/toxicity-grading-scale-healthy-adult-and-adolescent-volunteers-enrolled-preventive-vaccine-clinical> (2007).

[Download references](#)

Acknowledgements

We thank M. Dolsten for advice during drafting of the manuscript; P. Adams-Quack, C. Anders, C. Anft, N. Beckmann, K. Bissinger, P. Cienskowski, K. Clarke, C. Ecker, A. Engelmann, M. Fierek, D. Harjanto, A. Heinen, M. Hossainzadeh, S. Jägle, L. Jeck, O. Kahl, D. Kallin, M. Knezovic, T. Kotur, M. Kretschmer, A. Kruithof, J. Mc Gee, B. Mehlhase, C. Müller, S. Murphy, L.-M. Schmid, K. Schmoldt, R. Schulz, L. Srinivasan, B. Sänger, M. Vehreschild, A.-K. Wallisch, T. Weisenburger and S. Wessel for technical support, project management and advice; K. Swanson, H. Cai, W. Chen and R. Sarkar for synthesizing an S-encoding gene used for pseudovirus neutralization testing against the B.1.351-lineage S; S. Rothmeier for data analysis; O. Kistner, S. Liebscher, J. Loschko and K. Swanson for expert advice; J. Absalon for manuscript advice; the CRS Team (Mannheim and Berlin) for study conduct (S. Armani, M. Berse, M. Casjens, B. Ehrlich, F. Seitz and M. Streckebein); W. Kalina, I. Scully and the Pfizer Vaccines Clinical Assays Team and the Pfizer Aviation Team for technical and logistical support of serology analyses; and the GISAID nucleotide database for sharing of SARS-CoV-2 complete genome sequences. BioNTech is the sponsor of the study and responsible for the design, data collection, data analysis, data interpretation and writing of the report. Pfizer advised on the study and the manuscript, generated serological data and contracted for the generation of serological data. The authors had full access to all of the data in the study and had final responsibility for the decision to submit the data for publication. All study data were available to all authors. This study was not supported by any external funding at the time of submission.

Author information

Affiliations

1. BioNTech, Mainz, Germany

Ugur Sahin, Alexander Muik, Isabel Vogler, Evelyn
Derhovanessian, Lena M. Kranz, Mathias Vormehr, Jasmin
Quandt, Nicole Bidmon, Alexander Ulges, Daniel Maurus, Sebastian
Brachtendorf, Verena Lörks, Julian Sikorski, Peter Koch, Rolf
Hilker, Dirk Becker, Ann-Kathrin Eller, Jan Grützner, Manuel

Tonigold, Carsten Boesler, Corinna Rosenbaum, Ludwig Heesen, Marie-Cristine Kühnle, Ulrich Luxemburger, Alexandra Kemmer-Brück, David Langer, Stefanie Bolte, Tania Palanche, Azita J. Mahiny, Gábor Boros, Jonas Reinholtz, Gábor T. Szabó, Katalin Karikó & Özlem Türeci

2. TRON gGmbH – Translational Oncology at the University Medical Center of the Johannes Gutenberg University, Mainz, Germany

Ugur Sahin

3. Regeneron Pharmaceuticals, Inc., Tarrytown, NY, USA

Alina Baum, Kristen E. Pascal & Christos A. Kyratsous

4. BioNTech US, Cambridge, MA, USA

Asaf Poran & Jesse Z. Dong

5. Bexon Clinical Consulting LLC, Upper Montclair, NJ, USA

Martin Bexon

6. CRS Clinical Research Services Mannheim GmbH, Mannheim, Germany

Armin Schultz

7. CRS Clinical Research Services Berlin GmbH, Berlin, Germany

Sybille Baumann

8. University of Texas Medical Branch, Galveston, TX, USA

Pei-Yong Shi & Camila Fontes-Garfias

9. Pfizer, Pearl River, NY, US

John L. Perez, Mark Cutler, David Cooper, Philip R. Dormitzer & Kathrin U. Jansen

Authors

1. Ugur Sahin

[View author publications](#)

You can also search for this author in [PubMed](#) [Google Scholar](#)

2. Alexander Muik

[View author publications](#)

You can also search for this author in [PubMed](#) [Google Scholar](#)

3. Isabel Vogler

[View author publications](#)

You can also search for this author in [PubMed](#) [Google Scholar](#)

4. Evelyn Derhovanessian

[View author publications](#)

You can also search for this author in [PubMed](#) [Google Scholar](#)

5. Lena M. Kranz

[View author publications](#)

You can also search for this author in [PubMed](#) [Google Scholar](#)

6. Mathias Vormehr

[View author publications](#)

You can also search for this author in [PubMed](#) [Google Scholar](#)

7. Jasmin Quandt

[View author publications](#)

You can also search for this author in [PubMed](#) [Google Scholar](#)

8. Nicole Bidmon

[View author publications](#)

You can also search for this author in [PubMed](#) [Google Scholar](#)

9. Alexander Ulges

[View author publications](#)

You can also search for this author in [PubMed](#) [Google Scholar](#)

10. Alina Baum

[View author publications](#)

You can also search for this author in [PubMed](#) [Google Scholar](#)

11. Kristen E. Pascal

[View author publications](#)

You can also search for this author in [PubMed](#) [Google Scholar](#)

12. Daniel Maurus

[View author publications](#)

You can also search for this author in [PubMed](#) [Google Scholar](#)

13. Sebastian Brachtendorf

[View author publications](#)

You can also search for this author in [PubMed](#) [Google Scholar](#)

14. Verena Lörks

[View author publications](#)

You can also search for this author in [PubMed](#) [Google Scholar](#)

15. Julian Sikorski

[View author publications](#)

You can also search for this author in [PubMed](#) [Google Scholar](#)

16. Peter Koch

[View author publications](#)

You can also search for this author in [PubMed](#) [Google Scholar](#)

17. Rolf Hilker

[View author publications](#)

You can also search for this author in [PubMed](#) [Google Scholar](#)

18. Dirk Becker

[View author publications](#)

You can also search for this author in [PubMed](#) [Google Scholar](#)

19. Ann-Kathrin Eller

[View author publications](#)

You can also search for this author in [PubMed](#) [Google Scholar](#)

20. Jan Grützner

[View author publications](#)

You can also search for this author in [PubMed](#) [Google Scholar](#)

21. Manuel Tonigold

[View author publications](#)

You can also search for this author in [PubMed](#) [Google Scholar](#)

22. Carsten Boesler

[View author publications](#)

You can also search for this author in [PubMed](#) [Google Scholar](#)

23. Corinna Rosenbaum

[View author publications](#)

You can also search for this author in [PubMed](#) [Google Scholar](#)

24. Ludwig Heesen

[View author publications](#)

You can also search for this author in [PubMed](#) [Google Scholar](#)

25. Marie-Cristine Kühnle

[View author publications](#)

You can also search for this author in [PubMed](#) [Google Scholar](#)

26. Asaf Poran

[View author publications](#)

You can also search for this author in [PubMed](#) [Google Scholar](#)

27. Jesse Z. Dong

[View author publications](#)

You can also search for this author in [PubMed](#) [Google Scholar](#)

28. Ulrich Luxemburger

[View author publications](#)

You can also search for this author in [PubMed](#) [Google Scholar](#)

29. Alexandra Kemmer-Brück

[View author publications](#)

You can also search for this author in [PubMed](#) [Google Scholar](#)

30. David Langer

[View author publications](#)

You can also search for this author in [PubMed](#) [Google Scholar](#)

31. Martin Bexon

[View author publications](#)

You can also search for this author in [PubMed](#) [Google Scholar](#)

32. Stefanie Bolte

[View author publications](#)

You can also search for this author in [PubMed](#) [Google Scholar](#)

33. Tania Palanche

[View author publications](#)

You can also search for this author in [PubMed](#) [Google Scholar](#)

34. Armin Schultz

[View author publications](#)

You can also search for this author in [PubMed](#) [Google Scholar](#)

35. Sybille Baumann

[View author publications](#)

You can also search for this author in [PubMed](#) [Google Scholar](#)

36. Azita J. Mahiny

[View author publications](#)

You can also search for this author in [PubMed](#) [Google Scholar](#)

37. Gábor Boros

[View author publications](#)

You can also search for this author in [PubMed](#) [Google Scholar](#)

38. Jonas Reinholtz

[View author publications](#)

You can also search for this author in [PubMed](#) [Google Scholar](#)

39. Gábor T. Szabó

[View author publications](#)

You can also search for this author in [PubMed](#) [Google Scholar](#)

40. Katalin Karikó

[View author publications](#)

You can also search for this author in [PubMed](#) [Google Scholar](#)

41. Pei-Yong Shi

[View author publications](#)

You can also search for this author in [PubMed](#) [Google Scholar](#)

42. Camila Fontes-Garfias

[View author publications](#)

You can also search for this author in [PubMed](#) [Google Scholar](#)

43. John L. Perez

[View author publications](#)

You can also search for this author in [PubMed](#) [Google Scholar](#)

44. Mark Cutler

[View author publications](#)

You can also search for this author in [PubMed](#) [Google Scholar](#)

45. David Cooper

[View author publications](#)

You can also search for this author in [PubMed](#) [Google Scholar](#)

46. Christos A. Kyratsous

[View author publications](#)

You can also search for this author in [PubMed](#) [Google Scholar](#)

47. Philip R. Dormitzer

[View author publications](#)

You can also search for this author in [PubMed](#) [Google Scholar](#)

48. Kathrin U. Jansen

[View author publications](#)

You can also search for this author in [PubMed](#) [Google Scholar](#)

49. Özlem Türeci

[View author publications](#)

You can also search for this author in [PubMed](#) [Google Scholar](#)

Contributions

U.S. conceived the work and strategy, supported by Ö.T. Experiments were planned or supervised by N.B., E.D., C.F.-G., C.A.K., U.L., A.M., J.Q., P.-Y.S., A.U. and I.V. A.B., N.B., D.C., M.C., C.F.-G., K.E.P., J.Q., A.U. and P.-Y.S. performed experiments. D.B., S. Brachtendorf, E.D., P.R.D., J.G., K.U.J., A.-K.E., P.K., M.T., L.M.K., M.-C.K., V.L., A.M., J.Q., J.S., N.B., A.U., I.V. and M.V. analysed data. A.P. prioritized epitopes for pMHC multimer assay. J.Z.D. supervised the manufacturing and delivery of peptides for pMHC multimer assay. D.M. planned and supervised dashboards for the analysis of clinical trial data. R.H. was responsible for data normalization and adaption. C.B., L.H. and C.R. were responsible for the management of the biomarker and research and development programmes. G.B., K.K., A.J.M., J.R. and G.T.S. optimized mRNA characteristics. A.K.-B., S. Baumann, A.S., D.L., M.B., S. Bolte and T.P. coordinated operational conduct of the clinical trial. J.L.P. advised on the trial. U.S. and Ö.T., supported by M.B., N.B., E.D., P.R.D., K.U.J., L.M.K., A.M., A.U., I.V. and M.V., interpreted data and wrote the manuscript. All authors supported the review of the manuscript.

Corresponding author

Correspondence to [Ugur Sahin](#).

Ethics declarations

Competing interests

Ö.T. and U.S. are management board members and employees at BioNTech SE (Mainz, Germany); A.K.-B., A.M., A.J.M., A.-K.E., A.U., C.R., D.B., D.L., D.M., E.D., G.B., G.T.S., I.V., J.G., J.Q., J.R., J.S., K.K., L.H., L.M.K., M.-C.K., M.V., N.B., P.K., R.H., S. Bolte, S. Brachtendorf, T.P., U.L. and V.L. are employees at BioNTech SE; A.P. and J.Z.D. are employees at BioNTech US; M.B. is an employee at Bexon Clinical Consulting LLC; A.B., C.A.K. and K.E.P. are employees of Regeneron Pharmaceuticals Inc; A.M., K.K., Ö.T. and U.S. are inventors on patents and patent applications related to RNA technology and COVID-19 vaccines; A.K.-B., A.M., A.J.M., A.P., C.R., D.B., D.L., E.D., G.B., I.V., J.Z.D., J.G., K.K., L.H., L.M.K., M.V., N.B., Ö.T., R.H., S. Bolte, U.L. and U.S. have securities from BioNTech SE; D.C., J.L.P., K.U.J., M.C. and P.R.D. are employees at Pfizer and may have securities from Pfizer; C.A.K. is an officer at Regeneron Pharmaceuticals, Inc; A.B., C.A.K. and K.E.P. have securities from Regeneron Pharmaceuticals, Inc; C.F.-G. and P.-Y.S. received compensation from Pfizer to perform the neutralization assay; the authors declare that there are no other relationships or activities that could appear to have influenced the submitted work.

Additional information

Peer review information *Nature* thanks Antonio Bertoletti and the other, anonymous, reviewer(s) for their contribution to the peer review of this work.

Publisher's note Springer Nature remains neutral with regard to jurisdictional claims in published maps and institutional affiliations.

Extended data figures and tables

[Extended Data Fig. 1 Vaccination schedule and sample collection.](#)

Study participants received a priming dose with BNT162b2 on day 1 and a booster dose on day 22 ± 2 . Sera were obtained on day 1 (pre-prime), day 8 ± 1 (post-prime), day 22 ± 2 (pre-boost), day 29 ± 3 , day 43 ± 4 , day

50 ± 4 and day 85 ± 7 (post-boost). PBMCs were obtained on day 1 (pre-prime), day 29 ± 3 , day 43 ± 4 and day 85 ± 7 (post-boost).

Extended Data Fig. 2 Solicited adverse events.

a, b, Number of participants with local (**a**) or systemic (**b**) solicited adverse events. Participants were immunized with BNT162b2 on day 1 and day 22 (prime: $n = 12$ per dose cohort except for boost of the 1- and 100 μ g dose cohorts, for which $n = 11$); participants discontinued for non-vaccine-related reasons). Grey shading indicates number of participants at each time point. As per protocol, adverse events were recorded up to one week after each immunization (days 1–7 and 22–28) to determine reactogenicity; for some participants, data from 1–3 additional days of follow-up were available and are presented. Grading of adverse events was performed according to US Food and Drug Administration recommendations⁵³.

Extended Data Fig. 3 Pharmacodynamic markers.

a, b, Participants were immunized with BNT162b2 on day 1 and day 22 ($n = 12$ per dose cohort). One participant in the 1- μ g dose cohort (outlier on day 8 in **a** and highest dataset in **b**) presented with a non-treatment-related gastroenteritis on days 6–8. **a**, Kinetics of C-reactive protein (CRP) level. **b**, Kinetics of lymphocyte counts. **c**, Kinetics of neutrophil counts. Dotted lines indicate upper and lower limit of reference range. In **a**, for values below the LLOQ (of 0.3), LLOQ/2 values were plotted.

Extended Data Fig. 4 BNT162b2-induced antibody responses.

Vaccination schedule and serum sampling are described in Extended Data Fig. 1. Participants were immunized with BNT162b2 on day 1 and day 22 ($n = 12$ per dose cohort; from day 22 onwards $n = 11$ for the 1- μ g and 10- μ g dose cohorts). Arrowheads indicate days of vaccination. Pre-dose responses across all dose levels were combined. Samples from individuals who had been infected with SARS-CoV-2 or had recovered from COVID-19 (HCS) ($n = 38$) were obtained at least 14 days after PCR-confirmed diagnosis and at a time at which the donors were no longer symptomatic. **a–d**, Each serum was tested in duplicate and IgG GMCs (**a, c**) and geometric

mean 50% (pseudo)neutralizing titres (GMTs) (**c**, **d**) were plotted. For values below the LLOQ (1.27 (S1 IgG), 1.15 (RBD IgG) (**a**), 20 (VNT₅₀) (**c**) and 300 (pVNT₅₀) (**d**)), LLOQ/2 values were plotted. **a**, Recombinant S1- and RBD-binding IgG group GMCs (values above bars) with 95% confidence intervals. **b**, Fraction of participants with ≥ 4 -fold-increased 50% serum neutralizing response above baseline (from Fig. [1a](#)) at each time point. Fractions with exact 95% Clopper–Pearson confidence intervals. **c**, Non-parametric Spearman correlation of recombinant S1-binding IgG GMCs (from **a**) with VNT₅₀ from day 29 sera (from Fig. [1a](#)) with data points for participants with GMCs and GMTs below the LLOQ (open circles) excluded. **d**, pVNT₅₀ across a pseudovirus panel displaying 19 SARS-CoV-2 S variants on a Wuhan-Hu-1 strain background, including 18 with RBD single-nucleotide-exchange mutations and the dominant D614G variant (1-, 10- and 30- μ g dose cohorts, $n = 1$ or 2 representative sera each; day 29).

[Extended Data Fig. 5 BNT162b2-induced S-specific CD4 \$^+\$ and CD8 \$^+\$ T cells.](#)

CD4 $^+$ or CD8 $^+$ T cell effector-enriched fractions of PBMCs obtained from trial participants on day 1 (pre) and day 29 (1-, 10- and 20- μ g dose cohorts, $n = 9$ each; 30- μ g dose cohort, $n = 10$) were stimulated overnight with overlapping peptide pools covering the wild-type SARS-CoV-2 S (S pool 1 and S pool 2) or RBD for assessment by IFNy ELISpot. Each data point represents the normalized mean spot count from duplicate wells for one study participant, after subtraction of the medium-only control. Spot count data from two participants from the 20- μ g dose cohort could not be normalized and are not plotted. **a**, **b**, RBD-specific (**a**) and S-specific (**b**) CD4 $^+$ and CD8 $^+$ T cell responses for each dose cohort. T cell responses against S pool 1 and S pool 2 were combined for each participant. Numbers above each dataset represent the number of participants with a positive T cell response over the total number of participants tested. **c**, ELISpot example of CD4 $^+$ and CD8 $^+$ T cell responses for a 30- μ g dose cohort participant on day 1 (pre) and day 29 (post). **d**, Mapping of vaccine-induced responses of participants with evaluable baseline data ($n = 34$ for CD4 $^+$ and

$n = 37$ for CD8 $^{+}$ T cell responses) to different portions of S on day 29. De novo-induced or amplified responses are classified as BNT162b2-induced responses; no responses or pre-existing responses that were not amplified by the vaccinations are classified as no vaccine response (none). **e**, Response to S pool 1 on day 29 in individuals with or without a pre-existing response to S pool 2. Data from the 1- μ g dose cohort are excluded, as no baseline response to S pool 2 was present in this cohort. Horizontal bars represent the median of each group. **f**, ELISpot example of CD4 $^{+}$ and CD8 $^{+}$ T cell responses on day 85.

Extended Data Fig. 6 Correlation of antibody and T cell responses induced by BNT162b2.

a–c, Data are plotted for all prime–boost-vaccinated participants (1-, 10-, 20- and 30- μ g dose cohorts) from day 29, with data points for participants with no detectable T cell response (open circles; **b, c**) excluded from correlation analysis. S1-specific IgG responses from Fig. 1a, S-specific T cell responses from Extended Data Fig. 5a ($n = 37$). Non-parametric Spearman correlations are shown. **a**, Correlation of S1-specific IgG responses with S-specific CD4 $^{+}$ T cell responses. **b**, Correlation of S-specific CD4 $^{+}$ with CD8 $^{+}$ T cell responses. **c**, Correlation of S1-specific IgG responses with S-specific CD8 $^{+}$ T cell responses.

Extended Data Fig. 7 Cytokine profiles and reactivities of BNT162b2-induced T cells.

a–e, PBMCs obtained on day 1 (pre), day 29 (dose cohorts 1 μ g, $n = 8$; 10, 20 and 30 μ g, $n = 11$ each) (**a–d**), day 43 and day 85 (30- μ g dose cohort, $n = 8$) (**e**) and donors who had recovered from COVID-19 (HCS) ($n = 18$) (**b, d**) were stimulated overnight with three overlapping peptide pools representing different portions of the wild-type sequence of SARS-CoV-2 S (N-terminal pools S pool 1 and RBD, and the C-terminal S pool 2), and analysed by flow cytometry (gating strategy in Supplementary Fig. 1). Participant PBMCs were tested without replicates (**b–e**). **a**, Examples of pseudocolour flow cytometry plots of cytokine-producing CD4 $^{+}$ and CD8 $^{+}$ T cells from a participant in the 30- μ g dose cohort in response to S pool 1

and S pool 2 on day 1 (pre) and day 29 (post). **b**, S-specific CD4⁺ T cells (S pool 1, S pool 2 and RBD) producing the indicated cytokine as a fraction of total circulating T cells of the same subset on day 29. Values above data points indicate mean fractions per dose cohort. **c**, Fraction of vaccine-induced, S-specific IFN γ ⁺ CD4⁺ T cells plotted against IL-4⁺ CD4⁺ T cells on day 29. ICS stimulation was performed using a peptide mixture of S pool 1 and S pool 2. Each data point represents one study participant (dose cohorts 1 μ g, $n = 8$; 10 and 30 μ g, $n = 11$; 20 μ g, $n = 10$). One participant from the 20- μ g dose cohort with a strong pre-existing CD4⁺ T cell response to S pool 2 was excluded. **d**, S-specific CD8⁺ T cells (S pool 1, S pool 2 and RBD) producing the indicated cytokine as a fraction of total circulating T cells of the same subset on day 29. Values above data points indicate mean fractions per dose cohort. **e**, Response kinetics of S-specific CD4⁺ and CD8⁺ T cells stimulated with S pool 2 and producing the indicated cytokine as a fraction of total circulating T cells of the same subset. Vertical dotted lines indicate days of vaccination. **f**, Epitopes recognized by BNT162b2-induced T cells (from Fig. 4a) and aligned with the corresponding sequences in four SARS-CoV-2 lineages. Non-consensus amino acids are highlighted in red. **g**, Epitope-specific CD8⁺ T cell frequencies determined by pMHC class I multimer staining (per cent multimer⁺ of CD8⁺), ICS and ELISpot (per cent IFN γ ⁺ of CD8⁺) from the three participants in Fig. 4. Signals for S pool 1 and S pool 2 were merged for each assay.

Extended Data Table 1 Demographic characteristics

[Full size table](#)

Extended Data Table 2 Participant disposition and analysis sets

[Full size table](#)

Extended Data Table 3 Summary of solicited local and systemic reactions

[Full size table](#)

Supplementary information

[Supplementary Figures](#)

This file contains Supplementary Figures 1-2 which contain examples of the flow cytometry gating strategy.

Reporting Summary

Rights and permissions

Reprints and Permissions

About this article



Check for
updates

Cite this article

Sahin, U., Muik, A., Vogler, I. *et al.* BNT162b2 vaccine induces neutralizing antibodies and poly-specific T cells in humans. *Nature* **595**, 572–577 (2021). <https://doi.org/10.1038/s41586-021-03653-6>

Download citation

- Received: 09 December 2020
- Accepted: 19 May 2021
- Published: 27 May 2021
- Issue Date: 22 July 2021
- DOI: <https://doi.org/10.1038/s41586-021-03653-6>

Comments

By submitting a comment you agree to abide by our [Terms](#) and [Community Guidelines](#). If you find something abusive or that does not comply with our terms or guidelines please flag it as inappropriate.

[Download PDF](#)

Advertisement

This article was downloaded by **calibre** from <https://www.nature.com/articles/s41586-021-03653-6>

| [Section menu](#) | [Main menu](#) |

- Article
- [Published: 16 June 2021](#)

Tissue-resident macrophages provide a pro-tumorigenic niche to early NSCLC cells

- [María Casanova-Acebes](#) ORCID: orcid.org/0000-0002-5790-1163^{1,2,3 nAff19},
- [Erica Dalla](#)^{4,5,6,7 na1},
- [Andrew M. Leader](#)^{1,2,3 na1},
- [Jessica LeBeriche](#)^{1,2,3 na1},
- [Jovan Nikolic](#)⁸,
- [Blanca M. Morales](#)⁹,
- [Markus Brown](#)⁹,
- [Christie Chang](#) ORCID: orcid.org/0000-0002-7651-7220^{1,2,3},
- [Leanna Troncoso](#)^{1,2,3},
- [Steven T. Chen](#)^{1,2,3},
- [Ana Sastre-Perona](#)^{10,11},
- [Matthew D. Park](#)^{1,2,3},
- [Alexandra Tabachnikova](#)^{1,2,3},
- [Maxime Dhainaut](#)^{2,3,12},
- [Pauline Hamon](#)^{1,2,3},
- [Barbara Maier](#)^{1,2,3 nAff20},
- [Catherine M. Sawai](#)¹³,
- [Esperanza Agulló-Pascual](#)¹⁴,
- [Markus Schober](#)¹⁰,
- [Brian D. Brown](#) ORCID: orcid.org/0000-0002-3670-8778^{2,3,12,17},
- [Boris Reizis](#) ORCID: orcid.org/0000-0003-1140-7853¹⁵,
- [Thomas Marron](#)^{1,2,3,4,16},

- [Ephraim Kenigsberg](#) [ORCID: orcid.org/0000-0002-4107-3295^{2,17}](#),
- [Christine Moussion](#) [ORCID: orcid.org/0000-0002-1641-4094⁹](#),
- [Philippe Benaroch⁸](#),
- [Julio A. Aguirre-Ghiso](#) [ORCID: orcid.org/0000-0002-6694-6507^{1,2,3,4,5,6,7 na2}](#) &
- [Miriam Merad](#) [ORCID: orcid.org/0000-0002-4481-7827^{1,2,3,18 na2}](#)

Nature volume **595**, pages 578–584 (2021) [Cite this article](#)

- 24k Accesses
- 340 Altmetric
- [Metrics details](#)

Subjects

- [Cancer microenvironment](#)
- [Medical research](#)
- [Monocytes and macrophages](#)
- [Pathogenesis](#)

Abstract

Macrophages have a key role in shaping the tumour microenvironment (TME), tumour immunity and response to immunotherapy, which makes them an important target for cancer treatment^{1,2}. However, modulating macrophages has proved extremely difficult, as we still lack a complete understanding of the molecular and functional diversity of the tumour macrophage compartment. Macrophages arise from two distinct lineages. Tissue-resident macrophages self-renew locally, independent of adult haematopoiesis^{3,4,5}, whereas short-lived monocyte-derived macrophages arise from adult haematopoietic stem cells, and accumulate mostly in inflamed lesions¹. How these macrophage lineages contribute to the TME and cancer progression remains unclear. To explore the diversity of the macrophage compartment in human non-small cell lung carcinoma

(NSCLC) lesions, here we performed single-cell RNA sequencing of tumour-associated leukocytes. We identified distinct populations of macrophages that were enriched in human and mouse lung tumours. Using lineage tracing, we discovered that these macrophage populations differ in origin and have a distinct temporal and spatial distribution in the TME. Tissue-resident macrophages accumulate close to tumour cells early during tumour formation to promote epithelial–mesenchymal transition and invasiveness in tumour cells, and they also induce a potent regulatory T cell response that protects tumour cells from adaptive immunity. Depletion of tissue-resident macrophages reduced the numbers and altered the phenotype of regulatory T cells, promoted the accumulation of CD8⁺ T cells and reduced tumour invasiveness and growth. During tumour growth, tissue-resident macrophages became redistributed at the periphery of the TME, which becomes dominated by monocyte-derived macrophages in both mouse and human NSCLC. This study identifies the contribution of tissue-resident macrophages to early lung cancer and establishes them as a target for the prevention and treatment of early lung cancer lesions.

Access options

Subscribe to Journal

Get full journal access for 1 year

\$199.00

only \$3.90 per issue

[Subscribe](#)

All prices are NET prices.

VAT will be added later in the checkout.

Tax calculation will be finalised during checkout.

Rent or Buy article

Get time limited or full article access on ReadCube.

from \$8.99

[Rent or Buy](#)

All prices are NET prices.

Additional access options:

- [Log in](#)
- [Access through your institution](#)
- [Learn about institutional subscriptions](#)

Fig. 1: scRNA-seq of lineage-traced blood-derived macrophages reveals two ontogenically distinct populations of macrophages in NSCLC lesions.

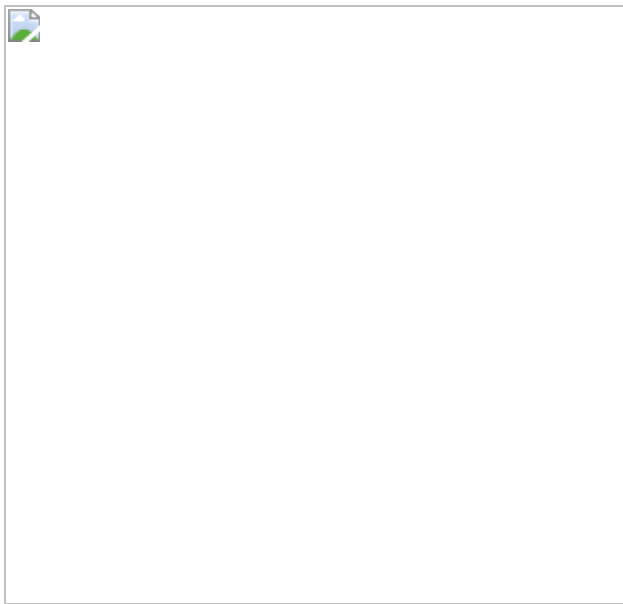


Fig. 2: TRMs localize in close proximity to tumour cells after seeding and enhance their antigen presentation and tissue remodelling programs in response to tumour cues.

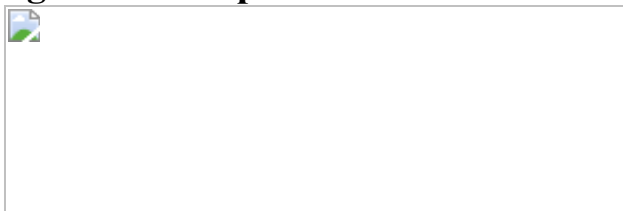


Fig. 3: TRMs induce NSCLC cells to undergo EMT and promote tumour cell invasiveness.

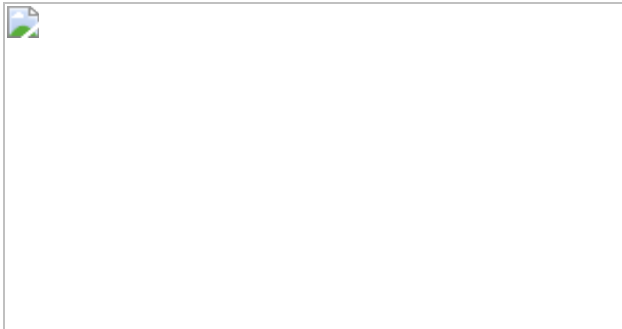
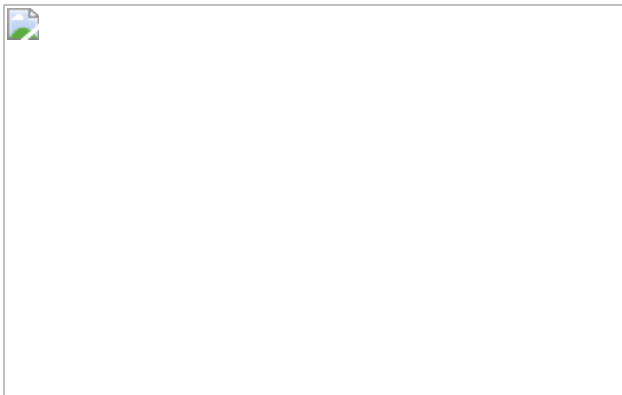


Fig. 4: Depletion of TRMs before tumour engraftment leads to reduced tumour burden and enhances T cell infiltration.



Data availability

All mice sequencing data are publicly available (GEO accession code [GSE147671](#)). The human dataset is available at the Sequence Read Archive (SRA) with BioProject accession [PRJNA609924](#). [Source data](#) are provided with this paper.

Code availability

The clustering analysis used here is described fully in its source manuscript⁶.

References

1. 1.

Lavin, Y., Mortha, A., Rahman, A. & Merad, M. Regulation of macrophage development and function in peripheral tissues. *Nat. Rev. Immunol.* **15**, 731–744 (2015).

[CAS](#) [PubMed](#) [PubMed Central](#) [Article](#) [Google Scholar](#)

2. 2.

Mantovani, A., Marchesi, F., Malesci, A., Laghi, L. & Allavena, P. Tumour-associated macrophages as treatment targets in oncology. *Nat. Rev. Clin. Oncol.* **14**, 399–416 (2017).

[CAS](#) [PubMed](#) [PubMed Central](#) [Article](#) [Google Scholar](#)

3. 3.

Ginhoux, F. et al. Fate mapping analysis reveals that adult microglia derive from primitive macrophages. *Science* **330**, 841–845 (2010).

[ADS](#) [CAS](#) [PubMed](#) [PubMed Central](#) [Article](#) [Google Scholar](#)

4. 4.

Hashimoto, D. et al. Tissue-resident macrophages self-maintain locally throughout adult life with minimal contribution from circulating monocytes. *Immunity* **38**, 792–804 (2013).

[CAS](#) [PubMed](#) [Article](#) [Google Scholar](#)

5. 5.

Schulz, C. et al. A lineage of myeloid cells independent of Myb and hematopoietic stem cells. *Science* **336**, 86–90 (2012).

[ADS](#) [CAS](#) [PubMed](#) [Article](#) [Google Scholar](#)

6. 6.

Leader, A. M. et al. CITEseq analysis of non-small-cell lung cancer lesions reveals an axis of immune cell activation associated with tumor antigen load and TP53 mutations. Preprint at <https://doi.org/10.1101/2020.07.16.207605> (2020).

7. 7.

Martin, J. C. et al. Single-cell analysis of Crohn's disease lesions identifies a pathogenic cellular module associated with resistance to anti-TNF therapy. *Cell* **178**, 1493–1508 (2019).

[CAS](#) [PubMed](#) [PubMed Central](#) [Article](#) [Google Scholar](#)

8. 8.

Schneider, C. et al. Induction of the nuclear receptor PPAR- γ by the cytokine GM-CSF is critical for the differentiation of fetal monocytes into alveolar macrophages. *Nat. Immunol.* **15**, 1026–1037 (2014).

[CAS](#) [PubMed](#) [Article](#) [Google Scholar](#)

9. 9.

Xue, W. et al. Response and resistance to NF- κ B inhibitors in mouse models of lung adenocarcinoma. *Cancer Discov.* **1**, 236–247 (2011).

[CAS](#) [PubMed](#) [PubMed Central](#) [Article](#) [Google Scholar](#)

10. 10.

Zilionis, R. et al. Single-cell transcriptomics of human and mouse lung cancers reveals conserved myeloid populations across individuals and species. *Immunity* **50**, 1317–1334 (2019).

[CAS](#) [PubMed](#) [PubMed Central](#) [Article](#) [Google Scholar](#)

11. 11.

Leach, S. M. et al. Human and mouse transcriptome profiling identifies cross-species homology in pulmonary and lymph node mononuclear phagocytes. *Cell Rep.* **33**, 108337 (2020).

[CAS](#) [PubMed](#) [PubMed Central](#) [Article](#) [Google Scholar](#)

12. 12.

Sawai, C. M. et al. Hematopoietic stem cells are the major source of multilineage hematopoiesis in adult animals. *Immunity* **45**, 597–609 (2016).

[CAS](#) [PubMed](#) [PubMed Central](#) [Article](#) [Google Scholar](#)

13. 13.

Yona, S. et al. Fate mapping reveals origins and dynamics of monocytes and tissue macrophages under homeostasis. *Immunity* **38**, 79–91 (2013).

[CAS](#) [PubMed](#) [Article](#) [Google Scholar](#)

14. 14.

Russell, D. G., Cardona, P. J., Kim, M. J., Allain, S. & Altare, F. Foamy macrophages and the progression of the human tuberculosis granuloma. *Nat. Immunol.* **10**, 943–948 (2009).

[CAS](#) [PubMed](#) [PubMed Central](#) [Article](#) [Google Scholar](#)

15. 15.

DuPage, M., Dooley, A. L. & Jacks, T. Conditional mouse lung cancer models using adenoviral or lentiviral delivery of Cre recombinase. *Nat. Protocols* **4**, 1064–1072 (2009).

[CAS](#) [PubMed](#) [Article](#) [Google Scholar](#)

16. 16.

Sutherland, K. D. et al. Multiple cells-of-origin of mutant K-Ras-induced mouse lung adenocarcinoma. *Proc. Natl Acad. Sci. USA* **111**, 4952–4957 (2014).

[ADS](#) [CAS](#) [PubMed](#) [PubMed Central](#) [Article](#) [Google Scholar](#)

17. 17.

Nieto, M. A., Huang, R. Y., Jackson, R. A. & Thiery, J. P. Emt: 2016. *Cell* **166**, 21–45 (2016).

[CAS](#) [PubMed](#) [Article](#) [Google Scholar](#)

18. 18.

Lim, J. & Thiery, J. P. Epithelial–mesenchymal transitions: insights from development. *Development* **139**, 3471–3486 (2012).

[CAS](#) [PubMed](#) [Article](#) [Google Scholar](#)

19. 19.

Ye, X. et al. Distinct EMT programs control normal mammary stem cells and tumour-initiating cells. *Nature* **525**, 256–260 (2015).

[ADS](#) [CAS](#) [PubMed](#) [PubMed Central](#) [Article](#) [Google Scholar](#)

20. 20.

Rhim, A. D. et al. EMT and dissemination precede pancreatic tumor formation. *Cell* **148**, 349–361 (2012).

[CAS](#) [PubMed](#) [PubMed Central](#) [Article](#) [Google Scholar](#)

21. 21.

Krebs, A. M. et al. The EMT-activator Zeb1 is a key factor for cell plasticity and promotes metastasis in pancreatic cancer. *Nat. Cell Biol.* **19**, 518–529 (2017).

[CAS](#) [PubMed](#) [Article](#) [Google Scholar](#)

22. 22.

Thiery, J. P. Epithelial-mesenchymal transitions in tumour progression. *Nat. Rev. Cancer* **2**, 442–454 (2002).

[CAS](#) [PubMed](#) [Article](#) [Google Scholar](#)

23. 23.

Yang, J. et al. Twist, a master regulator of morphogenesis, plays an essential role in tumor metastasis. *Cell* **117**, 927–939 (2004).

[CAS](#) [PubMed](#) [Article](#) [Google Scholar](#)

24. 24.

Dongre, A. & Weinberg, R. A. New insights into the mechanisms of epithelial–mesenchymal transition and implications for cancer. *Nat. Rev. Mol. Cell Biol.* **20**, 69–84 (2019).

[CAS](#) [PubMed](#) [Article](#) [Google Scholar](#)

25. 25.

Lavin, Y. et al. innate immune landscape in early lung adenocarcinoma by paired single-cell analyses. *Cell* **169**, 750–765 (2017).

[CAS](#) [PubMed](#) [PubMed Central](#) [Article](#) [Google Scholar](#)

26. 26.

Tada, Y. et al. Targeting VEGFR2 with Ramucirumab strongly impacts effector/ activated regulatory T cells and CD8⁺ T cells in the tumor microenvironment. *J. Immunother. Cancer* **6**, 106 (2018).

[PubMed](#) [PubMed Central](#) [Article](#) [Google Scholar](#)

27. 27.

Battaglia, A. et al. Metastatic tumour cells favour the generation of a tolerogenic milieu in tumour draining lymph node in patients with early cervical cancer. *Cancer Immunol. Immunother.* **58**, 1363–1373 (2009).

[PubMed](#) [Article](#) [Google Scholar](#)

28. 28.

He, F. et al. PLAU inferred from a correlation network is critical for suppressor function of regulatory T cells. *Mol. Syst. Biol.* **8**, 624 (2012).

[PubMed](#) [PubMed Central](#) [Article](#) [CAS](#) [Google Scholar](#)

29. 29.

Mucida, D. et al. Reciprocal T_H17 and regulatory T cell differentiation mediated by retinoic acid. *Science* **317**, 256–260 (2007).

[ADS](#) [CAS](#) [PubMed](#) [Article](#) [Google Scholar](#)

30. 30.

Soroosh, P. et al. Lung-resident tissue macrophages generate $Foxp3^+$ regulatory T cells and promote airway tolerance. *J. Exp. Med.* **210**, 775–788 (2013).

[CAS](#) [PubMed](#) [PubMed Central](#) [Article](#) [Google Scholar](#)

31. 31.

Mizukami, Y. et al. CCL17 and CCL22 chemokines within tumor microenvironment are related to accumulation of $Foxp3^+$ regulatory T cells in gastric cancer. *Int. J. Cancer* **122**, 2286–2293 (2008).

[CAS](#) [PubMed](#) [Article](#) [Google Scholar](#)

32. 32.

Liu, Z. et al. Fate mapping via Ms4a3-expression history traces monocyte-derived cells. *Cell* **178**, 1509–1525 (2019).

[CAS](#) [PubMed](#) [Article](#) [Google Scholar](#)

33. 33.

Miyake, Y. et al. Critical role of macrophages in the marginal zone in the suppression of immune responses to apoptotic cell-associated antigens. *J. Clin. Invest.* **117**, 2268–2278 (2007).

[CAS](#) [PubMed](#) [PubMed Central](#) [Article](#) [Google Scholar](#)

34. 34.

Karasawa, K. et al. Vascular-resident CD169-positive monocytes and macrophages control neutrophil accumulation in the kidney with ischemia-reperfusion injury. *J. Am. Soc. Nephrol.* **26**, 896–906 (2015).

[CAS](#) [PubMed](#) [Article](#) [Google Scholar](#)

35. 35.

Langmead, B., Trapnell, C., Pop, M. & Salzberg, S. L. Ultrafast and memory-efficient alignment of short DNA sequences to the human genome. *Genome Biol.* **10**, R25 (2009).

[PubMed](#) [PubMed Central](#) [Article](#) [CAS](#) [Google Scholar](#)

36. 36.

Li, H. et al. The sequence alignment/map format and SAMtools. *Bioinformatics* **25**, 2078–2079 (2009).

[PubMed](#) [PubMed Central](#) [Article](#) [CAS](#) [Google Scholar](#)

37. 37.

Zhang, Y. et al. Model-based analysis of ChIP-seq (MACS). *Genome Biol.* **9**, R137 (2008).

[PubMed](#) [PubMed Central](#) [Article](#) [CAS](#) [Google Scholar](#)

38. 38.

Love, M. I., Huber, W. & Anders, S. Moderated estimation of fold change and dispersion for RNA-seq data with DESeq2. *Genome Biol.* **15**, 550 (2014).

[PubMed](#) [PubMed Central](#) [Article](#) [CAS](#) [Google Scholar](#)

39. 39.

Ramírez, F., Dündar, F., Diehl, S., Grüning, B. A. & Manke, T. deepTools: a flexible platform for exploring deep-sequencing data. *Nucleic Acids Res.* **42**, W187–W191 (2014).

[PubMed](#) [PubMed Central](#) [Article](#) [CAS](#) [Google Scholar](#)

40. 40.

Sastre-Perona, A. et al. De novo PITX1 expression controls bi-stable transcriptional circuits to govern self-renewal and differentiation in squamous cell carcinoma. *Cell Stem Cell* **24**, 390–404 (2019).

[CAS](#) [PubMed](#) [PubMed Central](#) [Article](#) [Google Scholar](#)

41. 41.

McLean, C. Y. et al. GREAT improves functional interpretation of cis-regulatory regions. *Nat. Biotechnol.* **28**, 495–501 (2010).

[CAS](#) [PubMed](#) [PubMed Central](#) [Article](#) [Google Scholar](#)

42. 42.

Robinson, J. T. et al. Integrative genomics viewer. *Nat. Biotechnol.* **29**, 24–26 (2011).

[CAS](#) [PubMed](#) [PubMed Central](#) [Article](#) [Google Scholar](#)

43. 43.

Buenrostro, J. D., Giresi, P. G., Zaba, L. C., Chang, H. Y. & Greenleaf, W. J. Transposition of native chromatin for fast and sensitive epigenomic profiling of open chromatin, DNA-binding proteins and nucleosome position. *Nat. Methods* **10**, 1213–1218 (2013).

[CAS](#) [PubMed](#) [PubMed Central](#) [Article](#) [Google Scholar](#)

44. 44.

Schindelin, J. et al. Fiji: an open-source platform for biological-image analysis. *Nat. Methods* **9**, 676–682 (2012).

[CAS](#) [PubMed](#) [PubMed Central](#) [Article](#) [Google Scholar](#)

45. 45.

Schmidt, U., Weigert, M., Broaddus, C. & Myers, G. Cell detection with star-convex polygons. In *International Conference on Medical Image Computing and Computer-Assisted Intervention –MICCAI 2018* (eds Frangi, A. et al.) 265–273 (Springer, 2018).

46. 46.

Remark, R. et al. In-depth tissue profiling using multiplexed immunohistochemical consecutive staining on single slide. *Sci. Immunol.* **1**, aaf6925 (2016).

[PubMed](#) [Article](#) [Google Scholar](#)

47. 47.

Bankhead, P. et al. QuPath: open source software for digital pathology image analysis. *Sci. Rep.* 7, 16878 (2017).

[ADS](#) [PubMed](#) [PubMed Central](#) [Article](#) [CAS](#) [Google Scholar](#)

[Download references](#)

Acknowledgements

This work was supported by an HFSP postdoctoral fellowship (LT000110/2015-L/1) and an AACR–AstraZeneca Immuno-oncology Research Fellowship (20-40-12-CASA) to M.C.-A.; T32 CA078207 to A.L.; F30 CA243210 to S.T.C.; and ANR-10-IDEX-0001-02 PSL and ANR-11-LABX-0043 and Fondation ARC pour la recherche sur le cancer to P.B. This research was supported in part by the Tisch Cancer Institute at Mount Sinai P30 CA196521-Cancer Center Support Grant. We thank the Human Immune Monitoring Center for all the single-cell profiling and epigenetic studies; the Merad laboratory and A. Lujambio for discussions and reagents; the Flow Cytometry and the Imaging Core at Mount Sinai; and the Cancer Biorepository at MSSM for sample acquisition. This work was also supported by National Institutes of Health (NIH)–National Cancer Institute grants CA257195, CA254104, AT011326, AI128949 and R56AI137244 to M.M., who is also a Samuel Waxman Cancer Research Foundation Investigator; CA109182, CA216248 and CA218024 to J.A.A.-G., who is also a Samuel Waxman Cancer Research Foundation Investigator; CA257195, CA254104, AT011326 and AI128949 to B.D.B.; NCI grant T32 CA078207 to E.D.; and NIH grant AG049074 to B.R.

Author information

Author notes

1. María Casanova-Acebes

Present address: Cancer Immunity Laboratory, Molecular Oncology Program, Spanish National Cancer Centre, Madrid, Spain

2. Barbara Maier

Present address: CeMM, Research Center for Molecular Medicine of the Austrian Academy of Sciences, Vienna, Austria

3. These authors contributed equally: Erica Dalla, Andrew Leader, Jessica LeBerichel

4. These authors jointly supervised this work: Julio A. Aguirre-Ghiso, Miriam Merad

Affiliations

1. Department of Oncological Sciences, Icahn School of Medicine at Mount Sinai, New York, NY, USA

María Casanova-Acebes, Andrew M. Leader, Jessica LeBerichel, Christie Chang, Leanna Troncoso, Steven T. Chen, Matthew D. Park, Alexandra Tabachnikova, Pauline Hamon, Barbara Maier, Thomas Marron, Julio A. Aguirre-Ghiso & Miriam Merad

2. Precision Immunology Institute, Icahn School of Medicine at Mount Sinai, New York, NY, USA

María Casanova-Acebes, Andrew M. Leader, Jessica LeBerichel, Christie Chang, Leanna Troncoso, Steven T. Chen, Matthew D. Park, Alexandra Tabachnikova, Maxime Dhainaut, Pauline Hamon, Barbara Maier, Brian D. Brown, Thomas Marron, Ephraim Kenigsberg, Julio A. Aguirre-Ghiso & Miriam Merad

3. Tisch Cancer Institute, Icahn School of Medicine at Mount Sinai, New York, NY, USA

María Casanova-Acebes, Andrew M. Leader, Jessica LeBerichel, Christie Chang, Leanna Troncoso, Steven T. Chen, Matthew D. Park, Alexandra Tabachnikova, Maxime

Dhainaut, Pauline Hamon, Barbara Maier, Brian D. Brown, Thomas Marron, Julio A. Aguirre-Ghiso & Miriam Merad

4. Division of Hematology and Oncology, Icahn School of Medicine at Mount Sinai, New York, NY, USA

Erica Dalla, Thomas Marron & Julio A. Aguirre-Ghiso

5. Department of Medicine, Icahn School of Medicine at Mount Sinai, New York, NY, USA

Erica Dalla & Julio A. Aguirre-Ghiso

6. Black Family Stem Cell Institute, Icahn School of Medicine at Mount Sinai, New York, NY, USA

Erica Dalla & Julio A. Aguirre-Ghiso

7. Department of Otolaryngology, Icahn School of Medicine at Mount Sinai, New York, NY, USA

Erica Dalla & Julio A. Aguirre-Ghiso

8. Institut Curie, PSL Research University, INSERM U932, Paris, France

Jovan Nikolic & Philippe Benaroch

9. Department of Cancer Immunology, Genentech, South San Francisco, CA, USA

Blanca M. Morales, Markus Brown & Christine Moussion

10. The Ronald O. Perleman Department of Dermatology, New York University Grossman School of Medicine, New York, NY, USA

Ana Sastre-Perona & Markus Schober

11. Experimental Therapies and Novel Biomarkers in Cancer, Hospital La Paz Institute for Health Research (IdiPAZ), Madrid, Spain

Ana Sastre-Perona

12. Department of Genetics and Genomic Sciences, Icahn School of Medicine at Mount Sinai, New York, NY, USA

Maxime Dhainaut & Brian D. Brown

13. INSERM U1218 ACTION, University of Bordeaux, Bordeaux, France

Catherine M. Sawai

14. Microscopy CoRE, Dean's CoREs, Icahn School of Medicine at Mount Sinai, New York, NY, USA

Esperanza Agulló-Pascual

15. Department of Pathology, New York University Grossman School of Medicine, New York, NY, USA

Boris Reizis

16. Institute of Thoracic Oncology, Icahn School of Medicine at Mount Sinai, New York, NY, USA

Thomas Marron

17. Icahn Genomics Institute, Icahn School of Medicine at Mount Sinai, New York, NY, USA

Brian D. Brown & Ephraim Kenigsberg

18. Human Immune Monitoring Center, Icahn School of Medicine at Mount Sinai, New York, NY, USA

Miriam Merad

Authors

1. María Casanova-Acebes

[View author publications](#)

You can also search for this author in [PubMed](#) [Google Scholar](#)

2. Erica Dalla

[View author publications](#)

You can also search for this author in [PubMed](#) [Google Scholar](#)

3. Andrew M. Leader

[View author publications](#)

You can also search for this author in [PubMed](#) [Google Scholar](#)

4. Jessica LeBerichel

[View author publications](#)

You can also search for this author in [PubMed](#) [Google Scholar](#)

5. Jovan Nikolic

[View author publications](#)

You can also search for this author in [PubMed](#) [Google Scholar](#)

6. Blanca M. Morales

[View author publications](#)

You can also search for this author in [PubMed](#) [Google Scholar](#)

7. Markus Brown

[View author publications](#)

You can also search for this author in [PubMed](#) [Google Scholar](#)

8. Christie Chang

[View author publications](#)

You can also search for this author in [PubMed](#) [Google Scholar](#)

9. Leanna Troncoso

[View author publications](#)

You can also search for this author in [PubMed](#) [Google Scholar](#)

10. Steven T. Chen

[View author publications](#)

You can also search for this author in [PubMed](#) [Google Scholar](#)

11. Ana Sastre-Perona

[View author publications](#)

You can also search for this author in [PubMed](#) [Google Scholar](#)

12. Matthew D. Park

[View author publications](#)

You can also search for this author in [PubMed](#) [Google Scholar](#)

13. Alexandra Tabachnikova

[View author publications](#)

You can also search for this author in [PubMed](#) [Google Scholar](#)

14. Maxime Dhainaut

[View author publications](#)

You can also search for this author in [PubMed](#) [Google Scholar](#)

15. Pauline Hamon

[View author publications](#)

You can also search for this author in [PubMed](#) [Google Scholar](#)

16. Barbara Maier

[View author publications](#)

You can also search for this author in [PubMed](#) [Google Scholar](#)

17. Catherine M. Sawai

[View author publications](#)

You can also search for this author in [PubMed](#) [Google Scholar](#)

18. Esperanza Agulló-Pascual

[View author publications](#)

You can also search for this author in [PubMed](#) [Google Scholar](#)

19. Markus Schober

[View author publications](#)

You can also search for this author in [PubMed](#) [Google Scholar](#)

20. Brian D. Brown

[View author publications](#)

You can also search for this author in [PubMed](#) [Google Scholar](#)

21. Boris Reizis

[View author publications](#)

You can also search for this author in [PubMed](#) [Google Scholar](#)

22. Thomas Marron

[View author publications](#)

You can also search for this author in [PubMed](#) [Google Scholar](#)

23. Ephraim Kenigsberg

[View author publications](#)

You can also search for this author in [PubMed](#) [Google Scholar](#)

24. Christine Mousson

[View author publications](#)

You can also search for this author in [PubMed](#) [Google Scholar](#)

25. Philippe Benaroch

[View author publications](#)

You can also search for this author in [PubMed](#) [Google Scholar](#)

26. Julio A. Aguirre-Ghiso

[View author publications](#)

You can also search for this author in [PubMed](#) [Google Scholar](#)

27. Miriam Merad

[View author publications](#)

You can also search for this author in [PubMed](#) [Google Scholar](#)

Contributions

M.M. and M.C.-A. conceived the project. M.M., M.C.-A., P.B. and J.A.A.-G. designed the experiments. M.C.-A., E.D., J.A.A.-G. and M.M. wrote the manuscript. A.L., C.C., A.S.-P., E.A.-P., M.D.P. and E.K. performed computational analysis. M.C.-A., E.D., J.N., B.M.M., S.T.C., M.D.P., M.D., A.T., L.T., P.H., B.M. and J.L. performed experiments. B.B. and M.S. provided reagents. M.B. and C.M. performed image analysis of KP tumours. T.M. provided intellectual input and facilitated access to human samples. C.M.S. and B.R. provided *Pdzkip1-creER R26Tom/Tom* mice. All authors contributed to manuscript editing.

Corresponding authors

Correspondence to [María Casanova-Acebes](#) or [Miriam Merad](#).

Ethics declarations

Competing interests

J.A.A.-G. is a scientific co-founder of, scientific advisory board member and equity owner in HiberCell and receives financial compensation as a

consultant for HiberCell, a Mount Sinai spin-off company focused on therapeutics that prevent or delay cancer recurrence. M.M. serves on the scientific advisory boards of Compugen Inc., Innate Pharma Inc., Morphic Therapeutic, Myeloid Therapeutics, Celsius Therapeutics and Genenta. M.M. receives funding from Genentech Inc., Regeneron Inc., Boehringer Ingelheim Inc. and Takeda Inc. M.M. has ownership interest of less than 5% in Compugen Inc., Celsius Therapeutics Inc., Dren Bio Inc., and Asher Bio Inc. B.M.M., M.B. and C.M. declare that they are Genentech/Roche employees.

Additional information

Peer review information *Nature* thanks the anonymous reviewers for their contribution to the peer review of this work.

Publisher's note Springer Nature remains neutral with regard to jurisdictional claims in published maps and institutional affiliations.

Extended data figures and tables

[Extended Data Fig. 1 Macrophage distribution and profile in NSCLC lesions.](#)

a, Gating strategy for sorting of myeloid cells from naive and KP tumour-bearing lungs of *Map17creER^{+/+}* *R26tdTom* mice for scRNA-seq analysis. Monocytes and macrophages in the lung were gated as singlets, DAPI⁻CD45⁺Lin⁻CD11b^{-/+}Ly6G⁻CD11c^{lo-int/+}SIGLECF⁺ and Tom⁻ or Tom⁺. **b**, Confocal imaging of tdTomato⁺ bone-marrow-derived leukocytes and TRMs (CD206⁺, yellow). Images are representative of a single experiment and three tumours imaged. **c**, Gating strategy for sorting of myeloid cells from naive and KP tumour-bearing lungs of *Cx3cr1creER^{+/+}* *R26YFP* mice. Monocytes and macrophages were gated as in **a** and further separated based on YFP expression. **d**, Confocal imaging of YFP⁺ bone-marrow-derived leukocytes (red) and TRMs (CD206⁺, yellow). Scale bar, 50 μm. Images are representative of a single experiment and

three tumours imaged. **e**, Spearman correlation of variable gene expression between the human monocyte and macrophage clusters detected in ref. [6](#) and those in ref. [10](#). **f**, The log₂-transformed fold change (FC) between human TRM expression and the maximum cluster expression of non-TRM monocytes and macrophages, determined from data in ref. [6](#) (x axis) or ref. [10](#) (y axis). The human alveolar macrophage genes published previously^{[11](#)} are highlighted in red. **g**, Spearman correlation of variable gene expression between the mouse monocyte and macrophage clusters detected in the present study and in ref. [10](#). **h**, Average expression of selected mouse genes from scRNA-seq data in cluster groups I to IV (see Supplementary Table [2](#)). **i**, Average expression of selected human genes from scRNA-seq data (see Supplementary Table [1](#)). **j**, Confocal imaging of *CD169*^{cre/+} *R26tdTom* KP lesions (day 30, KP-GFP, green) with CD206 (yellow). Scale bar, 100 μm. Images are representative of a single experiment and three tumours imaged. **k**, Gating strategy for the identification of TRMs and MDMs in naive lungs. TRMs were gated as live/dead[−]CD45⁺Ly6G[−]CD64⁺MERTK⁺CD2⁺CD169⁺CD206⁺SIGLECF⁺; MDMs were gated as singlets, live/dead[−]CD45⁺Ly6G[−]CD64⁺Mertk⁺CD2[−]CD11b^{hi}CD169[−]CD206[−]SIGLE CF[−].

Source data

Extended Data Fig. 2 Fate-mapping of macrophages in KP tumours.

a, Lineage tracing experiment in *Map17*^{creER/+} *R26tdTom* mice. **b**, Fraction of labelled (red, tdTom⁺) cells in the peripheral blood and lung of non-tumour-bearing *Map17*^{creER/+} *R26tdTom* mice 6 months after tamoxifen injection ($n = 6$ blood, $n = 5$ lung; two independent experiments). Blood Ly6C^{hi} monocytes were identified as singlets, DAPI[−]CD45⁺CD11b⁺CD115⁺Ly6C^{hi} or Ly6C^{lo} monocytes as CD45⁺CD11b⁺CD115⁺Ly6C^{lo}. Lung monocytes were gated as CD45⁺CD11b⁺CX3CR1⁺Ly6C^{hi} or Ly6C^{lo}. Neutrophils in blood and lungs were identified as singlets, DAPI[−]CD45⁺CD11b⁺Ly6G⁺. TRMs were

identified as singlets, DAPI⁻CD45⁺Ly6G⁻CD11b^{lo/}
⁻SIGLECF^{hi}CD11c^{hi}CD206^{hi}CD169^{hi}. Data are mean ± s.e.m. **c**,
 Frequencies of labelled (red, tdTom⁺) or not labelled (grey, tdTom⁻) cells
 within each cluster groups as defined in **b** in tumour-bearing mice. **d**,
 Lineage tracing experiment in *Cx3cr1creER/+ R26YFP* mice. **e**, Fraction of
 labelled (green, YFP⁺) cells in the peripheral blood and lung of non-
 tumour-bearing mice ($n=8$, pool of two independent experiments). Data are
 mean ± s.e.m. **f**, Frequency of labelled (green, YFP⁺) and non-labelled
 (grey, YFP⁻) cells within each cluster groups as defined in **b** in KP tumour-
 bearing mice.

Source data

Extended Data Fig. 3 Longitudinal analysis of TRMs in NSCLC.

a, TRMs (red, CD206⁺) distribution in KP-GEMMs (green) 14 weeks (wks) after injection of adenovirus-SPC5^{Cre} in KP mice. White dotted lines delimit the tumour area. Unpaired two-tailed Student's *t*-test; **P* = 0.020. CD206⁺ macrophage distribution was analysed in $n=4$ tumour-bearing mice from one experiment. Data are mean ± s.e.m. **b**, Gene Ontology categories for ATAC-seq significant (*P* < 0.05) open (day 15) and closed (day 30) chromatin regions identified in KP-associated TRMs. **c**, Longitudinal analysis of CD45⁺ leukocytes, TRMs and Ly6C^{hi} and Ly6C^{lo} monocytes in naive ($n=5$) and in day-15 ($n=5$) and day-30 ($n=4$) KP-bearing mice. One-way ANOVA with Tukey's test. Data are mean ± s.e.m. TRMs were gated as singlets, live/dead⁻GFP⁻CD45⁺Ly6G⁻CD64⁺MERTK⁺CD2⁺CD169⁺CD206⁺Siglecf⁺; MDMs were gated as singlets, live/dead⁻GFP⁻CD45⁺Ly6G⁻CD64⁺MERTK⁺CD2⁻CD11b^{hi}CD169⁻SIGLECF⁻. Lung monocytes were gated as CD45⁺CD11b⁺CX3CR1⁺Ly6C^{hi} or Ly6C^{lo}. **d**, Longitudinal imaging analysis of TRMs identified by the co-expression of CD206 (red) and SIGLECF (yellow) in the KP-GFP orthotopic model. KP tumour cells, green. White asterisks indicate CD206⁺SIGLECF⁻ macrophages. Yellow asterisks depict

SIGLECF⁺CD206⁻ leukocytes, which are also found in overt tumours and are most probably SIGLECF⁺ eosinophils. Scale bars, 50 µm (D5, D10 and D15); 100 µm (D25–30). Images are representative of one experiment; $n = 3\text{--}5$ mice; 2–3 tumours analysed per time point. **e**, Longitudinal imaging analysis of TRMs in the KP-GEMM model. Tumour cells are identified by positive staining with pan-cytokeratin in green. Images are representative of one experiment; 2–3 tumours analysed per mouse; 3 mice per time point. Scale bars, 50 µm. **f**, Immunohistochemistry converted to pseudofluorescence image of CD206 (red), CD10 (yellow) and cytokeratin (CK, green) staining in non-involved lung and NSCLC tissue. White asterisks indicate CD206⁺CD10⁺ TRMs. Scale bars, 250 µm (bottom images); 250 µm (top images). Images are representative of one experiment. **g**, Immunohistochemistry converted to pseudofluorescence image of CD206 (red), FABP4 (yellow) and cytokeratin (CK, green) staining in non-involved lung and NSCLC tissue. White asterisks indicate CD206⁺FABP4⁺ TRMs. Scale bars, 500 µm (left); 400 µm (right). Dotted lines delineate tumour border. Representative images from two non-involved lung and two NSCLC tumours. Images are representative of one experiment.

[Source data](#)

[**Extended Data Fig. 4 Bulk RNA-seq and ATAC-seq of KP TRMs.**](#)

a, Heat map of DEGs of TRMs in naive lungs, day-15 and day-30 KP tumours. Red indicates the most significant upregulated and blue the most significant downregulated gene transcripts ($P < 0.05$, log₂-transformed fold change ($\log_2\text{FC}$) > 1 and $\log_2\text{FC} < 1$, respectively). TRMs were sorted as singlets, DAPI⁻CD45⁺Ly6G⁻CD11b^{lo/}
⁻CD64⁺MERTK⁺CD2⁺CD169⁺SIGLECF^{hi}CD206⁺. **b**, Gene Ontology analysis of upregulated DEGs between naive and early KP-TRMs (day 15) ($P < 0.05$ and $\log_2\text{FC} > 1$). **c**, Number of peaks and heat map representing average ATAC-seq peaks (pks) unchanged (cluster 1), differentially closed (cluster 2) or opened (cluster 3) in TRMs at different times after KP injection. **d**, **e**, Representative tracks of significant TRM DEGs ($P < 0.05$) showing increased chromatin accessibility (dotted red lines) (**d**) or lower

chromatin accessibility (**e**) in TRMs. Tracks are representative of three pooled mice examined over one single experiment. Data are mean \pm s.e.m.

[Source data](#)

Extended Data Fig. 5 TRMs promote EMT and a pro-invasive signature in KP spheroids, whereas MDMs favour growth.

a, Venn diagrams for DEGs upregulated and downregulated in spheroids co-cultured with TRMs or bone marrow monocytes (BMMs). The number of DEGs uniquely controlled by TRMs or BMMs is shown in blue (TRMs) and red (BMMs). **b**, Gene Ontology (GO) analysis of significant DEGs ($P < 0.05$) with upregulated signature controlled by TRMs (blue) and by BMMs (red), respectively. **c**, Gating strategy for BALF (bronchoalveolar fluid) TRMs gated as $CD45^+CD11b^{lo}CD11c^+SIGLECF^+CD206^+CD169^+$ and purity quantification in $n = 4$ mice. BALF routinely showed around 85% pure TRMs among $CD45^+$ leukocytes. **d**, Confocal representative images and quantification of E-cadherin (red), TWIST1 (white) and β -catenin (red) in KP spheroids cultured alone or with TRMs or BMMs. Scale bars, 5 μ m (inset) and 25 μ m. One-way ANOVA with Tukey's test. Data are mean \pm s.e.m. Two independent experiments. **e**, Bar graphs showing the expression (in transcripts per million, TPM) of EMT-signature selected genes in KP-spheroids alone, with TRMs or BMMs. Data are mean \pm s.e.m. Results are representative of one experiment. **f**, Size quantification for KP oncospheres co-cultured with TRMs or BMMs. Data are mean \pm s.e.m. Data are representative of two independent experiments. **g**, Quantification of the number of KP oncospheres in co-cultures with TRMs (blue) or BMMs (red) compared to KP alone in the presence of GM-CSF (light blue) or M-CSF (light red), respectively. Data are mean \pm s.e.m. Data are representative of two independent experiments. **h**, Quantification of KP 3D-matrigel spheroids with invasive protrusions co-cultured with TRMs or BMMs and their respective controls. Data are mean \pm s.e.m. Data are representative of two independent experiments. One-way ANOVA with Tukey's test (**f–h**). **i**, Bright-field microscopy images of the spheroids quantified in **h**. Scale bars, 100 μ m. **j**, **k**, Number (**j**) and size (**k**) of KP oncospheres cultured alone or co-cultured with tumour-associated tTRMs or tMDMs. Results are representative of two independent experiments

analysed using one-way ANOVA. Data are mean \pm s.e.m. * $P < 0.05$, ** $P < 0.01$, *** $P < 0.0001$.

[Source data](#)

Extended Data Fig. 6 Immune suppression is governed by TRMs in early KP tumours.

a, Frequency, CTLA-4 and CD73 MFI levels of T_{reg} cells induced by tTRMs and tMDMs with naive CD62L $^+$ CD44 $^-$ CD4 $^+$ T cells (one-way ANOVA with Tukey's test and two-tailed unpaired t -test). Two independent experiments. **b**, Frequency and phenotype of T_{reg} cells in TRM-depleted mice at day 15 after KP injection. $n = 5$ mice per group. Two-tailed unpaired t -test; ** $P = 0.003$, * $P = 0.025$; *** $P = 0.0003$ and **** $P < 0.0001$, respectively. **c**, Expression of *Ccl17* and *Tgfb1* in TRMs from naive mice (grey) and tumour-bearing mice (day 15 light green, day 30 dark green). Data from DEGs ($P < 0.05$ likelihood ratio test) list in Fig. 2d (see Supplementary Table 3). One experiment, $n = 3$ naive, $n = 2$ KP-TRM day 15 and $n = 3$ KP-TRM day 30 mice. **d**, Imaging of TRM-sufficient and deficient mice after instillation of diphtheria toxin. SIGLECF, green; CD206, red. Quantification of Ly6C $^{hi/lo}$ monocytes, neutrophils, MDMs and TRMs in wild-type or *CD169-DTR* lungs one week after the last dose of diphtheria toxin. $n = 5$ mice per group. Two-tailed unpaired t -test. TRMs were gated as singlets, live/dead $^-$ CD45 $^+$ Ly6G $^-$ CD64 $^+$ MERTK $^+$ CD2 $^+$ CD169 $^+$ SIGLECF $^+$ CD206 $^+$; MDMs as singlets, live/dead $^-$ CD45 $^+$ Ly6G $^-$ CD64 $^+$ MERTK $^+$ CD2 $^-$ CD11b hi CD169 $^-$ SIGLECF $^-$; monocytes as CD45 $^+$ CD11b $^+$ CX3CR1 $^+$ Ly6C hi or Ly6C lo (Ly6C hi and Ly6C lo , respectively); and neutrophils as live/dead $^-$ CD45 $^+$ CD11b $^+$ Ly6G $^+$. **e**, Levels of CD169 in Tomato $^+$ monocytes (CD45 $^+$ CD11b $^+$ CX3CR1 $^+$) and MDMs (live/dead $^-$ CD45 $^+$ Ly6G $^-$ CD64 $^+$ MERTK $^+$ CD2 $^-$ CD11b hi SIGLECF $^-$) in naive and two-week KP lesions from *Ms4a3-tdTom* reporter mice. $n = 3$ mice per group. Two-way ANOVA with Tukey's multiple comparisons test; ns, not significant. **f**, Frequencies of MDMs in wild-type and *CD169-DTR* lungs after DT treatment with diphtheria toxin in naive mice and KP lesions (two weeks). $n = 5$ per genotype for naive mice and $n = 3$ per genotype for

the KP tumour group. Two-way ANOVA with Tukey's multiple comparisons test. **g**, Quantification of T_{reg} cells in spleen and lymph nodes of tumour-bearing mice (day 15) in WT + DT (black) and CD169-DTR + DT mice (red). $n = 6$ mice per group. Unpaired two-tailed *t*-test. **h**, Percentage of KP cells from lungs of wild-type or CD169-DTR mice treated with diphtheria toxin, 24 h after KP injection. $n = 6$ mice per group. Two-tailed unpaired *t*-test. **i**, Image analysis of Ki67⁺ and CC3⁺ KP cells in day-15 lesions, and p27⁺ KP cells in day-5 lesions of WT + DT and CD169-DTR + DT mice. Asterisks show positive KP cells. One-tailed unpaired *t*-test. $n = 3$ WT + DT and $n = 4$ CD169-DTR + DT for Ki67 and CC3; $n = 3$ WT + DT and $n = 4$ CD169-DTR + DT for p27. Two to three independent experiments. Scale bars, 25 μm (main images); 10 μm (inset). Data are mean \pm s.e.m. (**a–i**). **j**, Diphtheria toxin treatment and KP injections in wild-type or CD169-DTR mice. **k**, Tumour burden in wild-type or CD169-DTR mice that were TRM-depleted after tumour implantation. **l**, Quantification of T_{reg} cells, IFN γ ⁺TNF⁺CD8⁺ effector cells and ratio of CD8/T_{reg} cells in mice from **k**. Effector T cells were gated as singlets, DAPI[−]CD45⁺TCR⁺CD8⁺; T_{reg} cells as singlets, DAPI[−]CD45⁺TCR⁺CD4⁺FOXP3⁺. $n = 5$ WT + DT and $n = 7$ CD169-DTR + DT mice. Three independent experiments. Data are mean \pm s.e.m.; two-tailed unpaired *t*-test. (**k, l**). **m**, Imaging and quantification of infiltrating FOXP3⁺ T_{reg} cells (top) and CD3⁺ T cells (bottom) in WT + DT or CD169-DTR + DT mice at days 12 and 15 after KP injection. Two-tailed unpaired *t*-test. Data are mean \pm s.e.m. Two independent experiments. Scale bar, 100 μm .

Extended Data Fig. 7 TRMs modulate T cell effector function in an antigen-independent manner.

a, Scheme of OT-I and OT-II adoptive transfer experiments in B16-F10/OVA wild-type and CD169-DTR mice. **b**, Relative quantification of OT-I T cells in the lungs and tumour-draining lymph nodes (tdLN). OT-I T cells were gated as viable, CD45.1⁺TCR⁺CD8⁺. $n = 4$ —5 mice. Data are representative of two independent experiments. **c**, Quantification of OT-I cells in the tumours of mice in **b**. CD45.1⁺ OT-I T cells were quantified in

7–8 tumours from mice in **b**. $n= 7$ WT + DT and $N= 8$ *CD169-DTR* + DT from one experiment. Scale bar, 50 μ m. **d**, Quantification of OT-II cells in the tumours of mice in **b**. OT-II T cells were gated as viable, CD45.1 $^{+}$ TCR $^{+}$ CD4 $^{+}$. $n = 5$ –8 mice per group. Data are representative of one experiment. Data are mean \pm s.e.m; unpaired two-tailed *t*-test (**b**–**d**). **e**, Scheme of the contribution of the TRM compartment and MDMs to tumour progression. This scheme was created with BioRender.com.

Supplementary information

Reporting Summary

Supplementary Table 1

scRNAseq differential average expression of cells per group over transcript expression in all groups of monocytes and macrophages in human.

Supplementary Table 2

scRNAseq differential average expression of cells per group over transcript expression in all groups of monocytes and macrophages in mouse.

Supplementary Table 3

Differential expression gene list in bulk RNA-seq of TRMs (alveolar macrophages, AM) in naïve, KP D15 and KP D30 tumours. Significant genes (KP D15 over naïve) are included (p-value <0.05). All data is also included in this table with no further statistical test.

Supplementary Table 4

Differential expression ATAC-seq peaks detected in TRMs in naïve, KP D15 and KP D30 tumours. Significant genes (KP D15 over naïve and KP D30 over naïve) are included (p-value <0.05).

Supplementary Table 5

Differential expression gene list in bulk RNA-seq of KP-spheroids co-cultured with TRMs and BMMs. Significant genes uniquely found in either KP+TRM over KP alone, and KP+BMM over KP alone are included (p-value<0.05), as well as significant genes found in both conditions.

Supplementary Tables 6-8

These tables include the list of antibodies used for flow cytometry (Supplementary Table 6), antibodies used for Multiplexed immunohistochemical consecutive staining on a single slide (Supplementary Table 7) and antibodies used for Clearing imaging (Supplementary Table 8).

Supplementary Data

This zipped file includes the Supplementary Imaging Macros and a guide.

Video 1

KP-spheroids co-cultured with TRMs. KP-GFP expressing spheroids were co-cultured with alveolar macrophages and imaged for 4 hours. Invasive protrusions are visualized. Scale bar corresponds to 200 μ m.

Video 2

KP-Spheroids co-cultured with BMMs. KP-GFP expressing spheroids were co-cultured with bone-marrow monocytes and imaged for 4 hours. Note the size of KP-GFP spheroids co-cultured under these conditions. Scale bar corresponds to 200 μ m.

Source data

Source Data Fig. 1

Source Data Fig. 2

[**Source Data Fig. 3**](#)

[**Source Data Fig. 4**](#)

[**Source Data Extended Data Fig. 1**](#)

[**Source Data Extended Data Fig. 2**](#)

[**Source Data Extended Data Fig. 3**](#)

[**Source Data Extended Data Fig. 4**](#)

[**Source Data Extended Data Fig. 5**](#)

Rights and permissions

[Reprints and Permissions](#)

About this article



Check for
updates

Cite this article

Casanova-Acebes, M., Dalla, E., Leader, A.M. *et al.* Tissue-resident macrophages provide a pro-tumorigenic niche to early NSCLC cells. *Nature* **595**, 578–584 (2021). <https://doi.org/10.1038/s41586-021-03651-8>

[Download citation](#)

- Received: 01 March 2020
- Accepted: 18 May 2021

- Published: 16 June 2021
- Issue Date: 22 July 2021
- DOI: <https://doi.org/10.1038/s41586-021-03651-8>

Comments

By submitting a comment you agree to abide by our [Terms](#) and [Community Guidelines](#). If you find something abusive or that does not comply with our terms or guidelines please flag it as inappropriate.

[Access through your institution](#)

[Change institution](#)

[Buy or subscribe](#)

Advertisement

This article was downloaded by **calibre** from <https://www.nature.com/articles/s41586-021-03651-8>

| [Section menu](#) | [Main menu](#) |

- Article
- [Published: 23 June 2021](#)

Clonal fitness inferred from time-series modelling of single-cell cancer genomes

- [Sohrab Salehi](#)^{1,na1},
- [Farhia Kabeer](#)^{1,2,na1},
- [Nicholas Ceglia](#)³,
- [Mirela Andronescu](#)^{1,2},
- [Marc J. Williams](#) [ORCID: orcid.org/0000-0001-5524-4174](#)³,
- [Kieran R. Campbell](#) [ORCID: orcid.org/0000-0003-1981-5763](#)⁴,
- [Tehmina Masud](#)¹,
- [Beixi Wang](#)¹,
- [Justina Biele](#)¹,
- [Jazmine Brimhall](#)¹,
- [David Gee](#)¹,
- [Hakwoo Lee](#)¹,
- [Jerome Ting](#)¹,
- [Allen W. Zhang](#) [ORCID: orcid.org/0000-0002-7606-089X](#)¹,
- [Hoa Tran](#) [ORCID: orcid.org/0000-0002-9547-8650](#)¹,
- [Ciara O'Flanagan](#)¹,
- [Fatemeh Dorri](#)^{1,5},
- [Nicole Rusk](#) [ORCID: orcid.org/0000-0003-2663-6288](#)³,
- [Teresa Ruiz de Algara](#)¹,
- [So Ra Lee](#)¹,
- [Brian Yu Chieh Cheng](#) [ORCID: orcid.org/0000-0002-9258-8184](#)¹,
- [Peter Eirew](#)¹,
- [Takako Kono](#)¹,

- [Jenifer Pham¹](#),
- [Diljot Grewal³](#),
- [Daniel Lai ORCID: orcid.org/0000-0001-9203-6323¹](#),
- [Richard Moore⁶](#),
- [Andrew J. Mungall⁶](#),
- [Marco A. Marra ORCID: orcid.org/0000-0001-7146-7175⁶](#),
- [IMAXT Consortium](#),
- [Andrew McPherson³](#),
- [Alexandre Bouchard-Côté⁷](#),
- [Samuel Aparicio ORCID: orcid.org/0000-0002-0487-9599^{1,2}](#) &
- [Sohrab P. Shah ORCID: orcid.org/0000-0001-6402-523X³](#)

Nature volume **595**, pages 585–590 (2021)[Cite this article](#)

- 10k Accesses
- 180 Altmetric
- [Metrics details](#)

Subjects

- [Cancer genomics](#)
- [Preclinical research](#)

Abstract

Progress in defining genomic fitness landscapes in cancer, especially those defined by copy number alterations (CNAs), has been impeded by lack of time-series single-cell sampling of polyclonal populations and temporal statistical models^{1,2,3,4,5,6,7}. Here we generated 42,000 genomes from multi-year time-series single-cell whole-genome sequencing of breast epithelium and primary triple-negative breast cancer (TNBC) patient-derived xenografts (PDXs), revealing the nature of CNA-defined clonal fitness dynamics induced by *TP53* mutation and cisplatin chemotherapy. Using a new Wright–Fisher population genetics model^{8,9} to infer clonal fitness, we

found that *TP53* mutation alters the fitness landscape, reproducibly distributing fitness over a larger number of clones associated with distinct CNAs. Furthermore, in TNBC PDX models with mutated *TP53*, inferred fitness coefficients from CNA-based genotypes accurately forecast experimentally enforced clonal competition dynamics. Drug treatment in three long-term serially passaged TNBC PDXs resulted in cisplatin-resistant clones emerging from low-fitness phylogenetic lineages in the untreated setting. Conversely, high-fitness clones from treatment-naive controls were eradicated, signalling an inversion of the fitness landscape. Finally, upon release of drug, selection pressure dynamics were reversed, indicating a fitness cost of treatment resistance. Together, our findings define clonal fitness linked to both CNA and therapeutic resistance in polyclonal tumours.

Access options

Subscribe to Journal

Get full journal access for 1 year

\$199.00

only \$3.90 per issue

[Subscribe](#)

All prices are NET prices.

VAT will be added later in the checkout.

Tax calculation will be finalised during checkout.

Rent or Buy article

Get time limited or full article access on ReadCube.

from \$8.99

[Rent or Buy](#)

All prices are NET prices.

Additional access options:

- [Log in](#)
- [Access through your institution](#)
- [Learn about institutional subscriptions](#)

Fig. 1: Replicate branch of p53 mutant cells and engineered mixture experiment.

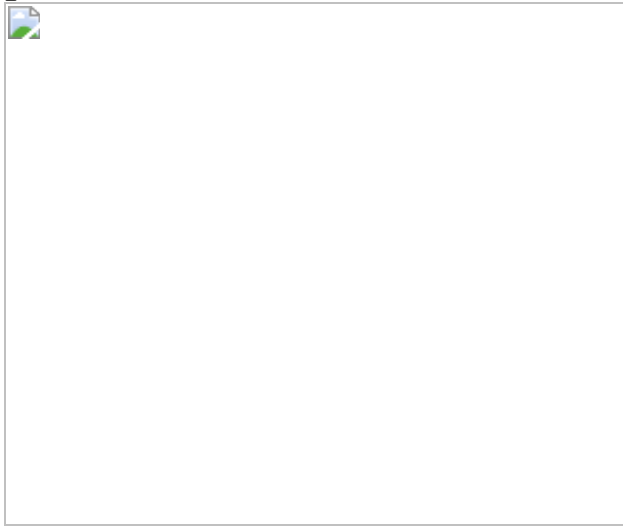


Fig. 2: Fitness landscapes of untreated TNBC-SA609 PDX.

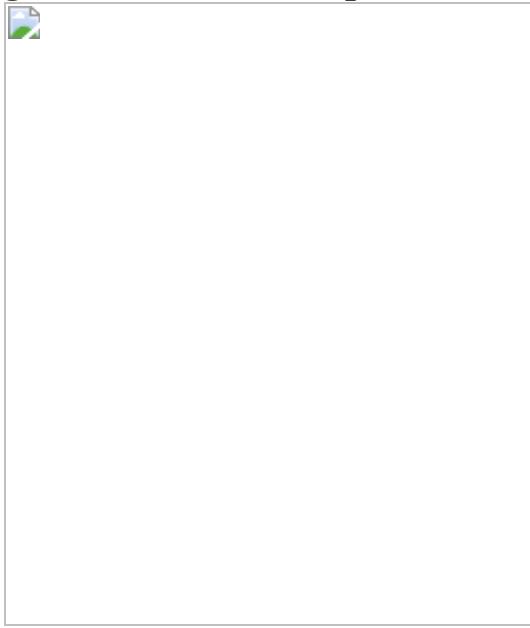


Fig. 3: Positive selection in untreated TNBC PDX.

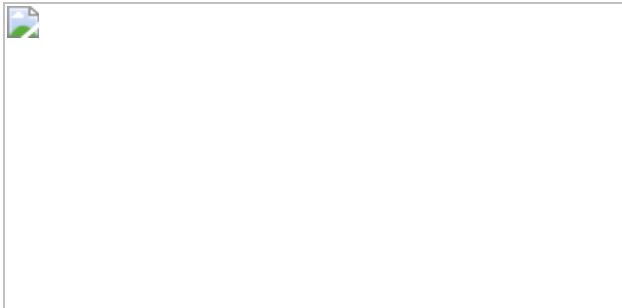
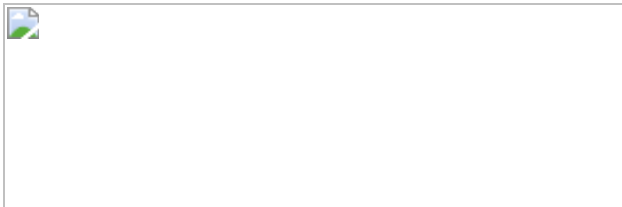


Fig. 4: Fitness landscape reversal in early cisplatin treatment in TNBC PDX models.



Data availability

Raw sequencing data for DLP⁺ and 10x scRNA-seq are available from the European Genome-Phenome under study ID [EGAS00001004448](#). Single-cell data from this report may be visualized in an instance of our scWGS exploration platform, Alhena, available at <https://www.cellmine.org>. [Source data](#) are provided with this paper.

Code availability

The software implementation of fitClone is available at <https://github.com/UBC-Stat-ML/fitclone>.

References

1. 1.

Gerstung, M. et al. The evolutionary history of 2,658 cancers. *Nature* **578**, 122–128 (2020).

[ADS](#) [CAS](#) [PubMed](#) [PubMed Central](#) [Article](#) [Google Scholar](#)

2. 2.

Williams, M. J. et al. Quantification of subclonal selection in cancer from bulk sequencing data. *Nat. Genet.* **50**, 895–903 (2018).

[CAS](#) [PubMed](#) [PubMed Central](#) [Article](#) [Google Scholar](#)

3. 3.

Salichos, L., Meyerson, W., Warrell, J. & Gerstein, M. Estimating growth patterns and driver effects in tumor evolution from individual samples. *Nat. Commun.* **11**, 732 (2020).

[ADS](#) [CAS](#) [PubMed](#) [PubMed Central](#) [Article](#) [Google Scholar](#)

4. 4.

Shah, S. P. et al. The clonal and mutational evolution spectrum of primary triple-negative breast cancers. *Nature* **486**, 395–399 (2012).

[ADS](#) [CAS](#) [PubMed](#) [Article](#) [Google Scholar](#)

5. 5.

Li, Y. et al. Patterns of somatic structural variation in human cancer genomes. *Nature* **578**, 112–121 (2020).

[ADS](#) [CAS](#) [PubMed](#) [PubMed Central](#) [Article](#) [Google Scholar](#)

6. 6.

Nik-Zainal, S. et al. Landscape of somatic mutations in 560 breast cancer whole-genome sequences. *Nature* **534**, 47–54 (2016).

[ADS](#) [CAS](#) [PubMed](#) [PubMed Central](#) [Article](#) [Google Scholar](#)

7. 7.

Curtis, C. et al. The genomic and transcriptomic architecture of 2,000 breast tumours reveals novel subgroups. *Nature* **486**, 346–352 (2012).

[CAS](#) [PubMed](#) [PubMed Central](#) [Article](#) [Google Scholar](#)

8. 8.

Wright, S. The distribution of gene frequencies in populations. *Proc. Natl Acad. Sci. USA* **23**, 307–320 (1937).

[ADS](#) [CAS](#) [PubMed](#) [PubMed Central](#) [MATH](#) [Article](#) [Google Scholar](#)

9. 9.

Tataru, P., Simonsen, M., Bataillon, T. & Hobolth, A. Statistical inference in the Wright–Fisher model using allele frequency data. *Syst. Biol.* **66**, e30–e46 (2017).

[PubMed](#) [Google Scholar](#)

10. 10.

Vasan, N., Baselga, J. & Hyman, D. M. A view on drug resistance in cancer. *Nature* **575**, 299–309 (2019).

[ADS](#) [CAS](#) [PubMed](#) [PubMed Central](#) [Article](#) [Google Scholar](#)

11. 11.

Ben-David, U. & Amon, A. Context is everything: aneuploidy in cancer. *Nat. Rev. Genet.* **21**, 44–62 (2020).

[CAS](#) [PubMed](#) [Article](#) [Google Scholar](#)

12. 12.

Sunshine, A. B. et al. The fitness consequences of aneuploidy are driven by condition-dependent gene effects. *PLoS Biol.* **13**, e1002155

(2015).

[PubMed](#) [PubMed Central](#) [Article](#) [CAS](#) [Google Scholar](#)

13. 13.

Sheltzer, J. M., Torres, E. M., Dunham, M. J. & Amon, A. Transcriptional consequences of aneuploidy. *Proc. Natl Acad. Sci. USA* **109**, 12644–12649 (2012).

[ADS](#) [CAS](#) [PubMed](#) [PubMed Central](#) [Article](#) [Google Scholar](#)

14. 14.

Williams, M. J., Werner, B., Barnes, C. P., Graham, T. A. & Sottoriva, A. Identification of neutral tumor evolution across cancer types. *Nat. Genet.* **48**, 238–244 (2016).

[CAS](#) [PubMed](#) [PubMed Central](#) [Article](#) [Google Scholar](#)

15. 15.

Nik-Zainal, S. et al. The life history of 21 breast cancers. *Cell* **149**, 994–1007 (2012).

[CAS](#) [PubMed](#) [PubMed Central](#) [Article](#) [Google Scholar](#)

16. 16.

Martincorena, I. et al. Universal patterns of selection in cancer and somatic tissues. *Cell* **171**, 1029–1041.e21 (2017).

[CAS](#) [PubMed](#) [PubMed Central](#) [Article](#) [Google Scholar](#)

17. 17.

Khan, K. H. et al. Longitudinal liquid biopsy and mathematical modeling of clonal evolution forecast time to treatment failure in the

PROSPECT-C phase II colorectal cancer clinical trial. *Cancer Discov.* **8**, 1270–1285 (2018).

[CAS](#) [PubMed](#) [PubMed Central](#) [Article](#) [Google Scholar](#)

18. 18.

Gerlinger, M. et al. Genomic architecture and evolution of clear cell renal cell carcinomas defined by multiregion sequencing. *Nat. Genet.* **46**, 225–233 (2014).

[CAS](#) [PubMed](#) [PubMed Central](#) [Article](#) [Google Scholar](#)

19. 19.

Jamal-Hanjani, M. et al. Tracking the evolution of non–small-cell lung cancer. *N. Engl. J. Med.* **376**, 2109–2121 (2017).

[CAS](#) [Article](#) [Google Scholar](#)

20. 20.

López, S. et al. Interplay between whole-genome doubling and the accumulation of deleterious alterations in cancer evolution. *Nat. Genet.* **52**, 283–293 (2020).

[PubMed](#) [PubMed Central](#) [Article](#) [CAS](#) [Google Scholar](#)

21. 21.

McPherson, A. et al. Divergent modes of clonal spread and intraperitoneal mixing in high-grade serous ovarian cancer. *Nat. Genet.* **48**, 758–767 (2016).

[CAS](#) [PubMed](#) [Article](#) [Google Scholar](#)

22. 22.

Good, B. H., McDonald, M. J., Barrick, J. E., Lenski, R. E. & Desai, M. M. The dynamics of molecular evolution over 60,000 generations. *Nature* **551**, 45–50 (2017).

[ADS](#) [PubMed](#) [PubMed Central](#) [Article](#) [CAS](#) [Google Scholar](#)

23. 23.

Dorri, F. et al. Efficient Bayesian inference of phylogenetic trees from large scale, low-depth genome-wide single-cell data. Preprint at <https://doi.org/10.1101/2020.05.06.058180> (2020).

24. 24.

Burleigh, A. et al. A co-culture genome-wide RNAi screen with mammary epithelial cells reveals transmembrane signals required for growth and differentiation. *Breast Cancer Res.* **17**, 4 (2015).

[PubMed](#) [PubMed Central](#) [Article](#) [CAS](#) [Google Scholar](#)

25. 25.

de la Vega, M. R., Chapman, E. & Zhang, D. D. NRF2 and the Hallmarks of cancer. *Cancer Cell* **34**, 21–43 (2018).

[PubMed Central](#) [Article](#) [CAS](#) [PubMed](#) [Google Scholar](#)

26. 26.

The Cancer Genome Atlas Network. Comprehensive molecular portraits of human breast tumours. *Nature* **490**, 61–70 (2012).

[ADS](#) [Article](#) [CAS](#) [Google Scholar](#)

27. 27.

Patch, A.-M. et al. Whole-genome characterization of chemoresistant ovarian cancer. *Nature* **521**, 489–494 (2015).

[ADS](#) [CAS](#) [PubMed](#) [PubMed Central](#) [Article](#) [Google Scholar](#)

28. 28.

Laks, E. et al. Clonal decomposition and DNA replication states defined by scaled single-cell genome sequencing. *Cell* **179**, 1207–1221 (2019).

[CAS](#) [PubMed](#) [PubMed Central](#) [Article](#) [Google Scholar](#)

29. 29.

Hather, G. et al. Growth rate analysis and efficient experimental design for tumor xenograft studies. *Cancer Inform.* **13**, 65–72 (2014).

[PubMed](#) [PubMed Central](#) [Google Scholar](#)

30. 30.

Bielski, C. M. et al. Genome doubling shapes the evolution and prognosis of advanced cancers. *Nat. Genet.* **50**, 1189–1195 (2018).

[CAS](#) [PubMed](#) [PubMed Central](#) [Article](#) [Google Scholar](#)

31. 31.

Bakhoum, S. F. et al. Chromosomal instability drives metastasis through a cytosolic DNA response. *Nature* **553**, 467–472 (2018).

[ADS](#) [CAS](#) [PubMed](#) [PubMed Central](#) [Article](#) [Google Scholar](#)

32. 32.

Davoli, T., Uno, H., Wooten, E. C. & Elledge, S. J. Tumor aneuploidy correlates with markers of immune evasion and with reduced response to immunotherapy. *Science* **355**, eaaf8399 (2017).

[PubMed](#) [PubMed Central](#) [Article](#) [CAS](#) [Google Scholar](#)

33. 33.

Acar, A. et al. Exploiting evolutionary steering to induce collateral drug sensitivity in cancer. *Nat. Commun.* **11**, 1923 (2020).

[ADS](#) [CAS](#) [PubMed](#) [PubMed Central](#) [Article](#) [Google Scholar](#)

34. 34.

Eirew, P. et al. Dynamics of genomic clones in breast cancer patient xenografts at single-cell resolution. *Nature* **518**, 422–426 (2015).

[ADS](#) [CAS](#) [PubMed](#) [Article](#) [Google Scholar](#)

35. 35.

Li, D. et al. Enhanced tumor suppression by adenoviral PTEN gene therapy combined with cisplatin chemotherapy in small-cell lung cancer. *Cancer Gene Ther.* **20**, 251–259 (2013).

[ADS](#) [CAS](#) [PubMed](#) [Article](#) [Google Scholar](#)

36. 36.

Wang, Y. et al. Klotho sensitizes human lung cancer cell line to cisplatin via PI3k/Akt pathway. *PLoS ONE* **8**, e57391 (2013).

[ADS](#) [CAS](#) [PubMed](#) [PubMed Central](#) [Article](#) [Google Scholar](#)

37. 37.

O'Flanagan, C. H. et al. Dissociation of solid tumor tissues with cold active protease for single-cell RNA-seq minimizes conserved collagenase-associated stress responses. *Genome Biol.* **20**, 210 (2019).

[PubMed](#) [PubMed Central](#) [Google Scholar](#)

38. 38.

Roth, A. et al. PyClone: statistical inference of clonal population structure in cancer. *Nat. Methods* **11**, 396–398 (2014).

[CAS](#) [PubMed](#) [PubMed Central](#) [Article](#) [Google Scholar](#)

39. 39.

Beaumont, M. A., Cornuet, J.-M., Marin, J.-M. & Robert, C. P. Adaptive approximate Bayesian computation. *Biometrika* **96**, 983–990 (2009).

[MathSciNet](#) [MATH](#) [Article](#) [Google Scholar](#)

40. 40.

Foll, M. et al. Influenza virus drug resistance: a time-sampled population genetics perspective. *PLoS Genet.* **10**, e1004185 (2014).

[PubMed](#) [PubMed Central](#) [Article](#) [CAS](#) [Google Scholar](#)

41. 41.

Bollback, J. P., York, T. L. & Nielsen, R. Estimation of 2Nes from temporal allele frequency data. *Genetics* **179**, 497–502 (2008).

[CAS](#) [PubMed](#) [PubMed Central](#) [Article](#) [Google Scholar](#)

42. 42.

Malaspinas, A.-S., Malaspinas, O., Evans, S. N. & Slatkin, M. Estimating allele age and selection coefficient from time-serial data. *Genetics* **192**, 599–607 (2012).

[PubMed](#) [PubMed Central](#) [Article](#) [Google Scholar](#)

43. 43.

Ferrer-Admetlla, A., Leuenberger, C., Jensen, J. D. & Wegmann, D. An approximate Markov model for the Wright–Fisher diffusion and its

application to time series data. *Genetics* **203**, 831–846 (2016).

[CAS](#) [PubMed](#) [PubMed Central](#) [Article](#) [Google Scholar](#)

44. 44.

Beskos, A. et al. Exact simulation of diffusions. *Ann. Appl. Probab.* **15**, 2422–2444 (2005).

[MathSciNet](#) [MATH](#) [Article](#) [Google Scholar](#)

45. 45.

Pollock, M. et al. On the exact and ε -strong simulation of (jump) diffusions. *Bernoulli* **22**, 794–856 (2016).

[MathSciNet](#) [MATH](#) [Article](#) [Google Scholar](#)

46. 46.

Jenkins, P. A. et al. Exact simulation of the Wright–Fisher diffusion. *Ann. Appl. Probab.* **27**, 1478–1509 (2017).

[MathSciNet](#) [MATH](#) [Article](#) [Google Scholar](#)

47. 47.

Blanchet, J. Exact simulation for multivariate Itô diffusions. *Adv. Appl. Probab.* **52**, 1003-1 (2020).

[Article](#) [Google Scholar](#)

48. 48.

Jorde, P., Palm, S. & Ryman, N. Estimating genetic drift and effective population size from temporal shifts in dominant gene marker frequencies. *Mol. Ecol.* **8**, 1171–1178 (1999).

[Article](#) [Google Scholar](#)

[Download references](#)

Acknowledgements

This project was generously supported by the BC Cancer Foundation at BC Cancer and Cycle for Survival supporting Memorial Sloan Kettering Cancer Center. S.P.S. holds the Nicholls Biondi Chair in Computational Oncology and is a Susan G. Komen Scholar (GC233085). S.A. holds the Nan and Lorraine Robertson Chair in Breast Cancer and is a Canada Research Chair in Molecular Oncology (950-230610). Additional funding provided by the Terry Fox Research Institute Grant 1082, Canadian Cancer Society Research Institute Impact program Grant 705617, CIHR Grant FDN-148429, Breast Cancer Research Foundation award (BCRF-18-180, BCRF-19-180 and BCRF-20-180), MSK Cancer Center Support Grant/Core Grant (P30 CA008748), National Institutes of Health Grant (1RM1 HG011014-01), CCSRI Grant (705636), the Cancer Research UK Grand Challenge Program, Canada Foundation for Innovation (40044) to S.A., S.P.S. and A.B.-C. We thank S. P. Otto, E. Laks, D. Min and E. Zaikova for their contribution to the project.

Author information

Author notes

1. These authors contributed equally: Sohrab Salehi, Farhia Kabeer

Affiliations

1. Department of Molecular Oncology, BC Cancer, Vancouver, British Columbia, Canada

Sohrab Salehi, Farhia Kabeer, Mirela Andronescu, Tehmina Masud, Beixi Wang, Justina Biele, Jazmine Brimhall, David Gee, Hakwoo Lee, Jerome Ting, Allen W. Zhang, Hoa Tran, Ciara O'Flanagan, Fatemeh Dorri, Teresa Ruiz de Algara, So Ra Lee, Brian Yu Chieh Cheng, Peter Eirew, Takako Kono, Jenifer Pham, Daniel

Lai, Emma Laks, Yangguang Li, Ciara H. O'Flanagan, Austin Smith, Teresa Ruiz, Daniel Lai & Samuel Aparicio

2. Department of Pathology and Laboratory Medicine, University of British Columbia, Vancouver, British Columbia, Canada

Farhia Kabeer, Mirela Andronescu, Emma Laks, Daniel Lai, Andrew Roth & Samuel Aparicio

3. Computational Oncology, Department of Epidemiology and Biostatistics, Memorial Sloan Kettering Cancer Center, New York, NY, USA

Nicholas Ceglia, Marc J. Williams, Nicole Rusk, Diljot Grewal, Ignacio Vázquez-García, Andrew McPherson & Sohrab P. Shah

4. Lunenfeld-Tanenbaum Research Institute Mount Sinai Hospital Joseph & Wolf Lebovic Health Complex, Molecular Genetics, University of Toronto, Toronto, Ontario, Canada

Kieran R. Campbell & Andrew Roth

5. Department of Computer Science, University of British Columbia, Vancouver, British Columbia, Canada

Fatemeh Dorri

6. Canada's Michael Smith Genome Sciences Centre, BC Cancer, Vancouver, British Columbia, Canada

Richard Moore, Andrew J. Mungall & Marco A. Marra

7. Department of Statistics, University of British Columbia, Vancouver, British Columbia, Canada

Alexandre Bouchard-Côté

8. Cancer Research UK Cambridge Institute, Li Ka Shing Centre,
University of Cambridge, Cambridge, UK

Gregory J. Hannon, Giorgia Battistoni, Dario Bressan, Ian Gordon Cannell, Hannah Casbolt, Atefeh Fatemi, Cristina Jauset, Tatjana Kovačević, Claire M. Mulvey, Fiona Nugent, Marta Paez Ribes, Isabella Pearsall, Fatime Qosaj, Kirsty Sawicka, Sophia A. Wild, Elena Williams, Shankar Balasubramanian, Maximillian Lee, Maurizio Callari, Wendy Greenwood, Giulia Lerda, Simon Tavaré & Eyal Fisher

9. Department of Chemistry, University of Cambridge, Cambridge, UK

Shankar Balasubramanian & Maximillian Lee

10. School of Clinical Medicine, University of Cambridge, Cambridge, UK

Shankar Balasubramanian

11. Department of Quantitative Biomedicine, University of Zurich, Zurich, Switzerland

Bernd Bodenmiller, Marcel Burger, Laura Kuett, Sandra Tietscher & Jonas Windhager

12. McGovern Institute, Departments of Biological Engineering and Brain and Cognitive Sciences, Massachusetts Institute of Technology, Cambridge, MA, USA

Edward S. Boyden, Shahar Alon, Yi Cui, Amauche Emenari, Dan Goodwin, Emmanouil D. Karagiannis, Anubhav Sinha & Asmamaw T. Wassie

13. Department of Oncology and Cancer Research UK Cambridge Institute, University of Cambridge, Cambridge, UK

Carlos Caldas, Alejandra Bruna, Yaniv Eyal-Lubling, Oscar M. Rueda & Abigail Shea

14. Súil Interactive Ltd, Dublin, Ireland

Owen Harris, Robby Becker, Flaminia Grimaldi, Suvi Harris, Sara Lisa Vogl & Joanna Weselak

15. Department of Oncology and Ludwig Institute for Cancer Research,
University of Lausanne, Lausanne, Switzerland

Johanna A. Joyce & Spencer S. Watson

16. Herbert and Florence Irving Institute for Cancer Dynamics, Columbia
University, New York, NY, USA

Simon Tavaré, Khanh N. Dinh & Russell Kunes

17. New York Genome Center, New York, NY, USA

Simon Tavaré

18. Institute of Astronomy, University of Cambridge, Cambridge, UK

Nicholas A. Walton, Mohammad Al Sa'd, Nick Chornay, Ali Dariush, Eduardo A. González-Solares, Carlos González-Fernández, Aybüke Küpcü Yoldas, Neil Millar & Tristan Whitmarsh

19. Howard Hughes Medical Institute, Harvard University, Cambridge,
MA, USA

Xiaowei Zhuang, Jean Fan, Hsuan Lee, Leonardo A. Sepúlveda, Chenglong Xia & Pu Zheng

20. Department of Physics, Harvard University, Cambridge, MA, USA

Xiaowei Zhuang, Jean Fan, Hsuan Lee, Leonardo A. Sepúlveda, Chenglong Xia & Pu Zheng

21. Department of Chemistry and Chemical Biology, Harvard University,
Cambridge, MA, USA

Xiaowei Zhuang, Jean Fan, Hsuan Lee, Leonardo A. Sepúlveda, Chenglong Xia & Pu Zheng

Authors

1. Sohrab Salehi

[View author publications](#)

You can also search for this author in [PubMed](#) [Google Scholar](#)

2. Farhia Kabeer

[View author publications](#)

You can also search for this author in [PubMed](#) [Google Scholar](#)

3. Nicholas Ceglia

[View author publications](#)

You can also search for this author in [PubMed](#) [Google Scholar](#)

4. Mirela Andronescu

[View author publications](#)

You can also search for this author in [PubMed](#) [Google Scholar](#)

5. Marc J. Williams

[View author publications](#)

You can also search for this author in [PubMed](#) [Google Scholar](#)

6. Kieran R. Campbell

[View author publications](#)

You can also search for this author in [PubMed](#) [Google Scholar](#)

7. Tehmina Masud

[View author publications](#)

You can also search for this author in [PubMed](#) [Google Scholar](#)

8. Beixi Wang

[View author publications](#)

You can also search for this author in [PubMed](#) [Google Scholar](#)

9. Justina Biele

[View author publications](#)

You can also search for this author in [PubMed](#) [Google Scholar](#)

10. Jazmine Brimhall

[View author publications](#)

You can also search for this author in [PubMed](#) [Google Scholar](#)

11. David Gee

[View author publications](#)

You can also search for this author in [PubMed](#) [Google Scholar](#)

12. Hakwoo Lee

[View author publications](#)

You can also search for this author in [PubMed](#) [Google Scholar](#)

13. Jerome Ting

[View author publications](#)

You can also search for this author in [PubMed](#) [Google Scholar](#)

14. Allen W. Zhang

[View author publications](#)

You can also search for this author in [PubMed](#) [Google Scholar](#)

15. Hoa Tran

[View author publications](#)

You can also search for this author in [PubMed](#) [Google Scholar](#)

16. Ciara O'Flanagan

[View author publications](#)

You can also search for this author in [PubMed](#) [Google Scholar](#)

17. Fatemeh Dorri

[View author publications](#)

You can also search for this author in [PubMed](#) [Google Scholar](#)

18. Nicole Rusk

[View author publications](#)

You can also search for this author in [PubMed](#) [Google Scholar](#)

19. Teresa Ruiz de Algara

[View author publications](#)

You can also search for this author in [PubMed](#) [Google Scholar](#)

20. So Ra Lee

[View author publications](#)

You can also search for this author in [PubMed](#) [Google Scholar](#)

21. Brian Yu Chieh Cheng

[View author publications](#)

You can also search for this author in [PubMed](#) [Google Scholar](#)

22. Peter Eirew

[View author publications](#)

You can also search for this author in [PubMed](#) [Google Scholar](#)

23. Takako Kono

[View author publications](#)

You can also search for this author in [PubMed](#) [Google Scholar](#)

24. Jenifer Pham

[View author publications](#)

You can also search for this author in [PubMed](#) [Google Scholar](#)

25. Diljot Grewal

[View author publications](#)

You can also search for this author in [PubMed](#) [Google Scholar](#)

26. Daniel Lai

[View author publications](#)

You can also search for this author in [PubMed](#) [Google Scholar](#)

27. Richard Moore

[View author publications](#)

You can also search for this author in [PubMed](#) [Google Scholar](#)

28. Andrew J. Mungall

[View author publications](#)

You can also search for this author in [PubMed](#) [Google Scholar](#)

29. Marco A. Marra

[View author publications](#)

You can also search for this author in [PubMed](#) [Google Scholar](#)

30. Andrew McPherson

[View author publications](#)

You can also search for this author in [PubMed](#) [Google Scholar](#)

31. Alexandre Bouchard-Côté

[View author publications](#)

You can also search for this author in [PubMed](#) [Google Scholar](#)

32. Samuel Aparicio

[View author publications](#)

You can also search for this author in [PubMed](#) [Google Scholar](#)

33. Sohrab P. Shah

[View author publications](#)

You can also search for this author in [PubMed](#) [Google Scholar](#)

Consortia

IMAXT Consortium

- Gregory J. Hannon
- , Giorgia Battistoni
- , Dario Bressan
- , Ian Gordon Cannell
- , Hannah Casbolt
- , Atefeh Fatemi
- , Cristina Jauset
- , Tatjana Kovačević
- , Claire M. Mulvey
- , Fiona Nugent
- , Marta Paez Ribes
- , Isabella Pearsall
- , Fatime Qosaj
- , Kirsty Sawicka
- , Sophia A. Wild
- , Elena Williams
- , Samuel Aparicio
- , Emma Laks
- , Yangguang Li
- , Ciara H. O'Flanagan
- , Austin Smith
- , Teresa Ruiz
- , Daniel Lai

- , Andrew Roth
- , Shankar Balasubramanian
- , Maximillian Lee
- , Bernd Bodenmiller
- , Marcel Burger
- , Laura Kuett
- , Sandra Tietscher
- , Jonas Windhager
- , Edward S. Boyden
- , Shahar Alon
- , Yi Cui
- , Amauche Emenari
- , Dan Goodwin
- , Emmanouil D. Karagiannis
- , Anubhav Sinha
- , Asmamaw T. Wassie
- , Carlos Caldas
- , Alejandra Bruna
- , Maurizio Callari
- , Wendy Greenwood
- , Giulia Lerda
- , Yaniv Eyal-Lubling
- , Oscar M. Rueda
- , Abigail Shea
- , Owen Harris
- , Robby Becker
- , Flaminia Grimaldi
- , Suvi Harris
- , Sara Lisa Vogl
- , Joanna Weselak
- , Johanna A. Joyce
- , Spencer S. Watson
- , Sohrab P. Shah
- , Andrew McPherson
- , Ignacio Vázquez-García
- , Simon Tavaré
- , Khanh N. Dinh

- , Eyal Fisher
- , Russell Kunes
- , Nicholas A. Walton
- , Mohammad Al Sa'd
- , Nick Chornay
- , Ali Dariush
- , Eduardo A. González-Solares
- , Carlos González-Fernández
- , Aybüke Küpcü Yoldas
- , Neil Millar
- , Tristan Whitmarsh
- , Xiaowei Zhuang
- , Jean Fan
- , Hsuan Lee
- , Leonardo A. Sepúlveda
- , Chenglong Xia
- & Pu Zheng

Contributions

S.P.S. and S.A.: project conception and oversight, manuscript writing, senior responsible authors; A.B.-C.: statistical inference method development and oversight; S.S.: computational method development, data analysis, manuscript writing; F.K.: mouse modelling, tissue procurement, data generation, manuscript writing; N.C., M.A., M.J.W., K.R.C., A.W.Z., F.D., J.P., D. Gee, D.L., A.M.: computational biology, data analysis; D. Grewal, C.O., T.M., B.W., J. Brimhall., J. Biele, J.T., H.L., T.R.d.A., S.R.L., B.Y.C.C., P.E., T.K.: tissue procurement, biological substrates and data generation; R.M., A.J.M., M.A.M.: genome sequencing; N.R.: manuscript editing.

Corresponding authors

Correspondence to [Samuel Aparicio](#) or [Sohrab P. Shah](#).

Ethics declarations

Competing interests

S.P.S. and S.A. are shareholders and consultants of Canexia Health Inc.

Additional information

Peer review information *Nature* thanks the anonymous reviewers for their contribution to the peer review of this work. Peer reviewer reports are available.

Publisher's note Springer Nature remains neutral with regard to jurisdictional claims in published maps and institutional affiliations.

Extended data figures and tables

[Extended Data Fig. 1 Schematic overview of experimental design for quantitatively modelling clone-specific fitness.](#)

a, b, Time-series sampling from in vitro (**a**) and PDX (**b**) systems. Grey circles represent un-treated, blue represents cisplatin treated and grey with a blue outline denotes drug-holiday samples. **c**, Clonal dynamics of cell populations observed over time. Whole genome single cell sequencing of time-series samples gives copy number (left) that in turn is used to infer a phylogenetic tree (middle), and clonal fractions over time (right). **d**, fitClone: mathematical modelling of fitness with diffusion approximation to the K-type Wright–Fisher model. **e**, fitClone inputs of clonal dynamics measured over time series (left), and inferred trajectories (middle) and posterior distributions of fitness coefficients (right). Box plots are as defined in Fig. [1b](#).

[Extended Data Fig. 2 Impact of *p53* mutation on fitness in 184hTERT cells.](#)

a, Heatmap representation of copy number profiles of 2,713 *p53*^{WT} cells, grouped in 6 phylogenetic clades. **b**, Phylogeny of cells over the time series

$p53^{WT}$ where nodes are groups of cells (scaled in size by number) with shared copy number genotype and edges represent distinct genomic breakpoints. Shaded areas represent clones. Tree root is denoted by the red circle. **c**, Observed clonal fractions over time, inferred trajectories and quantiles of the posterior distributions over selection coefficients of fitClone model fits to $p53^{WT}$ with respect to the reference clone F. **d**, Analogous to **a** but for $p53^{-/-}a$ ($n = 3,264$ $p53^{-/-}a$ cells). **e**, Clonal genotypes of three representative clones for $p53^{-/-}b$ showing high level amplification of *TSHZ2* in clone D, chromosome 4 loss in clone E. Reference diploid clone I is shown for comparison. **f, g**, Analogous to **b, c**, but for $p53^{-/-}b$ ($n = 4,881$ $p53^{-/-}b$ cells; reference clone I). **h**, Number of segments per clone in hTERT WT and $p53^{-/-}a$ and $p53^{-/-}b$ branches. **i**, Number of mutations in $p53^{-/-}a$ and $p53^{-/-}b$ branches. Box plots are as defined in Fig. 1b.

Extended Data Fig. 3 PDX tumour growth and clonal dynamics with cisplatin.

a, Experimental design of cisplatin treatment in PDX. The solid blue colour representing cisplatin treated tumours (UT, UTT, UTTT, UTTTT); blue outlined in grey as drug holiday (UTU, UTTU, UTTTU); grey as untreated series. **b–d**, Tumour response curves in TNBC-SA609, TNBC-SA535 and TNBC-SA1035 treated with Cisplatin (blue), in drug Holiday (green) and untreated (red) where each tumour replicate is shown in a different shade. The vertical axis on the right denotes the status of tumours and on the left denotes the tumour volumes. The top horizontal axis represents number of cisplatin cycles and at the bottom days from palpable tumours to collection. The red arrows indicate the start of treatment and the black arrows indicate the tumour sampled for scDNaseq. The bottom horizontal axis shows the tumour passage number. Each line in the big box is an individual tumour showing the growth over time. **e**, Top, clonal trajectories of the clone with the highest inferred selection coefficient in the treatment regime (solid black line) and the drug holiday counterpart (dashed red line) at each time point, in the three TNBC PDX time series; bottom, as the top row, but for a clone that grows back in the holiday regime.

Source data

Extended Data Fig. 4 Comparison of fitness landscapes of breast cancer PDX models.

a, Heatmap representation of copy number profiles of 2,015 cells from TNBC-SA1035, grouped in 11 phylogenetic clades. **b**, Phylogeny for TNBC-SA1035. **c**, Observed clonal fractions, inferred fitClone trajectories and quantiles of the selection coefficients with respect to the reference clone A for the TNBC-SA1035 UnRx model. **d–f**, Analogous to **a–c** but for HER2⁺ SA535 ($n = 1,549$ cells; reference clone C). **g–i**, Analogous to **a–c** but for HER2⁺ SA532 ($n = 2,193$ cells; reference clone A). Box plots are as defined in Fig. 1b.

Extended Data Fig. 5 Impact of pharmacologic perturbation with cisplatin on fitness landscapes in TNBC-SA1035.

a, Copy number genotype of clone E from the untreated time series. **b**, Copy number genotype of clone H from treated time series (arrows indicate differences to clone E). **c**, Evolution in absence of treatment and as a function of drug treatment. For each sample, the phylogeny with clonal abundance from DLP⁺ is shown, reflecting selection. **d, e**, The observed clonal abundances (**d**) and the summarized clonal phylogenetic tree (**e**).

Extended Data Fig. 6 Tumour evolution in absence of pharmacologic perturbation in TNBC-SA609 line 1.

a, b, Copy number genotype of clone E (**a**) and copy number genotype of clone C, the reference clone (arrows indicate differences to clone E) (**b**). **c**, Evolution in absence of treatment. For each sample, the phylogeny with clonal abundance from DLP⁺ is shown, reflecting selection. **d, e**, The observed clonal abundances (**d**) and the summarized clonal phylogenetic tree (**e**).

Extended Data Fig. 7 Mixture experiment in TNBC-SA609 PDX Line 1.

a, Clonal proportions of TNBC-SA609 Line 1 X3 and X8 used to generate the initial mixture M0 and subsequent serial passaging, yielding 5 samples for mixture experiment b (mixture b). **b**, Forward simulations from the original time series and starting population proportions in the initial experimental mixture b. Simulated trajectories are shown superimposed with mean simulation (red line) and observed clonal fractions (blue dots). The observation time is adjusted to match the simulation diffusion time. **c**, Summary phylogenetic tree, inferred trajectories and fitness coefficients (relative to reference clone C) for mixture a. **d**, As in **c** but for mixture b (relative to reference clone C). Box plots are as defined in Fig. [1b](#).

Extended Data Fig. 8 Fitness landscape reversal in early cisplatin treatment in TNBC PDX models.

In each column, the left and right sub-panels are from the untreated and treated branches respectively. **a**, Phylogenetic trees annotated with fittest clones in –Rx and Rx. **b**, **c**, Inferred trajectories, first coloured by clonal assignment, and then coloured by fitness rank (**b**), and quantiles of selection coefficients of fitClone model fits to each branch with respect to the reference Clone C in TNBC-SA609, Clone C in TNBC-SA535, and clone A in TNBC-SA1035 (**c**). **d**, Distribution over the probability of positive selection over pairs of clones for each series. Box plots are as defined in Fig. [1b](#).

Extended Data Fig. 9 Impact of pharmacologic perturbation with cisplatin on fitness landscapes in TNBC-SA609.

a, Copy number genotype of clone H from untreated time series. **b**, Copy number genotype of clone A from the treated time series (arrows indicate differences to clone H). **c**, Evolution in absence of treatment (top) and as a function of treatment (bottom). For each sample, the phylogeny with clonal abundance from DLP⁺ is shown, reflecting selection. **d**, The observed

clonal abundances. Starred time points are identical and reproduced to denote the identical starting point. **e**, Summarized clonal phylogenetic tree.

Extended Data Fig. 10 Impact of pharmacologic perturbation with cisplatin on fitness landscapes in TNBC-SA535.

a, Copy number genotype of clone G from untreated time series. **b**, Copy number genotype of clone A from treated time series (arrows indicate differences to clone E). **c**, Evolution in absence of treatment and as a function of drug treatment. For each sample, the phylogeny with clonal abundance from DLP⁺ is shown, reflecting selection. **d**, **e**, The observed clonal abundances (**d**) and the summarized clonal phylogenetic tree (**e**).

Supplementary information

Supplementary Information

This file contains Supplementary Methods, Supplementary Figures 1-6 a guide to Supplementary Tables 1-8 and Supplementary References.

Reporting Summary

Supplementary Tables

This file contains Supplementary Tables 1-8 – see Supplementary Information document for full guide.

Source Data

This file contains Source Data for Supplementary Figure 1.

Peer Review File

Source data

[Source Data Extended Data Fig. 3](#)

Rights and permissions

[Reprints and Permissions](#)

About this article



Check for
updates

Cite this article

Salehi, S., Kabeer, F., Ceglia, N. *et al.* Clonal fitness inferred from time-series modelling of single-cell cancer genomes. *Nature* **595**, 585–590 (2021). <https://doi.org/10.1038/s41586-021-03648-3>

[Download citation](#)

- Received: 08 May 2020
- Accepted: 17 May 2021
- Published: 23 June 2021
- Issue Date: 22 July 2021
- DOI: <https://doi.org/10.1038/s41586-021-03648-3>

Comments

By submitting a comment you agree to abide by our [Terms](#) and [Community Guidelines](#). If you find something abusive or that does not comply with our terms or guidelines please flag it as inappropriate.

[Access through your institution](#)

[Change institution](#)

[Buy or subscribe](#)

Advertisement

This article was downloaded by **calibre** from <https://www.nature.com/articles/s41586-021-03648-3>

| [Section menu](#) | [Main menu](#) |

- Article
- [Published: 23 June 2021](#)

Phase separation drives aberrant chromatin looping and cancer development

- [Jeong Hyun Ahn](#)^{1,2},
- [Eric S. Davis](#) ORCID: orcid.org/0000-0003-4051-3217³,
- [Timothy A. Daugird](#)⁴,
- [Shuai Zhao](#)^{1,2},
- [Ivana Yoseli Quiroga](#) ORCID: orcid.org/0000-0002-6799-0059⁵,
- [Hidetaka Uryu](#)^{1,2},
- [Jie Li](#)^{1,6},
- [Aaron J. Storey](#)⁷,
- [Yi-Hsuan Tsai](#) ORCID: orcid.org/0000-0003-2107-4300¹,
- [Daniel P. Keeley](#)⁸,
- [Samuel G. Mackintosh](#)⁷,
- [Ricky D. Edmondson](#)⁷,
- [Stephanie D. Byrum](#) ORCID: orcid.org/0000-0002-1783-3610⁷,
- [Ling Cai](#)^{1,2,9},
- [Alan J. Tackett](#)⁷,
- [Deyou Zheng](#) ORCID: orcid.org/0000-0003-4354-5337¹⁰,
- [Wesley R. Legant](#)^{4,11},
- [Douglas H. Phanstiel](#) ORCID: orcid.org/0000-0003-2123-0051^{1,3,5,12} [na1](#) &
- [Gang Greg Wang](#) ORCID: orcid.org/0000-0002-7210-9940^{1,2,4,6} [na1](#)

- 13k Accesses
- 1 Citations
- 250 Altmetric
- [Metrics details](#)

Subjects

- [Acute myeloid leukaemia](#)
- [Cancer epigenetics](#)
- [Chromatin structure](#)

Abstract

The development of cancer is intimately associated with genetic abnormalities that target proteins with intrinsically disordered regions (IDRs). In human haematological malignancies, recurrent chromosomal translocation of nucleoporin (NUP98 or NUP214) generates an aberrant chimera that invariably retains the nucleoporin IDR—tandemly dispersed repeats of phenylalanine and glycine residues^{1,2}. However, how unstructured IDRs contribute to oncogenesis remains unclear. Here we show that IDRs contained within NUP98–HOXA9, a homeodomain-containing transcription factor chimera recurrently detected in leukaemias^{1,2}, are essential for establishing liquid–liquid phase separation (LLPS) puncta of chimera and for inducing leukaemic transformation. Notably, LLPS of NUP98–HOXA9 not only promotes chromatin occupancy of chimera transcription factors, but also is required for the formation of a broad ‘super-enhancer’-like binding pattern typically seen at leukaemogenic genes, which potentiates transcriptional activation. An artificial HOX chimera, created by replacing the phenylalanine and glycine repeats of NUP98 with an unrelated LLPS-forming IDR of the FUS protein^{3,4}, had similar enhancing effects on the genome-wide binding and target gene activation of the chimera. Deeply sequenced Hi-C revealed that phase-separated NUP98–HOXA9 induces CTCF-independent chromatin loops that are enriched at proto-oncogenes. Together, this report describes a

proof-of-principle example in which cancer acquires mutation to establish oncogenic transcription factor condensates via phase separation, which simultaneously enhances their genomic targeting and induces organization of aberrant three-dimensional chromatin structure during tumourous transformation. As LLPS-competent molecules are frequently implicated in diseases^{[1,2,4,5,6,7](#)}, this mechanism can potentially be generalized to many malignant and pathological settings.

Access options

Subscribe to Journal

Get full journal access for 1 year

\$199.00

only \$3.90 per issue

[Subscribe](#)

All prices are NET prices.

VAT will be added later in the checkout.

Tax calculation will be finalised during checkout.

Rent or Buy article

Get time limited or full article access on ReadCube.

from \$8.99

[Rent or Buy](#)

All prices are NET prices.

Additional access options:

- [Log in](#)
- [Access through your institution](#)

- [Learn about institutional subscriptions](#)

Fig. 1: IDR_s within chimeric transcription factor oncoproteins establish phase-separated assemblies, inducing leukaemogenesis.

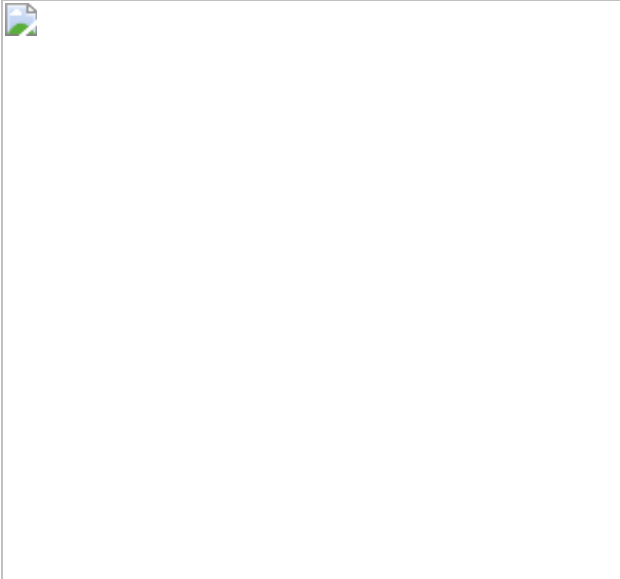


Fig. 2: Phase separation markedly enhances chromatin binding of NUP98–HOXA9, featured with broad, super-enhancer-like genomic occupancy.

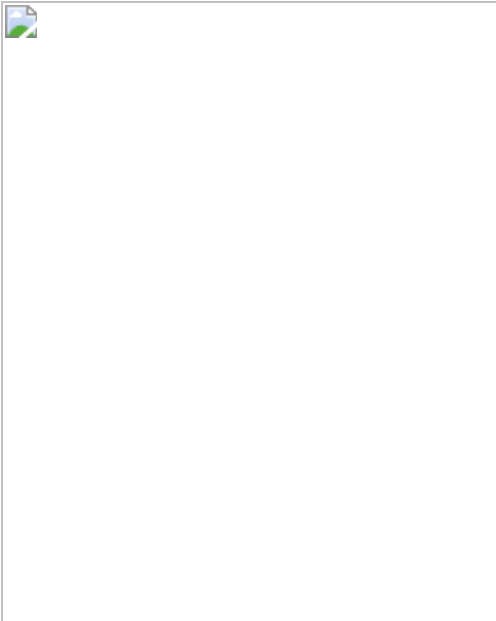
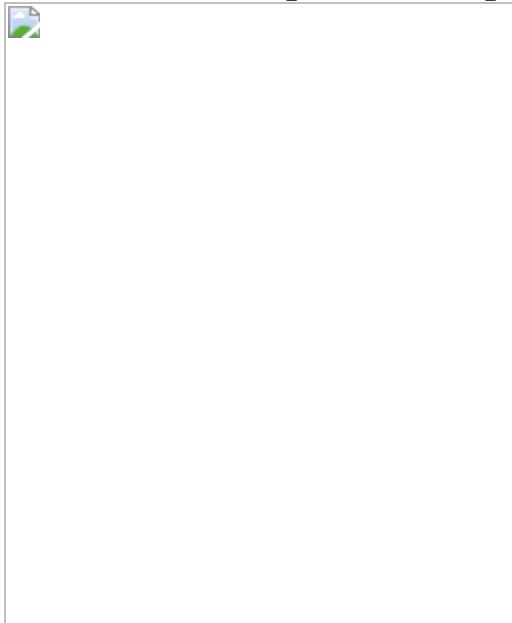


Fig. 3: Creation of an artificial F-IDR/A9 chimera and alteration of the FG-repeat valency in NUP98–HOXA9 demonstrate a role for IDR and LLPS in promoting target oncogene activation and cancerous transformation.



Fig. 4: Phase-separation-competent IDRs within NUP98–HOXA9 induce CTCF-independent looping at oncogenes.



Data availability

Next-generation sequencing datasets including those of ChIP–seq, RNA-seq and Hi-C used in this current study are deposited in the NCBI GEO under the accession number [GSE144643](#). The mass spectrometry-based proteomics data have been deposited to the ProteomeXchange Consortium via the PRIDE partner repository with the dataset identifier PXD023548 and 10.6019/PXD023548. [Source data](#) are provided with this paper.

Code availability

The scripts for genomic data analyses and all other data are available from the corresponding author upon request.

References

1. 1.

Gough, S. M., Slape, C. I. & Aplan, P. D. NUP98 gene fusions and hematopoietic malignancies: common themes and new biologic insights. *Blood* **118**, 6247–6257 (2011).

[CAS](#) [PubMed](#) [PubMed Central](#) [Article](#) [Google Scholar](#)

2. 2.

Mendes, A. & Fahrenkrog, B. NUP214 in leukemia: it's more than transport. *Cells* **8**, E76 (2019).

[PubMed](#) [Article](#) [CAS](#) [Google Scholar](#)

3. 3.

Murray, D. T. et al. Structure of FUS protein fibrils and its relevance to self-assembly and phase separation of low-complexity domains. *Cell* **171**, 615–627.e16 (2017).

[CAS](#) [PubMed](#) [PubMed Central](#) [Article](#) [Google Scholar](#)

4. 4.

Alberti, S. & Hyman, A. A. Biomolecular condensates at the nexus of cellular stress, protein aggregation disease and ageing. *Nat. Rev. Mol. Cell Biol.* **22**, 196–213 (2021).

[CAS](#) [PubMed](#) [Article](#) [Google Scholar](#)

5. 5.

Boija, A., Klein, I. A. & Young, R. A. Biomolecular condensates and cancer. *Cancer Cell* **39**, 174–192 (2021).

[CAS](#) [PubMed](#) [Article](#) [Google Scholar](#)

6. 6.

Wan, L. et al. Impaired cell fate through gain-of-function mutations in a chromatin reader. *Nature* **577**, 121–126 (2020).

[ADS](#) [CAS](#) [PubMed](#) [Article](#) [Google Scholar](#)

7. 7.

Kovar, H. Dr. Jekyll and Mr. Hyde: the two faces of the FUS/EWS/TAF15 protein family. *Sarcoma* **2011**, 837474 (2011).

[PubMed](#) [Article](#) [CAS](#) [Google Scholar](#)

8. 8.

Sabari, B. R. et al. Coactivator condensation at super-enhancers links phase separation and gene control. *Science* **361**, eaar3958 (2018).

[PubMed](#) [PubMed Central](#) [Article](#) [CAS](#) [Google Scholar](#)

9. 9.

Nair, S. J. et al. Phase separation of ligand-activated enhancers licenses cooperative chromosomal enhancer assembly. *Nat. Struct. Mol. Biol.* **26**, 193–203 (2019).

[CAS](#) [PubMed](#) [PubMed Central](#) [Article](#) [Google Scholar](#)

10. 10.

Chong, S. et al. Imaging dynamic and selective low-complexity domain interactions that control gene transcription. *Science* **361**, eaar2555 (2018).

[PubMed](#) [PubMed Central](#) [Article](#) [CAS](#) [Google Scholar](#)

11. 11.

Wang, G. G. et al. Haematopoietic malignancies caused by dysregulation of a chromatin-binding PHD finger. *Nature* **459**, 847–851 (2009).

[ADS](#) [CAS](#) [PubMed](#) [PubMed Central](#) [Article](#) [Google Scholar](#)

12. 12.

Jankovic, D. et al. Leukemogenic mechanisms and targets of a NUP98/HHEX fusion in acute myeloid leukemia. *Blood* **111**, 5672–5682 (2008).

[CAS](#) [PubMed](#) [Article](#) [Google Scholar](#)

13. 13.

Pak, C. W. et al. Sequence determinants of intracellular phase separation by complex coacervation of a disordered protein. *Mol. Cell* **63**, 72–85 (2016).

[CAS](#) [PubMed](#) [PubMed Central](#) [Article](#) [Google Scholar](#)

14. 14.

LaRonde-LeBlanc, N. A. & Wolberger, C. Structure of HoxA9 and Pbx1 bound to DNA: Hox hexapeptide and DNA recognition anterior to posterior. *Genes Dev.* **17**, 2060–2072 (2003).

[CAS](#) [PubMed](#) [PubMed Central](#) [Article](#) [Google Scholar](#)

15. 15.

Calvo, K. R., Sykes, D. B., Pasillas, M. & Kamps, M. P. Hoxa9 immortalizes a granulocyte-macrophage colony-stimulating factor-dependent promyelocyte capable of biphenotypic differentiation to neutrophils or macrophages, independent of enforced meis expression. *Mol. Cell. Biol.* **20**, 3274–3285 (2000).

[CAS](#) [PubMed](#) [PubMed Central](#) [Article](#) [Google Scholar](#)

16. 16.

Frey, S., Richter, R. P. & Görlich, D. FG-rich repeats of nuclear pore proteins form a three-dimensional meshwork with hydrogel-like properties. *Science* **314**, 815–817 (2006).

[ADS](#) [CAS](#) [PubMed](#) [Article](#) [Google Scholar](#)

17. 17.

Kasper, L. H. et al. CREB binding protein interacts with nucleoporin-specific FG repeats that activate transcription and mediate NUP98-HOXA9 oncogenicity. *Mol. Cell. Biol.* **19**, 764–776 (1999).

[CAS](#) [PubMed](#) [PubMed Central](#) [Article](#) [Google Scholar](#)

18. 18.

Xu, H. et al. NUP98 fusion proteins interact with the NSL and MLL1 complexes to drive leukemogenesis. *Cancer Cell* **30**, 863–878 (2016).

[CAS](#) [PubMed](#) [PubMed Central](#) [Article](#) [Google Scholar](#)

19. 19.

Kroon, E., Thorsteinsdottir, U., Mayotte, N., Nakamura, T. & Sauvageau, G. NUP98-HOXA9 expression in hemopoietic stem cells induces chronic and acute myeloid leukemias in mice. *EMBO J.* **20**, 350–361 (2001).

[CAS](#) [PubMed](#) [PubMed Central](#) [Article](#) [Google Scholar](#)

20. 20.

Wang, J. et al. A molecular grammar governing the driving forces for phase separation of prion-like RNA binding proteins. *Cell* **174**, 688–699.e16 (2018).

[CAS](#) [PubMed](#) [PubMed Central](#) [Article](#) [Google Scholar](#)

21. 21.

Qamar, S. et al. FUS phase separation is modulated by a molecular chaperone and methylation of arginine cation- π interactions. *Cell* **173**, 720–734.e15 (2018).

[CAS](#) [PubMed](#) [PubMed Central](#) [Article](#) [Google Scholar](#)

22. 22.

Hansen, A. S. et al. Robust model-based analysis of single-particle tracking experiments with Spot-On. *eLife* **7**, e33125 (2018).

[PubMed](#) [PubMed Central](#) [Article](#) [Google Scholar](#)

23. 23.

Strom, A. R. et al. Phase separation drives heterochromatin domain formation. *Nature* **547**, 241–245 (2017).

[ADS](#) [CAS](#) [PubMed](#) [PubMed Central](#) [Article](#) [Google Scholar](#)

24. 24.

Wang, L. et al. Histone modifications regulate chromatin compartmentalization by contributing to a phase separation mechanism. *Mol. Cell* **76**, 646–659.e6 (2019).

[CAS](#) [PubMed](#) [Article](#) [Google Scholar](#)

25. 25.

Gibson, B. A. et al. Organization of chromatin by intrinsic and regulated phase separation. *Cell* **179**, 470–484.e21 (2019).

[CAS](#) [PubMed](#) [PubMed Central](#) [Article](#) [Google Scholar](#)

26. 26.

Shin, Y. et al. Liquid nuclear condensates mechanically sense and restructure the genome. *Cell* **175**, 1481–1491.e13 (2018).

[CAS](#) [PubMed](#) [PubMed Central](#) [Article](#) [Google Scholar](#)

27. 27.

Calvo, K. R., Sykes, D. B., Pasillas, M. P. & Kamps, M. P. Nup98-HoxA9 immortalizes myeloid progenitors, enforces expression of Hoxa9, Hoxa7 and Meis1, and alters cytokine-specific responses in a manner similar to that induced by retroviral co-expression of Hoxa9 and Meis1. *Oncogene* **21**, 4247–4256 (2002).

[CAS](#) [PubMed](#) [Article](#) [Google Scholar](#)

28. 28.

Fahrenkrog, B. et al. Expression of leukemia-associated Nup98 fusion proteins generates an aberrant nuclear envelope phenotype. *PLoS One* **11**, e0152321 (2016).

[PubMed](#) [PubMed Central](#) [Article](#) [CAS](#) [Google Scholar](#)

29. 29.

Yu, M. et al. A resource for cell line authentication, annotation and quality control. *Nature* **520**, 307–311 (2015).

[ADS](#) [CAS](#) [PubMed](#) [Article](#) [Google Scholar](#)

30. 30.

Xu, B. et al. Selective inhibition of EZH2 and EZH1 enzymatic activity by a small molecule suppresses MLL-rearranged leukemia. *Blood* **125**, 346–357 (2015).

[CAS](#) [PubMed](#) [PubMed Central](#) [Article](#) [Google Scholar](#)

31. 31.

Cai, L. et al. An H3K36 methylation-engaging Tudor motif of polycomb-like proteins mediates PRC2 complex targeting. *Mol. Cell* **49**, 571–582 (2013).

[CAS](#) [PubMed](#) [Article](#) [Google Scholar](#)

32. 32.

Wang, G. G., Cai, L., Pasillas, M. P. & Kamps, M. P. NUP98-NSD1 links H3K36 methylation to Hox-A gene activation and leukaemogenesis. *Nat. Cell Biol.* **9**, 804–812 (2007).

[CAS](#) [PubMed](#) [Article](#) [Google Scholar](#)

33. 33.

Chen, B.-C. et al. Lattice light-sheet microscopy: imaging molecules to embryos at high spatiotemporal resolution. *Science* **346**, 1257998 (2014).

[PubMed](#) [PubMed Central](#) [Article](#) [CAS](#) [Google Scholar](#)

34. 34.

Stauffer, W., Sheng, H. & Lim, H. N. EzColocalization: An ImageJ plugin for visualizing and measuring colocalization in cells and organisms. *Sci. Rep.* **8**, 15764 (2018).

[ADS](#) [PubMed](#) [PubMed Central](#) [Article](#) [CAS](#) [Google Scholar](#)

35. 35.

Wang, G. G. et al. Quantitative production of macrophages or neutrophils ex vivo using conditional Hoxb8. *Nat. Methods* **3**, 287–293 (2006).

[CAS](#) [PubMed](#) [Article](#) [Google Scholar](#)

36. 36.

Wang, G. G., Pasillas, M. P. & Kamps, M. P. Meis1 programs transcription of FLT3 and cancer stem cell character, using a mechanism that requires interaction with Pbx and a novel function of the Meis1 C-terminus. *Blood* **106**, 254–264 (2005).

[CAS](#) [PubMed](#) [PubMed Central](#) [Article](#) [Google Scholar](#)

37. 37.

Lu, R. et al. Epigenetic perturbations by Arg882-mutated dnmt3a potentiate aberrant stem cell gene-expression program and acute leukemia development. *Cancer Cell* **30**, 92–107 (2016).

[CAS](#) [PubMed](#) [PubMed Central](#) [Article](#) [Google Scholar](#)

38. 38.

Roux, K. J., Kim, D. I. & Burke, B. BioID: a screen for protein–protein interactions. *Curr. Protoc. Protein Sci.* **74**, 19.23.11–19.23.14 (2013).

[Article](#) [Google Scholar](#)

39. 39.

Roux, K. J., Kim, D. I., Burke, B. & May, D. G. BioID: a screen for protein–protein interactions. *Curr. Protoc Protein Sci.* **91**, 19.23.11–19.23.15 (2018).

[Article](#) [CAS](#) [Google Scholar](#)

40. 40.

Li, J. et al. ZMYND11-MBD1 induces leukemogenesis through hijacking NuA4/TIP60 acetyltransferase complex and a PWWP-mediated chromatin association mechanism. *Nat. Commun.* **12**, 1045 (2021).

[ADS](#) [CAS](#) [PubMed](#) [PubMed Central](#) [Article](#) [Google Scholar](#)

41. 41.

Nesvizhskii, A. I., Keller, A., Kolker, E. & Aebersold, R. A statistical model for identifying proteins by tandem mass spectrometry. *Anal. Chem.* **75**, 4646–4658 (2003).

[CAS](#) [PubMed](#) [Article](#) [Google Scholar](#)

42. 42.

Cai, L. et al. ZFX Mediates non-canonical oncogenic functions of the androgen receptor splice variant 7 in castrate-resistant prostate cancer. *Mol. Cell* **72**, 341–354 (2018).

[CAS](#) [PubMed](#) [PubMed Central](#) [Article](#) [Google Scholar](#)

43. 43.

Egan, B. et al. An alternative approach to ChIP-Seq normalization enables detection of genome-wide changes in histone H3 lysine 27 trimethylation upon ezh2 inhibition. *PLoS One* **11**, e0166438 (2016).

[PubMed](#) [PubMed Central](#) [Article](#) [CAS](#) [Google Scholar](#)

44. 44.

Dobin, A. et al. STAR: ultrafast universal RNA-seq aligner. *Bioinformatics* **29**, 15–21 (2013).

[CAS](#) [PubMed](#) [Article](#) [Google Scholar](#)

45. 45.

Zhang, Y. et al. Model-based analysis of ChIP-Seq (MACS). *Genome Biol.* **9**, R137 (2008).

[PubMed](#) [PubMed Central](#) [Article](#) [CAS](#) [Google Scholar](#)

46. 46.

Ramírez, F. et al. deepTools2: a next generation web server for deep-sequencing data analysis. *Nucleic Acids Res.* **44** (W1), W160–W165 (2016).

[PubMed](#) [PubMed Central](#) [Article](#) [CAS](#) [Google Scholar](#)

47. 47.

Lovén, J. et al. Selective inhibition of tumor oncogenes by disruption of super-enhancers. *Cell* **153**, 320–334 (2013).

[PubMed](#) [PubMed Central](#) [Article](#) [CAS](#) [Google Scholar](#)

48. 48.

Ren, Z. et al. PHF19 promotes multiple myeloma tumorigenicity through PRC2 activation and broad H3K27me3 domain formation. *Blood* **134**, 1176–1189 (2019).

[CAS](#) [PubMed](#) [PubMed Central](#) [Article](#) [Google Scholar](#)

49. 49.

Wang, K. et al. MapSplice: accurate mapping of RNA-seq reads for splice junction discovery. *Nucleic Acids Res.* **38**, e178 (2010).

[PubMed](#) [PubMed Central](#) [Article](#) [CAS](#) [Google Scholar](#)

50. 50.

Li, B. & Dewey, C. N. RSEM: accurate transcript quantification from RNA-Seq data with or without a reference genome. *BMC Bioinformatics* **12**, 323 (2011).

[CAS](#) [PubMed](#) [PubMed Central](#) [Article](#) [Google Scholar](#)

51. 51.

Anders, S. & Huber, W. Differential expression analysis for sequence count data. *Genome Biol.* **11**, R106 (2010).

[CAS](#) [PubMed](#) [PubMed Central](#) [Article](#) [Google Scholar](#)

52. 52.

Subramanian, A. et al. Gene set enrichment analysis: a knowledge-based approach for interpreting genome-wide expression profiles. *Proc. Natl Acad. Sci. USA* **102**, 15545–15550 (2005).

[ADS](#) [CAS](#) [PubMed](#) [PubMed Central](#) [Article](#) [Google Scholar](#)

53. 53.

Grimm, J. B. et al. A general method to improve fluorophores for live-cell and single-molecule microscopy. *Nat. Methods* **12**, 244–250, 3, 250 (2015).

[CAS](#) [PubMed](#) [PubMed Central](#) [Article](#) [Google Scholar](#)

54. 54.

Tinevez, J.-Y. et al. TrackMate: An open and extensible platform for single-particle tracking. *Methods* **115**, 80–90 (2017).

[CAS](#) [PubMed](#) [Article](#) [Google Scholar](#)

55. 55.

Virtanen, P. et al. SciPy 1.0: fundamental algorithms for scientific computing in Python. *Nat. Methods* **17**, 261–272 (2020).

[CAS](#) [PubMed](#) [PubMed Central](#) [Article](#) [Google Scholar](#)

56. 56.

Rao, S. S. P. et al. A 3D map of the human genome at kilobase resolution reveals principles of chromatin looping. *Cell* **159**, 1665–

1680 (2014).

[CAS](#) [PubMed](#) [PubMed Central](#) [Article](#) [Google Scholar](#)

57. 57.

Durand, N. C. et al. Juicer provides a one-click system for analyzing loop-resolution Hi-C experiments. *Cell Syst.* **3**, 95–98 (2016).

[CAS](#) [PubMed](#) [PubMed Central](#) [Article](#) [Google Scholar](#)

58. 58.

Knight, P. A. & Ruiz, D. A fast algorithm for matrix balancing. *IMA J. Numer. Anal.* **33**, 1029–1047 (2012).

[MathSciNet](#) [MATH](#) [Article](#) [Google Scholar](#)

59. 59.

Love, M. I., Huber, W. & Anders, S. Moderated estimation of fold change and dispersion for RNA-seq data with DESeq2. *Genome Biol.* **15**, 550 (2014).

[PubMed](#) [PubMed Central](#) [Article](#) [CAS](#) [Google Scholar](#)

60. 60.

Ren, Y., Seo, H.-S., Blobel, G. & Hoelz, A. Structural and functional analysis of the interaction between the nucleoporin Nup98 and the mRNA export factor Rae1. *Proc. Natl Acad. Sci. USA* **107**, 10406–10411 (2010).

[ADS](#) [CAS](#) [PubMed](#) [PubMed Central](#) [Article](#) [Google Scholar](#)

61. 61.

Yung, E. et al. Delineating domains and functions of NUP98 contributing to the leukemogenic activity of NUP98-HOX fusions.

Leuk. Res. **35**, 545–550 (2011).

[CAS](#) [PubMed](#) [Article](#) [Google Scholar](#)

[Download references](#)

Acknowledgements

We thank M. Kamps, B. Strahl, B. Fahrenkrog, J. Schwaller, J. van Deursen, J. Song and J. Hao for providing reagents used in the study and the Wang laboratory members and J. Bear for discussion and technical support. We thank J. Lippincott-Schwartz for help with lattice light sheet microscopy and J. Rowley and A. Gladfelter for discussion and input. We thank UNC for facilities, including Imaging Core, High-Throughput Sequencing Facility (HTSF), Bioinformatics Core, Flow Cytometry Core, Tissue Culture Facility and Animal Studies Core, for their professional assistance of this work. We thank S. Pattenden for use of the Covaris LE220 instrument which was provided by the North Carolina Biotechnology Center Institute Development Program grant 2017-IDG-1005. The cores affiliated to UNC Cancer Center are supported in part by the UNC Lineberger Comprehensive Cancer Center Core Support Grant P30-CA016086 and UNC Neuroscience Microscopy Core supported, in part, by funding from the NIH-NINDS Neuroscience Center Support Grant P30 NS045892 and the NIH-NICHD Intellectual and Developmental Disabilities Research Center Support Grant U54 HD079124. This work was supported by NIH grants (R01-CA215284 and R01-CA218600 to G.G.W.; R35-GM128645 to D.H.P.; DP2GM136653 to W.R.L.; P20GM121293, R24GM137786, R01CA236209, S10OD018445, and TL1TR003109 to A.J.T; R01HL148128 and R01HL153920 to D.Z.), a Kimmel Scholar Award (to G.G.W.), Gabrielle's Angel Foundation for Cancer Research (to G.G.W.), Gilead Sciences Research Scholars Program in haematology/oncology (to G.G.W.), When Everyone Survives (WES) Leukemia Research Foundation (to G.G.W.) and UNC Lineberger Stimulus Awards (to D.H.P. and to L.C.). E.S.D. was supported by the NIH-NIGMS training grant T32-GM067553. W.R.L. is a Searle Scholar, a Beckman Foundation Young Investigator, and a Packard Fellow for Science and Engineering. G.G.W. is an American Cancer Society (ACS) Research

Scholar, an American Society of Hematology (ASH) Scholar in basic science, and a Leukemia and Lymphoma Society (LLS) Scholar.

Author information

Author notes

1. These authors jointly supervised this work: Douglas H. Phanstiel, Gang Greg Wang

Affiliations

1. Lineberger Comprehensive Cancer Center, University of North Carolina at Chapel Hill School of Medicine, Chapel Hill, NC, USA
Jeong Hyun Ahn, Shuai Zhao, Hidetaka Uryu, Jie Li, Yi-Hsuan Tsai, Ling Cai, Douglas H. Phanstiel & Gang Greg Wang
2. Department of Biochemistry and Biophysics, University of North Carolina at Chapel Hill School of Medicine, Chapel Hill, NC, USA
Jeong Hyun Ahn, Shuai Zhao, Hidetaka Uryu, Ling Cai & Gang Greg Wang
3. Curriculum in Bioinformatics and Computational Biology, University of North Carolina at Chapel Hill, Chapel Hill, NC, USA
Eric S. Davis & Douglas H. Phanstiel
4. Department of Pharmacology, University of North Carolina at Chapel Hill School of Medicine, Chapel Hill, NC, USA
Timothy A. Daugird, Wesley R. Legant & Gang Greg Wang
5. Thurston Arthritis Research Center, University of North Carolina at Chapel Hill, Chapel Hill, NC, USA
Ivana Yoseli Quiroga & Douglas H. Phanstiel

6. Curriculum in Genetics and Molecular Biology, University of North Carolina at Chapel Hill, Chapel Hill, NC, USA

Jie Li & Gang Greg Wang

7. Department of Biochemistry and Molecular Biology, University of Arkansas for Medical Sciences, Little Rock, AR, USA

Aaron J. Storey, Samuel G. Mackintosh, Ricky D. Edmondson, Stephanie D. Byrum & Alan J. Tackett

8. UNC Neuroscience Center and Carolina Institute for Developmental Disabilities, University of North Carolina at Chapel Hill, Chapel Hill, NC, 27599, USA

Daniel P. Keeley

9. Department of Genetics, University of North Carolina at Chapel Hill School of Medicine, Chapel Hill, NC, USA

Ling Cai

10. Departments of Genetics, Neurology, and Neuroscience, Albert Einstein College of Medicine, Bronx, NY, USA

Deyou Zheng

11. Joint Department of Biomedical Engineering, University of North Carolina, Chapel Hill, and North Carolina State University, Raleigh, NC, USA

Wesley R. Legant

12. Department of Cell Biology and Physiology, University of North Carolina at Chapel Hill School of Medicine, Chapel Hill, NC, USA

Douglas H. Phanstiel

Authors

1. Jeong Hyun Ahn
[View author publications](#)

You can also search for this author in [PubMed](#) [Google Scholar](#)

2. Eric S. Davis
[View author publications](#)

You can also search for this author in [PubMed](#) [Google Scholar](#)

3. Timothy A. Daugird
[View author publications](#)

You can also search for this author in [PubMed](#) [Google Scholar](#)

4. Shuai Zhao
[View author publications](#)

You can also search for this author in [PubMed](#) [Google Scholar](#)

5. Ivana Yoseli Quiroga
[View author publications](#)

You can also search for this author in [PubMed](#) [Google Scholar](#)

6. Hidetaka Uryu
[View author publications](#)

You can also search for this author in [PubMed](#) [Google Scholar](#)

7. Jie Li
[View author publications](#)

You can also search for this author in [PubMed](#) [Google Scholar](#)

8. Aaron J. Storey
[View author publications](#)

You can also search for this author in [PubMed](#) [Google Scholar](#)

9. Yi-Hsuan Tsai

[View author publications](#)

You can also search for this author in [PubMed](#) [Google Scholar](#)

10. Daniel P. Keeley

[View author publications](#)

You can also search for this author in [PubMed](#) [Google Scholar](#)

11. Samuel G. Mackintosh

[View author publications](#)

You can also search for this author in [PubMed](#) [Google Scholar](#)

12. Ricky D. Edmondson

[View author publications](#)

You can also search for this author in [PubMed](#) [Google Scholar](#)

13. Stephanie D. Byrum

[View author publications](#)

You can also search for this author in [PubMed](#) [Google Scholar](#)

14. Ling Cai

[View author publications](#)

You can also search for this author in [PubMed](#) [Google Scholar](#)

15. Alan J. Tackett

[View author publications](#)

You can also search for this author in [PubMed](#) [Google Scholar](#)

16. Deyou Zheng

[View author publications](#)

You can also search for this author in [PubMed](#) [Google Scholar](#)

17. Wesley R. Legant

[View author publications](#)

You can also search for this author in [PubMed](#) [Google Scholar](#)

18. Douglas H. Phanstiel

[View author publications](#)

You can also search for this author in [PubMed](#) [Google Scholar](#)

19. Gang Greg Wang

[View author publications](#)

You can also search for this author in [PubMed](#) [Google Scholar](#)

Contributions

J.H.A. designed the research, performed experiments, interpreted data and wrote the manuscript. J.H.A., Y-H. T., H.U., J. L., L. C., D.Z. and G.G.W. performed genomic data analysis. J.H.A. and S.Z. performed in vitro phase separation assays. D.P.K. conducted imaging quantification analysis. A.J.S., S.G.M., R.D.E. and S.D.B. performed proteomic analysis under the supervision of A.J.T. T.A.D. and J.H.A. performed single molecule tracking studies under the supervision of W.R.L. J.H.A. and J.L. performed murine leukaemia assays. E.S.D., I.Y.Q. and J.H.A. performed Hi-C mapping, data analysis and interpretation under the supervision of D.H.P. G.G.W. conceived the idea, supervised and designed the research, interpreted data, and wrote the manuscript with the inputs from all authors.

Corresponding authors

Correspondence to [Douglas H. Phanstiel](#) or [Gang Greg Wang](#).

Ethics declarations

Competing interests

The authors declare no competing interests.

Additional information

Peer review information *Nature* thanks Ari Melnick, Tanja Mittag and the other, anonymous, reviewer(s) for their contribution to the peer review of this work.

Publisher's note Springer Nature remains neutral with regard to jurisdictional claims in published maps and institutional affiliations.

Extended data figures and tables

[Extended Data Fig. 1 IDR retained within the leukaemia-related NUP98–HOXA9 chimera forms phase-separated condensates in vitro and is essential for establishing phase-separated chimeric transcription factor assemblies in the nucleus.](#)

a, Schematic showing the domain architecture of normal NUP98 (top), normal HOXA9 (middle) and leukaemic NUP98–HOXA9 chimera (bottom; with either GFP or 3×HA–3×Flag tag fused to C terminus). The GLFG or non-GLFG (xFG) motif contents, which make up IDR, and other important domains are shown. GLEBS represents the GLE2-binding sequence, which directs the NUP98 interaction with GLE2 (also known as RAE1) for mRNA export when NUP98 acts as component of nuclear pore complex⁶⁰. Red arrows indicate the common breakage point of NUP98 and HOXA9. **b**, Immunoblotting of NUP98–HOXA9, either full-length (WT) or with GLEBS deleted (Δ132–224; see **a**), as detected by the indicated antibodies after stable transduction into primary mouse HSPCs. For gel source data, see Supplementary Fig. 1. **c**, Mouse HSPCs stably transduced with wild-type or GLEBS-deleted NUP98–HOXA9 showed similar proliferation in liquid cultures ($n = 3$ independent cell cultures per group), in agreement to previous reports^{17,61}. Empty vector (EV)-infected HSPCs served as a control. Data are mean ± s.d. **d**, Live-cell fluorescence imaging (GFP; with

zoomed-in and zoomed-out views shown in the top and bottom panels, respectively) of 293FT cells with stable transduction of GFP-tagged NUP98–HOXA9, wild-type, GLEBS-deleted (also referred to as N-IDR_{WT}/A9; see Fig. [1a](#)) or carrying a DNA-binding-defective mutation in homeodomain (HD_{N51S}) or a Phe-to-Ser mutation that substitutes Phe residues within all FG repeats to Ser (IDR_{FS}, also referred to as N-IDR_{FS}/A9; see Fig. [1a](#)). The right panel shows immunoblotting of endogenous normal NUP98 in 293FT cells, as well as the stably transduced exogenous NUP98–HOXA9, either wild-type (lane 1) or GLEBS-deleted (lane 2), as detected by antibodies against GLEBS of NUP98^{[17](#)}. For gel source data, see Supplementary Fig. [1](#). Scale bars, 10 μm. **e**, Schematic of the indicated N-IDR fusion domains with a varying number of FG repeats. The IDR portion used for in vitro assay in main Fig. [1d](#) is indicated by a red dotted line. **f**, SDS–PAGE images showing recombinant N-IDR domain protein with the indicated varying number of FG repeats (His6[×]-tagged; see **e**), purified with Ni-column and an additional size exclusion column purification step. The protein size is labelled above the recombinant protein. **g**, Anti-GFP immunoblotting for GFP-tagged NUP98–HOXA9 chimera with the indicated varying number of FG repeats described in **e** after stable transduction in 293FT cells. For gel source data, see Supplementary Fig. [1](#). **h**, Live-cell fluorescence imaging for the N51S-mutated N-IDR/A9 (GFP-tagged) with either wild-type (top) or the Phe-to-Ser mutated IDR (bottom) in 293FT stable expression lines before (left) and after (right) treatment with 10% 1,6-hexanediol for 1 min. The left panels show zoomed-in images of a representative cell from the right panels of zoomed-out cell images. Scale bar, 10 μm.

Extended Data Fig. 2 IDR contained within chimeric transcription factor is required for leukaemic transformation of primary mouse HSPCs.

a, b, Immunoblotting (**a**) and fixed cell immunostaining (**b**; anti-Flag) of the LLPS-competent N-IDR_{WT}/A9 and LLPS-incompetent N-IDR_{FS}/A9 after stable transduction in 293FT cells. The left panel of **b** shows a zoomed-in view on the right panel. Scale bars, 10 μm. For gel source data, see Supplementary Fig. [1](#). **c**, Venn diagram shows significant overlap

between the N-IDR_{WT}/A9 and N-IDR_{FS}/A9 interactomes as detected by BioID, with the cut-off value set as the log₂-transformed fold change value above 2 compared with control. Examples of the detected interacting proteins are shown below. **d–f**, Immunostaining (**d**; anti-GFP), Wright–Giemsa staining (**e**) and FACS with the indicated surface markers (**f**) using mouse HSPCs 1 month after transduction of N-IDR_{WT}/A9 (GFP or 3×HA-3×Flag-tagged), which revealed a typical acute myeloid leukaemia phenotype (cKit⁺, CD34+, Mac1^{high}, CD19[−], B220[−]). The insert in **d** shows a zoomed-in view of the representative cell. Scale bars, 5 μm. For FACS gating strategy, see Supplementary Fig. 1. **g**, H&E-stained spleen section images for the indicated cohort at 10 × magnification. White pulp (WP) is outlined with white line for the sample from mice transplanted with empty vector-infected HSPCs (top). Note that clear demarcation between white pulp and red pulp (RP), as observed in cohorts receiving either empty vector or the mutant forms of fusion (bottom), is lost in those with N-IDR_{WT}/A9 and F-IDR_{WT}/A9 (middle) due to an excessive expansion of transformed leukaemia cells that infiltrated into spleen, leading to splenomegaly observed in **i** and Fig. 1k. **h**, Live-cell fluorescence (GFP) imaging of 293FT cells with stable expression of an artificial HOXA9 chimera created by replacing the NUP98 FG repeats with an unrelated IDR of the RNA-binding protein FUS, either wild-type or Tyr-to-Ser mutated (hereafter referred to as the F-IDR_{WT}/A9 and F-IDR_{YS}/A9 fusion, respectively; see Fig. 1a), before and after treatment with 10% 1,6-hexanediol for 1 min. Scale bar, 10 μm. **i**, Representative image of spleen from mice 7 months after transplantation of mouse HPSCs stably transduced with either F-IDR_{WT}/A9 (left) or F-IDR_{YS}/A9 (right).

Extended Data Fig. 3 ChIP-seq reveals binding patterns of NUP98–HOXA9 that carries either wild-type or an Phe-to-Ser mutated IDR.

- a**, Summary of the counts of ChIP-seq read tags for the indicated samples.
- b**, Scatterplots showing correlation of global N-IDR_{WT}/A9 (left) or N-IDR_{FS}/A9 (right) ChIP-seq signals using either HA (*x* axis) or GFP (*y* axis) antibodies in two biological replicates of 293FT stable cells. Coefficient of

determination (R^2) is determined by Pearson correlation. **c**, Total number of the called HA ChIP-seq peaks in stable 293FT cell lines expressing HA-tagged N-IDR_{WT}/A9 (left) or N-IDR_{FS}/A9 (middle) or empty vector control (right). **d, e**, Pie chart showing distribution of the indicated annotation feature among the called N-IDR_{WT}/A9 (**d**) or N-IDR_{FS}/A9 (**e**) ChIP-seq peaks in 293FT stable expression cells. **f, g**, Summary of the most enriched motifs identified within the called N-IDR_{WT}/A9 (**f**) or N-IDR_{FS}/A9 (**g**) ChIP-seq peaks in 293FT stable expression cells. Motif enrichment was statistically determined by ZOOPS scoring (zero or one occurrence per sequence) coupled with the hypergeometric enrichment calculations. **h**, Gene Ontology analysis of genes associated with broad super-enhancer-like peaks of N-IDR_{WT}/A9 as identified in 293FT stable cells. *P* values were determined by Fisher's exact test.

Extended Data Fig. 4 Enhanced chromatin occupancy, as well as a broad super-enhancer-like binding pattern typically seen at leukaemia-related genomic loci, is characteristic for the LLPS-competent NUP98–HOXA9 (N-IDR_{WT}/A9) and not its LLPS-incompetent IDR mutant (N-IDR_{FS}/A9).

a–e, Integrative genomics viewer (IGV) views for the indicated ChIP-seq signal at the well-known leukaemia-associated loci such as the *HOXA* (**a**), *HOXB* (**b**) and *HOXD* (**c**) gene clusters, *MEIS1* (**d**) and *MEIS2* (**e**). Samples from top to bottom are HA (tracks 1–3) and H3K27ac (tracks 4–6) ChIP-seq signals in the 293FT cells stably expressed with either empty vector (tracks 1 and 4; EV in track 1 acts as a negative control for HA ChIP) or the HA-tagged N-IDR_{WT}/A9 (tracks 2 and 5) or N-IDR_{FS}/A9 (tracks 3 and 6), GFP ChIP-seq signals (tracks 7–12) in the 293FT cells stably expressed with GFP-tagged N-IDR_{WT}/A9 (tracks 7–8 represent samples after treatment with vehicle or 10% 1,6-hexanediol, respectively, for 1 min), N-IDR_{FS}/A9 (tracks 9–10 represent samples after treatment with vehicle or 1,6-hexanediol, respectively), F-IDR_{WT}/A9 (track 11) or F-IDR_{YS}/A9 (track 12), as well as CTCF ChIP-seq in 293FT cells with N-IDR_{WT}/A9 (track 13) or N-IDR_{FS}/A9 (track 14). HA and CTCF ChIP-seq signals were

normalized to input signals, whereas GFP ChIP-seq, conducted in the spike-in controlled experiments, normalized to the spike-in *Drosophila* chromatin signals (those from antibody of a *Drosophila*-specific histone, H2Av).

Extended Data Fig. 5 Formation of the enhanced and broad super-enhancer-like binding patterns of leukaemia-related chimera transcription factors requires an intact phase-separation-competent IDR.

a, b, Hockey-stick plot shows distribution of the input-normalized ChIP-seq signals of N-IDR_{WT}/A9 (**a**) or H3K27ac (**b**) across all enhancers annotated by H3K27ac peaks (transcriptional start site \pm 2.5 kb regions were excluded) in 293FT cells. Dotted line indicates the threshold level set by the ROSE algorithm to call super-enhancers. Relative rankings of super-enhancers associated with some example genes are shown. **c**, Venn diagram illustrates overlap among super-enhancers called based on N-IDR_{WT}/A9 and H3K27ac ChIP-seq signals. **d, e**, Box plots showing averaged ChIP-seq signals for *k*-means clustered peaks (see Fig. [2b](#)) of the LLPS-competent N-IDR_{WT}/A9 (WT; **d**) show a marked reduction in binding after treatment of 293FT stable cells with 1,6-hexanediol (WT+H), relative to treatment with vehicle control (WT+V); this reduction is particularly significant for peak clusters 1–3 shown in Fig. [2b](#). By contrast, genomic binding of N-IDR_{FS}/A9 (FS; **e**) shows general insensitivity to the same treatment of 1,6-hexanediol (FS+H) in comparison to mock (FS+V). Right, averaged ChIP-seq signal distribution profiles are shown for N-IDR_{WT}/A9 and N-IDR_{FS}/A9 over a 10-kb region in the indicated peak cluster as an example. Box plots as defined in Fig. [3f](#). **f**, Venn diagram to compare genes associated with the broad super-enhancer-like peaks of N-IDR_{WT}/A9 after treatment with 1,6-hexanediol (+H), relative to vehicle control (+V), after treatment for 1 min. **g**, Hierarchical clustered heat maps for the pairwise correlation of ChIP-seq signals between each of the indicated sample. The coefficients were determined by Pearson correlation. HA and GFP represent ChIP-seq for HA-tagged and GFP-tagged chimera transcription factors, respectively.

Extended Data Fig. 6 The phase-separation-promoting property within F-IDR is sufficient to induce the enhanced binding of the chimeric transcription factor.

a, Heat maps showing the k -mean clustering of ChIP-seq signals for chimeric transcription factors that contain the NUP98 IDR (N-IDR_{WT}/A9 and N-IDR_{FS}/A9, two panels on the left) or FUS IDR (F-IDR_{WT}/A9 and F-IDR_{YS}/A9, two panels on the right) reveal a similarly enhanced binding for the LLPS-competent chimera that carries a wild-type form of IDR, relative to its LLPS-incompetent IDR mutant, in 293FT stable expression cells. Note that, although to a lesser degree, the artificially created F-IDR_{WT}/A9 fusion also displays a broad, super-enhancer-like binding pattern at the same sites observed with the N-IDR_{WT}/A9 fusion. **b**, Pie chart showing percentage distribution of the indicated genomic annotation feature among the ChIP-seq peaks of GFP-tagged F-IDR_{WT}/A9 (left) or F-IDR_{YS}/A9 (right) in the 293FT stable expression cells. **c**, Heat maps (left) and its averaged ChIP-seq signal distribution profiles (right) for k -mean clustered peaks of N-IDR_{WT}/A9 in the transformed mouse HPSCs. **d**, Venn diagram showing overlap between the annotated genes associated with the clusters 1–3 of N-IDR_{WT}/A9 ChIP-seq peaks detected in the transformed mouse HPSCs (left) and the 293FT stable expression cells (right). Examples of the shared oncogenes are shown below. **e**, IGV views of N-IDR_{WT}/A9 ChIP-seq signals (GFP-tagged) at the indicated loci in mouse HSPCs transformed by this chimera. **f**, ChIP-qPCR to assess the binding of GFP-tagged N-IDR_{WT}/A9 or N-IDR_{FS}/A9 at *CCL15* (a negative control region), *PBX3* and *HOXA9* in the 293FT stable cells after treatment with 10% 1,6-hexanediol for 1 min (+H), relative to mock (+V). ChIP signals, normalized to those of input, are presented as mean \pm s.d. of three replicate experiments. **g**, ChIP-qPCR to assess the binding of GFP-tagged F-IDR_{WT}/A9 or F-IDR_{YS}/A9 at *CCL15* (a negative control region), *PBX3* and *HOXA9* in the 293FT stable cells. ChIP signals, normalized to those of input, are presented as mean \pm s.d. of three replicates.

[Source data](#)

Extended Data Fig. 7 Single-molecule tracking shows that phase-separation-competent N-IDR_{WT}/A9 proteins behave with less dynamic characteristics, compared with phase-separation-incompetent N-IDR_{FS}/A9.

a, Representative images of single-molecule particles identification in an N-IDR_{WT}/A9-expressing cell, either the original captured image (left) or after processing to remove background (right). Scale bars, 5 μ m. **b, c**, Single-particle tracks for mean speed (**b**) and mean displacement (**c**) of either N-IDR_{WT}/A9 or N-IDR_{FS}/A9 single molecules within the temporally registered reference frame binned into 1-s intervals. **d, e**, Displacement (**d**) and mean velocity (**e**) of single-particle tracks indicate that N-IDR_{WT}/A9 with the LLPS-competent IDR (WT) is less mobile and navigates nuclear space at a slower rate than its LLPS-incompetent IDR mutant (FS). Dots indicate mean values in a single cell. Line indicates one standard deviation. *P* values determined by two-sided *t*-test. **f, g**, The diffusion coefficient for chromatin-bound (**f**) and freely diffusing states (**g**) of N-IDR_{WT}/A9 or N-IDR_{FS}/A9, calculated based on single-molecule tracking studies of its 293FT stable expression cells. *P* values determined by two-sided *t*-test.

Extended Data Fig. 8 An LLPS-competent IDR within the leukaemia-related transcription factor chimera is essential for potentiating transcriptional activation of the downstream oncogenic gene-expression program.

a, Fixed cell immunostaining for the 3 \times HA-3 \times Flag-tagged N-IDR_{WT}/A9 (left; anti-Flag) and the indicated histone modification (middle) in the 293FT stable expression cells. Top panels show the enlarged images of an example region within the white dotted box shown in the bottom panels, in which the transcription factor chimera is co-localized with H3K27ac (top) and not H3K9me3 (bottom). Scale bars, 10 μ m. **b**, Pearson's correlation coefficient values between N-IDR_{WT}/A9 and the indicated histone modification. The red dotted line indicates the calculated average value of each plot. The calculated means (red dotted lines) were compared with an

independent two-tailed Student's *t*-test. n, the number of cells analysed. **c**, RT-qPCR to assess the effect of phase separation in target gene expression in 293FT cells. All of the tested *HOX* and *MEIS2* genes are direct targets of both N-IDR_{WT}/A9 and N-IDR_{FS}/A9 based on ChIP-seq, whereas *MYC* is not and serves as a negative control. Note that LLPS-competent N-IDR_{WT}/A9 induces significantly more upregulation of target genes, relative to LLPS-incompetent N-IDR_{FS}/A9. PCR signals were normalized first to those of an internal control (18S RNA) and then to vector-expressing cells and presented as mean \pm s.d. of three replicated experiments. ****P* < 0.001; *****P* < 0.0001; two-sided *t*-test. n.s., not significant. **d**, Heat map illustrating relative expression of the 374 genes that show significant upregulation post-transduction of F-IDR_{WT}/A9, compared to empty vector and its IDR-mutant form (F-IDR_{YS}/A9), in 293FT stable expression cells. **e**, Venn diagrams showing the overlap of the significantly downregulated genes identified 7 days after transduction of the indicated construct into mouse HPSCs. **f**, Gene set enrichment analysis (GSEA) shows that, compared with that of N-IDR_{FS}/A9, the expression N-IDR_{WT}/A9 in mouse HPSCs is positively correlated with the indicated leukaemia- or HSPC-related gene sets (top) and negatively correlated with the indicated differentiation-related gene sets (bottom). The *P* value was calculated by an empirical phenotype-based permutation test; the false discovery rate (*q*) is adjusted for gene set size and several hypotheses testing whereas the *P* value is not. **g**, Venn diagrams showing the overlap of the significantly upregulated (left) or downregulated (right) genes identified after transduction of the indicated construct into mouse HPSCs.

Source data

Extended Data Fig. 9 Hi-C mapping reveals that a phase-separation-competent IDR within NUP98–HOXA9 is required to induce formation of CTCF-independent chromatin loops at the leukaemia-related genomic loci.

a, Matrix of Pearson correlation coefficients of loop counts among and between biological replicates of N-IDR_{WT}/A9 (WT; *n* = 4 replicates) or N-

IDR_{FS}/A9 (FS; $n = 4$ replicates) conditions. Numbers following WT or FS indicate biological replicate for that condition. **b**, Example correlation plots of loop counts between biological replicates and conditions. **c**, All loops were partitioned into either WT- or FS-specific loops and split into separate loop anchors. Loop anchors were then intersected with ChIP-seq peaks of N-IDR/A9 or CTCF. The percentage of observed (Obs.) overlaps for each feature is shown as a vertical blue line. The red line shows the expected (Exp.) distribution of overlaps as determined by randomly sampling loop anchors and calculating the overlap of each feature 1,000 times. P values were determined by summing the number of expected values greater than (or less than if the observed value was less than the mean) the observed value for that feature. **d–g**, 3C-qPCR assays measuring the change in crosslinking frequency of either an N-IDR_{WT}/A9-specific loop at the *PBX3* locus (**d**, **e**) or a CTCF-dependent loop (**f**, **g**; at Chr17 (41604677–41883642)) after treatment of 293FT stable cells with 10% 1,6-hexanediol for 1 min (+H), relative to mock (+V). The IGV view panels at **d** and **f** show the indicated ChIP-seq signals, with positions of the used 3C-PCR primers labelled under IGV tracks. PCR was performed using the same constant forward primer (C) paired with a differently numbered reverse primer (P1 to P4) at each locus tested. Panels **e** and **g** are plotted with signals of 3C-qPCR measuring the relative crosslinking frequency at *PBX3* (**d**, **e**) or a Chr17 locus with CTCF loop (**f**, **g**) before (V) and after (H) treatment with 1,6-hexanediol. Signals in **e** are normalized to those of the N-IDR_{FS}/A9-expressing cells ($n = 3$ replicated experiments). P values were determined by two-sided *t*-test. Data are mean \pm s.d. of three or six replicates.

[Source data](#)

[**Extended Data Fig. 10 Hi-C mapping reveals the chromatin loops specific to cells with the LLPS-competent NUP98-HOXA9, compared with the LLPS-competent mutant, at leukaemia-relevant gene loci.**](#)

Views for Hi-C mapping, RNA-seq and ChIP-seq for CTCF, N-IDR/A9 and H3K27ac at the *HOXB* (**a**), *EYA4* (**b**), and *SKAP2-HOXA* loci (**c**) in

293FT stable cells expressing either N-IDR_{WT}/A9 (WT) or N-IDR_{FS}/A9 (FS). Hi-C mapping views (top) show results from the N-IDR_{WT}/A9 or N-IDR_{FS}/A9 expressing cells (bottom and top diagonal, respectively). Corresponding ChIP-seq and gene tracks are shown below each Hi-C plot. N-IDR_{WT}/A9 loops are indicated by red arrows.

Extended Data Fig. 11 Model illustrating requirement of LLPS-competent IDR within NUP98–HOXA9 for leukaemogenesis and activation of the oncogenic gene-expression program.

The LLPS-competent IDR contained with NUP98–HOXA9 is crucial for promoting long-distance chromatin looping between proto-oncogene promoter and enhancers, which thus induces an oncogenic gene-expression program and malignant development.

Supplementary information

Supplementary Information

This file contains the Supplementary Discussion, Supplementary references and Supplementary Figures 1-2 (the gel source data and FACS gating strategy).

Reporting Summary

Supplementary Table 1

List of protein partners associated with either N-IDR_{WT}/A9 or N-IDR_{FS}/A9 in 293 cells as detected by the BioID approach.

Supplementary Table 2

List of the broad ChIP-seq peaks of N-IDR_{WT}/A9 in 293 stable cells after treatment with 10% of 1,6-hexanediol, relative to mock, for one minute, as

well as H3K27ac and N-IDR_{WT}/A9 associated super-enhancers defined by ROSE.

Supplementary Table 3

List of genes directly bound by N-IDR_{WT}/A9 (HA- or GFP-tagged) and F-IDR_{WT}/A9 in 293 stable cells as detected by ChIP-seq.

Supplementary Table 4

RNA-seq reveals transcripts showing the significant expression changes post-transduction of N-IDR_{WT}/A9, in comparison to empty vector (EV) or N-IDR_{FS}/A9, in 293 stable expression cells.

Supplementary Table 5

RNA-seq reveals transcripts showing significant expression changes post-transduction of F-IDR_{WT}/A9, in comparison to EV or F-IDR_{YS}/A9, in 293 stable expression cells.

Supplementary Table 6

RNA-seq reveals transcripts showing significant expression changes post-transduction of N-IDR_{WT}/A9, in comparison to EV or N-IDR_{FS}/A9, into primary murine HSPC cells.

Supplementary Table 7

RNA-seq reveals transcripts showing significant expression changes post-transduction of F-IDR_{WT}/A9, in comparison to EV, into primary murine HSPC cells.

Supplementary Table 8

List of reagents (such as plasmid, primers and antibodies) used in this study.

Video 1

Live cell imaging readily detects the fusion events of aggregates formed by GFP-tagged N-IDR_{WT}/A9_{N51S} upon its induced expression in the HeLa stable cell line. Each frame represents 24 seconds. This video is rendered at 10 frames per second. Example screen shots illustrating fusion events observed in this video are presented in Fig. 1h.

Source data

[Source Data Fig. 3](#)

[Source Data Extended Data Fig. 6](#)

[Source Data Extended Data Fig. 8](#)

[Source Data Extended Data Fig. 9](#)

Rights and permissions

[Reprints and Permissions](#)

About this article



Check for
updates

Cite this article

Ahn, J.H., Davis, E.S., Daugird, T.A. *et al.* Phase separation drives aberrant chromatin looping and cancer development. *Nature* **595**, 591–595 (2021).
<https://doi.org/10.1038/s41586-021-03662-5>

Download citation

- Received: 17 January 2020
- Accepted: 21 May 2021
- Published: 23 June 2021
- Issue Date: 22 July 2021
- DOI: <https://doi.org/10.1038/s41586-021-03662-5>

Further reading

- [**Fusion proteins form onco-condensates**](#)
 - Tanja Mittag
 - & Aseem Z. Ansari

Nature Structural & Molecular Biology (2021)

Comments

By submitting a comment you agree to abide by our [Terms](#) and [Community Guidelines](#). If you find something abusive or that does not comply with our terms or guidelines please flag it as inappropriate.

[Access through your institution](#)

[Change institution](#)

[Buy or subscribe](#)

Associated Content

[**Fusion proteins form onco-condensates**](#)

- Tanja Mittag
- Aseem Z. Ansari

Oncogenesis by phase separation

- Grant Otto

Advertisement

This article was downloaded by **calibre** from <https://www.nature.com/articles/s41586-021-03662-5>

| [Section menu](#) | [Main menu](#) |

A condensate-hardening drug blocks RSV replication in vivo

[Download PDF](#)

- Article
- [Published: 07 July 2021](#)

A condensate-hardening drug blocks RSV replication in vivo

- [Jennifer Risco-Ballester](#)¹,
- [Marie Galloux](#)²,
- [Jingjing Cao](#)³,
- [Ronan Le Goffic](#) [ORCID: orcid.org/0000-0002-2012-0064](#)²,
- [Fortune Hontonnou](#)²,
- [Aude Jobart-Malfait](#)¹,
- [Aurore Desquesnes](#)¹,
- [Svenja M. Sake](#)⁴,
- [Sibylle Haid](#)⁴,
- [Miaomiao Du](#)³,
- [Xiumei Zhang](#)³,
- [Huanyun Zhang](#)³,
- [Zhaoguo Wang](#)⁵,
- [Vincent Rincheval](#)¹,
- [Youming Zhang](#)³,
- [Thomas Pietschmann](#) [ORCID: orcid.org/0000-0001-6789-4422](#)⁴,
- [Jean-François Eléouët](#) [ORCID: orcid.org/0000-0002-7361-4885](#)²,
- [Marie-Anne Rameix-Welti](#) [ORCID: orcid.org/0000-0002-5901-3856](#)^{1,6 na1} &
- [Ralf Altmeyer](#) [ORCID: orcid.org/0000-0003-2794-459X](#)^{3 na1 nAff7}

[Nature](#) volume 595, pages 596–599 (2021) [Cite this article](#)

- 14k Accesses
- 50 Altmetric
- [Metrics details](#)

Subjects

- [Antivirals](#)
- [Cellular imaging](#)
- [Small molecules](#)

Abstract

Biomolecular condensates have emerged as an important subcellular organizing principle¹. Replication of many viruses, including human respiratory syncytial virus (RSV), occurs in virus-induced compartments called inclusion bodies (IBs) or viroplasm^{2,3}. IBs of negative-strand RNA viruses were recently shown to be biomolecular condensates that form through phase separation^{4,5}. Here we report that the steroidal alkaloid cyclopamine and its chemical analogue A3E inhibit RSV replication by disorganizing and hardening IB condensates. The actions of cyclopamine and A3E were blocked by a point mutation in the RSV transcription factor M2-1. IB disorganization occurred within minutes, which suggests that these molecules directly act on the liquid properties of the IBs. A3E and cyclopamine inhibit RSV in the lungs of infected mice and are condensate-targeting drug-like small molecules that have in vivo activity. Our data show that condensate-hardening drugs may enable the pharmacological modulation of not only many previously undruggable targets in viral replication but also transcription factors at cancer-driving super-enhancers⁶.

[Download PDF](#)

Main

RSV is a major cause of respiratory illness in young children, the older people and individuals who are immunocompromised worldwide^{7,8}. Currently, multiple targets are pursued for the development of a safe and effective therapy to treat RSV infections⁹.

In infected cells, RSV induces the formation of cytoplasmic IBs, in which nucleoprotein (N), phosphoprotein (P), polymerase L, the transcription factor M2-1 and viral genomic RNA are concentrated. We recently demonstrated that IBs are ‘viral factories’ in which viral RNA synthesis occurs³. The morphology of IBs suggests that they are condensates formed by liquid–liquid phase separation (LLPS). A recent study showed that N and P were sufficient to drive the formation of pseudo-IB condensates through LLPS in vitro, both in cells and in biochemical assays¹⁰. However, these N–P pseudo-IB condensates are not functional, as they do not shelter RNA synthesis and do

not reflect the complexity of IBs in virus-infected cells, which have multiple compartments. Strikingly similar in size and phase organization to the nucleolus condensate¹¹, RSV IBs are multiphasic and contain a sub-compartment called the IB-associated granule (IBAG), which is composed of newly synthesized viral mRNA and M2-1^{3,12}. Condensates have emerged as an important subcellular organizing principle¹. An important question in anti-viral drug development—and medicinal chemistry more generally—is whether these condensates are druggable. In principle, a drug that dissolved or hardened would prevent viral replication. Neither mechanism has yet been reported.

Chemical analogues without hedgehog antagonism

We previously identified the hedgehog (HH) pathway antagonist cyclopamine (CPM) as a potent inhibitor of RSV replication¹³. Inhibition of Sonic hedgehog (SHH) signalling is an unwanted feature of CPM as an RSV inhibitor. On the basis of the binding model of the Smoothened (SMO) receptor–CPM ligand binary complex¹⁴ (Protein Data Bank (PDB) 4O9R) and data on chemical analogues with enhanced SMO binding and HH signalling antagonism activity¹⁵, we designed CPM analogues with a modified A-ring (Extended Data Fig. 1) in order to engineer-out inhibitory HH signalling activity. The A-ring 3'-hydroxyl group was replaced with methoxy (A3M), ethoxy (A3E) and propoxy (A3P) groups, all of which show greatly reduced SHH-mediated signalling (Fig. 1a and Extended Data Fig. 2). The 3' ring modification in A3E and A3P resulted in near-complete loss of the HH activity (half-maximal inhibitory concentration (IC_{50}) > 20 μ M in SHH reporter assays). A3E is more potent against RSV *in vitro* than A3P (A3E, $IC_{50} = 1.0 \pm 0.34 \mu$ M; A3P, $IC_{50} = 3 \pm 1 \mu$ M) (Extended Data Fig. 2b,d,f) and was selected for all further studies. In addition to RSV reference strains, A3E and CPM also inhibit minimally laboratory-experienced strains of RSV (Extended Data Fig. 3). Although the selectivity index of A3E was lower compared with CPM, it consistently ranged above 10. Future studies will need to identify whether chemical modifications can be made to the CPM scaffold that eliminate the SMO binding and HH signalling while maintaining or even improving RSV activity. Of note, the mechanism of RSV inhibition probably remains unchanged as the same of R151K substitution in M2-1 confers resistance to both A3E and CPM (Fig. 1a).

Fig. 1: A drug-like steroidal alkaloid derivative inhibits RSV replication and disrupts IB organization.



a, The potency of A3E and CPM was determined using RSV–Luc- and RSV–M2-1(R151K)–Luc-infected HEp-2 cells and SHH-induced Gli-dependent luciferase-reporter-expressing NIH3T3 cells. The results are expressed as mean \pm s.d. for a representative of three independent experiments performed in triplicate. IC₅₀ concentrations in μ M are indicated. **b**, RSV–M2-1–mGFP-infected HEp-2 cells treated with A3E or CPM for 1 h (see Extended Data Fig. 4). Representative images from four independent experiments are shown. Poly(A) RNA is shown in red and nuclei are shown in blue. Scale bar, 10 μ m. White arrowheads indicate IBs.

[Source data](#)

[Full size image](#)

Disorganization of IBs by A3E and CPM

Formation of IBAGs inside RSV viral factories depends on the de novo synthesis of viral mRNA, which recruits M2-1 and which was proposed to result from phase separation³. We used a recombinant RSV expressing a functional M2-1–mGFP fusion protein to analyse the effect of A3E and CPM on the subcellular localization of M2-1. In untreated cells, M2-1 homogenously distributed in the cytoplasm and concentrated in IBAGs as revealed by FISH (fluorescence in situ hybridization) poly(A)-RNA staining (Fig. 1b and Extended Data Fig. 4). By contrast, IBAGs were no longer visible in compound-treated cells and M2-1–mGFP together with poly(A) RNA was detected throughout the entire IB. Complete loss of the organization of IB and IBAGs was observed after a 1-h treatment with compounds at a concentration equivalent to

$0.5 \times$ the IC₉₀ (Extended Data Fig. 4). Time-lapse fluorescence imaging revealed that the loss of IB and IBAG partitioning occurred within minutes after the addition of A3E and CPM (Supplementary Videos 1–3). This suggests that both compounds abolished the phase separation between IBs and IBAGs that could be mediated by M2-1-mRNA complexes.

Condensate-hardening small molecules

We hypothesized that RSV viral factories are condensates formed by LLPS¹⁰. The dynamic nature of RSV IBs was shown in cells infected with recombinant RSV expressing a fluorescent P protein that had typical liquid-like behaviour showing frequent fusion events between IBs followed by rapid coalescence to form a larger spherical IB (Fig. 2a and Supplementary Video 4). As expected for condensates, IBs disassembled upon osmotic shock and 1,6-hexanediol treatment, which disrupts hydrophobic protein–protein interactions (Fig. 2b,c and Extended Data Fig. 5a,b). To further confirm the liquid nature of IBs, we analysed the fluorescence recovery after photobleaching (FRAP) of IBs in RSV–P–BFP-infected cells. We observed a full and rapid recovery of the fluorescence, which is consistent with the rapid diffusion of P within IBs. By contrast, in compound-treated cells we did not observe any redistribution of P and fluorescence recovery (Fig. 2d,e). Moreover, IBs were no longer sensitive to osmotic shock, they lost their ability to fuse with each other and exhibited a slight decrease in mobility (Extended Data Fig. 5c,d and Supplementary Videos 5–7). The shape of the IBs, but not the surface area, was also altered in compound-treated cells, which resulted in the partial loss of the characteristic spherical shape of liquid condensates (Extended Data Fig. 5e).

Fig. 2: RSV IBs are LLPS condensates that can be hardened by A3E and CPM.

 **figure2**

a–g, HEp-2 cells were infected for 24 h with RSV-P-BFP (**a–e**), RSV-M2-1-mGFP (**f**) or RSV-M2-1(R151K)-P-BFP (**g**) and treated with 5 μ M CPM, 25 μ M A3E or DMSO for 1 h. **a**, Dynamic behaviour of RSV IBs. Arrowheads indicates a fusion event. Images are representative of ten videos from two experiments. Scale bar, 5 μ m. **b, c**, Hypotonic shock was applied and cells were imaged at the indicated times. Measurements labelled R (recovery) were taken after 5 min of shock followed by 5 min in culture medium. **b**, The mean \pm s.d. number of IBs per image is expressed as the percentage of the pre-shock control. Data are from ten acquisitions in two independent experiments. NS, not significant; *** P < 0.001; Kruskal–Wallis test with two-tailed Dunn’s test for multiple comparisons. **c**, Representative images. Scale bar, 10 μ m. **d–g**, Hardening of RSV IBs by A3E and CPM is shown using FRAP. The spontaneous re-distribution of fluorescence after photobleaching was recorded, the background and bleaching were corrected for during post-bleach imaging and normalized to the pre-bleach signal. **e, g**, Data are from 24 FRAP events in two independent experiments. **d, f**, Representative images of time-lapse microscopy from FRAP experiments are shown for P-BFP (**d**) and M2-1-mGFP (**f**). Scale bars, 2 μ m. White arrowheads indicate the bleached area.

[Source data](#)

[Full size image](#)

We further analysed the mobility of M2-1 by performing FRAP on IBAGs in RSV–M2-1-mGFP-infected cells. In untreated cells, photobleached areas of the IBAG

structures were readily replenished with M2-1–mGFP within 10 s, revealing rapid diffusion of M2-1 into IBAGs and active trafficking of M2-1 between the IB and IBAGs (Fig. 2f). However, in RSV–M2-1–mGFP-infected and A3E- or CPM-treated cells, M2-1 proteins were no longer able to redistribute into the photobleached area and remained in a hardened state (Fig. 2f). Taken together, our data show that RSV IBs are condensates formed by LLPS that can be hardened by small molecules A3E and CPM. Hardening of IB condensates does not result in the formation of solid fibrillar material as they do not stain positive with thioflavin S coloration¹⁶ (Extended Data Fig. 6a). We investigated the permeability of hardened IBs by analysing the diffusion of micro-injected fluorescent dextran beads in infected and treated cells¹⁷. The 10-kDa dextran beads, which have a hydrodynamic radius (R_h) of 2–3 nm, fully penetrate the IBs whereas the larger 70-kDa beads ($R_h > 6$ nm) are excluded from IBs in any experimental condition tested (Extended Data Fig. 6b,c). Notably, the mid-size 40-kDa beads ($R_h = 4.5$ nm) can enter the hardened IB in treated cells, which suggests that there is an increase in the IB mesh size after treatment with the compounds. This surprising finding warrants further investigation into the biophysical mechanism of IB condensate hardening.

We engineered an RSV–P–BFP recombinant virus that expresses the previously described M2-1(R151K) substitution that confers resistance to CPM¹³ and analysed IB dynamics and properties in compound-treated cells. In RSV–M2-1(R151K)–P–BFP-infected cells, treatment with CPM or A3E no longer resulted in a loss of roundness, resistance to hypotonic shock or change in the organization of IBs and IBAGs (Extended Data Figs. 7–9). FRAP data show that P mobility in IBs is no longer affected by CPM and A3E treatment (Fig. 2g). Taken together, these data demonstrate that the antiviral effect and the condensate-hardening properties of these small molecules are dependent on the M2-1 protein.

Viruses replicate or assemble in foci in which viral macromolecules locally concentrate, although many—such as positive-strand RNA viruses, including coronaviruses—are not known to form large IB condensates. Notably, small condensates formed by the nucleocapsid of SARS-CoV-2 were recently reported¹⁸. Whether smaller viral replication foci can be hardened and inhibited in a manner similar to RSV IB condensates is an interesting avenue of future research.

Efficacy of A3E in the RSV mouse model

To our knowledge, no condensate-targeted compounds have demonstrated *in vivo* efficacy to date. We therefore analysed whether the RSV condensate-hardening compounds A3E and CPM were able to block RSV replication in a mouse model¹⁹. We infected mice with RSV–Luc and treated animals twice daily with various doses of

CPM and A3E, starting on the day of infection. Treatment of mice with A3E resulted in significant and dose-dependent inhibition of RSV replication in the lungs (Fig. 3a, b). At the peak of viral infection at 4 days after infection (d.p.i.), the luminescent signal was barely visible in the lungs of treated mice (Fig. 3a, b and Extended Data Fig. 10a). Although typically only minor pathological changes can be seen in the lungs of RSV-A2-infected mice, A3E and CPM reduce the inflammation and exfoliation of lungs of treated animals, which are shown as a combined histopathology score in Fig. 3c. Furthermore, we show that RSV-Luc expressing the resistance substitution (R151K) in M2-1 could not be inhibited by either compound *in vivo* ($P > 0.05$) (Fig. 3a, b), which validates M2-1 as the main viral protein targeted by A3E and CPM. Taken together, these data confirm that the hardening of IB condensates in infected cells *in vitro* translates to antiviral efficacy in RSV-infected mice. The efficacy of A3E in suppressing virus replication is similar but appears to be slightly lower than CPM, which could be due to the lower potency of A3E observed *in vitro* (Fig. 3a, b). We believe that further investigations using a large-animal disease model of RSV infection can clarify this issue²⁰.

Fig. 3: A3E and CPM inhibit RSV replication in the lungs of mice through a mechanism involving M2-1.

 **figure3**

a, b, Mice were infected with RSV–Luc and treated twice daily with CPM ($n = 12$ mice), A3E (5 mg kg^{-1} , $n = 8$; 15 mg kg^{-1} , $n = 12$; 30 mg kg^{-1} , $n = 7$) or vehicle ($n = 27$) from 0 to 3 d.p.i. or infected with RSV–M2-1(R151K)–Luc and treated with CPM (15 mg kg^{-1} , $n = 8$), A3E (15 mg kg^{-1} , $n = 8$) or vehicle ($n = 13$). **a**, Bioluminescence reading was done at 4 d.p.i. and representative images of ventral views of infected animals are shown. The average radiance is expressed as the sum of the photons per second from each pixel inside the region of interest per the number of pixels ($\text{p s}^{-1} \text{ cm}^{-2} \text{ sr}^{-1}$). Normalized bioluminescence results are expressed as mean \pm s.e.m. from at least two experiments. * $P < 0.05$, ** $P < 0.01$, *** $P < 0.0001$; Kruskall–Wallis test with two-tailed Dunn’s tests for multiple comparisons. **c**, Histopathological changes in the lungs of mice infected with RSV A2 strain and treated with A3E (15 mg kg^{-1} , $n = 6$), CPM (15 mg kg^{-1} , $n = 3$) or vehicle ($n = 3$). Virus in lung was titred and tissue sections were prepared as described in the Methods. * $P < 0.05$; one-way Brown–Forsythe and Welch’s ANOVA, followed by two-sided Dunn’s tests for multiple comparisons. Two lung sections per mouse were analysed by

three independent pathologists and the mean score was calculated. Data are mean \pm s.e.m.

[Source data](#)

[Full size image](#)

Our in vitro data (Supplementary Videos [2](#), [3](#)) show that A3E and CPM act on RSV IBs within minutes. We therefore assessed the antiviral efficacy of condensate-hardening compounds in a more realistic setting by comparing RSV replication in mice treated with A3E and CPM at 1, 2 or 3 d.p.i., followed by luminescence measurement at 4 d.p.i. (Extended Data Fig. [10b,c](#)). The reduction in virus replication can be seen when treated up to 2 d.p.i. for both compounds, although significance was not reached for A3E at deferred treatment points.

A fast action is an expected feature of a condensate-hardening drug and was observed in cell culture experiments (Supplementary Videos [1–3](#)). This might be an important advantage of this new class of drugs for acute viral infections that have a limited treatment window. Indeed, RSV causes an acute respiratory disease that is characterized by a peak in viral replication in the lungs^{[21](#)}. Patients typically present themselves to physicians several days after the onset of symptoms. Comparative studies with development stage inhibitors of RSV F, L and N proteins should be done to determine the inhibition kinetics of current development-stage RSV inhibitors in vitro and in vivo.

Conclusion

Here we show that condensates formed by a liquid–liquid phase transition can be hardened by small drug-like molecules, resulting in the inhibition of virus replication in vivo. Targeting viral condensates could prove to be valuable for the development of drugs with broad-spectrum activity against future emerging viral pathogens by targeting proteins that are critical for condensate formation and conserved across the virus family. Condensate-targeting drugs may enable the pharmacological modulation of many previously undruggable targets. In recent years, biomolecular condensates have indeed been demonstrated in various physiological processes such as embryonic development, cellular response to stress and pathological protein aggregation in neurodegenerative diseases and cancer.

Methods

Design and synthesis of CPM analogues

CPM (Selleck) was used as the starting material based on the crystal structure of the CPM–SMO complex (PDB 4JKV and PDB 4O9R)¹⁴, which shows polar interactions of the A-ring 3'-hydroxyl group with the amino acids in the extracellular domain of the SMO receptor. We designed analogues as shown in Fig. 1a and Extended Data Fig. 1. The synthesis work was performed at WuxiAppTec. To a solution containing CPM (600 mg, 1.46 mM, 1.0 eq) in methanol (5 ml), Boc₂O (382.37 mg, 1.75 mM, 402.49 µl, 1.20 eq) was added. The reaction mixture was stirred at 20 °C for 16 h. Thin-layer chromatography (TLC) (petroleum ether/ethyl acetate (PE/EtOAc) = 3/1, Retention factor (Rf) = 0.45, KMnO₄) showed no starting material. The solvent was removed to obtain the residue. The residue was purified by column chromatography on silica gel (PE/EtOAc = 10/1) to give an intermediate compound (550 mg, 1.07 mM, 73.62% yield) as a white solid, which was named CPM-IM-1 (intermediate product 1). Next, to a solution of CPM-IM-1 (250 mg, 488.54 µM, 1.0 eq) in THF (4 ml), NaH (39.08 mg, 977.08 µM, 60% purity, 2.0 eq) was added at 20 °C. The reaction mixture was stirred at 60 °C for 20 min. MeI (346.72 mg, 2.44 mM, 152.07 µl, 5.0 eq) was added to the reaction mixture and stirred at 60 °C for 2 h. TLC (PE/EtOAc = 3/1, Rf = 0.70, KMnO₄) showed no starting material. The reaction mixture was diluted with water (40 ml), extracted with EtOAc (25 ml × 2), washed with brine (30 ml), dried over Na₂SO₄ and concentrated to give the crude product. The crude product was purified by column chromatography on silica gel (PE/EtOAc = 10/1) to give intermediate product 2 (CPM-IM-2; 250 mg, 475.50 µM, 48.67% yield) as a white solid. Next, to a solution of CPM-IM-2 (150 mg, 285.3 µM, 1.0 eq) and 2,6-lutidine (91.71 mg, 855.90 µM, 99.68 µl, 3.0 eq) in DCM (3.00 ml), TMSOTf (95.12 mg, 427.95 µM, 77.33 µl, 1.50 eq) was added at 0 °C. The reaction mixture was stirred at 0 °C for 30 min. TLC (PE/EtOAc = 3/1, Rf = 0.00, KMnO₄) showed no starting material. The reaction mixture was diluted with saturated NaHCO₃ (30 ml), extracted with EtOAc (30 ml × 2), washed with brine (30 ml), dried over Na₂SO₄ and concentrated to give the crude product. The crude product was purified by prep-HPLC (NH₄HCO₃) to give A3M (13.0 mg, 30.54 µM, 10.70% yield) as a white solid. A3E and A3P were synthesized with the same procedure, shown in Extended Data Fig. 1.

Cells

HEp-2 cells (ATCC, CCL-23) were maintained in Dulbecco's modified Eagle's medium (DMEM). ATCC number CCL-23 is derived from a HeLa cell contaminant and is recommended to grow RSV. BSRT7/5 cells—BHK-21 cells that constitutively express the T7 RNA polymerase²²—were maintained in Glasgow's MEM¹⁹. HH-signalling-pathway Gli-dependent luciferase-reporter-expressing NIH3T3 cells (BPS Bioscience, 60409) were maintained in DMEM. Cells were grown in medium supplemented with 10% heat-inactivated fetal bovine serum (FBS) supplemented with

penicillin–streptomycin solution. In addition, 0.5 mg ml⁻¹ of geneticin was added to BSRT7/5 cells and Gli-dependent luciferase-reporter-expressing NIH3T3 cells. Cells were grown in an incubator at 37 °C in 5% CO₂. Cell lines were not authenticated. BSRT7/5 and HEp-2 cells tested negative for mycoplasma using a MycoAlert PLUS Mycoplasma Detection Kit (Lonza).

Virus strains and recombinant virus rescue

RSV Long strain (ATCC, VR-26) was used for infection assays. The recombinant viruses, RSV–Luc, which expresses firefly luciferase and RSV–M2-1–mGFP, which expresses M2-1 fused to monomeric GFP, were prepared as described previously¹⁹. Recombinant RSV expressing the Luciferase reporter gene and encoding a Arg-to-Lys substitution at position 151 in the M2-1 protein (RSV–M2-1(R151K)–Luc) was engineered using the pACNR-rHRSV-Luc vector (GenBank accession, KF713491.1) as a template to amplify seven fragments covering the whole RSV genome. The fragments were assembled along with the p15A-Chl vector fragment using Gibson Assembly Master Mix (NEB, E2611). Recombinant RSV–M2-1(R151K)–Luc (GenBank accession, MW039343), RSV–P–BFP (GenBank accession, MT994243) and RSV–M2-1(R151K)–P–BFP (GenBank accession, MT994242) were rescued by reverse genetics and amplified in HEp-2 cells as described previously¹⁹.

RSV inhibition assays

HEp-2 cells were seeded at 5 × 10⁴ cells per well in 96-well plates the day before and infected with 10⁴ plaque forming units (PFU) of RSV–Luc in the presence of various concentrations of compounds. CPM (Selleck, S1146), CPM analogues and GDC-0449 (also known as Vismodegib; Selleck, S1082) were solubilized in DMSO at 8 mM, 8 mM and 10 mM, respectively. Compounds were further diluted serially in DMEM containing 0.25% DMSO to final concentrations ranging from 20 μM to 0.0005 μM. In cell and virus control wells, 0.25% DMSO was added. Compound dilutions were pre-incubated with viral suspensions for 5 min at 37 °C before addition to the cell monolayers in 96-well plates. Plates were incubated at 37 °C for 24 h for RSV–Luc before analysis. Luminescent readings were performed with a Bright Glo Luciferase System (Promega, E2610) and a Bioteck Synergy H1 plate reader. Relative light units indicate the luciferase activity relative to the mean control value (expressed as a percentage). The IC₅₀ was defined as the compound concentration required to achieve a 50% reduction in the maximal virus replication. In addition, cytotoxicity assays were done with the CellTiter-Glo Luminescent Cell Viability Assay (Promega, G7570) after incubation with the compounds to test the cell viability. The 50% cytotoxic concentration (CC₅₀) was defined as a 50% reduction in luminescence compared to

control wells. IC₅₀ and CC₅₀ values were calculated by fitting the data to a sigmoidal curve equation in GraphPad software (GraphPad Prism 5).

Minimally laboratory-experienced RSV isolates

Primary RSV isolates were obtained at the Hannover Medical School, Germany, in 2013 and 2016 from children with respiratory tract infections and with a multiplex RT-PCR-confirmed diagnosis of RSV infection²³. HEp-2 cells were inoculated with nasal swab, bronchial lavage fluid or throat swab material for 4 h at 37 °C. After a change to fresh medium, cells were incubated and, if necessary, passaged for several days until strong syncytia formation was visible. the supernatant and cells were collected, and cell-associated virus was released by three freeze-thaw cycles in liquid nitrogen. Cell debris was removed from the media by centrifugation at 1,000g and aliquots of the supernatant were snap-frozen in liquid nitrogen and stored at –80 °C. Viral RNA was isolated, reverse transcribed and RSV subtypes (RSV A GA2, RSV A ON1 and RSV B) were determined by Sanger sequencing of the G protein gene (or next-generation sequencing of the complete viral genome) and aligned to known sequences found using Nucleotide BLAST.

Assays to test HH antagonism of CPM analogues

The screening of compounds for HH antagonism was conducted at BPS Bioscience using the Gli-luciferase reporter system²⁴. In brief, Gli-dependent luciferase-reporter-expressing NIH3T3 cells, stably transfected with a Gli-dependent firefly luciferase expression plasmid, were seeded into white 96-well microplates and cultured overnight. After 24 h, the medium was changed to Opti-MEM containing diluted compounds and the cells were incubated for an additional 2 h, followed by addition of 1 µg ml⁻¹ recombinant mouse SHH protein. Untreated cells were used as control. After treatment for 24 h, cells were lysed and luciferase assay was performed using ONE-Step luciferase assay system (BPS bioscience, 60690). Luminescence was measured using a luminometer (BioTek SynergyTM 2 microplate reader). Reporter assays were performed in triplicate for each concentration and the luminescence intensity (L) was analysed using Graphpad Prism. The luminescence intensity in the absence of a compound was used as a positive control (L_p) and scored as 100%. The signal recorded in the absence of cells (L_b) was scored as 0%. The percentage luminescence in the presence of each compound was calculated according to the following equation: Luminescence (%) = $(L - L_b)/(L_p - L_b)$. The values of the percentage of luminescence for various concentrations of the same compound were then plotted using nonlinear regression analysis followed by calculation of the IC₅₀ value.

Quantification of IB and IBAG disorganization following compound treatment

HEp-2 cells were grown on glass coverslips and infected with RSV–M2-1–mGFP or RSV-M2-1(R151K)–P–BFP at a multiplicity of infection (MOI) of 1. At 24 h after infection, cells were treated with CPM or A3E at the indicated concentrations for 1 h. FISH was performed as previously described³. In brief, cells were fixed with 4% formaldehyde in PBS (v/v) for 10 min at 4 °C and endogenous biotin was blocked in PBS–1% BSA (w/v) supplemented with free streptavidin (4 µg ml⁻¹) for 1 h. Coverslips were incubated in hybridization mix (2× SSC, 300 mM NaCl and 30 mM sodium citrate), 10% dextran (w/v), 20% formamide (v/v), 1 mg ml⁻¹ herring sperm DNA and 1 µM of poly(dT) probe in a humidified chamber at 37 °C for 3 h. After serial washes, probes were detected by incubating the cells with streptavidin–Alexa Fluor 647 conjugate (8 µg ml⁻¹) in PBS–1% BSA (w/v) and then stained with rabbit polyclonal anti-N antibody³. z-stack image acquisitions of approximately 50 infected cells per condition were performed using a WLL Leica SP8 microscope with a 63× oil-immersion objective and a numerical zoom of ×2. The specific N antibody labelling was used for automatic detection of IBs in ImageJ software using the Analysis Particles function and a size threshold at >3 µm². The presence of IBAG(s) was then assessed manually based on M2-1–mGFP (if relevant) and poly(A) RNA signals.

Time-lapse microscopy and photobleaching experiments

Live-cell imaging and FRAP experiments were done using HEp-2 cells seeded in Ibidi µ-dishes with a polymer coverslip bottom that were infected with recombinant viruses (RSV–P–BFP, RSV–M2-1(R151K)–P–BFP or RSV–M2-1–mGFP) at high MOI for 20 h to 24 h. Image acquisition was performed using an Olympus FV3000 inverted confocal microscope with a 60× oil-immersion objective and a ×2.5 numerical zoom. Cells were maintained in a climate-controlled chamber (37 °C, 5% CO₂) during imaging. To analyse IB dynamics, images were acquired every 30 s for 15–30 min using cells treated for 1 h with 5 µM CPM or 25 µM A3E, or mock-treated (DMSO). Images and videos are representative of ten videos from two experiments. Ten 15-min-long videos from two independent experiments were analysed to quantify fusion events and IB mobility. Image editing was performed using both ImageJ and Icy software. IBs were detected using the Spot Detector plugin of the Icy software and fusion events were counted manually. Maximum velocities were obtained using the Spot Detector plugin with a size-filtering option and the Track Manager plugin of Icy software.

To visualize IBAG dynamics after CPM and A3E treatment, images were acquired every 6 s. After 5 min, the chemical compound (5 μ M CPM or 25 μ M A3E) was added and image acquisition was carried out for 20 min. Videos are representative of nine videos from three independent experiments.

FRAP acquisition was performed 1 h after addition of 5 μ M CPM, 25 μ M A3E or DMSO (mock, control). All FRAP experiments were realized using the same settings: 6 s pre-bleach, 5 ms bleach and 60 s post-bleach at a frame rate of 1 image every 126 ms. Bleaching was performed in a circular region at 100% and 80% laser intensity for GFP and BFP, respectively. Target IBs were close to other IB controls, which were used to correct for the loss of fluorescence due to photobleaching. The average fluorescence intensity as a function of the time of every bleached region was obtained using the Icy software. Background intensity was estimated by measuring a region outside the cell as far as possible from the target IB. Normalization of the recovery curves was performed using the easyFRAP, a MATLAB stand-alone application²⁵. For each experimental condition, two individual experiments were performed in which 12 IBs were analysed. To obtain the FRAP images displayed in Fig. 2, one image was acquired 5 s before bleaching and regions of interest were bleached with full power laser beam for 10 ms. Images were then acquired every 30 s (after a first image at 10 s). Image editing was performed using both ImageJ and Icy software.

Characterization of RSV IB area and shape

HEp-2 cells grown on glass coverslips were infected with RSV–P–BFP at MOI = 1 for 24 h and exposed to the indicated treatments (DMSO, CPM or A3E) for 1 h. Then, cells were fixed with PBS–4% formaldehyde (v/v) for 10 min at room temperature and permeabilized with PBS containing 1% BSA (w/v) and 0.1% Triton X-100 (v/v) for 10 min. Cells were incubated for 1 h with Hoechst 33342 (1 μ g ml⁻¹) and after washing in PBS, coverslips were mounted in ProLong Diamond antifade reagent (Thermofisher). z-stack image acquisitions of 100 cells per condition from 2 independent experiments were performed using a WLL Leica SP8 microscope with a 63 \times oil-immersion objective and a numerical zoom of \times 2. The shape and area measurements of RSV IBs were performed with the ImageJ software using the Analysis Particles function. After adjusting the threshold and converting the images to black and white, this command enables the automatic detection of IBs, calculation of the area and the roundness using the formula $\sqrt{\frac{4\pi A}{b^2}}$ (where A corresponds to the area and b to the major axis) of each IB. For multiple comparisons between different groups of treatments a Welch's ANOVA was performed followed by a Games–Howell post hoc test using the R statistical language (<https://www.r-project.org/>).

Sensitivity of IBs to osmotic shock and to 1,6-hexanediol treatment

HEp-2 cells were seeded on Ibidi μ-Dish polymer coverslips and infected with RSV–P–BFP or RSV–M2-1(R151K)–P–BFP at high MOI. At 24 h after infection, cells were exposed to 5 µM CPM or 25 µM A3E for 1 h at 37 °C. Image acquisition was performed using an Olympus FV3000 inverted confocal microscope with a 60× oil-immersion objective and a numerical zoom of ×2.5. Cells were maintained in a climate-controlled chamber (37 °C, 5% CO₂) during multi-position imaging. Five individual positions were studied per experiment and one image was acquired before treatment in two independent experiments. Hypotonic shock was performed by incubating the cells in 10% MEM diluted in water (v/v) for 5 min. To study a possible recovery of IBs after the shock, fresh 100% MEM was added, and the cells were imaged every 1 min for 5 min. To assess 1,6-hexanediol sensitivity, cells were incubated with 10% 1,6-hexanediol (w/v) and imaged every 2 min for 20 min after treatment. Image thresholding and IB detection was performed automatically in Icy software using the Otsu threshold clustering algorithm from the Best Threshold plugin and the Spot Detector plugin by defining a minimum (0,8 µm²) and maximum (50 µm²) ROI size.

Microinjection experiments

HEp-2 cells seeded on Ibidi μ-Dish polymer coverslips were infected with RSV–P–BFP for 24 h and exposed to CPM, A3E or DMSO at the indicated concentrations for 1 h at 37 °C. Cell microinjections were carried out with a FemtoJet microinjector (Eppendorf) mounted on an Olympus IX73 inverted microscope using Femtotips II needles (Eppendorf). Tetramethylrhodamine–dextran (40 kDa and 70 kDa, Sigma-Aldrich) and Texas-Red–dextran (10 kDa, Sigma-Aldrich) were prepared in injection buffer (48 mM K₂HPO₄, 4.5 mM KH₂PO₄, 14 mM NaH₂PO₄, pH 7.2) at final concentrations of 6 mg ml⁻¹. The 10-kDa, 40-kDa and 70-kDa dextrans have a hydrodynamic radius of approximately 2–3 nm, 4–5 nm and >6 nm, respectively¹⁷. Cells were imaged 2–5 min after microinjection using a 63× oil-immersion objective and average fluorescence intensity values of every region (cytoplasm, condensates and background) were obtained using the Icy software. Average fluorescence intensity of every region was corrected by subtracting the background (a region outside the cell).

Thioflavin S staining

HEp-2 cells were grown on glass coverslips, infected with RSV–P–BFP for 24 h and then treated with CPM, A3E or DMSO at the indicated concentrations at 37 °C for 1 h. Cells were then fixed with 4% formaldehyde in PBS (v/v) and permeabilized with PBS containing 1% BSA (w/v) and 0.1% Triton X-100 (v/v) for 10 min at room temperature. Thioflavin S (Sigma-Aldrich) was dissolved in water at 1% (w/v) and filtered before use. Cells were incubated for 1 h at room temperature with 0.01%

thioflavin S in 10% FBS and 0.5% Tween-20 in PBS (v/v). After serial washes with 0.5% Tween-20 in PBS (v/v), cell nuclei were stained with Hoechst 33342 ($1 \mu\text{g ml}^{-1}$). Mouse PrP amyloid fibrils were adsorbed on fixed cells and treated in parallel as a positive control of amyloid fibrils at a concentration of $1 \mu\text{M}$. Image acquisition was performed using a WLL395 Leica SP8 microscope with a $63\times$ oil-immersion objective and a numerical zoom of $\times 4$ and image editing was performed using the Icy software.

Flow-cytometry-based assay to quantify minimally laboratory-experienced RSV

HEp-2 cells were seeded at 2×10^4 cells per well in 96-well plates the day before virus inoculation. Cells were infected at MOI = 1 in the presence of the respective compound. After 2 h, the supernatant was removed and fresh medium containing the same concentration of the compound was added. At 24 h after inoculation, cells were washed once with PBS, and detached by trypsin treatment. Cells were washed, centrifuged at 400g, resuspended in fixation buffer (0.5% PFA and 1% FBS in PBS) and incubated at 4°C for at least 30 min or stored overnight. Subsequently, cells were permeabilized with 0.1% saponin and 1% FBS in PBS on ice for 20 min. Purified mouse anti-RSV phosphoprotein hybridoma supernatant was diluted 1:500 in permeabilization buffer and incubated with the cells on ice for 45 min²⁶. Cells were then washed with 1% FBS in PBS once and afterwards incubated with goat anti-mouse-Alexa 488 secondary antibody (ThermoFisher) in permeabilization buffer in the dark on ice for 1 h. After two additional washes with 1% FBS in PBS, cells were resuspended in fixation buffer and stored at 4°C overnight. Samples were analysed using a 99% attenuation filter in a BD Accuri C6 Flow Cytometer. Results were analysed using FlowJo V10. FSC-A versus SSC-A was used to gate on living cells. Living cells that had a higher FL1-A signal compared to stained but uninfected cells were considered RSV-positive. For each virus infection in the presence of a compound, infection was normalized to infected, DMSO-treated control cells.

Mouse infection and compound administration

Female BALB/c mice (approximately 8 weeks of age) were purchased from the Centre d'Elevage R. Janvier. Mice were housed under standard conditions with air filtration in a specific-pathogen-free animal facility using unbleached tissue nesting material, and water and food were provided ad libidum. Mice were acclimatized for 1 week before experiments started. For infection experiments, mice were housed in cages inside stainless-steel separate isolation cabinets that were ventilated under negative pressure with high-efficiency particulate-filtered air. Before infection, mice were anaesthetized using a mixture of ketamine and xylazine (1 mg and 0.2 mg per mouse, respectively)

and infected with 50 µl of PBS containing 6×10^4 PFU of RSV–Luc or RSV–M2-1(R151K)–Luc through the intranasal inoculation route. For compound administration to animals, compounds were dissolved in a sodium phosphate/citrate buffer (pH 3) containing 10% 2-hydropropyl- β -cyclodextrin (w/v). Compounds were administered by intraperitoneal injection at the indicated doses in a volume of 200 µl twice a day. The control group received vehicle only.

In vivo luminescence measurements

For in vivo imaging, mice were anaesthetized with ketamine and xylazine, but for daily imaging experiments, anaesthesia was induced using isoflurane in a well-ventilated room and a scavenging system. Calculations of sample size and randomization were not carried out in these experiments. In brief, mice were placed in the chamber (XGI-8, Caliper Life Sciences), the anaesthesia unit was turned on with a flow of 100% oxygen at a rate of 1.5–2 l min⁻¹ mixed with around 4–5% (v/v) isoflurane delivered to the anaesthesia chamber. Then, the deeply anaesthetized mice were injected by intranasal injection with 50 µl of PBS containing d-luciferin at 0.75 mg kg⁻¹. After 2 min, mice were placed with their back on a plate in the IVIS 200 imaging system (Xenogen, Perkin Elmer) with a nose cone providing 100% oxygen mixed with around 1.5–2% (v/v) isoflurane. Living Image software (v.4.0, Caliper Life Sciences) was used to measure luciferase activity. Bioluminescence images were acquired for 1 min with f/stop = 1 and binning = 8. A digital false-colour photon-emission image of the mouse was generated, and photons were counted within a constant region of interest corresponding to the surface of the chest encompassing the whole-airway area. Photon emission was measured as radiance in p s⁻¹ cm⁻² sr⁻¹.

Histopathology of RSV-infected mice

Female BALB/c mice were housed in individually ventilated cages in the biosafety level-2 laboratories of WuXi AppTec after quarantine. Animal care and use followed the WuXi IACUC-approved animal use protocol (IACUC no. ID01-QD029-2020v1.0).

Compounds (CPM or A3E) were administered at a dose of 15 mg kg⁻¹ intraperitoneally twice daily for 4 days, from 0 d.p.i. Mice were anaesthetized using a mixture of zoletil 50 and xylazine (30 mg kg⁻¹ and 6 mg kg⁻¹, respectively) and inoculated through intranasal injection with around 10⁵ PFU in 50 µl of RSV A2 strain. The control group received vehicle only. At 4 d.p.i., mice were euthanized, and the lung tissue was collected and snap-frozen in Hanks' balanced salt solution in a volume equal to tenfold the tissue weight (w/v) for further assays. Virus titration was performed as previously described¹³. The supernatant of tissue homogenates or virus

stock was used to infect the HEp-2 cells in 12-well plates. After a 4-h incubation, cells were washed and subsequently overlaid with 0.625% low-melting agarose in DMEM supplemented with antibiotics and 2% FBS, and then incubated for 96 h.

Subsequently, cells were fixed with 4% PFA for 30 min at room temperature, washed, blocked with BSA at room temperature for 1 h, and incubated for around 2–3 h at room temperature with mouse anti-RSV fusion protein monoclonal antibody (Abcam, ab94968) in 1× TBS, followed by a washing step with PBS–0.02% Tween-20.

Antigen–antibody complexes were revealed by incubating the cells for 2–4 h at room temperature with a secondary goat anti-mouse HRP-conjugated antibody (Abcam, ab6728) in 1× TBS. Cells were then washed with PBS–0.02% Tween-20 and overlaid with 4CN (4-chloro-1-naphthol) and H₂O₂ for 0.5 h. The plates were then rinsed with water and dried for counting foci. Final RSV titres are expressed as log₁₀-transformed PFU per g lung.

Histopathological analysis of mice was carried out at WuxiAppTec. Lobules of lung tissue were taken, fixed in 4% PFA for 24 h before being transferred to a 70% ethanol solution. Subsequently, the samples were paraffin-embedded and cut into 5-μm thick sections. Sections were stained with haematoxylin and eosin, and examined under a wide-field microscope by three independent pathologists, who were blinded to the treatment group of the animals. Lung inflammation and exfoliation was recorded and scored semiquantitatively. The degree of pathological changes was graded on a minimal, mild, moderate and marked scale corresponding to the numbers 0 to 3.

Ethics statement

The in vivo work of this study was carried out in accordance with INRAE guidelines in compliance with European animal welfare regulations. The protocols were approved by the Animal Care and Use Committee at the ‘Centre de Recherche de Jouy-en-Josas’ (COMETHEA) under relevant institutional authorization (“Ministère de l’éducation nationale, de l’enseignement supérieur et de la recherche”, authorization number 2015100910396112v1 (APAFIS#1487)). All experimental procedures were performed in a biosafety level-2 facility.

Reporting summary

Further information on research design is available in the [Nature Research Reporting Summary](#) linked to this paper.

Data availability

All experimental data shown in Figs. 1–3 and Extended Data Figs. 1–10 are available from the corresponding authors upon reasonable request. Sequences of newly described viruses are accessible from the GenBank under accession numbers [MW039434](#), [MT994243](#) and [MT994242](#). [Source data](#) are provided with this paper.

Code availability

No new custom computer code or algorithm was used to generate the results reported in the paper.

References

1. 1.

Wheeler, R. J. & Hyman, A. A. Controlling compartmentalization by non-membrane-bound organelles. *Phil. Trans. R. Soc. Lond. B* **373**, 20170193 (2018).

[Article](#) [Google Scholar](#)

2. 2.

Wileman, T. Aggresomes and pericentriolar sites of virus assembly: cellular defense or viral design? *Annu. Rev. Microbiol.* **61**, 149–167 (2007).

[CAS](#) [Article](#) [Google Scholar](#)

3. 3.

Rincheval, V. et al. Functional organization of cytoplasmic inclusion bodies in cells infected by respiratory syncytial virus. *Nat. Commun.* **8**, 563 (2017).

[ADS](#) [Article](#) [Google Scholar](#)

4. 4.

Nikolic, J. et al. Negri bodies are viral factories with properties of liquid organelles. *Nat. Commun.* **8**, 58 (2017).

[ADS](#) [Article](#) [Google Scholar](#)

5. 5.

Guseva, S. et al. Measles virus nucleo- and phosphoproteins form liquid-like phase-separated compartments that promote nucleocapsid assembly. *Sci. Adv.* **6**, eaaz7095 (2020).

[ADS](#) [CAS](#) [Article](#) [Google Scholar](#)

6. 6.

Sabari, B. R. et al. Coactivator condensation at super-enhancers links phase separation and gene control. *Science* **361**, eaar3958 (2018).

[Article](#) [Google Scholar](#)

7. 7.

Nam, H. H. & Ison, M. G. Respiratory syncytial virus infection in adults. *Br. Med. J.* **366**, l5021 (2019).

[Article](#) [Google Scholar](#)

8. 8.

Pneumonia Etiology Research for Child Health (PERCH) Study Group. Causes of severe pneumonia requiring hospital admission in children without HIV infection from Africa and Asia: the PERCH multi-country case-control study. *Lancet* **394**, 757–779 (2019).

[Article](#) [Google Scholar](#)

9. 9.

Heylen, E., Neyts, J. & Jochmans, D. Drug candidates and model systems in respiratory syncytial virus antiviral drug discovery. *Biochem. Pharmacol.* **127**, 1–12 (2017).

[CAS](#) [Article](#) [Google Scholar](#)

10. 10.

Galloux, M. et al. minimal elements required for the formation of respiratory syncytial virus cytoplasmic inclusion bodies in vivo and in vitro. *mBio* **11**, e01202-20 (2020).

[CAS](#) [Article](#) [Google Scholar](#)

11. 11.

Feric, M. et al. Coexisting liquid phases underlie nucleolar subcompartments. *Cell* **165**, 1686–1697 (2016).

[CAS](#) [Article](#) [Google Scholar](#)

12. 12.

Richard, C. A. et al. RSV hijacks cellular protein phosphatase 1 to regulate M2-1 phosphorylation and viral transcription. *PLoS Pathog.* **14**, e1006920 (2018).

[Article](#) [Google Scholar](#)

13. 13.

Bailly, B. et al. Targeting human respiratory syncytial virus transcription anti-termination factor M2-1 to inhibit in vivo viral replication. *Sci. Rep.* **6**, 25806 (2016).

[ADS](#) [CAS](#) [Article](#) [Google Scholar](#)

14. 14.

Weierstall, U. et al. Lipidic cubic phase injector facilitates membrane protein serial femtosecond crystallography. *Nat. Commun.* **5**, 3309 (2014).

[ADS](#) [Article](#) [Google Scholar](#)

15. 15.

Peluso, M. O. et al. Impact of the Smoothened inhibitor, IPI-926, on smoothened ciliary localization and Hedgehog pathway activity. *PLoS ONE* **9**, e90534 (2014).

[ADS](#) [Article](#) [Google Scholar](#)

16. 16.

Barron, R. M. et al. PrP aggregation can be seeded by pre-formed recombinant PrP amyloid fibrils without the replication of infectious prions. *Acta Neuropathol.* **132**, 611–624 (2016).

[CAS](#) [Article](#) [Google Scholar](#)

17. 17.

Wei, M. T. et al. Phase behaviour of disordered proteins underlying low density and high permeability of liquid organelles. *Nat. Chem.* **9**, 1118–1125 (2017).

[CAS](#) [Article](#) [Google Scholar](#)

18. 18.

Iserman, C. et al. Genomic RNA elements drive phase separation of the SARS-CoV-2 nucleocapsid. *Mol. Cell* **80**, 1078–1091.e6 (2020).

[CAS](#) [Article](#) [Google Scholar](#)

19. 19.

Rameix-Welti, M. A. et al. Visualizing the replication of respiratory syncytial virus in cells and in living mice. *Nat. Commun.* **5**, 5104 (2014).

[ADS](#) [CAS](#) [Article](#) [Google Scholar](#)

20. 20.

Blodörn, K. et al. A bovine respiratory syncytial virus model with high clinical expression in calves with specific passive immunity. *BMC Vet. Res.* **11**, 76 (2015).

[Article](#) [Google Scholar](#)

21. 21.

Kirsebom, F., Michalaki, C., Agueda-Oyarzabal, M. & Johansson, C. Neutrophils do not impact viral load or the peak of disease severity during RSV infection. *Sci. Rep.* **10**, 1110 (2020).

[ADS](#) [CAS](#) [Article](#) [Google Scholar](#)

22. 22.

Buchholz, U. J., Finke, S. & Conzelmann, K. K. Generation of bovine respiratory syncytial virus (BRSV) from cDNA: BRSV NS2 is not essential for virus replication in tissue culture, and the human RSV leader region acts as a functional BRSV genome promoter. *J. Virol.* **73**, 251–259 (1999).

[CAS](#) [Article](#) [Google Scholar](#)

23. 23.

Blockus, S. et al. Labyrinthopeptins as virolytic inhibitors of respiratory syncytial virus cell entry. *Antiviral Res.* **177**, 104774 (2020).

[CAS](#) [Article](#) [Google Scholar](#)

24. 24.

Mullor, J. L., Sánchez, P. & Ruiz i Altaba, A. Pathways and consequences: Hedgehog signaling in human disease. *Trends Cell Biol.* **12**, 562–569 (2002).

[CAS](#) [Article](#) [Google Scholar](#)

25. 25.

McNally, J. G. Quantitative FRAP in analysis of molecular binding dynamics in vivo. *Methods Cell Biol.* **85**, 329–351 (2008).

[CAS](#) [Article](#) [Google Scholar](#)

26. 26.

Haid, S., Grethe, C., Bankwitz, D., Grunwald, T. & Pietschmann, T. Identification of a human respiratory syncytial virus cell entry inhibitor by using a novel lentiviral pseudotype system. *J. Virol.* **90**, 3065–3073 (2016).

[CAS](#) [Article](#) [Google Scholar](#)

[Download references](#)

Acknowledgements

We thank T. Mitchison for discussions, interpretation of the data and reading the manuscript, H. Rezaei for mouse PrP amyloid fibrils and discussions, D. Descamps and M. Bauducel for help with animal work, C. Sizun for NMR assays, J. Fix for virus amplification, G. Hansen and M. Wetzke for collection of primary RSV isolates, H. Wang for technical assistance in DNA recombination and D. Xu for logistic support and helpful advice; W.-L. (Billy) NG for reviewing the SI chemistry; staff of the MIMA2 platform for access to the IVIS200 station, which was acquired with funds from the Ile de France région (SESAME); and staff of the Cymages platform for access to the Leica SP8 microscope and Olympus FV3000 inverted confocal microscope, which was supported by grants from the region Ile-de-France. This work

was supported by grants from the Natural Science Foundation of China Youth Project (31900147) to J.C., Fondation Air Liquide grant to J.-F.E. and R.A., the 111 Project (B16030), ATIP-AVENIR INSERM program and the Fondation Del Duca-Institut de France grant to J.R.-B. and M.-A.R.-W., a Sino-German Helmholtz International Lab grant (10000089395401) to Y.Z. and T.P., and People's Livelihood Technology Project of Qingdao City (17-3-3-2-nsh) to Z.W.

Author information

Author notes

1. Ralf Altmeyer

Present address: School of Public Health, University of Hong Kong, Hong Kong SAR, P. R. China

2. These authors contributed equally: Marie-Anne Rameix-Welti, Ralf Altmeyer

Affiliations

1. Université Paris-Saclay, INSERM, Université de Versailles St Quentin, UMR 1173 (2I), Versailles, France

Jennifer Risso-Ballester, Aude Jobart-Malfait, Aurore Desquesnes, Vincent Rincheval & Marie-Anne Rameix-Welti

2. Unité de Virologie et Immunologie Moléculaires (UR892), INRAE, Université Paris-Saclay, Jouy-en-Josas, France

Marie Galloux, Ronan Le Goffic, Fortune Hontonnou & Jean-François Eléouët

3. Helmholtz International Lab for Anti-Infectives, State Key Laboratory of Microbial Technology, Microbial Technology Institute, Shandong University, Qingdao, P. R. China

Jingjing Cao, Miaomiao Du, Xiumei Zhang, Huanyun Zhang, Youming Zhang & Ralf Altmeyer

4. Helmholtz International Lab for Anti-Infectives, Institute for Experimental Virology, Twincore - Centre for Experimental and Clinical Infection Research, Hannover, Germany

Svenja M. Sake, Sibylle Haid & Thomas Pietschmann

5. Qingdao Municipal Center for Disease Control and Prevention, Qingdao, P. R. China

Zhaoguo Wang

6. Assistance Publique des Hôpitaux de Paris, Université Paris Saclay, Hôpital Ambroise Paré, Laboratoire de Microbiologie, Boulogne-Billancourt, France

Marie-Anne Rameix-Welti

Authors

1. Jennifer Risso-Ballester

[View author publications](#)

You can also search for this author in [PubMed](#) [Google Scholar](#)

2. Marie Galloux

[View author publications](#)

You can also search for this author in [PubMed](#) [Google Scholar](#)

3. Jingjing Cao

[View author publications](#)

You can also search for this author in [PubMed](#) [Google Scholar](#)

4. Ronan Le Goffic

[View author publications](#)

You can also search for this author in [PubMed](#) [Google Scholar](#)

5. Fortune Hontonnou

[View author publications](#)

You can also search for this author in [PubMed](#) [Google Scholar](#)

6. Aude Jobart-Malfait

[View author publications](#)

You can also search for this author in [PubMed](#) [Google Scholar](#)

7. Aurore Desquesnes

[View author publications](#)

You can also search for this author in [PubMed](#) [Google Scholar](#)

8. Svenja M. Sake

[View author publications](#)

You can also search for this author in [PubMed](#) [Google Scholar](#)

9. Sibylle Haid

[View author publications](#)

You can also search for this author in [PubMed](#) [Google Scholar](#)

10. Miaomiao Du

[View author publications](#)

You can also search for this author in [PubMed](#) [Google Scholar](#)

11. Xiumei Zhang

[View author publications](#)

You can also search for this author in [PubMed](#) [Google Scholar](#)

12. Huanyun Zhang

[View author publications](#)

You can also search for this author in [PubMed](#) [Google Scholar](#)

13. Zhaoguo Wang

[View author publications](#)

You can also search for this author in [PubMed](#) [Google Scholar](#)

14. Vincent Rincheval

[View author publications](#)

You can also search for this author in [PubMed](#) [Google Scholar](#)

15. Youming Zhang

[View author publications](#)

You can also search for this author in [PubMed](#) [Google Scholar](#)

16. Thomas Pietschmann

[View author publications](#)

You can also search for this author in [PubMed](#) [Google Scholar](#)

17. Jean-François Eléouët

[View author publications](#)

You can also search for this author in [PubMed](#) [Google Scholar](#)

18. Marie-Anne Rameix-Welti

[View author publications](#)

You can also search for this author in [PubMed](#) [Google Scholar](#)

19. Ralf Altmeyer

[View author publications](#)

You can also search for this author in [PubMed](#) [Google Scholar](#)

Contributions

J.R.-B., J.C., V.R., M.G., J.-F.E., M.-A.R.-W. and R.A. designed experiments, analysed data and wrote the manuscript. R.A. initiated and designed the overall RSV drug discovery programme and designed the chemical analogues. M.-A.R.-W., J.-F.E., T.P. and R.A. reviewed the manuscript. R.A. and J.C. designed, performed and analysed the experiments, and analysed the data relative to the effects of the drugs on RSV replication and HH antagonism. H.Z., M.D. and X.Z. participated in the antiviral and HH compound testing. T.P., S.H. and S.M.S. designed, performed and analysed the inhibition assay with minimally laboratory-experienced RSV. J.R.-B., V.R., J.-F.E. and M.-A.R.-W. designed the experiments and analysed the data relative to the effects of the drugs on condensates in infected cells. J.R.-B. performed the experiments. V.R. performed experiments and provided expertise to analyse condensate disorganization and A.M.-J. provided support and expertise for the dextran micro-injection experiments. R.A., M.G. and R.L.G. designed and analysed the animal experiments. M.G., R.L.G., A.D. and F.H. infected and handled mice for animal efficacy studies. Y.Z. and Z.W. provided critical logistic and infrastructure support. Z.W., Y.Z., T.P., J.-F.E., M.-A.R.-W. and R.A. obtained funding for the study. All authors reviewed the manuscript.

Corresponding authors

Correspondence to [Jean-François Eléouët](#) or [Marie-Anne Rameix-Welti](#) or [Ralf Altmeyer](#).

Ethics declarations

Competing interests

R.A. and J.J.C. are inventors of patents 2016100874979.4 (China), 10,035,816 B2 (USA), 6588156 (Japan) and patent application 17749894.6 (EU) held by Shandong University. The other authors declare no competing interests.

Additional information

Peer review information *Nature* thanks the anonymous reviewers for their contribution to the peer review of this work.

Publisher's note Springer Nature remains neutral with regard to jurisdictional claims in published maps and institutional affiliations.

Extended data figures and tables

[Extended Data Fig. 1 Synthetic route of the CPM analogues.](#)

The detailed synthesis protocol is described in the [Supplementary Methods](#). The IDs of the end products are A3M (A-ring, 3'-methoxy-cyclopamine; compound 4), A3E (A-ring, 3'-ethoxy-cyclopamine, compound 6) and A3P (A-ring, 3'-propoxy-cyclopamine, compound 8). The name of A3E (3'-ethoxy-cyclopamine) according to IUPAC nomenclature is *3S,3'R,3a'S,6aS,6bS,6'S,7a'R,9R,11aS,11bR*-3-ethoxy-*3',6',10,11b*-tetramethyl-*1,2,3,3a',4,4',5',6,6a,6b,6',7,7',7a',8,11,11a,11b*-octadecahydro-*3'H*-spiro[benzo[*a*]fluorene-9,2'-furo[3,2-*b*]pyridine].

[Extended Data Fig. 2 Biological activity of CPM chemical analogues in vitro.](#)

a, c, e, g, Potency of compounds to inhibit SHH signalling was tested in Gli-dependent luciferase-reporter-expressing NIH3T3 cells. Data are expressed as the percentage \pm s.d. of the DMSO control. Data are representative of two experiments performed in triplicate. **b, d, f, h**, Potency of compounds to inhibit RSV replication was tested in RSV–Luc-infected HEp-2 cells. Luciferase activity was measured at 24 h after infection and expressed as the percentage \pm s.d. of the DMSO control. The cytotoxicity of compounds was measured in parallel in either HEp-2 or NIH3T3 reporter cells after treatment for 24 h (data not shown) or 72 h. IC₅₀ and CC₅₀ values

were calculated with GraphPad software. Data shown are representative of two (**b**, **f**) or three (**d**, **h**) experiments performed in triplicate.

[Source data](#)

Extended Data Fig. 3 Ability of A3E and CPM to inhibit minimally laboratory-experienced RSV.

a, Inhibition of minimally laboratory-experienced RSV was tested in HEp-2 cells infected for 24 h with two RSV A or one RSV B isolates and analysed by flow cytometry as described in the Methods. The results are expressed as mean \pm s.d. from three independent experiments performed in duplicate. **b**, **c**, IC₅₀ values are calculated from three independent experiments performed in duplicate. CC₅₀ values are from a representative experiment out of three experiments performed in triplicate. The selectivity index (SI) is calculated as SI = CC₅₀/IC₅₀.

[Source data](#)

Extended Data Fig. 4 Disorganization of IB and IBAG architecture in RSV–M2-1–mGFP-infected and compound-treated cells.

HEp-2 cells were infected with RSV–M2-1–mGFP for 24 h and then treated for 1 h with A3E and CPM at the indicated concentrations and stained to detect poly(A) RNA and N protein as described in the Methods. **a**, Representative images from two independent experiments are shown. Poly(A) RNA (red), N (white), M2-1–mGFP (green) and nuclei (blue) were visualized. A merged image of red, green and blue channels is shown (merge). Scale bars, 10 μ m. **b**, The presence of IBAGs within IBs was quantified and indicated as IBAG (+) when visible and IBAG (−) when absent (described in the Methods) for approximately 50 infected cells per condition from two independent experiments.

[Source data](#)

Extended Data Fig. 5 RSV IBs lose velocity and the ability to fuse but remain sensitive to 1,6-hexanediol.

a, **b**, HEp-2 cells infected with RSV–P–BFP for 24 h were treated for 1 h with DMSO, CPM (5 μ M) or A3E (25 μ M) and then exposed to 10% 1,6-hexanediol (Hex), imaged at 10 min and quantified (see [Methods](#)). Data are from 10 acquisitions captured in two independent experiments. Representative images are shown in **a**. Scale bar, 10 μ m. The mean \pm s.d. number of IBs per image is expressed as the percentage of the pre-

treatment control. ** $P < 0.01$; two-tailed Wilcoxon signed-rank test. **c, d**, HEp-2 cells were infected with RSV-P-BFP for 24 h and treated for 1 h with DMSO, CPM (5 μ M) or A3E (25 μ M) and then imaged as described in the Methods. Fusion events were quantified as described in the Methods. Results are expressed as mean \pm s.d. from 10 videos (15 min) from two independent experiments (**c**). Maximum velocities were obtained by automatic tracking of IBs from 10 videos (15 min) from two independent experiments (see [Methods](#)). Box plots show the median (centre line) and the first and third quartiles (upper and lower hinges). Statistical analysis of maximum velocities was done using Kruskal–Wallis tests followed by Dunn’s test for multiple comparisons (**d**). * $P < 0.05$; *** $P < 0.001$. **e**, HEp-2 cells were infected for 24 h with RSV-P-BFP and treated with CPM (5 μ M), A3E (25 μ M) or DMSO as control for 1 h. IBs shape was analysed as described in the Methods. Box plots indicate the median (centre line) and the first and third quartiles (upper and lower hinges). ** $P < 0.01$; Welch’s ANOVA followed by a Games–Howell post hoc test.

[Source data](#)

Extended Data Fig. 6 A3E and CPM do not induce the formation of fibrillar solids but increase the mesh size of IBs.

a, HEp-2 cells infected with RSV-P-BFP for 24 h and treated with CPM (5 μ M) or A3E (25 μ M) for 1 h, then fixed and stained with ThS. Purified mouse PrP amyloid fibrils adsorbed on fixed cells and treated in parallel were used as positive control. IBs are shown by P-BFP fluorescence (blue) and ThS is shown in green. Representative images from two independent experiments are shown. Scale bar, 10 μ m. **b, c**, Fluorescent dextran beads were selected based on their approximate hydrodynamic radius (Rh) and micro-injected into HEp-2 cells that were infected with RSV-P-BFP for 20–24 h and treated for 1 h with A3E (25 μ M) or CPM (5 μ M). Cells were imaged 2–5 min after micro-injection under a wide-field microscope. Representative images from two independent experiments are shown in **c**. Scale bar, 2 μ m. The fluorescent dextran signal inside IBs relative to the cytoplasm was quantified as described in the Methods. Data are mean \pm s.e.m. of the signal ratio from at least 25 IBs from two independent experiments. **** $P < 0.0001$; ns, not significant; Kruskal–Wallis test followed by Dunn’s test for multiple comparisons.

[Source data](#)

Extended Data Fig. 7 Variation in the size and shape of IBs in compound-treated RSV-infected cells.

a, b, HEp-2 cells were infected with RSV-P-BFP or RSV-M2-1(R151K)-P-BFP for 24 h and treated for 1 h with A3E (25 μ M), CPM (5 μ M) or DMSO at 24 h after

infection. Cells were fixed, stained and analysed by confocal microscopy as described in the Methods. The size (**a**) and roundness (**b**) of IBs were quantified. Results of 50 cells from two independent experiments are shown. Box plots indicate the median (centre line) and the first and third quartiles (upper and lower hinges). Statistical significance analysis of size and roundness data was performed using Welch's ANOVA followed by a Games–Howell test for multiple comparisons. ** $P < 0.01$.

[Source data](#)

Extended Data Fig. 8 IBs in RSV–M2-1(R151K)–P–BFP-infected and compound-treated cells are still susceptible to hypotonic shock.

a, b, HEp-2 cells were infected for 24 h and treated with A3E (25 μ M), CPM (5 μ M) or DMSO for 1 h. Hypotonic shock was applied for 10 min and cells were imaged at the indicated times and the signals were quantified. Measurements labelled ‘Rec’ (recovery period) were taken after 5 min of shock followed by 5 min in culture medium. **a**, Representative images from two independent experiments and ten acquisitions are shown. Scale bar, 10 μ m. **b**, Data are expressed as the mean \pm s.d. number of IBs per image and compared to pre-shock values. Statistical significance analysis was performed using Kruskal–Wallis tests followed by two-sided Dunn’s test for multiple comparisons; ** $P < 0.01$, *** $P < 0.001$, **** $P < 0.0001$.

[Source data](#)

Extended Data Fig. 9 IB and IBAG architecture is unaffected by compound treatment in cells infected with the RSV–M2-1(R151K) mutant virus.

a, b, HEp-2 cells were infected with RSV–M2-1(R151K)–P–BFP for 24 h and then treated for 1 h with A3E (25 μ M) or CPM (5 μ M) followed by staining for poly(A) RNA and N protein as described in the Methods. **a**, Representative images from two independent experiments are shown. Poly(A) RNA, N and P–BFP are shown in red, white and blue, respectively. Merge of poly(A) RNA, N and P–BFP or poly(A) RNA and P–BFP are shown in the fifth and fourth column, respectively. Scale bar, 10 μ m. **b**, The presence of IBAGs within IBs was quantified and scored as IBAG (+) when visible and IBAG (−) when absent from approximately 50 infected cells per condition from two independent experiments (see [Methods](#)).

[Source data](#)

Extended Data Fig. 10 Time course and treatment window for A3E and CPM in RSV–Luc-infected mice.

a, Time course of RSV–Luc infection in compound-treated mice. Mice were infected intranasally with 5×10^4 PFU ml⁻¹ RSV–Luc and treated with the indicated compounds twice daily from 0 to 3 d.p.i. and bioluminescence readings were obtained at 3, 4, 5 and 6 d.p.i. One representative of two time-course experiments performed is shown. The mean \pm s.e.m. radiance is expressed as the sum of the photons per second from each pixel inside the region of interest per the number of pixels (p s⁻¹ cm⁻² sr⁻¹). Vehicle group, $n = 10$ mice; all treatment groups, $n = 5$ mice. **b**, Experimental design to determine the A3E and CPM treatment window for RSV–Luc-infected mice. Viral replication in lungs was determined by bioluminescence imaging as described in **a** and the Methods. Mice were infected with 5×10^4 PFU ml⁻¹ RSV–Luc, treated with compounds at 15 mg kg⁻¹ twice daily for the indicated time periods and imaged at 4 d.p.i. **c**, Results are expressed as the percentage of RSV replication compared to vehicle control and are shown as mean \pm s.e.m. for a specified number of RSV–Luc-infected animals. Vehicle group, $n = 27$ mice, $n = 4$ experiments; CPM 0–3 d.p.i., $n = 12$ mice, $n = 3$ experiments; CPM 1–3 d.p.i., $n = 4$ mice, $n = 1$ experiment; CPM 2–3 d.p.i., $n = 4$ mice, $n = 1$ experiment; CPM 3 d.p.i., $n = 4$ mice, $n = 1$ experiment; A3E 0–3 d.p.i., $n = 12$ mice, $n = 2$ experiments; A3E 1–3 d.p.i., $n = 4$ mice, $n = 1$ experiment; A3E 2–3 d.p.i., $n = 4$ mice, $n = 1$ experiment; A3E 3 d.p.i., $n = 4$ mice, $n = 1$ experiment. Statistical significance analysis was performed using Kruskall–Wallis tests followed by two-sided Dunn’s test for multiple comparisons. * $P < 0.05$, ** $P < 0.01$, **** $P < 0.0001$.

[Source data](#)

Supplementary information

[Supplementary Information](#)

This file contains details of the chemical synthesis of A3M, A3E and A3P, including a List of compounds, synthesis scheme and images of analytical data.

[Reporting Summary](#)

[Supplementary Video 1](#)

IBAG dynamics in compound-treated cells. Time-lapse microscopy of IBAGs in HEp-2 cells infected with RSV-M2-1-mGFP. At 24 hpi, images were taken every 6 s in a CO₂-controlled chamber heated at 37 °C, with an Olympus FV3000 inverted confocal microscope. After five minutes, cells were treated with DMSO (mock, Supplementary Video 1), 5 µM CPM (Supplementary Video 2) or 25 µM A3E (Supplementary Video 3) and subsequently images were taken for another 20 min. The resulting videos were

visualized using Image J software (10 fps). A representative video from three independent experiments in which 3 videos were acquired is shown. Scale bar 10 μ m.

Supplementary Video 2

IBAG dynamics in compound-treated cells. Cells were treated with 5 μ M CPM; see legend for Supplementary Video 1.

Supplementary Video 3

IBAG dynamics in compound-treated cells. Cells were treated with 25 μ M A3E; see legend for Supplementary Video 1.

Supplementary Video 4

IB dynamics. Time-lapse microscopy of IBs in HEp-2 cells infected with RSV-P-BFP. At 24 hpi, cells were imaged every 30 s in a CO₂-controlled chamber heated at 37 °C, with an Olympus FV3000 inverted confocal microscope. The resulting videos were visualized under the Image J software (10 pfs). A representative video from 10 videos from 2 independent experiments is shown. Scale bar 10 μ m.

Supplementary Video 5

IB dynamics and mobility. Time-lapse microscopy of IBs in HEp-2 cells infected with RSV-P-BFP. At 24 hpi, cells were treated for 1 h with DMSO (mock, Supplementary Video 5), 5 μ M CPM (Supplementary Video 6) or 25 μ M A3E (Supplementary Video 7) and subsequently imaged every 30s for 15 min in a CO₂-controlled chamber heated at 37 °C, with an Olympus FV3000 inverted confocal microscope. The resulting videos were visualized under Image J and ICY software (10 pfs). A representative video from 10 videos from 2 independent experiments is shown. Scale bar 10 μ m.

Supplementary Video 6

IB dynamics and mobility. Cells were treated with 5 μ M CPM; see legend for Supplementary Video 5.

Supplementary Video 7

IB dynamics and mobility. Cells were treated with 25 μ M A3E; see legend for Supplementary Video 5.

Source data

[Source Data Fig. 1](#)

[Source Data Fig. 2](#)

[Source Data Fig. 3](#)

[Source Data Extended Data Fig. 2](#)

[Source Data Extended Data Fig. 3](#)

[Source Data Extended Data Fig. 4](#)

[Source Data Extended Data Fig. 5](#)

[Source Data Extended Data Fig. 6](#)

[Source Data Extended Data Fig. 7](#)

[Source Data Extended Data Fig. 8](#)

[Source Data Extended Data Fig. 9](#)

[Source Data Extended Data Fig. 10](#)

Rights and permissions

[Reprints and Permissions](#)

About this article



Check for
updates

Cite this article

Risso-Ballester, J., Galloux, M., Cao, J. *et al.* A condensate-hardening drug blocks RSV replication in vivo. *Nature* **595**, 596–599 (2021). <https://doi.org/10.1038/s41586-021-03703-z>

[Download citation](#)

- Received: 09 June 2020
- Accepted: 07 June 2021
- Published: 07 July 2021
- Issue Date: 22 July 2021
- DOI: <https://doi.org/10.1038/s41586-021-03703-z>

Comments

By submitting a comment you agree to abide by our [Terms](#) and [Community Guidelines](#). If you find something abusive or that does not comply with our terms or guidelines please flag it as inappropriate.

[Download PDF](#)

Associated Content

[Targeting viruses in their phase](#)

- Paulina Strzyz

Advertisement

This article was downloaded by **calibre** from <https://www.nature.com/articles/s41586-021-03703-z>

- Article
- [Published: 14 July 2021](#)

Structures of rhodopsin in complex with G-protein-coupled receptor kinase 1

- [Qiuyan Chen^{1,2}](#),
- [Manolo Plasencia³](#),
- [Zhuang Li ORCID: orcid.org/0000-0002-7249-9029¹](#),
- [Somnath Mukherjee ORCID: orcid.org/0000-0001-5447-4496⁴](#),
- [Dhabaleswar Patra ORCID: orcid.org/0000-0001-6520-6972^{1,2}](#),
- [Chun-Liang Chen ORCID: orcid.org/0000-0003-4625-4340^{1,2}](#),
- [Thomas Klose ORCID: orcid.org/0000-0002-2150-9792¹](#),
- [Xin-Qiu Yao ORCID: orcid.org/0000-0003-2706-2028⁵](#),
- [Anthony A. Kossiakoff^{4,6}](#),
- [Leifu Chang ORCID: orcid.org/0000-0002-6107-5271¹](#),
- [Philip C. Andrews^{3,7,8}](#) &
- [John J. G. Tesmer ORCID: orcid.org/0000-0003-1125-3727^{1,2}](#)

[Nature](#) volume **595**, pages 600–605 (2021) [Cite this article](#)

- 4680 Accesses
- 67 Altmetric
- [Metrics details](#)

Subjects

- [Cryoelectron microscopy](#)

- [Endocytosis](#)
- [Enzyme mechanisms](#)
- [Hormone receptors](#)

Abstract

G-protein-coupled receptor (GPCR) kinases (GRKs) selectively phosphorylate activated GPCRs, thereby priming them for desensitization¹. Although it is unclear how GRKs recognize these receptors^{2,3,4}, a conserved region at the GRK N terminus is essential for this process^{5,6,7,8}. Here we report a series of cryo-electron microscopy single-particle reconstructions of light-activated rhodopsin (Rho*) bound to rhodopsin kinase (GRK1), wherein the N terminus of GRK1 forms a helix that docks into the open cytoplasmic cleft of Rho*. The helix also packs against the GRK1 kinase domain and stabilizes it in an active configuration. The complex is further stabilized by electrostatic interactions between basic residues that are conserved in most GPCRs and acidic residues that are conserved in GRKs. We did not observe any density for the regulator of G-protein signalling homology domain of GRK1 or the C terminus of rhodopsin. Crosslinking with mass spectrometry analysis confirmed these results and revealed dynamic behaviour in receptor-bound GRK1 that would allow the phosphorylation of multiple sites in the receptor tail. We have identified GRK1 residues whose mutation augments kinase activity and crosslinking with Rho*, as well as residues that are involved in activation by acidic phospholipids. From these data, we present a general model for how a small family of protein kinases can recognize and be activated by hundreds of different GPCRs.

Access options

Subscribe to Journal

Get full journal access for 1 year

\$199.00

only \$3.90 per issue

[Subscribe](#)

All prices are NET prices.

VAT will be added later in the checkout.

Tax calculation will be finalised during checkout.

Rent or Buy article

Get time limited or full article access on ReadCube.

from \$8.99

[Rent or Buy](#)

All prices are NET prices.

Additional access options:

- [Log in](#)
- [Access through your institution](#)
- [Learn about institutional subscriptions](#)

Fig. 1: Trapping an activation-dependent complex between rhodopsin and GRK1.

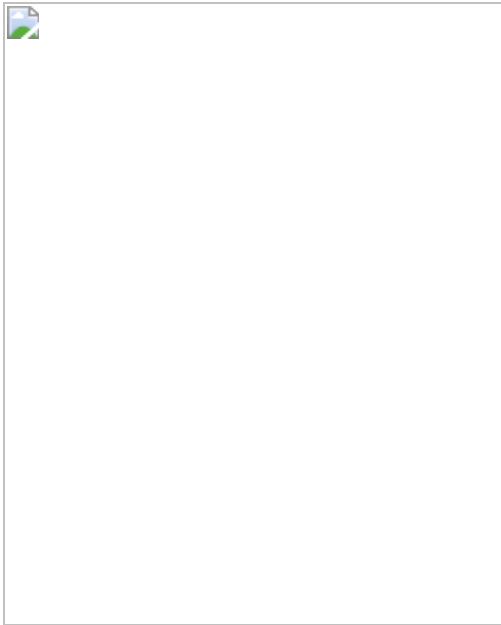


Fig. 2: Cryo-EM single-particle reconstructions reveal the prominent role of the GRK1 α N helix and AST in forming the interface with Rho*.



Fig. 3: Interactions within GRK1 and Rho* involve highly conserved elements in each protein family.

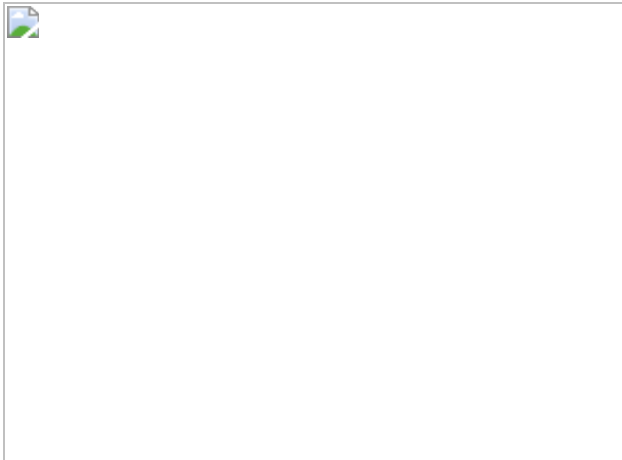


Fig. 4: CLMS confirms the cryo-EM structure and reveals dynamics in the receptor C-terminal tail.

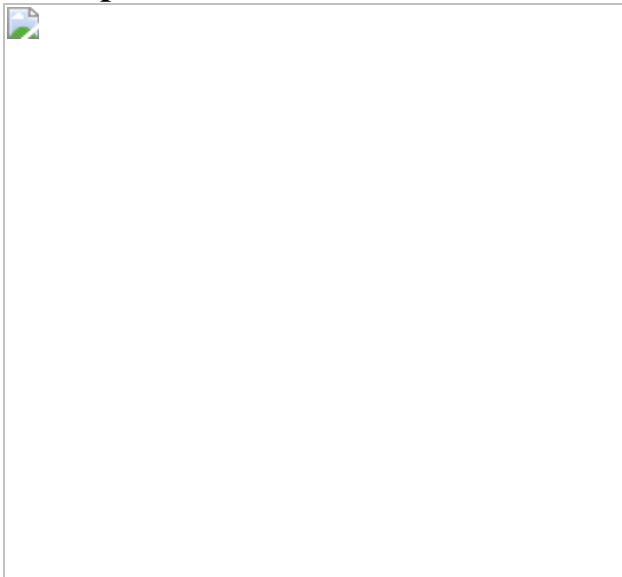


Fig. 5: A generalized model for GRK activation by anionic lipids and activated GPCRs.



Data availability

All data needed to evaluate the conclusions in the paper are presented in the paper and/or the [Supplementary Materials](#). Additional data related to this paper are available upon reasonable request from the authors. The structures of the four Rho*-GRK1 complexes (Rho*-GRK1, Rho*-GRK1(S5E/EE), Rho*-GRK1(S5E/EE)-Fab1, and Rho*-GRK1(S5E/EE)-Fab6) and their associated data have been deposited into the Protein Data Bank under accession codes [7MT9](#), [7MT8](#), [7MTA](#), and [7MTB](#), and the Electron Microscopy Data Bank under accession codes [EMD-23978](#), [EMD-23977](#), [EMD-23979](#), and [EMD-23980](#), respectively. CLMS data have been deposited to the ProteomeXchange Database (<http://www.proteomexchange.org/>) via the PRIDE⁷⁰ partner repository with dataset identifier PXD019215.

References

1. 1.

Gurevich, E. V., Tesmer, J. J., Mushegian, A. & Gurevich, V. V. G protein-coupled receptor kinases: more than just kinases and not only for GPCRs. *Pharmacol. Ther.* **133**, 40–69 (2012).

[CAS](#) [Google Scholar](#)

2. 2.

Cato, M. C. et al. The open question of how GPCRs interact with GPCR kinases (GRKs). *Biomolecules* **11**, 447 (2021).

[CAS](#) [PubMed](#) [PubMed Central](#) [Google Scholar](#)

3. 3.

Komolov, K. E. et al. Structural and functional analysis of a β_2 -adrenergic receptor complex with GRK5. *Cell* **169**, 407–421.e16 (2017).

[CAS](#) [PubMed](#) [PubMed Central](#) [Google Scholar](#)

4. 4.

He, Y. et al. Molecular assembly of rhodopsin with G protein-coupled receptor kinases. *Cell Res.* **27**, 728–747 (2017).

[CAS](#) [PubMed](#) [PubMed Central](#) [Google Scholar](#)

5. 5.

Beautrait, A. et al. Mapping the putative G protein-coupled receptor (GPCR) docking site on GPCR kinase 2: insights from intact cell phosphorylation and recruitment assays. *J. Biol. Chem.* **289**, 25262–25275 (2014).

[CAS](#) [PubMed](#) [PubMed Central](#) [Google Scholar](#)

6. 6.

Boguth, C. A., Singh, P., Huang, C. C. & Tesmer, J. J. Molecular basis for activation of G protein-coupled receptor kinases. *EMBO J.* **29**, 3249–3259 (2010).

[CAS](#) [PubMed](#) [PubMed Central](#) [Google Scholar](#)

7. 7.

Noble, B., Kallal, L. A., Pausch, M. H. & Benovic, J. L. Development of a yeast bioassay to characterize G protein-coupled receptor kinases. Identification of an NH₂-terminal region essential for receptor phosphorylation. *J. Biol. Chem.* **278**, 47466–47476 (2003).

[CAS](#) [Google Scholar](#)

8. 8.

Palczewski, K., Buczyłko, J., Lebioda, L., Crabb, J. W. & Polans, A. S. Identification of the N-terminal region in rhodopsin kinase involved in its interaction with rhodopsin. *J. Biol. Chem.* **268**, 6004–6013 (1993).

[CAS](#) [Google Scholar](#)

9. 9.

Lefkowitz, R. J. Seven transmembrane receptors: something old, something new. *Acta Physiol. (Oxf.)* **190**, 9–19 (2007).

[CAS](#) [Google Scholar](#)

10. 10.

Brinks, H. & Koch, W. J. Targeting G protein-coupled receptor kinases (GRKs) in heart failure. *Drug Discov. Today Dis. Mech.* **7**, e129–e134 (2010).

[CAS](#) [PubMed](#) [PubMed Central](#) [Google Scholar](#)

11. 11.

Nogués, L. et al. G protein-coupled receptor kinases (GRKs) in tumorigenesis and cancer progression: GPCR regulators and signaling hubs. *Semin. Cancer Biol.* **48**, 78–90 (2018).

[Google Scholar](#)

12. 12.

Kannan, N., Haste, N., Taylor, S. S. & Neuwald, A. F. The hallmark of AGC kinase functional divergence is its C-terminal tail, a cis-acting regulatory module. *Proc. Natl Acad. Sci. USA* **104**, 1272–1277 (2007).

[ADS](#) [CAS](#) [PubMed](#) [PubMed Central](#) [Google Scholar](#)

13. 13.

Lodowski, D. T., Pitcher, J. A., Capel, W. D., Lefkowitz, R. J. & Tesmer, J. J. Keeping G proteins at bay: a complex between G protein-coupled receptor kinase 2 and G $\beta\gamma$. *Science* **300**, 1256–1262 (2003).

[ADS](#) [CAS](#) [Google Scholar](#)

14. 14.

Gao, Y. et al. Structures of the rhodopsin-transducin complex: insights into G-protein activation. *Mol. Cell* **75**, 781–790.e3 (2019).

[CAS](#) [PubMed](#) [PubMed Central](#) [Google Scholar](#)

15. 15.

Maeda, S., Qu, Q., Robertson, M. J., Skiniotis, G. & Kobilka, B. K. Structures of the M1 and M2 muscarinic acetylcholine receptor/G-protein complexes. *Science* **364**, 552–557 (2019).

[ADS](#) [CAS](#) [PubMed](#) [PubMed Central](#) [Google Scholar](#)

16. 16.

Huang, W. et al. Structure of the neuropeptide Y receptor 1 in complex with β -arrestin 1. *Nature* **579**, 303–308 (2020).

[ADS](#) [CAS](#) [PubMed](#) [PubMed Central](#) [Google Scholar](#)

17. 17.

Staus, D. P. et al. Structure of the M2 muscarinic receptor– β -arrestin complex in a lipid nanodisc. *Nature* **579**, 297–302 (2020).

[ADS](#) [CAS](#) [PubMed](#) [PubMed Central](#) [Google Scholar](#)

18. 18.

Kato, H. E. et al. Conformational transitions of a neuropeptide Y receptor 1–G_{i1} complex. *Nature* **572**, 80–85 (2019).

[CAS](#) [PubMed](#) [PubMed Central](#) [Google Scholar](#)

19. 19.

Pulvermüller, A., Palczewski, K. & Hofmann, K. P. Interaction between photoactivated rhodopsin and its kinase: stability and kinetics of complex formation. *Biochemistry* **32**, 14082–14088 (1993).

[Google Scholar](#)

20. 20.

Kühn, H. & Dreyer, W. J. Light dependent phosphorylation of rhodopsin by ATP. *FEBS Lett.* **20**, 1–6 (1972).

[Google Scholar](#)

21. 21.

Kühn, H., Cook, J. H. & Dreyer, W. J. Phosphorylation of rhodopsin in bovine photoreceptor membranes. A dark reaction after illumination. *Biochemistry* **12**, 2495–2502 (1973).

[Google Scholar](#)

22. 22.

Clifford-Nunn, B., Showalter, H. D. & Andrews, P. C. Quaternary diamines as mass spectrometry cleavable crosslinkers for protein interactions. *J. Am. Soc. Mass Spectrom.* **23**, 201–212 (2012).

[ADS](#) [CAS](#) [Google Scholar](#)

23. 23.

Hagen, S. E. et al. Synthesis of CID-cleavable protein crosslinking agents containing quaternary amines for structural mass spectrometry. *Org. Biomol. Chem.* **16**, 8245–8248 (2018).

[Google Scholar](#)

24. 24.

Bayburt, T. H. et al. Monomeric rhodopsin is sufficient for normal rhodopsin kinase (GRK1) phosphorylation and arrestin-1 binding. *J. Biol. Chem.* **286**, 1420–1428 (2011).

[CAS](#) [Google Scholar](#)

25. 25.

Palczewski, K., Kahn, N. & Hargrave, P. A. Nucleoside inhibitors of rhodopsin kinase. *Biochemistry* **29**, 6276–6282 (1990).

[CAS](#) [Google Scholar](#)

26. 26.

Waldschmidt, H. V. et al. Structure-based design, synthesis, and biological evaluation of highly selective and potent G protein-coupled receptor kinase 2 inhibitors. *J. Med. Chem.* **59**, 3793–3807 (2016).

[CAS](#) [PubMed](#) [PubMed Central](#) [Google Scholar](#)

27. 27.

Komolov, K. E. et al. Structure of a GRK5–calmodulin complex reveals molecular mechanism of GRK activation and substrate targeting. *Mol. Cell* **81**, 323–339.e11 (2021).

[CAS](#) [Google Scholar](#)

28. 28.

Huang, C. C., Yoshino-Koh, K. & Tesmer, J. J. G. A surface of the kinase domain critical for the allosteric activation of G protein-coupled receptor kinases. *J. Biol. Chem.* **284**, 17206–17215 (2009).

[CAS](#) [PubMed](#) [PubMed Central](#) [Google Scholar](#)

29. 29.

Madhusudan, A., Akamine, P., Xuong, N. H. & Taylor, S. S. Crystal structure of a transition state mimic of the catalytic subunit of cAMP-dependent protein kinase. *Nat. Struct. Biol.* **9**, 273–277 (2002).

[CAS](#) [Google Scholar](#)

30. 30.

Yao, X. Q. et al. Navigating the conformational landscape of G protein-coupled receptor kinases during allosteric activation. *J. Biol. Chem.* **292**, 16032–16043 (2017).

[CAS](#) [PubMed](#) [PubMed Central](#) [Google Scholar](#)

31. 31.

Zhou, X. E. et al. Identification of phosphorylation codes for arrestin recruitment by G protein-coupled receptors. *Cell* **170**, 457–469.e13 (2017).

[CAS](#) [PubMed](#) [PubMed Central](#) [Google Scholar](#)

32. 32.

Farrens, D. L., Altenbach, C., Yang, K., Hubbell, W. L. & Khorana, H. G. Requirement of rigid-body motion of transmembrane helices for light activation of rhodopsin. *Science* **274**, 768–770 (1996).

[ADS](#) [CAS](#) [Google Scholar](#)

33. 33.

Pao, C. S., Barker, B. L. & Benovic, J. L. Role of the amino terminus of G protein-coupled receptor kinase 2 in receptor phosphorylation. *Biochemistry* **48**, 7325–7333 (2009).

[CAS](#) [Google Scholar](#)

34. 34.

Huang, C. C., Orban, T., Jastrzebska, B., Palczewski, K. & Tesmer, J. J. Activation of G protein-coupled receptor kinase 1 involves interactions between its N-terminal region and its kinase domain. *Biochemistry* **50**, 1940–1949 (2011).

[CAS](#) [Google Scholar](#)

35. 35.

Jones Brunette, A. M., Sinha, A., David, L. & Farrens, D. L. Evidence that the rhodopsin kinase (GRK1) N-terminus and the transducin G α C-terminus interact with the same “hydrophobic patch” on rhodopsin TM5. *Biochemistry* **55**, 3123–3135 (2016).

[CAS](#) [Google Scholar](#)

36. 36.

Kelleher, D. J. & Johnson, G. L. Characterization of rhodopsin kinase purified from bovine rod outer segments. *J. Biol. Chem.* **265**, 2632–2639 (1990).

[CAS](#) [Google Scholar](#)

37. 37.

Buczyłko, J., Gutmann, C. & Palczewski, K. Regulation of rhodopsin kinase by autophosphorylation. *Proc. Natl Acad. Sci. USA* **88**, 2568–2572 (1991).

[ADS](#) [PubMed](#) [PubMed Central](#) [Google Scholar](#)

38. 38.

Kunapuli, P., Gurevich, V. V. & Benovic, J. L. Phospholipid-stimulated autophosphorylation activates the G protein-coupled receptor kinase GRK5. *J. Biol. Chem.* **269**, 10209–10212 (1994).

[CAS](#) [Google Scholar](#)

39. 39.

Premont, R. T., Koch, W. J., Inglese, J. & Lefkowitz, R. J. Identification, purification, and characterization of GRK5, a member of the family of G protein-coupled receptor kinases. *J. Biol. Chem.* **269**, 6832–6841 (1994).

[CAS](#) [Google Scholar](#)

40. 40.

Ping, Y. Q. et al. Structures of the glucocorticoid-bound adhesion receptor GPR97-G_o complex. *Nature* **589**, 620–626 (2021).

[ADS](#) [CAS](#) [Google Scholar](#)

41. 41.

Dhami, G. K. & Ferguson, S. S. Regulation of metabotropic glutamate receptor signaling, desensitization and endocytosis. *Pharmacol. Ther.* **111**, 260–271 (2006).

[CAS](#) [Google Scholar](#)

42. 42.

Dhami, G. K. et al. G Protein-coupled receptor kinase 2 regulator of G protein signaling homology domain binds to both metabotropic glutamate receptor 1a and Galphaq to attenuate signaling. *J. Biol. Chem.* **279**, 16614–16620 (2004).

[CAS](#) [Google Scholar](#)

43. 43.

Iacovelli, L. et al. Regulation of group II metabotropic glutamate receptors by G protein-coupled receptor kinases: mGlu2 receptors are resistant to homologous desensitization. *Mol. Pharmacol.* **75**, 991–1003 (2009).

[CAS](#) [Google Scholar](#)

44. 44.

Ohguro, H., Palczewski, K., Ericsson, L. H., Walsh, K. A. & Johnson, R. S. Sequential phosphorylation of rhodopsin at multiple sites. *Biochemistry* **32**, 5718–5724 (1993).

[CAS](#) [Google Scholar](#)

45. 45.

Yang, J. et al. Crystal structure of an activated Akt/protein kinase B ternary complex with GSK3-peptide and AMP-PNP. *Nat. Struct. Biol.* **9**, 940–944 (2002).

[CAS](#) [Google Scholar](#)

46. 46.

Reiter, E., Ahn, S., Shukla, A. K. & Lefkowitz, R. J. Molecular mechanism of β-arrestin-biased agonism at seven-transmembrane receptors. *Annu. Rev. Pharmacol. Toxicol.* **52**, 179–197 (2012).

[CAS](#) [Google Scholar](#)

47. 47.

Nobles, K. N. et al. Distinct phosphorylation sites on the β(2)-adrenergic receptor establish a barcode that encodes differential functions of β-arrestin. *Sci. Signal.* **4**, ra51 (2011).

[CAS](#) [PubMed](#) [PubMed Central](#) [Google Scholar](#)

48. 48.

Shoemaker, B. A., Portman, J. J. & Wolynes, P. G. Speeding molecular recognition by using the folding funnel: the fly-casting mechanism. *Proc. Natl Acad. Sci. USA* **97**, 8868–8873 (2000).

[ADS](#) [CAS](#) [PubMed](#) [PubMed Central](#) [Google Scholar](#)

49. 49.

Singh, P., Wang, B., Maeda, T., Palczewski, K. & Tesmer, J. J. Structures of rhodopsin kinase in different ligand states reveal key elements involved in G protein-coupled receptor kinase activation. *J. Biol. Chem.* **283**, 14053–14062 (2008).

[CAS](#) [PubMed](#) [PubMed Central](#) [Google Scholar](#)

50. 50.

Palczewski, K. et al. Crystal structure of rhodopsin: a G protein-coupled receptor. *Science* **289**, 739–745 (2000).

[ADS](#) [CAS](#) [Google Scholar](#)

51. 51.

Pitcher, J. A. et al. Feedback inhibition of G protein-coupled receptor kinase 2 (GRK2) activity by extracellular signal-regulated kinases. *J. Biol. Chem.* **274**, 34531–34534 (1999).

[CAS](#) [Google Scholar](#)

52. 52.

Yu, Q. M. et al. The amino terminus with a conserved glutamic acid of G protein-coupled receptor kinases is indispensable for their ability to phosphorylate photoactivated rhodopsin. *J. Neurochem.* **73**, 1222–1227 (1999).

[CAS](#) [Google Scholar](#)

53. 53.

Sterne-Marr, R. et al. GRK2 activation by receptors: role of the kinase large lobe and carboxyl-terminal tail. *Biochemistry* **48**, 4285–4293

(2009).

[CAS](#) [Google Scholar](#)

54. 54.

Komolov, K. E., Bhardwaj, A. & Benovic, J. L. Atomic structure of GRK5 reveals distinct structural features novel for G protein-coupled receptor kinases. *J. Biol. Chem.* **290**, 20629–20647 (2015).

[CAS](#) [PubMed](#) [PubMed Central](#) [Google Scholar](#)

55. 55.

Lodowski, D. T. et al. The role of G $\beta\gamma$ and domain interfaces in the activation of G protein-coupled receptor kinase 2. *Biochemistry* **44**, 6958–6970 (2005).

[CAS](#) [Google Scholar](#)

56. 56.

Baameur, F. et al. Role for the regulator of G-protein signaling homology domain of G protein-coupled receptor kinases 5 and 6 in $\beta 2$ -adrenergic receptor and rhodopsin phosphorylation. *Mol. Pharmacol.* **77**, 405–415 (2010).

[CAS](#) [PubMed](#) [PubMed Central](#) [Google Scholar](#)

57. 57.

Lodowski, D. T., Tesmer, V. M., Benovic, J. L. & Tesmer, J. J. The structure of G protein-coupled receptor kinase (GRK)-6 defines a second lineage of GRKs. *J. Biol. Chem.* **281**, 16785–16793 (2006).

[CAS](#) [Google Scholar](#)

58. 58.

Papermaster, D. S. Preparation of retinal rod outer segments. *Methods Enzymol.* **81**, 48–52 (1982).

[CAS](#) [Google Scholar](#)

59. 59.

Paduch, M. et al. Generating conformation-specific synthetic antibodies to trap proteins in selected functional states. *Methods* **60**, 3–14 (2013).

[CAS](#) [Google Scholar](#)

60. 60.

Miller, K. R. et al. T cell receptor-like recognition of tumor in vivo by synthetic antibody fragment. *PLoS ONE* **7**, e43746 (2012).

[ADS](#) [CAS](#) [PubMed](#) [PubMed Central](#) [Google Scholar](#)

61. 61.

Suloway, C. et al. Automated molecular microscopy: the new Leginon system. *J. Struct. Biol.* **151**, 41–60 (2005).

[CAS](#) [Google Scholar](#)

62. 62.

Zivanov, J. et al. New tools for automated high-resolution cryo-EM structure determination in RELION-3. *eLife* **7**, e42166 (2018).

[PubMed](#) [PubMed Central](#) [Google Scholar](#)

63. 63.

Zheng, S. Q. et al. MotionCor2: anisotropic correction of beam-induced motion for improved cryo-electron microscopy. *Nat. Methods* **14**, 331–332 (2017).

[CAS](#) [PubMed](#) [PubMed Central](#) [Google Scholar](#)

64. 64.

Zhang, K. Gctf: real-time CTF determination and correction. *J. Struct. Biol.* **193**, 1–12 (2016).

[ADS](#) [CAS](#) [PubMed](#) [PubMed Central](#) [Google Scholar](#)

65. 65.

Punjani, A., Rubinstein, J. L., Fleet, D. J. & Brubaker, M. A. cryoSPARC: algorithms for rapid unsupervised cryo-EM structure determination. *Nat. Methods* **14**, 290–296 (2017).

[CAS](#) [PubMed](#) [Google Scholar](#)

66. 66.

Tan, Y. Z. et al. Addressing preferred specimen orientation in single-particle cryo-EM through tilting. *Nat. Methods* **14**, 793–796 (2017).

[CAS](#) [PubMed](#) [PubMed Central](#) [Google Scholar](#)

67. 67.

Bouley, R. et al. Structural determinants influencing the potency and selectivity of indazole-paroxetine hybrid G protein-coupled receptor kinase 2 inhibitors. *Mol. Pharmacol.* **92**, 707–717 (2017).

[CAS](#) [PubMed](#) [PubMed Central](#) [Google Scholar](#)

68. 68.

Ludtke, S. J., Baldwin, P. R. & Chiu, W. EMAN: semiautomated software for high-resolution single-particle reconstructions. *J. Struct. Biol.* **128**, 82–97 (1999).

[CAS](#) [Google Scholar](#)

69. 69.

Yang, Z., Fang, J., Chittuluru, J., Asturias, F. J. & Penczek, P. A. Iterative stable alignment and clustering of 2D transmission electron microscope images. *Structure* **20**, 237–247 (2012).

[CAS](#) [PubMed](#) [PubMed Central](#) [Google Scholar](#)

70. 70.

Perez-Riverol, Y. et al. The PRIDE database and related tools and resources in 2019: improving support for quantification data. *Nucleic Acids Res.* **47**, D442–D450 (2019).

[CAS](#) [PubMed](#) [Google Scholar](#)

71. 71.

Rasmussen, S. G. et al. Crystal structure of the $\beta 2$ adrenergic receptor-Gs protein complex. *Nature* **477**, 549–555 (2011).

[ADS](#) [CAS](#) [PubMed](#) [PubMed Central](#) [Google Scholar](#)

72. 72.

Bujacz, A. Structures of bovine, equine and leporine serum albumin. *Acta Crystallogr. D* **68**, 1278–1289 (2012).

[CAS](#) [Google Scholar](#)

73. 73.

Combe, C. W., Fischer, L. & Rappsilber, J. xiNET: cross-link network maps with residue resolution. *Mol. Cell. Proteomics* **14**, 1137–1147 (2015).

[CAS](#) [PubMed](#) [PubMed Central](#) [Google Scholar](#)

[Download references](#)

Acknowledgements

This work was supported by National Institutes of Health grants HL071818, HL122416, and CA221289 (to J.J.G.T.), GM117372 (to A.A.K.), GM095832, GM105942, GM109896, and GM105920 (to P.C.A.), an American Heart Association Post-Doctoral Fellowship (19POST34450193, to Q.C.), and National Science Foundation grant MCB-1517617 (to X.-Q.Y.). J.J.G.T. was also supported by the Walther Cancer Foundation. We thank the Purdue Cryo-EM Facility for equipment access and support.

Author information

Affiliations

1. Department of Biological Sciences, Purdue University, West Lafayette, IN, USA

Qiuyan Chen, Zhuang Li, Dhabaleswar Patra, Chun-Liang Chen, Thomas Klose, Leifu Chang & John J. G. Tesmer

2. Department of Medicinal Chemistry and Molecular Pharmacology, Purdue University, West Lafayette, IN, USA

Qiuyan Chen, Dhabaleswar Patra, Chun-Liang Chen & John J. G. Tesmer

3. Department of Biological Chemistry, University of Michigan, Ann Arbor, MI, USA

Manolo Plasencia & Philip C. Andrews

4. Department of Biochemistry and Molecular Biology, University of Chicago, Chicago, IL, USA

Somnath Mukherjee & Anthony A. Kossiakoff

5. Department of Chemistry, Georgia State University, Atlanta, GA, USA

Xin-Qiu Yao

6. Institute for Biophysical Dynamics, University of Chicago, Chicago, IL, USA

Anthony A. Kossiakoff

7. Department of Computational Medicine and Bioinformatics, University of Michigan, Ann Arbor, MI, USA

Philip C. Andrews

8. Department of Chemistry, University of Michigan, Ann Arbor, MI, USA

Philip C. Andrews

Authors

1. Qiuyan Chen

[View author publications](#)

You can also search for this author in [PubMed](#) [Google Scholar](#)

2. Manolo Plasencia

[View author publications](#)

You can also search for this author in [PubMed](#) [Google Scholar](#)

3. Zhuang Li

[View author publications](#)

You can also search for this author in [PubMed](#) [Google Scholar](#)

4. Somnath Mukherjee

[View author publications](#)

You can also search for this author in [PubMed](#) [Google Scholar](#)

5. Dhabaleswar Patra

[View author publications](#)

You can also search for this author in [PubMed](#) [Google Scholar](#)

6. Chun-Liang Chen

[View author publications](#)

You can also search for this author in [PubMed](#) [Google Scholar](#)

7. Thomas Klose

[View author publications](#)

You can also search for this author in [PubMed](#) [Google Scholar](#)

8. Xin-Qiu Yao

[View author publications](#)

You can also search for this author in [PubMed](#) [Google Scholar](#)

9. Anthony A. Kossiakoff

[View author publications](#)

You can also search for this author in [PubMed](#) [Google Scholar](#)

10. Leifu Chang

[View author publications](#)

You can also search for this author in [PubMed](#) [Google Scholar](#)

11. Philip C. Andrews

[View author publications](#)

You can also search for this author in [PubMed](#) [Google Scholar](#)

12. John J. G. Tesmer

[View author publications](#)

You can also search for this author in [PubMed](#) [Google Scholar](#)

Contributions

Q.C. and J.J.G.T. conceptualized the study. Q.C. produced and purified rhodopsin and GRK1, and performed crosslinking and kinetic assays. S.M., Q.C., J.J.G.T., and A.A.K. selected the Fabs. Q.C., J.J.G.T., Z.L., and L.C. collected data and performed structure determinations of Rho*-GRK1 and Rho*-GRK1(S5E/EE). Q.C. and J.J.G.T collected data and performed structure determinations of Rho*-GRK1(S5E/EE)-Fab1 and Rho*-GRK1(S5E/EE)-Fab6. T.K. assisted with cryo-EM data collection for all four reconstructions. M.P. and P.C.A. performed the mass spectrometry analysis. D.P. collected and performed negative-stain EM analysis. C.-L.C., J.J.G.T and Q.C. performed docking and molecular simulations. X.-Q.Y. performed the PCA analysis. Q.C. wrote the original draft and all authors further edited the manuscript. Q.C., J.J.G.T. and P.C.A. contributed funding.

Corresponding author

Correspondence to [John J. G. Tesmer](#).

Ethics declarations

Competing interests

The authors declare no competing interests.

Additional information

Peer review information *Nature* thanks Vsevolod Gurevich, Carol Robinson and Patrick M. Sexton for their contribution to the peer review of this work.

Publisher's note Springer Nature remains neutral with regard to jurisdictional claims in published maps and institutional affiliations.

Extended data figures and tables

Extended Data Fig. 1 Modulation of GRK1 activity by anionic lipids, Rho* C-terminal modifications, and Fab fragments.

a, Kinetic analysis of GRK1 phosphorylation of Rho* in ROS or LMNG or LMNG + c8-PtdIns(4,5)P₂. Mean ± s.d., $n = 4$ technical replicates.

Reactions were performed in 50 mM HEPES (pH 8.0), 10 mM MgCl₂ for 2 min at room temperature. **b**, Kinetic analysis of GRK1 phosphorylation of Rho* in ROS or POPC nanodiscs containing 40% POPG or 40% POPS or 10% PtdIns(4,5)P₂. Mean ± s.d., $n = 3$ technical replicates. Reactions were performed in 50 mM HEPES (pH 8.0), 10 mM MgCl₂ for 2 min at room temperature. **c**, Representative Michaelis–Menten kinetics measurement with varying ATP. Rho* was reconstituted with POPC nanodiscs containing 40% POPG (black squares) or 40% POPS (black triangles) and compared with Rho* in ROS (black circles). GRK1(5A) activity was greatly diminished relative to GRK1 under these conditions (blue symbols) but was still somewhat responsive to anionic lipids. **d**, Approximate location of the five positively charged residues places them close to the lipid bilayer. **e**, The crosslinking yield (corresponding to the amount of complex formed divided by the sum of the input GRK1 and Rho*) of GRK1(5A) was significantly lower than that of GRK1 in the presence of c8-PtdIns(4,5)P₂ but not in its absence. The crosslinking level of GRK1(5A) was compared with that of GRK1 using a two-sided *t*-test ($n = 3$ technical replicates) in the presence or absence of c8-PtdIns(4,5)P₂. For gel source data, see Supplementary Fig.

[5f](#). **f**, The crosslinking yield of p-Rho* (with estimated 6–8 phosphates out of 7 incorporated based on a standard curve) with GRK1 was compared with that of unphosphorylated rhodopsin using two-sided *t*-test ($n = 4$ technical replicates). For gel source data, see Supplementary Fig. [5h](#). **g**, The crosslinking yield of Asp-N-truncated Rho* (cleavage site N-terminal to Asp329) was compared with that of full-length Rho* using two-sided *t*-test ($n = 5$ technical replicates; N.S., not significant). For gel source data, see Supplementary Fig. [5i](#). The GRK1(K479R) mutant, which eliminates the other prominent crosslinking site, also did not affect our ability to trap the complex (data not shown). Mean ± s.d. **h**, ELISA analysis of Fab1 and Fab6

binding to GRK1 yielded EC₅₀ values of 2 and 5 nM, respectively ($n = 3$ technical replicates). Mean \pm s.d. **i**, Michaelis–Menten analysis of GRK1 in the absence or presence of threefold molar excess Fab1 or Fab6 ($n = 3$ technical replicates). Data were normalized to the fit $V_{\max, \text{Rho}}$ of GRK1. Mean \pm s.d.

Extended Data Fig. 2 Workflow of cryo-EM data processing and resolution analysis of Rho*-GRK1.

a, Representative raw cryo-EM micrograph from a total of 2,542. From these, 2.7 million particles were automatically picked in RELION-3 and were used to generate 2D class averages (shown are representative good classes). After screening out bad classes, 705,966 particles remained. Three major classes from 3D classification were generated in RELION-3 using an initial model generated by cryoSPARC. Class 2 (183,717 particles) showed the best quality and was selected for 3D auto-refinement, resulting in a final map at a global resolution of 7.0 Å (FSC cut-off = 0.143). **b**, Directional FSC indicated that the resolutions in the x and z directions are similar to the global resolution, whereas the resolution in the y direction is lower because fewer particles have this axis resolved. **c**, Plots of the global FSC together with the spread of directional resolution values defined by $\pm 1\sigma$ from the mean and a histogram of 100 such values evenly sampled over the 3D FSC. **d**, Local resolution map as estimated by RELION-3.

Extended Data Fig. 3 Workflow of cryo-EM data processing and resolution analysis of Rho*-GRK1(S5E/EE).

a, Representative raw cryo-EM micrograph from a total of 2,130. From these, 2.7 million particles were automatically picked in cryoSPARC and were used to generate 2D class averages (shown are representative good classes). After screening out bad classes, the 584,674 remaining particles were imported to RELION-3 and used to generate six major classes from 3D classification in RELION-3 using an initial model generated by cryoSPARC. Class 6 (132,721 particles) showed the best quality and was selected for 3D auto-refinement, resulting in a final map at a global resolution of 5.8 Å (FSC cut-off = 0.143). **b**, Directional FSC indicates that

the resolutions in the x and z directions are similar to the global resolution, whereas the resolution in the y direction is lower. **c**, Plots of the global FSC together with the spread of directional resolution values defined by $\pm 1\sigma$ from the mean and a histogram of 100 such values evenly sampled over the 3D FSC. **d**, Local resolution map as estimated by RELION-3.

Extended Data Fig. 4 Workflow of cryo-EM data processing and resolution analysis of Rho*-GRK1(S5E/EE)-Fab1.

a, Representative raw cryo-EM micrograph from a total of 5,501. From these, 5.7 million particles were automatically picked in cryoSPARC and were used to generate 2D class averages (shown are representative good classes). After screening out bad classes, the 421,682 remaining particles were further processed using heterogeneous refinement. Classes 2 and 3 showed similar quality and were selected for homogeneous refinement and then non-uniform refinement in cryoSPARC, resulting in a final map at a global resolution of 4.1 Å (FSC cut-off = 0.143). **b**, Directional FSC indicates that the resolutions in the x and z directions are similar to the global resolution, whereas the resolution in the y direction is lower. **c**, Plots of the global FSC together with the spread of directional resolution values defined by $\pm 1\sigma$ from the mean and a histogram of 100 such values evenly sampled over the 3D FSC. **d**, Local resolution map as estimated by cryoSPARC.

Extended Data Fig. 5 Flow chart of cryo-EM data processing and resolution analysis of Rho*-GRK1(S5E/EE)-Fab6, and comparison of the Fab1 and Fab6 complexes.

a, A representative raw cryo-EM micrograph from a total of 8,358. From these, 7.5 million particles were automatically picked in cryoSPARC and were used to generate 2D class averages (shown are representative good classes). After screening out bad classes, the 352,864 remaining particles were further processed using heterogeneous refinement. Classes 2 and 3 showed similar quality and were selected for homogeneous refinement and then non-uniform refinement in cryoSPARC. The resolution of the final map is estimated to be 4.0 Å. Global resolution was determined by FSC

with a cut-off of 0.143. **b**, Directional FSC indicates that the resolutions in the x and z directions are similar to the globular resolution, whereas the resolution in the y direction is lower. **c**, Plots of the global FSC together with the spread of directional resolution values defined by $\pm 1\sigma$ from the mean and a histogram of 100 such values evenly sampled over the 3D FSC. **d**, Local resolution map as estimated by cryoSPARC. **e**, Overlay of Rho* from the Fab1 (red) and Fab6 (blue) complexes after alignment of the small lobes of their kinase domains. Rho* pivots by about 5.5° , largely around an axis roughly parallel to a vector joining the ICL1 and ICL3 loops of the receptor. The key interactions between Rho* and GRK1, namely that of TM3, TM5 and TM6 with α N, and ICL1 with the C-terminal end of the AST, stay intact. This is because the α N helix and the N-terminal half of the AST loop region of GRK1 shift with the receptor, which is reasonable given that these elements are known to be dynamic from crystal structures of GRKs. Motion of these elements is likely to be responsible for the observed difference in kinase domain conformation exhibited by the Fab1 and Fab6 complexes because they directly affect the hinge region of the kinase domain. There are, however, small conformational differences at the end of TM1 and the beginning of the ICL1 loop in Rho* that probably occur because the bound GPCR is trying to maintain optimal interactions with phosphosites at the end of the AST in each state. The conformation of ICL2 is also likely to change between the structures, but this region could not be accurately modelled. Because our PC analysis (Fig. 2e) suggests that the Fab6 complex features a less active conformation of the GRK1 kinase domain, it may represent an intermediate state in which α N and AST have engaged the receptor, but the kinase domain has yet to fully adopt a transition state-like conformation.

Extended Data Fig. 6 Assessment of ligand density, of the presence of all-trans retinal, and of the conformational heterogeneity of the GRK1 RH domain.

a, Electron density of all-*trans* retinal, contoured at 17σ (Fab1 map) and 13σ (Fab6 map); Sgv, contoured at 24σ (Fab1 map) and 26σ (Fab6 map); and α N, contoured at 21σ (Fab1 map) and 25σ (Fab6 map). **b**, Light- and GRK ligand-dependence of the crosslinking reaction between rhodopsin and GRK1. 11-*cis* retinal undergoes isomerization upon light exposure to

all-*trans* retinal, which serves as a full agonist for rhodopsin. The crosslinking level of GRK1 with rhodopsin in the dark ($n = 4$ technical replicates) and in the light with excess 11-*cis* retinal ($n = 3$ technical replicates) were compared to that of GRK1 with rhodopsin in the light using one-way ANOVA followed by a Dunnett's multiple comparisons test. Mean \pm s.d. **c**, Density for the RH domain was not observed by cryo-EM in any of our reconstructions. The map of Rho*-GRK1(S5E/EE)-Fab1 is shown here as an example. **d**, A representative negative-stain EM micrograph of the Rho*-GRK1 complex solubilized in LMNG (left) along with representative 2D averages (right), indicating heterogeneity in the bound GRK1. The smaller, variably positioned domain is interpreted as the RH domain.

Extended Data Fig. 7 GRK α N interactions, kinase domain conformational changes, and comparison of the interactions between Rho* and its three principal downstream targets.

a–d, The GRK N terminus folds into a helix (α N) that packs against the small lobe and AST of the kinase domain, forming a docking side for Rho* (**a**, **b**; GRK1 with Fab1 and Fab6 complexes, respectively), Ca²⁺·CaM (**c**; GRK5 in PDB entry 6PJX²⁷), or a twofold related crystal lattice contact (**d**; GRK6 in PDB entry 3NYN⁶). The interfaces shown are mediated by the same highly conserved hydrophobic residues (side chains shown with spheres). **e**, The cytoplasmic cleft and ICL1 of activated β_2 AR in its G-protein-bound conformation (PDB entry 3SN6⁷¹) readily accommodates α N and AST of GRK1. **f–h**, Kinase domain small lobes from different ‘active’ GRK structures were aligned to highlight differences in closure. **i–l**, Comparison of downstream proteins bound to the cytoplasmic surface of Rho*. The side chains of residues interacting with GRK1 in the Fab1 complex (**i**; PDB entry 7MTA), GRK1 in the Fab6 complex (**j**; PDB entry 7MTB), G α_t (transducin) (**k**; PDB entry 6OYA¹⁴) and arrestin-1 (**l**; PDB entry 5W0P³¹) are shown as yellow spheres. Note that α N of GRK1 and α 5 of G α bind with opposite polarity. **m**, **n**, Cartoon representations of GRK1 α N helix docked to Rho* in the Fab1 (**m**) and Fab6 (**n**) models. **o**, G α_t C

terminus bound to Rho* (PDB entry 6OYA¹⁴). **p**, Arrestin-1 finger loop bound to Rho* (PDB entry 5W0P³¹).

Extended Data Fig. 8 Interactions of GRK1 with intracellular loops of Rho* and development of autophosphorylation mimetic variants.

a, Interactions of GRK1 α N with the cytoplasmic cleft and H8 of Rho*. GRK1-Ser5 was modelled in a phosphorylated state to demonstrate proximity to Rho*-Lys311 and Arg314. **b**, GRK1 AST interaction with ICL1. The key participating residues are shown with stick side chains. Ser488 and Thr489 are autophosphorylation sites in GRK1. **c–g**, Kinetic and crosslinking analysis of GRK1 and phosphomimetic mutants of Rho* autophosphorylation (S5E; S488E and T489E (EE); S488D and T489D (DD); S5E, S488E, and T489E (S5E/EE)). One-way ANOVA followed by Dunnett’s multiple comparison test was carried out to compare each mutant with GRK1. Reactions were performed in 50 mM HEPES (pH 8.0), 10 mM MgCl₂ for 2 min at room temperature. Data were normalized to the $V_{\max,Rho}$ or $V_{\max,ATP}$ of GRK1. For Rho kinetics: S5E, $n = 4$; EE, $n = 5$; DD, $n = 3$; S5E/EE, $n = 3$. For ATP kinetics: S5E, $n = 3$; EE, $n = 3$; DD, $n = 4$; S5E/EE, $n = 4$ (all technical replicates). All data shown as mean \pm s.d. **f**, Time courses of tubulin phosphorylation by GRK1 and variants are similar. Data were normalized to the phosphorylation level of tubulin by GRK1 at 30 min ($n = 3$ technical replicates). **g**, Crosslinking yield of GRK1 variants relative to GRK1 ($n = 3$ technical replicates). For gel source data, see Supplementary Fig. 5. **h**, Interaction of the GRK1 small lobe with ICL2 of Rho*. The GRK1 α 0 helix from a basal ATP-bound structure (PDB entry 3C4Z⁴⁹) is modelled by aligning its small lobe with that in the Rho*-GRK1(S5E/EE)-Fab1 complex, demonstrating a potential clash between ICL2 and α 0. **i**, Interaction of GRK1 AST with ICL3.

Extended Data Fig. 9 MC4 crosslinker properties and liquid chromatography tandem mass spectrometry peptide coverage of the Rho*–GRK1 complex.

a, MC4 has two symmetrical amine-reactive NHS esters separated by a C4 linker attached to a quaternary *N*-morpholine group. *Conformational analyses of in vacuo MD simulations suggest an average carboxy C–C distance of approximately 6 Å. **b**, Characterization of MC4 reactive distance using BSA. The *y*-axis shows the frequency (expressed as %) of experimentally identified crosslinked lysine pairs within a certain Ca – Ca distance (*x*-axis) based on a BSA crystal structure (PDB entry 4F5S⁷²). **c**, Peptide sequence coverage obtained for the purified crosslinked Rho*–GRK1 complex after multistep digestion with *Staphylococcus aureus* Protease V8 (GluC)/mix (1:1 mixture of GluC/trypsin and GluC/chymotrypsin) or GluC/trypsin. **d**, Intramolecular and intermolecular crosslinks summarized from Supplementary Data Tables 2, 3 are shown with a bar plot generated by XiNET⁷³. Dashed green lines represent rare intermolecular crosslinks that were too distant to react in our cryo-EM models.

Extended Data Table 1 GRK mutations and their effects on kinase activity towards Rho* or a soluble substrate

[Full size table](#)

Extended Data Table 2 Cryo-EM data collection, refinement, and validation statistics

[Full size table](#)

Supplementary information

[Supplementary Information](#)

This file contains Supplementary Methods, Supplementary Figures 1-5, Supplementary Tables 1-4, a Supplementary Discussion and Supplementary References.

[Reporting Summary](#)

[Video 1](#)

: 360° rotation of the model for the Rho*-GRK1_{S5E/EE}-Fab1 complex fitted into its cryo-EM map. Corresponding map was contoured at 6 σ with the detergent micelle density omitted for clarity. Videos were generated using UCSF Chimera.

Video 2

: 360° rotation of the model for the Rho*-GRK1_{S5E/EE}-Fab6 complex fitted into its cryo-EM map. Corresponding map was contoured at 6 σ with the detergent micelle density omitted for clarity. Videos were generated using UCSF Chimera.

Video 3

: Conformational change associated with principal component 1 (PC1) derived from known GRK and PKA kinase domain structures. PC1 represents the dominant conformational change observed in the kinase domain (10% of variance). Images were generated by PyMOL2 (Schrödinger LLC) and videos were rendered with Photoshop 2020 (Adobe Inc).

Video 4

: Conformational changes associated with principal component 2 (PC2) derived from known GRK and PKA kinase domain structures. PC2 represents the second largest conformational change observed in the kinase domain (10% of variance). Images were generated by PyMOL2 (Schrödinger LLC) and videos were rendered with Photoshop 2020 (Adobe Inc).

Rights and permissions

[Reprints and Permissions](#)

About this article



Cite this article

Chen, Q., Plasencia, M., Li, Z. *et al.* Structures of rhodopsin in complex with G-protein-coupled receptor kinase 1. *Nature* **595**, 600–605 (2021). <https://doi.org/10.1038/s41586-021-03721-x>

[Download citation](#)

- Received: 25 May 2020
- Accepted: 11 June 2021
- Published: 14 July 2021
- Issue Date: 22 July 2021
- DOI: <https://doi.org/10.1038/s41586-021-03721-x>

Comments

By submitting a comment you agree to abide by our [Terms](#) and [Community Guidelines](#). If you find something abusive or that does not comply with our terms or guidelines please flag it as inappropriate.

[Access through your institution](#)

[Change institution](#)

[Buy or subscribe](#)

Associated Content

Receptor–enzyme complex structures show how receptors start to switch off

- Vsevolod V. Gurevich
- Eugenia V. Gurevich

Advertisement

This article was downloaded by **calibre** from <https://www.nature.com/articles/s41586-021-03721-x>

| [Section menu](#) | [Main menu](#) |

- Article
- [Published: 30 June 2021](#)

cAMP binding to closed pacemaker ion channels is non-cooperative

- [David S. White^{1,2} ✉ nAff4](#),
- [Sandipan Chowdhury¹ ✉ nAff5](#),
- [Vinay Idikuda](#) [ORCID: orcid.org/0000-0001-6324-5839](#)¹ nAff6,
- [Ruohan Zhang^{1,2}](#),
- [Scott T. Rettner³](#),
- [Randall H. Goldsmith](#) [ORCID: orcid.org/0000-0001-9083-8592](#)² &
- [Baron Chanda](#) [ORCID: orcid.org/0000-0003-4954-7034](#)¹ nAff6

[Nature](#) volume **595**, pages 606–610 (2021) [Cite this article](#)

- 2501 Accesses
- 38 Altmetric
- [Metrics details](#)

Subjects

- [Cyclic nucleotide-gated cation channels](#)
- [Ligand-gated ion channels](#)
- [Single-molecule biophysics](#)

Abstract

Electrical activity in the brain and heart depends on rhythmic generation of action potentials by pacemaker ion channels (HCN) whose activity is

regulated by cAMP binding¹. Previous work has uncovered evidence for both positive and negative cooperativity in cAMP binding^{2,3}, but such bulk measurements suffer from limited parameter resolution. Efforts to eliminate this ambiguity using single-molecule techniques have been hampered by the inability to directly monitor binding of individual ligand molecules to membrane receptors at physiological concentrations. Here we overcome these challenges using nanophotonic zero-mode waveguides⁴ to directly resolve binding dynamics of individual ligands to multimeric HCN1 and HCN2 ion channels. We show that cAMP binds independently to all four subunits when the pore is closed, despite a subsequent conformational isomerization to a flip state at each site. The different dynamics in binding and isomerization are likely to underlie physiologically distinct responses of each isoform to cAMP⁵ and provide direct validation of the ligand-induced flip-state model^{6,7,8,9}. This approach for observing stepwise binding in multimeric proteins at physiologically relevant concentrations can directly probe binding allostery at single-molecule resolution in other intact membrane proteins and receptors.

Access options

Subscribe to Journal

Get full journal access for 1 year

\$199.00

only \$3.90 per issue

[Subscribe](#)

All prices are NET prices.

VAT will be added later in the checkout.

Tax calculation will be finalised during checkout.

Rent or Buy article

Get time limited or full article access on ReadCube.

from \$8.99

[Rent or Buy](#)

All prices are NET prices.

Additional access options:

- [Log in](#)
- [Access through your institution](#)
- [Learn about institutional subscriptions](#)

Fig. 1: fcAMP binding to intact HCN channels in ZMWs.

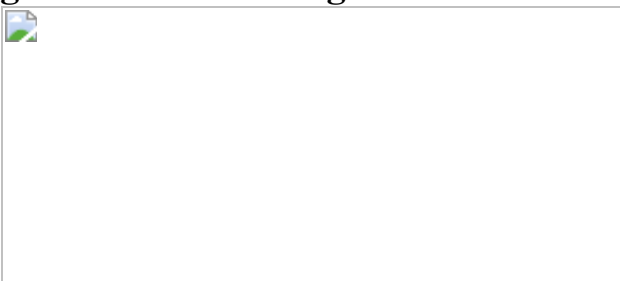


Fig. 2: fcAMP binds non-cooperatively to both HCN isoforms.

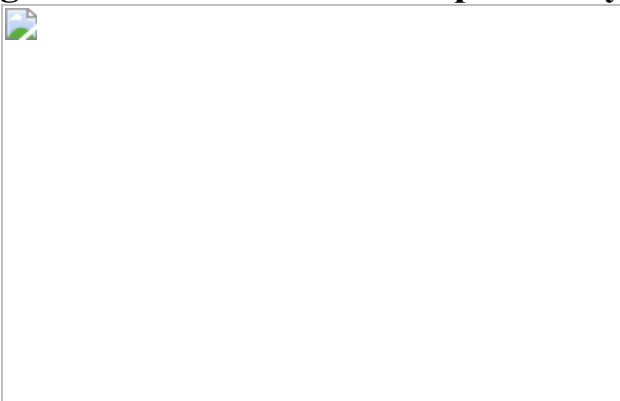


Fig. 3: Ligand binding induces a conformational change at each HCN subunit.

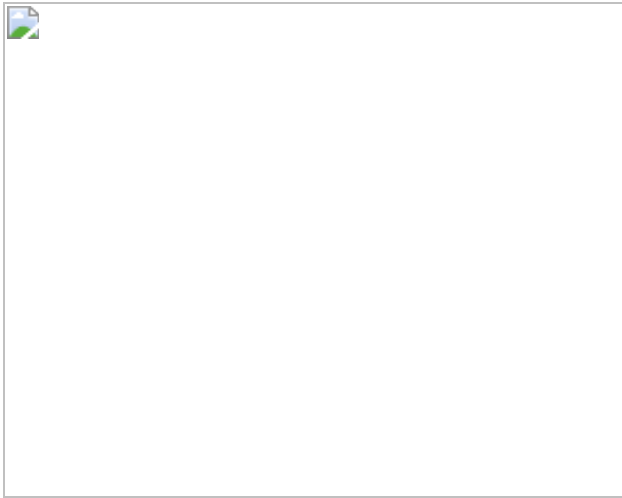
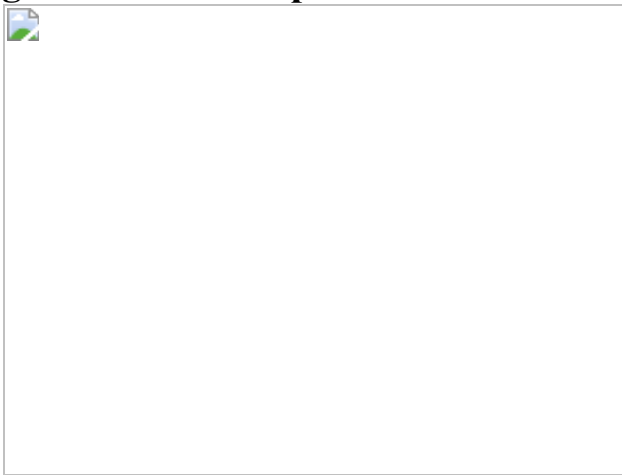


Fig. 4: A revised flip-state model.



Data availability

All experimental data are available upon reasonable request. [Source data](#) are provided with this paper.

Code availability

The DISCO software package is available at <https://github.com/ChandaLab/DISC> and fully described elsewhere³⁶. All additional MATLAB scripts for single-molecule analysis and image processing are available upon reasonable request.

References

1. 1.

Wahl-Schott, C. & Biel, M. HCN channels: structure, cellular regulation and physiological function. *Cell. Mol. Life Sci.* **66**, 470–494 (2009).

[CAS](#) [PubMed](#) [Article](#) [Google Scholar](#)

2. 2.

Kusch, J. et al. How subunits cooperate in cAMP-induced activation of homotetrameric HCN2 channels. *Nat. Chem. Biol.* **8**, 162–169 (2011).

[PubMed](#) [Article](#) [CAS](#) [Google Scholar](#)

3. 3.

Thon, S., Schulz, E., Kusch, J. & Benndorf, K. Conformational flip of nonactivated HCN2 channel subunits evoked by cyclic nucleotides. *Biophys. J.* **109**, 2268–2276 (2015).

[ADS](#) [CAS](#) [PubMed](#) [PubMed Central](#) [Article](#) [Google Scholar](#)

4. 4.

Levene, M. J. et al. Zero-mode waveguides for single-molecule analysis at high concentrations. *Science* **299**, 682–686 (2003).

[ADS](#) [CAS](#) [PubMed](#) [Article](#) [Google Scholar](#)

5. 5.

Wainger, B. J., DeGennaro, M., Santoro, B., Siegelbaum, S. A. & Tibbs, G. R. Molecular mechanism of cAMP modulation of HCN pacemaker channels. *Nature* **411**, 805–810 (2001).

[ADS](#) [CAS](#) [PubMed](#) [Article](#) [Google Scholar](#)

6. 6.

Lape, R., Colquhoun, D. & Sivilotti, L. G. On the nature of partial agonism in the nicotinic receptor superfamily. *Nature* **454**, 722–727 (2008).

[ADS](#) [CAS](#) [PubMed](#) [PubMed Central](#) [Article](#) [Google Scholar](#)

7. 7.

Jadey, S. & Auerbach, A. An integrated catch-and-hold mechanism activates nicotinic acetylcholine receptors. *J. Gen. Physiol.* **140**, 17–28 (2012).

[CAS](#) [PubMed](#) [PubMed Central](#) [Article](#) [Google Scholar](#)

8. 8.

Abele, R., Keinanen, K. & Madden, D. R. Agonist-induced isomerization in a glutamate receptor ligand-binding domain. A kinetic and mutagenetic analysis. *J. Biol. Chem.* **275**, 21355–21363 (2000).

[CAS](#) [PubMed](#) [Article](#) [Google Scholar](#)

9. 9.

Cheng, Q., Du, M., Ramanoudjame, G. & Jayaraman, V. Evolution of glutamate interactions during binding to a glutamate receptor. *Nat. Chem. Biol.* **1**, 329–332 (2005).

[CAS](#) [PubMed](#) [Article](#) [Google Scholar](#)

10. 10.

DiFrancesco, D. The role of the funny current in pacemaker activity. *Circ. Res.* **106**, 434–446 (2010).

[CAS](#) [PubMed](#) [Article](#) [Google Scholar](#)

11. 11.

DiFrancesco, D. & Tortora, P. Direct activation of cardiac pacemaker channels by intracellular cyclic AMP. *Nature* **351**, 145–147 (1991).

[ADS](#) [CAS](#) [PubMed](#) [Article](#) [Google Scholar](#)

12. 12.

Kusch, J. et al. Interdependence of receptor activation and ligand binding in HCN2 pacemaker channels. *Neuron* **67**, 75–85 (2010).

[CAS](#) [PubMed](#) [Article](#) [Google Scholar](#)

13. 13.

Chow, S. S., Van Petegem, F. & Accili, E. A. Energetics of cyclic AMP binding to HCN channel C terminus reveal negative cooperativity. *J. Biol. Chem.* **287**, 600–606 (2012).

[CAS](#) [PubMed](#) [Article](#) [Google Scholar](#)

14. 14.

Hines, K. E., Middendorf, T. R. & Aldrich, R. W. Determination of parameter identifiability in nonlinear biophysical models: a Bayesian approach. *J. Gen. Physiol.* **143**, 401–416 (2014).

[CAS](#) [PubMed](#) [PubMed Central](#) [Article](#) [Google Scholar](#)

15. 15.

Wyman, J. The binding potential, a neglected linkage concept. *J. Mol. Biol.* **11**, 631–644 (1965).

[CAS](#) [PubMed](#) [Article](#) [Google Scholar](#)

16. 16.

Sigg, D. A linkage analysis toolkit for studying allosteric networks in ion channels. *J. Gen. Physiol.* **141**, 29–60 (2013).

[CAS](#) [PubMed](#) [PubMed Central](#) [Article](#) [Google Scholar](#)

17. 17.

Chowdhury, S. & Chanda, B. Free-energy relationships in ion channels activated by voltage and ligand. *J. Gen. Physiol.* **141**, 11–28 (2013).

[CAS](#) [PubMed](#) [PubMed Central](#) [Article](#) [Google Scholar](#)

18. 18.

Chowdhury, S. & Chanda, B. Estimating the voltage-dependent free energy change of ion channels using the median voltage for activation. *J. Gen. Physiol.* **139**, 3–17 (2012).

[CAS](#) [PubMed](#) [PubMed Central](#) [Article](#) [Google Scholar](#)

19. 19.

Vafabakhsh, R., Levitz, J. & Isacoff, E. Y. Conformational dynamics of a class C G-protein-coupled receptor. *Nature* **524**, 497–501 (2015).

[ADS](#) [CAS](#) [PubMed](#) [PubMed Central](#) [Article](#) [Google Scholar](#)

20. 20.

Gregorio, G. G. et al. Single-molecule analysis of ligand efficacy in β_2 AR-G-protein activation. *Nature* **547**, 68–73 (2017).

[ADS](#) [CAS](#) [PubMed](#) [PubMed Central](#) [Article](#) [Google Scholar](#)

21. 21.

Liauw, B. W., Afsari, H. S. & Vafabakhsh, R. Conformational rearrangement during activation of a metabotropic glutamate receptor. *Nat. Chem. Biol.* **17**, 291–297 (2021).

[CAS](#) [PubMed](#) [PubMed Central](#) [Article](#) [Google Scholar](#)

22. 22.

Wang, Y. et al. Single molecule FRET reveals pore size and opening mechanism of a mechano-sensitive ion channel. *eLife* **3**, e01834 (2014).

[PubMed](#) [PubMed Central](#) [Article](#) [CAS](#) [Google Scholar](#)

23. 23.

Dolino, D. M. et al. The structure–energy landscape of NMDA receptor gating. *Nat. Chem. Biol.* **13**, 1232–1238 (2017).

[CAS](#) [PubMed](#) [PubMed Central](#) [Article](#) [Google Scholar](#)

24. 24.

Wang, S., Vafabakhsh, R., Borschel, W. F., Ha, T. & Nichols, C. G. Structural dynamics of potassium-channel gating revealed by single-molecule FRET. *Nat. Struct. Mol. Biol.* **23**, 31–36 (2016).

[CAS](#) [PubMed](#) [Article](#) [Google Scholar](#)

25. 25.

Jiang, Y. et al. Sensing cooperativity in ATP hydrolysis for single multisubunit enzymes in solution. *Proc. Natl Acad. Sci. USA* **108**, 16962–16967 (2011).

[ADS](#) [CAS](#) [PubMed](#) [PubMed Central](#) [Article](#) [Google Scholar](#)

26. 26.

Hoskins, A. A. et al. Ordered and dynamic assembly of single spliceosomes. *Science* **331**, 1289–1295 (2011).

[ADS](#) [CAS](#) [PubMed](#) [PubMed Central](#) [Article](#) [Google Scholar](#)

27. 27.

Holzmeister, P., Acuna, G. P., Grohmann, D. & Tinnefeld, P. Breaking the concentration limit of optical single-molecule detection. *Chem. Soc. Rev.* **43**, 1014–1028 (2014).

[CAS](#) [PubMed](#) [Article](#) [Google Scholar](#)

28. 28.

Wu, J. Y., Stone, M. D. & Zhuang, X. A single-molecule assay for telomerase structure-function analysis. *Nucleic Acids Res.* **38**, e16 (2010).

[PubMed](#) [Article](#) [CAS](#) [Google Scholar](#)

29. 29.

Morse, J. C. et al. Elongation factor-Tu can repetitively engage aminoacyl-tRNA within the ribosome during the proofreading stage of tRNA selection. *Proc. Natl Acad. Sci. USA* **117**, 3610–3620 (2020).

[CAS](#) [PubMed](#) [PubMed Central](#) [Article](#) [Google Scholar](#)

30. 30.

Zheng, J. & Trudeau, M. C. *Handbook of Ion Channels* (CRC, 2015).

31. 31.

Zhu, P. & Craighead, H. G. in *Annual Review of Biophysics* Vol. 41 (ed. D. C. Rees) 269–293 (2012).

32. 32.

Goldschen-Ohm, M. P. et al. Structure and dynamics underlying elementary ligand binding events in human pacemaking channels. *eLife* **5**, e20797 (2016).

[PubMed](#) [PubMed Central](#) [Article](#) [CAS](#) [Google Scholar](#)

33. 33.

Uemura, S. et al. Real-time tRNA transit on single translating ribosomes at codon resolution. *Nature* **464**, 1012–1017 (2010).

[ADS](#) [CAS](#) [PubMed](#) [PubMed Central](#) [Article](#) [Google Scholar](#)

34. 34.

Eid, J. et al. Real-time DNA sequencing from single polymerase molecules. *Science* **323**, 133–138 (2009).

[ADS](#) [CAS](#) [Article](#) [Google Scholar](#)

35. 35.

Goldschen-Ohm, M. P., White, D. S., Klenchin, V. A., Chanda, B. & Goldsmith, R. H. Observing single-molecule dynamics at millimolar concentrations. *Angew. Chem. Int. Ed.* **56**, 2399–2402 (2017).

[CAS](#) [Article](#) [Google Scholar](#)

36. 36.

White, D. S., Goldschen-Ohm, M. P., Goldsmith, R. H. & Chanda, B. Top-down machine learning approach for high-throughput single-molecule analysis. *eLife* **9**, e53357 (2020).

[PubMed](#) [PubMed Central](#) [Article](#) [Google Scholar](#)

37. 37.

Wang, J., Chen, S. & Siegelbaum, S. A. Regulation of hyperpolarization-activated HCN channel gating and cAMP modulation due to interactions of COOH terminus and core transmembrane regions. *J. Gen. Physiol.* **118**, 237–250 (2001).

[CAS](#) [PubMed](#) [PubMed Central](#) [Article](#) [Google Scholar](#)

38. 38.

Korlach, J. et al. Selective aluminum passivation for targeted immobilization of single DNA polymerase molecules in zero-mode waveguide nanostructures. *Proc. Natl Acad. Sci. USA* **105**, 1176–1181 (2008).

[ADS](#) [CAS](#) [PubMed](#) [PubMed Central](#) [Article](#) [Google Scholar](#)

39. 39.

Ding, S. & Sachs, F. Evidence for non-independent gating of P2X₂ receptors expressed in *Xenopus* oocytes. *BMC Neurosci.* **3**, 17 (2002).

[PubMed](#) [PubMed Central](#) [Article](#) [Google Scholar](#)

40. 40.

Collauto, A. et al. Rates and equilibrium constants of the ligand-induced conformational transition of an HCN ion channel protein domain determined by DEER spectroscopy. *Phys. Chem. Chem. Phys.* **19**, 15324–15334 (2017).

[CAS](#) [PubMed](#) [PubMed Central](#) [Article](#) [Google Scholar](#)

41. 41.

Zagotta, W. N. et al. Structural basis for modulation and agonist specificity of HCN pacemaker channels. *Nature* **425**, 200–205 (2003).

[ADS](#) [CAS](#) [PubMed](#) [Article](#) [Google Scholar](#)

42. 42.

Qin, F., Auerbach, A. & Sachs, F. A direct optimization approach to hidden Markov modeling for single channel kinetics. *Biophys. J.* **79**, 1915–1927 (2000).

[CAS](#) [PubMed](#) [PubMed Central](#) [Article](#) [Google Scholar](#)

43. 43.

Nicolai, C. & Sachs, F. Solving ion channel kinetics with the QuB software. *Biophys. Rev. Lett.* **8**, 191–211 (2013).

[Article](#) [Google Scholar](#)

44. 44.

Schwarz, G. Estimating dimension of a model. *Ann. Stat.* **6**, 461–464 (1978).

[MathSciNet](#) [MATH](#) [Article](#) [Google Scholar](#)

45. 45.

Lolicato, M. et al. Tetramerization dynamics of C-terminal domain underlies isoform-specific cAMP gating in hyperpolarization-activated cyclic nucleotide-gated channels. *J. Biol. Chem.* **286**, 44811–44820 (2011).

[CAS](#) [PubMed](#) [PubMed Central](#) [Article](#) [Google Scholar](#)

46. 46.

Lee, C. H. & MacKinnon, R. Structures of the human HCN1 hyperpolarization-activated channel. *Cell* **168**, 111–120.e11 (2017).

[CAS](#) [PubMed](#) [PubMed Central](#) [Article](#) [Google Scholar](#)

47. 47.

Goehring, A. et al. Screening and large-scale expression of membrane proteins in mammalian cells for structural studies. *Nat. Protoc.* **9**, 2574–2585 (2014).

[CAS](#) [PubMed](#) [PubMed Central](#) [Article](#) [Google Scholar](#)

48. 48.

Idikuda, V. et al. Singlet oxygen modification abolishes voltage-dependent inactivation of the sea urchin spHCN channel. *J. Gen. Physiol.* **150**, 1273–1286 (2018).

[CAS](#) [PubMed](#) [PubMed Central](#) [Article](#) [Google Scholar](#)

[Download references](#)

Acknowledgements

This research was supported by the NIH grants to B.C. (NS-116850, NS-101723, and NS-081293), D.S.W. (T32 fellowship GM007507) and NSF to R.H.G. (CHE-1856518). We thank K. A. Knapper and C. H. Vollbrecht for assistance with cover glass cleaning at the Wisconsin Centers for Nanoscale Technologies; M. P. Goldschen-Ohm and M. Smith for helpful discussions; C. Lingle and L. Anson for their feedback on the manuscript; and M. Jackson for sparking this collaboration. ZMWs were fabricated at the Center for Nanophase Materials Sciences at Oak Ridge National Laboratory, which is a DOE Office of Science User Facility.

Author information

Author notes

1. David S. White

Present address: Department of Biochemistry, University of Wisconsin-Madison, Madison, WI, USA

2. Sandipan Chowdhury

Present address: Department of Molecular Physiology and Biophysics, University of Iowa Carver College of Medicine, Iowa City, IA, USA

3. Vinay Idikuda & Baron Chanda

Present address: Center for Investigation of Membrane Excitability Diseases, Department of Anesthesiology, Washington University School of Medicine, St Louis, MO, USA

4. These authors contributed equally: David S. White, Sandipan Chowdhury

Affiliations

1. Department of Neuroscience, University of Wisconsin-Madison, Madison, WI, USA

David S. White, Sandipan Chowdhury, Vinay Idikuda, Ruohan Zhang & Baron Chanda

2. Department of Chemistry, University of Wisconsin-Madison, Madison, WI, USA

David S. White, Ruohan Zhang & Randall H. Goldsmith

3. Center for Nanophase Materials Sciences, Oak Ridge National Laboratory, Oak Ridge, TN, USA

Scott T. Rettner

Authors

1. David S. White

[View author publications](#)

You can also search for this author in [PubMed](#) [Google Scholar](#)

2. Sandipan Chowdhury

[View author publications](#)

You can also search for this author in [PubMed](#) [Google Scholar](#)

3. Vinay Idikuda

[View author publications](#)

You can also search for this author in [PubMed](#) [Google Scholar](#)

4. Ruohan Zhang

[View author publications](#)

You can also search for this author in [PubMed](#) [Google Scholar](#)

5. Scott T. Rettner

[View author publications](#)

You can also search for this author in [PubMed](#) [Google Scholar](#)

6. Randall H. Goldsmith

[View author publications](#)

You can also search for this author in [PubMed](#) [Google Scholar](#)

7. Baron Chanda

[View author publications](#)

You can also search for this author in [PubMed](#) [Google Scholar](#)

Contributions

D.S.W., S.C., R.H.G. and B.C. conceived and designed the studies; V.I. performed electrophysiology experiments; S.C. performed molecular biology and protein purification; D.S.W. and R.Z. performed single-molecule experiments; D.S.W. analysed single-molecule data. D.S.W. fabricated ZMWs under supervision of S.T.R.; D.S.W., S.C., R.H.G. and B.C. wrote the manuscript with input from others.

Corresponding authors

Correspondence to [Randall H. Goldsmith](#) or [Baron Chanda](#).

Ethics declarations

Competing interests

The authors declare no competing interests.

Additional information

Peer review information *Nature* thanks the anonymous, reviewer(s) for their contribution to the peer review of this work. Peer reviewer reports are available.

Publisher's note Springer Nature remains neutral with regard to jurisdictional claims in published maps and institutional affiliations.

Extended data figures and tables

Extended Data Fig. 1 Characterization of HCN1SM and HCN2SM.

a, Representative electrophysiological recordings (top) of HCN1SM (left) and HCN2SM (right) with voltage protocol. Tail currents (arrow) were collected at -130 mV and were used to generate the activation curves. **b**, Normalized activation curves of HCN1SM (left) and HCN2SM (right) in the absence or presence of saturating concentrations (500 μ M) of internal cAMP with a Boltzmann fit (red). Data points are mean \pm s.e.m. ($n = 5$ patches). $V_{1/2}$ values for are HCN1SM -71.2 ± 0.4 mV without cAMP and -69.1 ± 0.5 mV with cAMP. $V_{1/2}$ values for are HCN2SM -105.2 ± 0.6 mV without cAMP and -84.6 ± 0.5 mV with cAMP. **c**, Size exclusion chromatography (SEC) profiles of HCN1SM (grey) and HCN2SM (orange dashed). Triangles indicate the peak fraction (0.3 ml) used for single-molecule measurements. **d**, Example fluorescence vs time trajectory of photobleaching eGFP-tagged HCN2SM tetramers via TIRFM. **e**, Distributions of photobleaching steps overlaid with a maximum likelihood estimate of a zero-truncated binomial distribution (red) for a tetrameric complex with a probability (P) of observing eGFP (HCN1: $P = 0.65$, 95% CI [0.63, 0.67], $n = 752$; HCN1: $P = 0.67$, 95% CI [0.65, 0.69], $n = 588$).

[Source data](#)

Extended Data Fig. 2 Non-specific binding in ZMWs.

a, Bright field image of ZMW array on single-molecule imaging set-up featuring a 512×512 pixel EMCCD and a $100\times$ objective. Each white dot (about 1,600 per field of view) is a ZMW. **b, c**, Test of specific binding of eGFP-tagged HCN2SM to ZMWs (**b**) and of fcAMP (**c**) to HCN2SM in ZMWs. For **b** and **c**, all images shown are averaged over the first 10 frames (1 s) and background subtracted for visualization. Brightness and contrast were adjusted for clarity. **d**, Representative and randomly selected fluorescence trajectories of empty (no HCN) and passivated ZMWs with 1,000 nM fcAMP fit with DISC (black). The first 50 frames (grey) were removed from analysis.

[Source data](#)

Extended Data Fig. 3 fcAMP binding to HCN1SM in ZMWs.

Representative fluorescence trajectories of fcAMP (100 nM to 900 nM) binding to HCN1SM in ZMWs with idealized fits (black) imaged at 100-ms resolution. The first 50 frames (grey) were removed from analysis.

[Source data](#)

Extended Data Fig. 4 fcAMP binding to HCN2SM in ZMWs.

Representative fluorescence trajectories of fcAMP (100 nM to 1,500 nM) binding to HCN2SM in ZMWs with idealized fits (black) imaged at 100-ms resolution. The first 50 frames (grey) were removed from analysis.

[Source data](#)

Extended Data Fig. 5 All state occupancy distributions.

a, b, Normalized state occupancy distributions for HCN1SM (**a**) and HCN2SM (**b**) across all recorded fcAMP concentrations. Each plot

indicates the total number of molecules (n) and data points (that is, frames, m) included in the analysis. P is the success rate of the optimized binomial distribution considering four binding sites. All obtained and expected state occupancies values are in Supplementary Table 2.

[Source data](#)

Extended Data Fig. 6 Isolated-B1 Events of HCN1SM.

a, Dwell time distributions of isolated-B1 events for HCN1SM at various fcAMP concentrations overlaid with maximum likelihood estimates for monoexponential (blue dashed) and biexponential (red) distributions (Supplementary Table 3). For inset, error bars are the error of a binomial distribution (Methods). **b, c**, Coordinates of identified single-molecules in the 512×512 pixel field of view superimposed across all ZMW arrays. The colour bars denote the average dwell time (**b**) and fluorescence (**c**) of the isolated-B1 state for each molecule (n). **d**, Correlation of fluorescence intensity and dwell times for each isolated-B1 event (m), where r is the Pearson correlation coefficient. Data are binned for visualization.

[Source data](#)

Extended Data Fig. 7 Isolated-B1 Events of HCN2SM.

a, Dwell time distributions of isolated-B1 events for HCN2SM at various fcAMP concentrations overlaid with maximum likelihood estimates for monoexponential (blue dashed) and biexponential (red) distributions (Supplementary Table 3). For inset, error bars are the error of a binomial distribution (Methods). **b, c**, Coordinates of identified single-molecules in the 512×512 pixel field of view superimposed across all ZMW arrays. The colour bars denote the average dwell time (**b**) and fluorescence (**c**) of the isolated-B1 state for each molecule (n). **d**, Correlation of fluorescence intensity and dwell times for each isolated-B1 event (m), where r is the Pearson correlation coefficient. Data are binned for visualization.

[Source data](#)

Extended Data Fig. 8 Isolated-B1 events do no exhibit static heterogeneity.

a, e, Average isolated-B1 dwell time of HCN1SM (**a**) and HCN2SM (**e**) for each molecule at 100 nM fcAMP. Outliers (diamonds) were identified by three scaled median absolute deviations. Data plotted as mean \pm s.d. of exponential distribution. The blue dashed line indicates the average B1 dwell time across all molecules (HCN1SM: $n = 176$; HCN2SM: $n = 77$). **b, f**, Histograms of average isolated-B1 dwell times for each HCN1SM (**b**) and HCN2SM (**f**) molecule. **c, g**, Parameters for a monoexponential fit (τ) to isolated-B1 dwell times of HCN1SM (**c**) and HCN2SM (**g**). **d, h**, Parameters for a biexponential fit (τ_1, τ_2, A_1) to isolated-B1 dwell times of HCN1SM (**d**) and HCN2SM (**h**). For **c, g, d, h**, the ordinate corresponds to the obtained parameter ($\tau, \tau_1, \tau_2, A_1$) and error bars are 95% confidence intervals. All parameters were obtained using maximum likelihood estimates across all isolated-B1 events in either all data (HCN1SM: $n = 8,229$; HCN2SM: $n = 2,676$) or inlier (HCN1SM: $n = 7,816$; HCN2SM: $n = 2,575$) groups, as indicated on the abscissa.

[Source data](#)

Extended Data Fig. 9 HCN1SM dwell time distributions.

Dwell time distributions of all liganded states of HCN1SM across all fcAMP concentrations overlaid with expectations from the optimized rates in Fig. 4b.

[Source data](#)

Extended Data Fig. 10 HCN2SM dwell time distributions.

Dwell time distributions of all liganded states of HCN2SM across all fcAMP concentrations overlaid with expectations from the optimized rates from in Fig. 4b.

[Source data](#)

Supplementary information

Supplementary Information

This file contains Supplementary Note 1, Supplementary Methods, Supplementary Tables 1-7, and Supplementary Figures 1-2.

Reporting Summary

Peer Review File

Source data

Source Data Fig. 1

Source Data Fig. 2

Source Data Fig. 3

Source Data Fig. 4

Source Data Extended Data Fig. 1

Source Data Extended Data Fig. 2

Source Data Extended Data Fig. 3

Source Data Extended Data Fig. 4

Source Data Extended Data Fig. 5

Source Data Extended Data Fig. 6

Source Data Extended Data Fig. 7

[**Source Data Extended Data Fig. 8**](#)

[**Source Data Extended Data Fig. 9**](#)

[**Source Data Extended Data Fig. 10**](#)

Rights and permissions

[Reprints and Permissions](#)

About this article



Check for
updates

Cite this article

White, D.S., Chowdhury, S., Idikuda, V. *et al.* cAMP binding to closed pacemaker ion channels is non-cooperative. *Nature* **595**, 606–610 (2021). <https://doi.org/10.1038/s41586-021-03686-x>

[Download citation](#)

- Received: 20 October 2020
- Accepted: 02 June 2021
- Published: 30 June 2021
- Issue Date: 22 July 2021
- DOI: <https://doi.org/10.1038/s41586-021-03686-x>

Comments

By submitting a comment you agree to abide by our [Terms](#) and [Community Guidelines](#). If you find something abusive or that does not comply with our terms or guidelines please flag it as inappropriate.

[Access through your institution](#)

[Change institution](#)

[Buy or subscribe](#)

Advertisement

This article was downloaded by **calibre** from <https://www.nature.com/articles/s41586-021-03686-x>

| [Section menu](#) | [Main menu](#) |

Amendments & Corrections

- **[Publisher Correction: A 20-year retrospective review of global aquaculture](#)** [06 July 2021]

Publisher Correction •

Publisher Correction: A 20-year retrospective review of global aquaculture
[Download PDF](#)

- Publisher Correction
- [Published: 06 July 2021](#)

Publisher Correction: A 20-year retrospective review of global aquaculture

- [Rosamond L. Naylor](#) ORCID: [orcid.org/0000-0002-1260-3322](#)^{1,2},
- [Ronald W. Hardy](#)³,
- [Alejandro H. Buschmann](#) ORCID: [orcid.org/0000-0003-3246-681X](#)⁴,
- [Simon R. Bush](#)⁵,
- [Ling Cao](#)⁶,
- [Dane H. Klinger](#) ORCID: [orcid.org/0000-0003-4178-8167](#)^{7,8},
- [David C. Little](#)⁹,
- [Jane Lubchenco](#) ORCID: [orcid.org/0000-0003-3540-5879](#)¹⁰,
- [Sandra E. Shumway](#)¹¹ &
- [Max Troell](#) ORCID: [orcid.org/0000-0002-7509-8140](#)^{12,13}

[Nature](#) volume 595, page E36 (2021)[Cite this article](#)

- 871 Accesses
- 9 Altmetric
- [Metrics details](#)

Subjects

- [Environmental impact](#)

- [Environmental sciences](#)

The [Original Article](#) was published on 24 March 2021

[Download PDF](#)

Correction to: *Nature* <https://doi.org/10.1038/s41586-021-03308-6>

Published online 24 March 2021

In this Review, the Competing Interests section should read as follows:
‘R.L.N. is a member of the Forest Protection Advisory Panel at Cargill, and the Center on Food Security and the Environment (FSE) has received funding from the Cargill Foundation for visiting scholars and staff support, but not for research activities. She is also on the Scientific Advisory Board for Oceana and is the President of the Board of Directors for the Aspen Global Change Institute. She participates on the editorial board of *Aquaculture Environment Interactions*. D.H.K. is a member of the Technical Advisory Group for the Aquaculture Stewardship Council and a member of the Aquaculture Technical Advisory Committee of Monterey Bay Aquarium’s Seafood Watch Program. S.E.S. serves on the Advisory Committee on Aquaculture Science for DFO Canada (<http://www.dfo-mpo.gc.ca/aquaculture/advisory-comm-consultatif-eng.html>). She is currently working on two white papers for the United Nations Food and Agricultural Organization, and has previously chaired the Aquaculture Stewardship Council’s Technical Advisory Committee and the Monterey Bay Seafood Watch Advisory Committee. She also serves as Editor-in-Chief for the *Journal of Shellfish Research*, and Editor-in-Chief for *Reviews in Fisheries Science & Aquaculture*. A.H.B. is on the Standards Oversight Committee of the Global Aquaculture Alliance. He has no affiliation with any for-profit company; all of his research is supported by the Chilean National Science Agency (ANID) and therefore has no conflict of interest with any aquaculture activity. S.R.B. is a member of the Standards Oversight Committee of the Global Aquaculture Alliance, the Multi-Stakeholder Group of Monterey Bay Aquarium’s Seafood Watch programme, the Technical Advisory Committee of the Good Fish Foundation in the Netherlands, and the Technical Advisory Committee of

the Aquaculture Program of the Sustainable Trade Initiative (IDH). He has received funding from the Monterey Bay Aquarium's Seafood Watch programme for the development of Aquaculture Governance Indicators. R.W.H. is Editor-in-Chief of *Aquaculture Research*. In the past five years, he served as Chair of a Global Aquaculture Alliance committee that revised and updated best practices standards for fish feeds, a project that was completed in 2019, prior to his participation on this Review. In the past, also prior to this Review, he has been a principal investigator for grants and contracts awarded to the University of Idaho and received grants and contracts from industry or industry groups including the United Soybean Board, Enz-A-Bac, Midwest Ag Enterprises, Ajinomoto NA and Knipbio to assess feed ingredients for sustainable aquaculture. L.C. is a judge of the global F3 (fish-free feed) challenge. She was on the Scientific Advisory Board for the Aquaculture Stewardship Council between 2017 and 2019. She has no affiliations with for-profit companies. D.C.L. has received in-kind and financial support from a wide range of commercial and non-commercial entities, serves as a committee member for standards organizations and is a director of a commercial tilapia hatchery in Thailand. J.L. until recently served on the boards of The David and Lucile Packard Foundation, Oceano Azul Foundation, Prince Albert II of Monaco Foundation, the National Geographic Society, and Seafood Businesses for Ocean Stewardship (SeaBOS). She also co-chaired the Expert Group for the High Level Panel for a Sustainable Ocean Economy. She resigned from all of these roles in February 2021 when she took up her new position in the White House. M.T. is a member of the Program committee for The Marine and Coastal Science for Management (WIOMSA/MASMA), member of Action Areas and Solution Clusters Working Groups – Blue foods, United Nations Forum on Sustainability Standards (UNFSS), scientific lead for SeaBOS, and a Review Editor for *Aquaculture Environment Interactions*.⁷ The Review has been corrected online.

Author information

Affiliations

1. Department of Earth System Science, Stanford University, Stanford, CA, USA

Rosamond L. Naylor

2. Center on Food Security and the Environment, Stanford University, Stanford, CA, USA

Rosamond L. Naylor

3. Aquaculture Research Institute, University of Idaho, Moscow, ID, USA

Ronald W. Hardy

4. Centro i-mar & CeBiB, Universidad de Los Lagos, Puerto Montt, Chile

Alejandro H. Buschmann

5. Environmental Policy Group, Wageningen University, Wageningen, The Netherlands

Simon R. Bush

6. School of Oceanography, Shanghai Jiao Tong University, Shanghai, China

Ling Cao

7. Center for Oceans, Conservation International, Arlington, VA, USA

Dane H. Klinger

8. Department of Nutrition, Harvard T. H. Chan School of Public Health, Boston, MA, USA

Dane H. Klinger

9. Institute of Aquaculture, University of Stirling, Stirling, UK

David C. Little

10. Department of Integrative Biology, Oregon State University, Corvallis, OR, USA

Jane Lubchenco

11. Department of Marine Sciences, University of Connecticut, Groton, CT, USA

Sandra E. Shumway

12. Beijer Institute, Royal Swedish Academy of Sciences, Stockholm, Sweden

Max Troell

13. Stockholm Resilience Centre, Stockholm University, Stockholm, Sweden

Max Troell

Authors

1. Rosamond L. Naylor

[View author publications](#)

You can also search for this author in [PubMed](#) [Google Scholar](#)

2. Ronald W. Hardy

[View author publications](#)

You can also search for this author in [PubMed](#) [Google Scholar](#)

3. Alejandro H. Buschmann

[View author publications](#)

You can also search for this author in [PubMed](#) [Google Scholar](#)

4. Simon R. Bush

[View author publications](#)

You can also search for this author in [PubMed](#) [Google Scholar](#)

5. Ling Cao

[View author publications](#)

You can also search for this author in [PubMed](#) [Google Scholar](#)

6. Dane H. Klinger

[View author publications](#)

You can also search for this author in [PubMed](#) [Google Scholar](#)

7. David C. Little

[View author publications](#)

You can also search for this author in [PubMed](#) [Google Scholar](#)

8. Jane Lubchenco

[View author publications](#)

You can also search for this author in [PubMed](#) [Google Scholar](#)

9. Sandra E. Shumway

[View author publications](#)

You can also search for this author in [PubMed](#) [Google Scholar](#)

10. Max Troell

[View author publications](#)

You can also search for this author in [PubMed](#) [Google Scholar](#)

Corresponding author

Correspondence to [Rosamond L. Naylor](#).

Rights and permissions

[Reprints and Permissions](#)

About this article



Check for
updates

Cite this article

Naylor, R.L., Hardy, R.W., Buschmann, A.H. *et al.* Publisher Correction: A 20-year retrospective review of global aquaculture. *Nature* **595**, E36 (2021). <https://doi.org/10.1038/s41586-021-03736-4>

[Download citation](#)

- Published: 06 July 2021
- Issue Date: 22 July 2021
- DOI: <https://doi.org/10.1038/s41586-021-03736-4>

Comments

By submitting a comment you agree to abide by our [Terms](#) and [Community Guidelines](#). If you find something abusive or that does not comply with our terms or guidelines please flag it as inappropriate.

[Download PDF](#)

Advertisement

This article was downloaded by **calibre** from <https://www.nature.com/articles/s41586-021-03736-4>

| [Section menu](#) | [Main menu](#) |

Focal Point